Flow Field Formation and Compositional Variations of Flood Basalt Eruptions

Thesis

Flow Field Formation and Compositional Variations of Flood Basalt Eruptions

A thesis submitted for the degree of

Doctor of Philosophy

September 2009

Charlotte Vye

BSc (Hons), Keele University, 2000

Volcano Dynamics Group,
Department of Earth and Environmental Sciences,
The Open University, Walton Hall, Milton Keynes, MK7 6AA. UK

CONTAINS

PULLOUTS

Flow Field Formation and Compositional Variations of Flood Basalt Eruptions

A thesis submitted for the degree of

Doctor of Philosophy

September 2009

Charlotte Vye

BSc (Hons), Keele University, 2000

Volcano Dynamics Group,
Department of Earth and Environmental Sciences,
The Open University, Walton Hall, Milton Keynes, MK7 6AA. UK

DATE of SUBMISSION: 11 SEPT 2009

DATE of AWARD: 11 FEB 2010

Abstract

Characterisation of three lava flow fields from the Columbia River Basalt Group (CRBG), USA, reveals compositional heterogeneity on all scales, from adjacent lava lobes to the intra-crystal scale. Simple flow fields can be traced from vent areas to distal reaches, but those with multiple-layered lobes present a degree of complexity that make lava pathways and eruption sequences difficult to identify. A 3-D model based on field investigation of a single flow field establishes a volcanological context for geochemical sampling. Compositional variation within each flow field suggests that small-scale geochemical heterogeneity is common within and between lobes of these flood basalt lavas. Lobe cores emplaced during the latter stages of an eruption have less evolved compositions and more enriched incompatible elements, suggesting progressive variation of magma composition caused by either recharge or sequential tapping of compositionally zoned magma.

Progressive crustal contamination of magma during a single eruption is indicated by Re-Os isotope ratios. Initial $^{187}Os/^{188}Os$ ratios range from 1.405 in the earlier emplaced lava crust to 0.128 in the latter emplaced lava core. These values are more radiogenic than any known enriched sources (normative mantle ~0.127, HIMU ~0.15) consistent with previous data that indicate that neither an enriched source nor sub-continental lithospheric mantle can be the source of CRBG magma. Os isotope signatures can be explained by different degrees of contamination of two isotopically distinct lithologies represented by the North American craton and Jurassic accreted terranes underlying the province.

Intra-crystal Sr isotope analyses within a flow field record variable histories in an open magmatic system. Results suggest crystal residences in an increasingly contaminated melt within the crust with several recharge events of less-contaminated more primitive basaltic melt. Assembly of melt and crystal cargo occurred immediately prior to eruption without significant residence times in the final host magma. The combined compositional evidence suggests that an extensive shallow-crustal network of dykes and sills supplied magma to the CRBG eruptions.

Acknowledgements

I would like to take this opportunity to thank my supervisors, Steve Self, Tiff Barry and Kevin Burton, for their support, company in the field, encouragement, advice and the opportunity to undertake this research project. I am indebted to my supervisors. Thanks also to the British Geological Survey for allowing my leave of absence for this PhD.

Mouhcine Gannoun and Bruce Charlier are thanked for their involvement and support of the project. For making laboratory space and resources available, teaching good clean suite practices and triton analyses and being always on-call for supervision of the osmium isotope and intra-crystal strontium isotope analyses. John Watson, Michelle Higgins, Kay Green, Sam Hammond and Nick Rogers made themselves and their labs available to me and are sincerely thanked for their help in sample preparation, XRF and ICP-MS analyses. Anne Jay and Sam Vye were outstanding field assistants and company.

The staff and students of the Volcano Dynamics Group at the OU all made my time at the OU thoroughly enjoyable. The company, afternoon tea, banter and memorable dinners at the Blue Orchid will be greatly missed.

Lastly, I would like to thank all my family and friends for their unending long suffering support, words of encouragement, kindness and accommodation of my shortage of free-time. To Rich, Sarah, Sue and my No.10 housemates - thank you for your love, friendship and motivational words. My dear family - Mum, Peter, Frances, Juliette, Samuel, Rich, and Tim - thank you for always being there to support and share my endeavours from the beginning to the very end.

Contents

Chapter 5 – Intra-crystal Sr isotopic variations

List of Figures

Chapter 1

Chapter 2

Chapter 3

Chapter 4

Chapter 5

List of Tables

Chapter 2

Chapter 3

Chapter 4

Chapter 5

View up the Snake River toward Lyons Ferry

Chapter 1. Introduction

1.1. Introduction

Flood basalt provinces contain the longest and most voluminous lava flows known on earth (Cashman *et al.* 1998). Early models of the emplacement of these lava flows hypothesised huge, literal floods, of lava smothering the landscape (Shaw and Swanson 1970; Walker 1971). Supply of lava at these scales invoked high eruption rates requiring a large volume reservoir of magma in the shallow crust. Such a model required that magma was erupted rapidly with a high magmatic head pressure along the full length of a fissure system. Voluminous eruptions on the scale of flood basalts are likely to have a severe impact on the environment, caused principally by loading the atmosphere with volcanic gases and fine ash (Thordarson *et al.* 2001; Self *et al.* 2005). However, high eruption rates and rapid emplacement may increase this impact or alter the conditions over which environmental impact are assessed.

The mechanisms that enable large volumes of lava to flow up to 500 km away from the eruption site has been debated, modelled numerically and compared with modern analogues (e.g. Hon *et al.* 1994; Keszthelyi and Self 1998; Self *et al.* 1998). Comparisons with modern volcanism have revealed similarities in the structure and characteristics of large and small lava flows (Hon *et al.* 1994; Self *et al.* 1996). An insulating mode of transport preserves molten lava without crystallisation prior to attaining the observed flow lengths (lava inflation). Insulated emplacement allows long lavas to develop from low effusion rates that are similar to observed eruption rates on Hawaii and Iceland (Ho and Cashman 1997; Keszthelyi and Self 1998). Understanding the emplacement of long lava flows is of importance because there is a need to estimate magma discharge rates and

eruption durations to set in context atmospheric studies and the links between flood basalts and mass extinction events (e.g. Wignall *et al.* 2009).

Various techniques have been applied to quantitatively assess the emplacement of lava flow emplacement. Numerical models (Keszthelyi and Self 1998), anisotropy of magnetic susceptibility (AMS) (Canon-Tapia and Coe 2002) and within-lava geochemical variations (e.g. Reidel 2005) have all revealed variations that may reflect the spatial development of a lava flow. Of these, compositional variations within the products of a single eruption have the greatest potential to provide insights into both emplacement and processes affecting a single batch of magma.

Compositional heterogeneity within individual lava flows has been observed from both historically active volcanic centres (Watkins *et al.* 1970; Lindstrom and Haskin 1981; Maclennan *et al.* 2003) and flood basalt provinces (Jensen 1980; Martin 1991; Reidel 2005). However, the presence and cause of such heterogeneity within the products of a single eruption has not been investigated using the physical structure of a lava flow to identify eruption sequence. Indeed, many lavas are still presumed to have homogeneous compositions or variation either within analytical error or less than the variation between successively erupted lavas (e.g. Hooper 2000).

The nature of compositional heterogeneity requires characterisation to identify the potential for problems in the application of chemostratigraphy to the subdivision of flood basalt provinces. Intra-lava compositional heterogeneity can be investigated at different scales: laterally across the lava field as a function of distance from the eruptive centre, vertically within the lobe of a single lava at the scale of whole-rock samples, within whole single crystal analyses and intra-crystal analyses. A thorough characterisation of intra-lava

compositional heterogeneity can reveal processes of magma genesis for large volumes of melt residing in the crust prior to eruption to form these extensive volcanic provinces.

1.2 Project aims

This thesis examines the degree of intra-lava compositional heterogeneity and characterises differential variation within single flood basalt eruptive units. Compositional heterogeneity is compared to the widely accepted lava inflation model for the emplacement of flood basalts (Hon *et al.* 1994; Self *et al.* 1997). This model is applied to individual flows to examine the cause of compositional heterogeneity by setting the variation in a temporal-spatial framework. This temporal framework is then used to investigate the source and components involved in petrogenesis of a large melt body associated with continental flood basalt volcanism.

1.3 The Columbia River Basalt Group

The Columbia River Basalt Group (CRBG) represents one of the most intensively studied flood basalt provinces. Much of the existing research on the CRBG was conducted during the 1980's, funded by the U.S. Department of Energy and summarily published in a Geological Society of America Special Paper (Reidel and Hooper 1989). As a result, abundant geochemical, palaeomagnetic and field mapping databases exist in addition to drill cores through the unexposed, thickest parts of the stratigraphy in the Pasco Basin.

1.3.1. Location and extent

The CRBG is the youngest continental flood basalt province and covers large parts of Washington, Oregon and Idaho in western USA (Fig. 1.1). Recent work on the province

has linked the main CRBG in Washington State to flood basalts from Steens Mountains and the Malheur River Gorge in Oregon. Based on this work, the province is calculated to be 234,000 km^3 (Camp *et al.* 2003) and is currently believed to have formed between 17.5 to 6.0 Ma, with approximately 90 % of its volume erupted in a period of roughly 1.3 My, around 16 Ma. Although the area of the CRBG is smaller than many other igneous provinces, the CRBG is possibly the most well-characterised. It is also one of the best preserved provinces and has experienced limited weathering in a semi-arid environment. This, in combination with good access, extensive canyon-side exposures for a three-dimensional perspective and a well-established stratigraphy, makes this province an ideal location for this project.

Whilst current attempts to quantify eruption duration and frequency have yet to provide an exact figure, qualitative approaches in the Columbia River Basalts estimate eruption durations of months to decades with intervals of hundreds to thousands of years between eruptions (Self *et al.* 1997; Keszthelyi and Self 1998). These eruption rates are significantly lower than those previously envisioned for a model of flooding basalt (Shaw and Swanson 1970). Through such an approach, timescales may be applied to petrogenetic processes accounting for observed geochemical heterogeneity between eruptions. This thesis represents the first such attempt to constrain magmatic processes on such a short time span within a CFB province.

The majority of CRBG flow fields are reported to exceed 1,000 km^3 and have travelled hundreds of kilometres from their vents (Reidel and Fecht 1987). It is claimed that the CRBG has the largest known terrestrial basalts (Reidel *et al.* 1989; Tolan *et al.* 1989; Reidel and Tolan 1992; Reidel 1998) though this may be due to more poorly constrained

individual eruption units elsewhere. Single lavas are commonly assumed to be compositionally homogeneous, enabling correlation with feeder dykes.

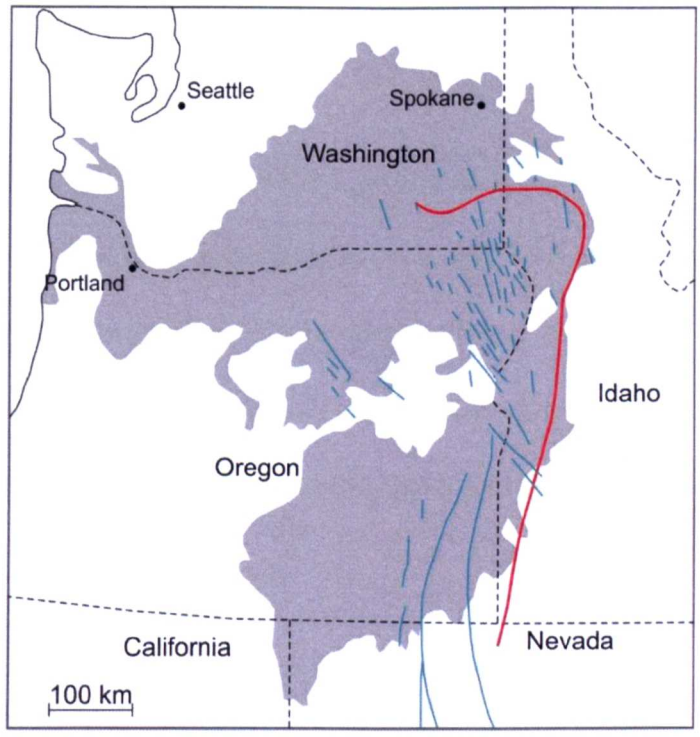

Figure 1.1 Map of the extent of the Columbia River flood basalt province after Tolan *et al.* 1989 and Wolff *et al.* 2008 showing the position of the suture boundary (red) and principal feeder dykes (blue).

Where the products of single eruptions can be identified, they have been shown to be voluminous, up to 2,600 km^3, and of tholeiitic basalt to basaltic andesite composition. Primitive lavas and silicic lavas, present in other flood basalt provinces, are absent from the CRBG. Flow fields advanced down a gentle 2-3 degree slope to the west and northwest up to 600 km away from the fissure vents (Hooper 1997).

Dyke swarms, mostly orientated NW-SE, occur in the SE quadrant of the province. Most dykes erupted through accreted Mesozoic oceanic crust to the south and west of a terrane boundary with Precambrian cratonic lithosphere (Fig. 1.1). However, the location of the island-arc / continent suture zone underlying the province is poorly constrained and is

hampered by the accumulation of up to 3,000 m of basalt obscuring the surface expression (Mohl and Thiessen 1995).

1.3.2. Stratigraphy

The size and accessibility of the CRBG has promoted research, resulting in thousands of representative geochemical analyses that have been used to map the province (Hooper and Hawkesworth 1993; Hooper 2000). The geochemical data, along with extensive field and petrologic studies, have enabled a detailed chemostratigraphic subdivision of the Columbia River basalt province with five principal stratigraphic units (Swanson *et al.* 1979; Tolan *et al.* 1989).

Much detailed research into chemostratigraphy and the emplacement of flood basalt lavas has focused on the CRBG, leading to the development of an established stratigraphy (Tolan *et al.* 1989). This framework allows for further small-scale studies. The current stratigraphy of the CRBG was originally compiled by Waters (1961) and Swanson *et al.* (1979), and was subsequently modified by Tolan *et al.* (1989) and Langdon and Long (1989) (Fig. 1.2). The CRBG, as described by Tolan *et al.* (1989), excluding the Oregon basalts, can be categorised into five parts:

1. The lowermost part of the sequence marks the onset of volcanism within the province. The Imnaha Basalt erupted in the south-eastern corner of the Columbia Plateau and buried irregular topography (Hooper 1982). The Imnaha Basalt is the most primitive of the CRBG formations and is considered to most closely represent the composition of underlying plume mantle (Hooper 2000).

2. The most voluminous eruptive phase in the CRBG is the Grande Ronde Basalt. The basalts from this formation are typically aphyric, have high SiO_2 and are enriched in large-ion lithophile incompatible elements relative to the underlying Imnaha Formation. The eruption of lavas in this formation spans four magnetostratigraphic intervals (Swanson *et al.* 1979). The formation is exposed in the south-eastern portion of Washington State, but is covered by younger basalts over the rest of the province.

3. The overlying Eckler Mountain Formation is less significant and consists of small volume lava flows of relatively limited extent (Tolan *et al.* 1989).

4. The Wanapum Basalt marks the waning of the main eruptive phase and follows a significant hiatus after the Grande Ronde Basalts. Some of the lavas in this part of the sequence are plagioclase phyric and are superbly exposed over most of the province.

5. The upper part of the stratigraphy, the Saddle Mountains Basalt, is predominantly composed of smaller volume lava flows (e.g. Pomona), many of which were topographically constrained by a combination of factors, including the uplift of the Cascade Mountains and topography developed by the underlying flow fields.

1.3.3 Petrogenesis of CRBG magmas

The Miocene-age CRBG is interpreted by some to be the product of the Yellowstone plume (Brandon and Goles 1988; Geist and Richards 1993; Takahahshi *et al.* 1998; Hooper *et al.* 2005), whilst others prefer backarc extension (Hart and Carlson, 1987), delamination or back-arc sub-continental lithospheric mantle (SCLM) melting (McDougall 1976;

Carlson 1984; Smith 1992; Camp and Ross 2004; Hales *et al.* 2005), or delamination triggered by a plume (Camp and Hanan 2008). The cause of the outpouring of these vast lavas in south-east Washington, western Idaho and north-east Oregon remains a contentious issue.

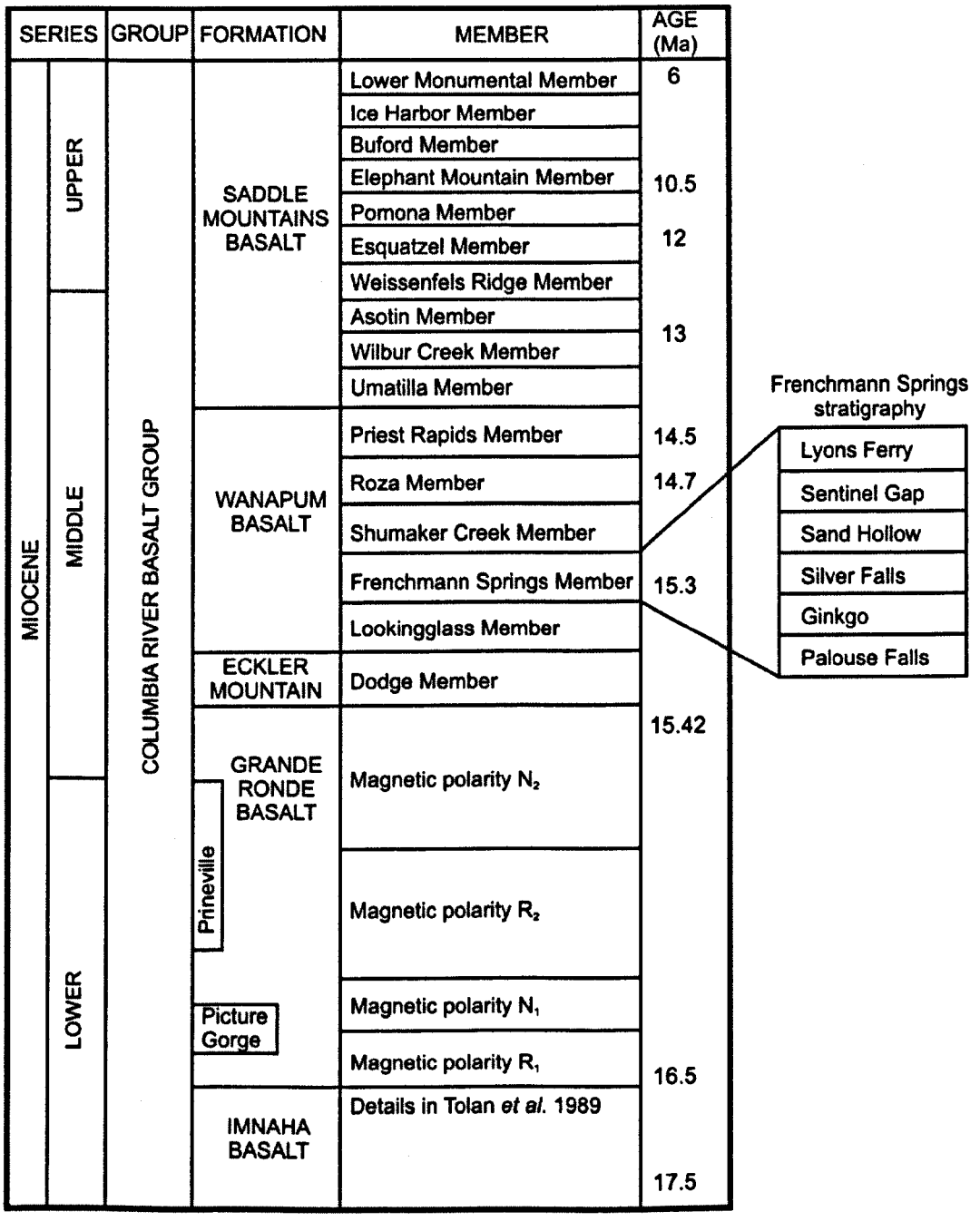

Figure 1.2 Stratigraphic sequence of basalts comprising the Columbia River flood basalt province (from Tolan *et al.* 1989 and Langdon and Long 1989) with age dating (from T. Barry unpublished data and Tolan *et al.* 1989) and stratigraphic subdivision of the Frenchman Springs Member (from Beeson *et al.* 1985).

Although existing research reveals contradictory conclusions regarding the origin, source and evolution of magma, there is a distinct pattern in the geochemistry of the stratigraphic units of the CRBG. The initiation of volcanism is recorded by the primitive Imnaha formation, that suggests relatively uncontaminated mantle plume composition (Dodson *et al.* 1997). Subsequent formations become sequentially more evolved. The thickest stratigraphic unit, the Grande Ronde Basalts, was erupted in quick succession with the geochemically similar Wanapum Basalts. Together they represent the most voluminous part of the province. The last erupted Saddle Mountains Basalt is suggested to involve significant crustal contamination (Carlson *et al.* 1981; Carlson 1984).

The available data have provided an interpretation of the genesis and source of the entire province. Additionally, since temporal and spatial intra-lava flow geochemical heterogeneity has been observed within single eruptive units (Reidel and Fecht 1987; Reidel 2005), compositional variation may be used to further investigate the character of the source. However, while small-scale heterogeneity questions the validity of using chemostratigraphic divisions across flood basalt provinces, it may prove important for understanding magmatic processes within the length-scale of single flood basalt eruptive events.

1.4. Thesis structure

This thesis investigates the presence and origin of intra-lava compositional heterogeneity within continental flood basalts. Chapter 2 presents field data on three flow fields for which the geochemical analyses are presented in subsequent chapters. The physical volcanological model of lava emplacement is outlined. The lava inflation model was applied during fieldwork and used to identify and trace three flow fields independent of

any chemostratrigraphic method. The latter part of this chapter evaluates the suitability of this model, accepted in other flood basalt provinces, to the Columbia River flood basalts and draws together all the field data to develop a 3-D understanding of individual flow field morphology.

The temporal and spatial implications of the development of a flow field are used in Chapter 3 to provide a framework against which to investigate compositional variability. The major and trace element composition of the Palouse Falls flow field, a simple small scale flood basalt flow field, is used to probe the nature of heterogeneity. Small-scale intra-lobe variations with height, sample-scale variations and large-scale variations between lobes and across the whole flow field are characterised. The origin of this variation is investigated and implications for models of flow field emplacement are evaluated within simple flow fields. Models of emplacement are then extrapolated to compound, larger-scale and more complex flow fields.

The role of pre-eruptive conditions in generating compositional heterogeneity is investigated using Re-Os isotope data for whole rock samples from one flow field in Chapter 4. This provides insights into the origin of the small-scale major and trace element heterogeneity. Mass balance calculations are used to extrapolate the relative contributions of the crust to a primitive melt composition. The results are used to discuss contamination and variation in the composition of a melt forming a single eruption to propose a model of pre-eruptive conditions.

Compositional variations within large single plagioclase crystals from one flow field are investigated using intra-crystal Sr isotope and electron microprobe data in Chapter 5. The origin of these plagioclase crystals is discussed in light of their petrologic characteristics,

whole rock Sr isotope composition and groundmass plagioclase compositions. The results provide a detailed view of the petrogenetic model proposed in Chapter 4 and support the existence of a complex plumbing system that is tapped for the duration of a flood basalt eruption.

A summary of the conclusions reached within each one of these chapters and areas for future research are presented in the concluding chapter.

Sand Hollow and Palouse Falls lobes overlying Grande Ronde lobes exposed at Palouse Falls state park

Chapter 2. Physical characteristics and flow field architecture

2.1 Introduction

Study of the physical volcanology of individual flood basalt flow fields provides an insight into the broad-scale emplacement mechanisms that influence the character and architecture of a flood basalt province. Understanding these mechanisms and the rates of emplacement are of significance due to their intrinsic link with factors such as lava supply, eruption style, and duration of eruptive episodes, e.g. controls on the amount and intensity of fire fountaining (Wilson and Head 1981; Bruce and Huppert 1989; Heliker *et al.* 2003). Furthermore, the nature of flood basalt eruptive events has implications for the release of volatiles and the potential environmental and climatic effects (e.g. Grattan 2005).

This chapter utilises current terminology, features and concepts of flood basalt lavas and their emplacement, which will be described in the following sections. I present a detailed study of three lava flow fields from the CRBG, and on the basis of the lava inflation model (Hon *et al.* 1994) investigate mechanisms of lobe and flow field formation. The three studied flow fields, Palouse Falls, Ginkgo and Sand Hollow, have each been previously defined as lava units of the Frenchman Springs Member of the Wanapum Formation (Beeson *et al.* 1985; Tolan *et al.* 1989).

Using my detailed investigation, I outline flow field architecture using 3-D models. Models representing the characteristics of a flow field provide insight into the emplacement style of individual flood basalt eruptions. A generalised model is sought to characterise the mechanism facilitating the advance of lava across a plain, in particular the forward propagation and radial spread of a flow field. Evidence provided by the physical

volcanology of each of the three flow fields shows that emplacement by inflation was the predominant mechanism in producing thick lobes. The inflation mechanism also enables existing lobes to transmit lava to form new lobes, thus extending the spread of the flow fields.

2.2 Emplacement by inflation and terminology used in this work

2.2.1 The inflation mechanism

The most widely applied, current explanation for pāhoehoe lava emplacement is the inflation (or lava rise) model. Originally described as a mechanism for the injection of liquid lava under pāhoehoe crusts that generates features such as tumuli and lava rises (Walker 1991), the idea was developed following a series of observations from active pāhoehoe lava flows at Kilauea, Hawaii (Hon *et al.* 1994). Each lobe of lava is initially emplaced as a thin body approximately 20-30 cm thick. A crust forms at the surface around each lobe and thickens as cooling accompanies progressive emplacement of fluid lava beneath the crust, with smaller lobes coalescing into larger lobes. The lava emplaced last constitutes the massive central zone of thicker larger units, known as the core (Self *et al.* 1997) (Fig. 2.1). The basal crust is always observed to be much thinner than the upper crustal zone (Hon *et al.* 1994; Self *et al.* 1998). The cooled, solidified brittle upper crustal zone is observed within Hawaiian flows to be more highly fractured than the core. Hon *et al.* (1994) suggest that the transition zone between the brittle crust and any internal liquid lava in an actively inflating lobe is a viscoelastic layer. This layer provides the tensile strength to retain lava behind the active flow front, ruptured only where breakouts occur, and maintains an evenly distributed hydrostatic pressure enabling uniform uplift of the solidifying crust.

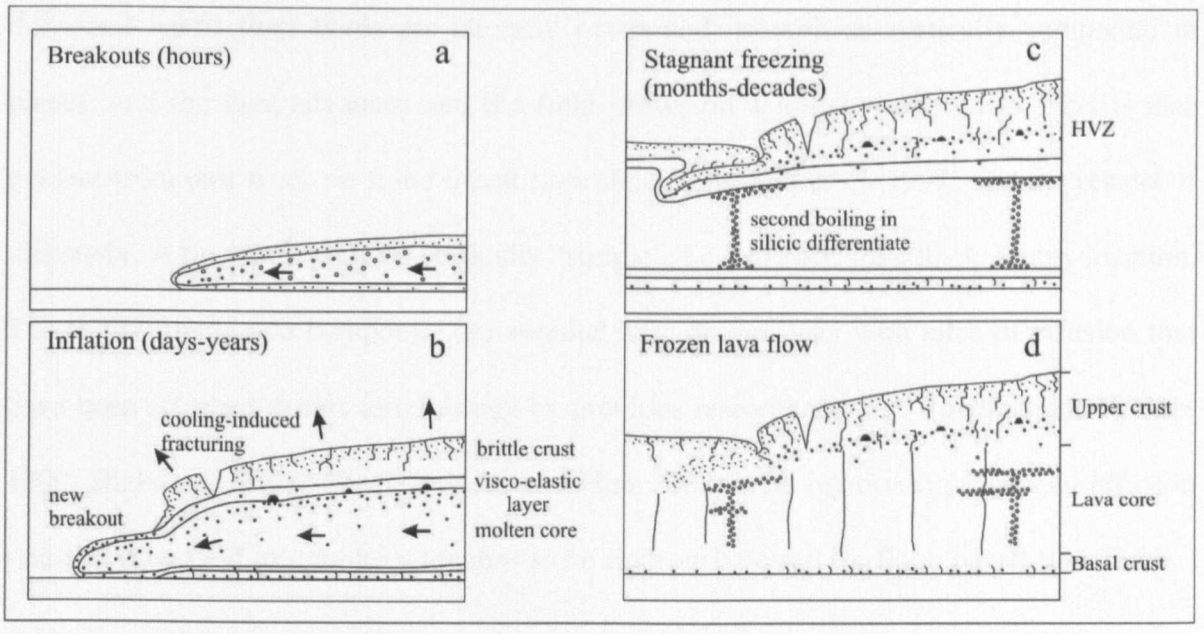

Figure 2.1 Cartoon demonstrating the progressive emplacement of a lava lobe through the inflation mechanism, after Self *et al.* (1997). a) a new lobe advances and a thin glassy chilled selvage develops, gradually thickening down into an upper crust, b) the lobe thickens by inflation as it extends, upper crustal zone thickens, bubbles from the moving lava are trapped in the crust as vesicles, breakout lobes occur from the lobe front c) de-pressurisation from the formation of a new breakout permits the formation of a horizontal vesicular zone as part of the upper crustal zone, d) flow stagnates, remaining vesicles rise to the base of the upper crust as segregation features, core begins to cool and solidify.

2.2.2 Previously applied terminology

Some of the first work on the morphology and volcanology of flood basalts was undertaken in the Deccan Volcanic Province (Walker 1971; Walker 1973). Walker developed a classification based on the concept of 'flow-units' (after Nichols 1936). Flow units are defined as a body of lava having a top that cooled significantly and solidified before another body of lava covered it. Walker (1971) identifies two basalt lava flow types: 'simple' flows consist of one flow unit, which he interpreted as the result of rapid rates of extrusion; and 'compound' flows are divisible into numerous, superimposed flow units that were thought to form due to low lava extrusion rates. However, Walker admits the limitations in the applicability of this terminology, stating that is it most appropriately applied on a localized or outcrop scale. Flow units in the terminology applied and described here could be considered the equivalent of sheet lobes, therefore compound flows are the amalgamation of numerous constituent lobes.

All flood basalt flow fields are laterally compound, as well as vertically compound in places, and the lava advances and the field grows on a lobe-by-lobe basis. This is also evident from past work on flood basalt flow fields (e.g. Self *et al.* 1997) and the results of this study. A flow field may be vertically "simple", i.e. only one lobe thick, in any location. The terms simple and compound are avoided here due to links with rates of effusion that have been attached to this terminology by previous researchers (e.g. Rowland and Walker 1990; Blake and Bruno 2000; Bondre and Hart 2008). The relationship between effusion rate and flow field morphology remains to be rigorously tested for flood basalt flow fields.

Other early examples of field studies within flood basalt provinces, especially within the CRBG, utilised the terms *colonnade* and *entablature* to provide a division of the complex internal structure of any lobe (e.g. Reidel *et al.* 1998). This nomenclature is based primarily on vertical changes in jointing style within a lobe, originally devised by Tomkeieff (1940) and further modified by Long and Wood (1986). The colonnade is defined as a tier of widely spaced joints with 40 to 200 cm spacing, which demark relatively planar-sided sub-vertical columns. The entablature zone is formed of closely spaced, 20 to 40 cm, planar to irregularly curved columns (Fig. 2.2). This division of jointing styles is a reflection of relative cooling rates within a flow and has been extensively applied in the CRBG. Key textural differences between the two divisions are also noted (further discussed in section 2.5.3). Distinct associations have been drawn between this nomenclature and cooling rates (Degraff *et al.* 1989; Kattenhorn and Schaefer 2008), linking water ingress through flooding of the lava surface by displaced drainage (Saemundsson 1970) to quench cool the entablature (Swanson 1967; Long and Wood 1986). This nomenclature is not adopted within this study due to associated assumptions on cooling rate and the complexities that arise in referral to multiple occurrences of both entablatures and colonnades within multi-tiered lava flows (Lyle 2000). In many of the

lobes observed in this study, however, the entablature zone approximates to what I call the upper crust or upper crustal zone.

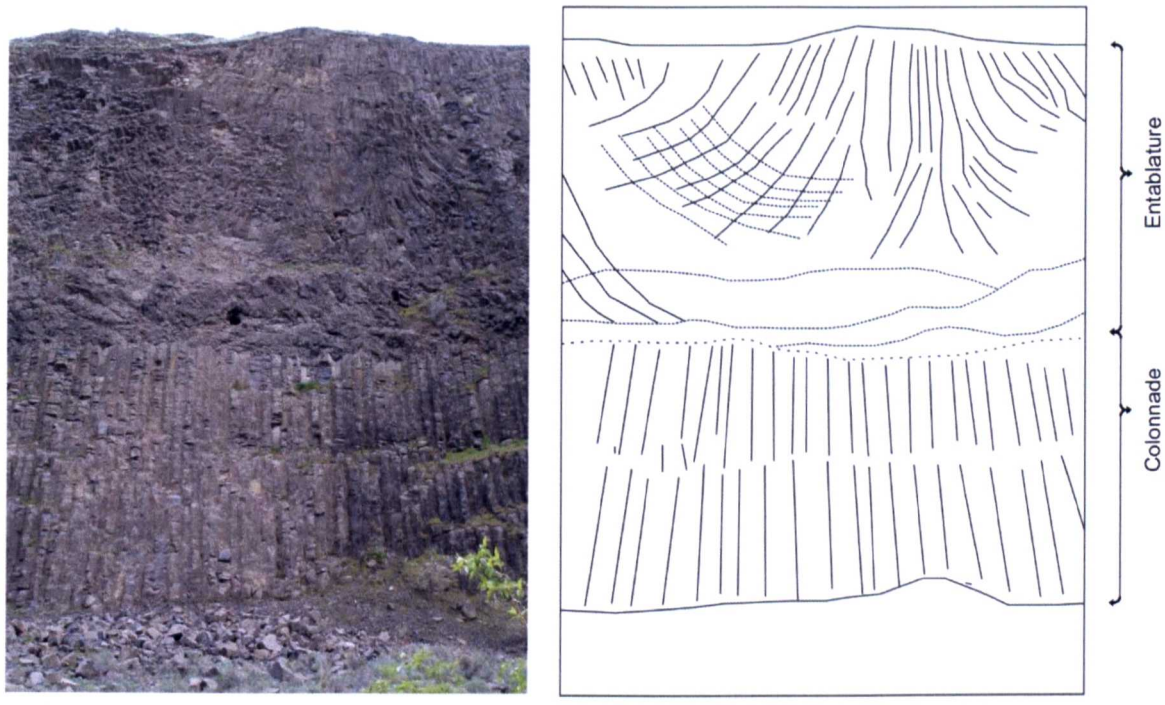

Figure 2.2 Example of the jointing style used to subdivide CRBG flows into the colonnade and entablature zones, within the Pomona flow field near Clarkston (N46°24.677' W117°11.215').

2.2.3 Currently used terminology

The nomenclature defined by Self *et al.* (1997 and 1998) of flow field, lava flow, flow lobe and upper crustal zone, core, basal crust are applied in this study. Observations and measurements on active lava flows provide a terminology for the description of pāhoehoe lava flows (Hon *et al.* 1994) that has been extrapolated and applied to the CRBG (Self *et al.* 1997) and North Queensland Cenozoic lavas (Stephenson *et al.* 1998). Since these initial descriptions, further volcanological accounts of inflated pāhoehoe morphologies have been recorded in the lavas of many flood basalt provinces including the Parana (Waichel *et al.* 2006), North Atlantic Igneous Province (Kent *et al.* 1998; Passey and Bell 2007), Etendeka (Jerram *et al.* 2000), Deccan Volcanic Province (Bondre *et al.* 2004) and Australia (Whitehead and Stephenson 1998) in addition to those in the CRBG (Ho and Cashman 1997; Self *et al.* 1997; Keszthelyi and Self 1998; Thordarson and Self 1998;

Guilbaud 2006). For simplicity, and to permit comparisons with existing characterisation of the physical volcanology of lavas from other flood basalt provinces, the terminology adopted here is from Self *et al.* (1997).

At the largest scale, a *flow field* (after Kilburn *et al.* 1988) is the product of a single eruption and may include one, or more lava flows. Flow fields can be identified in the field in ancient provinces where exposures are mainly vertical as lava units bounded by weathering horizons, soils, sedimentary beds or by evidence of erosion. The presence of any of these indicators infers that there was a long enough hiatus between eruptions to permit some (or all) of these features to develop.

A *lava flow* is the product of a single outpouring of lava composed of one or more lobes, separated from adjacent flows by weathering surfaces or sediments. New lava flows are usually generated due to a pause in an ongoing eruption, or a new vent opening during an eruption. New lava flows are often started during a new phase or episode in many long-lasting eruptions, e.g. Kilauea 1983 – present (Heliker *et al.* 2003). It may be possible for more than one lava flow to be simultaneously emplaced during the same eruption.

Sheet lobes are extensive lobes with smooth upper surfaces displaying little relief (Hon *et al.* 1994; Thordarson and Self 1998). Sheet lobes can be up to 200 m thick in some flood basalt provinces, and may be up to several kilometres across. The dominance of sheet lobes in flood basalt provinces is likely a result of the low slope angle ($<2^{o}$) upon which these lavas are emplaced (Hon *et al.* 1994). Low slope angles inhibit channelisation of flows and promote a uniform thickness of lava within lobes (Walker 1991). The use of this nomenclature does not imply a minimum flow thickness. The term *sheet flow* was previously used to describe extensive thin, lobate lava flows dominantly found in

submarine environments (Ballard *et al.* 1979) and its usage is avoided here to reduce confusion.

Lava lobes and *precursor lobes (or toes)* are the smallest discrete unit of lava. Lobes are single cooling units bounded by a chilled crust or glassy selvages.

The term *lava unit(s)* is used to describe individual packages of lava where the outcrop restricts recognition of which one of the above terms can be applied.

2.2.4 Structure of an inflated pāhoehoe sheet lobe

The broad structural division within an inflated pāhoehoe lobe is based on three zones: the upper crustal zone, lava core and basal (or lower) crust. The subdivision is based on variations in vesicle abundance, size and distribution as well as jointing style and petrographic textures. These zones and features are displayed on a section through a sheet lobe studied in this work (Fig. 2.3).

Thicknesses of upper crustal zones vary in the studied sheet lobes. The crust ranges from 13 to 55 % of the total lobe thickness, but most typically is 40 to 50 % of the total lobe thickness. The crust displays a high vesicularity which can be variable with horizontal bands of vesicle-rich and vesicle-poor basalt (Fig. 2.4). In general, vesicularity within a crust decreases downwards but vesicle size increases (Cashman and Kauahikaua 1997). Joints in the upper crust are highly variable, usually hackly and curvilinear, in contrast to the better-developed columns in the lava core. Variations in joint orientation are a reflection of the stress regime imposed on the crust during inflation (Keszthelyi *et al.* 1999). The outermost 5-10 cm of the upper crust has a hypohyaline glassy selvage (usually

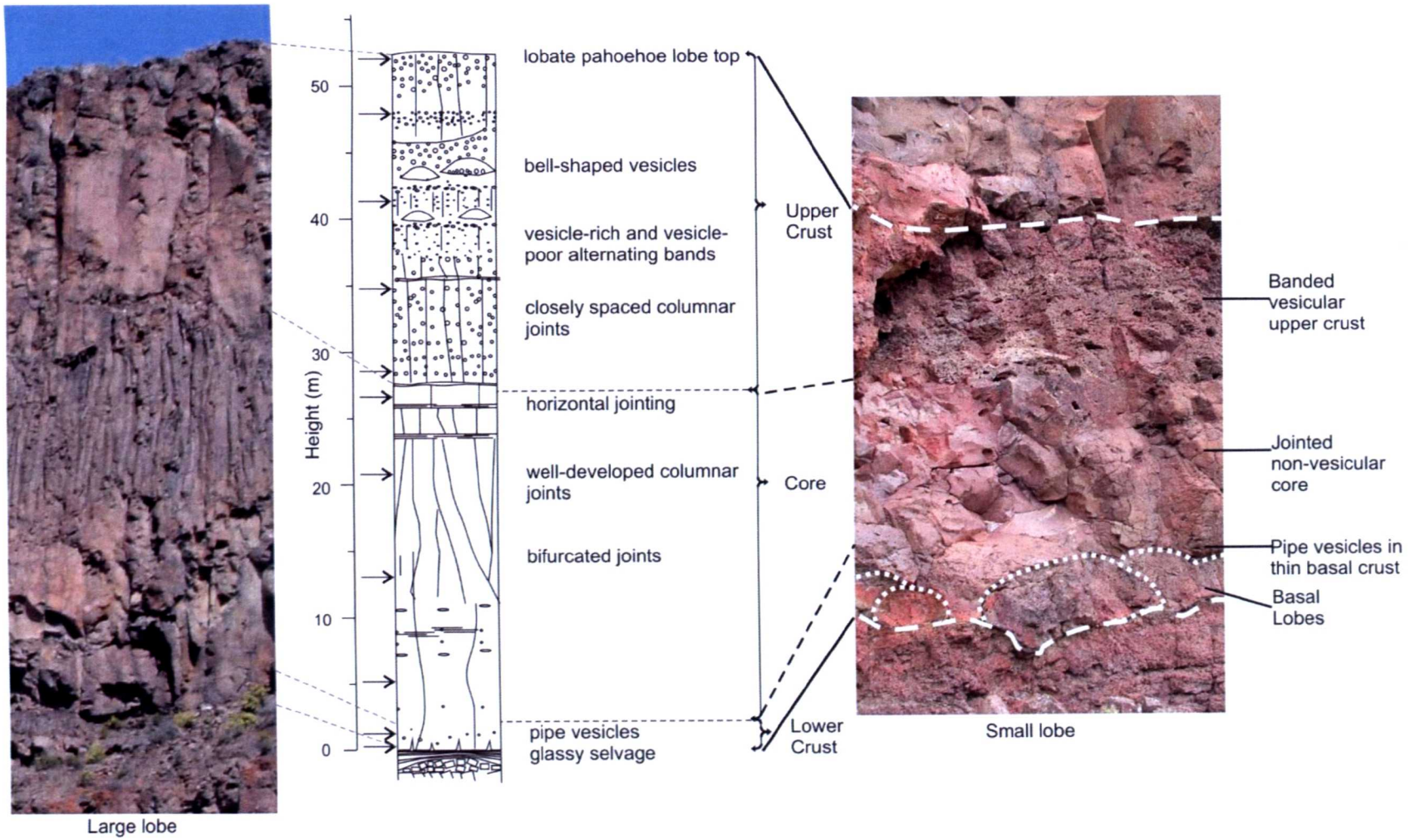

Figure 2.3 Example of a lithostratigraphic log of a lava lobe from the Grand Ronde Formation on the Snake River, Washington (N46°35.074' W118°29.814') demonstrating the typical range of features used to identify the three-tiered structure that relates to the inflation mechanism. On the right is a small lobe, 1.5 metres thick, showing a poorly developed core. On the left is a large lobe of typical flood basalt proportions, 32 metres thick, illustrating a well-developed core. At this scale the resolution at which features such as vesicle distribution can be illustrated is lost.

missing in ancient flood basalt provinces due to weathering and erosion between flow fields) and the rest is hypocrystalline.

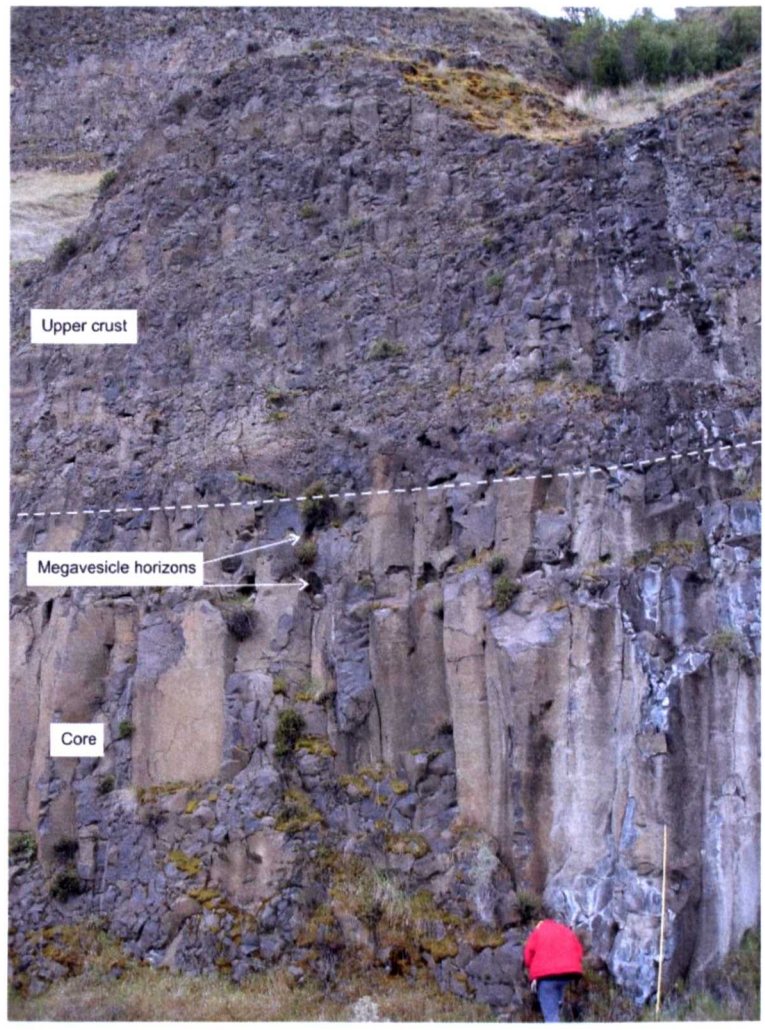

Figure 2.4 Changes in vesicular banding and megavesicle horizons marking the upper crust within a sheet lobe from the Grande Ronde Formation on the Starbuck Road cutting, Washington (N46°39.621' W118°10.892').

The lava core accounts for most of the remaining thickness of a lobe, generally ranging from 40 to 60 % of the total. The uppermost part of a core is defined as the transition from low vesicularity to high vesicularity, typical of the upper crust. The very uppermost part of a lava core often contains segregation features such as horizontal vesicle sheets (HVS, described in detail in section 2.5.2.3) and megavesicles. Joints are commonly well-developed, although poorly-developed in a few localities, forming distinct columns up to 2 metres wide. The texture is usually holocrystalline and more coarsely crystalline than the

upper crust. However, there are exceptions within the core (discussed in later sections) where finely jointed, glass-rich portions occur.

The basal zone or lower crust accounts for less than 10 % of the total lobe thickness. The boundary between this zone and the lava core is diffuse. Pipe vesicles are common at the base of many lobes and vesicularity is moderate. A quenched glassy selvage defines the outer margin of the lobe.

The three-tiered structure within single lobes enables an understanding to be gained of the physical link between constituent lobes of an eruption flow field. Lobe cores studied can be observed to provide a common lava flow pathway between lobes, which enabled flow field propagation beneath the insulating upper crust of separate lobes. The model thus relates chronologic development within a lobe to subsequent emplacement of adjacent lobes. This approach provides a temporal and spatial physical framework to examine the eruption sequence and the opportunity to relate that sequence to any changes in basalt composition.

Field observations have identified pāhoehoe sheet lobes throughout the CRBG succession (Reidel and Tolan 1992), occasionally exhibiting rubbly pāhoehoe surfaces (Keszthelyi *et al.* 2006). Subsequently, internal features have been interpreted as the product of inflation (Self *et al.* 1996; Self *et al.* 1997).

2.3 Flow fields in the Columbia River Basalt Group

All of the flow fields presented in this chapter (Palouse Falls, Sand Hollow and Ginkgo) are part of the Frenchman Springs Member of the Wanapum Formation. The subdivision

and characterisation of flow fields within this member are summarized by Beeson *et al.* (1985). Original identification of this part of the CRBG stratigraphy is based upon geochemical composition, predominantly Cr, P_2O_5, TiO_2 and MgO abundances, palaeomagnetic data, and stratigraphy. Previously, subdivision of the Frenchman Springs Member was made on the basis of plagioclase phenocryst abundance, which is a defining characteristic of this member relative to the mainly aphyric Grande Ronde Member (Bentley and Campbell 1983), along with texture and intraflow structures (Mackin 1961). The stratigraphy defined by Beeson *et al.* (1985) is used in this study. Emplacement of the Wanapum Formation followed the most voluminous phase of CRBG eruptions, the Grande Ronde, after which there was a substantial eruption hiatus represented over much of the province by a widespread but discontinuous saprolite and sediment horizon. This horizon provides a province-wide marker separating the Grande Ronde basalts from the lowermost Wanapum flow fields. In a restricted area, the lava flows of the Eckler Mountain Member (Tolan *et al.* 1989) occupy this horizon. They are petrographically distinct and easily recognized.

The Palouse Falls is a simple flow field and lies above a well-developed and extensive saprolite. Near-complete exposure is available through the long axis of the flow field. The Sand Hollow flow field is larger than the Palouse Falls flow field but has incomplete exposure between vent to medial localities and some distal localities, where it is only one sheet lobe thick. The Ginkgo is a complex flow field of similar volume to the Sand Hollow and is generally comprised at each locality by up to three lobes of varying sizes (and in a few places pillow lavas and small pāhoehoe lobes).

2.4 Field methods and procedures

The following section presents the justification for the selection of flow fields chosen for study and the field localities (Fig. 2.5). The method employed to correlate between sites and across the province for both medium-scale lobe-to-lobe mapping and large-scale flow field extent is outlined.

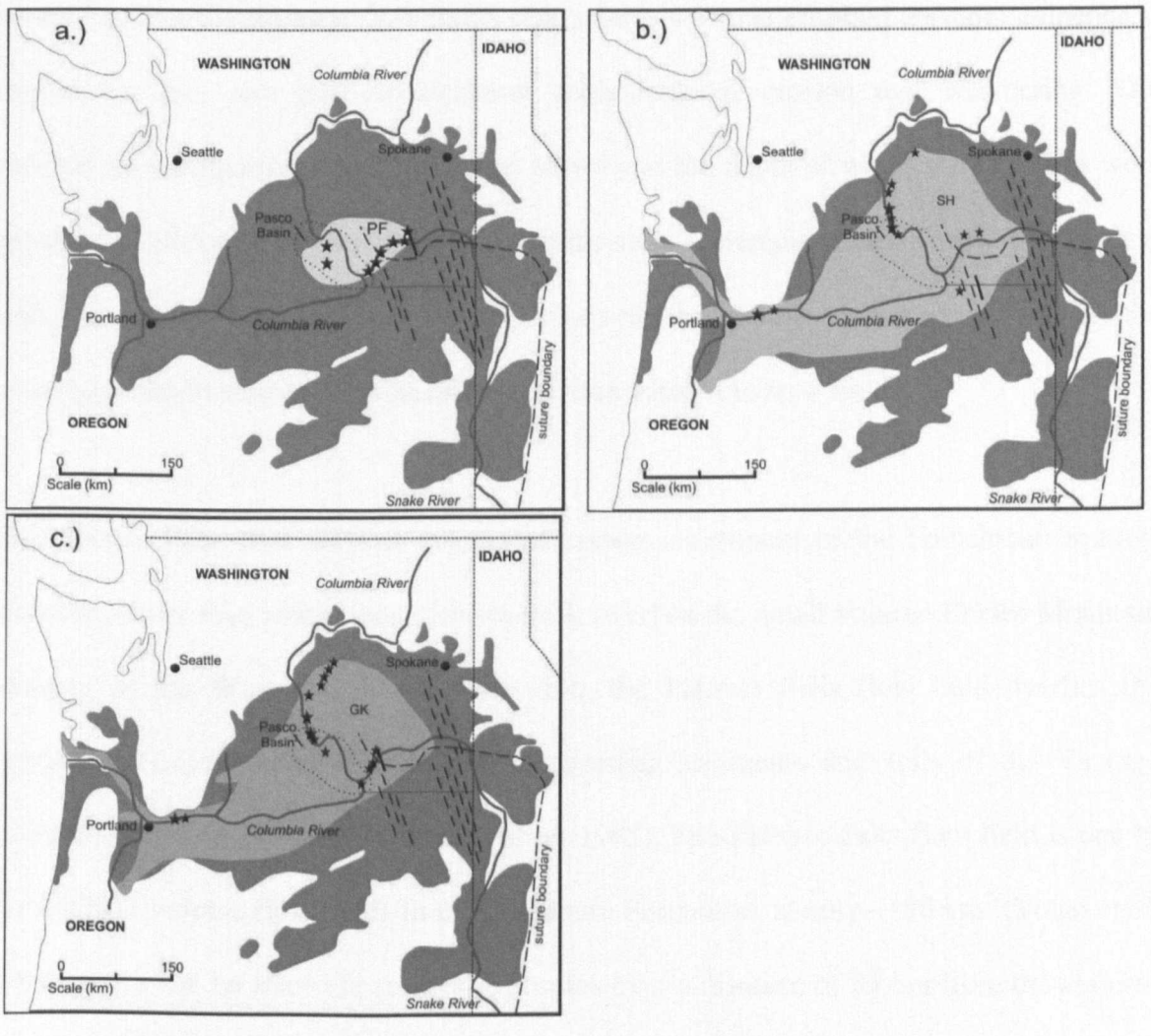

Figure 2.5 Mapped extent of each flow field within the province, compiled from existing mapped extents (Tolan *et al.* 1989) in combination with primary data acquisition from this study: a) Palouse Falls (PF), b) Sand Hollow (SH), c) Ginkgo (GK) flow fields. Dark grey areas show the full extent of the CRBG. Pale grey areas denote the extent of each flow field. Stars show localities reported within this thesis. Dashed lines represent areas of identified feeder dykes and fissure vents for the CRBG whilst solid lines show the location of feeder dykes for each of these flow fields.

2.4.1 Flow unit identification and correlation

The three flow fields were selected for detailed study because they can be clearly distinguished in the field from adjacent lavas in the Wanapum Formation (Beeson *et al.* 1985; Martin 1989) and the underlying Eckler Mountain and Grande Ronde Basalts. Also they are near to the top of the CRBG pile and are frequently exposed.

In order to identify discrete flow fields (the products of one eruptive episode) evidence is needed for pre- and post-emplacement sedimentation, erosion and weathering. The presence of sedimentary interbeds or ash layers and the depth of weathering profiles were utilised as lithostratigraphic markers. Additionally, internal features such as jointing, vesicular bands, and distinctive plagioclase-phyric characteristics of some of the constituent basalt were used to enable correlation across the flow field.

The Palouse Falls flow field is the oldest known component of the Frenchman Springs Member. Other than a few localities where it overlies the small volume Eckler Mountain Member of the Wanapum Basalt Formation, the Palouse Falls flow field overlies the uppermost Grande Ronde Basalts and intervening sediments and soils of the Vantage Interbed (Swanson *et al.* 1979; Beeson *et al.* 1985). The Palouse Falls flow field is one of the smallest-volume flow fields in the Wanapum Formation, at only ~190 km^3 (Tolan *et al.* 1989), and it can be traced in surface exposures over a distance of 55 km from the eastern-most exposure in the presumed vent area (S. Reidel *pers. comm.*) to the southwestern-most exposure near the edge of the Pasco Basin (Fig. 2.5a). Drill cores within the basin reveal the Palouse Falls lobes reach thicknesses up to twice that of lobes emplaced elsewhere in the flow field and expand the extent of the flow field to a minimum of 80 km from the vent area. The Palouse Falls basalt bears the same petrographic characteristics throughout; being sparsely phyric with small, tabular and equant plagioclase phenocrysts.

The Ginkgo flow field is clearly characterized by abundant plagioclase glomerocrysts and phenocrysts up to 3 cm in diameter. The collective volume of the 3-4 lava flows that constitute the flow field is ~1,570 km^3 (Tolan *et al.* 1989; Ho 1999). Ginkgo basalt overlies the Grande Ronde basalts in areas where the Palouse Falls and Eckler Mountain basalts are not found. In many locations the base of the Ginkgo consists of pillow basalts and hyaloclastites (Ho and Cashman 1997) and small (m-scale) pāhoehoe lobes and toes (personal observation, Soap Lake, Washington).

The Sand Hollow flow field is the most voluminous and laterally extensive of the Frenchman Springs eruptions, with an estimated volume of ~2,660 km^3 (Tolan *et al.* 1989) and one of the biggest described basalt lava units on Earth. The petrography of the basalt is variable within single lobes and between lobes, ranging from sparse to abundantly plagioclase phyric. The Sand Hollow flow field is up to 80 m thick, bounded above and below by ash and sediment deposits up to 60 cm thick. Individual lobe cores display variable joint patterns. A notable finely jointed glass-rich zone is persistent throughout the middle of the core. In places, the Sand Hollow basalt lies on the Silver Falls basalt, yet elsewhere it sits directly on the Ginkgo basalt. Therefore, identification of the Sand Hollow flow field is partly based on the mapped extent of the Silver Falls flow field (Tolan *et al.* 1989).

2.4.2 Field mapping

Field mapping of parts of each flow field was conducted on a metre to kilometre scale. Structures within individual lobes are recorded in logs for each locality (Figs. 2.6, 2.7 and 2.8). The structure and lateral extent of lobes are recognised through observations of lobe junctions (Fig. 2.9).

DISTAL
Pasco Basin

PROXIMAL

Palouse Falls Flow Field

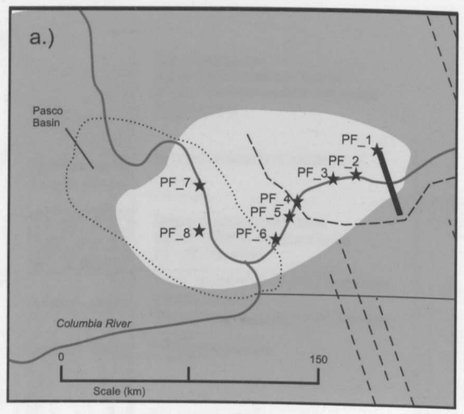

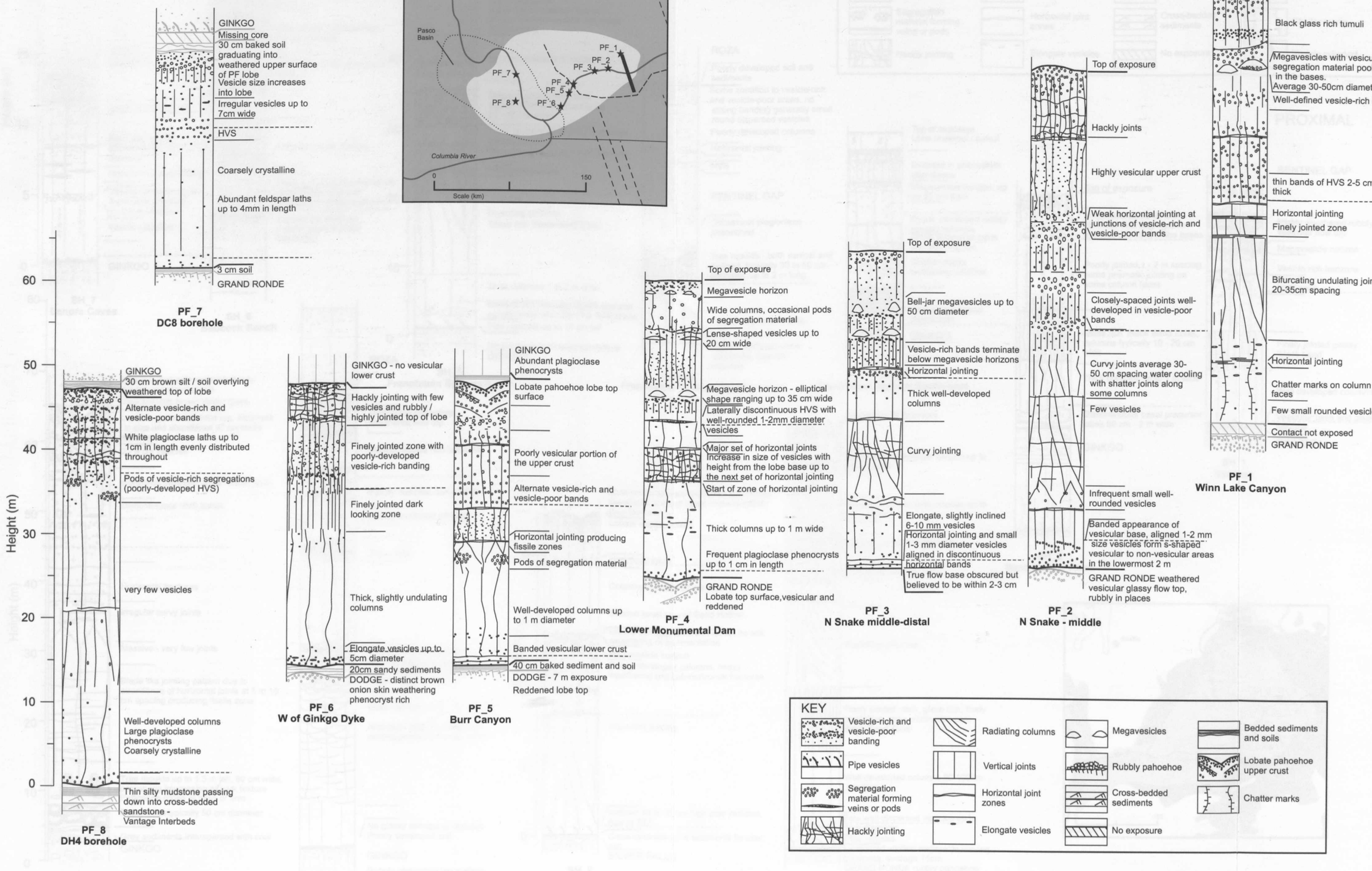

Figure 2.6. Logs constituting the Palouse Falls flow field

Sand Hollow Flow Field

DISTAL

PROXIMAL

KEY

- Vesicle-rich and vesicle-poor banding
- Pipe vesicles
- Segregation material forming veins or pods
- Hackly jointing
- Radiating columns
- Vertical joints
- Horizontal joint zones
- Elongate vesicles
- Megavesicles
- Rubbly pahoehoe
- Cross-bedded sediments
- No exposure
- Bedded sediments and soils
- Lobate pahoehoe upper crust
- Chatter marks
- Vesicle cylinders

Height (m)

SH_7 Lenore Caves

- ROZA
- Tulip joints
- Weak vertical joints
- Rare plagioclase glomerocrysts up to 2 cm diameter
- Horizontal vesicle sheets
- Vesicle rich layer up to 3 cm thick of small 1 - 2 mm vesicles
- Vesicle cylinders
- GINKGO

SH_6 Babcock Bench

- ROZA
- Thin sediments, max 10cm thick
- Few vesicle rich horizons up to 1 m thick
- Bifurcating HVS up to 2 cm thick
- Irregular hackly jointing
- Thick well-developed columns up to 80 cm wide with occasional vesicle cylinders
- Contact not exposed
- Lobate upper surface
- GINKGO

SH_5 Frenchman Springs North

- Top of exposure
- Upper lobe breakout / tumuli
- 20 cm diameter vesicle rich areas
- Phenocrysts
- Banded vesicle rich horizons
- Glassy highly jointed zone
- Slightly hackly, small columns 20 - 40 cm wide
- Thick columns divided by horizontal jointing horizons
- Glomerocrysts up to 7 mm diameter
- Horizontal jointing
- Diverging columns
- Glass rich 'Black Band Zone'
- Thick columns 1 to 2 m wide
- Banded thin vesicular layers and and patchy finely vesicular (1-2 mm) areas
- Pipe vesicles up to 10 cm tall
- Ripple cross-laminated sandstone
- GINKGO

SH_4 Frenchman Springs South

- ROZA
- Poorly developed soil and sediments
- Some zonation to vesicle-rich and vesicle-poor areas, no strong banding generally small round dispersed vesicles
- Poorly developed columns
- Horizontal jointing
- HVS
- SENTINEL GAP
- Occasional plagioclase phenocryst
- Tree moulds - both vertical and inclined, typically 30 to 50 cm diameter, up to 2 m long
- Columns up to 2 m wide
- Highly weathered zone, underlying lobe not exposed

SH_3 Frenchman Springs South-east

- Top of exposure
- Lobe breakout / tumuli
- Increase in phenocryst abundance
- Megavesicle horizon, up to 25 cm thick
- Poorly developed widely spaced columns
- Weak horizontal joints and few vesicles
- Chatter marks undulating columns
- Fissile, occasional phenocryst
- GINKGO

SH_2 Sand Hollow Road

- Top of exposure
- Megavesicles 10-20 cm diameter with segregation material collected in the bases
- Poorly jointed,1 - 2 m spacing, some prismatic jointing on some column faces
- Glass rich 'Black Band Zone', columns typically 10 - 20 cm wide
- Thick columns up to 1 m wide
- Discontinuous basal precursor lobes 50 cm - 2 m wide
- GINKGO

SH_1 Vantage

- SENTINEL GAP
- Highly weathered rubbly vesicular flow top
- Megavesicle horizon
- Vesicle rich horizons
- HVS zone
- Finely jointed glassy 'black band'
- Well developed columns
- Vesicular base and glassy selvage
- GINKGO

SH_11 Locke Lake

- Massive lava with vesicular base, occasional phenocrysts
- Thin soil with brown rotten glass
- Lobate, vesicle rich lobe top, decrease in size and abundance of vesicules with depth
- 2 - 3 cm vesicles
- Horizontal vesicular sheet (HVS) zone
- Discontinuous HVS zones
- Horizontal fractures
- Irregular curvy joints
- Massive - very few joints
- Blade like jointing pattern due to abundance of horizontal joints at 5 to 15 cm spacing producing fissile zone
- Tree moulds up to 1.3 m tall, 80 cm wide, preserving impression of bark texture
- Pahoehoe ropes at base of lava
- Basal lobes typically 50 cm diameter
- Grey sediments interspersed with coal
- GINKGO

SH_10 Lyle

- Undulating pahoehoe weathered flow top
- Distinct vesicle rich horizons
- Patchy vesicles, curvy joints
- Strong horizontal jointing
- Tulip joints
- Variable characteristics and thickness of tulip jointed zone, from 20 to 40m across a 400m wide exposure
- Weak vertical joints
- Abundant irregular horizontal jointing producing fissile basalt
- No glassy selvage or vesicles
- Poorly developed soil
- GINKGO
- Rubbly undulating top surface

SH_9 Upper Devils Canyon

- Overlain by laterally discontinuous poorly developed soil and lobes of the Sentinel Gap Member
- Lobate upper surface
- Horizontal joints
- Columns typically 50 cm wide
- Second small lobe of Sand Hollow
- Glassy selvages between lobes, no soil, weathering or sedimentation
- Megavesicle horizon
- Poorly developed columns, heavy weathering and sub-horizontal fractures
- Abundant jointing
- Inclined 20 to 30 cm high pipe vesicles, flow to 327°
- Cross-laminated fine sediments lie over ash
- SILVER FALLS

SH_8 Palouse Falls rapids

- Eroded top of exposure
- Elongate megavesicle horizon up to 25 cm wide
- Vesicle rich band with vesicles up to 7cm diamter
- Vesicles up to 1cm diameter
- Horizontal jointing
- Radiating columns
- Finely jointed, dark, glass rich, finely crystalline zone within lobe core Black Band Zone
- Well-developed columns 80-100cm spacing
- Few well-dispersed vesicles up to 1cm diameter
- Pipe vesicles
- Laminated vitrified sediments varying thickness, average 15cm
- GRAND RONDE rubbly pahoehoe 80cm thick top

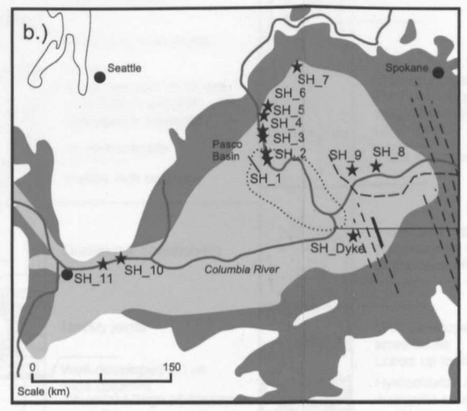

Figure 2.7. Logs constituting the Sand Hollow flow field

Figure 2.8. Logs constituting the Gingko flow field

Ginkgo Flow Field

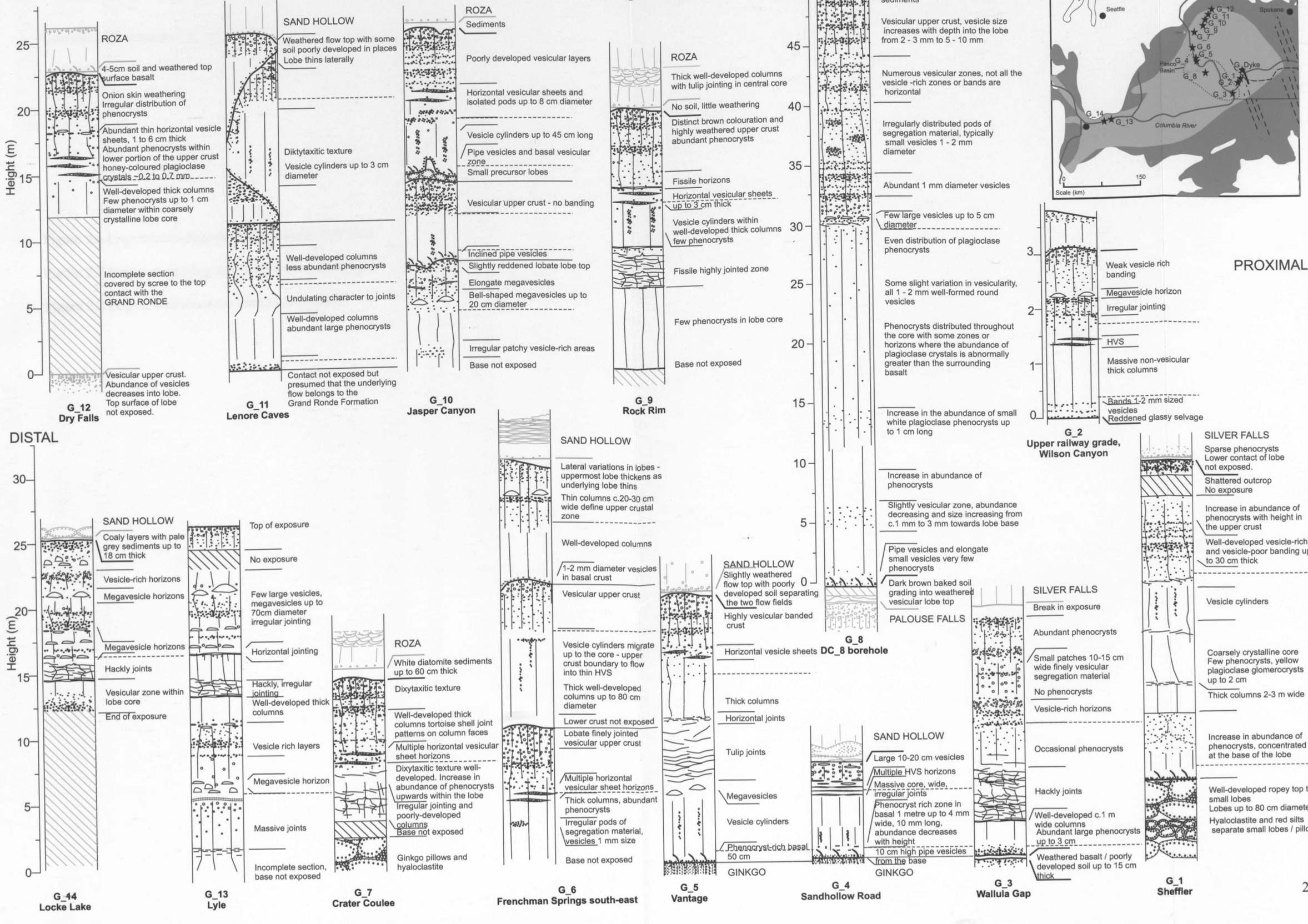

See inserts for Figures 2.6, 2.7 and 2.8.

Figure 2.6 Logs constituting the Palouse Falls flow field

Figure 2.7 Logs constituting the Sand Hollow flow field

Figure 2.8 Logs constituting the Ginkgo flow field

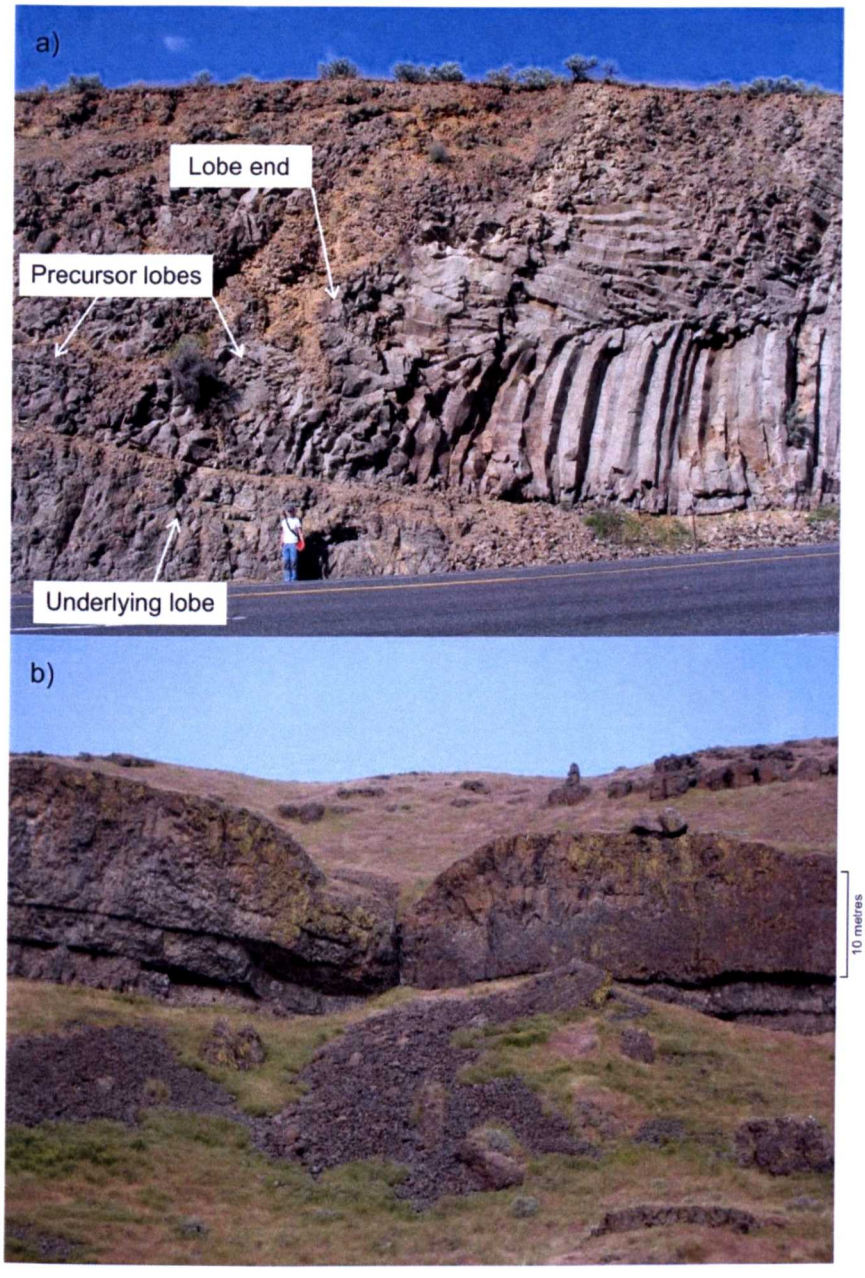

Figure 2.9 Junction between two adjacent sheet lobes within a) the Grande Ronde basalts outcropping to the west of Quincy (N47°09.080' W119°57.133'), and b) the Palouse Falls flow field, opposite Ayer on the northern bank of the Snake River (N46°35.074' W118°29.814').

Correlation of lobes constituting each flow field uses the features described above. Six field localities and two borehole cores for the Palouse Falls flow field were logged to establish a 90 km-long sequence of sections from the vent area to the Pasco Basin. In addition, this flow field was traced along near-continuous exposure (over ~20 km) on the northern banks of the Snake River from the vent area near Palouse Falls to the Lower

Monumental Dam area (N46°39.828' W118°13.377'). An example of the way in which flow fields can be correlated in this area is shown in Figure 2.10.

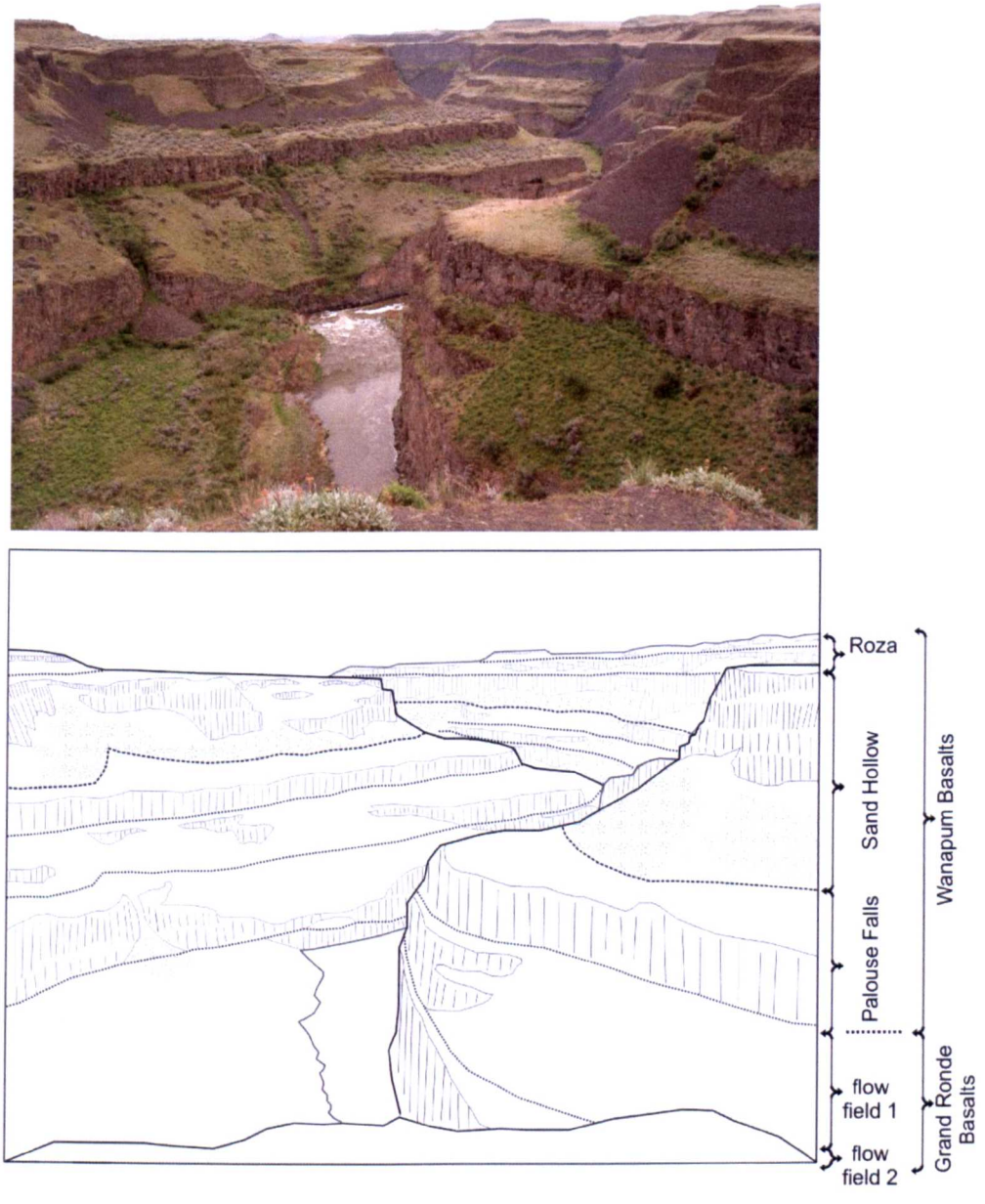

Figure 2.10 View point from Palouse Falls State Park (N46°39.744' W118°13.675') to the south along Palouse Falls River. Dashed lines represent the mapped contacts between adjacent flow fields. The Sand Hollow flow field is characteristically thick, 40 to 55 metres, in this vent proximal area with numerous vesicular and non-vesicular layers in the upper crust which can be identified from a distance by changes in the jointing style of columns. Palouse Falls flow field is typically 20 to 25 metres thick. The Grande Ronde flow fields in this area are labelled as flows 1 and 2 to avoid any confusion with existing literature and stratigraphy. These units are mapped to define the physical relationships and extent of flow fields. In this context comparison to stratigraphic nomenclature is not neccessary. Flow field 1 is 20 to 35 metres thick, and flow field 2 is 40 to 45 metres thick and forms the lowermost unit from the Palouse Falls waterfall to the confluence with the Snake River.

Observations at twelve localities were used to define the Ginkgo flow field in addition to a feeder-dyke outcrop and two borehole cores. Commonly, outcrops of the Ginkgo flow field are compound lobes of only the uppermost part of the flow field, with the underlying Ginkgo basalt covered by scree. Abundant exposures in the vicinity of the assumed feeder dyke (S. Reidel *pers. comm.*) (N46°28.069' W118°37.498') enable the relationships between lobes to be clearly established. Elsewhere exposures are discontinuous.

The Sand Hollow flow field was studied using eleven localities logged in detail starting with the type section at Sand Hollow in the Vantage area (N46°55.270' W119°56.988'). A further locality was recorded at a Sand Hollow dyke close to the southern limit of the flow field (N45°53.473' W118°17.192'). Extensive exposures from the Vantage area towards the north enable clear identification and correlation of lobe morphologies. Concurrent and post-volcanism tectonism caused folding, faulting and subsidence in some parts of the province that has limited exposure through the CRBG succession (Hooper *et al.* 2007). Access to complete thick lobes, which characterise this flow field, can be made along inclined road and rail cuttings, and where the unit dips in folds along the Columbia River Gorge.

2.5 Results

2.5.1 General characterisation of flow-field-wide features and lobes

The following presents a summary of the logs for each flow field (Figs. 2.6, 2.7 and 2.8). Identification of the features described and correlation of the lobes constituting a single flow field represent a substantial body of fieldwork. Here I review variations in the features across each flow field. The logs are used to construct fence diagrams of each flow field, presented in Figures 2.16, 2.18 and 2.21, that should accompany viewing of these descriptions.

2.5.1.1 Lobes

Lobes vary in thickness and lateral extent throughout each flow field. Early precursor lobes (1 to 5 metres thick), for which lava supply dwindled before extensive coalescence and inflation could occur, are seen on the banks of the Snake River in the Palouse Falls flow field (N46°25.600' W118°36.279'). Inflated sheet lobes in the Sand Hollow and Palouse Falls flow field range up to 80 metres thick, but are typically around 35 metres thick. The Ginkgo flow field generally has thinner lobes than the Sand Hollow and Palouse Falls flow fields. However, at each locality the Ginkgo flow field consists of a vertically stacked succession of two or three lobes, providing an average flow field thickness in the same range as that of the Sand Hollow and Palouse Falls. Lobe ends and the relationship between lobes in field exposures can be clearly seen using the intra-lobe structures such as vesicular zones and jointing styles, identification of glassy selvages and eruption units (Fig. 2.11).

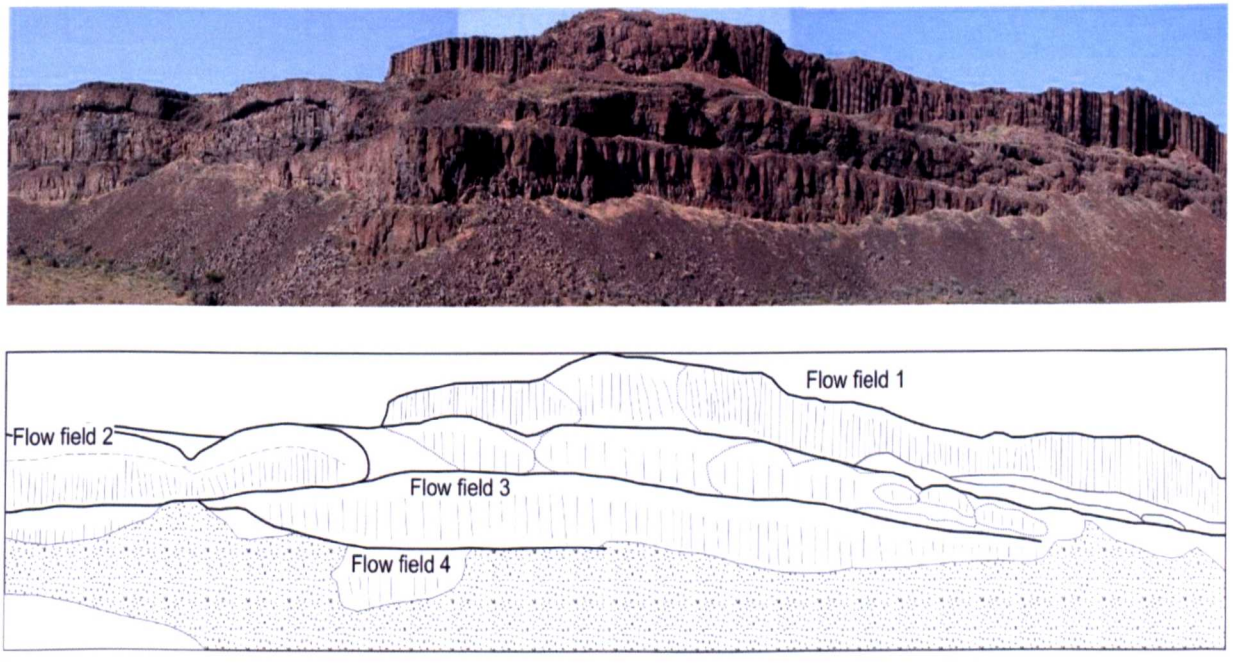

Figure 2.11 Annotated sketch and photo illustrating the relationships between lobes within a flow field at Babcock Bench (N47°10.251' W119°58.757'). Vertical lines denote jointed lobe cores. Dashed lines indicate the position of lobe boundaries within flow fields. Thick lines mark flow field limits.

2.5.1.2 Lobe top surface morphology

The contact between flow fields is distinct in all cases where exposed. In most localities it consists of a 1-2 cm thick glassy selvage with elongate deformed vesicles and a smooth pāhoehoe flow surface that grades down into the vesicular upper crust (Fig. 2.12).

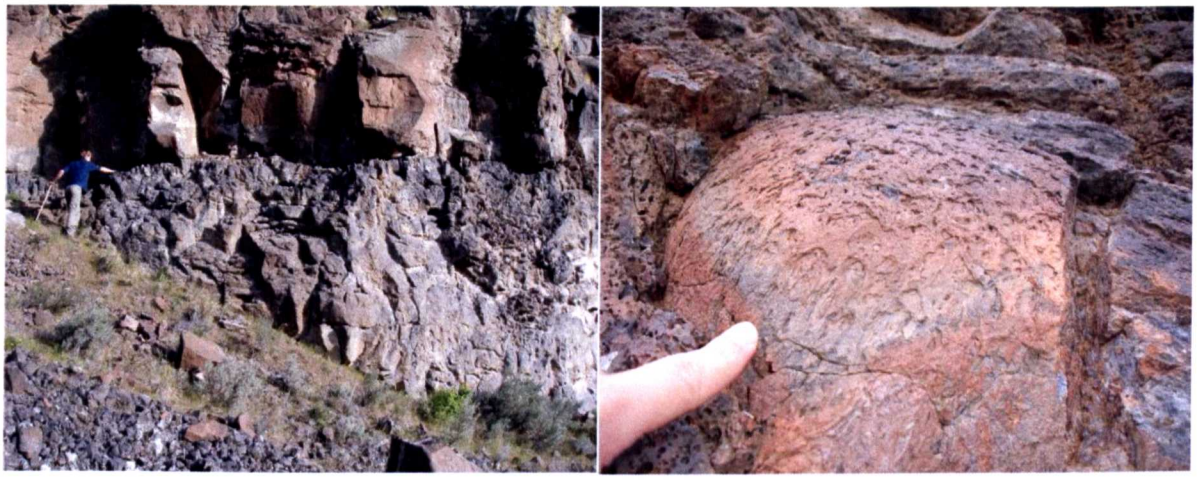

Figure 2.12 Lobate flow top morphologies typical of inflated sheet lobes illustrating amalgamated inflated precursor lobes; a) Dry Falls canyon (N47°35.289' W119°23.311') person for scale, b) Jasper Canyon (N47°34.192' W119°25.365') finger for scale.

Pāhoehoe ropes and small-scale lobate undulations of the smooth top surface are occasionally observed (e.g. N47°34.192' W119°25.365', Fig. 2.13).

Figure 2.13 Pāhoehoe ropes exposed on a flow top within the Grande Ronde Formation at Locke Lake (N45°41.972' W121°24.395').

In some localities a brecciated upper surface extending up to 50 cm thick into the upper crust is observed (e.g. Vantage, N46°55.883' W119°56.891', SH_1); interpreted as rubbly pāhoehoe generated by cycles of inflation and brecciation of the surface crust rather than post-emplacement mechanical weathering. Observations within the CRBG are in-keeping with definitions of rubbly pāhoehoe from elsewhere, i.e. irregular, fragmented, loose blocks of pāhoehoe lava crust generally <10 cm in size which grade into the flow to become coherent vesicular upper crust (Keszthelyi *et al.* 2004; Guilbaud *et al.* 2005).

2.5.1.3 Tumuli and upper crust breakout lobes

Breakouts from the upper crust of several lobes are identified within the Sand Hollow and Palouse Falls flow fields (Fig. 2.14). No soil, weathering, or sedimentary deposits occur between the main sheet lobe above and the breakout lobe. The breakout lobes vary from two to five metres thick (accounting for up to ~8 to 10 % of the thickness of the parent lobe at that position in the flow field) and exhibit inflation features including vesicular crusts, a well-jointed core and segregation structures.

Typically tumuli and lava rise pit features are associated with hummocky pāhoehoe flow fields that form on steeper and more irregular topography (Hon *et al.* 1994) than is common in the CRBG. The near-absence of these features suggests that each CRBG flow field studied covered the pre-existing flow fields without encountering strong topographic variations.

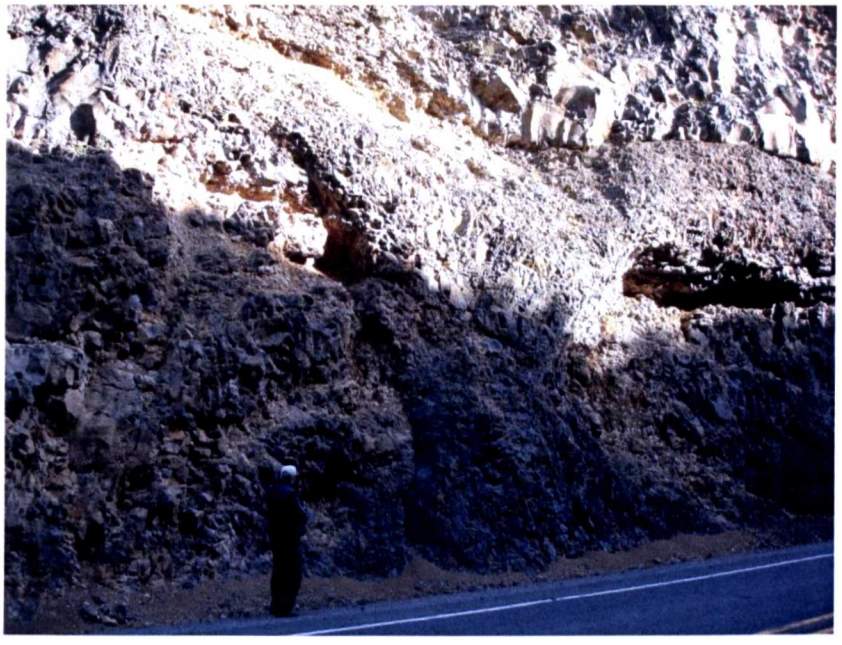

Figure 2.14 Surface break out from a lobe within the uppermost part of the Grande Ronde Formation exposed in a road cutting on the eastern banks of Banks Lake (N47°44.549' W119°13.877'). Basalt at the base of the outcrop is within the lobe core and cuts vertically upward through the vesicular upper crust to flow out on the surface to form a new lobe.

2.5.1.4 Lobe base morphology

The morphology of lobe bases varies and is dependent on the nature of the substrate, i.e. a lobe of a preceding eruption or a sedimentary succession that buries lobe morphology. In most outcrops the morphology of the base of a lobe is near-planar. Lobe bases are less variable than the undulating character of lobe top surfaces and consist of a thin outer glassy selvage, occasionally showing pāhoehoe ropes. At locations where the Ginkgo flow field overlies the Vantage Interbed sediments, the basal parts of the flow field are represented by pillow basalts and hyaloclastite (e.g. Museum Road, N46°57.020' W119°59.870'). These reflect initial propagation of the flow field over wet sediments or into shallow water bodies. The subsequently emplaced sheet lobes have planar bases.

Within other flow fields elsewhere in the province, lobate morphologies to the bases of lobes displace finely laminated silts and muds (Fig. 2.15). This is interpreted as the result of loading, which progressively increases during inflation. Disturbed sedimentary bedding suggests lateral migration of sediments but there is a notable absence of water-escape

structures. There is no inclusion of sediments into the basalt. The lobe contact consists of a thin glassy selvage and vesicular basalt, as seen in other lobe bases.

Figure 2.15 Lobate morphology of the basal contact of the Roza flow field on the Highway 14 road cutting in the Lyle area, northern bank of the Columbia River (N45°42.348' W121°19.047').

2.5.2 Characteristics of the Palouse Falls flow field

The Palouse Falls flow field is the smallest of the three flow fields studied, both volumetrically and in terms of the distance that lava travelled from the hypothesised vent area. Lobes vary from 2 metres thick at the southern margin of the flow field in the Snake River outcrops where the flow field consists of two lobes and is only 4 metres thick in total, to 58 metres thick in the proximal area. Lobes at the distal reaches of the flow field in the Pasco Basin, studied in cores, are up to 50 metres thick. Significant thinning of the whole flow field occurs with increasing distance from the vent area, apart from the Pasco Basin fill. Upper crusts constitute 37-54 % of total lobe thickness close to the vent; and average 38 % over the whole flow field. Upper crusts constitute just 21 % of the lobe thicknesses in the Pasco basin boreholes (PF_7 and PF_8, Fig. 2.16).

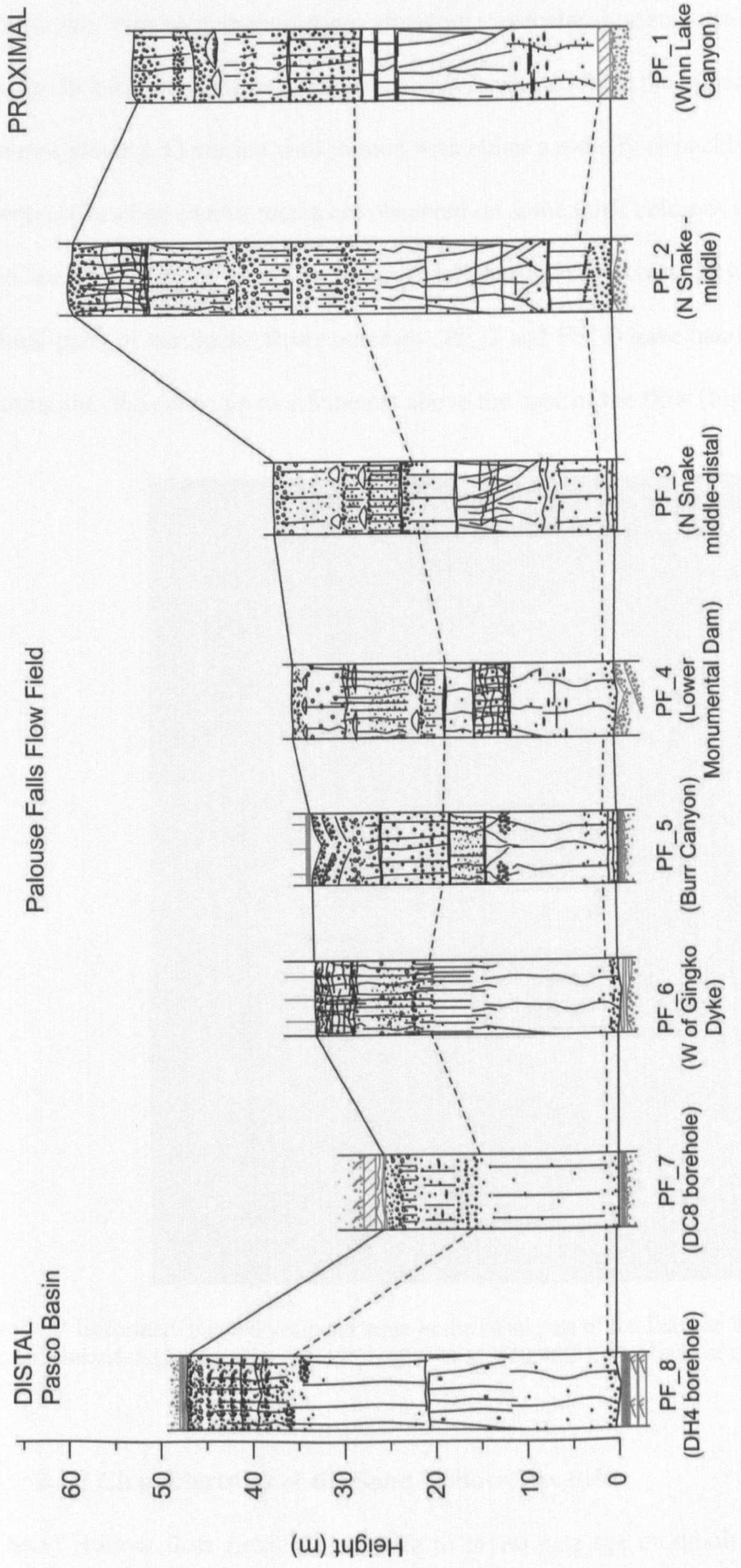

Figure 2.16 Fence diagram of the lithostratigraphic logs made within the Palouse Falls flow field extend from the vent area in the east (proximal) to the westernmost (distal) reaches of the flow field. The flow field extent is identified by a near-continuous exposure on the northern bank of the Snake River from Winn Lake Canyon (PF_1) to the Ginkgo dyke locality (PF_6). PF_7 and PF_8 are borehole localities within the Pasco Basin.

Upper crusts typically demonstrate abundant vesicular horizons and more than one megavesicle horizon. Lobe cores are frequently separated from the upper crust by a zone of horizontal jointing. Cores are well jointed with either a radially or hackly jointed section in the centre. Chisel or chatter marks are observed on some thick columns (> 80 cm diameter) within the lava core at localities along the Palouse Falls River. Lower crusts in more proximal parts of the Snake River outcrops (PF_2 and PF_3) have banded vesicular zones extending into the cores, up to 1.5 metres above the base of the flow (Fig. 2.17).

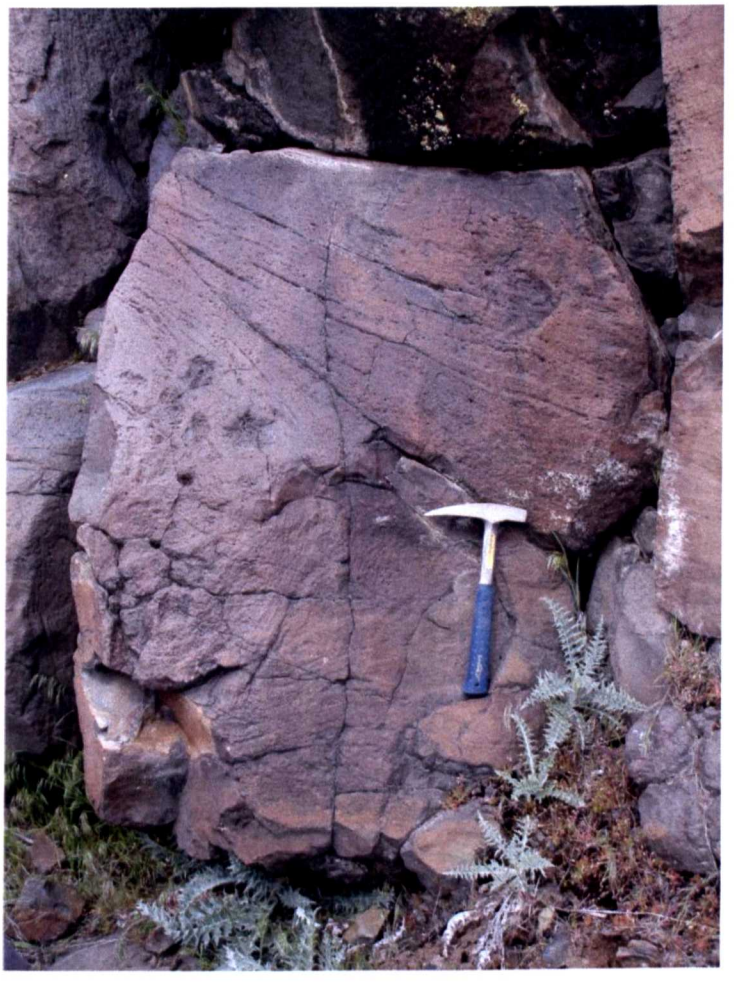

Figure 2.17 Deformed, banded vesicular zone in the basal part of the Palouse Falls flow field on the northern bank of the Snake River (N46°36.635' W118°19.402'). The base of the lobe is covered by vegetation.

2.5.3 Characteristics of the Sand Hollow flow field

The Sand Hollow flow field is used here to investigate the morphology of a large flow field, typical of the size found in many flood basalt provinces (<1,000-2,000 km^3 of lava

and hundreds of kilometres long). In all localities where the flow field is observed, it is only one lobe thick (Fig. 2.18). The vast extent of the Sand Hollow flow field and the lack of control on the order in which lobes were emplaced mean that some assumptions must be made. First, it is unknown if the northern or western edges of the flow field represent the last lava to be emplaced. Therefore, both are considered 'distal' to the eruption vent and localities converging to the south and east of the flow field are considered 'proximal'.

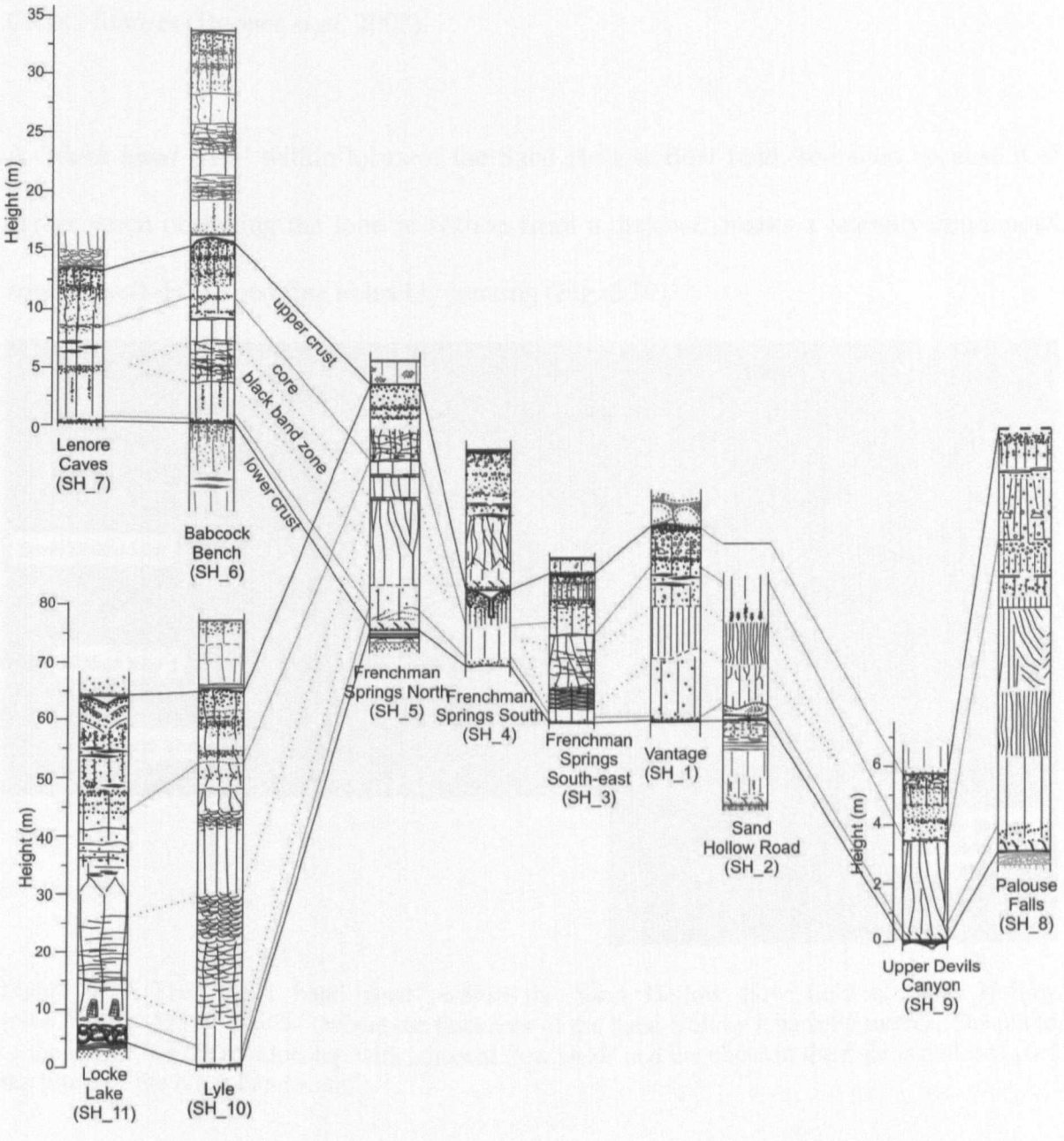

Figure 2.18 Fence diagram of the logs within the Sand Hollow flow field extending from the vent area in the southeast to the northern and western distal reaches of the flow field.

Second, in the absence of other constraints, this flow field is believed to have developed in a similar way to the younger Roza flow field (Martin 1989; Martin 1991; Thordarson and Self 1998; Hooper *et al.* 2007). This includes development of a northwestern portion of the flow field in addition to advancement of lava to the west down the palaeo-Snake River valley. This is related to the progressively north-westward migration of vents observed along the NW-SE trending Roza fissure system, believed to be a common trend for all CRBG fissures (Hooper *et al.* 2007).

A *'black band zone'* within lobes of the Sand Hollow flow field, so-called because it is darker when observing the lobe in section from a distance, marks a laterally continuous zone of well-developed fine to hackly jointing (Fig. 2.19).

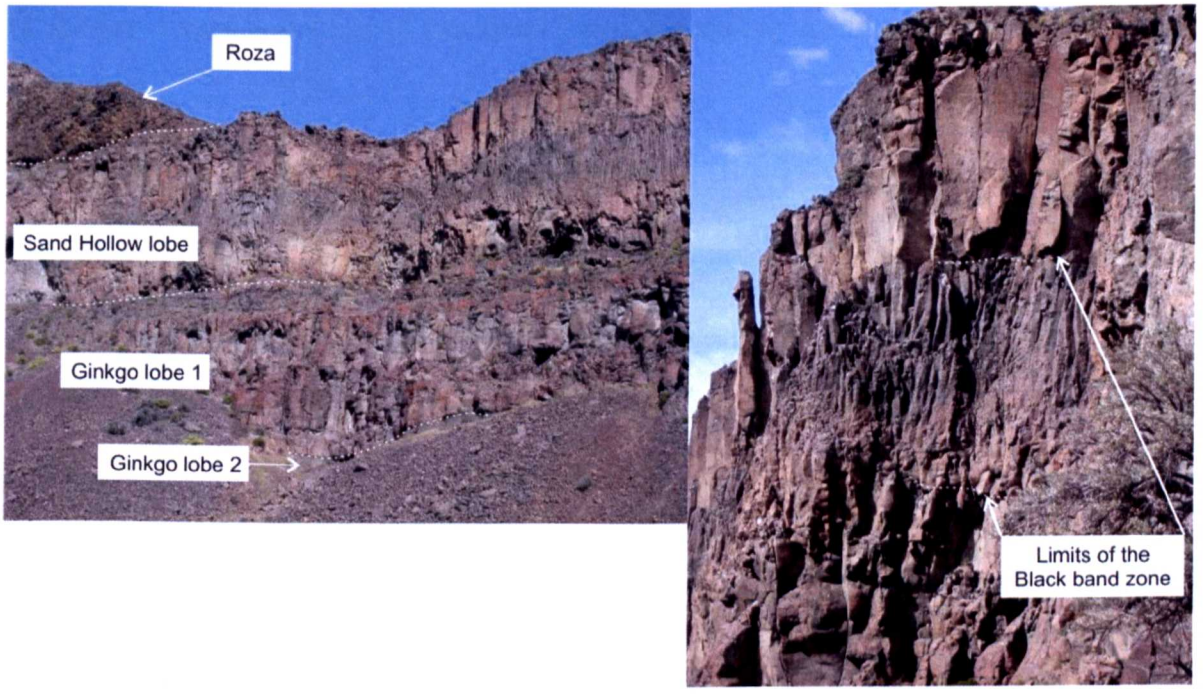

Figure 2.19 The 'black band zone' within the Sand Hollow flow field at Sand Hollow (N46°55.109' W119°56.928') where the thickness of the Sand Hollow lobe is 36 metres. The photo to the left shows the relationship with adjacent flow fields and the photo to the right is a close up of the limits of the black band zone.

The zone has an irregular thickness when traced laterally within the same lobe, but is persistent within lobes adjacent to a major lobe at Vantage (SH_1 on Fig. 2.18) for a

minimum distance of 16 km. The black band zone is located within the uppermost third of the lobe core in all cases, and is overlain by normally jointed core beneath the upper crust boundary. The petrography of this zone is distinctly glass-rich in comparison to the surrounding more coarsely crystalline core. From a distance, the margins of this zone appear sharp due to the abrupt change in column width and the presence of horizontal jointing; on closer inspection, however, the boundaries are diffuse over a 20-30 cm area.

Hypotheses developed within this thesis for the formation of this zone might include: 1) the zone represents the last emplaced portion of the lobe core introduced as a late-stage injection into a crystal mush; 2) percolation of surface waters into the lobe caused rapid cooling of the molten core; or 3) pressure release through brittle fracturing of the upper crust caused quench-cooling of the residual evolved melt in the lava core by volatile loss.

Physical features that indicate the ingress of water such as radial columns, sediment or hydrous mineral amygdaloidal cavity fills, and changes in the cooling regime within the core are absent. Despite the presence of 'tortoise shell joints' on column faces in some lobes, extensive flooding and pervasion by water into all lobes is not supported by the field and petrographic observations and this hypothesis is not considered plausible. It is not possible to distinguish between the other two hypotheses due to limited field evidence. The lateral persistence of a hackly jointed centre of Sand Hollow lobe cores suggests that either hypothesis is viable. At this time the processes considered most likely to have formed the black band zone are limited to either a change in cooling conditions or else cooling rates in the final stages of lobe formation. Thorough investigation of this zone requires special studies that are beyond the scope of this thesis.

In the most western distal locations (Lyle and Locke Lake, SH_10 and SH_11), the Sand Hollow flow field (like the Roza) is confined to the palaeo-Snake - Columbia River drainage channel (Tolan *et al.* 1989). Lobes between 60 - 80 metres thick outcrop on the banks of the present Columbia River channel. Upper crusts typically comprise <38 % of the total lobe thickness. The exact location of these sites in relation to the axis of the drainage channel in which they flowed is unknown. Curvilinear joints and tulip-jointing styles are observed within the lobe cores at these localities. The portion of the core within each lobe exhibiting these joints is glass-rich. This zone is believed to be a poorly-developed lateral equivalent of the 'black band zone'. Such well-developed tulip joints are infrequent in the CRBG but similar examples can be observed in the younger Roza and Rosalia flow fields from the Vantage (N46°55.270' W119°56.988') to Potholes Coulee (N47°10.251' W119°58.757') areas. This jointing style is hypothesised to represent a distinct change in the cooling rate of the lava core. One causative process could be the ingress of surface waters propagating along joints already established in the overlying lava. The lower crusts in these localities lack pipe vesicles, or other lower crustal vesicular zones, and the lower glassy selvage seen at other localities is not preserved.

Northernmost distal locations of the flow field thin and comprise of a single 13 metre thick lobe (N47°32.623' W119°25.232'). Such distal lobes continue to display segregation features. Upper crusts are thin and average 42 % of the total lobe thickness. The Lenore Caves outcrop (SH_7) marks the limit of the northerly exposure, and possibly the lateral extent, of this flow field.

Towards the central and proximal portions of the flow field all lobes display the hackly jointing of the characteristic 'black band zone'. Upper crusts constitute on average 30 % of

the total lobe thickness and have fewer well-defined vesicular zones than the Palouse Falls flow field.

In-situ upright tree moulds in growth position occur at the base of some locations within the flow field (Fig. 2.20). Additionally, recumbent tree moulds are found on top surfaces and between breakout lobes. These features provide evidence of environmental conditions and provide further evidence for emplacement by inflation. They also suggest that the hiatus since the last lava to be emplaced was sufficiently long for mature trees to develop. Tree moulds result from an advancing lava flow engulfing a tree; a crust forms at the point of contact and the tree either burns or decays over time leaving a cast within the lava (Lockwood and Williams 1978; Mackiewicz 1978). The height of the cast approximately indicates the height of the precursor lobe. Burnt trees around the height of the top surface may be felled onto the upper crust and be preserved by sediments or a successive lava flow.

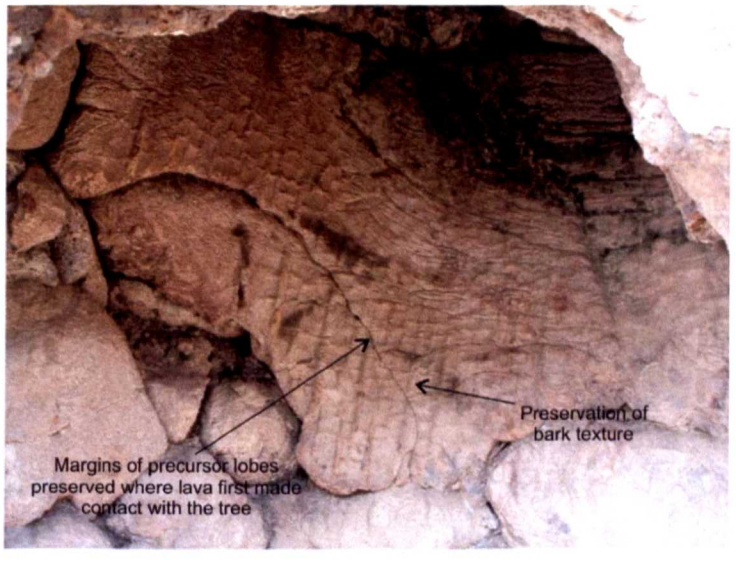

Figure 2.20 Tree moulds at the base of the Sand Hollow lobe exposed in the Locke Lake area (N45°41.916' W121°23.684') extend up to 1.5 metre vertically into the lobe.

2.5.4 Characteristics of the Ginkgo flow field

Throughout the Ginkgo flow field each locality consists of a vertical succession of at least two lobes. The logs in Figure 2.21 show the uppermost lobe and as many of the underlying lobes as are exposed at each locality.

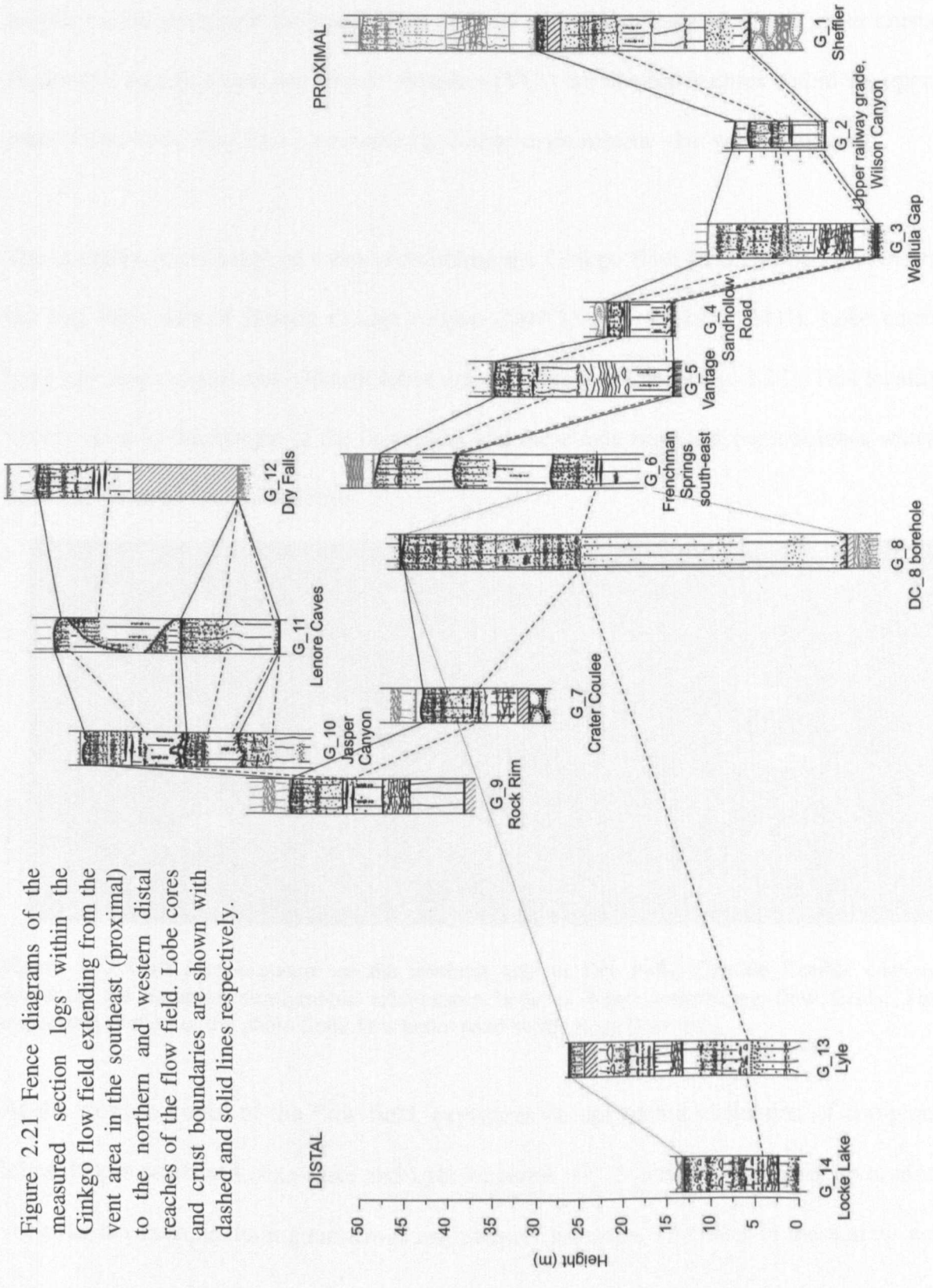

Figure 2.21 Fence diagrams of the measured section logs within the Ginkgo flow field extending from the vent area in the southeast (proximal) to the northern and western distal reaches of the flow field. Lobe cores and crust boundaries are shown with dashed and solid lines respectively.

At the northernmost reaches of the Ginkgo flow field, lobes range from 5 to 22 metres thick. Two or three laterally discontinuous lobes are present at Lenore caves (G_10) and Jasper Canyon (G_11) but only one lobe is exposed in the most northerly locality (Dry Falls, G_12) and Rock Rim (G_9). Within each lobe the physical characteristics are similar despite variations in lobe thickness. Two or three vesicle-rich bands form the upper crusts. Horizontal vesicle sheets and vesicle cylinders (VCs) are distinct features within the upper parts of the cores. The lobe cores typically comprise prominent ~1m wide columns.

The complex relationship of lobes constituting the Ginkgo flow field can be observed in the Dry Falls area of Grande Coulée canyon (N47°35.289' W119°23.311'). Lobe edges have low slope angles and adjacent lobes onlap preceeding lobes (Fig. 2.22). This locality is very close to the margin of the flow field, and these may represent pioneer lobes which have experienced limited inflation.

Figure 2.22 Cliff face exposure on the northern side of Dry Falls, Grande Coulée canyon, revealing the complex stratigraphic relationship between lobes constituting flow fields. The uppermost portion of the photo (lobe 5) is believed to be the Roza flow field.

At the western extent of the flow field, exposures do not permit evaluation of complete lobes. Upper crusts at Locke Lake and Lyle localities (G_13 and G_14) display up to nine vesicular horizons, including numerous megavesicle horizons. The lobes in these areas are

significantly thicker than those in any other part of the flow field. Localities that are medial and proximal to the vent have fewer vesicular horizons within the upper crusts, which comprise up to 60 % of the total lobe thickness, and thicknesses are highly variable between localities. Pillow lava and hyaloclastite deposits up to four metres thick are found underlying logged sections at the base of the Gingko flow field in a few localities: G_1, G_5 and G_7. These may represent river channels or standing bodies of water on the Grande Ronde basalts into and across which the Ginkgo flow field advanced.

Phenocrysts are abundant throughout the flow field. Typically these are white to honey-coloured single or glomerocryst plagioclase crystals up to 3 cm diameter. Locally within lobes the abundance of phenocrysts changes with height from 2 to 12 % over distances of 50 to 120 cm. Overall, Gingko is a good example of a large scale 'compound' flow field, i.e. more than one lobe is present at each locality. Ginkgo is an example of a flow field where the sheet lobes are usually small, <1 km in diameter and up to 25 metres thick, with innumerable smaller lobes, that are superposed in every part of the flow field examined.

2.5.5 Other features of the flow fields

The following presents a description of other features shown by the lithostratigraphic logs of the lava sequence in all three flow fields (Figs. 2.6, 2.7 and 2.8). These features are not present within every lobe or at every locality, but they are representative of the variety observed.

2.5.5.1 Feeder dykes and eruption vents

Two locations are known that represent parts of the feeder dykes for the Sand Hollow and Ginkgo flow fields. Correlations between the feeder dykes and flow fields are based on

chemostratigraphic characterisation (Hooper 2000); there is no physical link between the lobes and the dykes and there are no proximal deposits.

A Ginkgo feeder dyke on the north bank of the Snake River (N46°28.069' W118°37.498') striking to 350° is a near-vertical 10 metre-wide dyke of dense lava, dissecting the upper crust of a lobe of an upper Grande Ronde basalt. The contact zone is highly weathered and shattered and has a thin glassy selvage. Abundant honey-coloured plagioclase phenocrysts are evenly distributed throughout the dyke outcrop. Irregular jointing in the outer two metres develops into well-defined curvilinear columns perpendicular to the dyke margins that converge and become vertical towards the centre of the dyke (Fig. 2.23).

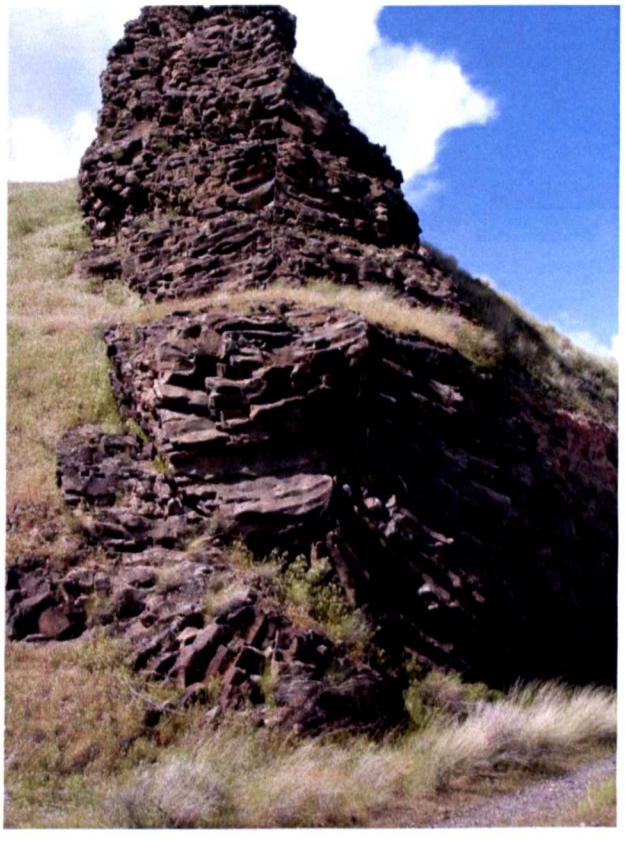

Figure 2.23 Outcrop of the Ginkgo feeder dyke on the northern bank of the Snake River (N46°28.069' W118°37.498') and contact with the Grande Ronde Formation (red weathered lobe top visible to the right of photo).

One Sand Hollow dyke is located amongst numerous other feeder dykes, at the western margin of the Wanapum Formation dyke swarm (S. Reidel *pers. comm.*; Hooper 2007)

(N45°53.473' W118°17.192'). The outcrop reveals an inclined 11 metre thick dyke dipping 60° to the south, trending north-east (Fig. 2.24). Plagioclase phenocrysts up to 1 cm long are sparse and irregularly distributed throughout the exposure. Higher concentrations of phenocrysts are found in poorly defined bands both close to the margins and in the central portions of the dyke.

Figure 2.24 Feeder dyke of the Sand Hollow flow field in the Walla Walla river area, Harris Country Park (N45°53.473' W118°17.192').

2.5.5.2 Vesicles

Description: The character of the *vesicular upper crust* varies between lobes within a flow field. Vesicle-rich and vesicle-poor banding generally appears to be laterally extensive within the confines of a lobe but the diffuse boundaries of such zones can make this difficult to trace. Bands vary from 10 cm to several metres thick (Fig. 2.25). Well-developed banding is not developed in all lobes, and where poorly developed there is a

decrease in vesicularity that accompanies an increase in vesicle size with depth from the top of the crust toward the core.

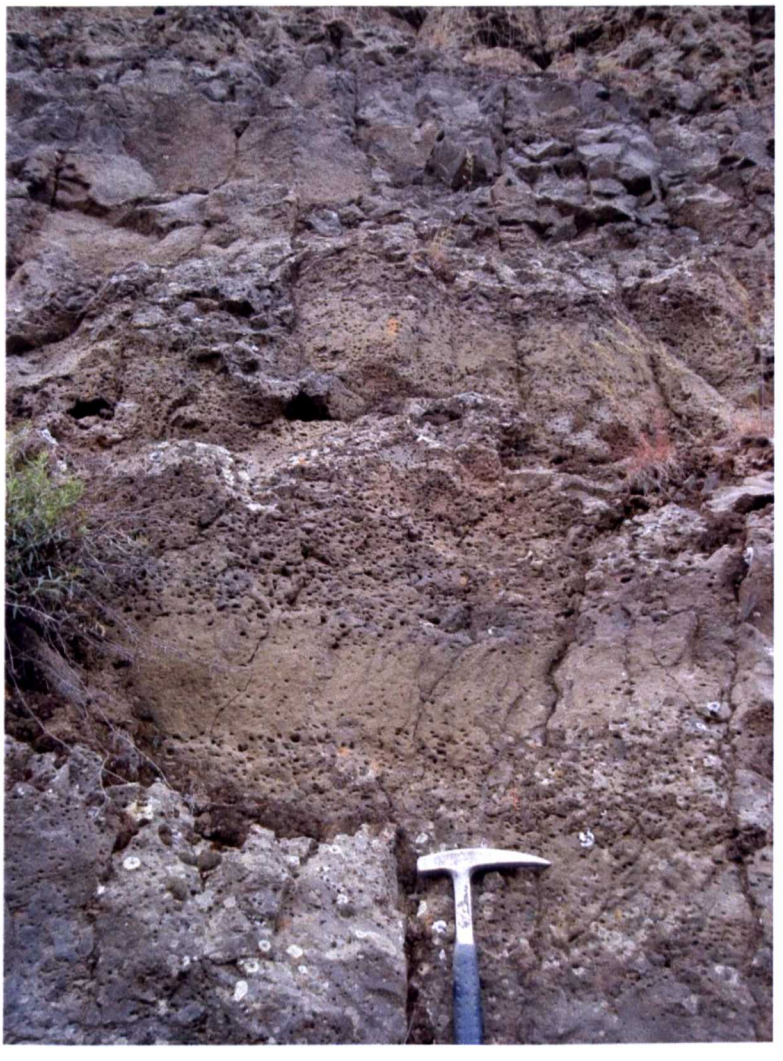

Figure 2.25 Fine-scale vesicular banding in the upper crust of the Palouse Falls sheet lobe exposed on the railway grade above Lower Monumental Dam (PF_4, N46°34.287' W118°32.549').

Interpretation: Differences in the distribution of vesicles within the upper crusts of lobes are thought to reflect variations in the rise of bubbles from the liquid core that are trapped where the lava meets the solidification front migrating into the flow from the upper crust (McMillan *et al.* 1987; Aubele *et al.* 1988; McMillan *et al.* 1989). Each vesicle-rich band, and associated vesicle-poor band, reflects a new pulse of volatile-rich lava introduced into the core. However, as Hon *et al.* (1994) observe on Kilauean lavas, patterns of vesiculation within inflated lobes are dependent on dynamic pressure changes, such as outbreaks, that cause pressure drops, or topographic influences causing deviations or blockages of flows

that result in pressure increases. Cashman and Kauahikaua (1997) suggest that the formation of small vesicle zones relate to falls in pressure caused by pauses in tube flow.

The processes causing changes in vesiculation within an actively inflating sheet lobe have yet to be determined. Despite the unconstrained variables, vesicle-rich and vesicle-poor banding is known to reflect physical changes within a lobe such as lava flow rates, flow style and pressure conditions (Hon *et al.* 1994). Alongside established influences on vesiculation such as changes in lava chemistry and volatile content (McMillan *et al.* 1989), breakouts and pulsed inflation (Anderson *et al.* 1999), vesicular banding could, in principle, be used in the future to reconstruct a detailed lobe history within the flow field.

Pipe vesicles occur within the basal 20 cm of most lobes. Average dimensions range from 1 to 3 cm wide and 5 to 20 cm long. Inclined upper parts of pipe vesicles indicate deformation during flow (Fig. 2.26). Such indicators of flow direction are usually limited to localised flow conditions, varying within a lobe, rather than providing a record of the principal axis of flow field elongation (Walker 1987). Particularly well-developed examples of pipe vesicles are seen at the Sand Hollow road cutting (N46°55.270' W119°56.988', SH_2). Pipe vesicles are absent in hyaloclastite and pillow lobes, and within some channel-confined flows. The occurrence of pipe vesicles does not correlate with lobe extent, thickness or proximity to the source region. Philpotts and Lewis (1987) suggest that pipe vesicles are the result of exsolution or retrograde boiling of the lava. Whereas others (e.g., Godinot 1988) attribute the presence of pipe vesicles in the lower crust as being due to the solidification front at the base of the flow growing into the lobe at a much slower rate than the upper crust.

Figure 2.26 Pipe vesicles within the basalt crust of the Ginkgo lobe at the Sand Hollow road cutting (N46°55.270' W119°56.988').

Bell-jar vesicles and megavesicles are not as common as pipe vesicles within the flow fields. They vary from classic bell-jar shaped cavities, up to 30 cm in diameter and extending up to 50 cm in height, to elongate vesicles, where the aspect ratio is the inverse of bell-jar vesicles but the volume is similar (Fig. 2.27). These are usually located within the uppermost metre of the core. The coalescence of gas at this horizon is due to the junction between the liquid lobe core and the upper crystallisation surface. The gas forming these megavesicles is released from both pipe vesicles at the flow base and vesiculation of the molten core.

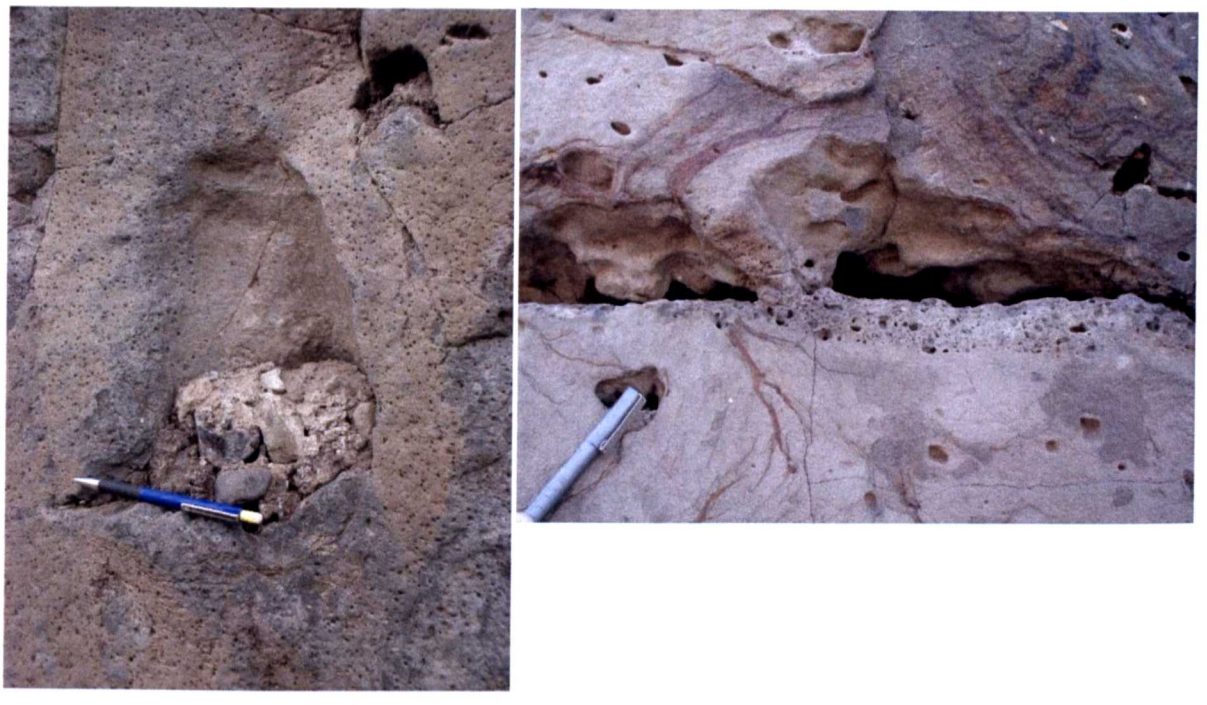

Figure 2.27 Megavesicles and bell-jar vesicles at the core-uppercrust boundary within the Sand Hollow flow field from the Vantage area (N46°55.883' W119°56.891').

2.5.5.3 Segregation features

Description: Segregation features are common in the cores of most sheet lobes in the flow fields. In contrast with the gradational margins of vesicular zones in the upper crust, segregation features are sharply defined zones of unusually highly vesicular basalt (Fig. 2.28). Often multiple horizontal vesicular sheet (HVS) layers occur and range from 2 to 5 cm thick with up to 20 cm of poorly vesicular lobe core between them. There is a notable absence of HVS where abundant megavesicle horizons occur in the upper-crust to core boundary. The presence of segregation features appears to be unrelated to any minimum or maximum lobe thickness.

Interpretation: Segregation features such as VCs and HVS or pods relate to the physical separation of residual melt and volatiles from the surrounding lava as crystallisation commences. The residuum is often more evolved, high SiO_2, volatile rich and more coarsely crystalline melt than the surrounding lava (Goff 1996). Due to the density contrast

between this differentiate and the surrounding crystal mush, it rises through the core as VCs and spreads laterally, trapped in layers, when it reaches the upper solidification interface (Anderson *et al.* 1984; Bideau and Hekinian 1984; Hon *et al.* 1994) to form HVS (Self *et al.* 1997).

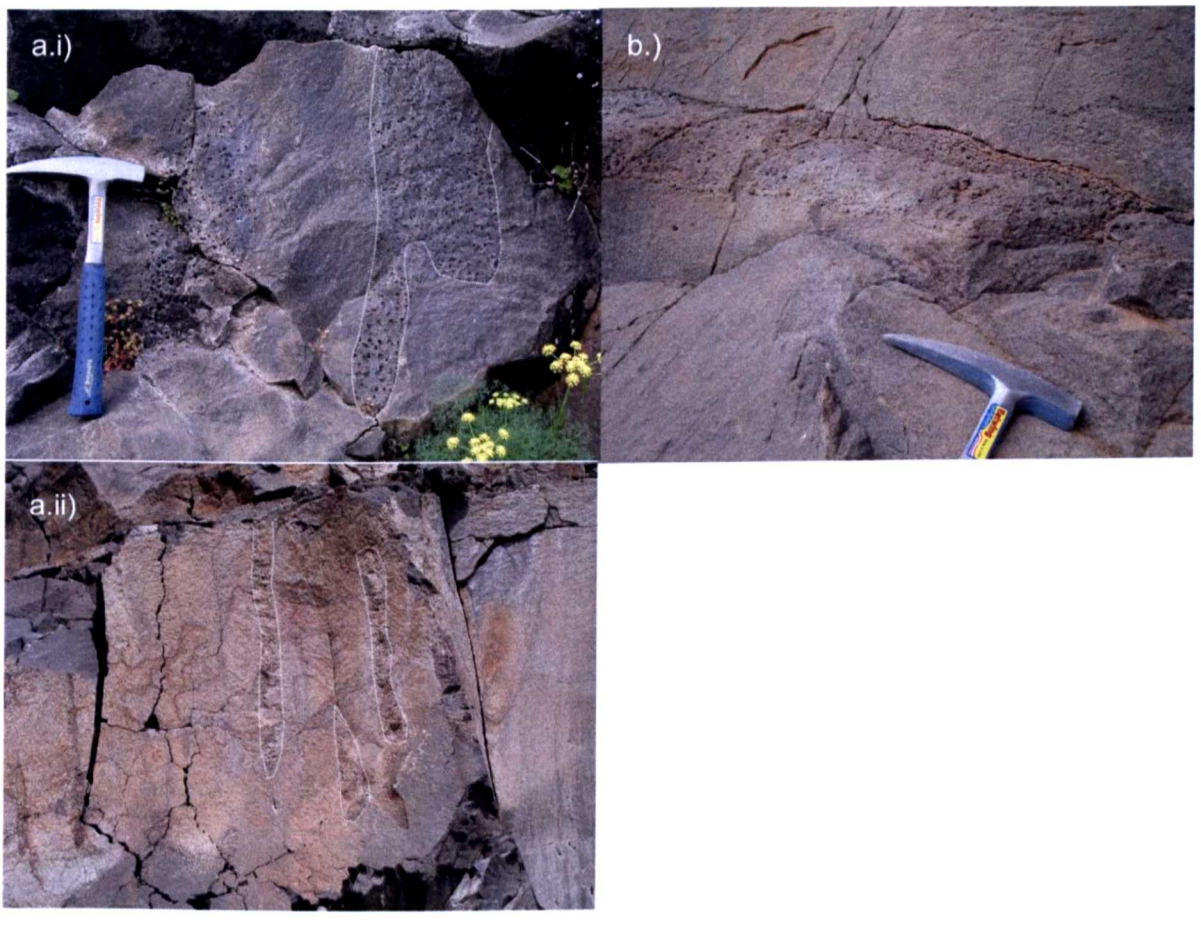

Figure 2.28 a.i) and a.ii)Vesicle cylinders of highly vesicular basalt in the lobe core at Locke Lake (N45°41.916' W121°23.684') within the Sand Hollow flow field, outlined in chalk for clarity b.) Horizontal vesicle sheets within the Grande Ronde basalts near Locke Lake (N45°41.972' W121°24.395').

The presence of such features is dependent on volatile content and bulk composition (McMillan *et al.* 1989) and on initial temperature, cooling and inflation history. Segregation features can also be formed in thick flows by secondary vesiculation events (Hon *et al.* 1994). It is unclear if multiple horizons of HVS within a lobe represent residual melts from multiple processes or are instead related to the same event. Such variations may be generated through multiple inflation events or variations in horizontal stresses during the movement of viscous lava (Thordarson and Self 1998). Evidence for variations in the

stress regime within inflated lobes is provided by anisotropy of magnetic susceptibility (AMS) studies, which identify variable shear rates and isolate late-stage shearing at the lava core-crust boundary (Canon-Tapia and Coe 2002).

2.5.5.4 Columns and jointing style

Description: Columns are well-developed in the lobe cores, less prominent in the vesicle-poor bands of the upper crust and under-developed in the vesicle-rich bands. Marked variations in the frequency and morphology of columnar joints are observed throughout each flow field. Columns range up to 2 metres wide with planar vertical joints in lava cores to 15 cm wide. Column surfaces may also undulate or radiate from a point, often near the boundary between the core and the upper crust (Fig. 2.29).

Interpretation: Radiating columns such as those found in the lobe core at Palouse Falls (N46°40.005' W118°13.407', SH_8) are speculated to have experienced cooling related to a specific event such as ingress of surface waters or brittle failure and fracturing of the overlying upper crust (Waters 1960). The columns grow perpendicular to the solidification or cooling front so that any perturbation in this front is represented in the column orientations. Column surfaces occasionally reveal 'chatter' or 'chisel' marks caused by repeated cycles of stress and relief (Ryan and Sammis 1978) and are considered to indicate the direction in which the column surface propagated (Degraff and Aydin 1987). Examples of these features can be seen in the south-western part of the province where drainage of lavas utilising the Columbia River palaeovalley would have repeatedly dammed and redirected the river drainage patterns.

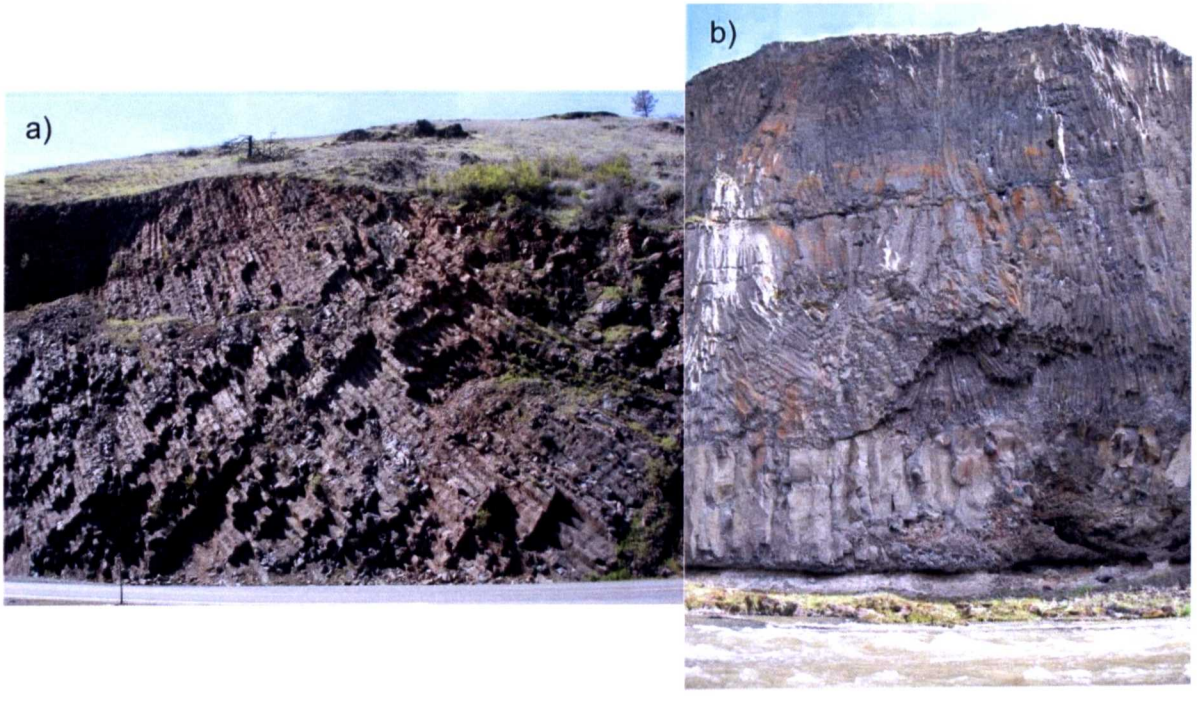

Figure 2.29 a) An example of radial jointing within a Grande Ronde lobe, Oregon; b) Radial columns from the boundary of the lobe core with the upper crust within the Palouse Falls flow field on the eastern bank of the Palouse River (N46°40.005' W118°13.407').

Phenomena referred to as 'tortoise shell cracks' or joints are suggested to represent further cooling by surface or ground water ingress causing 5 to 10 cm wide prismatic joints on some joint faces. Occurrences of these are rare but are observed on the Sand Hollow road log (N46°55.109' W119°56.928', SH_2).

2.5.6 Textural features

Textural variations with height and changing structural features within lava lobes have been observed elsewhere (Degraff *et al.* 1989). Iddings (1886) recognised the finely crystalline glass-rich nature of the entablature in contrast to the coarsely crystalline basal colonnade. These variations are interpreted to reflect the variable cooling and solidification history of a lobe (Long and Wood 1986). Samples from one lobe within the Sand Hollow flow field are used to record textural variations in light of the structural divisions, emplacement and cooling model related to inflation. These can be compared to the features recorded in the log SH_8 (Fig. 2.30).

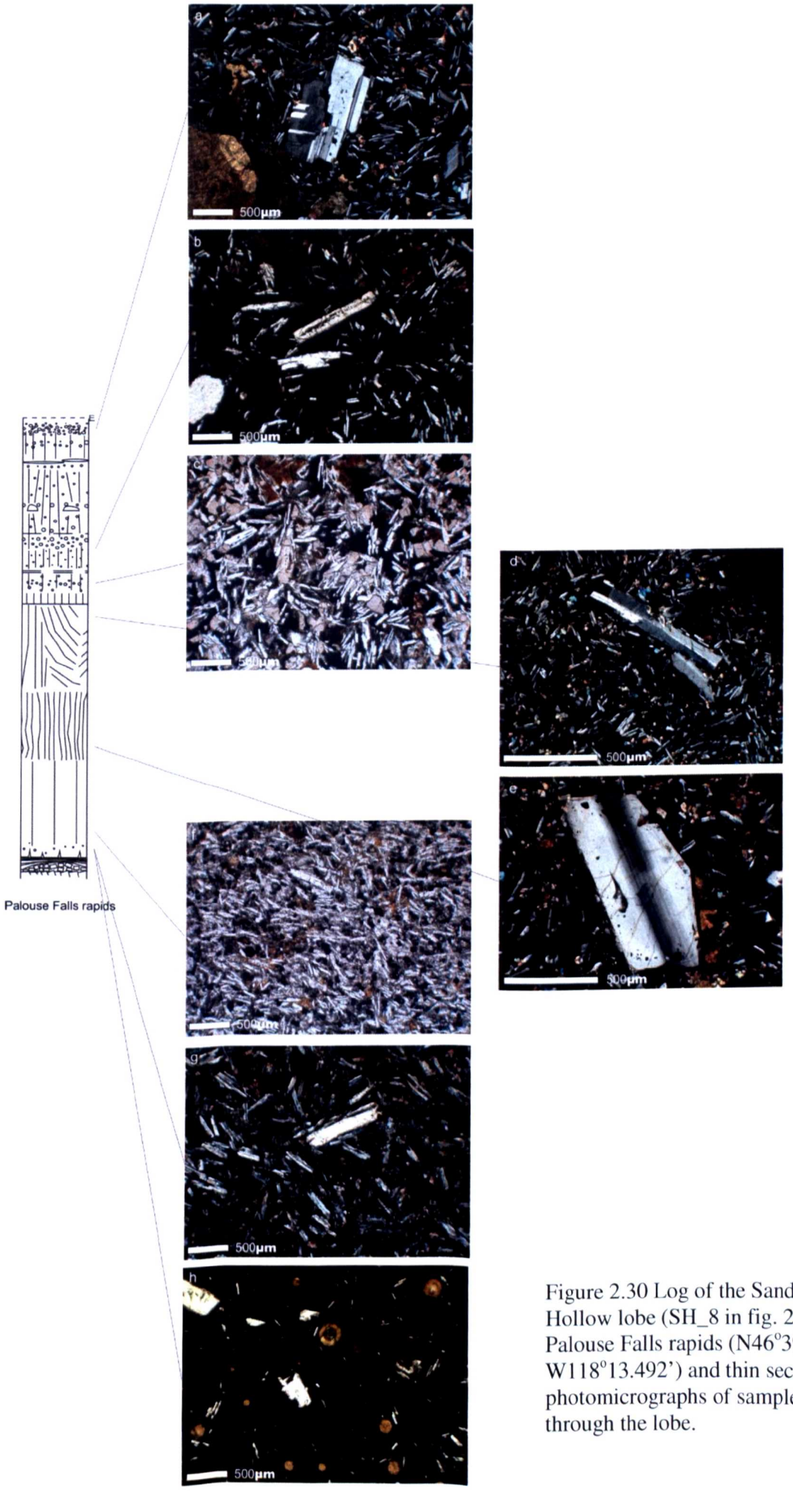

Figure 2.30 Log of the Sand Hollow lobe (SH_8 in fig. 2.6) at Palouse Falls rapids (N46°39.969' W118°13.492') and thin section photomicrographs of samples through the lobe.

The lowermost sample is within the lower crust, in the transition zone between the outer glassy selvage and the core. This hypocrystalline zone contains sparse plagioclase phenocrysts within a groundmass which contains both crystals and glass. The microcrystalline texture is so fine that it is difficult to differentiate the relative proportions of crystals and glass (Fig. 2.30 h).

The core samples (Figs. 2.30 d, f and g) demonstrate a marked increase in crystallinity relative to the crusts. The intersertal texture is consistent throughout the core, with brown glass and hypocrystalline material occupying the interstices between plagioclase laths. Sample CRB05_043 from the finely jointed zone within the core reveals a decrease in the size and abundance of microphenocrysts of plagioclase and is dominated by altered brown glass and finely crystalline subhedral pyroxenes and equant euhedral opaques (Fig. 2.30 e).

Samples from the upper crust show a decreasing crystallinity with increasing height within the lobe (Figs. 2.30 a, b and c). Intergranular interstitial textures characterise the basal portion of the upper crust with seriate textures occasionally observed. Towards the top, finely crystalline samples demonstrate seriate textures similar to the lower crust. The sample from the top of the upper crust lacks the finely crystalline intersertal texture observed in the basal crust (Fig. 2.30 h). This is an additional indication that the top of the exposure in this locality does not represent the top of the lobe, although the proportion of the upper crust as a function of the total lobe thickness suggests that it may be close.

The characteristics and abundances of plagioclase phenocrysts vary throughout the lobe. Phenocrysts are more abundant in the crusts than the lobe core. Single euhedral bladed plagioclase crystals exhibit discontinuous zoning, frequently with a zonal arrangement of melt inclusions and microlites in the outer rims and occasional embayments.

Glomerocrysts of 2 to 4 crystals are present, but are infrequent within this Palouse Falls lobe.

Textural variations observed in other eruption units within the CRBG can help interpret intra-lobe melt dynamics and differentiation (Philpotts and Burkett 1987; Philpotts and Philpotts 2005; Philpotts and Philpotts 2006). The dynamics proposed by Philpotts and Philpotts (2005) may be applicable within a stagnant lobe core. An insulated upper crust may permit sufficient time for differentiation processes such as crystal settling, and diapiric or effusive migration of residual melt. However, textural evidence found within the Cohassett flow field (of the Grande Ronde Formation) for orientation of plagioclase laths and trapped melt is not identified within this lobe (Fig. 2.31).

Figure 2.31 Figure extracted from (Philpotts and Philpotts 2005) to show example of textural variations. Photomicrograph of orientated phenocrysts indicating accumulation and trap of rising residual melts within the Cohassett flow field (Grande Ronde Formation) at Sentinel Bluffs. Sub-horizontal plagioclase phenocrysts in sample from 12 m above base of flow. All phenocrysts are shown in their correct orientation relative to drill-core axis, which is vertical. Groundmass plagioclase crystals tend to be stacked along upper surface of phenocrysts and patches of glass and late crystallizing magnetite are trapped beneath phenocrysts. The asymmetry of this texture, which resembles a lintel over a doorway, is evidence of relative motion of crystals and liquid. Phenocrysts in (D) to (F) are bent over supporting crystals. Width of each field: 1 mm. Partly crossed polars.

2.6 Discussion

2.6.1 Implications of field descriptions for styles of emplacement

It is evident from the descriptions provided above that the principal structural components of each flow field are similar. Whilst lobe thicknesses and extent varies between the constituent outcrops of each flow field, similar volcanological features are present at each locality. A summary of the features at each locality is presented in Table 2.1. Analysis of these localities supports the emplacement of each flow field through inflation processes.

2.6.1.1 Intra-lobe features

Many claim that the common occurrence of the described features enables comparison between voluminous flood basalts with modern active and historic lavas (Self *et al.* 1996; Ho and Cashman 1997; Keszthelyi and Self 1998; Thordarson and Self 1998; Waichel *et al.* 2006; Passey and Bell 2007). The variation in volume by several orders of magnitude between historic or active lava flows, such as those on Hawaii or Iceland, and continental flood basalts has given rise to speculation on whether models for the emplacement of relatively small volume lavas (<1 km^3) can be applied as analogues for large volume lavas (up to 6000 km^3, (Reidel and Fecht 1987). However, the similarities in morphologies, surface features, and internal zonation of pāhoehoe sheet lobes and inflated pāhoehoe sheet lobes in Hawaii (Hon *et al.* 1994; Self *et al.* 1996) has led to an increasing recognition of the importance of inflation in flood basalts. The inflation model has since been proposed to thicken flows from the scale of typical advancing lobes, roughly 15-50 cm thick (Hon *et al.* 1994; Keszthelyi and Denlinger 1996; Walker 1996) within the CRBG (Self *et al.* 1996; Thordarson and Self 1998), the Deccan (Bondre *et al.* 2000; Bondre *et al.* 2004), Etendeka - Parana (Jerram *et al.* 2000), and the North Atlantic Igneous Province (Passey and Bell 2007), other terrestrial and planetary long lava flows (Keszthelyi and Pieri 1993; Stephenson *et al.* 1998; Keszthelyi *et al.* 2004; Keszthelyi *et al.* 2006). Self *et al.* (1998)

suggest that the process should be referred to as the Standard Way of Emplacing Large Lavas, the SWELL hypothesis and this has generally been accepted as a valid emplacement mechanism.

Lobe	Log reference	Grid reference[a]	Flow field thickness[b]	No. of lobes	Lobe surface morphology[c]	Surface features[d]	Internal features[e]
Sand Hollow							
Locke Lake	SH_11	N45.41.916' W121.23.684'	62	1	pahoehoe	l, ps	vz, hvs, tm
Lyle	SH_10	N45.41.390' W121.16.322'	80	1	pahoehoe	l, ps	vz
Palouse Falls Rapids	SH_8	N46.40.032' W118.13.380'	50	1	N/E	ps	vz, mv, pv, tm
Lenore Caves	SH_7	N47.32.623' W119.25.232'	12	1	pahoehoe	l, ps	vz, hvs, vc
Babcock Bench	SH_6	N47.10.251' W119.58.757'	19	1	pahoehoe	l, ps	vz, hvs, vc
FSC N	SH_5	N47.01.542' W119.58.342'	42	1	pahoehoe	t, l, ps	vz, pv
FSC S	SH_4	N47.01.535' W119.58.051'	12	1	pahoehoe	l, ps	vz, hvs, pv
FSC SE	SH_3	N47.01.607' W119.57.975'	26	1	pahoehoe	t, l, ps	vz, mv
Vantage	SH_1	N46.56.147' W119.57.235'	32	1	rubbly pahoehoe	ps	vz, mv, hvs
Sand Hollow Road	SH_2	N46.55.109' W119.56.928'	25	1	N/E	ps	vz, mv
Black Band	—	N46.55.109' W119.56.928'	6	—	—	—	—
Devils Canyon	SH_9	N46.37.259' W118.33.450'	9	1	pahoehoe	r, l, ps	vz, mv, pv
Dyke	—	N45.53.473' W118.17.192'	10	—	—	—	—
Palouse Falls							
DH4	PF_8	N46.45.198' W119.21.064	47	1	weathered	ps	vz, sz
DC8	PF_7	N46.28.489' W119.23.125'	29	1	weathered	ps	vz, hvs
W of Ginkgo Dyke	PF_6	N46.27.664' W118.37.781'	34	1	rubbly pahoehoe	ps	vz
Burr Canyon	PF_5	N46.30.900' W118.36.444'	35	1	pahoehoe	r, l, ps	vz, sz
Lower Monumental Dam	PF_4	N46.33.640' W118.32.874'	35	1	N/E	ps	vz, mv, hvs
N Snake - middle-distal	PF_3	N46.35.719' W118.28.847'	36	1	N/E	l, ps	vz, mv
N Snake - middle	PF_2	N46.36.635' W118.19.402'	58	1	pahoehoe	l, ps	vz
Winn Lake Canyon	PF_1	N46.38.516' W118.12.230'	51	1	pahoehoe	t, l, ps	vz, mv, hvs
Ginkgo							
Locke Lake	G_14	N45.41.925' W121.23.552'	13	1	pahoehoe	ps	vz, mv
Lyle	G_13	N45.41.362' W121.16.619'	26.5	1	N/E	ps	vz, mv
Dry Falls	G_12	N47.35.289' W119.23.311'	18	1	pahoehoe	r, l ps	vz, mv, hvs
Jasper Canyon	G_10	N47.34.130' W119.25.372'	19	3	pahoehoe	r, l, ps	vz, mv, hvs, vc, pv
Lenore Caves	G_11	N47.32.623' W119.25.232'	24	3	pahoehoe	l, ps	vc
Rock Rim Village	G_9	N47.33.896' W119.26.358'	19.5	1	pahoehoe	l, ps	vz, hvs, vc
Crater Coulee	G_7	N47.14.960' W119.57.959'	15	2	pahoehoe	l, ps	vz, hvs
FSC SE	G_6	N47.01.607' W119.57.975'	30	3	pahoehoe	l, ps	vz, mv, hvs, vc
Vantage	G_5	N46.56.999' W119.57.393'	20	2	pahoehoe	l, ps	vz, hvs, mv, vc, pv
Sand Hollow Road	G_4	N46.55.270' W119.56.988'	15	2	pahoehoe	l	hvs, vc, pv
DC_8 borehole	G_8	N46.28.489' W119.23.125'	50	2	pahoehoe	l, ps	mv, sz, vz, pv
Wallula Gap	G_3	N46.01.835' W118.56.012'	18	1	N/E	ps	vz
Wilson Canyon	G_2	N46.27.921' W118.37.640'	3.4	2	pahoehoe	l,ps	mv, hvs, vz
Sheffler	G_1	N46.24.167' W118.38.615'	20	2	rubbly pahoehoe	ps	vc, vz, pv
Dyke	—	N46.28.069' W118.37.498'	11	—	—	—	—

[a] Principal locality used for log thickness representing the lobe
[b] average total thickness of the flow field including all constituent lobes at each locality
[c] lobe surface morphology
[d] surface features: l – small pāhoehoe lobes, ps – pāhoehoe sheet lobes, r – pāhoehoe ropes, t – tumuli
[e] internal features: vz – vesicular banding, hvs – horizontal vesicular sheets, mv – megavesicles, pv – pipe vesicles, sz – segregation zones (unclassified morphology), vc – vesicle cylinders, tm – tree moulds

Table 2.1 Features of flow fields and reference localities for all logs.

Several lines of evidence are repeatedly given to support emplacement by inflation. These are derived principally from volcanological features indicating endogenous growth, pāhoehoe morphology which includes compound flows with thick crusts and layering or

vesicular bands, and an abundance of features such as tumuli and lava rise pits (Walker 1991; Hon *et al.* 1994; Bondre *et al.* 2004). Additional evidence which points to the emplacement of long lava flows by inflation include: characteristic structural features (Thordarson and Self 1998), chemical variation and degrees of lava mixing (Reidel 1998), quantitative fluid dynamical and thermal constraints (Keszthelyi and Self 1998), and anisotropy of magnetic susceptibility (AMS). Changes in the AMS signature within one flood basalt sheet lobe identified 16 discrete injection events in the Birkett Flow of the Grande Ronde Basalts of the CRBG, thickening the lobe in each instance by 0.5 to 4.0 meters (Canon-Tapia and Coe 2002). The range of thickening by inflation coincides with that inferred for Hawaiian lavas (Hon *et al.* 1994).

2.6.1.2 Flow field wide morphology and sheet lobe geometry

The correlation of lobes that comprise individual flow fields and their tripartite structural division permits an evaluation of changes in the character of lobes spatially within a flow field. Changes in the structure of lobes across a flow field may relate to changes in the eruption rate, flow rate or style, constrained by physical parameters including topography, lava temperature, crystallisation and volatile content (Bruno *et al.* 1994; Walker 1996; Carrasco-Nunez 1997; Cashman *et al.* 1998; Keszthelyi and Self 1998; Thordarson and Self 1998; Blake and Bruno 2000; Duraiswami *et al.* 2002; Bondre *et al.* 2004; Solana *et al.* 2004). The relationships between the core and upper crust in individual lobes within the studied flow fields in the CRBG are shown in Tables 2.2 and 2.3. Absolute variations in the thickness of lobes within each flow field are shown in fence diagrams in Figures 2.16, 2.18 and 2.21. Thinning of individual lobes with increasing distance from the vent area is noted within the Palouse Falls flow field whilst the Sand Hollow and Ginkgo exhibit more complex thickness variations. Factors influencing these observations that require consideration include intermittent sampling of the larger two flow fields and linear

characterisation of the Palouse Falls field through a series of genetically linked lobes. This sampling resolution limits interpretation of the spatial development of each flow field.

Lobe	Log reference	Distance from source (km)	Thickness (m)			No. of lobes	% Upper crust	Exposed lobe extent (km)	Calculated duration of emplacement (days)
			Core	Upper crust	Total				
Sand Hollow									
Locke Lake	SH_11	242	45	17	62	1	27	0.5	1984
Lyle	SH_10	235	50	30	80	1	38	1	6180
Lenore Caves	SH_7	195	7	5	12	1	42	u/k	172
Babcock Bench	SH_6	180	10.5	8.5	19	1	45	5	496
FSC N	SH_5	174	31	11	42	1	26	2	831
FSC S	SH_4	173	9	3	12	1	25	0.5	62
FSC SE	SH_3	172.5	16	10	26	1	38	0.5	687
Vantage	SH_1	158	28	4	32	1	13	1	110
Sand Hollow Road	SH_2	157	20	—	25	1	—	1	—
Black Band	—	156.5	—	—	—	—	—	—	—
Palouse Falls Rapids	SH_8	150	31	19	50	1	38	2-5	2479
Devils Canyon	SH_9	76	4	5	9	1	56	0.1	172
Palouse Falls									
DH4	PF_8	85	37	10	47	1	21	—	687
DC8	PF_7	80	18	11	29	1	38	—	831
W of Ginkgo Dyke	PF_6	40	21	13	34	1	38	7-9	1160
Burr Canyon	PF_5	39	20	15	35	1	43	7-9	1545
Lower Monumental Dam	PF_4	30	21	14	35	1	40	2	1346
N Snake - middle-distal	PF_3	22	22	14	36	1	39	8-10	1346
N Snake - middle	PF_2	12	26	32	58	1	55	3-10	7031
Winn Lake Canyon	PF_1	5	26	25	51	1	49	4	4292

Table 2.2 Data summary of the lobe morphology, intra-lobe structures and calculated emplacement time for lobes constituting the Sand Hollow and Palouse falls flow fields. Ranges of the extent of lobes are gained from field observations of width and length dimensions, u/k = unknown. Emplacement time is calculated using equation 1, derived from (Hon *et al.* 1994). Blank cells indicate insufficient data available from incomplete lobes or exposures.

Lobe	Log reference	Distance from source (km)	Thickness (m)				No. of lobes	% Upper crust	Range of lobe extent (km)	Calculated duration of emplacement (days)
			Core	Upper crust	Lobe total	Flow field total				
Ginkgo										
Locke Lake	G_14	237.6	—	13	—	13	1	—	<1	
Lyle	G_13	227.2	—	20	—	26.5	1	—	<4	
Dry Falls	G_12	140.7	15	3	18	18	1	17	1	62
Jasper Canyon	G_10	135.8	7	6	13	19	3	46	1	247
Lenore Caves	G_11	134.4	9	4	13	24	3	31	0.2	110
Rock Rim Village	G_9	130.5	14	5.5	19.5	19.5	1	28	<1	208
Crater Coulee	G_7	138.1	7.5	7.5	15	15	2	50	<1	386
FSC SE	G_6	123	5	5	10	30	3	50	0.2	172
Vantage	G_5	115.6	15	5	20	20	2	25	0.5	172
Sand Hollow Road	G_4	113.8	10	5	15	15	2	33	2	172
DC_8 borehole	G_8	65	29	21	50	—	2	42	—	3028
Wallula Gap	G_3	42.6	10	8	18	18	1	44	3	439
Wilson Canyon	G_2	19.3	1.6	1.4	3	3.4	2	47	3	13
Sheffler	G_1	2.3	11	9	20	20	2	45	4	556
Dyke		0	—	—	—	11	—	—	—	—

Table 2.3 Data summary of the morphology, intra-lobe structures, and calculated emplacement time for lobes constituting the Ginkgo flow field. Thicknesses are derived from the uppermost lobe in each locality where multiple lobes are exposed. The relationship between the core and upper crust in the uppermost lobe is used to calculate the emplacement time. Therefore, the duration of flow field formation is a minimum value.

To facilitate a comparison of the relative spatial variation in each flow field between the cores and crusts of each lobe, the percentage of the lobe thickness that is comprised of the upper crustal zone is plotted as a function of distance from the vent (Fig. 2.32).

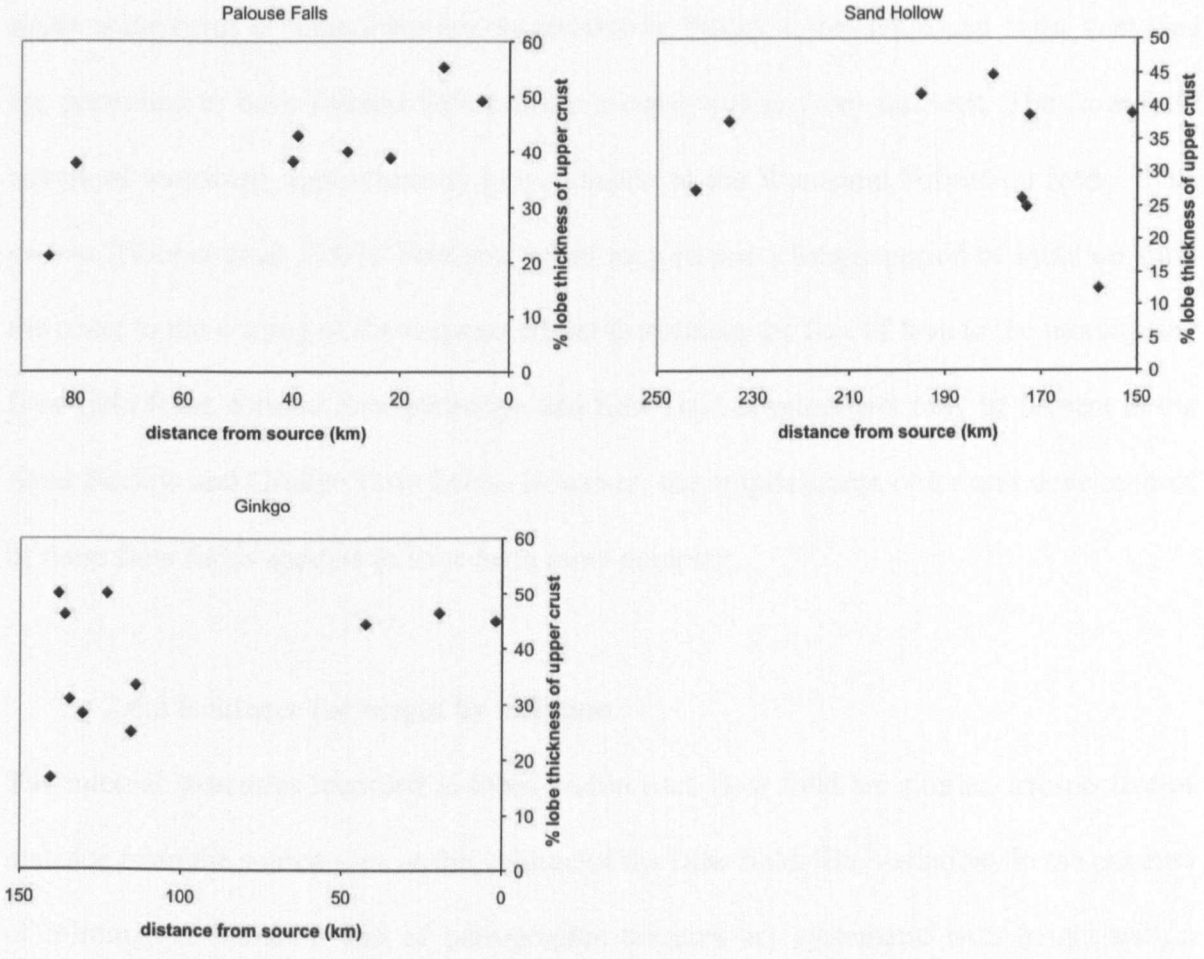

Figure 2.32 Thickness of the upper crust as a percentage of the total lobe thickness at each locality plotted against the distance from the vent within each flow field.

In the Palouse Falls and the Ginkgo flow fields a decrease in the proportion of a lobe which is upper crust from proximal to distal locations is apparent. The Sand Hollow flow field exhibits an inverse relationship with distance. It is assumed that the thicknesses observed are representative of lobes within each flow field aside from small localised fluctuations. Hon *et al.* (1994) observe uniform uplift within a lobe through inflation. In this case, the relative proportions of core and crust should be approximately the same throughout a sheet lobe except at the very margins.

Thinning of the Palouse Falls flow field with distance from the vent is interpreted to reflect a decrease in the time of emplacement and degree of inflation with distance during the eruption. A simple linear spatial and temporal relationship in the Palouse Falls flow field is made as the cores of some lobes are observed to be linked. Lobes emplaced in the vent area are presumed to have formed before those located further from the vent. The flow field advanced westward, approximately perpendicular to the Wanapum Formation feeder dyke swarm (Hooper *et al.* 2007). Proximal lobes may record a longer period of inflation from the onset to the waning of the eruption whilst facilitating the flux of lava to the propagating flow field front. Similar flow pathways and flow field development may be present in the Sand Hollow and Ginkgo flow fields. However, the emplacement order and development of these flow fields appears to have been more complex.

2.6.2 Evidence for origin by inflation

The internal structures recorded in lobes within each flow field are similar, irrespective of distance from the source area or the volume of the flow field. The variations in the patterns of jointing, vesiculation and of petrographic textures are systematic with height within each lobe. These characteristics are typical of the tripartite subdivision of lobes into a basal crust, core and upper crust that defines pāhoehoe inflated lobes.

Prior to identification of inflation processes, understanding of the emplacement mechanism of flood basalt lava flows was dominated by the presumption that extensive lavas must be emplaced rapidly, literally flooding the landscape (Shaw and Swanson 1970; Reidel and Tolan 1992). Rapid emplacement models invoking turbulent flow regimes (Shaw and Swanson 1970; Walker 1971) are inconsistent with the range of pāhoehoe surface structures and lava morphologies observed (Walker 1991; Keszthelyi and Pieri 1993; Chitwood 1994; Rossi and Gudmundsson 1996). The inflation model for sheet flow

emplacement in flood basalt provinces provides a more convincing alternative to the high lava supply rates necessary to support rapid emplacement (Shaw and Swanson 1970; Swanson *et al.* 1975) and the requirement for large magma chambers (Hooper *et al.* 2007). The 'lower' eruption rates implicit in the inflation model significantly reduce previous estimates to eruption durations of months or years (Murphy *et al.* 1991).

2.6.2.1 Alternative theories on emplacement of continental flood basalts

Alternative emplacement models are frequently based on evidence gleaned from a single province. Whilst it is acknowledged that small-scale variations in the morphology of flows occurs, a single model applicable to all provinces is sought to determine eruption rates (Jerram 2002; Bondre *et al.* 2004). Only through the collection of morphological accounts throughout multiple provinces can such a claim be made. A review of the alternative emplacement mechanisms is given below.

A laminar flow regime with progressive invasion and inflation of older lava units by younger units has been proposed to explain compositional heterogeneity within the Umatilla, Sillusi, Cohassett and Roza flow fields in the CRBG (Reidel 1998, Reidel 2005). These compositional zones within 'composite sheet flows' form individual lobes close to the vents and require simultaneous, geographically disparate fissure eruptions (Reidel and Fecht 1987; Martin 1989; Martin 1991; Reidel 2005). Thermal erosion of lava flows through sediments or basalt to inflate another lobe is required for compositionally distinct lava flows to mix and produce intermediate compositions (Greeley *et al.* 1998; Kerr 2001). This mechanism is not substantiated by field evidence in the Palouse Falls, Sand Hollow and Ginkgo flow fields.

Pulsed inflation (Anderson *et al.* 1999; Anderson *et al.* 2000; Self *et al.* 2000) of pāhoehoe lava flows requires varying strain rates within the flow to account for the dilated fractures seen in Hawaiian lavas. These are generated as a response to small pulses of lava emplaced as a sequence of 'pods' of lava beneath a crust in a network of preferred pathways. This model is based specifically on lavas emplaced on slopes and the fracture morphology relates to cooling and has not been applied elsewhere.

2.6.3 Timescales and rates of emplacement

Single eruptions may include several pulses or series of related eruptions (Cashman *et al.* 1998; Guilbaud *et al.* 2005). In many provinces (Deccan, Siberian and Parana) the total volume of erupted products has been divided by estimated emplacement times to calculate magma production rates of 0.1-2 km^3 / yr (Richards *et al.* 1989; White and McKenzie 1995; Turner *et al.* 1996). However, when considering the hiatus between eruptions, magma discharge rates are likely to be an order of magnitude higher (Cashman *et al.* 1998). As research has developed, models of eruption duration on individual lavas as flood basalt flow fields range from one week for a 'typical' 100 km^3 Yakima basalt in the CRBG (Shaw and Swanson 1970) to several years for the whole Roza flow field using the sheet lobe inflation model (Thordarson and Self 1998). Other indicators of longer duration emplacement times in the CRBG include limited evidence for either high fountains (Swanson *et al.* 1975) or the construction of lava shields (commonly associated with long-duration eruptive events, Greeley 1982), and signs of thermally efficient transport of lava in individual flows (Ho and Cashman 1997).

2.6.3.1 Quantifying the rate of emplacement

The features described within each flow field provide abundant evidence to qualitatively document inflation. However, the collection of data to quantitatively characterise

emplacement is more complicated. Quantification of rates is important as recent models question the assumption that typical pāhoehoe surface morphology indicates slow emplacement (Solana *et al.* 2004), calling for eruption rates and styles to be the dominant controls on lava flow morphology (Blake and Bruno 2000; Jerram 2002).

Existing methods applied to calculate eruption durations are based on conductive cooling models and crustal growth (Keszthelyi and Self 1998; Thordarson and Self 1998). These utilise constants derived from observations of Hawaiian lavas (Hon *et al.* 1994) to provide an empirical relationship with time:

$$t = 164.8\ H_c^2$$

Equation 2.1

where t is the time in hours and H_c is the thickness of the upper crust in metres. Such models are believed to be appropriate for flood basalts; application of this method to the 1801 Hualalai pāhoehoe lavas suggests that Hawaiian alkali basalt behaves similarly to tholeiitic basalt during emplacement (Hon *et al.* 1994) and shows a similar cooling rate. The thermal properties of lavas are examined by Keszthelyi *et al.* (2004) in a model presented by Keszthelyi and Denlinger (1996) which found that variations in thermal properties propagate a maximum 25 % uncertainty to such calculations.

Application of this equation to the three flow fields presented is shown in Tables 2.1 and 2.2 and plotted with a function of distance from the vent locality in Figure 2.33. Variations in the emplacement timescales for each eruption unit are diverse, ranging from 13 to 7031 days. Average emplacement times for each flow field are 3.2 ± 0.8 years for Sand Hollow, 6.3 ± 1.58 years for Palouse Falls and 1.36 ± 0.34 years for the uppermost portion of the Ginkgo field. The mean values in the Sand Hollow field are markedly skewed by the long

duration times calculated for the distal Locke Lake and Lyle localities (SH_10 and SH_11).

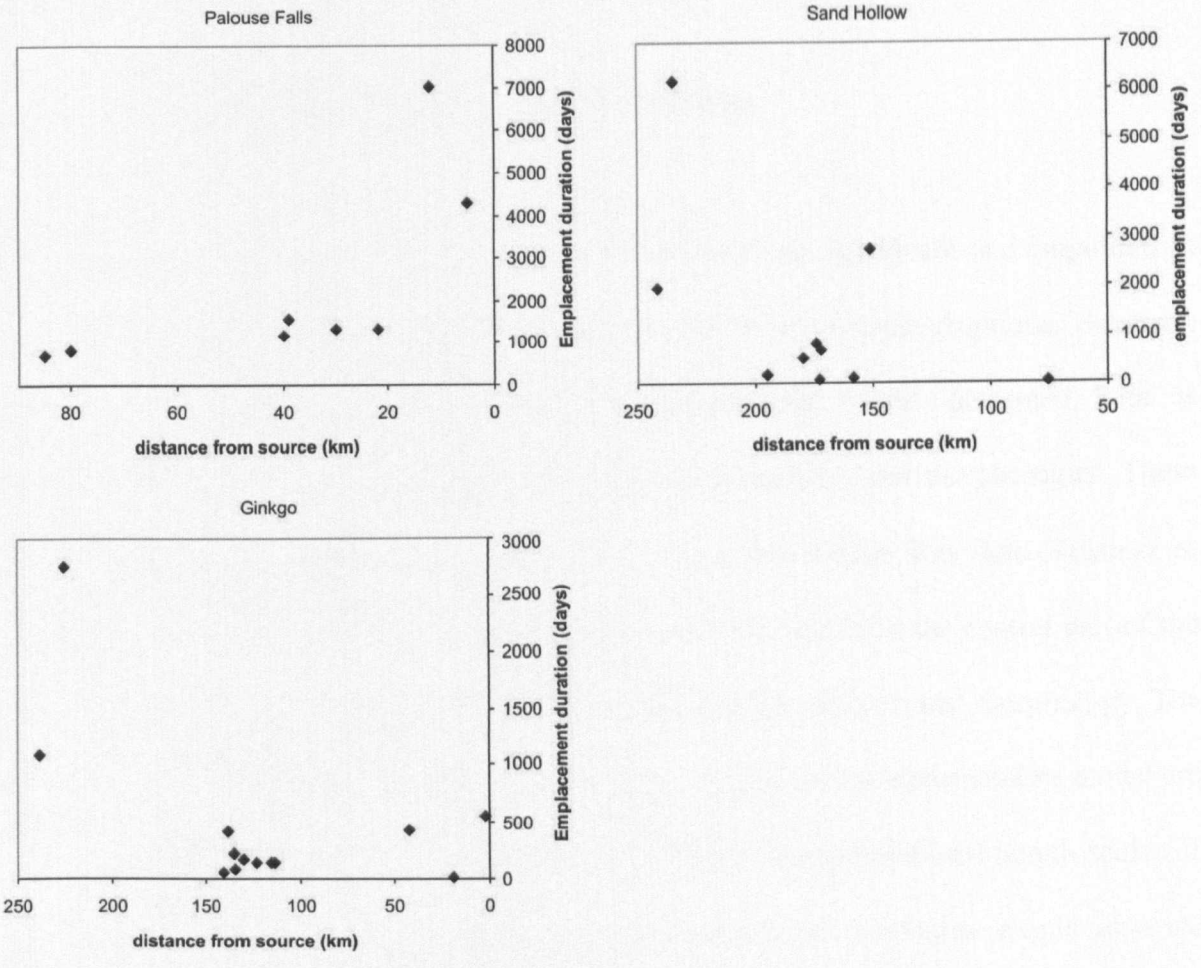

Figure 2.33 Emplacement time calculated from Equation 2.1 derived from (Hon *et al.* 1994), plotted against distance from the vent for each flow field.

Limitations of this method based solely on the rate of cooling include the lack of adjustment for variations in supply rates because the upper crust thickness may not reflect late stage core injection or inflation events, lava ponding or channelised flow. Lobes emplaced under such conditions may have thinner upper crusts due to the retardation of upper crust growth as a result of the flux of hot lava, in a similar way to tube pathways (Hon *et al.* 1994). Despite these caveats, the calculated emplacement times agree with those presented for the 40,350 km^2, 1,300 km^3 Roza flow field of 5 to 15 years (Thordarson 1995; Thordarson and Self 1998). Any quantification of the rate of emplacement is dependent on the number of exposures and the localities used. To fully understand and

quantify the temporal and spatial development of a flow field a three-dimensional appreciation of the flow field morphology is required.

2.6.4 Three-dimensional flow field morphology

The sizes and shapes of lobes constituting a flow field are significant and important in determining the eruptive style and the rate of effusion in flood basalt eruptions. However, these remain poorly constrained. The three-dimensional model presented here is constructed from field observations of lobe extents, boundaries and morphologies. These primary data are combined with existing maps of the extent of each flow field (Tolan *et al.* 1989), partial exposures and borehole data from the Pasco Basin in the central part of the province. This model is based on observations and quantification of lobe morphology. The limitations and assumptions made to facilitate the completion of a representative model are presented in Section 2.6.3.1. The quantification of vertical and horizontal length-scales of features such as lobes associated with known emplacement conditions should improve future interpretations of the conditions required for emplacement by inflation.

The construction of a realistic 3-D model for a flood basalt flow field is significant for sub-basalt imaging related to hydrocarbon exploration. To date, the morphology of basalts has been based on a broad-scale facies architecture approach to subdividing basaltic successions (Jerram 2002; Single and Jerram 2004). Detailed field studies reported in this chapter are the first to characterise a single flow field and provide a new level of detail which may be usefully employed in the understanding of the internal architecture of volcanic successions (Martini *et al.* 2005).

2.6.4.1 Identification of the vent locality

Distances from the source are calculated from a dyke outcrop in the case of the Ginkgo flow field; a dyke proposed by Steve Reidel (*pers comm.* 2006) to be part of the feeder system for the Sand Hollow flow field; and a postulated locality in the case of the Palouse Falls field. The calculated distances from these point sources are linear and do not reflect actual travel distances of lava from the point of eruption. The true flow distance may be greater due to anastomosing or deviated flow patterns. Thus the calculated distances provide a minimum distance.

Dykes identified in the field are used as point sources for the vents of each flow field. These feeder dykes may not be the only vent area as they may represent only a small part of an extensive fissure system which may include several active dyke segments. There are no known alternative dyke outcrops for these flow fields to further constrain this possibility.

The vent location for the Palouse Falls flow field is assumed as no lobes are correlated with this flow field further than 5 km east of the junction of the Palouse Falls and Snake Rivers. A feeder dyke has not been identified for this flow field. It could be suggested that the Palouse Falls was a phenocryst-poor early part of the Ginkgo eruption. However, the occurrence of intervening volcanic ash layers and sedimentary layers, together with reddened lobe surfaces, suggests that these two flow fields formed from separate eruptive episodes, separated by a distinct hiatus.

The Palouse Falls dyke may not outcrop. Other circumstances that may account for the absence of the dyke include: 1.) the feeder dyke system was re-used by a successive eruptions and dykes of Palouse Falls basalt are no longer preserved, 2.) compositional

correlation between dykes and flow fields is not possible due to geochemical variations in the erupted lava during a single eruption, 3.) there are no exposures, 4.) river canyons occupy the site of the dykes, so they are now lost through erosion.

2.6.4.2 Construction of lobes

The areal extent of lobes can be assessed from cross-cutting canyon exposures. The set of northerly trending canyons are roughly perpendicular to the main Snake River canyon which provides excellent exposure through this section of the Palouse Falls flow field. Elsewhere, exposures are limited or absent and the limitations on the accurate depiction of the Sand Hollow and Ginkgo flow fields are great by comparison with the Palouse Falls. Lobe ends are inferred where there is a break in exposure, revealing the underlying flow field, in combination with a progressive variation in the inclination of columns from near vertical to horizontal towards the break (Fig. 2.34).

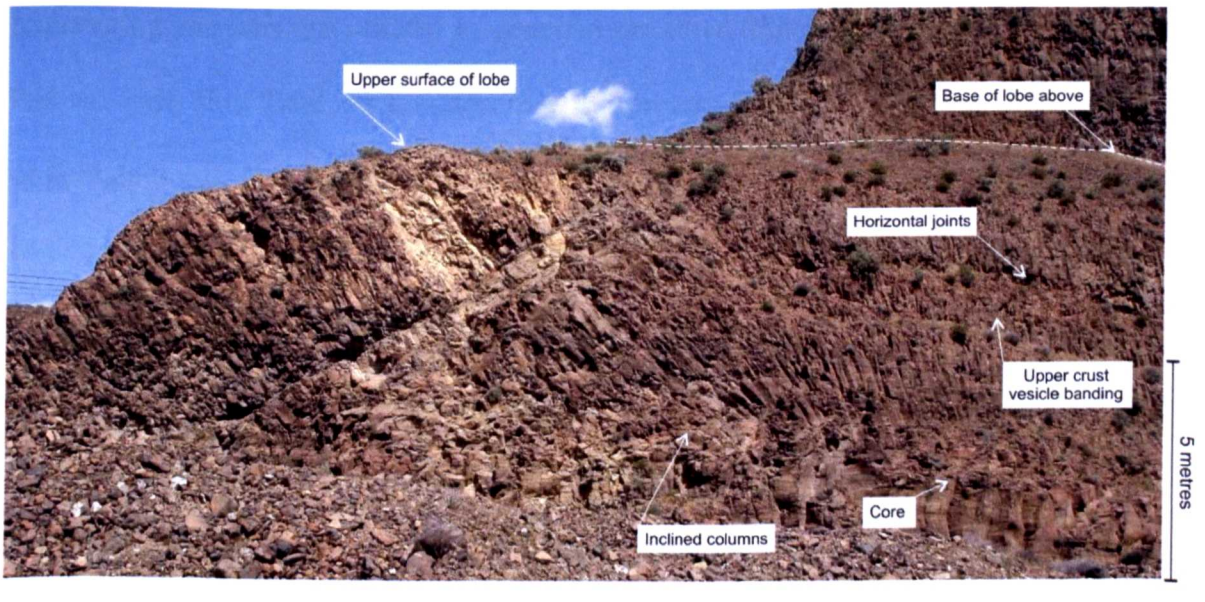

Figure 2.34 Variation in the orientation of columns indicating the termination of a lobe within the Palouse Falls flow field, exposed on the southern bank of the Snake River near Ayer (N46°34.634' W 118°23.349').

In these areas, the break in exposure is interpreted not to be selective erosion of part of a lobe, but preferential erosion of small lobes of a successive flow field. Intersecting canyon exposures are exploited to record the aspect ratios of lobes. The abundance of such outcrops in the Palouse Falls area enables a detailed examination of this flow field. There are fewer outcrops through the flow fields for the Ginkgo and Sand Hollow. Most exposures of these flow fields are limited to two-dimensional cliff-sides.

2.6.4.3 Interpretation of 3-D models

Figure 2.35 illustrates the model constructed using the methods described above for the Palouse Falls flow field.

2.6.4.4 Assumptions and limitations

Various assumptions have been made to produce a model of the Palouse Falls flow field where incomplete exposure prevents observation of all the constituent lobes. Whilst intersecting canyons are utilised to generate the three-dimensional extent of lobes in the Palouse Falls flow field, such exposure is not present in the more extensive Sand Hollow or Ginkgo fields. Hon *et al.* (1994) observed in the Pu-u'Oo and Kupaianaha flow fields on Kilauea volcano that pāhoehoe toes formed on low slopes (<2°) and have lateral flow velocities nearly equal to the forward velocity. This results in toes impinging on adjacent toes before a solid crust can form. This may apply to flood basalt lobes emplaced on a very low slope (generally <1°). Coalescence of these toes forms a single upper crust and a continuous liquid lava core. The resulting lobes will have equal length and width dimensions assuming that the lateral spread of lava occurs at the same rate as the longitudinal development of the field, on an even low slope without obstacles causing a preferential direction to the flow of lava. Where exposures permit, this characteristic has been observed within the Palouse Falls flow field and has been assumed elsewhere.

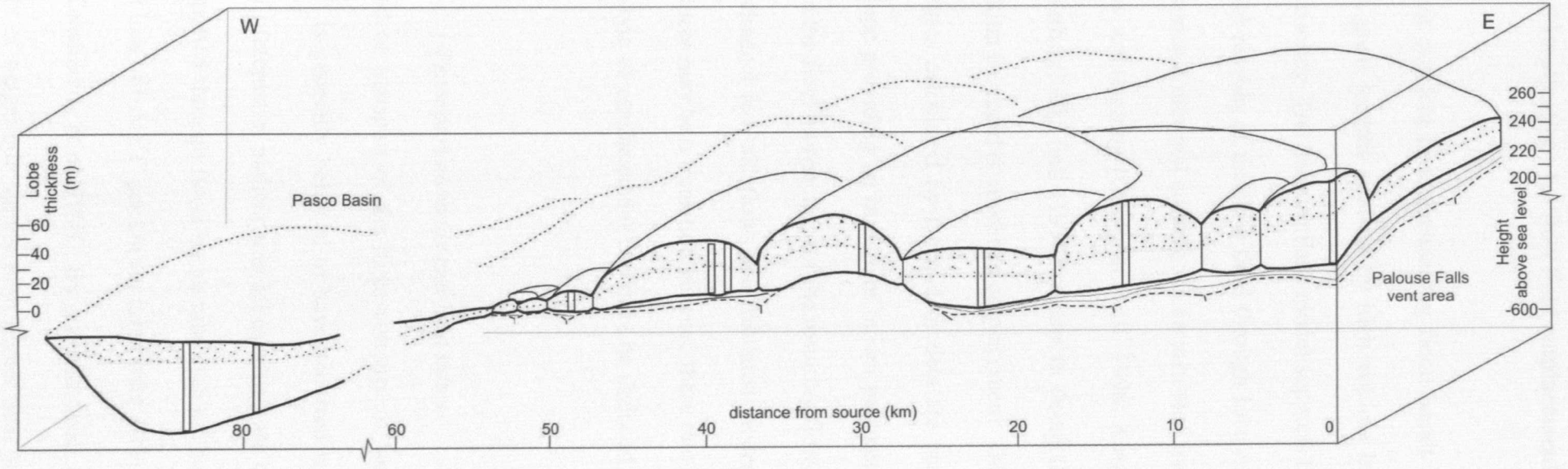

Figure 2.35 Three-dimensional model of the Palouse Falls flow field, extending from the vent area in the east to the distal reaches of the field in the Pasco Basin to the west. Vertical exaggeration is applied to the model to enable display. Actual lobe thicknesses are utilised along with locations and morphology of lobe ends and junctions. Upper crust thicknesses throughout the flow field are shown by the stippled area within each lobe. Underlying sediments and the contact with the Grande Ronde formation are indicated by dashed lines. Vertical bars show the location of the logs characterising the structure of the flow field. Dashed lines denote inferred lobes based on mapped lateral extent (Tolan *et al.* 1989; Heliker *et al.* 2003) to complete the model. The Pasco Basin is shown for reference, it is depressed by 800m relative to the surface outcrop of the remainder of the flow field.

2.6.5 Implications for flow field emplacement models

A significant problem in understanding flood basalt flow field construction has been to explain the great lengths attained by high volume lava flows without them undergoing significant cooling. The Palouse Falls model supports the propagation of lava from the vent area to distal reaches of the flow field through lobe cores. Existing research also suggests heat retention and minimal cooling via an insulated mode of transport but debates over the rate of flow are ongoing (Cashman *et al.* 1998; Keszthelyi and Self 1998; Solana *et al.* 2004). Keszthelyi and Self (1998) review in detail the key parameters influencing flow field formation for rapid or insulated emplacement. The range of effusion rates and channel flow velocities calculated by thermal models are markedly different for either scenario with the slope providing an important model parameter. However, significant differences are noted in the final morphology of the resulting flow. Rapid emplacement produces flows similar to channel fed 'aā' flows and insulated modes as tube-fed or sheet-like pāhoehoe flows. As there may be a transition between these two flow regimes within a flow field, the dominant style of emplacement can only be deduced through an examination of multiple localities.

2.6.5.1 Transport methods and lava tubes

The method of transport of the large volumes of lava in the studied flow fields (500 – 2,660 km^3) is generally believed to have occurred without substantial cooling through a network of preferential pathways in lobes which are no longer inflating (Hon *et al* 1994). Lava transported through flood basalt tube systems has an estimated velocity of 1-2 m/sec with a heat loss of 0.5-1°C per km for tubes over 10 km long (Helz *et al.* 1991; Cashman *et al* 1998; Kauahikaua *et al.* 1998). By contrast, sheet flow advance on Kilauea is noted to be an order of magnitude slower with higher heat loss (5-10°C / km (Hon *et al.* 1994).

According to the observations of Hon *et al* (1994), sheet flows stagnate and form overlapping rather than sequential flow lobes in the absence of tube systems.

The development of lava tubes is understood from laboratory and field data to be a response to an increase in frictional resistance to lava flow as the distance between cooled crusts is reduced due to advance of the solidification fronts. Through the reduction of space, the movement of lava is focused towards the centre of a flow (Hon *et al.* 1994 and references therein). Prior to work by Hon *et al.* (1994), lava tubes were perceived to be the result of roofing of active channels (Greeley 1971). According to the documented evolution of tubes on Kilauea from geoelectrical measurements (Zablocki 1978; Hon *et al.* 1994), the resulting decrease in cross-sectional area increases the lava flow velocity and crustal growth is retarded due to the influx of hot lava. This results in the presence of well-developed tubes within 2-4 weeks of sheet lobe formation. The rapid transport of lava through tubes may account for the occurrence of compositionally similar glasses at the proximal and distal ends of some CRBG flow units (Swanson *et al.* 1975; Mangan *et al.* 1986).

The presence and identification of lava tubes in continental flood basalt provinces remains controversial (e.g. Halliday 2002 and references therein). Tubes have been identified in the Deccan Volcanic Province (Duraiswami *et al.* 2002; Misra *et al.* 2002; Bondre *et al.* 2004; Duraiswami *et al.* 2005), Faroe Islands (North Atlantic Igneous Province (Passey and Bell 2007) and the Parana (Helz *et al.* 2003). However, these are scarce and there are few reports of tubes within flood basalt provinces. It has been suggested that some tubes may be mis-identified elongate or channel confined lobes (Kauahikaua *et al.* 1998; Bondre *et al.* 2004). The radiating joints within the elliptical cross-sections through lobes defined as 'war-bonnets' in The Dalles area of the Columbia River province (N45°41.911'

W121°23.693'), is one example. The radiating columns observed there have been proposed to be similar to the lava tubes observed in flow fields on Hawaii and are the principal feature of contention (Waters 1960; Greeley 1971; Greeley *et al.* 1998; Halliday 2002).

The tubes observed on Hawaii are distinct as they are usually at least partially drained and have an elliptical cross-section (Halliday 2002). By contrast, the conditions such as low slope angles that the CRBG were erupted onto (<2°; Hooper *et al.* 2007) would cause lava tubes to remain filled unless there is drainback near the vent. Any drainback is likely to affect only proximal areas. Lava in the tube crystallizes upon stagnation due to topographic blockage or reduction in lava supply rate and subsequent cooling (Peterson and Swanson 1974). If this is the case, the lack of observed lava tubes may simply reflect the difficulty in distinguishing them from the surrounding basalt succession. Alternatively, it is thought that a discrete tube may not develop in a rapidly emplaced lobe on a near flat surface, if the rate of lava input is sustained (Self *et al.* 1998). In contrast with hummocky pāhoehoe flows emplaced on irregular topography with discontinuous rates of emplacement, the whole sheet lobe may conduct lava from the proximal to distal end. Therefore, the identification of a three-dimensional model depicting the entire flow field permits an understanding of emplacement methods during a flood basalt eruption.

2.6.5.2 Flow field architecture

Published descriptions of sheet lobes have until recently accounted for vast proportions of flood basalt provinces. However, research into the architecture of these provinces (Jerram 2002; Jay 2005) suggests a more complex relationship of lobes than the 'layer-cake' stratigraphy which is often apparent on first inspection. Observations by Hon *et al.* (1994) suggest that a simplified sheet lobe model may be common as lobes genetically related through breakout maintain a fluid connection. Thus new lobes inflate to the same height as

previous lobes and the flow front is obliterated. This simple idea is in keeping with the observations within the Palouse Falls flow field. There are several related implications for the identification of lobes within flood basalt flow fields. First, it may not be possible to identify the initially emplaced lobes. Second, the aspect ratios of lobes may be overestimated due to the mis-identification of lobe geometries. Third, the implied lava supply and spreading rates, which are perceived to be the principal controls affecting lobe advance, may be overestimated.

Where a complicated architecture exists between lobes within a flow field such as that in the Ginkgo flow field, topography is frequently thought to be the dominant control (Beeson *et al.* 1989). Flows can be channelled along depressions such as river channels. However, the inflation of these lobes can result in the inversion of this topography, diverting the successive flow fields. Onlapping lobes from different flow fields creates the complex architecture observed in many provinces (Jerram 2002; Jay 2005; Passey and Bell 2007).

The observations reported within this chapter have been used to build a fence diagram and a three-dimensional model that identify genetic and spatial correlations in flow field development using the tripartite lobe structure. The Palouse Falls model records the propagation of a flow field through progressive emplacement by breakout of frontal lobes and subsequent inflation linking the cores of previously emplaced lobes. This simple linear model does not account for all the variations observed in the Sand Hollow and Ginkgo flow fields. The temporal genetic relationship between lobes constituting these fields remains poorly constrained. Models summarizing the various relationships between lobes in these flow fields are shown in Figure 2.36.

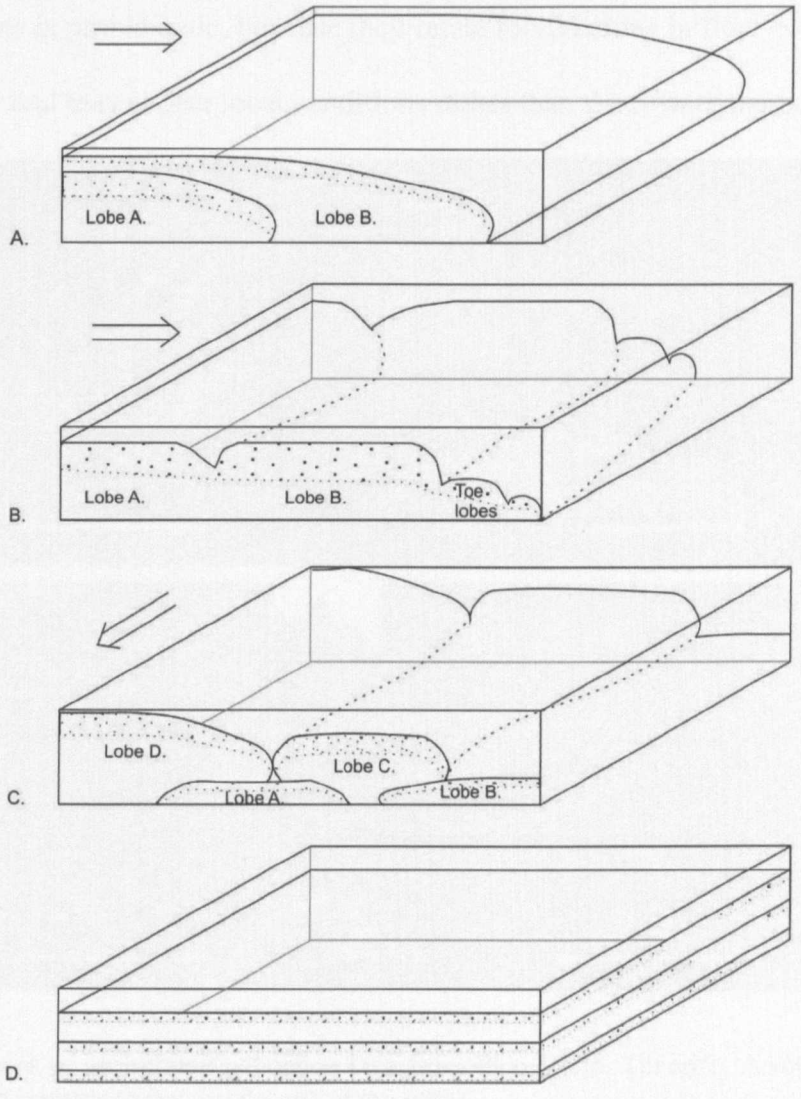

Figure 2.36 Three-dimensional cartoons illustrating the range of relationships of lobes within a flow field. A.) Lateral accretion due to vertical or lateral flow migration. B.) Lateral accretion by front lobe breakout. C.) Successive emplacement of overlapping lobes or topographic inversion by inflation. D.) Uniform lateral aggradation of sheet lobes.

The identification of these models from field observations depends on the nature of the exposure relative to the predominant flow direction. On a small-scale, palaeoflow indicators include the inclination of elongate vesicles and pipe vesicles, textures in megavesicles, pāhoehoe ropes on sheet lobe surfaces and jointing characteristics. Such features have been related to flow direction (Waters 1961; Walker 1987) and have been seem by the author in recent, small-volume inflated pāhoehoe lobes from Teide, Tenerife (Fig. 2.37). The use of these features in deriving flow field propagation directions in flood

basalt provinces is problematic, because they relate to variations in flow conditions caused by topography and may reflect local conditions rather than the flow dynamics of the lobe.

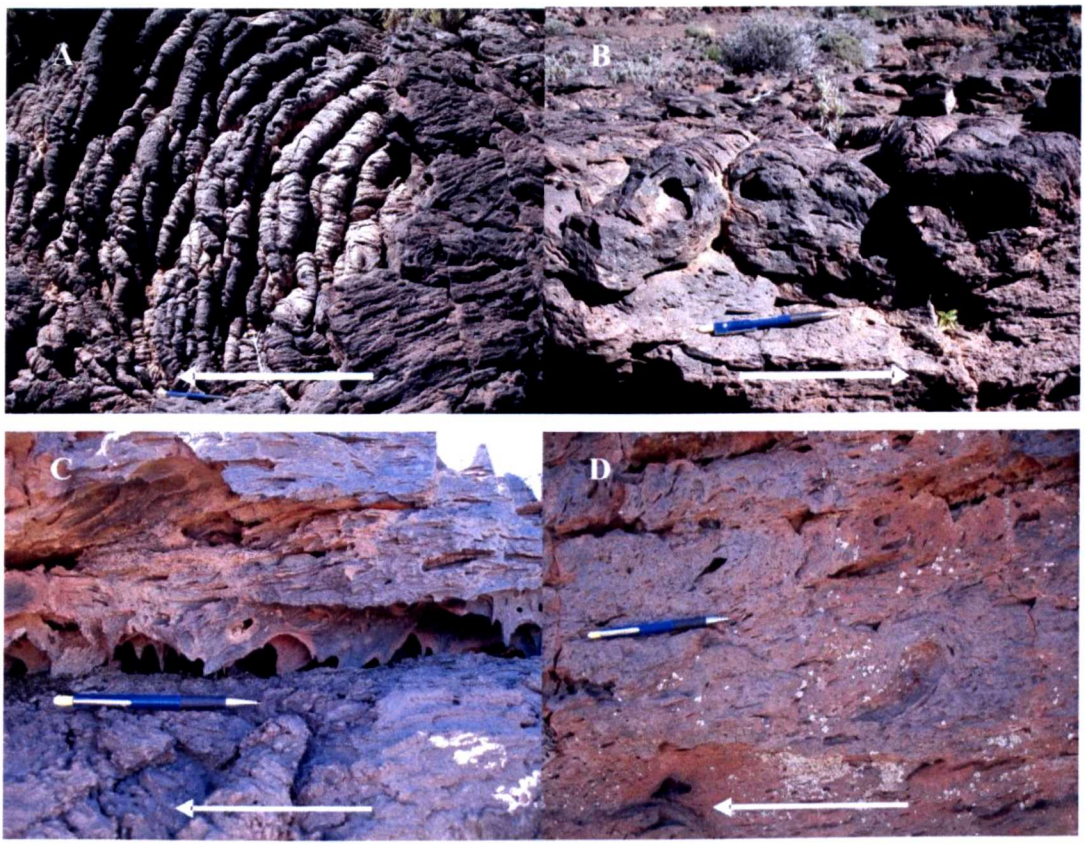

Figure 2.37 Photos of an inflated pāhoehoe lava from Pico Viejo, Tenerife. Arrows indicate flow direction from the source to the distal parts of the lobe.

On a large-scale, thickening of the flow field in proximal regions, like that observed in highly viscous lavas and ignimbrites (Branney and Kokelaar 2002), is only observed in the Palouse Falls flow field. It is likely that a combination of factors prevent the observation of this pattern in the other flow fields. These may include inadequate exposure, non-linear flow field characterisation, and divergence of flow pathways during emplacement, channelisation and topographic inversion. In the case of the Palouse Falls, all the lobes observed are genetically related across the flow field by linked lobe cores. Thus the process controlling thickening implies compression parallel to the lava transport direction (Iezzi and Ventura 2000), which in the case of basaltic flows is mainly controlled by magmatic pressure (Bruno *et al.* 1994).

2.7 Conclusions

- The Columbia River flood basalt eruptions that produced these three flow fields were voluminous (up to 2,660 km^3). The lavas have pāhoehoe and rubbly pāhoehoe surface morphologies and internal structures characterised by a three-tiered division comprising lower crust, lava core and upper crust. This structure is similar to that of smaller inflated pāhoehoe lobes on Hawaii, Tenerife and that seen in other flood basalt provinces.

- The inflation model appears to be the most satisfactory mechanism for emplacement of the lavas. The field observations suggest that small flow fields develop thicker lobes near the vent, thinning with increasing distance from the vent with small precursor or toe lobes in the distal reaches of the field. In small flow fields (<100 km across) such as the Palouse Falls, many lobe cores are physically linked, despite separate upper crusts, indicating the last emplaced lava in each lobe simultaneously inflates related lobes. A single simple group of lobes with linked lobe cores may be considered to be one lava flow within the flow field.

- All three flow fields can be traced across the Columbia River province over distances of ~ 240 km. Such high-resolution correlation of single eruptions based on physical parameters may not be feasible in other provinces, or where the duration of any hiatus between eruptions are too short to separate single eruptions from a succession.

- The 3-D characterisation of a flow field derived here potentially provides the closest analogue to off-shore seismic interpretations. This is particularly relevant for provinces such as the North Atlantic Igneous Province, and may aid interpretations of flow field morphology and help address the sub-basalt imaging problems in characterisation of long lava flows.

- This chapter provides some of the first data on the morphology and lateral extent of lobes within a flow field. The field observations reported reveal lobes that range in diameter from 0.2 to 10 km.
- The variation in the thicknesses of the upper crust and core indicates both a longer duration of inflation in the proximal lobes and a thicker lobe core, suggesting that the magmatic pressure driving inflation was higher nearer the vent.
- Model calculations suggest that the maximum duration of the Palouse Falls eruption varies from 1.9 to 19.2 years. The implications for emplacement of lava over a near-flat surface from a long duration flood basalt eruption arising from the construction of this model are that proximal sheet lobes transport lava through lobe cores to the distal margins of a flow field without developing physically identifiable lava tubes.
- Longer duration and higher volume eruptions generate more complex flow fields where the genetic and spatial development of the flow field cannot be disentangled using field observation alone.

The work presented in this chapter provides a relative temporal and spatial physical volcanological framework against which a detailed geochemical study of variation across flood basalt flow fields is compared in Chapter 3.

2.8 Further work

Identification of the physical volcanological structure and morphology of a single flow field may be developed in the future towards a detailed facies architecture approach to subdividing flood basalt provinces. It is hoped that such an approach will facilitate the comparison of eruptions throughout the history of a province, and eventually between different flood basalt provinces. This may have important implications for research into the size, style and duration of flood basalt eruptions.

Vantage cliffs on the east side of the Columbia River looking south

Chapter 3. Major and trace element compositional heterogeneity

3.1 Introduction

The geochemical signature of flood basalts is frequently used as a petrogenetic tracer of magmatic processes and source characteristics (Lassiter *et al.* 1995; Ali *et al.* 2005; Reichow *et al.* 2005) with province-wide geochemical variations informing changes in the role of source components (e.g. Mahoney *et al.* 2000). Investigations utilising broad-scale geochemistry are common. Whilst small-scale compositional variation within individual volcanoes and felsic eruption units is well documented (e.g. Hildreth 1983; Sumner and Branney 2002; Carrasco-Nunez and Branney 2005), reports of similar small-scale variation in mafic units are scarce. Potential variations within a single flood basalt flow field and the use of such information to provide insight to the assembly of the flow field have remained little explored. In addition, small-scale geochemical variations can provide insights to potential changes in source composition and eruption dynamics.

A number of implications arise from the relative homogeneity or heterogeneity of large volume flow fields that relate to the petrogenesis of magmas in continental settings. Uniform geochemical compositions imply a common source for basalts (Hooper 2000). Compositionally similar glasses found near vents and at the distal ends of some flow fields has been used to support the idea of rapid transport of lava within tube systems (Swanson *et al.* 1975; Mangan *et al.* 1986). Examples of flow fields or formations within flood basalt provinces with uniform chemistry include the Faroe Islands Basalt Group of the North Atlantic Igneous Province (Waagstein 1988; Larsen *et al.* 1999) and the Pomona flow field in the CRBG (Hooper 2000).

If a flood basalt eruption produces lavas that are homogeneous in composition it follows that the processes that generate such large volumes of magma are unlike those that govern magma genesis in other volcanic settings. Hooper (2000) suggests that compositional homogeneity of large volumes of magma reflects one of two possible processes: a) huge crustal level magma chambers with efficient convection that homogenises the effects of crystal fractionation and crustal assimilation processes (Griselin *et al.* 1997); or b) primary melts from iron-rich mantle derived from mantle plumes with significant components of subducted basaltic crust (Wright *et al.* 1989; Cordrey *et al.* 1997; Takahahshi *et al.* 1998). Thorough characterisation of any potential compositional heterogeneity within a single flow field is required to avoid unnecessary explanations for the genesis of large-volume homogeneous melts.

This chapter presents a detailed study characterising geochemical variation within and between constituent lobes of a flow field formed during one eruption. Major and trace element variations are compared to physical features observed in the field. This is then assessed for the significance of any geochemical variations. Using this method I investigate the presence and extent of heterogeneity from a vent area to more distal parts of a flow field, looking for variations within and between lobes. I have focused this work on the Palouse Falls, Sand Hollow and Ginkgo flow fields of the Wanapum Formation. Variations in composition are then related to eruption sequence to examine their origin. Finally, geochemical variations are used to provide an insight into the petrogenesis of magma(s) tapped during the lifespan of a single eruptive episode.

3.1.1 Existing research on compositional heterogeneity

There is variable evidence published for and against compositional homogeneity or heterogeneity of individual basaltic lava flows. Compositional heterogeneity has been

documented in some historical long lava flows (Watkins *et al.* 1970; Lindstrom and Haskin 1981; Maclennan *et al.* 2003; Spiegelman and Kelemen 2003), however, homogeneity of individual flood basalt eruptions is still claimed to be a common feature (Hooper *et al.* 2007). Until this present research most CRBG flow fields were believed to show limited compositional variation and be relatively uniform (Hooper and Camp 1981; Reidel 1983), with only a few lavas showing significant variations (Waters 1961; Wright *et al.* 1973; Swanson and Wright 1981; Reidel and Fecht 1987; Martin 1989; Martin 1991; Reidel 2005). A consensus has not been reached on either the cause of, or processes responsible for, these geochemical variations.

Variations within the Roza flow field are attributed to the simultaneous or subsequent eruption of lava from separate fissure segments with each eruption represented by a different chemical subtype (Martin 1991). Heterogeneities within flow fields from the Grande Ronde Formation have been interpreted as the result of either post-eruption flow emplacement conditions including thermal erosion and mixing of juxtaposed liquid lava flows (Reidel 2005) or in-situ differentiation and crystal settling (Philpotts and Philpotts 2005 and references therein).

Other flood basalt provinces from which intra-lava compositional variations have been observed include the Faeroe Islands (Jensen 1980), MORB (Rubin *et al.* 2001; Spiegelman and Kelemen 2003) and the Karoo province (Richardson 1979). These studies have focused on either compositional variability across a flow field i.e. sampling the same horizon across the flow field, such as the upper crust (Rubin *et al.* 2001; Maclennan *et al.* 2003), or vertical variations comparing the constituent members of a province (Richardson 1979; Jensen 1980; Philpotts 1998; Reiners 2002). The only existing research to combine

both these approaches is the sampling suite from the Roza flow field within the CRBG (Martin 1989; Martin 1991).

These previous studies provide a number of interpretations of processes that can account for heterogeneity. One explanation involves no quantifiable physical process and the composition is a factor of random variation (Lindstrom and Haskin 1981). Controls on composition have been identified as pre-eruptive source conditions, eruption conditions and post-eruption processes such as in-situ differentiation and contamination (Hartley and Thordarson 2009 in press). Existing literature on small-scale compositional variations concentrates on the possible causes of heterogeneity. However, the spatial and temporal extent of compositional heterogeneity within single eruption products remains unknown.

An inherent problem in attempting to associate any observed changes in melt chemistry to eruption sequence in flood basalt provinces has been the lack of a suitable physically-defined eruption unit or flow field. The difficulty is in identifying, unambiguously, a single flow field in an otherwise monotonous succession of rather similar-looking basaltic lavas. Application of the inflation model reported in Chapter 2 offers the first opportunity to resolve these outstanding issues. This chapter seeks to compare the relatively simple well-constrained physical emplacement and linear evolution of the Palouse Falls lava with the more extensive, less well-constrained Sand Hollow and Ginkgo flow fields. This approach will characterise variation within an initial simple flow field, and then apply the same technique to more complex flow fields. It will go on to test whether any further insight to the style of emplacement can be determined from such an approach.

3.2 Sampling methodology

The sampling strategy was based on physical lobe characteristics, defined by the inflation model (Self *et al.* 1997) and described in detail in Chapter 2. Samples were taken at regular intervals within each vertical section of each of the flow fields. The intervals typically range from 1 to 5 metres according to the physical features that characterise each locality. An example of the sampling strategy applied to most localities is shown in Figure 3.1.

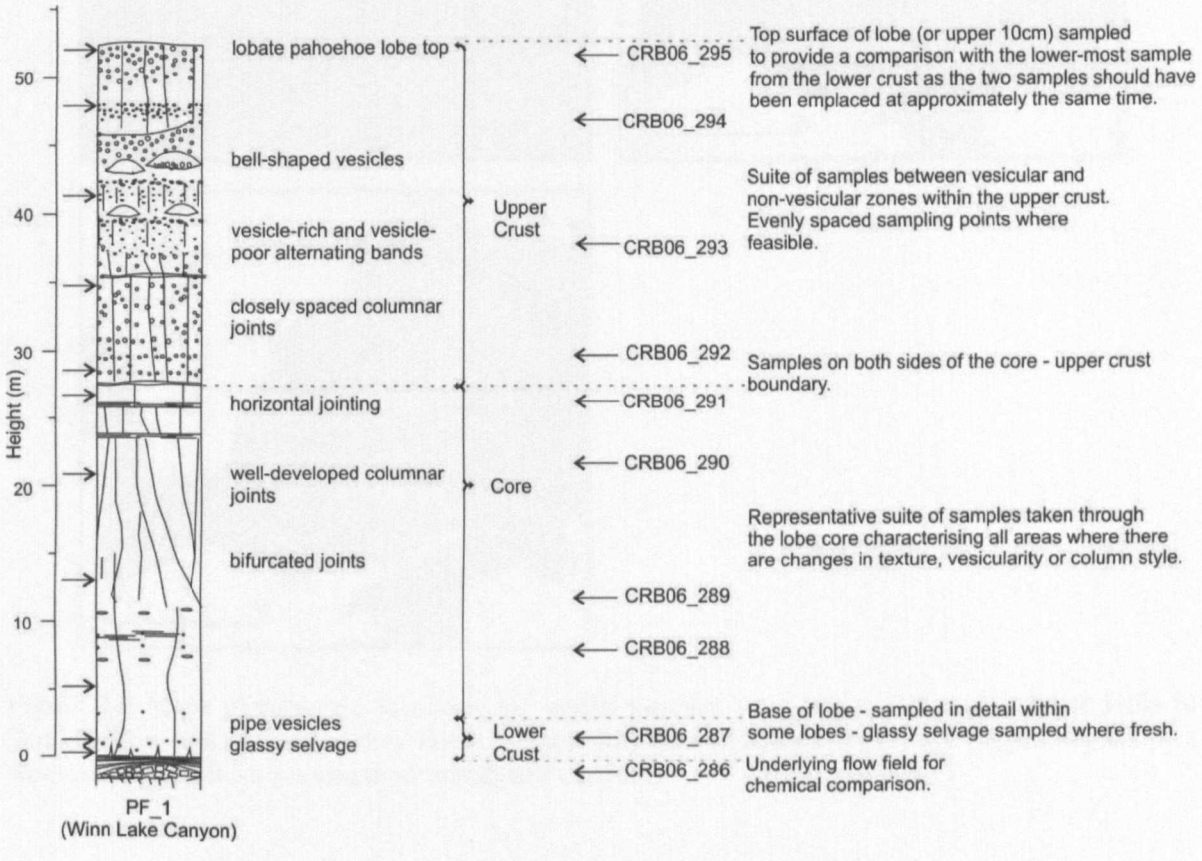

Figure 3.1 A typical log for a sampling site. Text in the column to the right gives an example of the justification used for the choice of sampling. Additional samples were collected for specific small-scale studies and are described later within this chapter.

Within the Palouse Falls flow field eight vertical sections were logged in the field along a near continuous outcrop from a source-proximal position to the distal reaches of the flow field (Fig. 3.2). Systematic sampling at 2 metre vertical intervals was conducted within one lobe of the Palouse Falls flow field to ensure no bias was introduced by the sampling interval. A subset of the localities defining the Sand Hollow and Ginkgo flow fields were

also sampled and analysed (Figs. 3.3 to 3.5). Further information on the localities of all samples collected are presented in Appendix A.

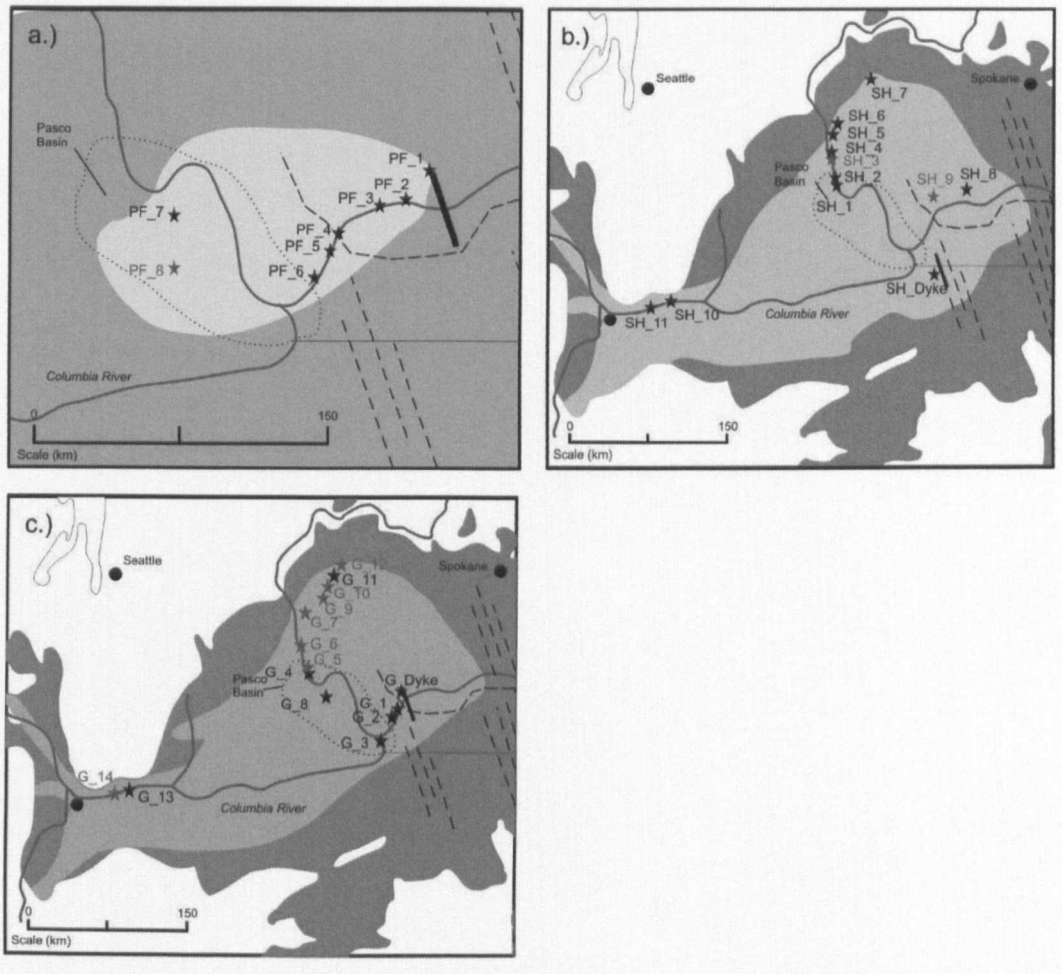

Figure 3.2 Maps plotting the localities for which samples were analysed for a) Palouse Falls b) Sand Hollow and c) Ginkgo flow fields. Sample localities indicated in grey are logged but samples were not analysed for presentation within this chapter.

The average sample size collected was 500g and altered rock was avoided. Samples were split to remove weathered or joint faces and powdered in an agate mill. Sample sizes of at least 300g were used to produce a homogeneous powder representative of the whole-rock sample. The quench cooled, glass-rich samples are finely crystalline in nature and lack phenocryst phases, and thus minimise sample heterogeneities ensuring analytical reproducibility. Major and trace element analyses were obtained by XRF on a wavelength dispersive ARL 8420 spectrometer at the Open University. A full methodology of the sample preparation and analyses employed in this study is provided in Appendix B.

Palouse Falls Flow Field

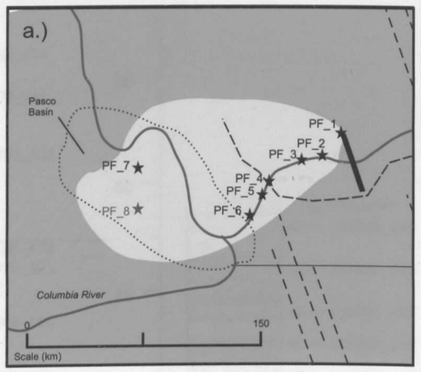

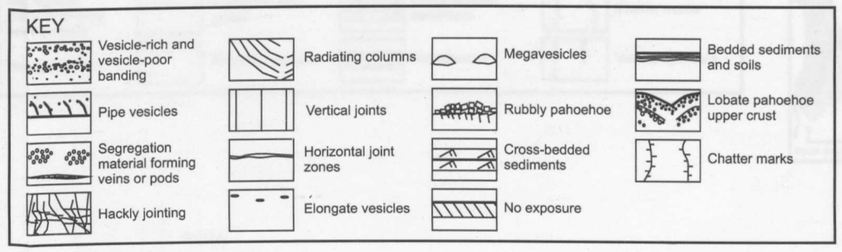

DISTAL
Pasco Basin

PROXIMAL

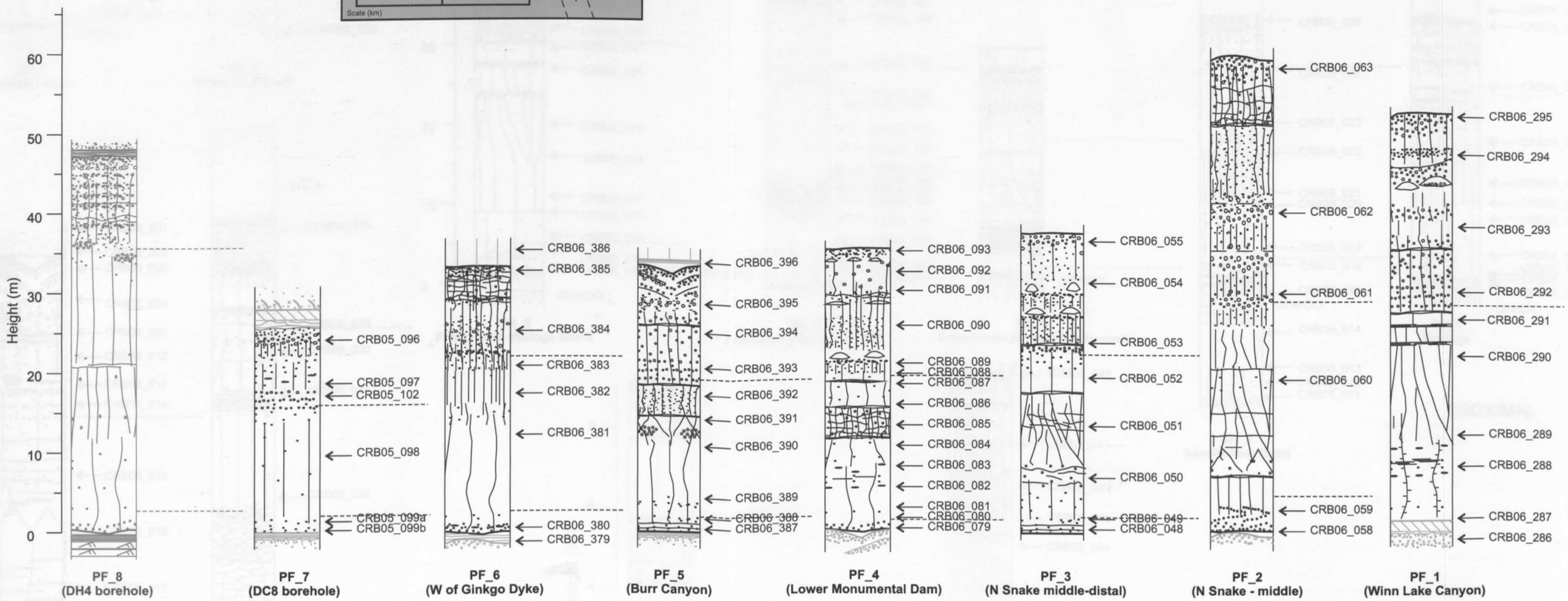

Figure 3.3 Sample localities within each vertical section of the Palouse Falls flow field

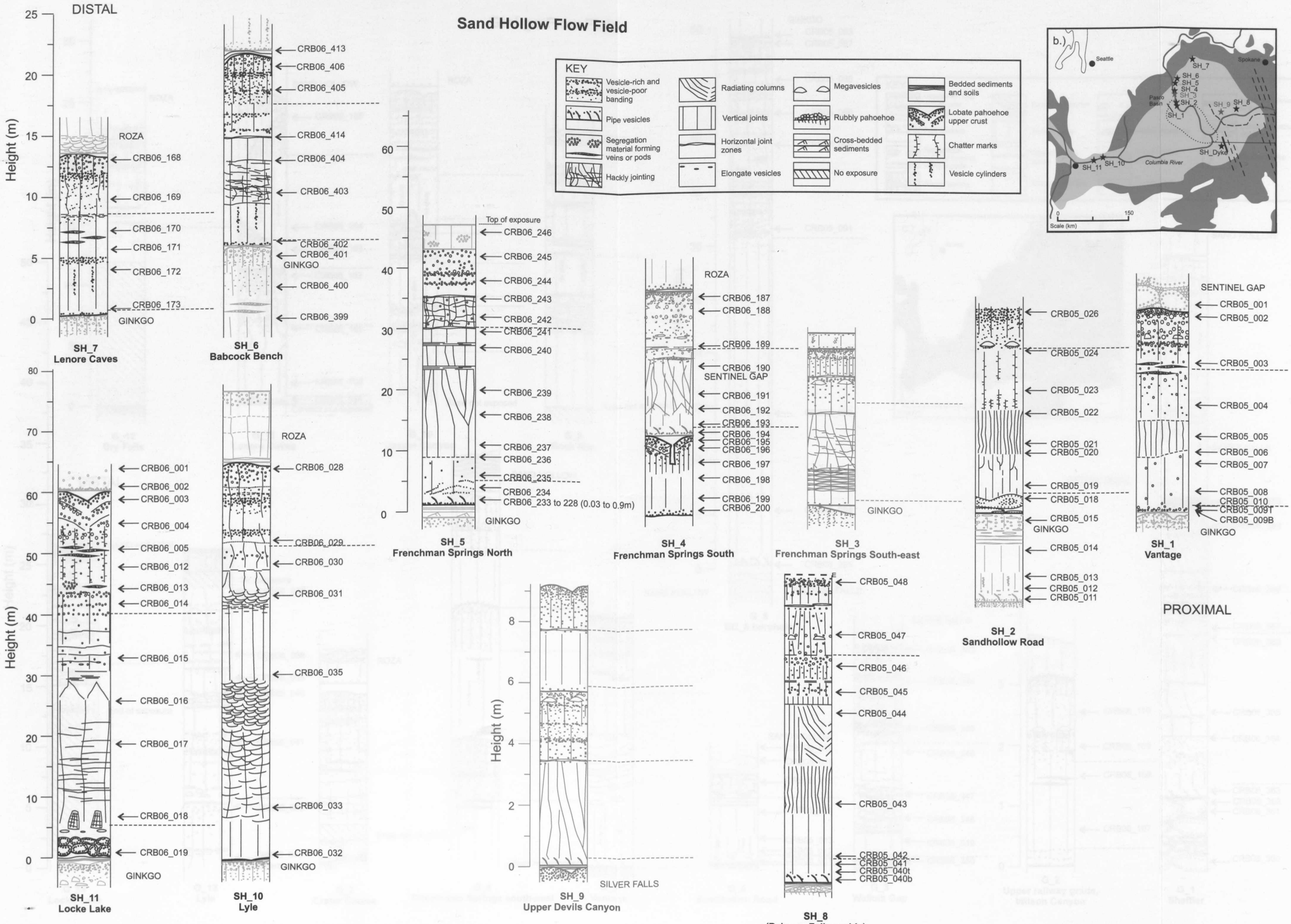

Figure 3.4 Sample localities within each vertical section of the Sand Hollow flow field

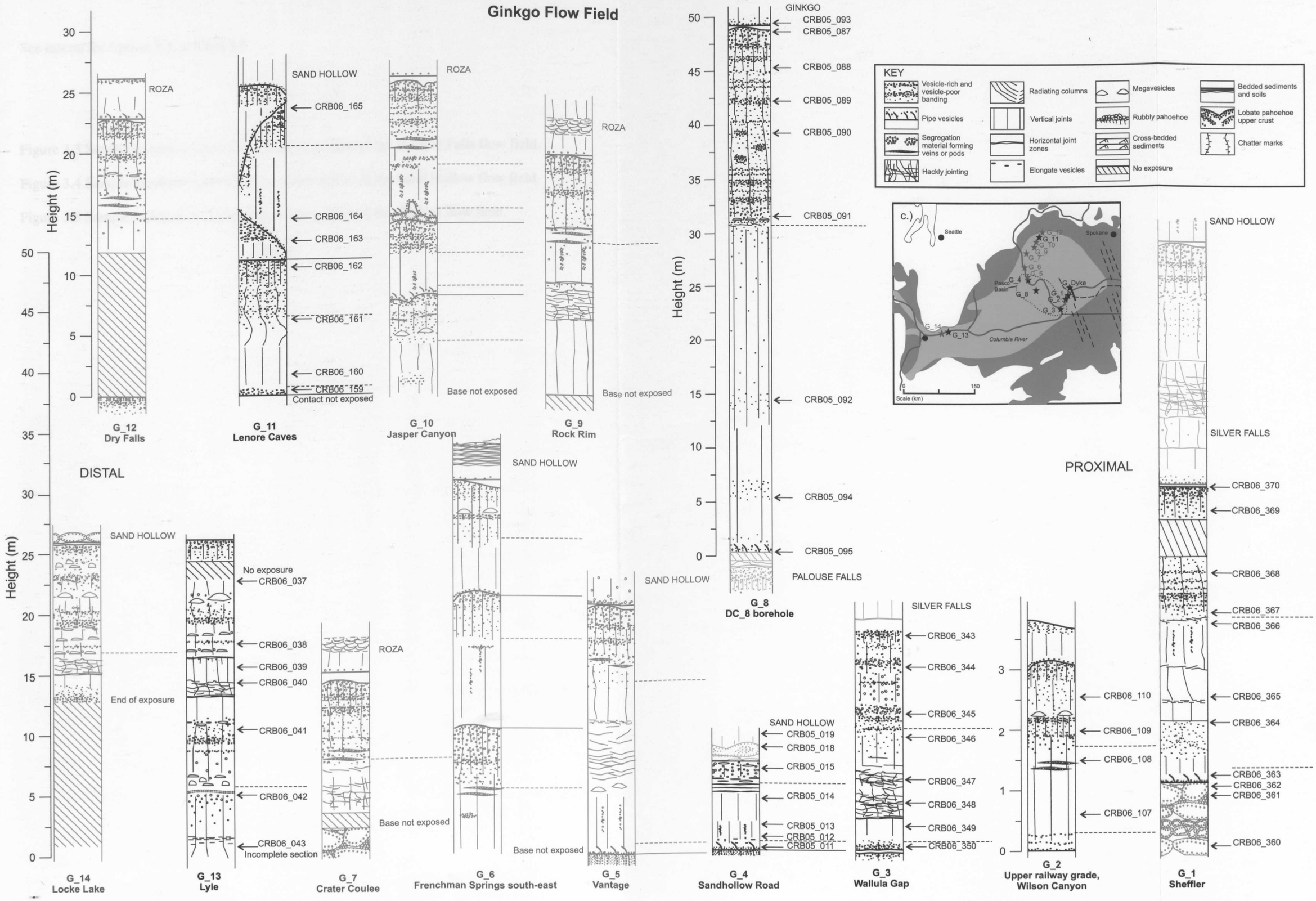

Figure 3.5 Sample localities within each vertical section of the Gingko Falls flow field

See inserts for figures 3.3, 3.4 and 3.5.

Figure 3.3 Sample localities within each vertical section of the Palouse Falls flow field.

Figure 3.4 Sample localities within each vertical section of the Sand Hollow flow field.

Figure 3.5 Sample localities within each vertical section of the Ginkgo flow field.

3.3 Chemostratigraphy

Geochemical studies to assess melt source, evolution and emplacement of flood basalts commonly employ a single sample-per-exposure technique (e.g. (Sweeney *et al.* 1994; Takahahshi *et al.* 1998; Sheth *et al.* 2004). This sampling resolution is then used to construct a chemostratigraphy of the volcanic succession. Flow fields and feeder dykes constituting the CRBG have been identified, correlated and traced across the plateau for hundreds of kilometres based on their chemical composition (Wright *et al.* 1973; Tolan *et al.* 1989; Hooper and Swanson 1990; Reidel and Tolan 1992; Hooper 2000). Numerous analyses throughout the stratigraphy enable a thorough classification of the composition of all formations within the CRBG (e.g. Hooper 2000 and references therein). Plots of TiO_2 versus P_2O_5 emphasise the principal differences between the CRBG formations such as the 'Ti gap' separating the Wanapum Formation from older formations (Fig. 3.6). Whilst further plots including SiO_2 / K_2O, Zr / Sr, SiO_2 / P_2O_5 and Cr / TiO_2 have been used to subdivide some formations to the level of individual flow fields, it is acknowledged that eruption units of the Wanapum Basalt are difficult to subdivide on this basis (Hooper 2000).

The successful application of a chemostratigraphic approach to the classification of a stratigraphy is dependent on the isolation of chemical subtypes of basalts which define distinct eruptive phases. It is also essential to acknowledge the possibility that the chemical signature of an individual flow field may not be unique. However, the use of a chemical mapping approach requires the assumption that individual flow fields are chemically homogeneous and the differences between them are a reflection of consistent variations through the stratigraphy. Heterogeneity within a single flow field would question the validity of chemostratigraphy as a standalone method in discriminating individual flow

fields where variations are subtle. The remainder of this chapter will present the results from three flow fields that have been identified in the field using physical parameters rather than chemostratigraphic techniques. These results will be used to assess compositional heterogeneity and review the use of chemostratigraphy within the Wanapum Formation.

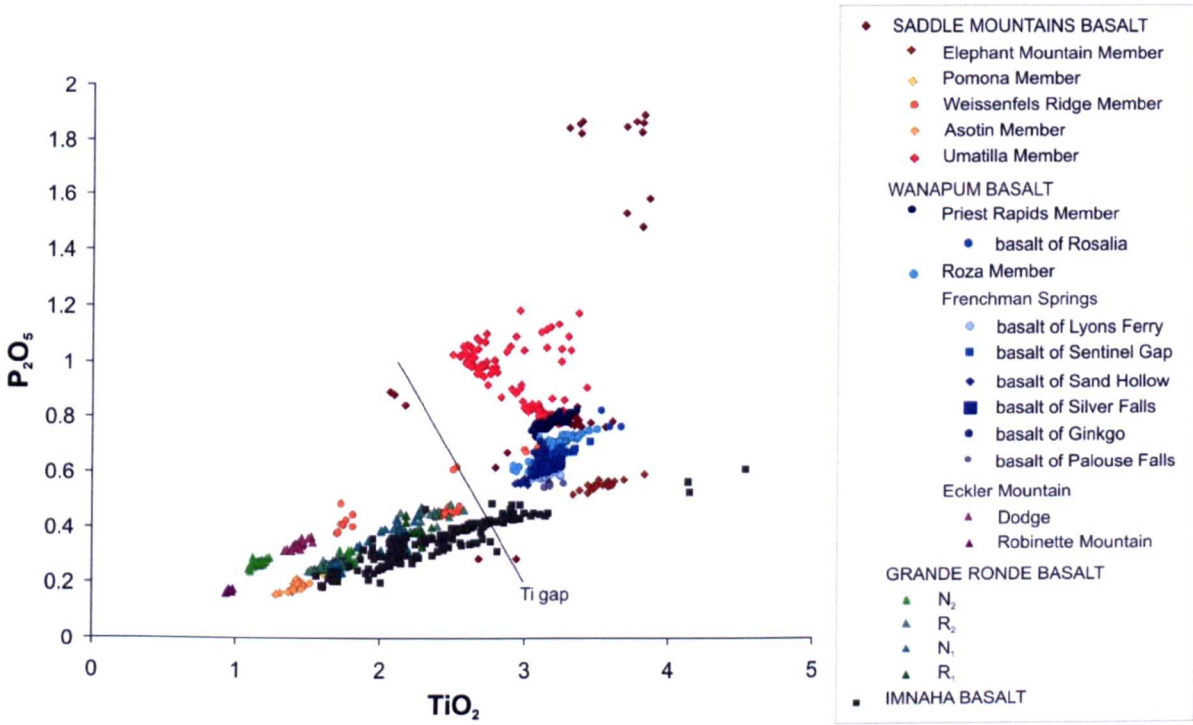

Figure 3.6 Compositional variation throughout the CRBG used to define the province stratigraphy, compiled from Hooper (2000). The 'Ti gap' of Seims *et al.* (1974) and Hooper (2000) separates formations. In accordance with the presentation of data in Hooper (2000) results for samples from this study are plotted using data re-calculated to 100 wt%.

3.4 Statistics and uncertainty

Before investigating the extent and causes of geochemical variation, consideration must first be given to analytical reproducibility. This is essential in order to establish the significance of any variations and provide confidence to the extent to which the cause of small scale compositional variation may be reliably calculated.

3.4.1 Analytical precision and accuracy

Analytical error and variance of the XRF data is calculated from multiple analyses of international standard powders (WS-E and OUG94) and repeats of each bead or pellet within each sample batch (Tables 3.1 and 3.2 with a full set of results presented in Appendix C). Repeat analyses are essential for the identification of any variance inherited from analytical variance rather than from real sample compositional heterogeneity.

	WS-E (n=28)				OUG94 (n=28)			
	mean average [a]	sum of square residuals (S) [b]	Std Dev [c]	Std Error [d]	mean average [a]	sum of square residuals (S) [b]	Std Dev [c]	Std Error [d]
SiO_2	51.06	0.31	0.106	0.020	69.92	0.31	0.106	0.020
TiO_2	2.43	0.01	0.021	0.004	0.31	0.00	0.004	0.001
Al_2O_3	13.89	0.03	0.033	0.006	14.63	0.05	0.043	0.008
Fe_2O_3	13.15	0.01	0.022	0.004	3.04	0.00	0.007	0.001
MnO	0.17	0.00	0.002	0.000	0.08	0.00	0.001	0.000
MgO	5.56	0.02	0.026	0.005	1.05	0.00	0.010	0.002
CaO	9.01	0.03	0.032	0.006	1.37	0.00	0.012	0.002
Na_2O	2.46	0.01	0.019	0.004	4.60	0.03	0.031	0.006
K_2O	0.99	0.00	0.005	0.001	2.97	0.00	0.011	0.002
P_2O_5	0.30	0.00	0.003	0.001	0.17	0.00	0.002	0.000

Table 3.1 Collated results of repeat analyses for major elements from international standards WS-E and OUG94.

[a] Average values for each element are calculated from the mean of 28 analyses.
[b] The residual value is the difference between each measurement and the mean value for the dataset. These values are squared and added together for each element in turn to produce 'S'.
[c] Standard Deviation is calculated from $StdDev = \sqrt{S/N}$ where N is the number of analyses conducted.
[d] Standard Error is calculated from $E = \frac{1}{\sqrt{N}} StdDev$

The standard error (Std error) is a measure of analytical precision. The calculated values are small and reflect a high number of repeat measurements. The calculated standard deviations for each element are used for error bars on all graphical plots in the remainder of this thesis.

	BHVO-1 (n=22)			
	mean average	sum of square residuals (S)	Std Dev	Std Error
Rb	9.60	7.45	0.582	0.124
Sr	403.48	53.90	1.565	0.334
Y	27.69	12.42	0.751	0.160
Zr	177.89	18.44	0.915	0.195
Nb	18.43	11.47	0.722	0.154
Ba	139.21	611.63	5.273	1.124
Pb	1.85	60.57	1.659	0.354
Th	1.81	33.06	1.226	0.261
U	0.16	12.75	0.761	0.162
Sc	31.89	49.92	1.506	0.321
V	313.05	573.30	5.105	1.088
Cr	290.87	192.90	2.961	0.631
Co	44.58	61.15	1.667	0.355
Ni	120.80	187.20	2.917	0.622
Cu	137.67	106.88	2.204	0.470
Zn	103.56	29.47	1.157	0.247
Ga	21.75	14.99	0.826	0.176
Mo	0.57	8.53	0.623	0.133
As	0.94	131.55	2.445	0.521
S	130.46	503.55	4.784	1.020

Table 3.2 Collated results for the standard deviation and standard error for trace elements from international standard BHVO-1. Average values for each element are calculated from the mean of 22 analyses. The calculations applied are the same as those described in Table 3.1.

3.4.2 Existing methods for quantifying significant variations

Two existing studies on small-scale compositional heterogeneity have applied methods to quantify any given geochemical variance within lava flows and therefore be able to quantitatively assess its significance (Rubin *et al.* 2001; Maclennan *et al.* 2003). The first attempt to quantify chemical heterogeneity was based on samples from Mauna Loa, Hawaii, using a calculation known as the 'homogeneity index' (HI) (Rhodes 1983). Application of the HI uses the results of multiple elements and oxides normalised to their analytical precision to quantify heterogeneity relative to analytical variance. The HI is defined as:

$$HI = \frac{\sum(S_i)/(P_i)}{n}$$

Where S_i is the standard deviation (2σ) about the mean, P_i is the analytical precision for element i, and n is the number of elements used in the calculation. Analytical precision is quantified from replicate analyses as described in section 3.4.1. Homogeneity index values of ≤ 1 indicate that no compositional heterogeneity can be identified outside analytical

variance. Rubin *et al.* (2001) applied the HI method to 10 MORB flow fields and refers to the HI as the 'heterogeneity index', a more appropriate name for a method of quantifying significant compositional heterogeneity that is adopted hereafter. Application of the HI as a quantitative measure offers the opportunity to investigate the variation of multiple elements as a function of distance and position within a flow field. HI values for each flow field are shown in Tables 3.3, 3.4 and 3.5.

PALOUSE FALLS

Location Name		Winn Lake Canyon	Joso lobe	N Snake - middle	N Snake - middle-distal	Lower Monumental Dam	Burr Canyon	W of Ginkgo Dyke	DC8
Log reference		PF_1	-	PF_2	PF_3	PF_4	PF_5	PF_6	PF_7
Grid reference		N46.38.516' W118.12.230'	N46.37.097' W118.13.116'	N46.36.635' W118.19.402'	N46.35.719' W118.28.847'	N46.33.640' W118.32.874'	N46.30.900' W118.36.444'	N46.27.664' W118.37.781'	N46.28.489' W119.23.125'
Samples analysed		n = 9	n = 4	n = 6	n = 8	n = 14	n = 10	n = 6	n = 5
Element	Analytical precision P_i (2σ)	S_i (2σ)	S_i (2σ)	S_i (2σ)	S_i (2σ)	S_i (2σ)	S_i (2σ)	S_i (2σ)	S_i (2σ)
SiO_2	0.212	0.469	0.148	0.358	0.678	0.383	0.522	0.582	0.890
TiO_2	0.042	0.101	0.010	0.062	0.070	0.080	0.082	0.035	0.050
Al_2O_3	0.066	0.136	0.040	0.119	0.120	0.123	0.425	0.123	0.170
Fe_2O_3	0.044	0.292	0.105	0.296	0.245	0.384	0.989	0.234	0.664
MgO	0.051	0.085	0.060	0.139	0.101	0.106	0.205	0.354	0.450
CaO	0.065	0.157	0.066	0.135	0.091	0.188	0.383	0.215	0.263
K_2O	0.010	0.166	0.064	0.087	0.210	0.125	0.268	0.152	0.223
P_2O_5	0.007	0.016	0.005	0.011	0.022	0.010	0.026	0.007	0.022
Rb	1.164	4.910	1.135	4.231	7.530	5.043	6.346	2.311	7.878
Sr	3.130	5.371	4.344	5.543	4.990	7.543	16.239	5.564	4.540
Y	1.503	0.704	1.135	0.311	0.822	0.534	0.843	0.993	1.258
Zr	1.831	12.032	2.053	1.754	6.560	3.571	3.976	2.584	5.473
Nb	1.444	1.307	0.263	0.305	0.884	0.626	0.694	0.601	1.197
Ba	10.545	56.930	20.311	35.067	31.924	22.601	43.362	46.786	84.308
Sc	3.013	4.127	1.812	1.278	2.987	1.654	2.159	1.550	1.868
V	10.210	13.693	2.650	23.207	12.321	11.562	24.836	14.228	17.916
Cr	5.922	2.308	1.283	9.265	6.333	4.323	2.389	2.225	3.399
Co	3.334	2.107	1.303	2.151	1.666	4.073	1.655	2.110	1.824
Ni	5.834	4.641	0.804	2.124	1.971	2.956	1.440	1.899	1.664
Cu	4.408	5.328	0.532	2.156	3.510	1.805	1.857	1.183	1.625
Zn	2.315	5.254	1.931	2.761	7.205	8.140	4.833	4.969	10.885
HI		3.020	1.048	2.085	3.019	2.513	4.676	2.538	4.320
Distance from vent (km)		5	6	12	22	30	39	40	80

Table 3.3 Mean average results for all samples within each lobe of the Palouse Falls flow field, standard deviation about the sample means within each lobe and standard deviation of the analytical precision calculated from reproducibility analyses of WS-E for major oxides and BHVO_1 for trace elements, used to calculate the HI value for each lobe.

SAND HOLLOW Location Name		Dyke	Black Band Zone	Sand Hollow Road	Vantage	FSC S	FSC N	Babcock Bench	Lenore Caves	Palouse Falls Rapids	Lyle	Locke Lake
Log reference		-	-	SH_2	SH_1	SH_4	SH_5	SH_6	SH_7	SH_8	SH_10	SH_11
Grid reference		N45.53.473' W118.17.192'	N46.55.109' W119.56.928'	N46.55.109' W119.56.928'	N46.56.147' W119.57.235'	N47.01.535' W119.58.051'	N47.01.542' W119.58.342'	N47.10.251' W119.58.757'	N47.32.623' W119.25.232'	N46.40.032' W118.13.380'	N45.41.390' W121.16.322'	N45.41.916' W121.23.684'
Samples analysed	Analytical precision	n = 5	n = 5	n = 8	n = 10	n = 6	n = 18	n = 6	n = 6	n = 10	n = 7	n = 11
Element	P_i (2σ)	S_i (2σ)	S_i (2σ)	S_i (2σ)	S_i (2σ)	S_i (2σ)	S_i (2σ)	S_i (2σ)	S_i (2σ)	S_i (2σ)	S_i (2σ)	S_i (2σ)
SiO_2	0.212	0.313	0.263	0.342	0.895	0.529	0.589	0.166	0.561	0.382	0.645	0.370
TiO_2	0.042	0.028	0.013	0.052	0.040	0.066	0.051	0.034	0.048	0.053	0.080	0.047
Al_2O_3	0.066	0.209	0.054	0.106	0.277	0.324	0.262	0.141	0.222	0.108	0.264	0.288
Fe_2O_3	0.044	0.767	0.070	0.414	0.999	0.808	0.949	0.312	0.321	0.299	0.711	0.584
MgO	0.051	0.408	0.040	0.167	0.385	0.522	0.264	0.196	0.345	0.236	0.276	0.489
CaO	0.065	0.147	0.040	0.143	0.737	0.234	0.155	0.270	0.156	0.122	0.235	0.222
K_2O	0.010	0.083	0.090	0.098	0.122	0.194	0.103	0.091	0.071	0.075	0.074	0.135
P_2O_5	0.007	0.008	0.007	0.011	0.034	0.027	0.030	0.013	0.027	0.008	0.034	0.021
Rb	1.164	3.786	1.539	2.364	3.506	3.271	2.535	0.859	4.538	2.537	4.314	4.568
Sr	3.130	5.295	3.897	11.793	11.707	6.084	8.991	6.416	4.894	3.268	10.679	5.165
Y	1.503	0.635	0.249	0.982	0.763	2.401	1.536	0.739	2.062	0.750	1.010	0.705
Zr	1.831	2.014	2.652	3.403	3.748	7.335	6.416	3.843	8.672	3.253	5.589	4.502
Nb	1.444	1.078	0.531	0.690	0.538	1.585	1.499	0.383	0.794	0.644	0.563	0.551
Ba	10.545	71.923	19.787	19.868	57.132	16.178	40.233	19.823	15.151	30.957	19.274	35.982
Sc	3.013	1.565	1.278	1.441	2.599	1.443	2.552	1.677	2.116	2.200	1.055	2.603
V	10.210	7.409	2.482	9.699	20.397	15.375	19.119	9.363	10.255	13.038	17.764	16.619
Cr	5.922	3.288	2.653	1.624	2.477	2.356	3.896	1.580	2.719	2.565	7.434	4.469
Co	3.334	2.372	2.263	1.880	2.325	2.260	4.231	1.028	1.255	2.196	2.443	2.160
Ni	5.834	1.221	2.027	1.095	2.602	3.371	3.947	1.906	1.694	1.438	1.987	2.111
Cu	4.408	0.942	1.305	1.423	2.151	1.286	1.452	1.428	0.903	1.197	1.958	1.397
Zn	2.315	4.087	3.081	4.106	7.302	7.219	5.590	5.015	6.525	4.370	7.423	9.559
HI		2.907	1.213	2.184	4.341	4.008	3.527	2.004	2.570	1.945	3.214	3.372
Distance from vent (km)		0	156.5	157	158	173	174	180	195	150	235	242

Table 3.4 Mean average results for all samples within each lobe of the Sand Hollow flow field, standard deviation about the sample means within each lobe and standard deviation of the analytical precision calculated from reproducibility analyses of WS-E for major oxides and BHVO_1 for trace elements, used to calculate the HI value for each lobe.

GINKGO Location Name		Lyle	Lenore Caves	Sand Hollow Road	DC_8 borehole	Wallula Gap	Wilson Canyon	Sheffler	Dyke
Log reference		G_13	G_11	G_4	G_8	G_3	G_2	G_1	—
Grid reference		N45.41.362' W121.16.619'	N47.32.623' W119.25.232'	N46.55.270' W119.56.988'	N46.28.489' W119.23.125'	N46.01.835' W118.56.012'	N46.27.921' W118.37.640'	N46.24.167' W118.38.615'	N46.28.069' W118.37.498'
Samples analysed		n = 7	n = 7	n = 5	n = 8	n = 8	n = 4	n = 8	n = 8
Element	Analytical precision P_i (2σ)	S_i (2σ)	S_i (2σ)	S_i (2σ)	S_i (2σ)	S_i (2σ)	S_i (2σ)	S_i (2σ)	S_i (2σ)
SiO_2	0.212	0.497	0.442	0.349	0.284	0.583	0.175	0.376	0.132
TiO_2	0.042	0.030	0.110	0.034	0.080	0.095	0.040	0.091	0.014
Al_2O_3	0.066	0.113	0.236	0.165	0.406	0.445	0.197	0.303	0.069
Fe_2O_3	0.044	0.255	0.466	0.337	0.425	0.466	0.174	0.281	0.180
MgO	0.051	0.151	0.244	0.160	0.218	0.282	0.064	0.387	0.041
CaO	0.065	0.142	0.269	0.234	0.158	0.264	0.052	0.304	0.041
K_2O	0.010	0.067	0.220	0.11	0.085	0.090	0.056	0.192	0.063
P_2O_5	0.007	0.035	0.041	0.02	0.019	0.014	0.016	0.034	0.007
Rb	1.164	1.870	7.937	3.753	6.471	4.594	0.412	6.729	1.915
Sr	3.130	10.615	7.714	9.383	10.782	18.864	5.542	7.799	2.514
Y	1.503	0.979	1.971	0.915	1.055	2.055	0.918	1.368	0.659
Zr	1.831	3.160	7.315	5.319	5.955	9.927	3.036	4.722	2.309
Nb	1.444	0.488	0.641	0.377	0.607	1.131	0.618	0.581	0.518
Ba	10.545	11.356	20.094	31.974	39.091	35.642	13.969	36.814	7.693
Sc	3.013	1.603	1.972	2.157	2.402	1.124	1.059	1.810	0.881
V	10.210	17.815	16.292	10.483	23.350	14.282	11.364	24.553	4.076
Cr	5.922	3.746	2.076	0.977	1.512	1.711	1.053	2.749	1.206
Co	3.334	1.477	2.010	1.481	4.337	2.970	2.005	3.796	
Ni	5.834	1.642	1.335	1.657	1.772	2.038	2.053	2.482	0.853
Cu	4.408	0.770	1.107	1.839	1.500	3.154	0.804	2.906	1.323
Zn	2.315	5.448	7.015	5.512	7.830	3.237	5.855	10.218	0.916
HI		2.021	3.772	2.463	2.978	3.292	1.436	3.658	1.030
Distance from vent (km)		227.2	134.4	113.8	65	42.6	19.3	2.3	0

Table 3.5 Mean average results for all samples within each lobe of the Ginkgo flow field, standard deviation about the sample means within each lobe and standard deviation of the analytical precision calculated from reproducibility analyses of WS-E for major oxides and BHVO_1 for trace elements, used to calculate the HI value for each lobe.

The average HI values within each flow field are similar from 2.6 to 2.9. Individual flow fields vary with the Palouse Falls hosting the largest range (1.04 – 4.68), intermediate ranges for the Sand Hollow (1.21 – 4.34) and lowest ranges for the Ginkgo flow field (1.03 – 3.77). Comparisons may be drawn between the spatial patterns of multiple geochemical analyses within a flow field as the HI serves as an indication of the degree of significant compositional variation at a single site. Position within the flow field is calculated as the linear distance from a point source (described in detail in Chapter 2). The distance is plotted against the HI for each lobe sampled within the flow fields in the subsequent diagrams.

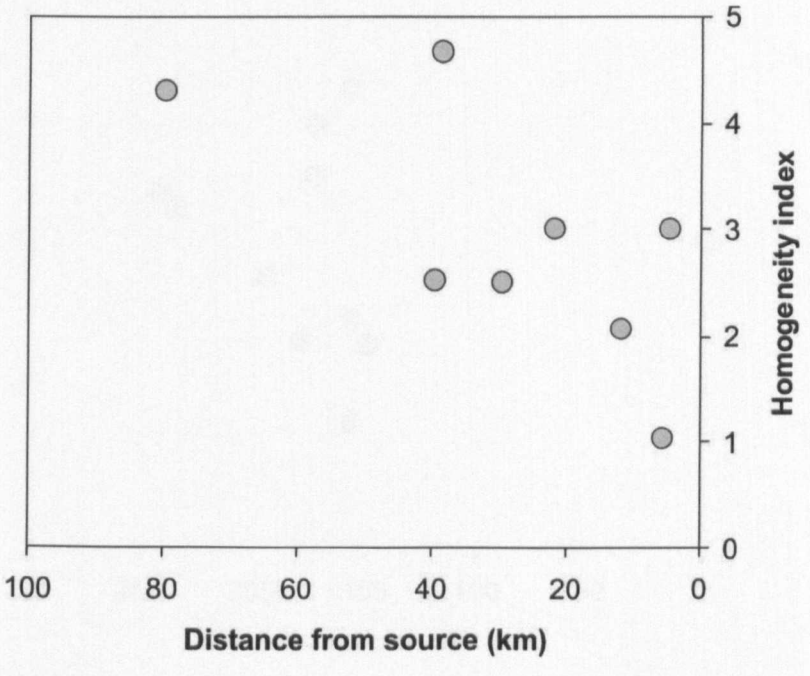

Figure 3.7 Plots of HI versus distance from the source for the Palouse Falls flow field.

The Palouse Falls flow field exhibits high HI values at distance from the source decreasing to low values in source proximal areas. The flow field is reported in Chapter 2 as a simple flow field with samples gathered from a series of interconnected lobes recording the linear development of the flow. In this case, the high HI values in distal portions of the flow field report increased compositional heterogeneity during the latter parts of the eruption sequence.

The Sand Hollow flow field shows a similar linear pattern with high HI values in distal areas decreasing to low values in source proximal parts of the flow field (Fig. 3.8). However, the three highest HI values are in the middle of the flow field. These areas in the Frenchman Springs and Vantage areas are geographically close to each other. The variation in degree of compositional heterogeneity is likely to be more complicated in extensive flow fields due to the character of deviated or anastomosing flow front advancement. The degree of compositional heterogeneity recorded in the Sand Hollow dyke is close to the mean for the whole flow field.

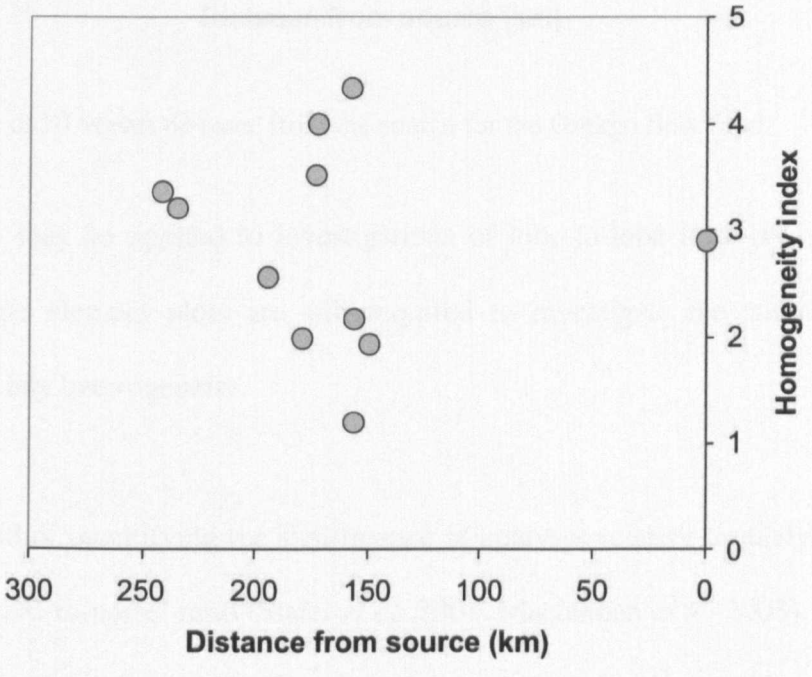

Figure 3.8 Plots of HI versus distance from the source for the Sand Hollow flow field.

The spatial relationship of HI values within the Ginkgo flow field is complicated further and there are insufficient data points to characterise the compositional heterogeneity (Fig. 3.9). In contrast with the Sand Hollow profile, the Ginkgo dyke samples have the least compositional heterogeneity than any other location sampled in the flow field.

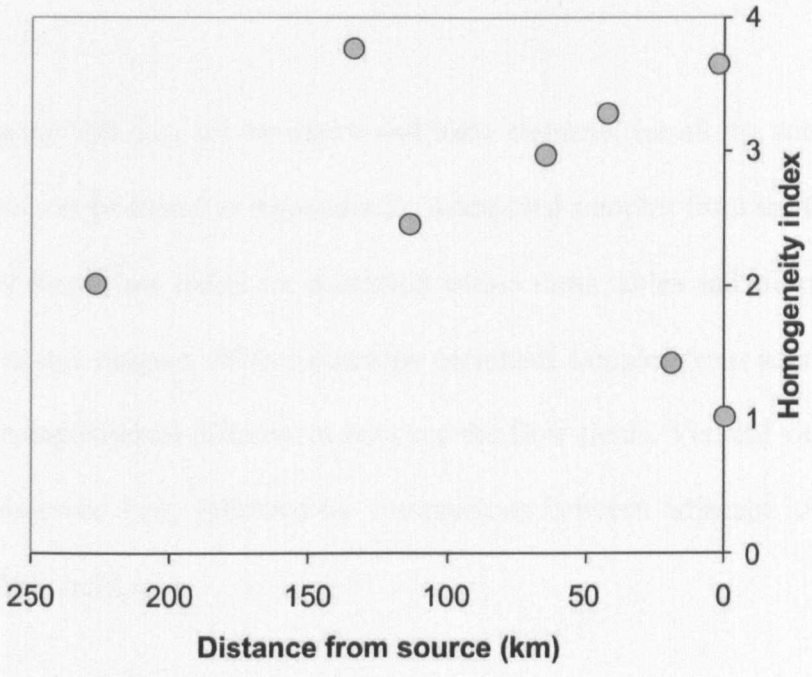

Figure 3.9 Plots of HI versus distance from the source for the Ginkgo flow field.

The HI values may be applied to investigations of lobe-to-lobe intra-lava heterogeneity. However, single element plots are still required to investigate the source and genetic relationship of any heterogeneity.

Another method of quantifying the significance of analyses relative to analytical error was termed the 'signal-to-noise' ratio (Slater *et al.* 2001; Maclennan *et al.* 2003). Much like the HI, the contribution of error to the observed heterogeneity is considered as the true standard deviation (σ_t) of a set of related data. True standard deviation is calculated from standard deviation of the data relative to the standard random error (σ_r) from repeat analyses, $\sigma_t^2 = \sigma_o^2 - \sigma_r^2$. Then the true standard deviation can be compared to the standard random error (σ_t / σ_r) which is referred to as the signal-to-noise ratio for each sample locality. Following application of the signal-to-noise ratio, elements with an index value below 2 are not considered further. This applies to Pb, Th and Nb.

3.5 Results

Tables plotting the full data set for major and trace elements for all the samples from the three flow fields can be found in Appendix D. Additional samples from the Grande Ronde, Silver Falls and Roza flow fields are contained within these tables and are plotted in some of the figures in this chapter. Where outcrops permitted samples from adjacent lavas, the data illustrate compositional differences between the flow fields. Vertical variations within lobes will be assessed first, followed by comparisons between adjacent lobes within the Palouse Falls flow field.

3.5.1 Palouse Falls intra-lobe variation

Intra-lobe compositional variation within each flow field can be assessed by analysing suites of samples taken at varying heights within a single lobe and compared to the physical structure of the lobe. Intra-lobe geochemical variation could occur vertically (as in the profile of a log) but also laterally. The latter will be investigated later in this chapter. A similar format is adopted for all diagrams within the results section. Figure 3.10 illustrates the sample frequency and physical structures used on geochemical plots within this section. These features are selected because they result from an important aspect of the inflation process that may have ramifications for altering a compositional profile. Tie-lines between sample results have been used in diagrams within this chapter to illustrate the character of intra-lobe variation. However, this is not a reflection of the absolute compositional variability and plots of analytical results with height within a lobe may have more step-like changes if the sampling frequency was greater than the current suites with their apparently smooth variations.

3.5.1.1 Vertical geochemical variations

Major and trace element analyses are presented for 62 samples from seven sections within the Palouse Falls flow field (shown in Figure 3.3 with raw data in Appendix D). The results of intra-lava sampling profiles will be presented from the vent proximal portions of the flow field first.

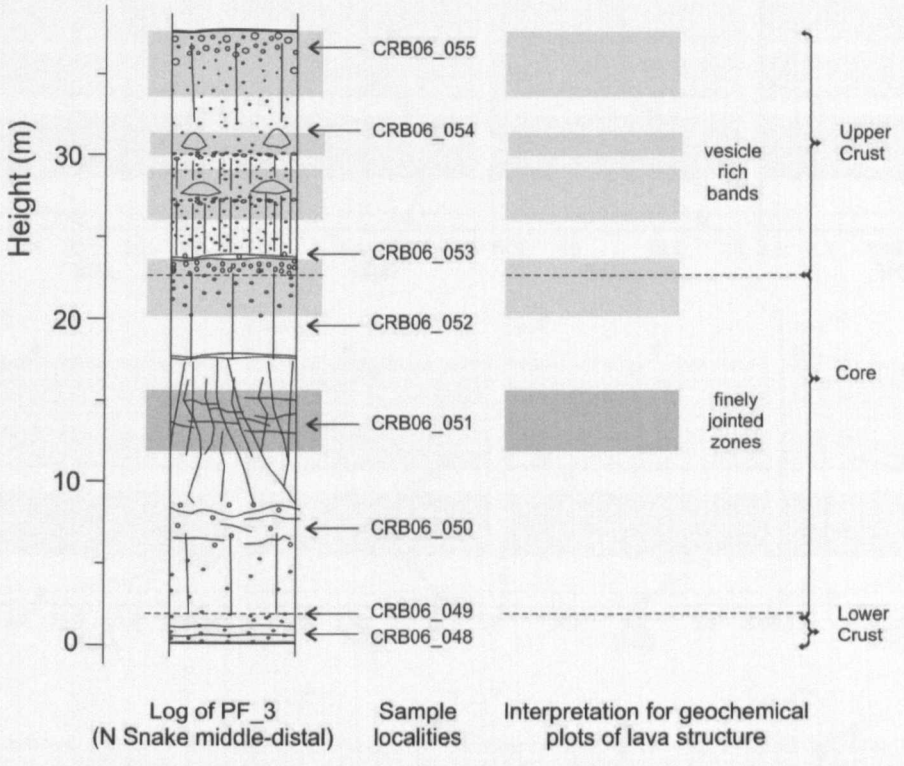

Figure 3.10 Example of the structural variations within a lobe from the Palouse Falls flow field used to illustrate intra-lobe geochemical plots to enable correlation with logs of each lobe.

Generally within the Palouse Falls flow field distinct variations are seen in some oxides and compatible elements. Some typically show an increase from lava crusts to core values e.g. MgO 3.24 to 4.23 wt%, Fe_2O_3 12.93 to 16.28 wt%, Cr 29 to 52 ppm, TiO_2 2.82 to 3.14 wt%. This is accompanied by a decrease in incompatible elements i.e. Y 47 to 43 ppm, Zr 207 to 172 ppm, and V 430 to 345 ppm. Variation in some elements (Cu, Ni, Th, Pb and Ga) within individual lobes is rarely reconcilable outside analytical error.

Vertical profiles within the proximal Winn Lake Canyon lobe (PF_1) display highly variable characteristics (Fig. 3.11). Sequential decreases in some incompatible elements

and oxides occur from the lobe crusts into the lobe core (e.g. TiO_2, Al_2O_3 and V) and increases in some compatible elements (e.g. Fe_2O_3, Sr, Cr and MnO). In either case two horizons impart a change in the compositional profile of this lobe: the upper crust to core boundary, and the lower contact of a finely jointed portion of the lobe core.

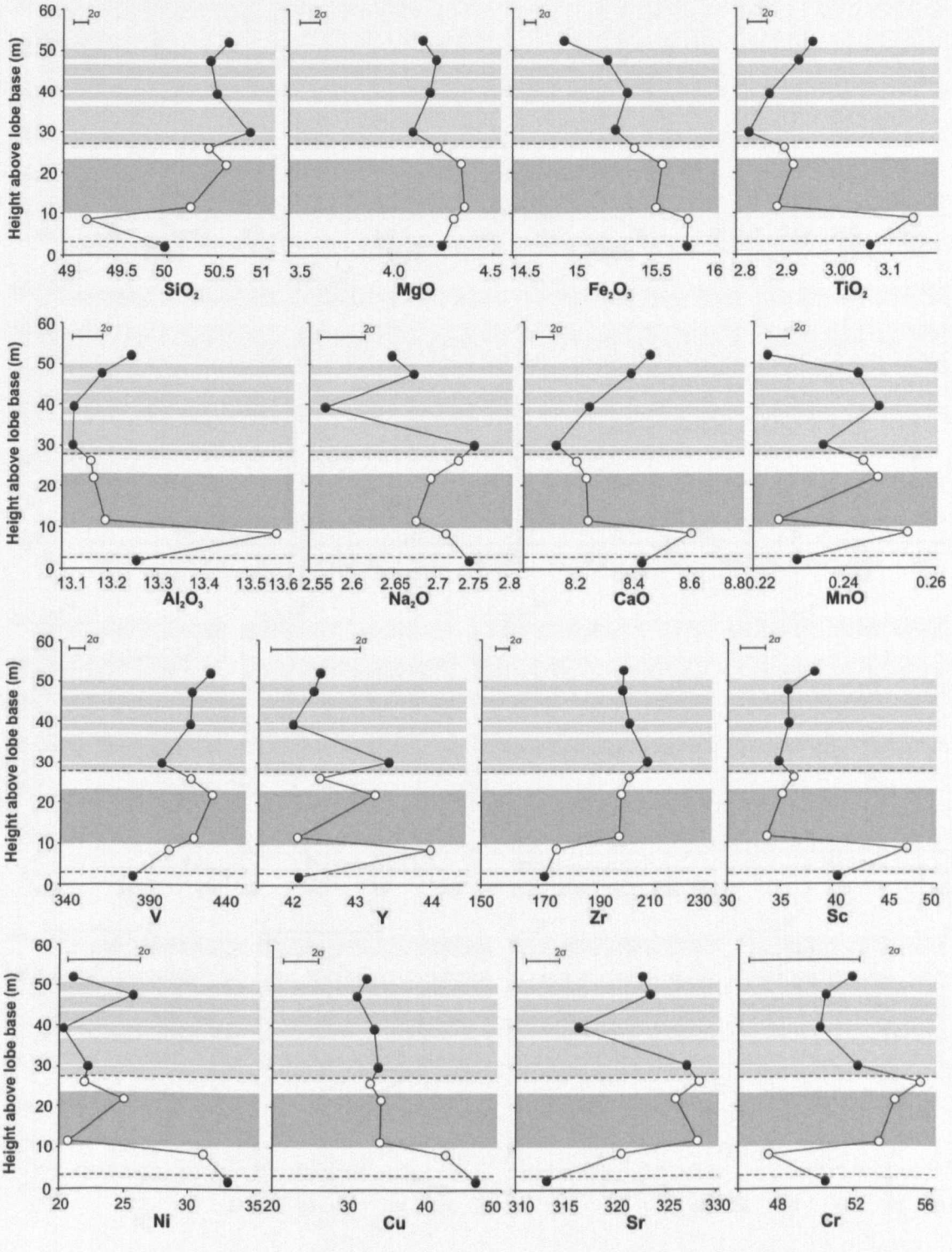

Figure 3.11 Compilation diagram of major oxides (wt %) and trace element (ppm) variations within the Winn Lake Canyon (PF_1) lobe of the Palouse Falls flow field. The dark grey band within the core denotes the finely jointed zone, pale grey bands indicate areas of vesicle-rich banding.

The following logs are presented with the most easterly (proximal) first and progressing along the Snake River outcrops to the westerly (distal) portions of the Palouse Falls flow field.

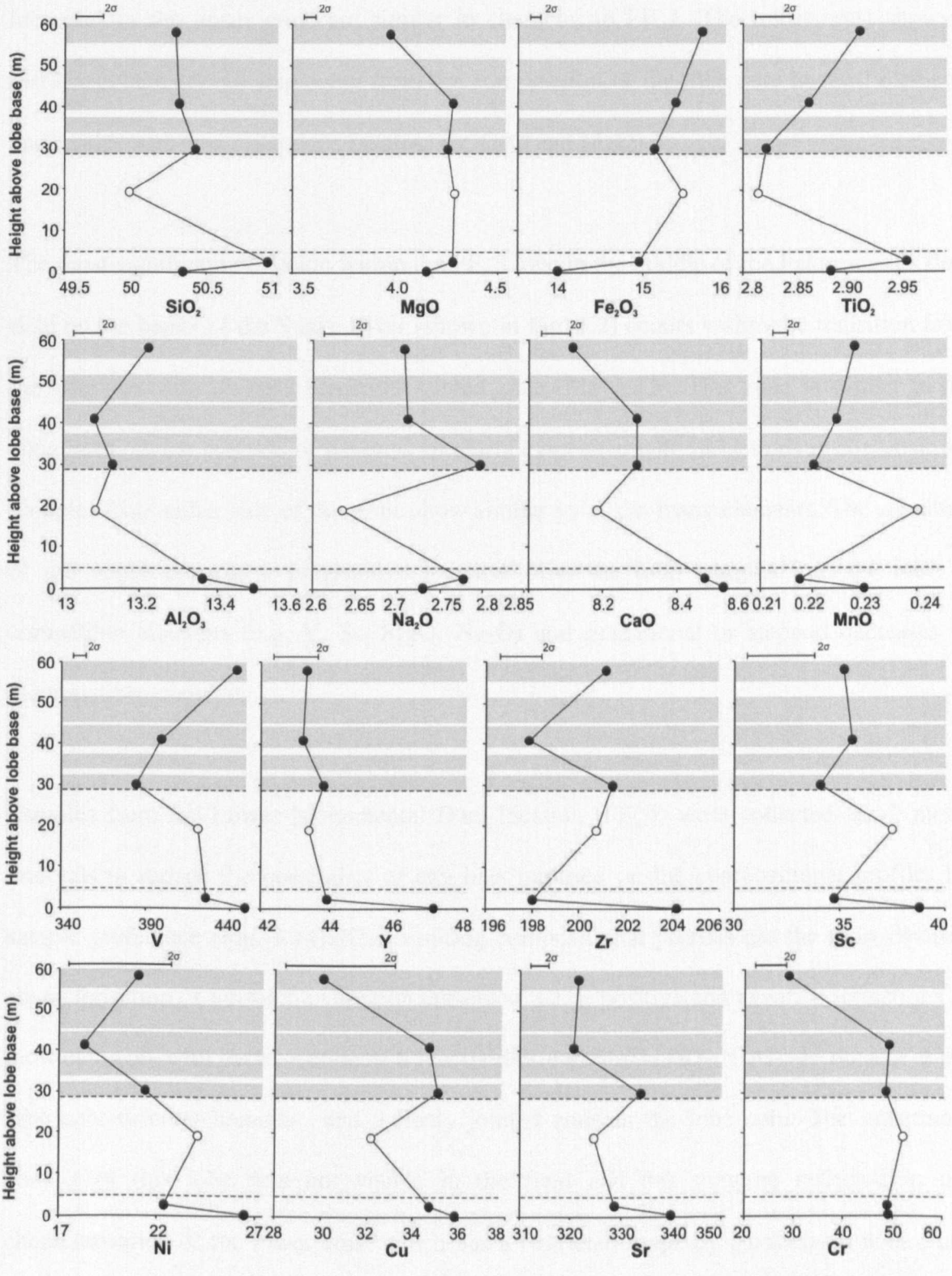

Figure 3.12 Compilation diagram of major oxides (wt %) and trace element (ppm) variations within the N Snake middle (PF_2) lobe of the Palouse Falls flow field. The dark grey band within the core denotes the finely jointed zone, pale grey bands indicate areas of vesicle-rich banding.

The next sampling location from the Snake River outcrops (N Snake middle, PF_2) reveals fewer oscillations in the compositional profiles (Fig. 3.12). Large sampling intervals may obscure absolute compositional heterogeneity. Apparently progressive decreases or increases in the upper crust are similar in character to PF_1. The lower crust shows a distinct compositional step away from the composition of the lobe core in most elements and oxides with few exceptions (such as Cr, CaO and MgO).

The most significant deviation within the PF_3 lobe in the middle of the Palouse Falls flow field on the banks of the Snake River (shown in Fig. 3.2) occurs within the transition from the lobe core into a finely vertically jointed zone (Fig. 3.13). This zone is similar to the zone in PF_2, the position of which is similarly associated with inflections in composition. Samples from either side of this zone show similar values in many elements. The signature of the upper crust is a progressive increase from the lobe margins into the lobe in compatible elements (e.g. V, Sr, MgO, Na_2O) and gradational or stepped decreases in incompatible elements.

Samples from the Lower Monumental Dam location (PF_4) were collected at ~2 metre intervals to reduce the possibility of any bias imposed on the compositional profiles by sample preference (Fig. 3.14). The resulting compositional profiles are the most detailed characterisation of intra-lobe variation presented. Clear positive and negative inflections in most elements with the exception of a few oxides (e.g. MgO, TiO_2, CaO) are present at the lobe core to crust boundary and a finely jointed zone in the lobe core. The lowermost contact of this lobe was not visible in the field and this may be reflected in the characterisation of the lower crust which has a restricted range by comparison with other lobes in the Palouse Falls flow field (e.g. PF_2).

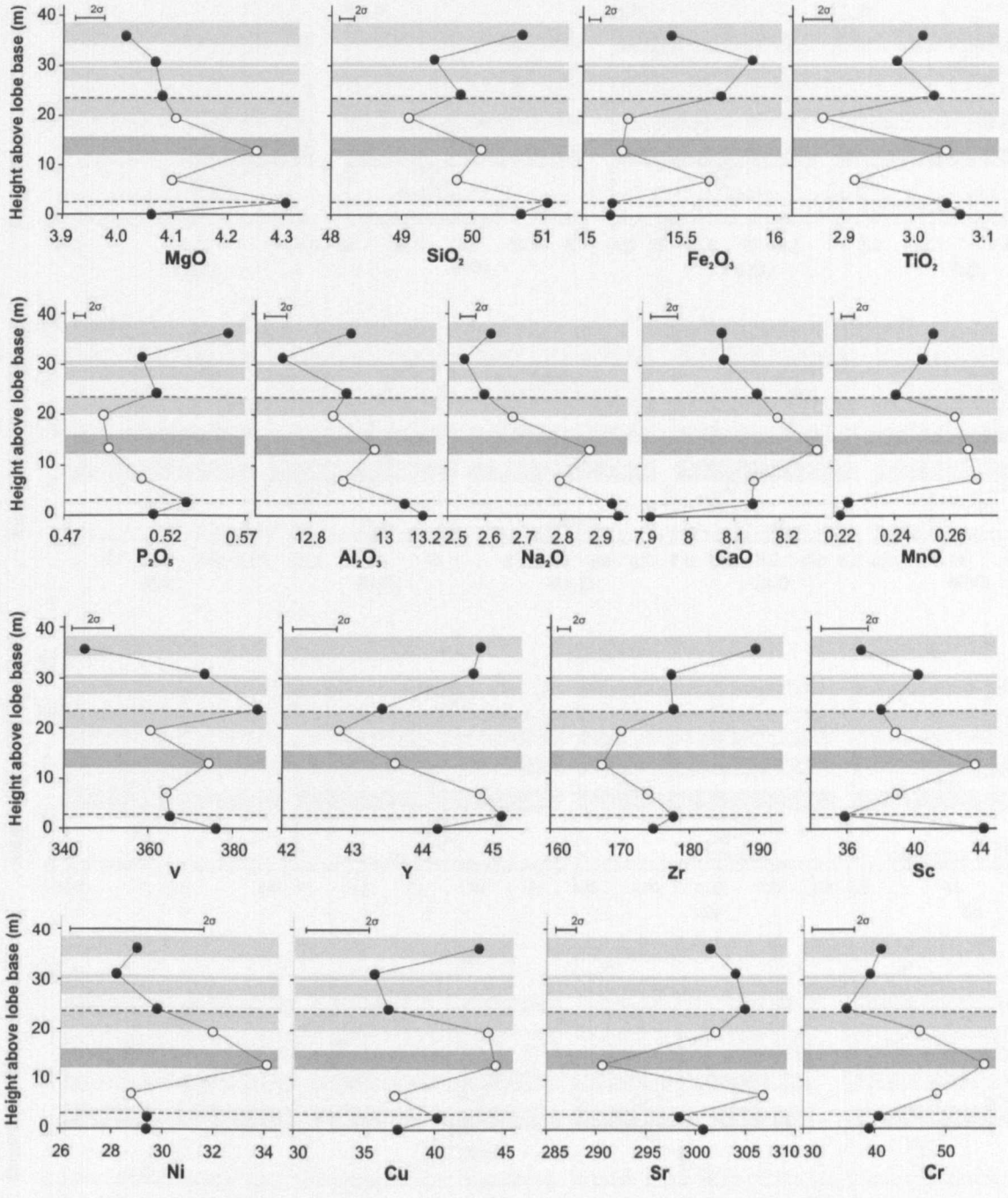

Figure 3.13 Compilation diagram of major oxides (wt %) and trace element (ppm) variations within the N Snake middle-distal (PF_3) lobe of the Palouse Falls flow field. The dark grey band within the core denotes the finely jointed zone, pale grey bands indicate areas of vesicle-rich banding.

The Burr Canyon lobe (PF_5, Fig. 3.2) reveals limited variation in the lobe core outside of 98 % certainty of analytical error (Fig. 3.15). Significant variations occur in both the upper and lower crusts and commonly the outermost crust samples have similar values to each other and thus provide a mirror image of the variation i.e. SiO_2, TiO_2, Sc, Zr, Y, MgO,

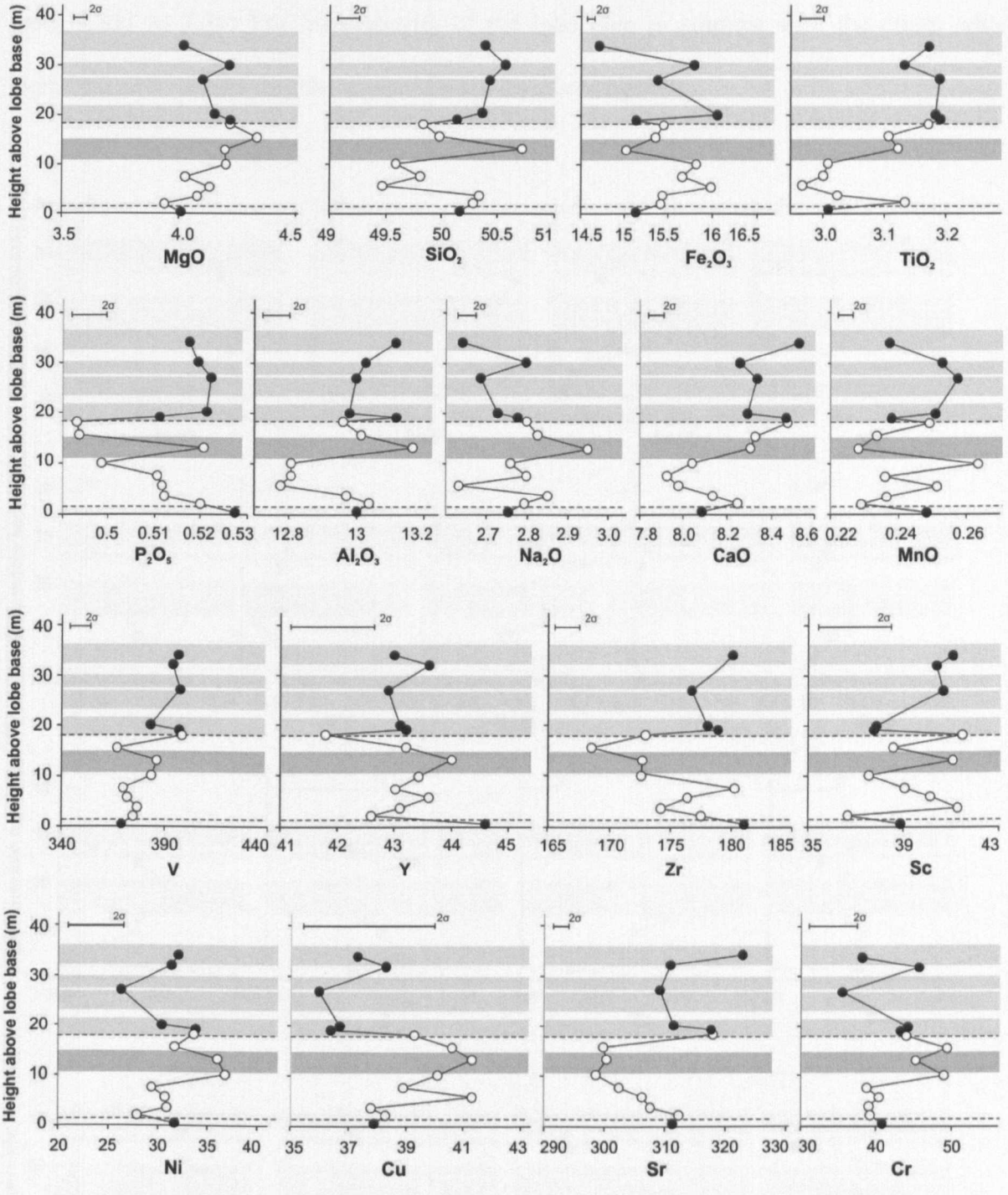

Figure 3.14 Compilation diagram of major oxides (wt %) and trace element (ppm) variations within the Lower Monumental Dam (PF_4) lobe of the Palouse Falls flow field. The dark grey band within the core denotes the finely jointed zone, pale grey bands indicate areas of vesicle-rich banding.

P_2O_5. Excluding the outer crust samples, PF_5 is the first lobe in the Palouse Falls flow field where many of the samples are within analytical error of each other. This is reflected in the calculated HI for this lobe which, on exclusion of the outermost samples, reduces

from 9.351 to 3.34. The homogeneity of the lobe core in contrast with the crusts adds significance to identifying the cause of intra-lava heterogeneity.

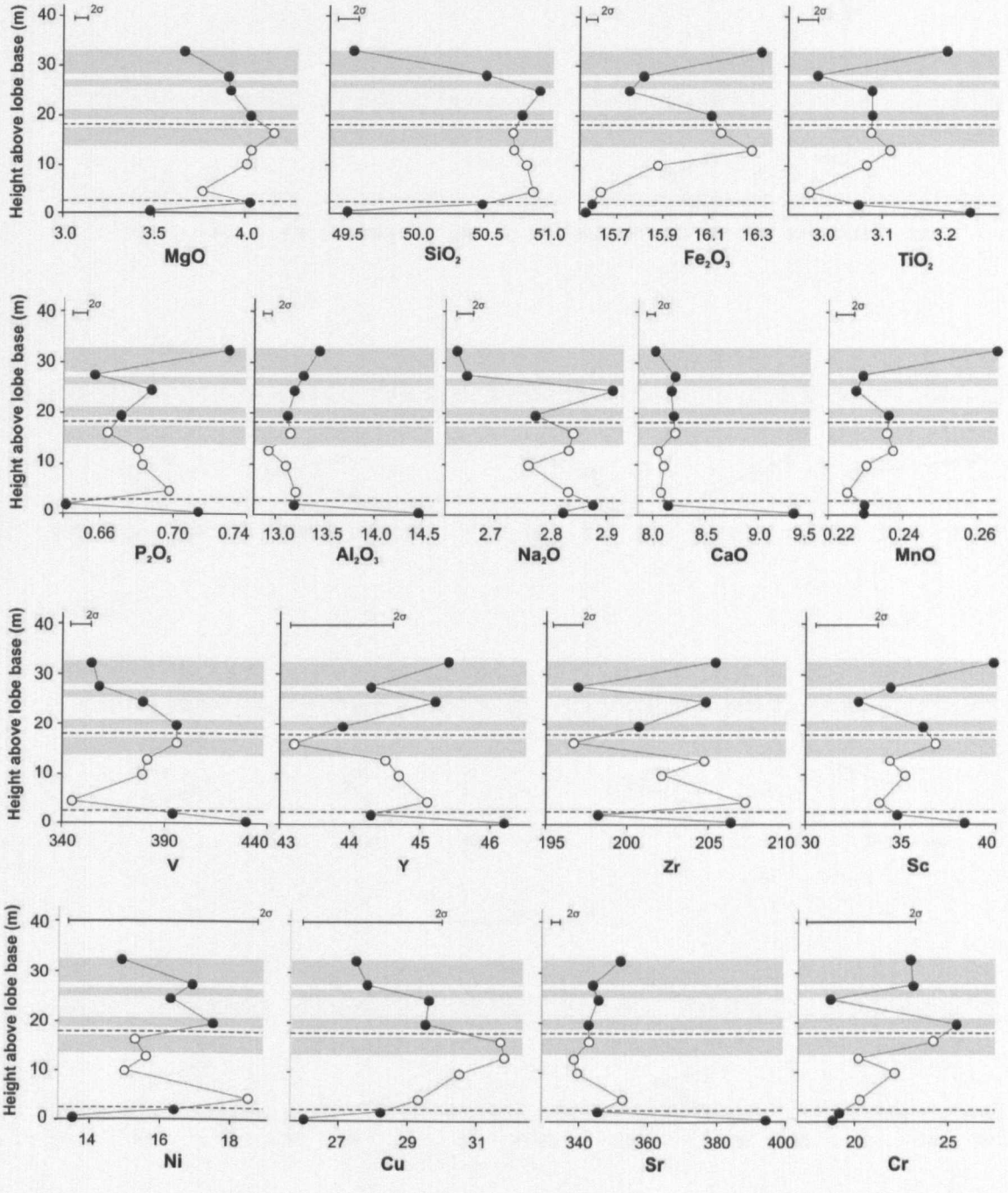

Figure 3.15 Compilation diagram of major oxides (wt %) and trace element (ppm) variations within the Burr Canyon (PF_5) lobe of the Palouse Falls flow field. Grey bands indicate areas of vesicle-rich banding within the lobe.

Compositional profiles from the Ginkgo Dyke area (PF_6) are similar to those from Snake River profile PF_2. Whilst care is taken not to over-interpret profiles with fewer sampling

points, variations with height within this lobe bear similarities such as systematic enrichment or depletion of elements and oxides (e.g. SiO_2, MgO, CaO, Zr) rather than the stepped compositional variation seen in the intervening lobes (Fig. 3.16).

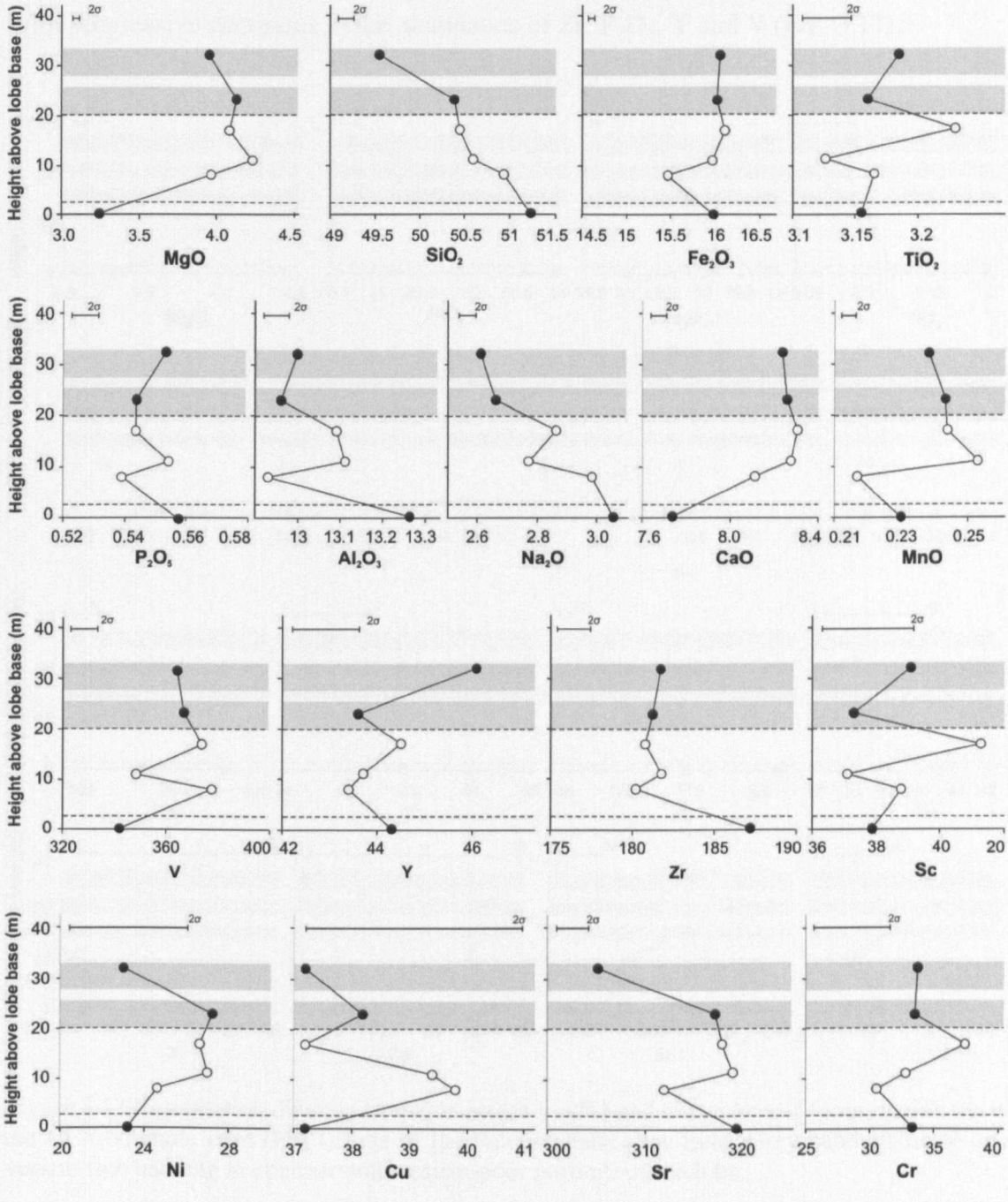

Figure 3.16 Compilation diagram of major oxides (wt %) and trace element (ppm) variations within the W of Ginkgo Dyke (PF_6) lobe of the Palouse Falls flow field. Grey bands indicate areas of vesicle-rich banding within the lobe.

A distinct contrast emerges when comparing the DC8 borehole (PF_7) from the Pasco Basin for the Palouse Falls lava with the exposed lava along the Snake River. None of the

characteristics identified between physical features or zones of the lobes seem to be observed within this lobe. Progressive increases in oxides and some trace elements (MgO, CaO, Sr and Cr) occur with height from the basal core to the upper crust in conjunction with progressive decreases in the abundance of Zr, P_2O_5, Y and V (Fig. 3.17).

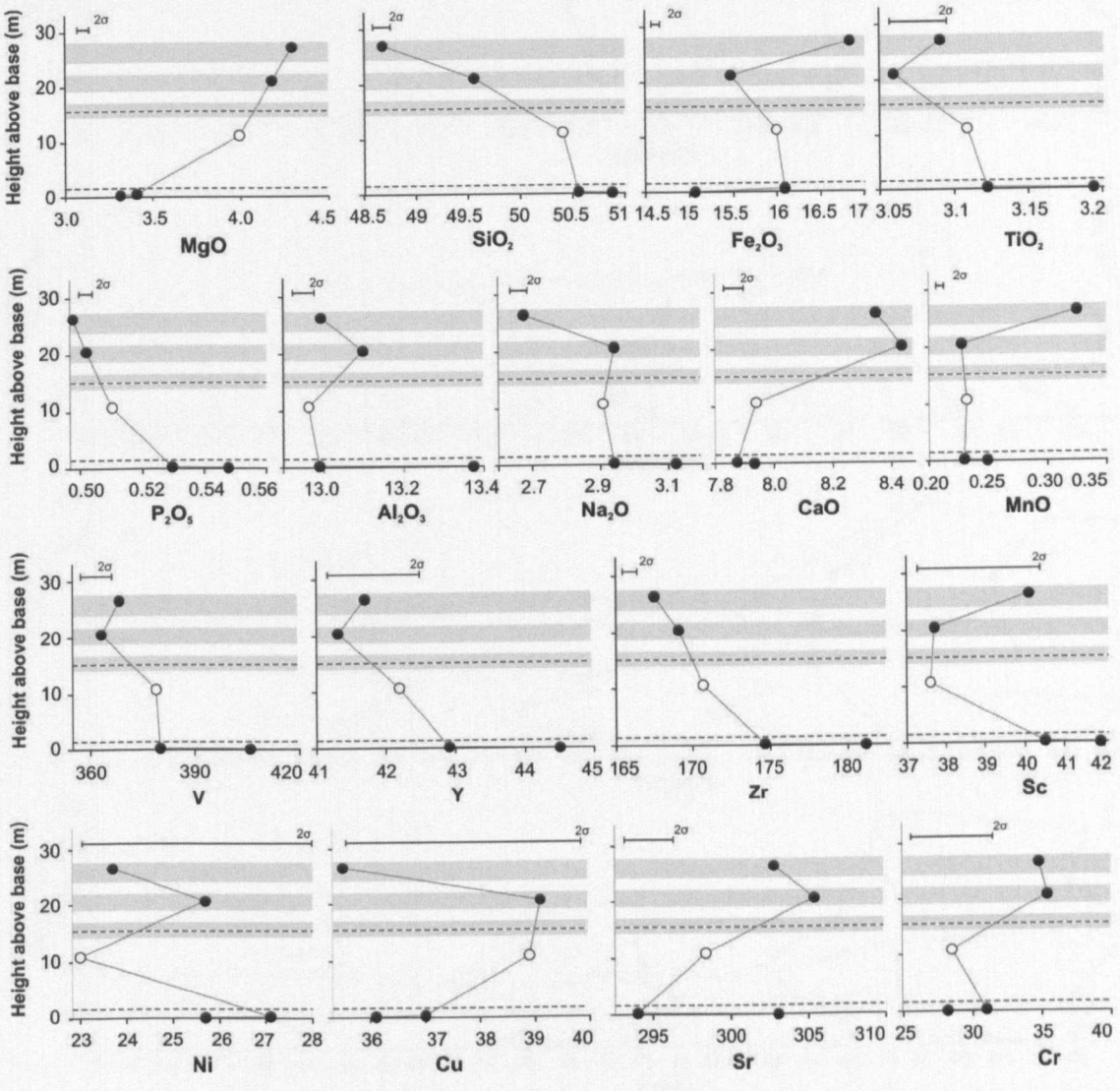

Figure 3.17 Compilation diagram of major oxides (wt %) and trace element (ppm) variations within the DC8 borehole core (PF_7) lobe of the Palouse Falls flow field. Grey bands indicate areas of vesicle-rich banding in contrast with vesicle-poor portions of the lobe.

3.5.2 Inter-lobe variations in the Palouse Falls flow field

The results for the entire flow field are now considered, using each lobe as a single locality and considering the relationship between samples from the lobe crusts and cores with distance from the vent area. The range of values in any lobe is greater in the proximal and

distal parts of the Palouse Falls flow field e.g. MgO ranging up to 0.75 wt% with reduced ranges in the middle of the field (Fig. 3.18).

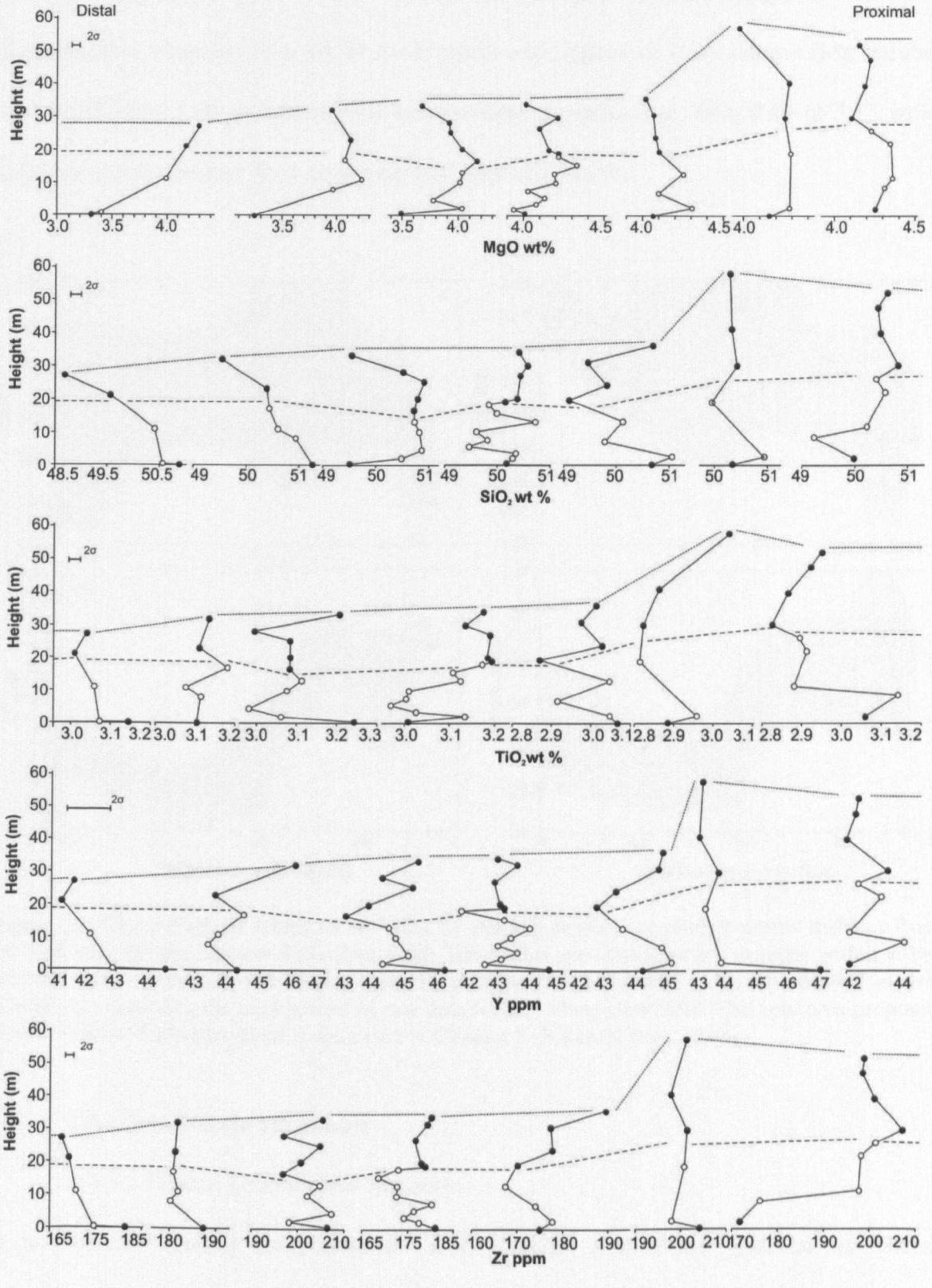

Figure 3.18 SiO_2, MgO, TiO_2 wt%, Y and Zr ppm variation plotted with height within each lobe of the Palouse Falls flow field from the vent proximal site in the east to the distal reaches of the flow field in the Pasco Basin to the west. Closed circles indicate samples within the upper or basal crust of each lobe. Open circles indicate samples from each lobe core.

Compositional heterogeneity between adjacent lobes and across the flow field reveals progressive variations with distance from the vent. Average values for samples from lava cores and crusts relative to the total range of sample values demonstrate general decreases in compatible elements (e.g. Cr 54 to 21 ppm) and indices of fractionation (Mg number 36.2 to 31.8) as well as increases in incompatible elements (e.g. TiO_2 2.83 to 3.13 wt%) with increasing distance from proposed vent area (Fig. 3.19).

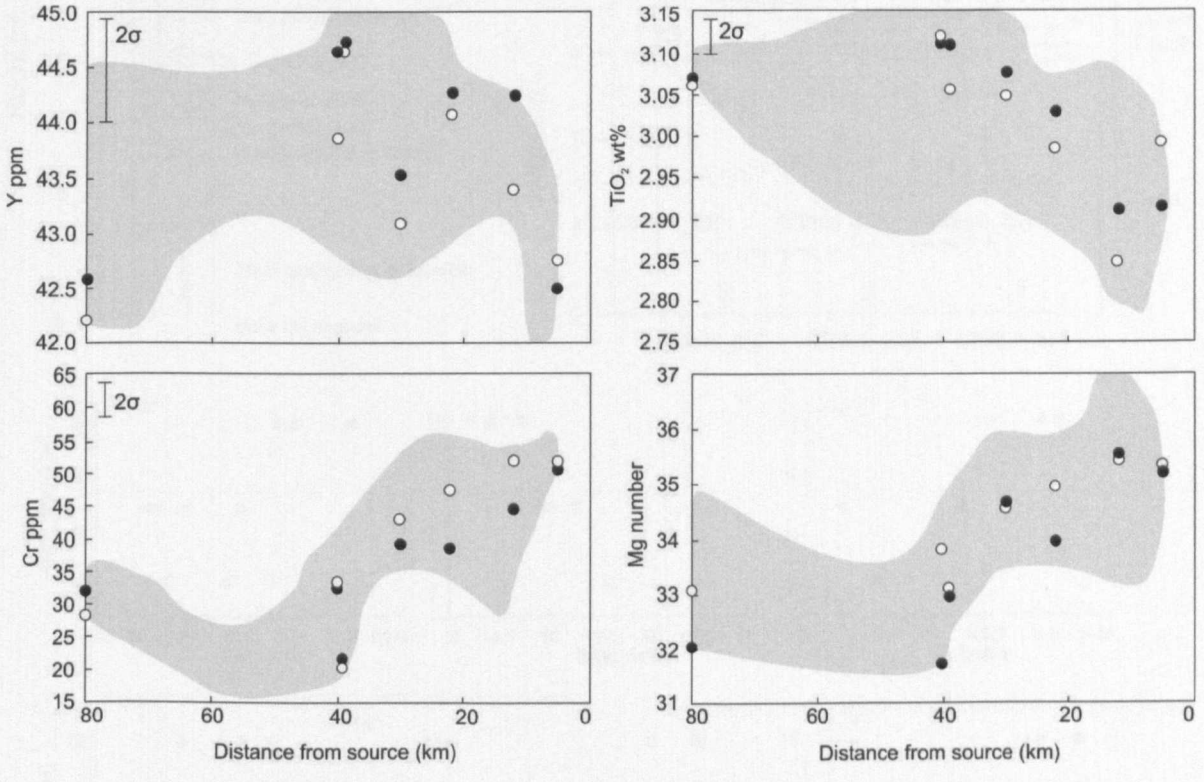

Figure 3.19 Mean average values for Y, TiO_2, Cr and Mg number are plotted against distance from the vent area for the Palouse Falls flow field. The values are calculated for samples within either the lobe core (open circles) or the upper and basal crusts (closed circles) for each locality. The grey shaded area indicates the total spread of raw data for the whole flow field. The vent area proposed for the Palouse Falls flow field is discussed in Chapter 2 (S.Reidel *pers. comm.*).

3.5.3 Small-scale variations

3.5.3.1 Lateral geochemical variations

In addition to vertical compositional variation there is also the potential for lateral compositional variations within a lobe (Fig. 3.20). Three horizons were sampled on either side of the core to upper crust transition zone with three samples taken at one metre

intervals at each horizon. The results show variation outside of analytical error for some elements but the average analysis at each horizon is generally distinct from the sample ranges in the other horizons. Significant compositional variation exists at the sample scale. Furthermore, the origin of such variations and the implications for the emplacement model and lava flow conditions will be discussed in section 3.7.2.

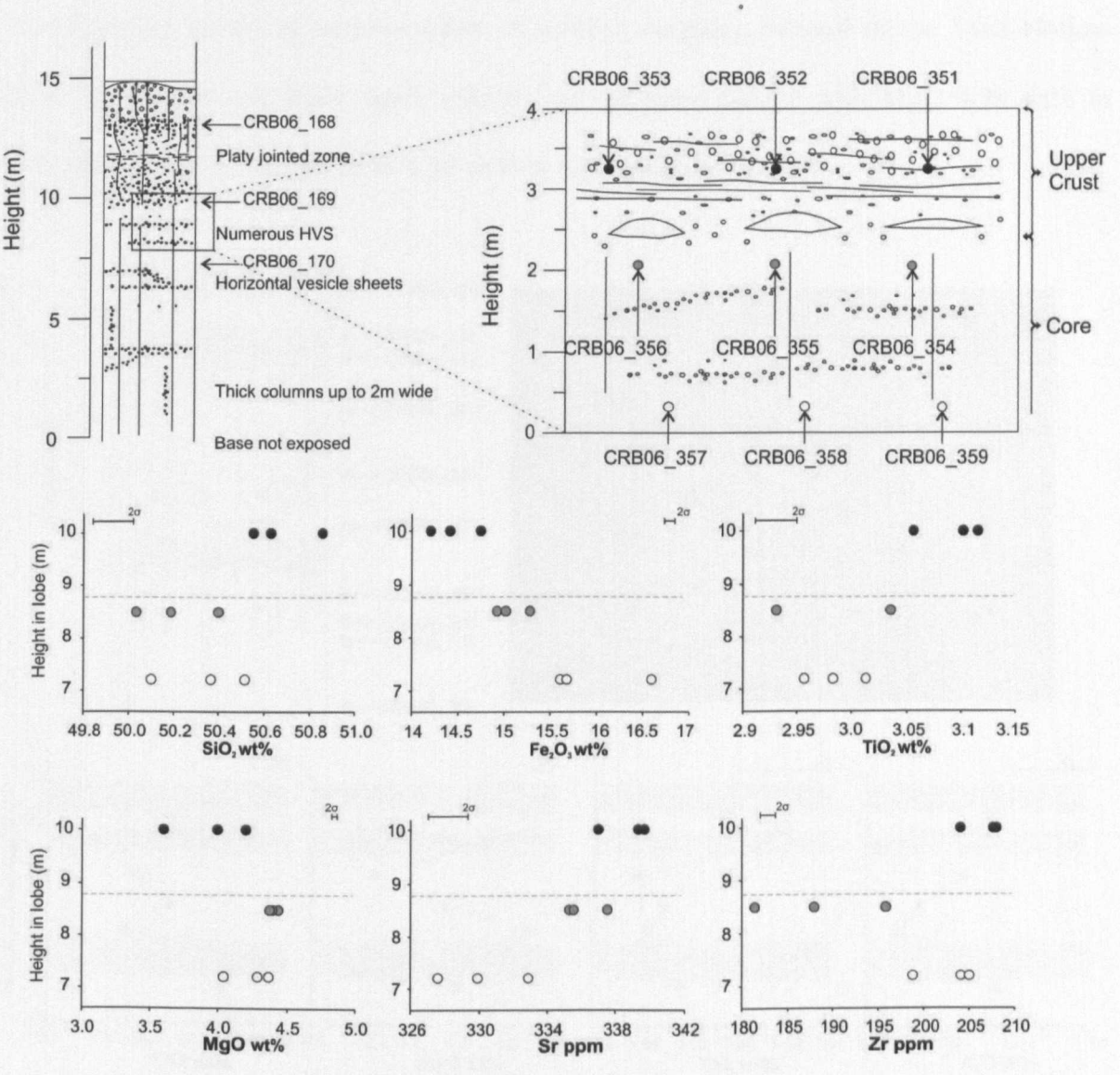

Figure 3.20 Lateral compositional variation in SiO_2, Fe_2O_3, TiO_2 and MgO (wt %), Sr and Zr (ppm) within three horizons from a Wanapum flow on the Kahlotus road section (N46°46.821' W118°05.603').

3.5.3.2 Small scale

Small-scale sampling suites offer the opportunity to investigate the degree and source of variation and the sensitivity of the heterogeneity to emplacement processes. Compositional

profiles from high resolution sampling at 20 cm intervals in vesicle-rich to vesicle-poor bands within the upper-crust show similar characteristics to whole intra-lobe profiles (Fig. 3.21). Degassed vesicular bands have slightly more evolved compositions than corresponding non-vesicular bands, e.g. MgO 4.95 wt% in vesicular band 1 as compared to 4.60 wt% in non-vesicular band 1. This suggests that the process responsible for the heterogeneity occurs at various scales. A similar sampling interval in the Sand Hollow flow field at Palouse Falls rapids (SH_8) has the same pattern with MgO 4.98 wt% in vesicular band 1 as compared to 4.36 wt% in non-vesicular band 1.

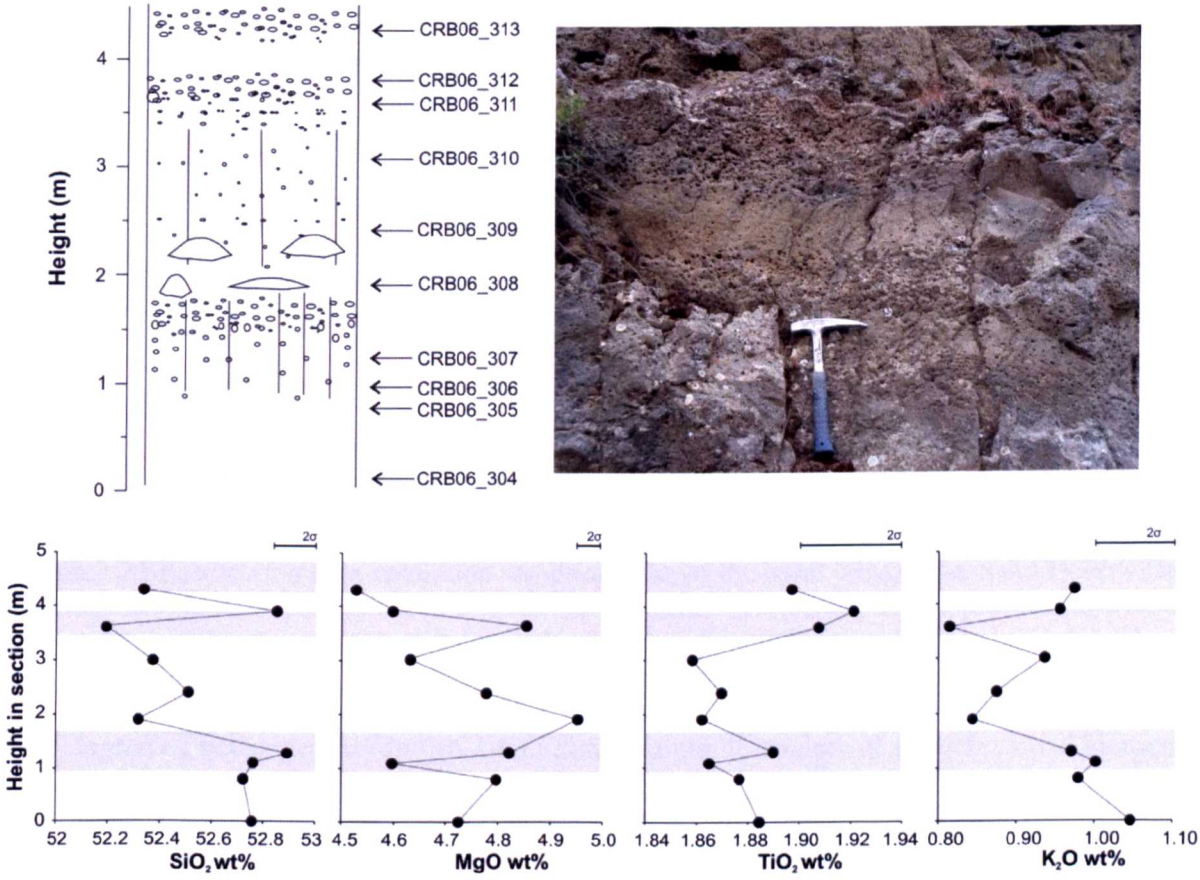

Figure 3.21 Sample positions and results of a high-resolution sampling suite within and between vesicular bands of the upper crust of a Grande Ronde flow field at Lyons Ferry Marina (N46°35.174' W118°13.345'). Grey bands show the position of vesicle-rich bands. Photo shows the outcrop shown in the log as indicated.

Similar small-scale investigations in the lower crust at 10 cm intervals reveal a range of compositions as extensive as those observed in the entire lobe (Fig. 3.22).

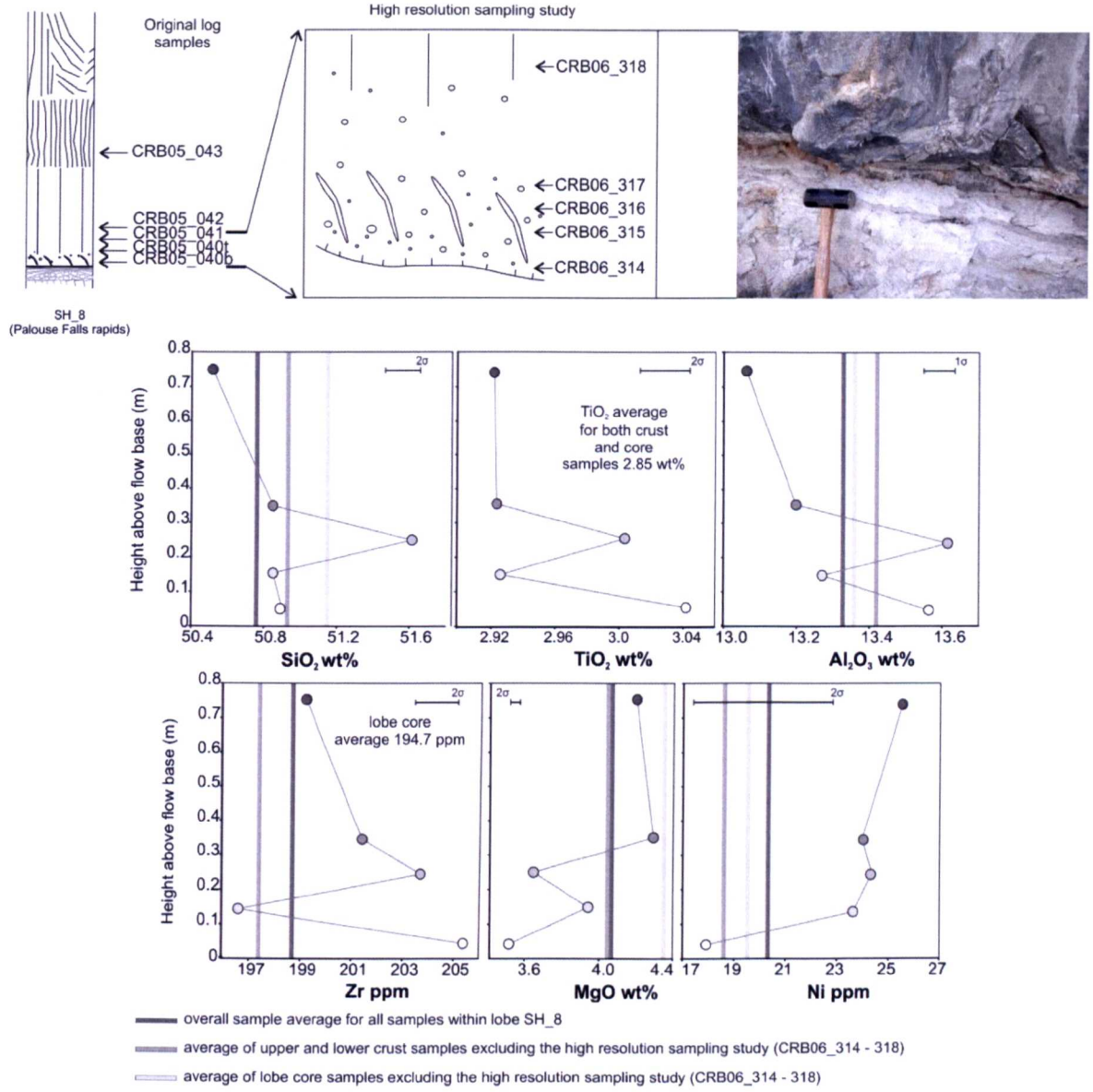

Figure 3.22 Results of a high-resolution sampling suite of the basal crust of the Sand Hollow flow field at Palouse Falls Rapids (SH_8). Solid bars indicate the average of samples throughout the lobe at this locality, the average of the crustal samples and the lobe core samples within this lobe.

The degree of heterogeneity in this small zone is outside analytical error for most elements but the high resolution sampling conducted here does not provide a greater insight to the cause of such variable compositions.

3.5.4 Comparisons with other flow fields

3.5.4.1 The Sand Hollow flow field

Results from a similar sampling strategy within a subset of lobes from the Sand Hollow flow field allow the degree and character of compositional heterogeneity within a flow

field of more typical flood basalt proportions to be investigated (~2600 km^3). The nine profiles with 82 samples (Fig. 3.4) in the Sand Hollow flow field typically show increases in compatible elements from the upper and lower crusts into the core (i.e. MgO 3.09 to 4.55 wt%, Fe_2O_3 12.2 to 15.8 wt% (Fig. 3.23) similar to the pattern seen in the Palouse Falls flow field. This is accompanied by a decrease in incompatible elements (i.e. Sr 356 to 313 ppm, Y 47 to 40 ppm, Zr 210 to 191 ppm, TiO_2 3.04 to 2.8 wt%, V 449 to 394 ppm and Sc 40 to 30 ppm (Fig. 3.24). Similar decreases are noted in some trace elements which should be moderately compatible (i.e. Ni 24 to 16 ppm). Some elements within the Vantage lobe of the Sand Hollow flow field (SH_1) demonstrate a mirror set of values in the upper and lower crusts as seen in the Palouse Falls flow field. This is expected during lava inflation as we might assume that the outer portions of the lobe are emplaced simultaneously from the same batch of lava. Variations toward the core of the flow may be a factor of the difference in emplacement times and supply of lava from later in the eruption sequence.

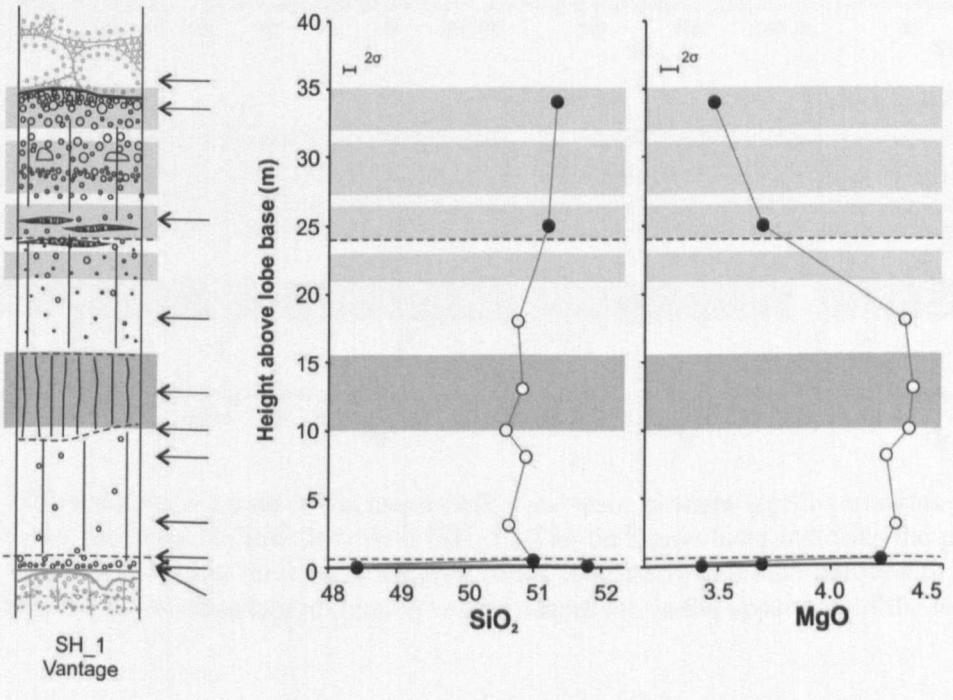

Figure 3.23 Example of the variation in wt% of SiO_2 and MgO compared with the physical structure of the Sand Hollow flow field within the Vantage sheet lobe (SH_1).

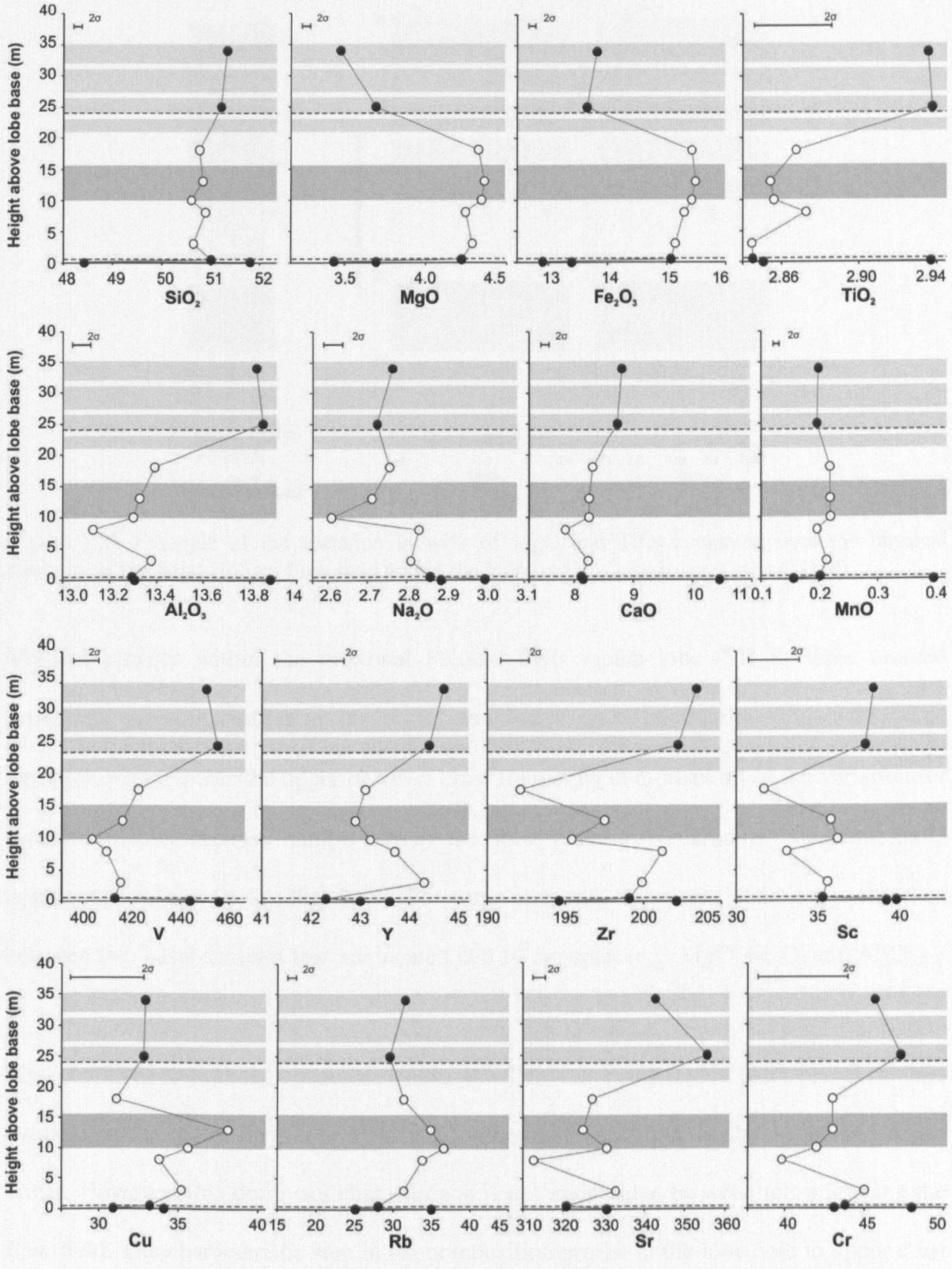

Figure 3.24 Compilation diagram of the major (wt%) and trace element (ppm) variations within the Vantage lobe of the Sand Hollow flow field (SH_1). The dark grey band indicates the position of the 'black band zone' within the lobe. Pale grey bands indicate vesicle rich portions of the upper crust and the presence of abundant horizontal vesicle sheets within the upper part of the lobe core.

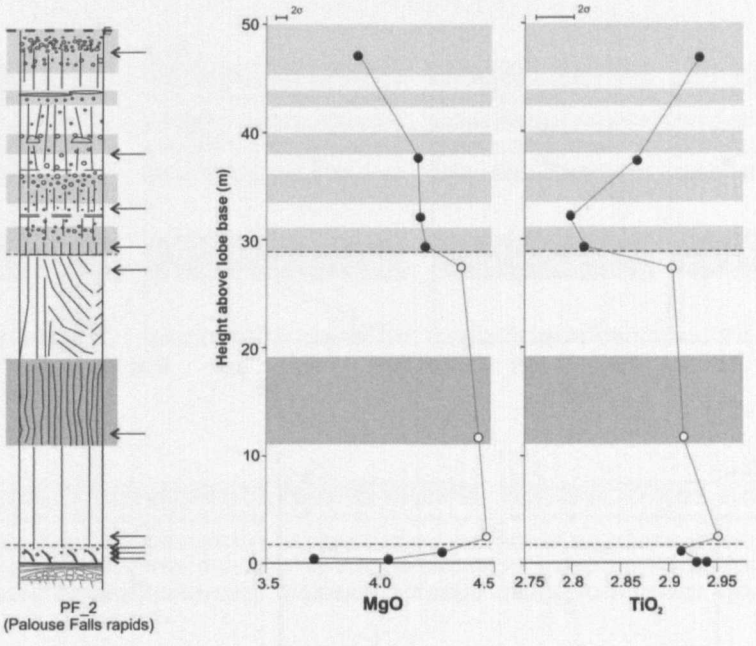

Figure 3.25 Example of the variation in wt% of MgO and TiO_2 compared with the physical structure of the Sand Hollow flow field within the Palouse Falls rapids sheet lobe (SH_8).

Vertical profiles within the proximal Palouse Falls rapids lobe (SH_8) show marked inflections in composition at the upper and lower crust boundaries (Fig. 3.25). The variation within either the upper or lower crust frequently comprises all of the variation for the whole lobe because samples from the lobe core are commonly compositionally homogeneous (e.g. Fe_2O_3, Fig. 3.26). For some elements significant variation is observed between two basal samples that are located just 10 cm apart (e.g. MgO, Fe_2O_3 and Al_2O_3).

The chemical variations observed within the Palouse Falls rapids lobe reveals a less evolved, more mafic lava core with weak systematic variation in the upper and lower crusts. However, this dominant characteristic is not maintained between lobes forming the flow field. The characteristic step in the composition profile at the lobe core to upper crust boundary is in marked contrast with many lobes from the Palouse Falls flow field (e.g. PF_4) which displays progressive variation across the upper crustal boundary.

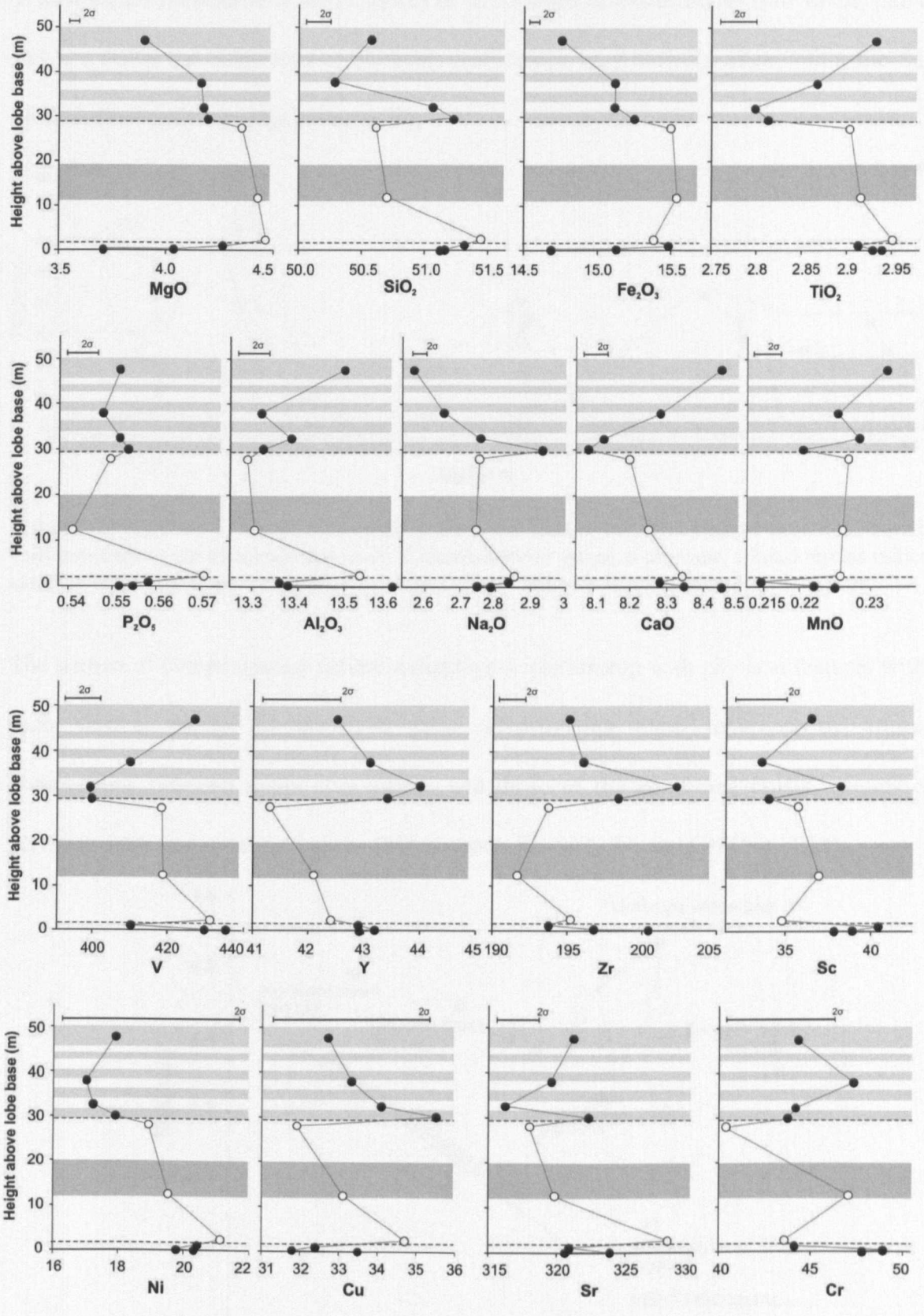

Figure 3.26 Compilation diagram of major oxides (wt %) and trace element (ppm) variations within the Palouse Falls rapids (SH_8) lobe of the Sand Hollow Falls flow field. Dashed lines denote the boundaries between the upper crust, core and lower crust of the lobe. The mid-grey area identifies the 'black band zone'. Pale grey bands in the upper crust identify the vesicle rich bands reported in the SH_8 log.

Whilst these characteristics seem typical of some lobes across different flow fields, like the Palouse Falls, the behaviour of elements and oxides vary between sites within the Sand Hollow flow field e.g. MgO (Fig. 3.27).

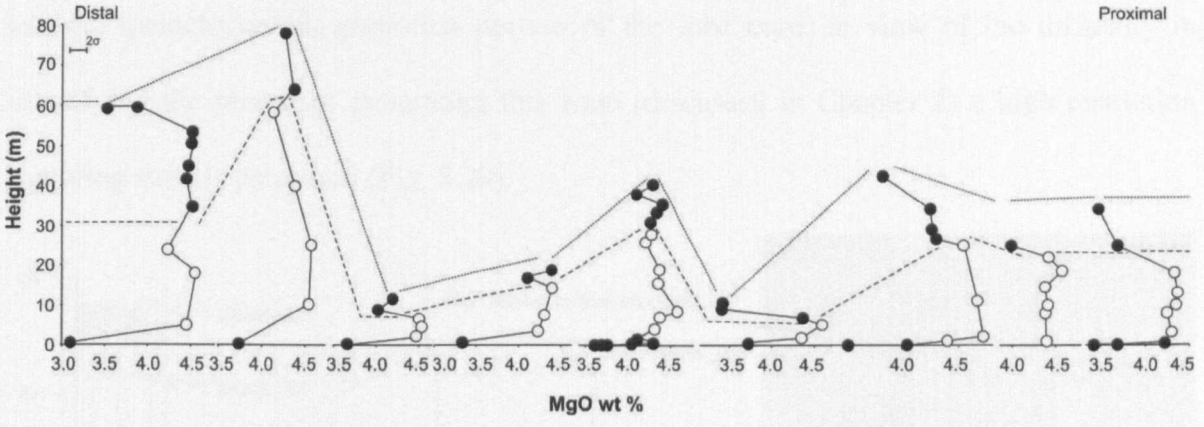

Figure 3.27 MgO wt% plotted with height within each lobe of the Sand Hollow flow field from the vent proximal to the distal reaches in the Columbia River gorge to the west. Closed circles indicate samples within the upper or basal crusts. Open circles indicate samples from each lobe core.

The pattern of compositional variation displays a relationship with physical features within each vertical profile of the flow field. Investigating these relations, by drawing comparisons between mean core values and those of the combined crusts, reveals co-variation with fractionation indices (Mg number, Fe, SiO_2, Ni and Cr) (Fig. 3.28).

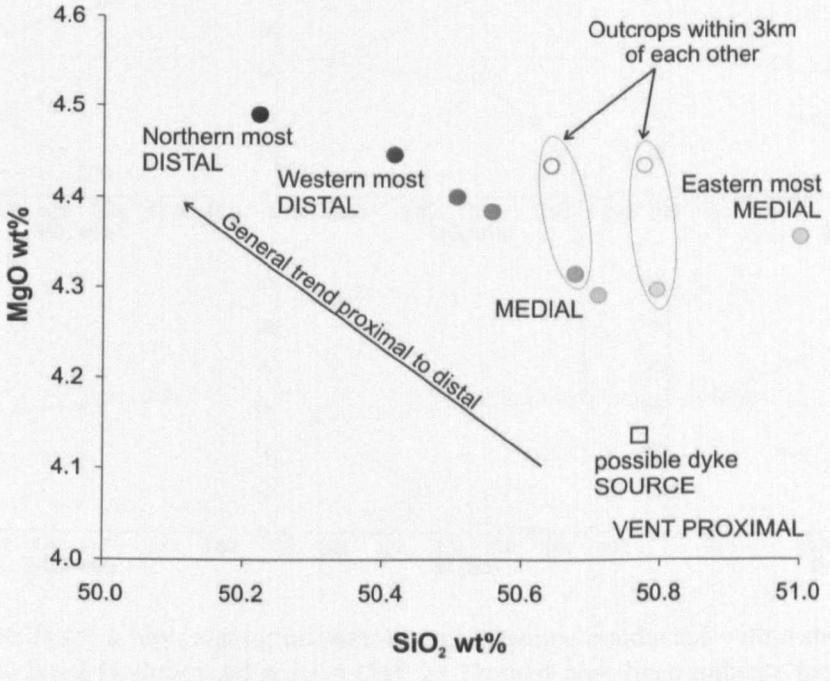

Figure 3.28 MgO wt% variation of the average values for samples from the lobe cores plotted with SiO_2 wt % within the Sand Hollow flow field indicating distance from the vent proximal site in the east to the fissure dyke to the northern and western-most distal reaches of the flow field.

The so-called 'black band zone' is a defining characteristic of the Sand Hollow flow field. The position of the black band within the lobe illustrated appears as a dark grey band. An inflection in some elements appears to be associated with the presence of this highly jointed, quench-cooled, glass-rich portion of the lobe core. In view of the difficulty in identifying the processes generating this zone (discussed in Chapter 2) a high resolution sampling suite is presented (Fig. 3.29).

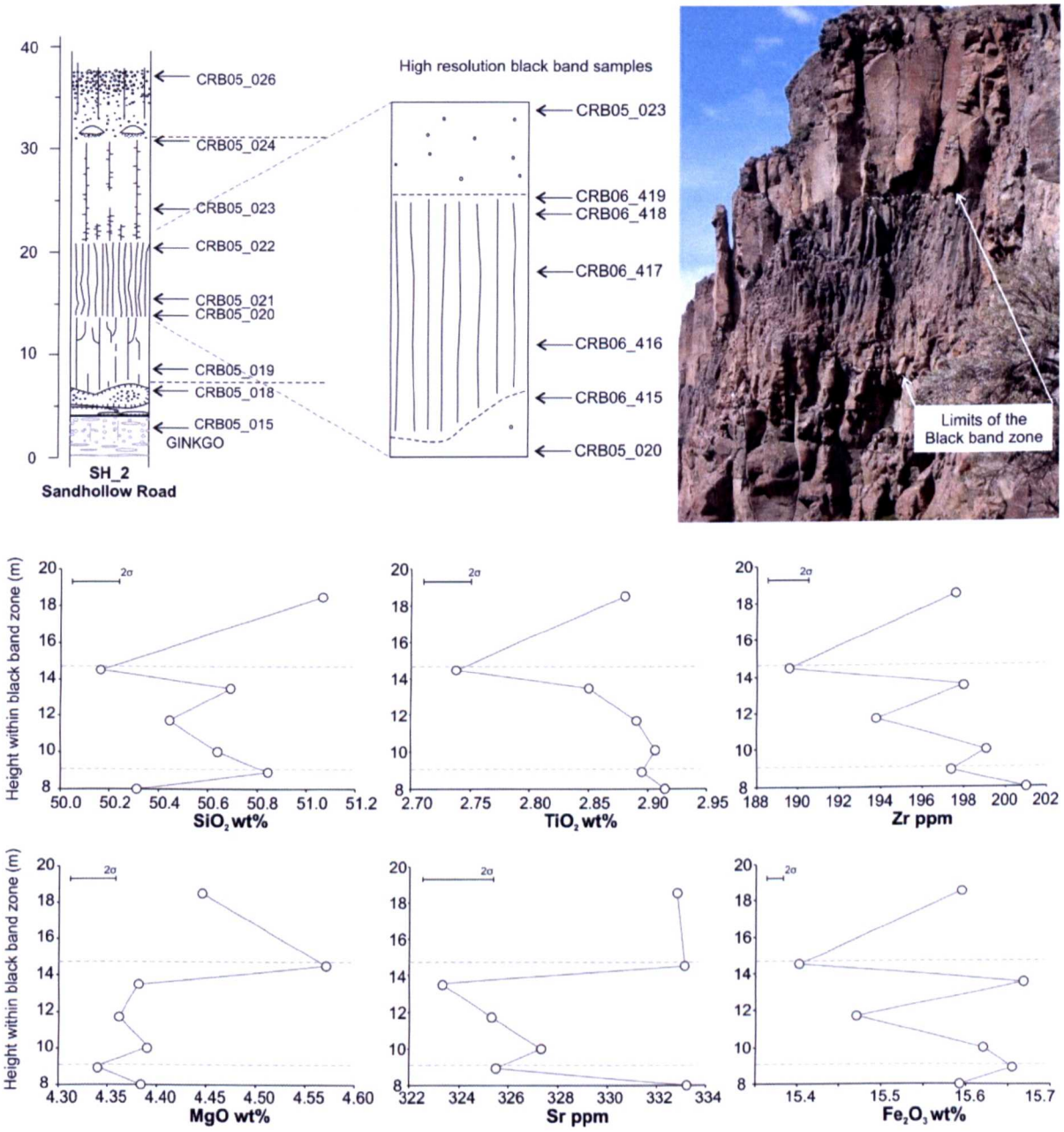

Figure 3.29 Results for a high resolution sampling programme conducted within the Sand Hollow flow field in the Sand Hollow road section (SH_2). Dashed grey lines indicate the boundaries of the black band zone. On close inspection the transition between this glass-rich finely jointed zone and the surrounding core is gradational and these boundaries are indicative of the cessation of closely spaced joints.

Comparison of these average values at each locality with distance from the area postulated to be the vent for this eruption (Tolan *et al.* 1989), reveals some relationship (Fig. 3.30) with an overall decrease in fractionation indices (Zr/Y and MgO) and systematic co-variation of SiO_2 as the more primitive samples are located furthest from the vent. The average composition of the cores records little variation with distance whilst the crusts are markedly variable.

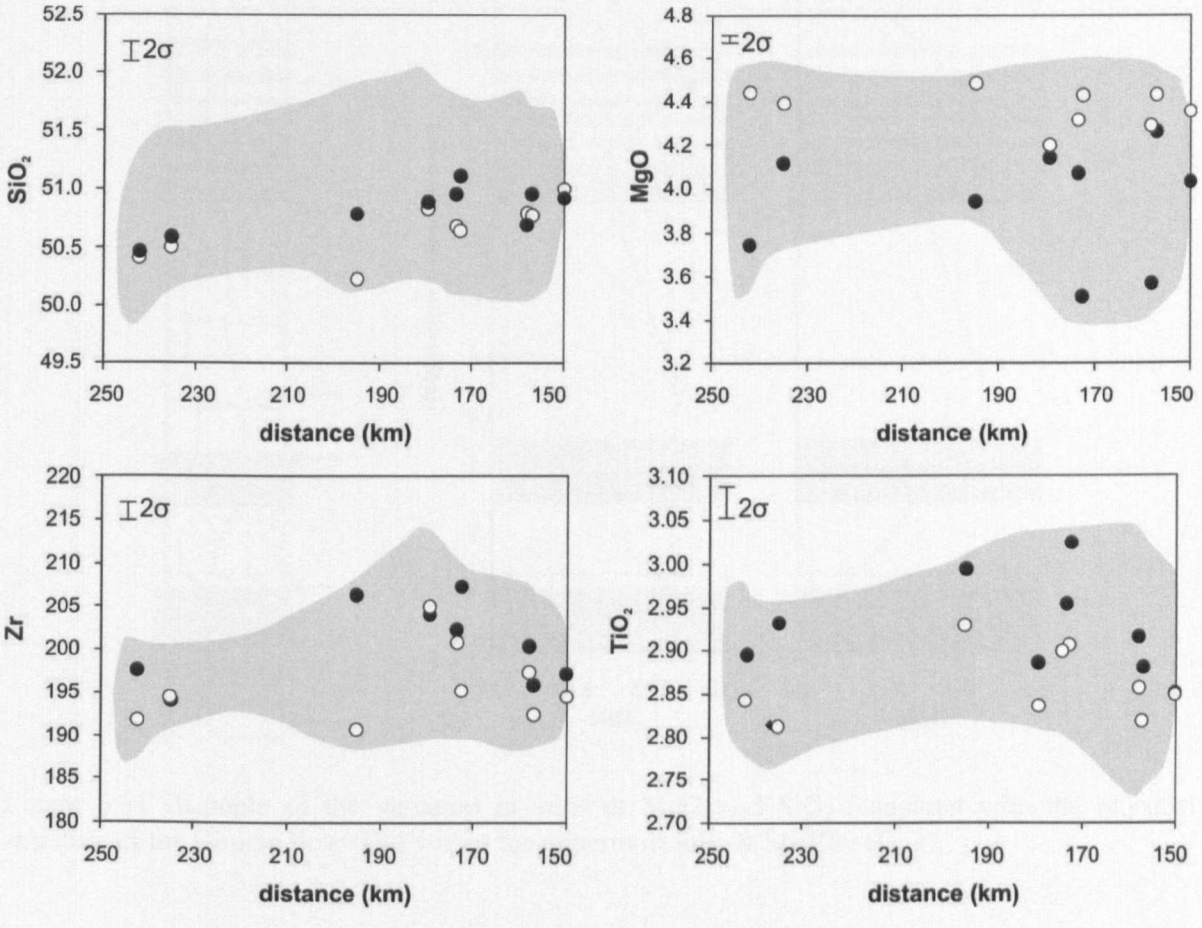

Figure 3.30 Average values SiO_2, MgO and TiO_2 wt% and Zr ppm for samples from the lobe core and crusts in each locality plotted with distance from the Sand Hollow vent area. Closed circles indicate the average value for samples from the lobe crusts. Open circles indicate average values for samples from each lobe core. Grey shaded areas indicate the total spread of data for all samples.

3.5.4.2 The Ginkgo flow field

The complex nature of the compound Ginkgo flow field was highlighted in Chapter 2. Analyses for 46 samples are shown from a subset of seven profiles characterising the Ginkgo flow field. To reduce the degree of complexity associated with investigating a flow

field involving numerous stacked lobes in any one locality results plotted below are from samples taken from the uppermost lobe at each site. Precursor lobes underlying the Ginkgo lobe are used as the temporal equivalent of the lower crust. Precursor lobes are indicated on the variation diagrams by dark grey zones as shown in Fig. 3.31.

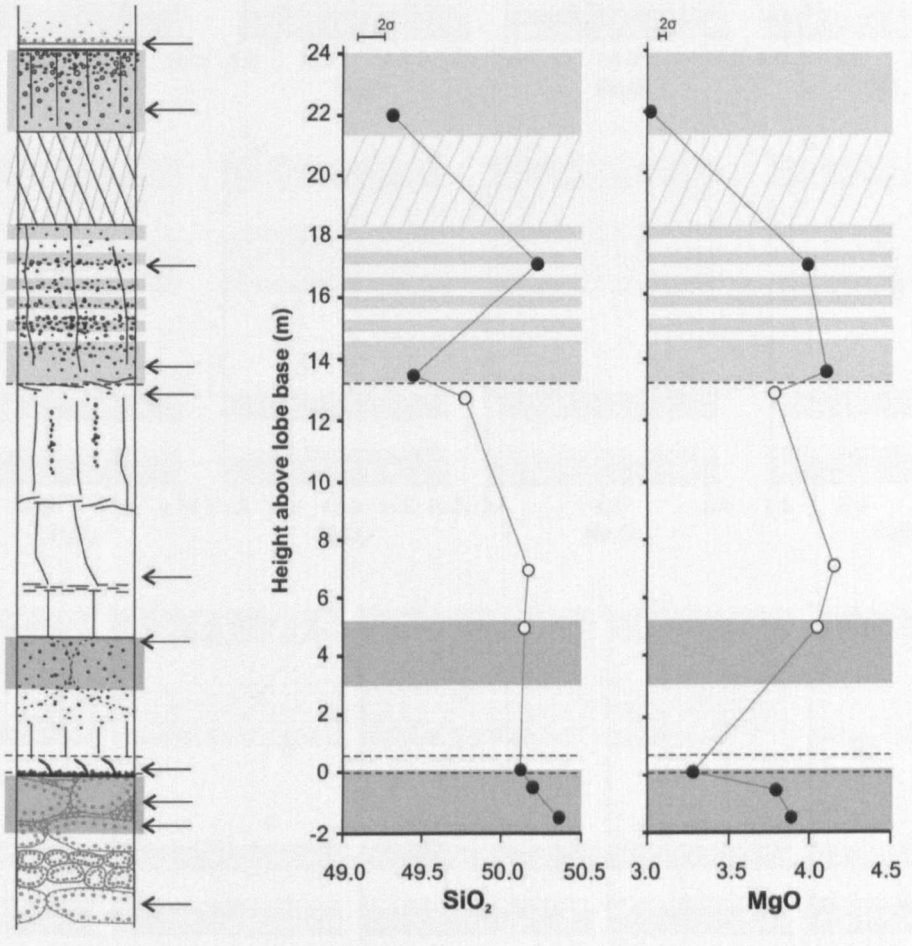

Figure 3.31 Example of the variation in wt% of MgO and SiO_2 compared with the physical structure of the Ginkgo flow field within the uppermost lobe at Sheffler (G_1).

Characteristics of vertical intra-lobe variation with the Sheffler lobe (Fig. 3.32) are reminiscent of the Vantage lobe in the Sand Hollow flow field (Fig. 3.24). Increases in incompatible elements (Zr, Y, V, TiO_2) and decreasing abundances of compatible elements (MgO and Ni) are observed with increasing height within the upper crust. Inflections within the core coincide with a change in the physical structure of the lobe such as vesicular horizons or jointing style changes. A step in the profile is located at the core to upper crust boundary.

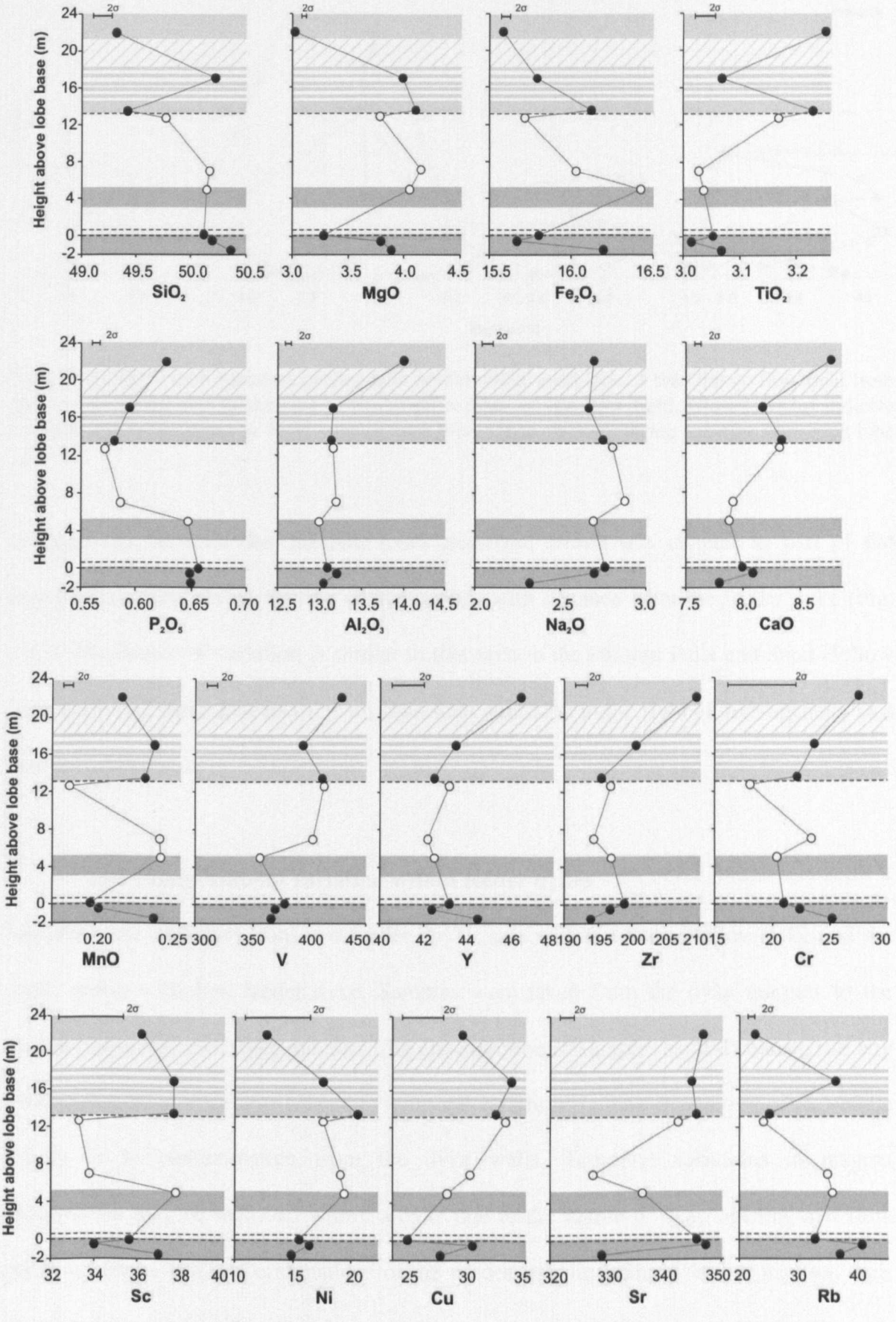

Figure 3.32 Compilation diagram of the principal major (wt %) and trace element (ppm) variations within the Ginkgo lobe at Sheffler (G_1), in the proximal part of the Ginkgo flow field.

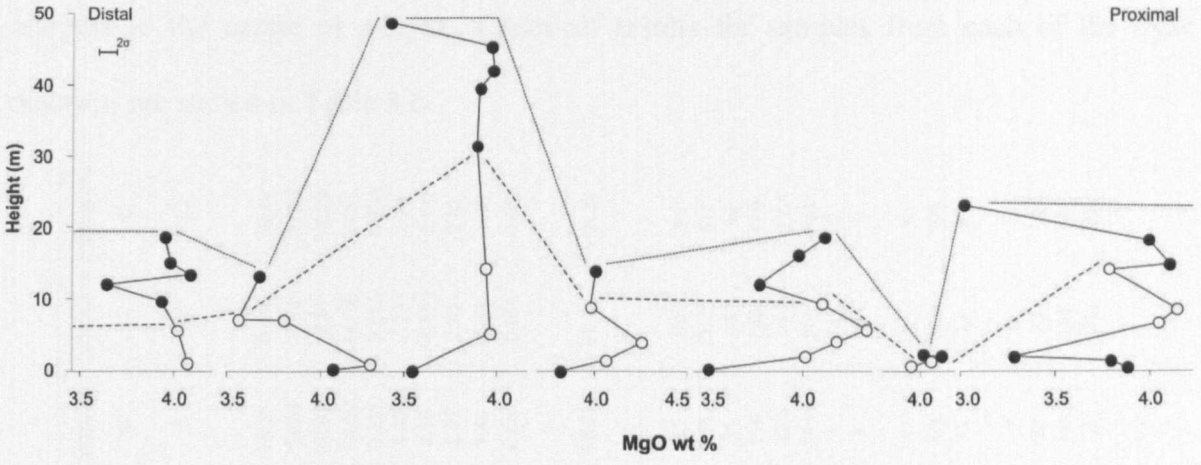

Figure 3.33 MgO wt% variation plotted with height within each lobe of the Ginkgo flow field from the vent proximal site in the east to the distal reaches of the flow field. Closed circles indicate samples within the upper or basal crust of each lobe. Open circles indicate samples from each lobe core.

Comparisons between the different lobes presented within this chapter as part of the Ginkgo flow field reveal varying characteristics with distance from the feeder dyke (Fig. 3.33). The degree of variation is similar to that seen in the Palouse Falls and Sand Hollow flow fields and there appears to be no consistent alteration in the style of heterogeneity as a function of distance.

3.5.5 Compositional variation within feeder dykes

Samples were collected from two feeder dykes; one within a Sand Hollow dyke and the other within a Ginkgo feeder dyke. Samples were taken from the dyke margins to the central portion of each dyke outcrop. The cross-section of samples should characterise any compositional heterogeneity related to temporal variations in the composition of the source supply or to contamination from the dyke walls. Temporal variations in magma composition may be recorded within a dyke due to the nature of dyke opening and flow pathways (Ross 1983). Combinations of the processes influencing dyke propagation such as cooling and crystallization from the margins towards the centre suggest that any temporal variation in composition may be recorded in a cross-section of samples from the

margins to the centre of a dyke. Chemical results for samples from each of the dyke outcrops are shown in Table 3.6.

Sample locality	Sand Hollow dyke - Harris country park							Ginkgo dyke - Snake River							
Sample no.	CRB06-329	CRB06-330	CRB06-331	CRB06-332	CRB06-333	CRB06-334		CRB06-112	CRB06-113	CRB06-114	CRB06-115	CRB06-116	CRB06-117	CRB06-118	CRB06-119
Flow field	SH	SH	SH	SH	SH	SH		G	G	G	G	G	G	G	G
Distance from dyke margin (m)	0	0.5	2	8	9	-0.2		0.3	0.7	1.4	1.9	2.5	3	3.8	4.2
Oxide wt. %															
SiO_2	51.26	50.73	50.73	50.39	50.74	54.78		50.55	50.28	50.35	50.57	50.45	50.67	50.35	50.44
TiO_2	2.898	2.850	2.890	2.904	2.925	2.114		3.065	3.049	3.079	3.097	3.079	3.068	3.069	3.076
Al_2O_3	13.69	13.25	13.29	13.16	13.22	13.40		12.95	12.92	12.92	13.05	12.82	12.97	12.87	12.89
FeO	12.39	13.69	14.05	14.07	13.74	11.94		13.83	14.12	14.32	14.38	14.22	14.03	14.18	14.31
MnO	0.216	0.241	0.241	0.233	0.217	0.214		0.223	0.230	0.233	0.236	0.234	0.235	0.232	0.233
MgO	3.44	4.23	4.46	4.41	4.15	3.24		4.17	4.21	4.23	4.28	4.22	4.30	4.23	4.22
CaO	8.60	8.28	8.37	8.25	8.26	6.94		8.12	8.08	8.10	8.14	8.03	8.10	8.06	8.03
Na_2O	2.71	2.69	2.75	2.71	2.81	2.75		2.81	2.85	2.79	2.79	2.80	2.77	2.81	2.81
K_2O	1.33	1.42	1.24	1.32	1.20	1.85		1.40	1.24	1.41	1.42	1.43	1.41	1.35	1.40
P_2O_5	0.549	0.541	0.554	0.542	0.532	0.363		0.664	0.660	0.661	0.646	0.667	0.662	0.666	0.662
LOI	0.88	0.06	0.08	0.02	0.19	1.33		-	-	-	-	-	-	-	-
Total	97.97	97.97	98.65	98.00	97.99	98.92		97.78	97.64	98.10	98.61	97.95	98.23	97.82	98.08
S %	0.09	0.10	0.08	0.08	0.06	0.02		-	-	-	-	-	-	-	-
Element ppm															
Rb	39	34	32	36	29	53		34	29	35	35	35	35	34	35
Sr	336	325	324	326	323	323		317	316	312	315	310	311	311	312
Y	41.7	40.8	40.3	41.5	40.4	39.5		40	39	38	38	39	38	39	39
Zr	195	193	192	195	197	200		181	181	180	175	182	178	180	179
Nb	14.7	16.0	17.5	16.0	17.0	14.3		13.3	12.9	13.7	13.5	14.0	12.8	13.2	12.4
Ba	712	533	557	555	600	669		585	564	578	564	574	564	566	574
Pb	7	2	8	7	5	8		7	8	8	6	6	6	8	7
Th	4	7	6	4	7	9		8	8	9	8	10	8	9	9
U	0	0	1	0	1	3		-	-	-	-	-	-	-	-
Sc	37	36	38	36	34	33		36	36	37	36	35	37	35	37
V	426	424	413	410	424	372		394	388	392	400	388	391	388	393
Cr	56	59	60	58	52	20		18	19	18	20	20	18	17	17
Co	44	38	39	40	39	33		-	-	-	-	-	-	-	-
Ni	26	28	26	25	25	9		17	17	16	15	16	17	18	18
Cu	32	33	31	34	33	16		19	21	22	20	21	22	23	22
Zn	148	141	141	137	140	133		146	144	143	144	143	145	143	144
Ga	22	21	21	25	23	23		23	22	22	20	23	21	21	21
Mo	1	1	3	0	1	0		-	-	-	-	-	-	-	-
As	0	1	0	0	4	1		-	-	-	-	-	-	-	-
S	416	513	477	419	423	113		-	-	-	-	-	-	-	-

Table 3.6 Compilation of the results for the Sand Hollow and Ginkgo feeder dykes. Ginkgo dyke samples were analysed at Washington State University. Cross-lab compatibility results are shown in Appendix E.

The Sand Hollow dyke samples reveal a systematic variation from the margins toward the centre of the dyke outcrop (Fig. 3.34). Samples become progressively less evolved with increasing distance from the margin to centre, e.g. MgO 3.44 to 4.46 wt%.

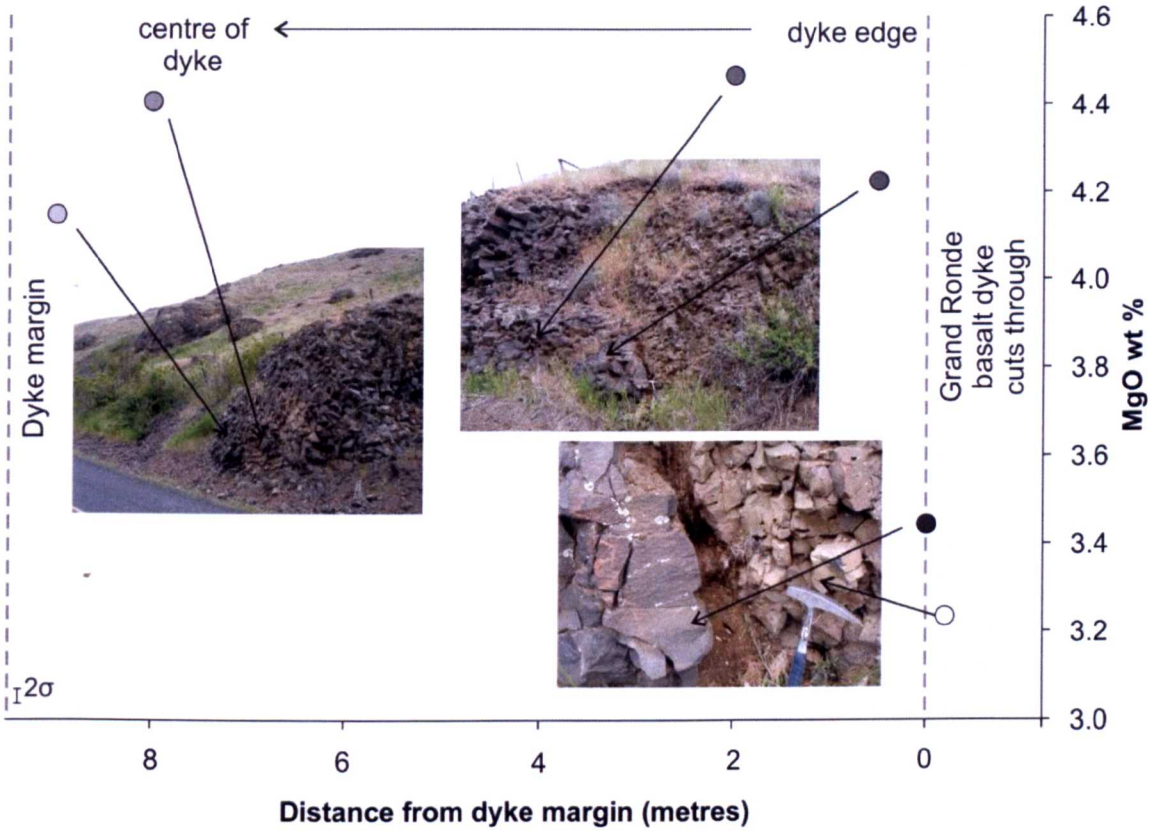

Figure 3.34 MgO wt% variations of samples from the margin to the centre of the feeder dyke of the Sand Hollow flow field in the Walla Walla river area, Harris Country Park (N45°53.473' W118°17.192').

By contrast the Ginkgo dyke results shown in Fig. 3.35 show little variation. The less evolved, more primitive composition of the dyke centre is similar to the intra-lobe vertical variations with high MgO values in the lobe cores. The pattern confirms a temporal relationship with more evolved lava erupted early in the eruption sequence and less evolved lava emplaced later in the sequence.

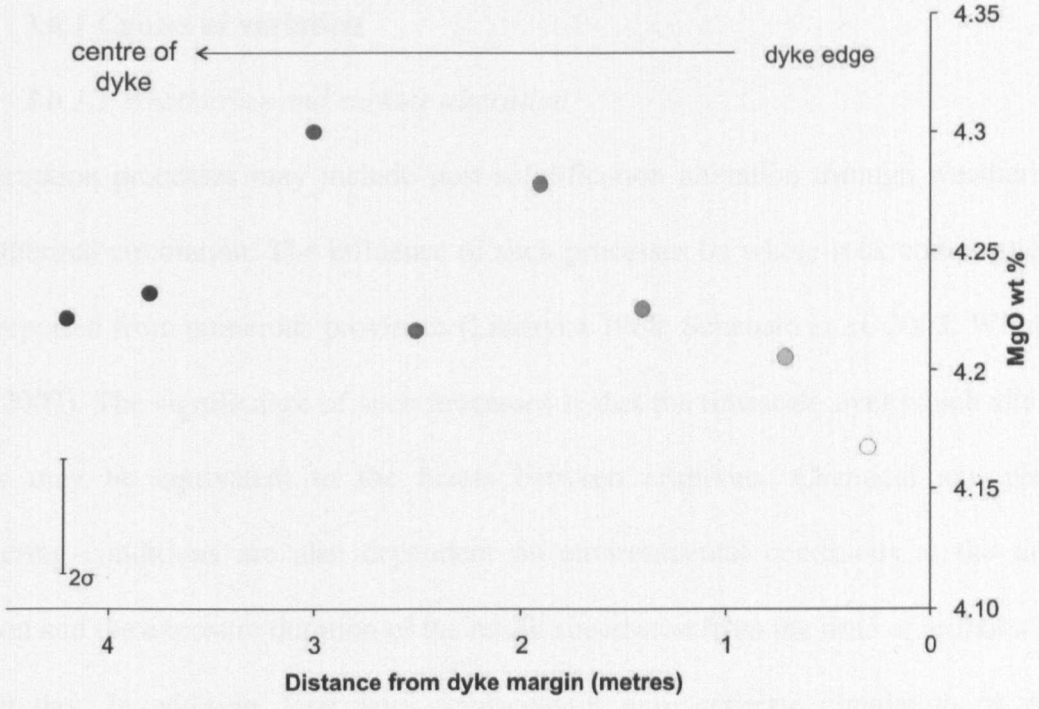

Figure 3.35 Compositional variations in samples from the margin to the core of the Ginkgo feeder dyke on the northern bank of the Snake River (N46°28.069' W118°37.498').

3.6 Discussion

Comparison of the results for the three flow fields presented within this chapter along with existing published data (summarised by Hooper, 2000) reveal distinct chemical subtypes defining each flow field. Within each subtype there is a small degree of overlap with adjacent subtypes. Application of chemostratigraphy works well on a broad scale for the identification of units across the entire province. However, the detailed analyses of Palouse Falls, Sand Hollow and Ginkgo flow fields reveal a significant overlap between the chemical subtypes suggesting that there is likely to be a limit to the scale at which a strict chemostratigraphy can be applied. At the scale of members across the province, Hooper (2000) clearly demonstrates the success of this approach, but the degree of chemical similarity between juxtaposed eruptions suggests that chemostratigraphy cannot be exclusively applied to define individual flow fields.

3.6.1 Causes of variation

3.6.1.1 Weathering and surface alteration

Post-eruption processes may include post-solidification alteration through weathering or hydrothermal circulation. The influence of such processes on whole-rock composition has been reported from numerous provinces (Lisitsyna 1968; Schenato *et al.* 2003; Wimpenny *et al.* 2007). The significance of such processes is that the timescale over which alteration occurs may be equivalent to the hiatus between eruptions. Chemical and physical weathering conditions are also dependent on environmental conditions at the time of eruption and the exposure duration of the basalt succession from the time of eruption to the present day. In addition, later lava emplacement may generate circulation of ground waters, facilitating precipitation of minerals and alteration of any repose period sedimentation (Chenet *et al.* 2008).

Mobile elements most susceptible to the effects of weathering (e.g. Ba, Ca, Na) do not systematically vary with height from the top of any flow. If any such post-emplacement (or secondary) alteration had occurred then depletion of mobile elements and corresponding enrichment of immobile elements would be expected to demonstrate a systematic loss from the top of a lobe most affected by weathering phenomena. Thus, I suggest that any of the compositional profiles presented here record the composition of the whole-rock mass at the point of crystallization, rather than secondary alteration processes.

3.6.1.2 Syn-emplacement contamination and thermal erosion

Contamination of basalt can occur by numerous processes at different stages of petrogenesis, eruption and emplacement of lava. Variations in the potential contribution of a contaminant must be evaluated to understand any cause of compositional heterogeneity. Identification of pre-eruption contamination is evaluated and discussed further in Chapter

4. Syn-emplacement contamination may occur at the interface between the flowing lava and the underlying substrate. Mechanisms facilitating such contamination include chemical diffusion, melting, mixing and other methods of mechanical incorporation such as thermal and mechanical erosion of the substrate by the advancing flow field front.

Erosion is a concept frequently associated with lava flows (Calvari and Pinkerton 1999). Both thermal and mechanical erosion are considered to play an important role in basaltic lavas and tubes in Hawaii (Peterson and Swanson 1974; Kauahikaua *et al.* 1998) and Etna (Greeley *et al.* 1998). It is also considered important in the development of komatiite lava flows (Huppert *et al.* 1984). Similarities between flow conditions within lava tubes and inflated sheet flows, where the entire width of a lobe may transport lava to the propagating flow front, imply that sub-lobe erosion may be present within flood basalt provinces.

Erosion by melting for Kilauean lava flows has been calculated at a rate approximating 10^{-7} m s^{-1}, or about 2.5 m/month (Hulme 1982). Hulme suggested that erosion through melting accounts for a small portion of the ground area; the majority is more likely to be removed as mechanical erosion by the lava. Mechanical erosion is dependent on the viscosity or coherence of the lava and a few days of continuous flow are required for melting to begin (Peterson and Swanson 1974). Erosion rates for mechanical removal have been calculated at typically 2 m per month (Hulme 1982). On Hawaii, the combined rates of both thermal and mechanical erosion add up to between 5 and 10 cm per day (Kauahikaua *et al.* 1998).

Thermal erosion of sediments from the substrate during turbulent flow conditions (Byerly and Swanson 1978; Camp and Hooper 1981; Kauahikaua *et al.* 1998; Beresford and Cas 2001) has been reported within CRBG flows (Reidel and Fecht 1987). However, contacts

in all examples studied here were glassy and chilled with no evidence for mixing or melting of sediments. Furthermore, there is no evidence of melting of any underlying lavas. Extensive erosion of the substrate should also lead to detectable chemical contamination of the lava (Huppert *et al.* 1984; Dragoni and Santini 2007). It is generally acknowledged that little contamination may occur following the development of a glassy selvage at the base of a lava flow (Fagents and Greeley 2001; Williams *et al.* 2004). In this case, contamination is likely to be negligible and is dismissed as a significant process.

3.6.1.3 Post-emplacement intra-lobe fractionation

Various mechanisms within a closed system, such as a lobe storing molten lava in the core (at least temporally prior to front lobe break-out, or through stagnation of flow advance) may generate physically separate differentiates of a starting composition. Detailed logs presented in Chapter 2 are recorded at each site to investigate the physical representation of any such processes, upon which to relate any chemical variation. Filter-pressing (Anderson *et al.* 1984) or the expulsion of differentiated melt and volatiles from the lower solidification interface (Hon *et al.* 1994) is one process which facilitates the physical separation of compositionally variable melts. Sufficient volume is required for the buoyancy of the differentiated melt layer to overcome viscosity and yield strength differences. However, it may be possible that the thickness of flood basalt lobes may result in higher pressures exerted upon the melt so that differentiates and volatile rich melt may never overcome viscosity or yield strength to produce physically separate and identifiable bodies. Whilst vesicle cylinders and horizontal vesicular sheets are evidence of late stage differentiation these are distinct and small in volume rather than processes effecting the composition of the whole lobe. Timescales of emplacement may prevent such closed system processes from occurring. For example, the lava lakes in Kilauea sustain melt in the core for decades as a stagnant differentiating lava. Lobe by lobe emplacement across a

flow field may sustain lava stored in the lobe cores for short periods of time prior to lobe front breakout. Whereas a continuously advancing flow front may act as an open system, systematically transferring new lava from a proximal lobe core to a distal margin.

Within-flow differentiation, such as that recorded in Hawaiian lava lakes (Helz *et al.* 1989; Barth *et al.* 1994), may generate compositional variation in a thick accumulation of lava (Worster *et al.* 1993). One method that may facilitate this is crystal accumulation and separation of solid phases from melt (Philpotts *et al.* 1998; Philpotts and Philpotts 2005). Within-flow differentiation by crystal separation requires the presence of large phenocrysts orientated with the c-axis parallel to flow direction that can trap rising, lower-density residual melt. Despite the presence of abundant segregation veins and vesicle-rich horizons in lava cores, there is no evidence for crystal accumulation. The flow fields studied here contain few phenocrysts and instead mainly consist of finely crystalline aphyric quench-cooled basalt. If there was any degree of internal differentiation, it must be concentrated in the lava core.

Segregation features are one of the physical indicators of intra-lava differentiation syn- or post-emplacement during a period of cooling when viscous deformation is still possible (Merle 1998). Progressive development of segregation features may be akin to fractional crystallisation processes in a magma chamber but in the former may result from filter-pressing (Anderson *et al.* 1984 and as described in Chapter 2). Merle (1998) reports a change in chemistry between samples from segregation structures and surrounding basalt. Segregated material from ocean floor basalt pillows shows compositional enrichment in Si, Fe, Ca, Na, Ti, P, and K and depletion in Mg and Al relative to bulk rock composition. This supports the suggestion that segregation structures result from physical separation of evolved residual melt from a crystallising mush. Segregation sheets are reported from the

Holyoke Basalt (Carroll *et al.* 1995) bearing textural and composition differences relative to the host basalt. Detailed studies have been conducted in volcanic provinces in USA (Wacaster and McConnell 2002; Hartley and Thordarson 2009, in press) and on long lavas (Bideau and Hekinian 1984; Caroff *et al.* 2000; Costa *et al.* 2006; Rogan *et al.* 1996; Stephenson *et al.* 2000) which summarise the extent that in-situ fractionation can generate compositionally evolved physically separate melts. Such processes, and the intricacies of them, are limited to the lava core in the last stages of crystallisation. Segregations are not sampled in this study as they are not the subject of this investigation.

3.6.1.4 Magmatic processes

A range of magmatic processes may affect the composition of a flow field that may be preserved as compositional heterogeneity if the transport of magma, style of eruption and emplacement do not act to homogenize the lava. Heterogeneity may reflect any one, or a combination of: fractional crystallization, recharge, magma mixing, crustal contamination and mantle source heterogeneity. Thoughts on hypothetical compositional variations reveal that four end-member scenarios may be identified within profiles of geochemical variation for any element or oxide with height within a sheet lobe (Fig. 3.36).

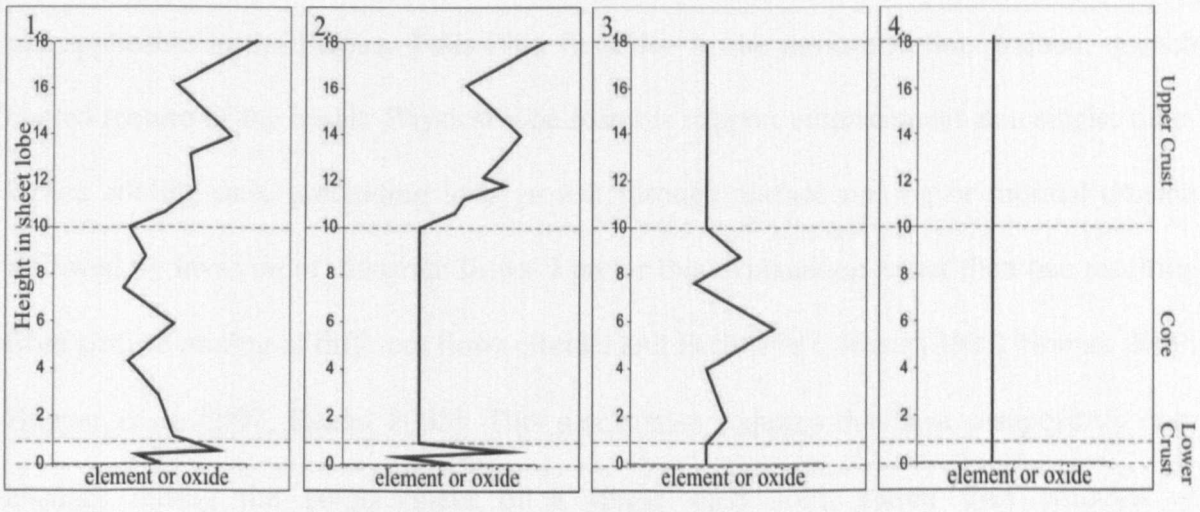

Figure 3.36 Hypothetical compositional variation diagrams.

These hypothetical variations can be interpreted as follows:

Scenario 1 - Both source variation and *in-situ* differentiation are active processes.

Scenario 2 - Changing composition of the source through time is recorded in the progressive cooling of the upper crust. The homogeneity of the core represents the composition of the last batch of magma. The heterogeneity of the source composition may be the result of a number of factors.

Scenario 3 - Fractional crystallisation and *in-situ* differentiation are the dominant processes represented by the observed variation.

Scenario 4 - The lava is emplaced and crystallises so rapidly that there is no time for either the composition of the lava to evolve or the composition to change significantly at source.

These hypotheses will be discussed in turn within the remainder of this chapter.

3.6.2 Explaining intra-lava variations

The major and trace element variation in the Palouse Falls flow field is coupled to intra-lava volcanological features. Such heterogeneity in lavas in other regions have been attributed to a variety of causative processes, including random variation (Lindstrom and Haskin 1981). Others explain such heterogeneity using textural or petrographic evidence such as crystal accumulation (Philpotts *et al.* 1999; Philpotts and Philpotts 2005). This is not applicable in the Palouse Falls flow field due to the uniformly fine grained, quench cooled texture of the basalt. Physical lobe features support emplacement as a single, time-lapsed cooling unit, precluding lobe growth through surface mixing or thermal erosion followed by invasion of disparate flows. I prefer this explanation rather than one resulting from surface mixing of different flows (Reidel and Fecht 1987; Martin 1991; Hooper 2000; Hooper *et al.* 2007; Reidel 2005). This mechanism requires that lava composition only changes during the emplacement of a single sheet lobe, rather than eruption of compositionally distinct lavas erupted simultaneously and mixing during flow

advancement. I further suggest that the progressive systematic variation is a result of magmatic heterogeneity from the point of eruption (Rubin *et al.* 2001) rather than controlled by post-eruption processes such as within lobe core fractionation or segregation (Philpotts and Philpotts 2005).

The Palouse Falls flow field is the volumetrically smallest of the three flow fields presented. It also bears the most limited range of heterogeneity within individual lobes. When compared with the Sand Hollow flow field, the intra-lobe variations appear to be systematic with fewer steps in the compositional profiles. Variations in the Sand Hollow flow field cannot be explained by post-eruptive processes or alteration. Whilst it is acknowledged that in-situ differentiation is an influential process within the cores of these lobes, the presence of physical indicators such as segregation material is limited to the upper part of each lobe core and thus has a limited effect on the compositional heterogeneity observed within an entire lobe. The complexity of multiple lobes in the Ginkgo flow field does not lend itself to this type of study. Comparisons between intra-lobe results and the hypothetical scenarios reveal the presence of scenarios 1, 2 and 3 with scenario 2 being common in the Sand Hollow flow field. It is proposed here that the principal compositional variation within a flow field is the result of the geochemistry of the magma feeding an eruption.

3.6.3 Source variation

Identification of compositional heterogeneity as a pre-eruptive feature offers the possibility of investigating processes that affect magma feeding a single eruption. Fractional crystallisation and recharge accompanying eruptions from large bodies of basaltic magma at crustal levels is likely to occur within such large volume flow fields (>1000 km^3). Fractional crystallisation has previously been used to explain geochemical signatures

between different flow fields of the CRBG stratigraphy (Hooper 1985; Hooper 1988), but not variations within single lava flow fields.

Mass balance calculations were run using PETROLOG software (Danyushevsky 2001) under two sets of conditions. Both models were run assuming a volatile content of 0.3-0.4 wt% H_2O, which is in agreement with values for Columbia River Basalt magmas (Thordarson and Self 1996; Hartley and Thordarson 2009). The first model uses the most primitive composition for all flow fields at increments of 0.1 % fractional crystallisation of a parent melt. The most evolved sample compositions from each of the flow fields are attained within 5 % fractional crystallisation. The second model uses an average composition for the Imnaha Basalts (Hooper 2000). The Imnaha was the first formation erupted in the CRBG and has been suggested to represent the most plume-like composition (e.g. Hooper 2000). Application of the model using identical parameters reveals a range in fractional crystallisation from 32-46 % to produce the observed values. With either of these models there is a large scatter in composition of samples from any of the three flow fields suggesting processes other than simply fractional crystallisation are involved in generating the compositional profiles.

Combination of modelling results with intra-lobe profiles suggests tapping of a layered or zoned magma chamber or network of sills and dykes undergoing replenishment during the eruption. The source of such variation may stem from a combination of processes. The relatively evolved characteristics and systematic variation of these basalts suggest that high level fractional crystallisation has been an important pre-eruption process (Takahahshi *et al.* 1998). The general absence of phenocrysts throughout the flow fields suggests that fractional crystallisation was extremely efficient. However, the extent of crustal assimilation cannot be robustly quantified due to the similarity in composition between the

likely assimilant, Jurassic accreted terrane, and the magma. Comparison with existing data for the Columbia River Basalts support an ocean island basalt-type magma source for these basalts (Hooper and Hawkesworth 1993; Hooper 2000). However, the nature of the heterogeneity cannot be explained by variations in partial melting of a compositionally diverse source. Further investigations are presented in Chapters 4 and 5.

3.7 Implications for emplacement models

Intra-lobe compositional variations appear to be coupled to physical, emplacement-related features both within lobes and with distance from source. Thus intra-lobe variations may record magmatic compositional differences, reflected in the lava emplacement. Consideration of the features inherent to inflated sheet lobes suggests that systematic variations from more evolved lobe crusts to more primitive lobe cores reflect the presence of compositionally distinct magmas that were available at the same time. Eruption may have occurred from either a stratified, periodically replenished, magma chamber or a network of separate chambers sequentially tapped during the ongoing eruption.

3.7.1 Evidence for inflation

Decreases in compatible element abundance and enrichment in incompatible elements appears to be consistent throughout the flow field. This supports the field evidence of sequential emplacement of lobes from the source to the distal reaches of the field as well as corroborating the intra-lobe temporal relationship of less-evolved melts emplaced later in the eruption, represented in the lobe cores.

Spatial compositional variations within the simple example of the Palouse Falls flow field supports emplacement of distal lobes via laminar flow of lava through a network of lobe

cores. Such emplacement would suggest that lobe cores are the last emplaced lava within each profile and the most distal core is likely to be emplaced before all the more proximal ones have crystallised. This is significant as the cores of proximal lobes are interpreted to act as feeders for more distal lobes. In detail, flow field formation must be highly complex. However, as the last distal lobe is being emplaced there must be at least one proximal near vent lobe (and a series of linked lobes all the way through the flow field), that is able to transfer the same composition lava through its core as in the most distal core. Thus, based on our model, preferential pathways of lava flow through lobe cores may be expected to have similar chemistry. Progressive variations from the source to distal areas are observed through the constituent lobes of the flow field. Excursions from this general trend may reflect lateral spread of the flow field in addition to longitudinal development. Therefore, lobes of differing composition are juxtaposed within a flow field.

3.7.2 Caveats in the inflation model

Variations in the compositional profile within a single vertical section are complicated by: 1) the very outer few centimeters of crust of a lobe, which should have the same composition, are often not sufficiently well preserved to provide samples for analysis; 2) the possibility that the upper crust need not be the compositional mirror of the lower crust due to inhibited development of the lower crust during lobe emplacement and thickening (see Keszthelyi and Self 1998). This may also be affected by rafting of cooled sections of the upper crust on lava flowing in the core. Furthermore, variation in the lower crust may be affected by variations in the flow dynamics at the base of the lava core including thermal or mechanical erosion; turbulence caused by topographic variations in the substrate; and shear deformation of a crystal lattice caused by flow of overlying lava.

Whilst thermal erosion may be theoretically possible, it appears that such a physical process is both unsupported by field observation and unlikely within this province (Greeley

et al. 1998; Kerr 2001). However, there are field observations to support shear deformation in the basal metre of the thick lava flows described here, as well as elsewhere (James *et al.* 2004). Evidence from other long lava flows also suggests shear deformation or strain accommodation in a cooling basalt (Lore *et al.* 2000). Shear deformation within the lower crustal zone would complicate the simplistic model of laminar flow associated with the pahoehoe inflation model but is a likely scenario enabling the propagation of lava to the advancing flow front once a crystal lattice has formed.

3.7.3 Comparison with emplacement of other magmatic bodies

Other volcanic products and igneous bodies display compositional heterogeneities thought to derive from dynamic processes within a single magma chamber. Ignimbrites display chemical and thermal heterogeneities in zones that may be used to trace the evolution and emplacement of the density current (Carrasco-Nunez and Branney 2005). Heterogeneities in the Fish Canyon Tuff, USA (Bachmann and Bergantz 2008), Bishop Tuff, USA (Hildreth and Wilson 2007), Valley of Ten Thousand Smokes, Alaska (Fierstein and Wilson 2005) and Zaragoza, Mexico (Carrasco-Nunez and Branney 2005) have been interpreted as the result of complex mixing and mingling within a stratified magma chamber. Whilst compositional zonation is common, simple interpretations are usually based on withdrawal from a density-stratified magma chamber. Bachmann and Bergantz (2008) describe long term heterogeneities within magmatic systems that may be induced by mixing, assimilation, internal phase changes and decompression and that are preserved due to inefficient convection. Furthermore, they state that the degree of heterogeneity (and efficiency of convection) is not related to the viscosity of the magma. Whilst basaltic magmatic systems may not preserve heterogeneity to the same extent as more evolved magmas the same processes are applicable. Therefore the length of repose periods between

eruptions may not be related to the degree of compositional heterogeneity within a single flow field.

Intrusive bodies such as sills contain compositional heterogeneities that have been interpreted to be a result of both the style and duration of emplacement (Gibb and Henderson 1996; Gibb and Henderson 2006), assimilation and contamination of the melt from the wallrock (DePaolo 1981) and magmatic heterogeneities preserved as a function of emplacement (Latypov 2003). Sub-horizontally emplaced sills have many similarities with thick lava lobes or sheet lobes; the outer portions of each body are emplaced first with younger magma emplaced into the core creating an age profile younging from the outer margins to the centre of each. The variations between the two bodies are related to the cooling style – whilst flood basalt sequences have an asymmetric cooling profile displayed in a thick upper crust and thin lower crust, sills are more likely to have a symmetrical cooling profile as both the upper and lower contacts have a similar thermal regime with the surrounding country rocks.

3.8 Conclusions

- Progressive systematic variation with height through individual sheet lobes provides supporting evidence for the emplacement of individual lobes by pahoehoe-type inflation.

- High resolution sampling and compositional analysis within single flow fields offers a significant advance in the understanding of emplacement mechanisms that are not revealed by lower resolution datasets.

- A combination of high-resolution sampling relative to volcanological features enable compositional fingerprinting of flow fields. Such compositional data provides a record of sequential development of the magmatic system over time.

- Intra-lobe differentiation, syn-emplacement contamination and post-emplacement alteration are ruled out as processes generating the observed compositional heterogeneity.

- Vertical and lateral variations within and between lobes constituting a single flow field reveal slightly more evolved upper and lower crusts and slightly more mafic cores. During emplacement of each flow field the composition of the magma progressively became slightly more primitive.

- Small-scale major and trace element compositional heterogeneity on whole-rock samples alone is insufficient evidence to constrain the petrogenesis of individual flood basalt eruptive units.

- With regards to chemostratigraphic characterisation of Columbia River basalts, intra-lava flow compositional heterogeneity may cause miscorrelation or misinterpretation of eruption units when based on single sample characterisation. This has implications for sampling for the purpose of establishing a chemostratigraphy. Even on a small-scale, it cannot be assumed that samples from the same point or height in a lobe enable cross-correlation. Across a province, compositional variations may not distinguish between, or correlate with, separate eruptions.

3.9 Further work

Further investigation may be merited on the mechanism of emplacement in the base of a flood basalt lava flow. Textural investigation accompanying compositional variation may provide an insight to understanding structural deformation and the style of lava flow in this basal zone. The possibility that shear deformation of the crystal lattice may assist propagation of lava to the advancing flow field front is comparable to shear deformation enabling movement within the basal zone of glaciers.

View to the south down the Palouse River canyon from Palouse Falls State Park

Chapter 4. Osmium Isotopes

4.1 Introduction

In light of the major and trace element heterogeneity in single flow fields presented in Chapter 3 and the failure to identify petrogenetic processes from trace element compositions it is important to investigate the possibility of isotopic heterogeneity. If this exists it could provide quantitative constraints on the length-scales over which magmatic processes occur within a province. Os isotopic analyses are applied here to investigate magmatic processes prior to a flood basalt eruption. This is the first study of Os isotope variations in the products of a single continental flood basalt eruption and the results provide some insights into the causes of intra-flow variations. The nature of this study allows a link between changes in flow chemistry with the textural and temporal evolution of the flow based on the inflation model.

The Re-Os system is applied here to examine heterogeneity and investigate the relative contributions from the assimilation of continental crust, source contamination and heterogeneity of the mantle source to the petrogenesis of these lavas. Accurate determinations of the relative contributions of continental crust and the mantle to flood basalts remain a significant barrier to understanding the genesis of large volume melts (Peng *et al.* 1994; Chesley *et al.* 2002; Krienitz *et al.* 2006). Crustal contamination is considered to be a key factor contributing to the compositional differences between continental flood basalts and their oceanic counterparts. It has been clearly demonstrated that the migration of magma through continental lithosphere results, in some cases, in crustal assimilation through bulk or selective contamination or assimilation with fractional crystallisation (AFC) (Carlson *et al.* 1981; Carlson 1991; Brandon *et al.* 1993). However,

some argue it is the source that is contaminated (e.g. by ancient subducted crust) prior to magma generation (Carlson 1991) that creates mantle heterogeneity, rather than contamination during magma ascent and eruption. In either case, it is essential to constrain the role of contamination on the composition of basaltic magmas prior to attributing such variations to mantle heterogeneity (Glazner and Farmer 1992; Chesley *et al.* 2002; Reiners 2002).

4.1.1 Existing Re-Os data for continental flood basalts

Re-Os isotopes have been used to provide some insight into the origins of continental flood basalt magmatism (e.g. Allègre and Luck 1980; Brauns *et al.* 2000; McBride *et al.* 2001) by enabling the sources of contamination (Hoefs *et al.* 1980) to be distinguished from the evolved isotopic signature inherited from the different potential sources of the basalts (Carlson 1991; Ellam *et al.* 1992; Smith 2003). There are few Os isotope data for continental flood basalts, however, distinct variations in $^{187}Os/^{188}Os$ within provinces have been reported for the Karoo (Ellam *et al.* 1992), Siberia (Horan *et al.* 1995), Ferrar (Molzahn *et al.* 1996), Deccan (Allègre *et al.* 1999), Emeishan (Xu *et al.* 2007) and Columbia River provinces (Chesley and Ruiz 1998) (Fig. 4.1). However, these studies selectively excluded samples representing the most evolved and potentially most contaminated basalts.

The source of these vast volumes of basaltic material, whether deep mantle plume, shallow asthenospheric mantle or sub-continental lithospheric mantle (SCLM), is highly debated. The SCLM typically has less radiogenic values than primitive upper mantle ($^{187}Os/^{188}Os$ = 0.1296; (Meisel *et al.* 1996), and plume-derived material is characterised by OIB-type mantle with $^{187}Os/^{188}Os$ ratios that range from ~0.13 to 0.15 (Shirey and Walker 1998). The sensitivity and systematics of the Re-Os system result in the development of distinct

isotopic signatures and offer the opportunity to reconcile contradictory models based on traditional lithophile element systems (Rb-Sr, Sm-Nd, U-Pb) that generally experience a smaller extent of fractionation during melting and magmatic processes.

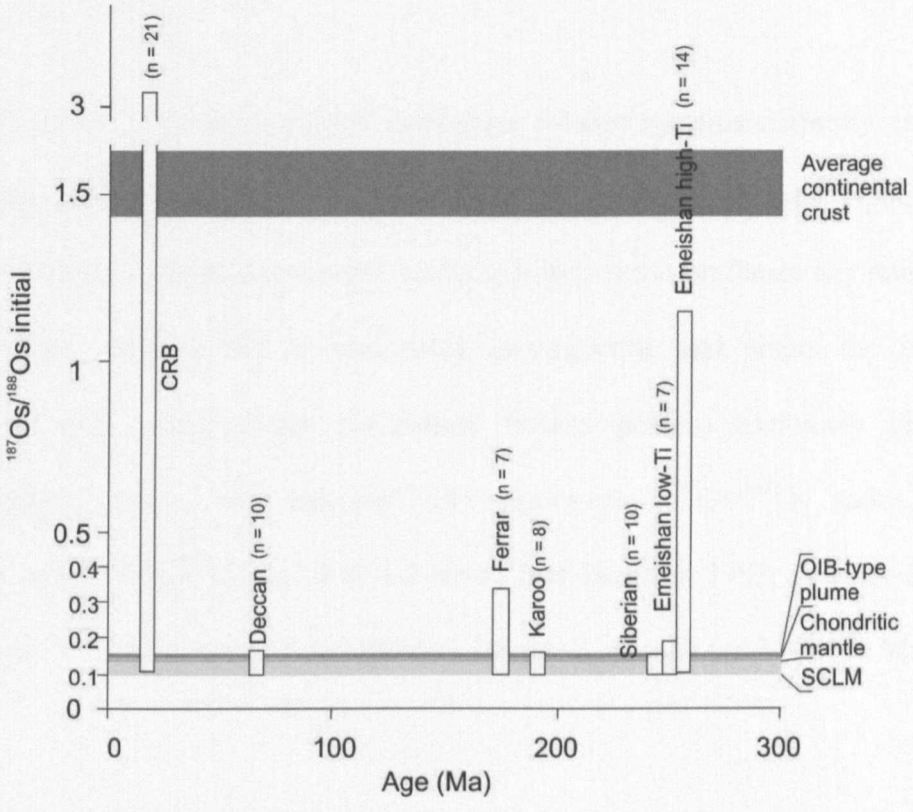

Figure 4.1 Schematic diagram showing the distribution of initial $^{187}Os/^{188}Os$ and ages for the Karoo (Ellam *et al.* 1992), Siberia (Horan *et al.* 1995), Ferrar (Molzahn *et al.* 1996), Deccan (Allègre *et al.* 1999), Emeishan (Xu *et al.* 2007) and Columbia River provinces (Chesley and Ruiz 1998) and references therein. $^{187}Os/^{188}Os$ values of potential sources from ocean island basalts (OIB, Shirey and Walker 1998), chondritic mantle (Meisel *et al.* 1996), SCLM (Shirey and Walker 1998) and average continental crust (Peucker-Ehrenbrink and Jahn 2001).

Existing studies have shown variations between provinces in Os isotopes and the resulting interpretations of petrogenesis of basaltic melts. However, no study has yet been undertaken which documents spatial and temporal variations in Os isotopes at high resolution, in particular at the scale of an individual flow. Investigation of the products of a single eruption potentially provides insight to both the petrogenesis of a single batch of melt and the significance of isotopic variability throughout individual provinces. Without

such investigation into the influence of shallow lithospheric processes and contamination it is not possible to interpret the primary source of continental flood basalts.

4.2 Re-Os systematics

The Re-Os system is unique amongst radiogenic isotope systems currently employed in earth systems science because of the sensitivity of osmium to crustal inputs. Osmium behaves as a highly compatible element during melting, and is preferentially retained in the residual mantle, whereas Re is moderately incompatible and enters the melt. As a consequence, both oceanic and continental basalts possess extremely high Re/Os (parent/daughter) ratios, and develop very radiogenic $^{187}Os/^{188}Os$ ratios, (average continental crust $^{187}Os/^{188}Os \approx 1.4$ to 1.9; Esser and Turekian 1993; Peucker-Ehrenbrink and Jahn 2001) relative to the contemporary depleted mantle (~0.12-0.13; Meisel *et al.* 1996).

4.2.1 Properties of Re and Os

Osmium is a platinum group element with seven naturally occurring isotopes, ^{184}Os, ^{186}Os, ^{187}Os, ^{188}Os, ^{189}Os, ^{190}Os and ^{192}Os (Table 4.1). Of these, ^{186}Os and ^{187}Os are products of radioactive decay from ^{190}Pt by alpha emission, and ^{187}Re by beta emission, respectively. Osmium may exist in a number of different oxidation states but the predominant natural states are 0, +III and +IV. Rhenium is a refractory metal with two natural isotopes, ^{185}Re and ^{187}Re and most commonly exists in natural samples with an oxidation state of +IV or +VI (Morgan 1997b; Ertel *et al.* 2001). Due to the low emission energy of the ^{187}Re decay, various methods have attempted to accurately measure the decay constant. Initial direct measurements of the decay constant yielded a value of 1.64×10^{-11} yr^{-1} (Lindner *et al.* 1989), which has since been refined to 1.666×10^{-11} yr^{-1} on the basis of high-precision Re-

Os chronology (Shen *et al.* 1996; Smoliar *et al.* 1996), and most recently 1.6668 ± 0.0034 x 10^{-11} yr^{-1} (Selby *et al.* 2007).

Isotope		Relative proportion (%)
Osmium	^{184}Os	0.02
	^{186}Os	1.59
	^{187}Os	1.96
	^{188}Os	13.24
	^{189}Os	16.15
	^{190}Os	26.26
	^{192}Os	40.78
Rhenium	^{185}Re	37.4
	^{187}Re	62.6

Table 4.1 Naturally occurring isotopes of Re and Os and their relative proportions.

The characteristics of both Re and Os during mantle melting have an important influence on the distribution of these elements. Os predominantly resides within sulphides (Roy-Barman *et al.* 1998) whereas Re is sited within silicate phases (Burton *et al.* 1999; Burton *et al.* 2002). However, Re is only partially controlled by silicates as it is compatible in sulphide phases and covaries with S in orogenic lherzolites and mantle peridotites (Morgan 1986; Reisberg and Lorand 1995). Despite the complexities of Re-Os partition coefficients, there is an intrinsic relationship between sulphur saturation and Re-Os abundances (Keays 1995; Lightfoot and Keays 2005). The low Os concentration of some oceanic basalts may be caused by olivine crystallisation in which Os is incompatible and causes sulphur saturation of the melt driving sulphide precipitation (Burton *et al.* 2002). Sulphur as an incompatible element is depleted in the lithospheric mantle and sulphur saturation can also occur through contamination at crustal levels. Therefore, consideration of sulphur concentrations alongside Re-Os isotopes provides insight to the origin and crustal level processes of the CRB magmas.

4.2.2 History of Re-Os analysis

The full potential of the Re-Os system was not realised until the 1990's with improvements in both chemistry and the analytical precision and accuracy of mass spectrometric techniques. The earliest successful rhenium and osmium results analysed gaseous OsO_4 but suffered from low precision (Hirt *et al.* 1963). Subsequent research focused on increasing the ion yield of Os, as the high ionization potential of Os (~9eV) requires greater temperatures than those possible using conventional thermal ionization mass spectrometery (TIMS). The use of secondary ionization mass spectrometry (SIMS) alongside improvements in the purification of Re and Os resulted in much greater precision in the 1980's (Luck *et al.* 1980; Luck and Allegre 1982). Other methods were also developed which successfully analysed positive ions of Os, albeit with low precision (acceleration mass spectrometry, Fehn *et al.* 1986), argon plasma torch from an inductively-coupled plasma mass spectrometer (ICP-MS) (Houk 1980), and resonance ionization mass spectrometry (Walker and Fassett 1986).

The breakthrough in analysis arrived with the advent of negative TIMS (N-TIMS) (Creaser *et al.* 1991; Volkening *et al.* 1991; Walczyk *et al.* 1991) as the yield of negative ions from solid Os samples permits analysis by conventional TIMS methods and dramatically improved precision. The improvement in results from analysis by N-TIMS facilitated research in low Os concentration samples. All the samples presented within this chapter were analysed by N-TIMS. In parallel with analytical developments improvements in methods of chemical separation have also extended the range of samples which can be measured at low levels of Re and Os. An ultra low blank chemistry involving bromine extraction and microdistillation (Birck et al. 1997) is employed in this study.

Early Os research typically reports isotope data as the $^{187}Os/^{186}Os$ ratio, however, ^{186}Os has been found to be the daughter isotope of radioactive decay from ^{190}Pt (McDaniel *et al.* 2004). Therefore, due to the variations in $^{186}Os/^{188}Os$ accompanying ingrowth of ^{186}Os (Walker *et al.* 1991), normalisation of ^{187}Os to the stable isotope ^{188}Os has been universally adopted. The $^{187}Os/^{188}Os$ reporting convention is used in this study to permit comparison with existing datasets. Where comparison with existing data reported as $^{187}Os/^{186}Os$ is required, a $^{186}Os/^{188}Os$ value of 0.12035 is applied to convert to $^{187}Os/^{188}Os$ (Snow and Reisberg 1995).

4.3 Sampling strategy and analytical methods

4.3.1 Sample selection

A total of 26 samples were selected for Re-Os analysis. The samples are a subset selected to represent three vertical transects through lobes of the Sand Hollow flow field (Fig. 4.2). Full geochemical characterisation of the Sand Hollow flow field was based on 82 samples from nine sections presented in Chapter 3.

The Sand Hollow flow field was selected for study due to the relative ease with which it can be recognised in the field, independent of chemostratigraphic discrimination. The hiatus following the Grande Ronde eruptions was marked by a significant period of sedimentation and is frequently represented in the field by a thick well-developed laterite. The first extensive Wanapum lava, the Ginkgo, is a plagioclase phenocryst-rich basalt flow field, that is a marked change from the strongly aphyric Grande Ronde flows. Such characteristics have been traced laterally in the field to map in detail the extent of the flow fields which stratigraphically precede the Sand Hollow flow field. The characteristics

observed and methods employed are described in Chapter 2. Such a rigorous approach to field mapping ensures that only lobes from the same eruptive event were sampled.

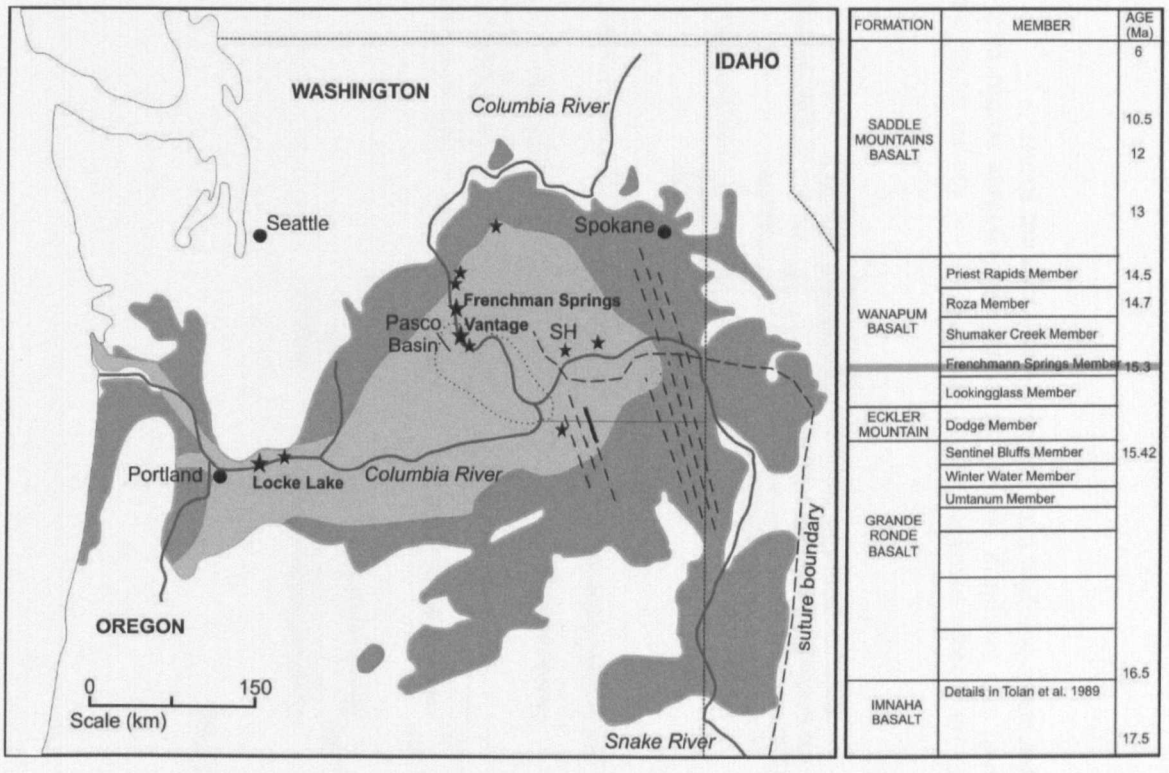

Figure 4.2 Map showing the extent of the Sand Hollow flow field (pale grey) within the CRB (dark grey), the location of sites used for major and trace element analyses (stars) and named sites for Re-Os analyses. Stratigraphic units of the Columbia River Basalt Group (Swanson *et al.* 1979; Beeson *et al.* 1985; Reidel and Fecht 1987; Tolan *et al.* 1989) and age dates (Snavely *et al.* 1973; Watkins and Baksi 1974; McKee *et al.* 1977; Long and Duncan 1983; Baksi and Farrar 1990; Hooper *et al.* 2002).

Of the three localities used for Re-Os analysis, the Vantage section is located closest to the feeder dyke area; the Frenchman Springs section lies 16 km further north. The Locke Lake section is the most distal locality, set in the palaeo-Columbia River valley, a topographic low in the high ground of the Cascades mountain range which funnelled lavas out to the west coast. These represent a range of localities across the flow field, and are thought to mark temporally distinct parts of the eruption that produced the whole flow field. Within each section, samples from the lower crust and the top of the upper crust were taken, with other samples taken at critical boundaries, at notable features and at evenly dispersed localities (Fig. 4.3).

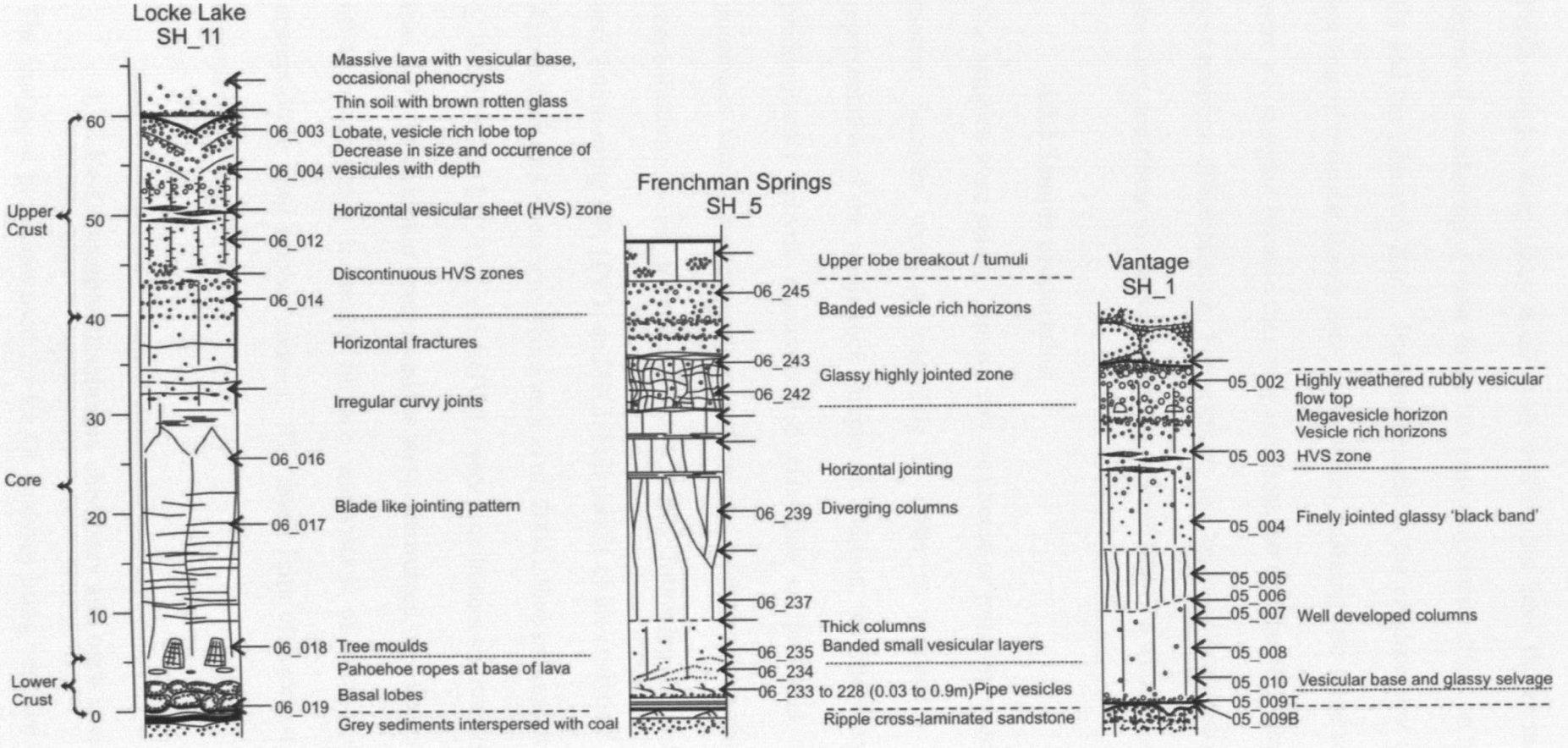

Figure 4.3 Logs of the three localities from which samples were taken for isotope analyses. Intra-lobe features are shown including jointing style, vesicular horizons, segregation features (zones of residual liquid) and sampling points. Structural subdivisions within each lobe are delineated by dashed lines separating the lower crust, lobe core and upper crust. Samples used for Re-Os analyses are shown.

Fresh samples were taken in all cases, and studies have shown that the low to moderate degree of weathering of these flows has only a moderate effect on mobile elements i.e. Ba, Ca and Na (Sheldon 2003). Features related to the emplacement of these flows (such as horizontal vesicular sheets and pipe vesicles, marking late stage residual melt migration) were not sampled because they may represent the end member composition of any in-situ post-eruption differentiation. Furthermore, the localised occurrence of late-stage features does not contribute to understanding the construction of a whole flow field.

4.3.2 Sample preparation

The samples were split to remove any weathered or joint faces and powdered in an agate mortar. Samples were at least 30g in order to produce a homogeneous powder representative of the whole-rock sample. In addition, the finely crystalline nature of these predominantly aphyric quench-cooled glass-rich samples that lack phenocryst phases minimises sample heterogeneities and ensures analytical reproducibility. Trace element concentrations were determined by ICP-MS following a method of Teflon® vial dissolution using HF, HNO_3 and HCl. Full details of the analytical procedures are given in Appendix B and elsewhere (Kisakurek *et al.* 2004). Five international rock standards (BIR-1, W2, DNC-1, BHVO-2 and AGV-1) were simultaneously run and reproducibility is less than 4 % (1σ). Sulphur concentrations were determined on a Leco CS230 at the University of Leicester using induction furnace combustion of samples followed by infra-red absorption to yield sulphur content. The lower limit of detection is 23 ppm and average reproducibility is 1.32 % (1σ).

4.3.3 Re-Os sample dissolution, chemistry and mass spectrometry

The analytical procedure used for Re-Os analyses using negative thermal ionisation mass spectrometry closely follows that outlined previously (Birck *et al.* 1997) and is described

below. Sample powders (~0.4g) and a mixed ^{185}Re-^{190}Os spike were digested in 2ml of 29M HF and 2ml 9M teflon distilled HBr in PFA pressure vials at 140°C for a minimum of 48 hours. Oxidation of osmium to ensure complete equilibration to Os +IV was achieved by the addition of CrO_3-HNO_3 and extracted into Br_2. These samples were purified by microdistillation. Rhenium extraction and purification was achieved by ethanol reduction of the supernatent from Os extraction and subsequent solvent extraction using iso-amylol and 2M HNO_3. Both Re and Os were analysed on Pt filaments as OsO_3- and ReO_4- using the electron multiplier on a ThermoFinnigan Triton® (Creaser *et al.* 1991; Volkening *et al.* 1991). Osmium isotopic ratios are normalised to $^{192}Os/^{188}Os$ 3.08271 (Luck and Turekian 1983) and corrected using $^{18}O/^{16}O$ and $^{17}O/^{16}O$ ratios of 0.002047 and 0.00037 respectively (Nier 1937).

4.3.3.1 Blanks

Total procedural blanks for Os ranged between 0.03 and 0.10 pg with a mean of 0.077pg (n=8). The mean $^{187}Os/^{188}Os$ ratio of the blanks was 0.267 ± 0.053. The blank corrections applied are appropriate for each reagent batch, rather than the long term mean. The contribution of the blank to Os recovered from the samples for the majority of data were less than 10 % with the exception of nine samples which range from 10 to 22 % where Os abundance is generally low (0.5 to 0.8 ppt). Rhenium blanks varied between 4.6 and 45.7 pg with a mean value of 15.8 pg.

4.3.3.2 Reproducibility

The 'nugget effect' in Re-Os whole-rock chemistry may be caused by heterogeneous distribution of Os rich-phases and, independent of the laboratory method, may cause misrepresentation of the actual sample value (Carlson and Turekian 2005). To ensure analytical accuracy, repeats of whole-rock powders were conducted on several samples,

including large sample batches of 4g of rock powder (Table 4.2). The results of these sample repeats are heterogeneous in both isotopic value and concentration.

Sample	$^{187}Os/^{188}Os$	2σ	Os ppt
CRB05_004	7.28059	0.01764	0.531
CRB05_004	6.04667	0.05043	0.423
CRB05_004_4g	4.61480	0.01767	0.373
CRB05_007	6.55232	0.01389	0.539
CRB05_007	5.55593	0.02987	0.415
CRB05_007_4g	3.17256	0.02229	0.403
CRB05_008	4.00340	0.01741	0.735
CRB05_008_4g	3.53040	0.00517	0.512
CRB05_010	2.99064	0.01616	0.759
CRB05_010_4g	4.45150	0.01469	0.408

Table 4.2 Results for normal sample sizes and 4g sample digestions.

4.3.3.3 Standards

Standards were run with every sample batch analysed. Standards run during this study show repeatedly good analytical precision and accuracy. Repeat 35pg aliquots of Johnson Mathey (JM) standard gave a mean value of 0.17388 ± 26 (Fig. 4.4). This is in good agreement with published values: 0.17394 ± 14 (Birck *et al.* 1997) and 0.17398 ± 35 (Schaefer *et al.* 2000).

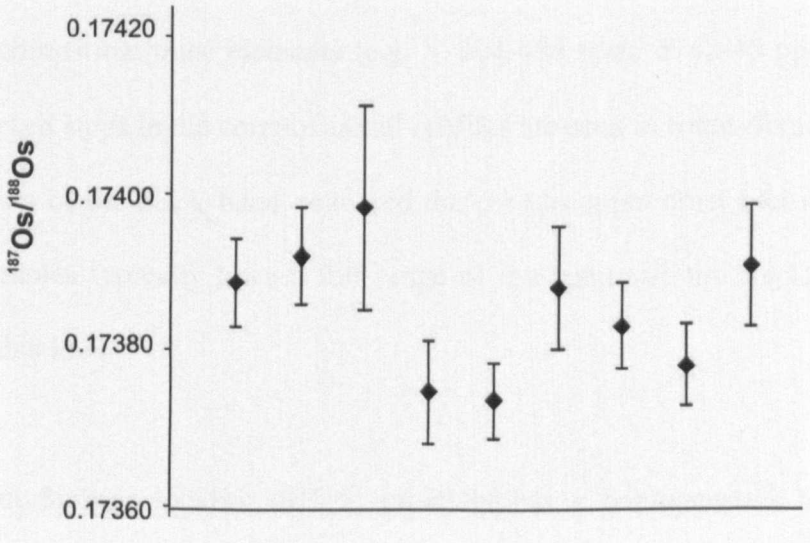

Figure 4.4 Results for 35pg aliquots of JM standard run at intervals throughout the analysis of samples to determine analytical accuracy and long term drift. Grey bar indicates the average value and dashed lines indicate the average 2σ precision.

4.4 Results

Results for each lobe analysed within the Sand Hollow flow field are shown in Table 4.3. Additional major and trace element results are presented in Chapter 3 (pages 114-121).

4.4.1 Major and trace element variations

Major and trace element variations within each of the three presented lobes (each representing a single locality) of the Sand Hollow flow field show some of the typical features and relationships with the structure of each lobe.

The Vantage locality (SH_1) displays compositional variation significantly outside analytical error for most elements (Fig. 4.5). Compatible major element oxides are especially homogeneous in the core of the lobe with an apparent step to more depleted upper and lower crusts (e.g. MgO 4.33 wt% in the core to 3.43 wt% in the crusts, Fe_2O_3 15.52 wt% down to 12.90 wt%). Other major oxides display profiles with the reverse signature (e.g. TiO_2 2.85 wt% in the lobe core to 2.94 wt% in the crusts) similar to the profiles for incompatible trace elements (e.g. V 404-456 ppm, Y 42-45 ppm and Zr 192-203 ppm). Marked steps in the compositional profiles are seen in some elements coinciding with the position of the black band zone and the core to upper crust transition zone. The lower crust samples typically have a full range of the compositions displayed by all the samples from this lobe.

The Frenchman Springs locality (SH_5) typically has a homogeneous lobe core with highly variable compositions limited to the upper portions of the upper crust and the lower crust (Fig. 4.6). The lower crust has distinct compositional variations, in some elements this mirrors the variation observed in the upper crust (e.g. SiO_2, TiO_2, Sc, Cu and Rb).

Compositional inflections in the upper crust are associated with transition from vesicle-poor to vesicle-rich bands.

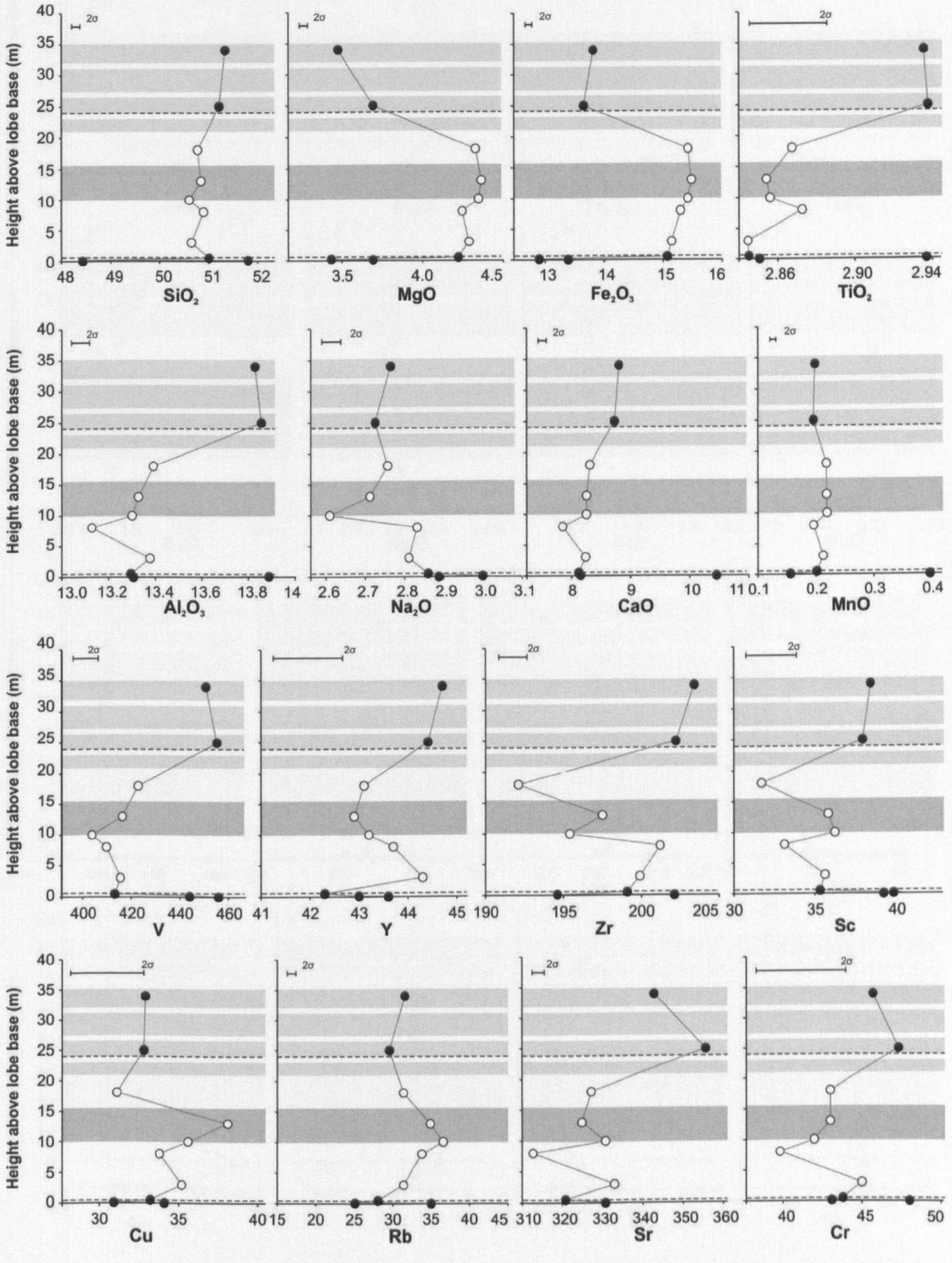

Figure 4.5 Diagrams plotting major oxides (wt%) and trace elements (ppm) against height within the Vantage lobe (SH_1) of the Sand Hollow flow field. Analytical error determined by repeat analyses are shown (2σ). Light grey bands indicate vesicular banding. Dark grey band shows the position of the black band zone within the lobe.

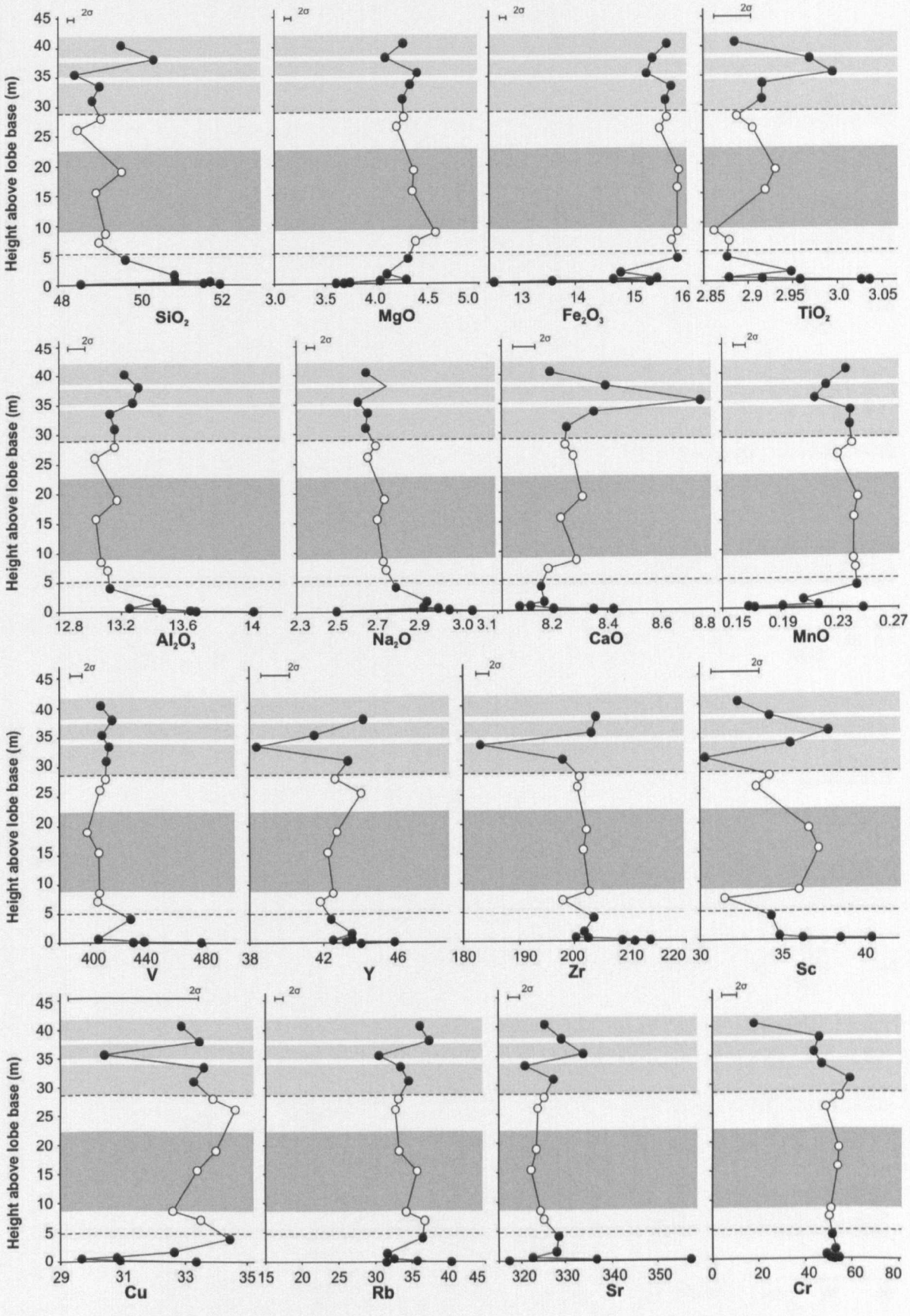

Figure 4.6 Diagrams plotting major oxides (wt%) and trace elements (ppm) against height within the Frenchman Springs lobe (SH_5) of the Sand Hollow flow field. Analytical error determined by repeat analyses are shown (2σ). Light grey bands indicate vesicular banding. Dark grey band shows the position of the black band zone within the lobe.

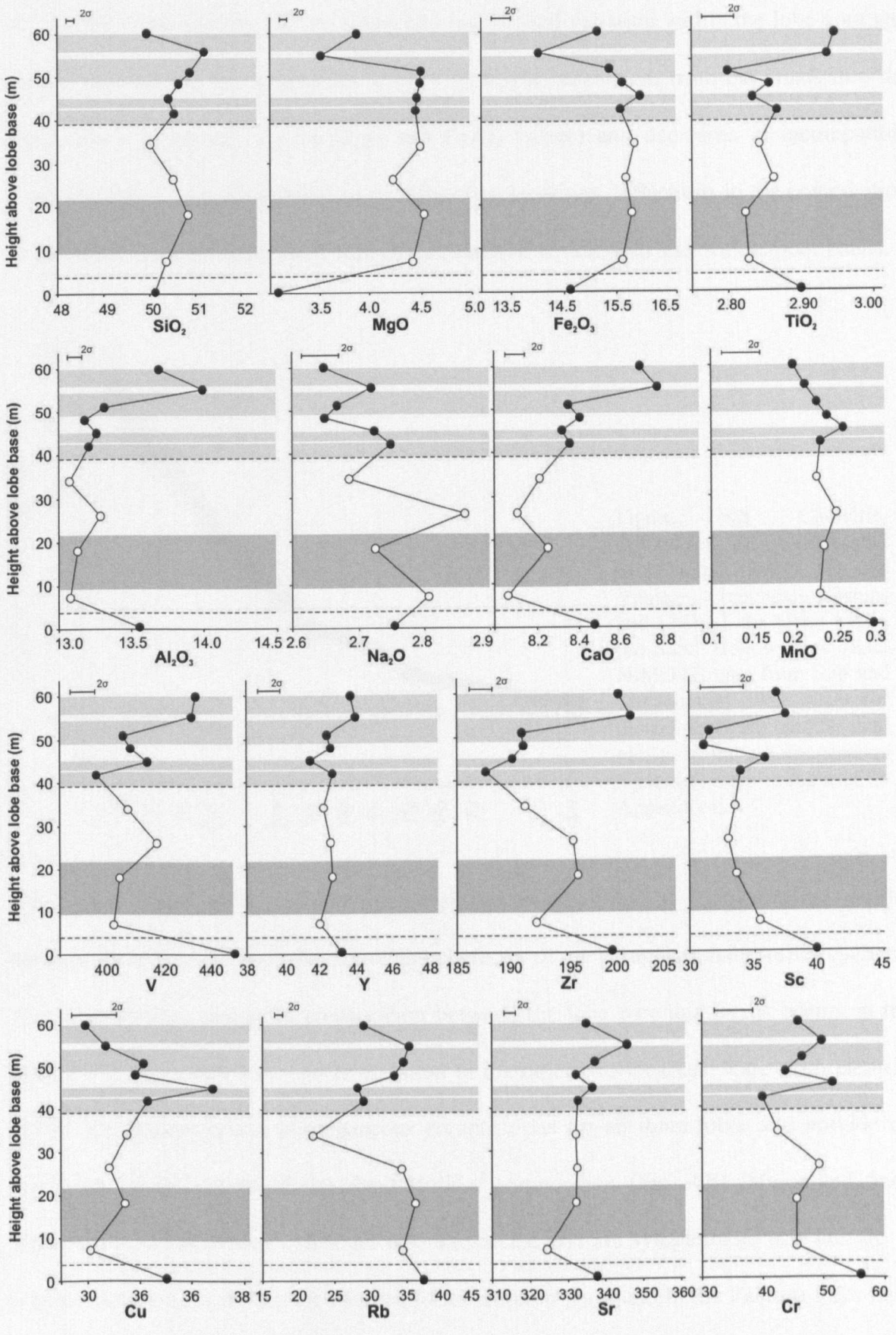

Figure 4.7 Diagrams plotting major oxides (wt%) and trace elements (ppm) against height within the Locke Lake lobe (SH_11) of the Sand Hollow flow field. Analytical errors determined by repeat analyses are shown (2σ). Light grey bands indicate vesicular banding. Dark grey band shows the approximate position of the poorly defined finely jointed area believed to represent the black band zone within this lobe.

The Locke Lake locality (SH_11) typically has limited variation within the lobe core and greater variation in the upper crust (Fig. 4.7). Slight enrichment from the crusts into the lobe core is observed (e.g. in MgO and Fe_2O_3 values) and decreases in incompatible elements (e.g. V and Rb) similar to the other two localities. Inflections in the composition of the upper crust are associated with the presence of vesicle-rich and vesicle-poor bands.

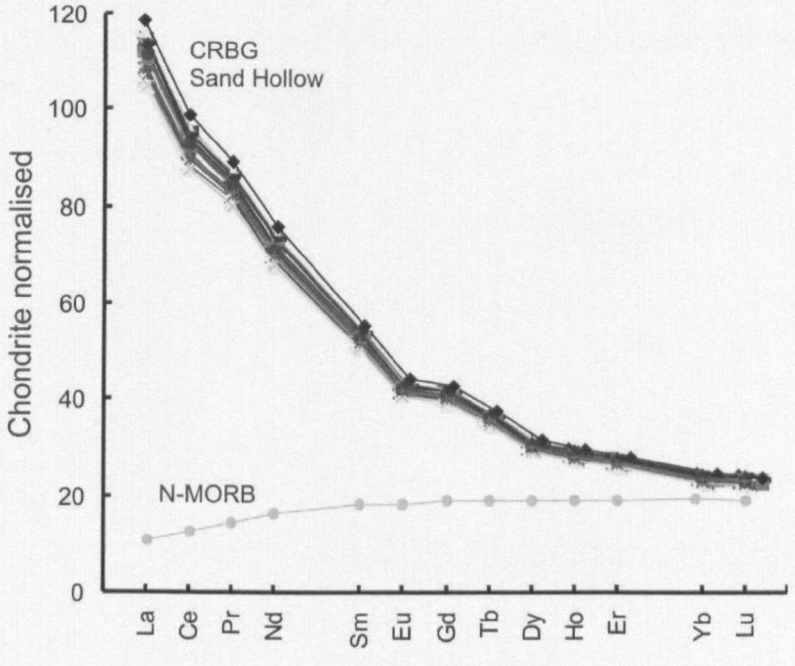

Figure 4.8 Chondrite normalised REE (Sun and McDonough 1989) for the Vantage, Frenchman Springs and Locke Lake lobes within the Sand Hollow flow field. N-MORB data from Sun and McDonough 1989. Data for these lobes are similar and plot to reveal a homogeneous signature. Data is reported in Appendix F.

The overall range in major and trace element compositions of each lobe are similar between localities although the nature and character of the compositional profiles changes. The most distinct change in composition between the lobe core and crusts occurs in the Vantage locality with less regular variation in the other two localites. Rare earth element (REE) abundances reveal homogeneous compositions for all three lobes and provide no constraint on the origin of the Sand Hollow composition (Fig. 4.8). Major and trace element variations between sites are not unexpected and are symptomatic of a change in magma composition during the lifetime of an eruption (as found in the Palouse Falls flow field presented in Chapter 3).

4.4.2 Re-Os elemental abundance

Re and Os concentrations show variable profiles and degrees of compositional heterogeneity between each site (Fig. 4.9). Overall, Os concentrations range from 0.37 to 12.05 ppt, with a mean value of 3.1 ppt. At each locality the Os concentrations are highly variable and the only systematic observation is depletion towards the core in the Vantage section. Although the high concentration Os samples correlate with low MgO at the Vantage section, such well-defined correlation is not observed in the other localities.

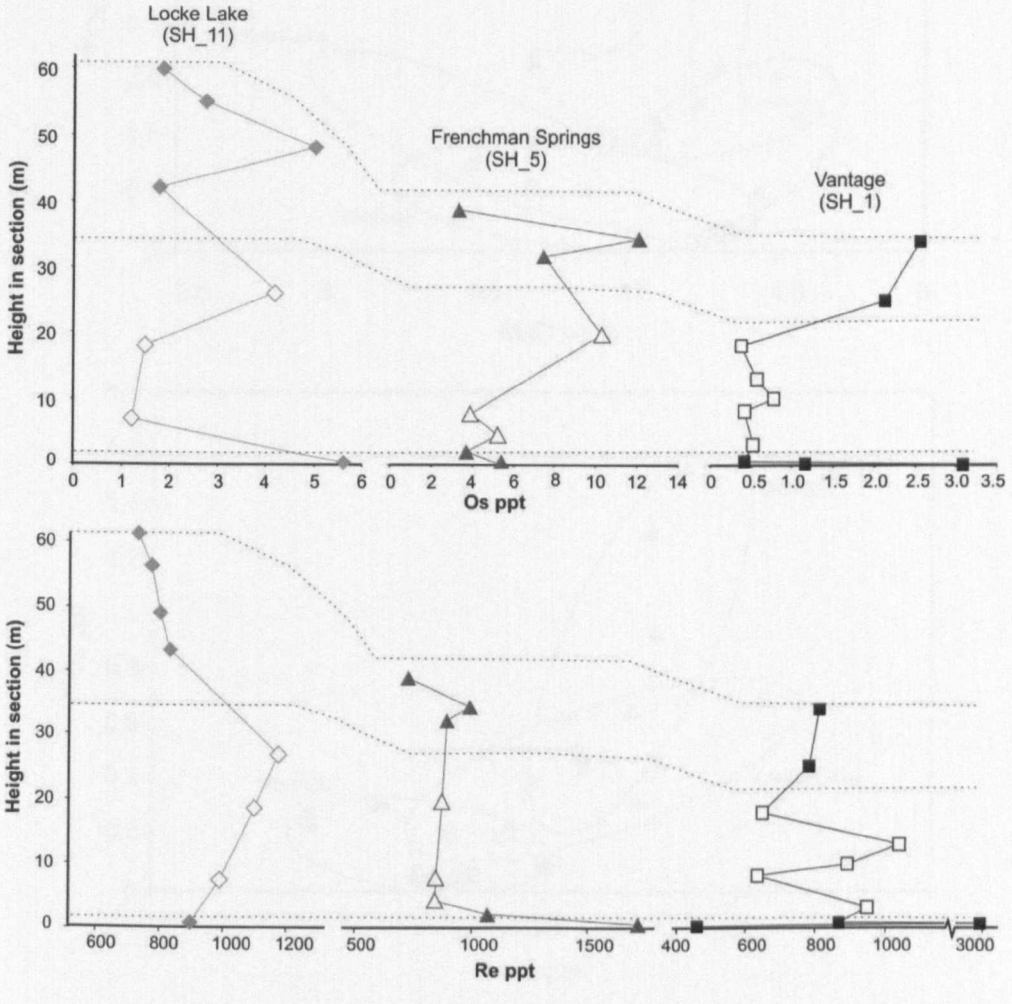

Figure 4.9 Re (ppt) and Os (ppt) concentrations plotted against height within each lobe of the Sand Hollow flow field.

Comparisons between each section reveal systematic variations with low concentrations at Vantage (~1 ppt), higher values at Locke Lake (~3 ppt) and the most enriched section is Frenchman Springs (~6 ppt). Co-variations are observed between ^{188}Os and other compatible elements (Mg and Ni), confirming the compatible behaviour of Os during

mantle melting (Fig. 4.10). ^{188}Os is plotted here as the non-radioactive isotope of osmium to investigate the concentration of Os without additional influences from isotopes of the element derived by isotopic decay (^{187}Os and ^{186}Os from ^{187}Re and ^{190}Pt respectively).

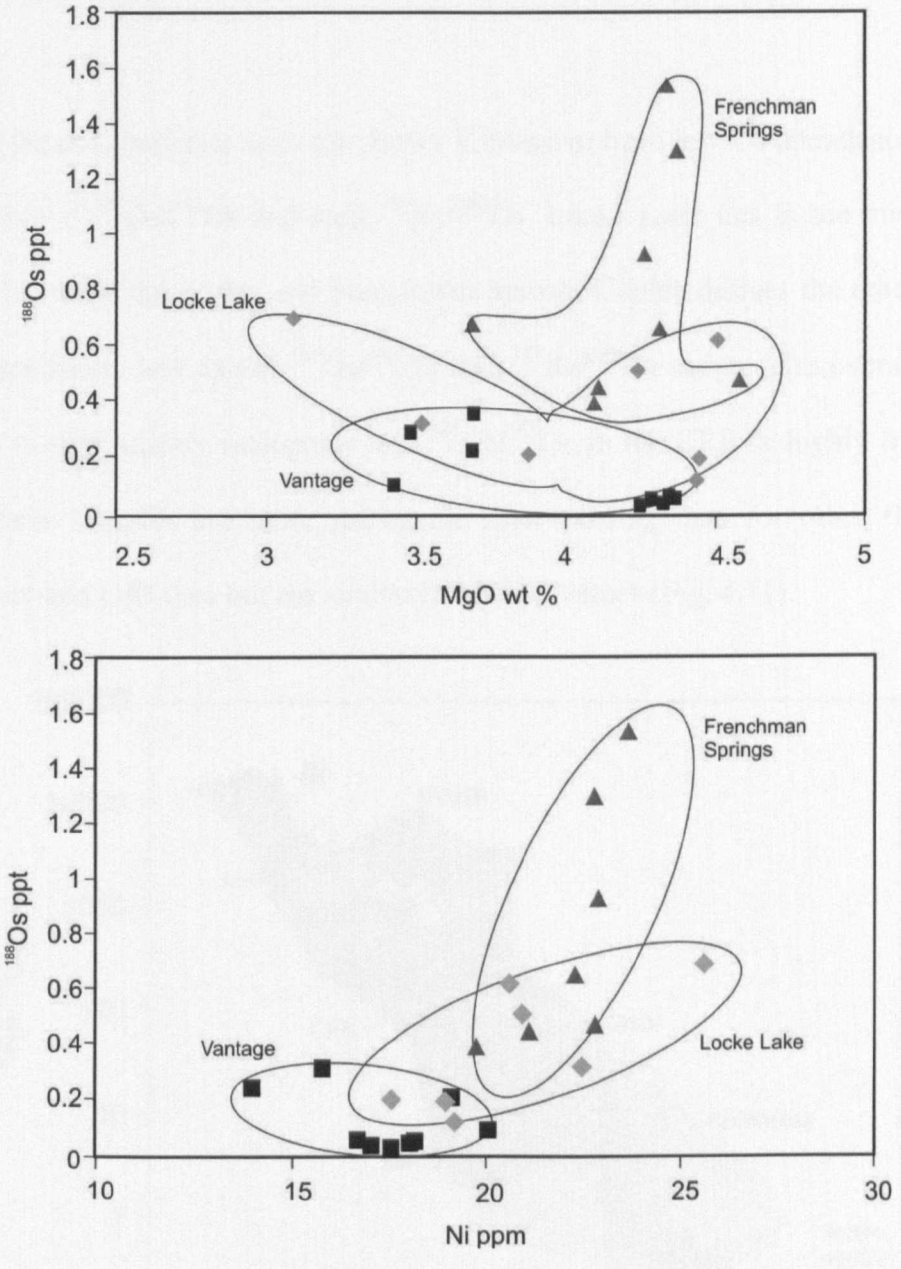

Figure 4.10 Co-variations in Ni abundance and MgO wt% with ^{188}Os abundance. Linework delineates predominant trends in the dataset for each locality. Squares indicate the Vantage (SH_1), diamonds indicate the Locke Lake (SH_11) and triangles indicate the Frenchman Springs (SH_5) localities within the flow field.

Rhenium concentrations range from 462 to 2921 ppt, with a mean value of 960 ppt. The Re concentrations for these samples are comparable to those previously measured from the Columbia River Basalts (Chesley and Ruiz 1998), but extend to lower Os concentrations.

These abundances are low, similar to MORB (average Os 10 ppt) and island arc basalts. By contrast, Re values are similar to the range observed for MORB (average range 927 to 1270 ppt) but higher than OIB (average Re 350 ppt) and arc basalts (Hauri and Hart 1997; Gannoun *et al.* 2007).

Comparing the data between each site shows Vantage to have low Os abundance, the most radiogenic initial $^{187}Os/^{188}Os$ and high $^{187}Re/^{188}Os$. Locke Lake lies in the middle of the data range for these three sites and Frenchman Springs Coulee defines the other end with high Os abundance, low initial $^{187}Os/^{188}Os$ and $^{187}Re/^{188}Os$ ratios. The overall range in $^{187}Os/^{188}Os$ is significantly radiogenic and $^{187}Re/^{188}Os$ in the CRB is highly fractionated. Some of these samples are more radiogenic than existing data for other flood basalt provinces, arc and OIB data but are similar to MORB values (Fig. 4.11).

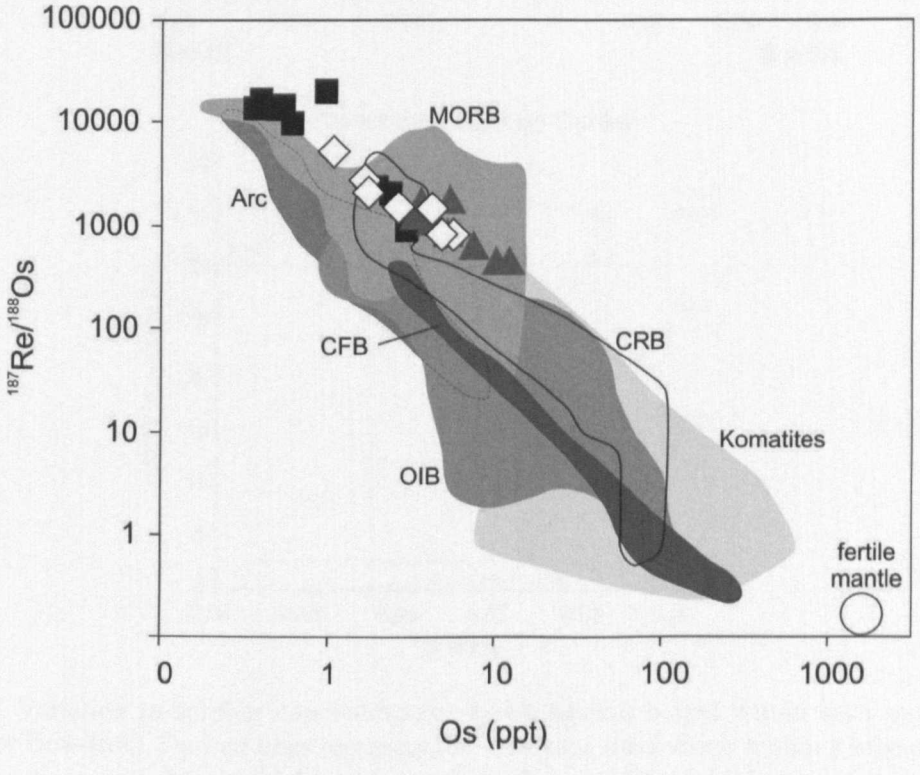

Figure 4.11 Vantage (black squares), Frenchman Springs Coulee (grey triangles) and Locke Lake (white diamonds) shown in relation to fertile mantle (Shirey and Walker 1998), Komatites (Walker *et al.* 1988; Shirey *et al.* 1994), OIB (Hauri and Hart 1993; Reisberg *et al.* 1993; Marcantonio *et al.* 1995; Roy-Barman and Allegre 1995; Bennett *et al.* 1996; Widom and Shirey 1996; Lassiter and Hauri 1998; Schiano *et al.* 2001), CFB (Horan *et al.* 1995; Molzahn *et al.* 1996), Arc (Alves *et al.* 2002), CRB (Chesley and Ruiz 1998) and MORB (Schiano *et al.* 1997; Gannoun *et al.* 2007).

4.4.3 Sulphur abundance

Sulphur concentrations determined by LECO analyses are heterogeneous within each lobe of the Sand Hollow flow field (Fig. 4.12). The Vantage and Locke Lake localities show a similar range of values (0.0171-0.0731 and 0.0328-0.0828) whereas the Frenchman Springs lobe has restricted values at the upper end of the range (~0.08 wt%).

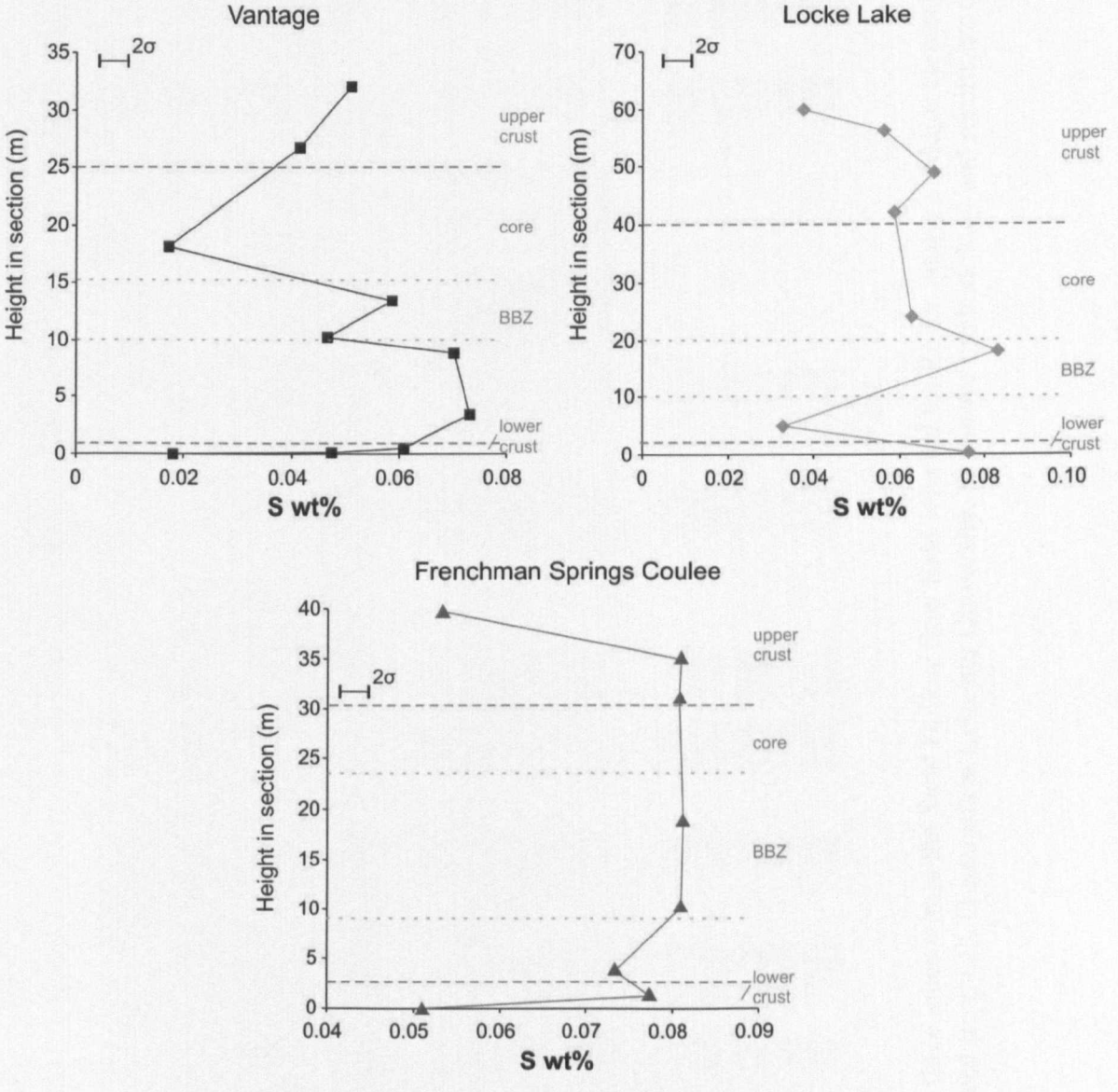

Figure 4.12 Variation in sulphur concentrations shown against height within each section of the Sand Hollow flow field. Dashed lines represent the structural subdivision within a lobe of the upper and lower crust separated by the lobe core which in this case bears the finely jointed black band zone (BBZ). Standard deviation (2σ) shown was provided for this sample suite by the Leicester University laboratory.

Sample reference	Mass (g)	[Re] (ppt)	[Os] (ppt)	$^{187}Re/^{188}Os$	$^{187}Os/^{188}Os$	2σ	$^{187}Os/^{188}Os$ initial age corrected to 15.3Ma	Blank effect (%)	$^{87}Sr/^{86}Sr$	2σ	MgO (wt.%)	SiO_2 (wt.%)	Al_2O_3 (wt.%)	TiO_2 (wt.%)	Ni (ppm)	S (ppm)
Vantage																
CRB05-002	0.409	809	2.557	2058	1.937	0.009	1.405	8.1			3.48	51.3	13.8	2.94	14.0	510
CRB05-003	0.400	776	2.121	2356	1.647	0.005	1.037	9.8			3.69	51.2	13.9	2.94	19.1	416
CRB05-004	4.048	647	0.373	13667	4.615	0.018	1.069	3.8								
CRB05-005	0.414	1038	0.569	14628	3.930	0.025		11.0			4.36	50.8	13.3	2.85	18.1	586
dupl.	0.438	1067	0.736	14039	3.467	0.016		22.2								
CRB05-006	0.439	889	0.766	8161	3.047	0.016	0.891	8.0			4.34	50.6	13.3	2.86	16.7	467
dupl.	0.406	867	0.817	10207	3.558	0.017	0.923	21.7								
CRB05-007	0.465	633	0.415	14137	5.556	0.030		14.0			4.24	50.9	13.1	2.87	17.0	701
CRB05-008	4.006	945	0.512	13191	3.530	0.005	0.128	2.8			4.29	50.6	13.4	2.84	18.0	731
CRB05-010	4.012	867	0.408	16557	4.452	0.015	0.180	3.5			4.22	51.0	13.3	2.85	18.0	610
CRB05-009t	0.414	2921	1.160	20019	2.619	0.014		16.0			3.43	48.4	13.3	2.85	20.0	476
CRB05-009b	0.405	462	3.080	916	1.601	0.007	1.362	6.8			3.69	51.8	13.9	2.94	15.8	180
Locke Lake																
CRB06_003	0.438	731	1.853	2297	0.976	0.004	0.414	6.7	0.705197	8.22E-06	3.87	49.9	13.7	2.95	17.5	377
CRB06_004	0.423	773	2.731	1558	0.692	0.003	0.310	4.8	0.705212	5.00E-06	3.52	51.1	14.0	2.94	22.4	562
CRB06_012	0.435	794	5.022	818	0.389	0.001	0.188	2.6	0.705206	5.91E-06	4.51	50.6	13.2	2.86	20.6	678
CRB06_014	0.425	833	1.764	2750	0.917	0.005	0.240	7.2	0.705204	5.98E-06	4.45	50.5	13.2	2.87	18.9	588
CRB06_016	0.412	1179	4.188	1501	0.573	0.003	0.200	3.3	0.705224	4.90E-06	4.23	50.4	13.3	2.86	20.9	629
CRB06_017	0.406	1101	1.495	4229	1.151	0.008		5.0	0.705223	5.62E-06	4.55	50.8	13.1	2.82	20.6	828
CRB06_018	0.436	992	1.203	5292	1.442	0.010	0.133	9.9	0.705210	5.59E-06	4.43	50.3	13.1	2.83	19.2	328
CRB06_019	0.444	902	5.620	837	0.481	0.002	0.274	2.3	0.705213	2.36E-05	3.09	50.1	13.6	2.90	25.6	760
Frenchman Springs																
CRB06_229	0.406	1727	5.442	1733	0.829	0.002	0.395	2.6			3.69	52.0	14.0	3.03	30.3	510
CRB06_234	0.402	1079	3.715	1551	0.537	0.002	0.153	3.8			4.11	51.4	13.4	2.95	21.1	773
CRB06_235	0.413	841	5.281	828	0.424	0.002	0.221	2.6			4.31	50.8	13.1	2.88	22.3	734
CRB06_237	0.412	850	3.910	1154	0.517	0.002	0.234	3.5			4.58	50.6	13.1	2.86	22.8	808
CRB06_239	0.426	870	10.252	428	0.297	0.001	0.192	1.3			4.37	50.8	13.2	2.93	22.8	812
CRB06_242	0.427	901	7.415	620	0.344	0.002	0.192	1.8			4.26	50.4	13.2	2.91	22.9	807
CRB06_243	0.411	1000	12.052	418	0.300	0.001	0.197	1.2			4.33	50.5	13.1	2.92	23.6	809
CRB06_245	0.411	730	3.282	1195	0.556	0.002	0.264	4.1			4.09	51.2	13.3	2.97	19.7	533

Table 4.3 Results of the three lobes within the Sand Hollow flow field selected for Re-Os analysis. Major element data is normalised to 100 wt % total oxides. S data derived from LECO analysis at Leicester University. Sr isotope methodology and results are described in full in Chapter 5.

4.4.4 Re-Os isotope data

The $^{187}Os/^{188}Os$ ratios for the Sand Hollow flow field are highly variable, but generally co-vary with $^{187}Re/^{187}Os$ (parent/daughter) ratios (Fig. 4.13). The Vantage locality demonstrates a considerable range of $^{187}Os/^{188}Os$ values (1.601 to 5.556), whilst the Frenchman Springs and Locke Lake localities have more restricted values at the lower end of the range (0.389 to 1.442 and 0.297 to 0.829 respectively).

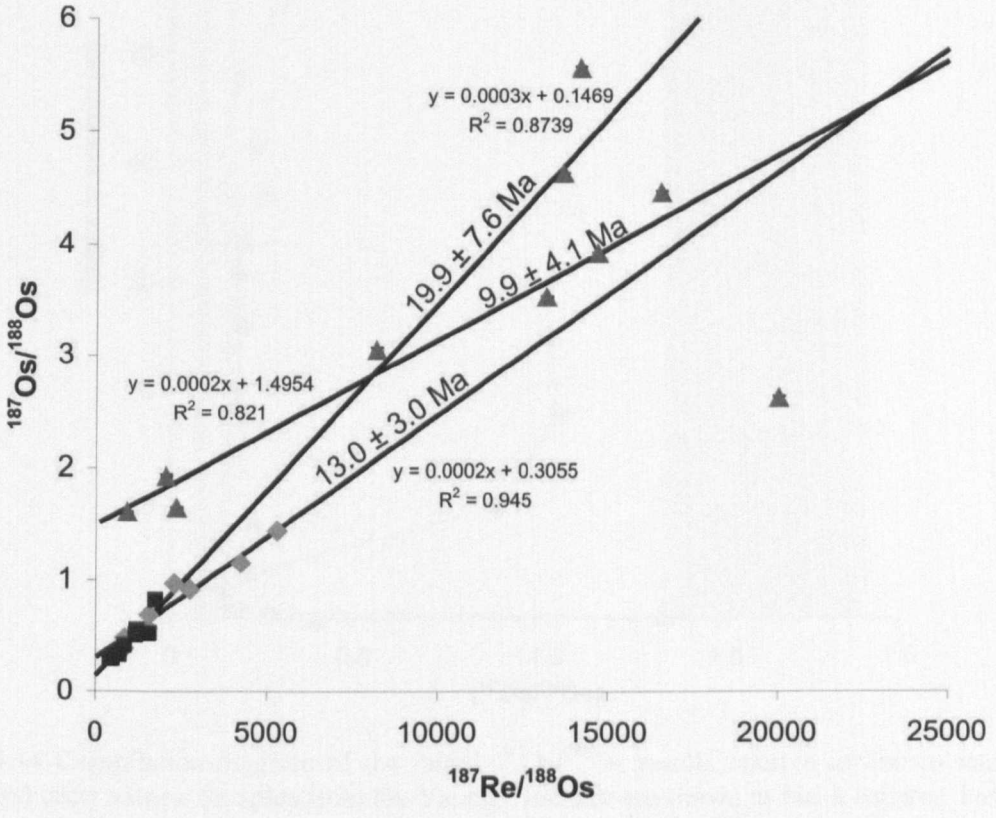

Figure 4.13 Re-Os isochron plotting $^{187}Os/^{188}Os$ versus $^{187}Re/^{188}Os$. Standard deviations for analyses of each sample are plotted but are generally smaller than the symbol size. Samples from the Vantage locality are shown as black squares, Frenchman Springs samples are dark grey triangles, Locke Lake samples are pale grey diamonds.

The $^{187}Os/^{188}Os$ have been age-corrected to 15.3 Ma, based on K-Ar and Ar-Ar age data (Tolan *et al.* 1989) and used to derive initial $^{187}Os/^{188}Os$ using the following equation:

$$(^{187}Os/^{188}Os)_i = {}^{187}Os/^{188}Os - (^{187}Re/^{188}Os * (EXP\ (1.663*15.3*0.00001)-1))$$

Correction of $^{187}Os/^{188}Os$ values in this way permits comparison of the data to source values and other datasets irrespective of age. The calculated initial $^{187}Os/^{188}Os$ values at the

lower end of the full range are comparable to the values for mantle (0.128; Hauri and Hart 1993; Reisberg *et al.* 1993; Schiano *et al.* 2001). However, values up to 1.405 are more akin to average continental crust (Esser and Turekian 1993; Peucker-Ehrenbrink and Jahn 2001) (Fig. 4.14).

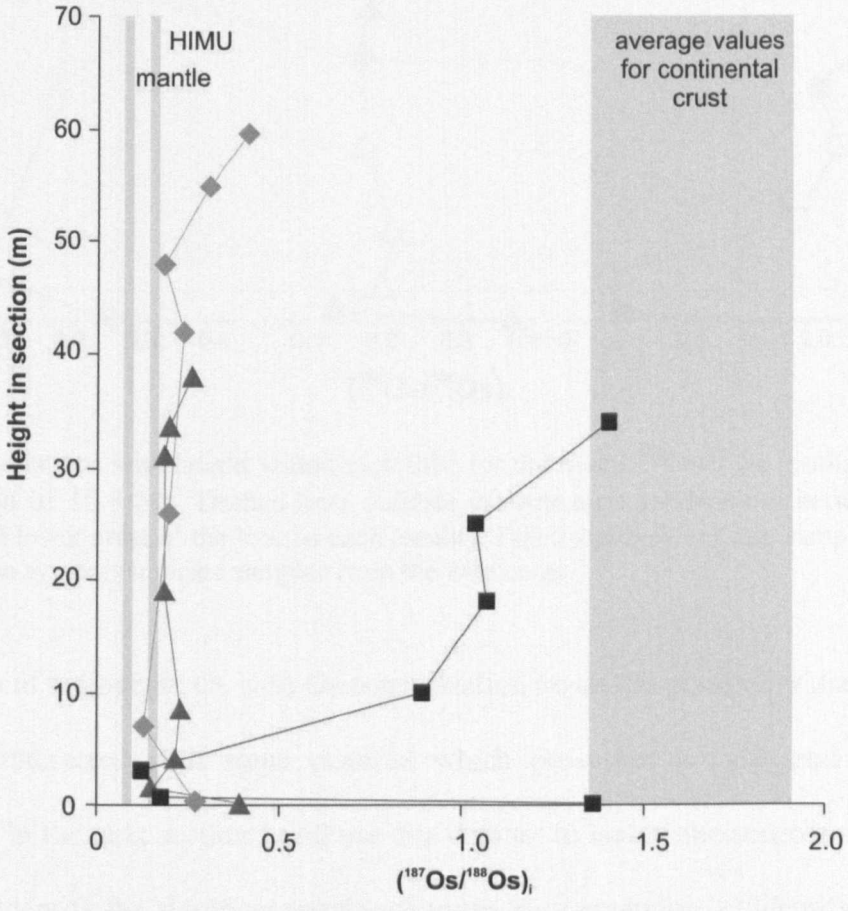

Figure 4.14 Compilation diagram of the initial $^{187}Os/^{186}Os$ results relative to known mantle and continental crust values. Samples from the Vantage locality are shown as black squares, Frenchman Springs samples are dark grey triangles, Locke Lake samples are pale grey diamonds.

Examination of the isotopic analyses in context with the physical volcanology shows that lobe cores are on average less radiogenic than the lower and upper crusts (Fig. 4.15). Placing this in a temporal framework, the lava emplaced early in the eruption came from a source that had high Re/Os ratios and subsequent radiogenic $^{187}Os/^{188}Os$; as the eruption evolved the magma progressed towards a more unradiogenic end member represented by the lava cores.

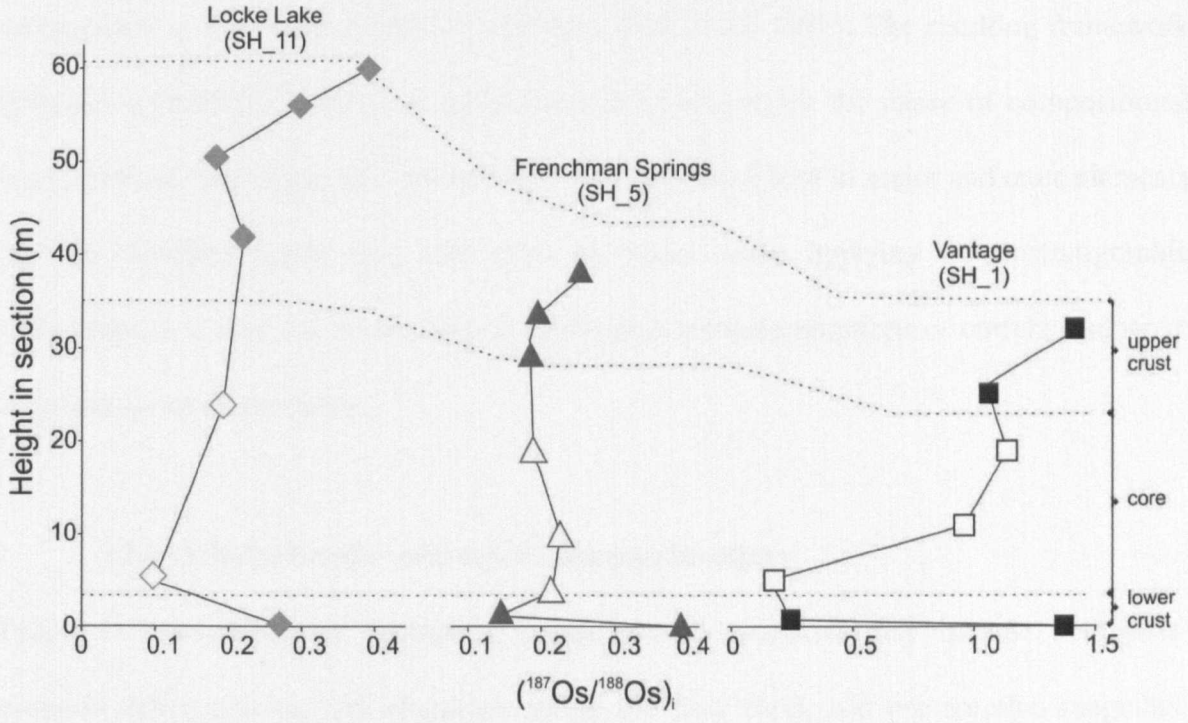

Figure 4.15 Variations with height within each lobe for the initial $^{187}Os/^{186}Os$ results based on an age correction of 15.3 Ma. Dashed lines indicate the structural subdivisions between the upper crust, core and lower crust of the lobe in each locality. Filled symbols indicate samples taken from the crusts, open symbols indicate samples from the lobe cores.

The variation in radiogenic Os with Os concentration raises the possibility that the magma, low in Os, interacted with some material which possessed a radiogenic Os isotopic composition. In the next section I will use this data to: a) isolate the sources and processes involved, b) identify the significance of each to the melt evolution, c) identify where these processes occurred, and d) summarise the cause of differential variations in chemistry within one individual magma batch?

4.5 Discussion

Intra-lobe elemental and isotopic variation throughout the flow field has the potential to unveil much about the genetic history of melt unit erupted during a single event as a flood basalt unit. Sample positions within and between the three sections taken to represent the Sand Hollow flow field are considered relative to the pahoehoe inflation model and

arrangements of lobe emplacement over time (Self *et al.* 1997). The resulting framework provides a temporal framework against which to investigate the cause of compositional heterogeneity. The compositional heterogeneity presented here in major and trace elements and Os isotopes imply that care must be taken when applying chemostratigraphic techniques as it may not be possible to distinguish between eruptions or correlate separate eruptions across a province.

4.5.1 Origin of major and trace element chemistry

Processes responsible for generating compositional variations may include both post-eruption differentiation and alteration within the flow field, and pre-eruption magmatic variation. Compositional variation may be induced by weathering (e.g mechanical weathering during repose periods) or chemical alteration (e.g. groundwater percolation or hydrothermal alteration) following solidification of lava. Such variation is most likely to be greater in the vesicular upper crust than in the core of a lobe as weathering profiles develop down into the lava from the exposed surface. Heterogeneity induced by these processes would produce asymmetric compositional profiles becoming more homogeneous with depth into any given lobe and would preferentially affect mobile elements. Absence of such profiles in the Sand Hollow flow field in Chapter 3 rejects the existence of post-eruption alteration processes.

In-situ differentiation may have a small role to play in intra-lava compositional heterogeneity. Segregation structures contain residual melt pockets with an evolved composition reflecting post-eruption fractionation (Goff 1996). However, through flow samples can not be linked to textural or petrographic observations which would support wide-scale post-eruption differentiation such as crystal accumulation, as has been previously proposed (Philpotts *et al.* 1999; Philpotts and Philpotts 2005). Instead,

compositional profiles for the Sand Hollow flow field and similarly with the Palouse Falls flow fields suggest progressive systematic variation in the basalt from the point of eruption. Therefore the heterogeneity records sequential development of the magmatic system over time.

Various pre-eruptive processes causing compositional variation can be assessed. Crustal contamination, fractional crystallisation, batch melting, recharge in the magma chamber and variations in the source may all cause sequential progressive variation in the lava composition. Co-variations in incompatible elements (e.g. TiO_2, Al_2O_3, V, Zr) and compatible elements (e.g. MgO, Fe_2O_3, Sr) suggest eruption of the Sand Hollow lava from a fractionally crystallised magma. Some of the variation may be accounted for by closed system evolution typified by separation of the melt fraction from crystals to produce a layered or zoned magma chamber, where the variation reflects the sequential eruption of zoned compositions. Recharge of this system is evident in the emplacement of a less evolved magma in the latter stages of the eruption. Whilst these relationships are most apparent in the Vantage locality, the cause of heterogeneities in the other localities is ambiguous.

Apparent homogeneity of REE for the Sand Hollow flow field samples combined with small trace element variations fail to identify any petrogenetic processes that can account for the major and trace element heterogeneity. The absence of significant variations in the REE signatures either between or within sections for this flow field produces a 'compositional type' for the eruption that may be employed as a chemostratigraphic tool. Processes such as assimilation along with fractional crystallisation (AFC) may be difficult to detect on the basis of trace element variations alone if the principle assimilated lithology is similar to the trace element composition of the magma (Powell 1984). Several distinct

areas form the continental crust under the Columbia River province and may have contaminated the Sand Hollow magma: Jurassic accreted terrain to the west and southwest; Precambrian cratonic lithosphere the north and east; and previously emplaced CRB basalts and/or gabbro. The absence of any significant variation in REE and trace elements means that distinguishing the roles of source variation, fractional crystallisation and contamination contributions in the major element and isotopic compositions is difficult.

4.5.2 Cause of Re and Os elemental variation

The Os concentration of all three sites within the Sand Hollow flow field is very low (ranging from 0.373 to 12.05 ppt). Reliable analyses of such low concentrations have only been made possible by recent developments in techniques. Low concentrations of Os in oceanic basalts (MORB (Schiano *et al.* 1997; Gannoun *et al.* 2007) and OIB (Marcantonio *et al.* 1995; Widom and Shirey 1996) have been attributed to either: partitioning into sulphide during mantle melting (Morgan and Baedecker 1983; Hart and Ravizza 1996; Burton *et al.* 1999), or partitioning into an unknown phase during magmatic fractional crystallisation (Hauri *et al.* 1996; Roy-Barman *et al.* 1998). Os concentration in the CRB samples may also be attributed to either process. Both these processes are believed to have a role in the CRB composition as co-variations in Mg-Ni-Os are consistent with the influence of olivine crystallisation on the composition of a residual melt and contemporaneous sulphide precipitation (Hauri *et al.* 1996; Burton *et al.* 2002).

Re and Os elemental variations within each locality may also be the result of surface processes rather than primary magmatic processes. A sharp decrease in the concentration of both elements at the top of the profiles may be an effect of mobility of these elements and caused by eruption hiatus environmental weathering. One explanation of this

phenomenon is the position of the palaeo-watertable (Wimpenny *et al.* 2007). However, the samples are fresh and young and post-emplacement alteration is minimal.

Differential loss of Re or Os either during the course of an eruption or through emplacement of the flow field may result in variations in the abundance of either element which is unrelated to the pre-erupted conditions. Volatile behaviour of osmium has been observed but not extensively documented (Krahenbuhl *et al.* 1992). The elemental budget of both of Re and Os has to be considered in the light of potential volatile loss. Loss of any element during emplacement of the flow field is thought to be minimal as the laminar emplacement method minimises turbulence and the insulating upper crust prevents escape pathways for the vesiculating lava (Thordarson 1995; Thordarson *et al.* 2001; MacKenzie and Canil 2006). Analysis of melt inclusions and glass suggest that most of the degassing occurs at the point of eruption (Thordarson and Self 1996). Under these conditions, the loss of any element is similar in any position within the flow field and samples therefore are still comparable.

Volatile loss of Re, either during primary degassing in shallow magma chambers, or during eruption and lava emplacement, has been clearly demonstrated to occur in MORB (Lassiter 2003; Sun *et al.* 2004). Experimentally derived constraints on the volatilisation of Re from basalt reveal comparable characteristics to Ar and CO_2 at 500 MPa (MacKenzie and Canil 2006). Therefore, Re can be released as a volatile and subaerial degassing may cause lower concentrations in arc-type and OIB lavas relative to MORB. Rhenium depletion may be present within each locality at the very upper portions of the Sand Hollow and Locke Lake lobes but these are very slight alterations and no such depletion is observed in the Vantage lobe (Fig. 4.9). Comparison of the CRB Re concentrations reveal no variation in the potential volatility of Re between samples (Fig. 4.16). Any volatile release of Re must

have affected the Re concentration of all areas of the Sand Hollow flow field equally. Significant Re depletion from a thick lava flow is deemed impossible due to the difference between lava cooling and solidification times and the diffusion, partitioning and migration to degass Re (MacKenzie and Canil 2006). However, the controls on volatility remain poorly understood (Norman *et al.* 2004).

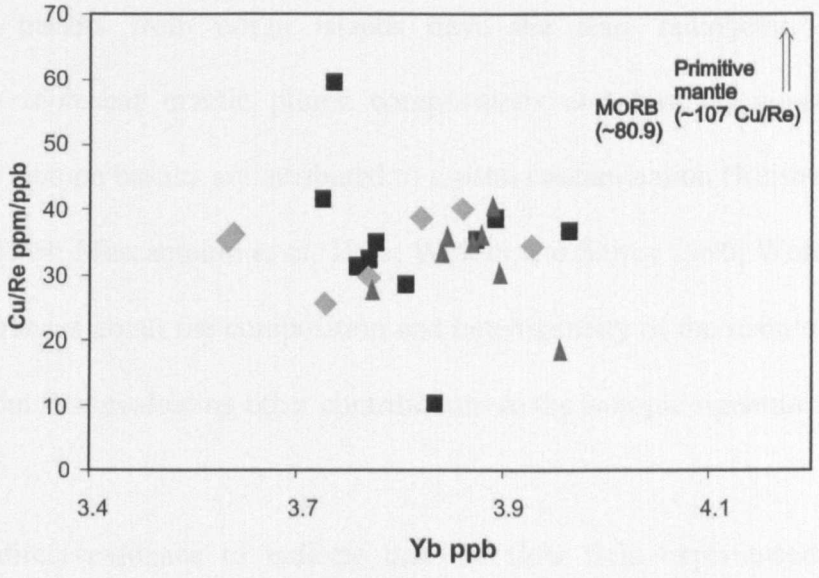

Figure 4.16 Cu/Re vs Yb for the CRB samples (Vantage – squares, Frenchman Springs – triangles, Locke Lake – diamonds) relative to data for MORB and estimations from primitive upper mantle (Bennett *et al.* 2000; Lassiter 2003). Yb is applied as an element with similar incompatibilities as Re and the Cu/Re ratio provides a measure of volatility (Lassiter 2003).

Isotope fractionation associated with volatile loss has not been identified in Re-Os systematics. If such fractionation occurred, the lighter isotopes would be preferentially depleted. This would result in a decrease in the $^{187}Os/^{188}Os$ ratio and therefore cannot be used to explain the observed results.

4.5.3 Origin of isotopic variations

Results for the Sand Hollow flow field are amongst the most radiogenic Os compositions with low Os concentrations for any flood basalt province. The source of these variations has important implications for the origin and assembly of a melt body erupted as a single flood basalt eruption. Determining the source of radiogenic Os from these data requires the

identification of the source composition of parental magmas, contaminants during transport to the point of eruption and post-eruption alteration of the isotopes. A review of currently existing Os isotopic values for sources of basaltic melt can be summarised as varying from 0.122 to 0.127 for lithospheric mantle (Luck and Allegre 1992; Snow and Reisberg 1995), 0.139 to 0.151 from HIMU plume-derived mantle (Widom *et al.* 1999). High Os concentration basalts from ocean islands have the least radiogenic Os signatures interpreted to represent mantle plume compositions and low Os concentration with radiogenic Os isotope basalts are attributed to crustal contamination (Reisberg *et al.* 1993; Martin *et al.* 1994; Marcantonio *et al.* 1995; Widom and Shirey 1996; Widom 1997). It is clear that inferences about the composition and heterogeneity of the mantle source cannot be made without first evaluating other contributions to the isotopic signature.

There is no direct evidence to indicate that the flow field experienced post-eruptive contamination, but neither is it possible to dismiss such interactions. Contamination might occur through the incorporation of sedimentary and volcaniclastic deposits on the land over which the lava advanced. Similarly, the lava could have interacted with water bodies, hydrothermal ground waters, or potentially re-melted basalt from an earlier eruption. Firstly, there is little evidence for any significant eruption hiatus sedimentation preceding this eruption. In most localities, the basalt overlies the reddened weathered top of the Ginkgo basalt, or a thick ash layer on top of the Silver Falls basalt. There is also no evidence for turbulent emplacement of the flow field, which would be necessary to cause thermal erosion into underlying sediments (Greeley *et al.* 1998; Kerr 2001). To the contrary, there is abundant evidence for passive laminar emplacement of the flows. Thus, if there is any exchange with an underlying deposit, such alteration would be limited to the glassy chilled rim of the basalt. Secondly, it is known that the environment at the time of these eruptions was a warm temperate climate (Leopold 1969; Barnett and Fisk 1980) with

lakes and river drainage networks re-established between each eruption. Within the Sand Hollow flow field there are no pillow basalts or hyaloclastite deposits associated with this eruption to suggest the presence of substantial bodies of water. Thirdly, there are few if any significant mineralised joint faces or amygdales.

Between the Sand Hollow flow field and the underlying flows, there is usually a reddened weathering horizon and distinct chilled margins, with preserved pahoehoe ropes and small-scale lobe structures. There is no fusing of the two flow fields vertically to one another. Therefore it would appear that the lower chilled margin of the Sand Hollow flow field was an effective insulator enabling the propagation of the flow field. However, there is potential for the assimilation of older basalts from this province through wall-rock contamination during the latter stages of magma ascent. The oldest CRB formation was erupted at 17.5 Ma, providing up to 2.2 Ma for the evolution of the radiogenic Os composition. Adjusting for this growth of ^{187}Os, relative to present day $^{187}Re/^{188}Os$ (500-2000 modelled) and mantle $^{187}Os/^{188}Os$ (0.128) (Saal *et al.* 1998), and using the ^{187}Re decay constant of 1.663×10^{-11} yr^{-1} (Shen *et al.* 1996) produces a range of $^{187}Os/^{188}Os$ from 0.146-0.201. However, these compositions are not sufficiently radiogenic to explain the high $^{187}Os/^{188}Os$ observed here.

Positive correlation between isotope fractionation and contamination indices precludes the involvement of deep, basal crust or mantle, magma chambers. Under these circumstances, any crustal contribution must have been assimilated during ascent and is therefore greater for primitive magmas with a higher thermal gradient between the melt and wallrock. This implies that contamination is a rapid process and such assimilation is likely to have a dominant role in more primitive magmas by comparison with cooler evolved magmas.

4.5.3.1 Comparison with existing data for the CRBG

In the Columbia River flood basalt province, data for a number of stratigraphic levels reveal significant variations in initial $^{187}Os/^{188}Os$ ratios (i.e. the isotope composition at the time of eruption) ranging from 0.13 to ~3 (Chesley and Ruiz 1998). These are attributed to the contamination of a mantle melt by mafic lower continental crust without any measurable involvement of the SCLM (Chesley and Ruiz 1998). Interpretation of the results is based on sample localities within flow fields. A geographic link is made between sample sites and the involvement of geochemically distinct contaminants, rather than the fissure vent location. Separate contaminants are implied to have been derived from the juxtaposition of the North American craton and Jurassic accreted terranes (Fig. 4.17). However, any link between pre-eruptive contamination and the composition of lava flows needs to consider the feeder dyke or vent location in addition to the sample location within a flow field.

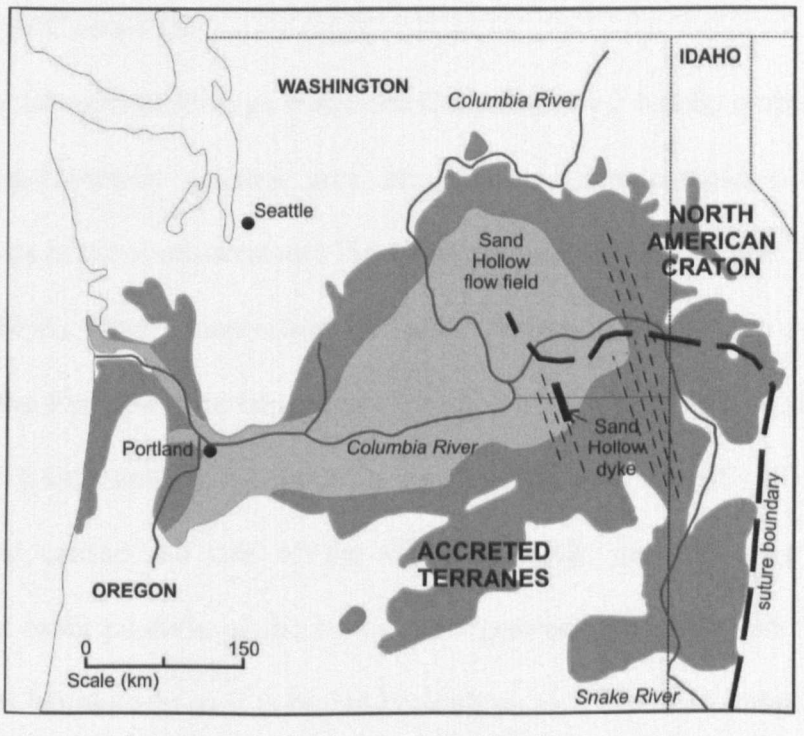

Figure 4.17 Areal extent of the Columbia River Basalt (modified from (Reidel *et al.* 1989; Tolan *et al.* 1989; Hooper and Hawkesworth 1993). The Mesozoic initial $^{87}Sr/^{86}Sr = 0.706$ isopleth separates the North American Craton from the Jurassic accreted terranes to the south and west (Reidel and Tolan 1994; Mohl and Thiessen 1995). Zones of the major feeder dike swarms are denoted by dashed lines (Tolan *et al.* 1989). The extent of the Sand Hollow flow field and source area for the feeder dike are shown (SH).

The Sand Hollow flow field has not been sampled in any previous analysis of the CRB, but data have been obtained for other flow fields within the same formation (Chesley and Ruiz 1998). DePaolo (1983) argues that there are several reasons that the compositional profile of the Columbia River Basalts does not necessarily invoke large amounts of crustal contamination in a response to Carlsons paper (Carlson *et al.* 1981). The supporting evidence is based on positive εNd values, trace element patterns do not require crustal assimilation in the modelling, there is no associated rhyolitic volcanism within the Columbia River province and the isotopic ratios correspond with both geographic position and composition. Comparison of the Sand Hollow flow field Os isotopic data with data from elsewhere in the stratigraphic sequence reveals a change in composition over time. The elevation in $^{187}Os/^{188}Os$ through time is interpreted as the result of the progressive contamination of magmas by a Re/Os rich component such as the continental crust.

4.5.3.2 AFC modelling

The continental lithosphere through which the Columbia River basalts erupted is composed of Mesozoic-aged oceanic volcanic arcs, accretionary prism complexes and associated basin successions to the south-west and Pre-Cambrian cratonic lithosphere to the north and east (Vallier 1995). The juxtaposition of these terranes is thought to result from the subduction of the Farallon plate beneath the North American plate during the Jurassic e.g. (Atwater 1970; Bunge and Grand 2000; Lui *et al.* 2008). Subsequently, the Juan de Fuca subducting slab caused the rise of the Cascade Range and resulting Cenozoic arc volcanism. The exact position of the suture zone between the craton and these accreted oceanic terranes is unknown as it is buried beneath up to 3,000 m of basalt. However, the major crustal lineaments and lithologies from outside the margins of the province have been extrapolated beneath the basalts (Mohl and Thiessen 1995) to provide some constraints on the crustal components present in the vicinity of the fissure vent and those

likely to be present at magma storage and transport sites, thereby giving some indication of potential contaminants to the magma.

A simple AFC mixing model is applied to the Sand Hollow flow field data to identify the likely composition and contribution of a crustal assimilant to explain the variation in isotopic values. Variable Os abundances and $^{187}Os/^{188}Os$ are applied for the continental crust and a basaltic melt (Equation 1):

$$^{187}Os/^{188}Os_{mix} = \frac{[(^{187}Os/^{188}Os)_{cc}*Os_{cc}*f] + [(^{187}Os/^{188}Os)_{B}*Os_{B}*(1-f)]}{[(Os_{cc}*f) + Os_{B}*(1-f)]}$$

Equation 1.

where f is the fraction of assimilated crust, cc is the isotopic ratio or elemental concentration of the crustal contaminant and B is that of the uncontaminated parent magma. Mixing curves are shown in Fig. 4.18, utilising the least radiogenic sample from each locality as an end-member for the model and a proxy for the uncontaminated mantle source component. Application of a range of $^{187}Os/^{188}Os$ and Os concentrations suggests the involvement of up to 5 % of a distinct assimilant for the Sand Hollow basalt at the Vantage section. By comparison, the data from the other two sections suggests up to 10 % contamination but by a much less radiogenic contaminant. Despite the strong dependence of these mixing lines on the elemental and isotopic composition of the end members, these calculations clearly demonstrate that the observed variations can be plausibly explained by crustal contamination of primitive mantle magmas.

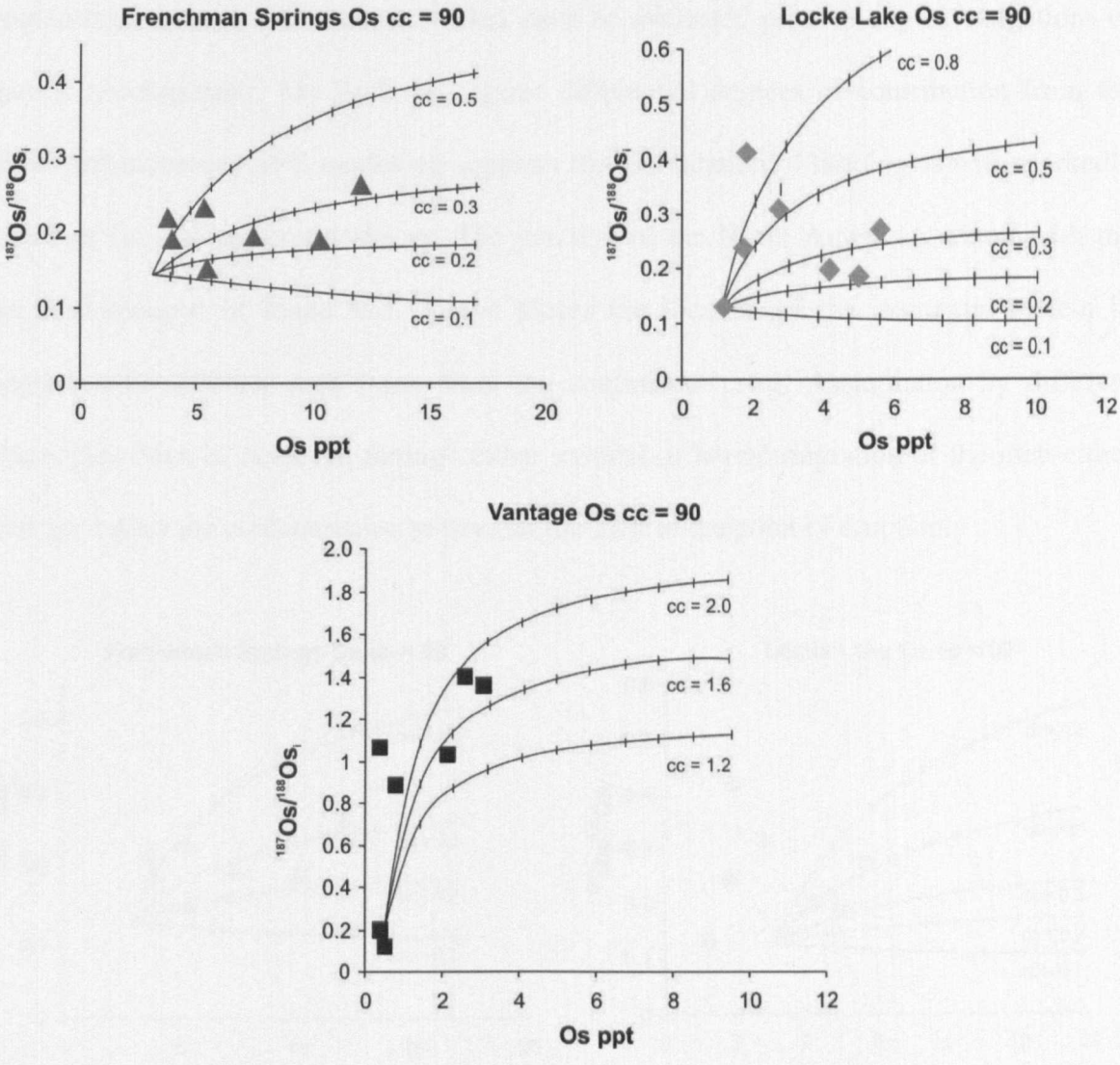

Figure 4.18 AFC models illustrating a range of parameters for crustal assimilation in continental crust with an Os concentration of 90 ppt. Starting composition for each model is the least radiogenic most primitive sample composition within each lobe. The different modelled scenarios are for different isotopic values (cc = x) of a hypothetical crustal assimilant as indicated for individual models. Tick marks on each modelled line are at 1 % intervals.

If a depleted mantle composition is applied to the same model only the Frenchman Springs locality can be modelled (Fig. 4.19). The other localities clearly cannot be derived from mantle composition alone as the sample suite is more radiogenic that even the most radiogenic mantle composition (e.g. HIMU $^{187}Os/^{188}Os$ ~0.15; Widom *et al.* 1999) and contamination must make a contribution to the isotopic signature.

Although at the present time, we cannot separate the contribution of crustal contamination from heterogeneity in Re-Os of the source, these findings show the significance of crustal

contamination on flood basalt melts that must be evaluated prior to any investigations of mantle heterogeneity. My findings suggest differential degrees of contribution from the crust, and moreover AFC modelling supports the assimilation of lithologies with markedly different Os isotopic compositions. The junction of the North American craton with the accreted terranes of Idaho and Oregon places the location of the magmatic system in contact with different rock types from the continental crust. Assimilation by different lithologies must be achieved through either vertical or lateral migration of the melt either during or after the contamination to transfer the melt to the point of eruption.

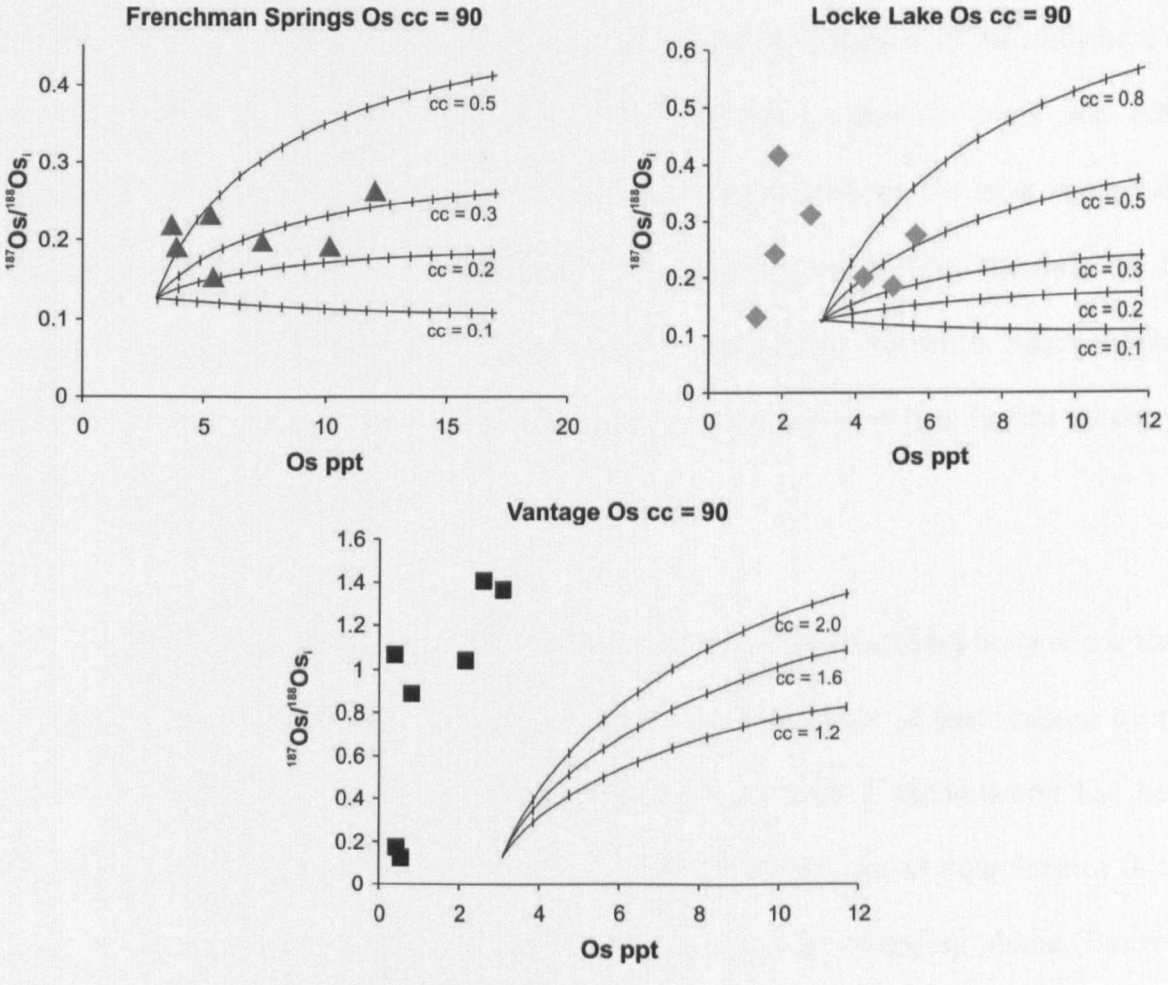

Figure 4.19 AFC models illustrating a range of parameters for crustal assimilation in a continental crust with an Os concentration of 90 ppt. Starting composition for the model is depleted mantle ($^{187}Os/^{188}Os$ - 0.128, Os - 2.99 ppt; Salters and Stracke 2004). The different modelled scenarios are for different isotopic values (cc = x) of a hypothetical crustal assimilant. Tick marks on each modelled line are at 1 % intervals.

4.5.4 Location of contamination

Results from the AFC modelling reinforce the model recently proposed for the Columbia River basalts of a shallow to mid-level crustal magmatic system that propagates magma to the point of eruption through a complex dyke network. The depth of this system (15-30 km; Wolff *et al.* 2008) is consistent with phenocryst compositions (Durand and Sen 2004; Caprarelli and Reidel 2005; Ramos *et al.* 2005). Wolff *et al.* (2008) state that the degree of magma-crust interaction is coupled to an increase in the eruption rates from Imnaha to Grande Ronde times. This may also be linked to an increase in the flux of the magma from the mantle into the crust. If this model holds true for large-scale development of the province, the same may be observed on the scale of a single eruption. In the study here on the Sand Hollow flow field, elevated $^{187}Os/^{188}Os$ are coupled to MgO and other fractionation indices to demonstrate an inverse relationship between the most isotopically contaminated and the most evolved samples. Throughout the flow field, and therefore for the duration of the eruption, the first emplaced / erupted lava represents magma with a greater contribution from the continental crust. The ensuing eruption is fuelled by deeper magmas, recharging the system.

Involvement of two isotopically distinct assimilants in the single erupted body of the Sand Hollow flow field could be explained through lateral migration of melt caused by the physical boundary of the cratonic lithosphere margin. Such a phenomenon has been suggested as a common occurrence in flood basalt provinces due to complexities in the physical structure of the lithosphere and the interaction of an ascending plume (Burov *et al.* 2007) but could also be related to the development of the magmatic plumbing system over time (Peate *et al.* 2008). Lateral migration is suggested for the CRB originating from the plume impact site to the south of the province (Fig. 4.20). Irregular occurrences of sparse plagioclase antecrysts throughout the Wanapum Formation flow fields support the

incorporation of pre-existing shallow level melts erupted in a single event (Ramos *et al.* 2005; see also Chapter 5). These most probably mixed just prior to or during the eruption, because the crystals are in neither chemical nor textural equilibrium with the host melt (Durand and Sen 2004; Ramos *et al.* 2005). These data suggest that lateral and vertical transport of magma to the point of eruption is likely and contamination occurred within a complex magmatic system which periodically ponded and was transported through both sides of the suture boundary.

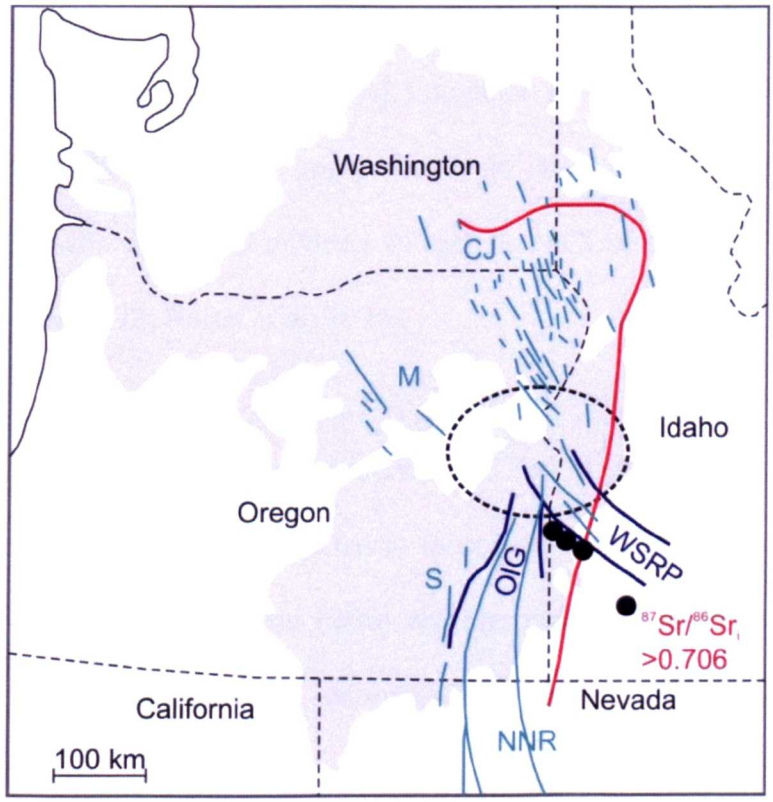

Figure 4.20 Map showing the full extent of the CRBG (including the Steens Basalts) from Wolff *et al.* (2008); the Mesozoic isopleth (red); dyke swarms (green - CJ = Chief Joseph; M = Monument; S = Steens; NNR = northern Nevada Rift); extensional structures (purple - WSRP - western Snake River Plain graben; OIG = Oregon-Idaho graben); and the present-day area in which crustal-level magma chambers for the CRBG are inferred to lie (dashed ellipse).

Laboratory (King and Anderson 1995) and numerical modelling (Burov *et al.* 2007) support the case for lateral transport of melt in the region of a continental suture zone. Such models have significant implications for the geochemistry and mineralogy of magmas erupted to form flood basalts (Johnston and Thorkelson 2000). The obvious complexity in sources and contaminants of any melt undergoing such physical translation

through the lithosphere adds further merit to analysis of suitably sensitive isotopic systems such as Re-Os to separate crustal level contributions to the signature of a melt prior to interpretations of the nature of the source where source heterogeneity may otherwise be invoked (Wang *et al.* 2007).

4.6 Comparison with other continental flood basalt provinces

Existing Re-Os isotopic data from the CRB and other provinces highlight the differences between this system and that of traditional lithophile systems. The Karoo province in Africa and Siberian basalt studies apply Re-Os to only the most Mg-rich samples, suggesting these basalts arise from mixtures of enriched SCLM and mantle plume-derived material (Ellam *et al.* 1992; Horan *et al.* 1995).

A study on the Ferrar province in Antarctica was the first to characterise the Os signature of a LIP where samples were not restricted to those with high-Mg, high-Os. High Re/Os ratios and low Os abundances in the Ferrar are interpreted to represent melting of the SCLM with the addition of subducted sediments (Molzahn *et al.* 1996). Consideration of the range of basaltic compositions in this and subsequent studies resulted in a change in the interpretation of the source and petrogenesis of continental flood basalts.

Analyses from the Deccan illustrate the difference in interpretation gained from Os isotopes in contrast to Sr and other lithophile isotope systems. Sr isotopes reveal heterogeneity originating from either crustal contamination or derivation from a metasomatized source (Allègre *et al.* 1982; Mahoney *et al.* 1982; Peng *et al.* 1994). The Os isotopes provide an important contribution revealing an isotopically homogeneous source

with slight variability gained from small amounts of crustal contamination up to 0.15 % (Allègre *et al.* 1999).

A study of basalts from the Emeishan province in China identifies two populations with distinct Os contents and isotopic signatures that correlate with high-Ti and low-Ti basalt groups within the province (Xu *et al.* 2007). The low-Ti basalt group shows high-Os concentrations with radiogenic Os and are interpreted as plume-derived (OIB-like) material. Whereas the high-Ti basalt group has high-Os with an unradiogenic signature, suggesting either derivation from the SCLM or contamination of lithospheric mantle (possibly plume) material through the SCLM.

A limited sampling study coincident to the CRB samples on a single lobe from the Deccan province reveals a similarly interesting degree of isotopic heterogeneity (Fig. 4.21). Preservation within the Deccan is poor relative to the CRB – a function of both age and climate, so that the physical structure of the lobe is difficult to identify (Jay 2005) and alteration caused by weathering may have more of an effect than in the CRB basalts (Wimpenny et al 2007). Despite these caveats isotopic heterogeneity occurs throughout the lobe and varies with height in a similar pattern to samples from the CRB. The range of $^{187}Os/^{188}Os_i$ is less than that observed in the CRB, closer to depleted mantle values (Hauri and Hart 1993). However, the presence of variable degrees of crustal assimilation in the genesis of continental flood basalts may be a common characteristic that requires thorough analysis prior to interpretations of the nature of mantle sources of these voluminous melts.

Many flood basalt provinces are situated at the junction between thin oceanic and continental crust represented by fracture zones or sutures i.e. Deccan, North Atlantic

Tertiary Province, Karoo-Parana and Columbia River, as well as Ascension and Cape Verde OIB (King and Anderson 1995).

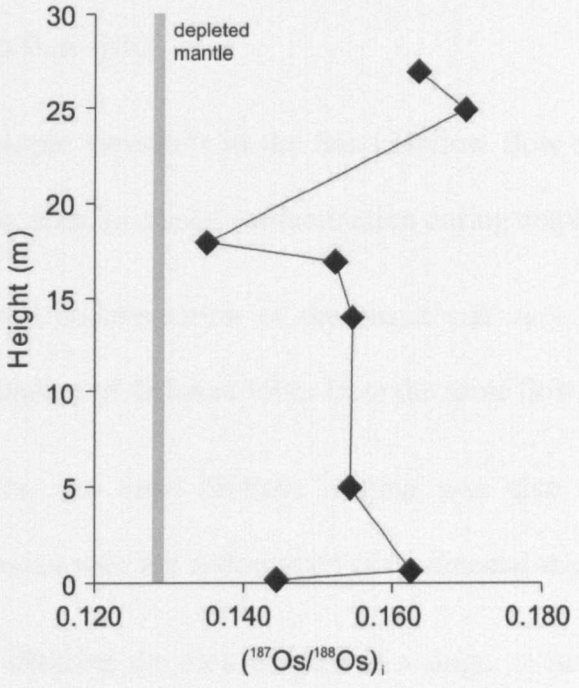

Figure 4.21 $^{187}Os/^{188}Os_i$ with height within a single lobe from Ambenali Ghat, India (N17°55'09.6" W073°37'39.2"; samples provided by A.Jay). Data is reported within Appendix G.

The subduction of oceanic crust is often omitted from models of plume impingement on the base of the crust and may have significant affects on thermal circulation models affecting the distribution of resulting melt (King and Anderson 1995). Such structural complexities in the magma generation and storage zones may impart distinct chemical signatures on the resulting melt (Anderson 1994). Such similarities between many provinces might suggest that the compositional heterogeneities observed within single lava flows in the Columbia River may be common elsewhere and provide insight to pre-eruptive storage processes.

4.7 Conclusions

- Small scale geochemical heterogeneity occurs within both elemental and isotopic compositions, within and between lobes produced during a single eruption. This variation was present at the time of emplacement and was acquired from pre-eruptive magmatic contamination, rather than surface processes.

- Variations in Re-Os isotopes highlight the difficulty in attempting to apply a chemostratigraphy for a single flow field because the composition varies from site to site across any given flow field.
- The $^{187}Os/^{188}Os$ isotopic variations in the Sand Hollow flow field suggest that there was a progressive decrease in crustal contamination during emplacement of the flow.
- The degree of crustal contamination of the basalt can vary within an eruption, as evidenced by examination of different lobes from the same flow field.
- During emplacement, the Sand Hollow magma was also affected by fractional crystallisation in parallel with the assimilation of continental material.
- Variable processes affecting the melt erupted in a single event are not a special case limited to the CRB province. Preliminary data for an individual lava flow from the Deccan Traps indicates a similar process to that seen in the CRB whereby maximum contamination is recorded in the crusts of a flood basalt rather than the core.

4.8 Further work

The commonality of coincidence between cratonic boundaries and the present of flood basalt provinces has led to the suggestion of an alternate mechanism of flood basalt formation (King and Anderson 1995; Lustrino 2005). Physical modelling identify a possibility that non-uniform boundary conditions between thick (cratonic) and thin (accreted) lithosphere may create small-scale forms of convection enabling shallow and sub-horizontal flow of magma (Lustrino 2005). Whilst this exists as an alternative to a plume model for genesis of the CRBG (Manea *et al.*; Arndt *et al.* 1993), verification of this versus alternative models is not examined here. Further accumulation of Re-Os data within individual eruption units for flood basalts may provide novel data to take this work forward.

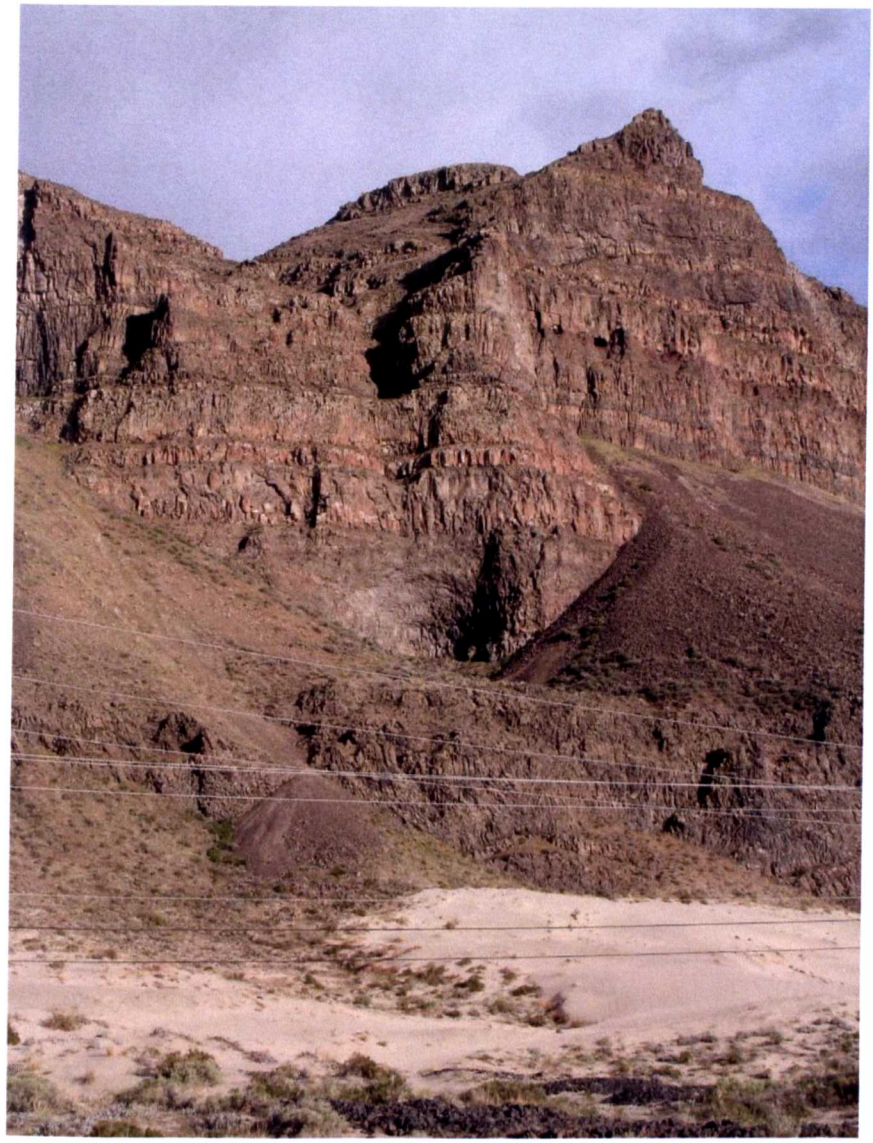

Upper Grande Ronde basalts at Sentinel Gap

Chapter 5. Sr isotopes

5.1 Introduction

Intra-crystal isotopic microsampling has been utilised over the last two decades to examine pre-eruptive histories of magmas (e.g. Davidson *et al.* 1998). It offers significant advantages over bulk rock analyses that typically provide only an averaged isotopic composition which can obscure potential compositional variations among individual mineral and melt components. As such, bulk rock analyses can only supply a partial view of the source and components of a melt (Ramos and Tepley 2008). Radiogenic isotopes, when combined with textural and major element analyses, within mineral grains offer high resolution information to determine the nature of magmatic systems. Such insights can in principle identify differentiation pathways within open systems and better constrain the isotopic composition of the end-members and mantle sources.

Microspatial analyses target individual growth zones within crystals. Growth of a phenocryst occurs from core to rim by the crystallisation of sequential layers of material. The layers record changes in the isotopic character of the magma in which the crystal grew. Plagioclase appears early in the crystallisation history of magma and crystallises over a large range of compositions (e.g. during differentiation of basalts to rhyolites), pressures and temperatures. This property enables the use of plagioclase crystals to record temporal compositional changes associated with magma chamber dynamics (e.g. Knesel and Davidson 1999). Combination of chemical and textural zoning may thus be used to reconstruct a) the conditions in which the plagioclase grew and b) the evolution of the magma in which the crystal has been exposed to (Grove *et al.* 1984; Ginibre *et al.* 2002). Compositional zoning of major elements in plagioclase typically reflects primary growth

compositions due to slow diffusion within the crustal structure (Grove *et al.* 1984; Giletti and Casserly 1994). High concentrations of Sr and low concentrations of Rb make plagioclase an ideal candidate for the investigation of $^{87}Sr/^{86}Sr$ recorded during the growth of a crystal. Low Rb contents mean that $^{87}Sr/^{86}Sr$ ratios are not measurably influenced by isotopic ingrowth and can be taken as recording the initial Sr isotope ratio.

Detailed studies of isotopic variations within a single crystal are referred to as crystal-isotope stratigraphy (CIS) studies (Tepley *et al.* 2000; Davidson *et al.* 2006). These studies have shown that crystals may record the source composition and magma pathways and the processes of mixing and contamination (Knesel *et al.* 1999; Tepley *et al.* 1999; Tepley *et al.* 2000; Davidson *et al.* 2001; Davidson *et al.* 2007; Morgan *et al.* 2007). Thus isolating the end-members involved in the magmatic system.

The CIS methodology has been mostly applied to andesitic and rhyolitic systems and single volcanoes rich in large crystals (e.g. Davidson *et al.* 2007) but only rarely applied to a flood basalt province (Wolff *et al.* 1999; Bryce and DePaolo 2004; Durand and Sen 2004; Ramos *et al.* 2005; Higgins and Chandrasekharam 2007; Font *et al.* 2008). Mixing and mobilisation of an existing crystal population with an incoming younger melt is a consistent conclusion from many silicic volcanic systems e.g. Soufriere Hills – Montserrat (Zellmer *et al.* 2005), Ruapehu (Gamble *et al.* 1999; Price *et al.* 2005) and Oruanui - New Zealand (Charlier *et al.* 2008). Crystal mushes have been shown to comprise chains and clusters of crystals with interstitial melt (Jerram *et al.* 2003), reflecting complex crystallisation events and recycling into younger melts (Marsh 2004). Heterogeneity resulting from magma mixing (e.g., Tepley et al., 1999), assimilation (e.g., Knesel *et al.* 1999; Davidson *et al.* 2001), recharge (e.g., Davidson and Tepley 1997; Morgan *et al.* 2006), and radioactive decay (e.g., Christensen and Depaolo 1993; Morgan and Blake

2006) is understandable in these evolved silicic magmas. Comparatively fewer studies document isotopic heterogeneities between melt bodies and their crystal cargo in less evolved magmas which typically have shorter residence times in magma chambers, higher temperature and lower viscosity melts (Cortini and van Calsteren 1985; Paslick *et al.* 1996; Knesel and Davidson 1999; Bryce and DePaolo 2004; Font *et al.* 2008). Analyses of multiple single crystals from an individual single flood basalt eruptive unit could provide novel data on the assembly of a melt body erupted during a single event. Furthermore, insight into crustal-level processes can provide additional evidence for shallow level processes versus compositions inherited from source signatures.

In this chapter the application of CIS (Davidson *et al.* 2005) enables the construction of two time sequences with which to investigate magmatic history. Firstly, growth zones from the core to rim of a crystal represent a recording through time of the host magma composition in which the crystal grew. Secondly, the relationship between the analysed crystals in the eruptive sequence provides a temporal sequence because they were extracted from samples at the upper crust, lower portion of the upper crust and at the lobe core of a single lobe within the Sand Hollow flow field. According to the inflation model of pahoehoe lava by Self *et al.* (1996) these samples represent a relative timeline from the first emplaced basalt (upper crust) to the last emplaced basalt (lobe core). This temporal framework enables comparison of potential variations that might have affected magma erupted as a single unit.

5.1.1 Existing intra-crystal research

Early isotopic studies of individual crystals that were undertaken in a textural and major element context helped constrain magma mixing histories (Geist *et al.* 1988). Studies examined enclave – host magma variations and xenocryst identification (Davidson *et al.*

1990). These micro-scale studies identified potential magmatic processes and the extent of these processes within magmatic systems (Davidson *et al.* 2005). As the application, precision and accuracy of isotopic analyses have become increasingly detailed, numerous studies have revealed a commonality in the results - the majority of crystals reveal isotopic heterogeneity (Geist *et al.* 1988; Davidson and Tepley 1997; Tepley *et al.* 1999; Charlier *et al.* 2006; Charlier *et al.* 2007; Charlier *et al.* 2008).

Numerous intra-crystal isotope studies revealed a highly complex series of processes that would otherwise have been overlooked from whole-rock averaging. All the studies utilised a combination of textural analyses, crystal major and trace element variations and isotope analyses from micromilling or laser-ablation. Complex models have been created for studies from El Chichón, Mexico (Tepley *et al.* 2000), Lassen Peak, USA (Tepley *et al.* 1999), Ngaruhoe Volcano, New Zealand (Davidson *et al.* 2007), Monte Cimino and Vico volcano, Italy (Perini *et al.* 2003) and Isle of Skye (Font *et al.* 2008). These models explain the compositions where crystals are derived from an older melt, magmas mix and hybridise prior to eruption. From this work it was recognised that many so-called phenocrysts had complex crystal characteristics due to recycling in volcanic systems. Such crystals were re-termed 'antecrysts' (Charlier *et al.* 2005 and references therein). Antecrysts are genetically related to the system but are not derived from the magma in which they are erupted (Davidson *et al.* 2007) and can be identified by virtue of being in isotopic disequilibrium with the surrounding groundmass.

5.1.2 Insights from earlier intra-crystal studies in the CRBG

Laser ablation sampling of $^{87}Sr/^{86}Sr$ of plagioclase from several formations in the CRBG have been reported (Wolff *et al.* 1999; Ramos *et al.* 2005). Results from the early erupted Imnaha lavas, which are generally thought to derive from a plume mantle source with little

significant crustal inputs, reveal a wide range of $^{87}Sr/^{86}Sr$ ratios from within plagioclase phenocrysts. This contrasts with only subtle variations in the host basalt (Eckberg *et al.* 2006). The intra-crystal work suggests that the plagioclase originated from a plume-related mantle and interacted with either accreted fluid-fluxed subcontinental mantle or cratonic crust encountered during ascent (Wolff *et al.* 2008). Subsequent eruptions of the Picture Gorge and Grande Ronde basalts reveal a wider range of $^{87}Sr/^{86}Sr$ values than the earlier Imnaha basalts (Ramos *et al.* 2004). The Picture Gorge signatures are suggested to reflect greater interaction with fluid-fluxed accreted materials, whereas the patterns in the Grande Ronde basalts are inferred to result from increased assimilation of cratonic crust (Eckberg *et al.* 2006).

As well as tracing sources and processes, $^{87}Sr/^{86}Sr$ have been used to evaluate crystal residence times (Ramos *et al.* 2005). All the studied crystals indicate disequilibrium with their host melt and can be described as antecrysts. Plagioclase crystals were incorporated through a crystal-melt exchange into large volume magmas at different times prior to eruption from 5 to 250 years (Wolff *et al.* 2008). These extremely short times, calculated from 1D diffusion modelling from the host magma composition at 1100°C, indicate that mineral and melt components of the flood basalt magmas were undergoing assembly immediately before or during the eruptions.

The approach to intra-crystal isotopic composition outlined in various previous research papers (e.g. Charlier *et al.* 2006; Davidson *et al.* 2007) is applied in this chapter to elucidate the assembly of a melt body erupted in a single flood basalt event. Sr isotopic analyses and electron microprobe (EMP) data from intra-crystal zones in large crystals are compared with small (<3 mm) groundmass crystals and whole-rock powders from a single locality. The data illustrate the extensive range of compositions within single crystals that

are not identified using only whole-rock analyses. As a result, detailed analyses of a few crystals reveal more information about these complex magmatic systems than multiple broad-scale province-wide geochemical profiles.

5.2 Sample choice

Three crystals from the Locke Lake lobe of the Sand Hollow flow field were selected for detailed analysis (Fig. 5.1). The samples were selected from the Re-Os sample suite (Chapter 4), in order to provide further constraints on the source and petrogenesis of the Sand Hollow flow field.

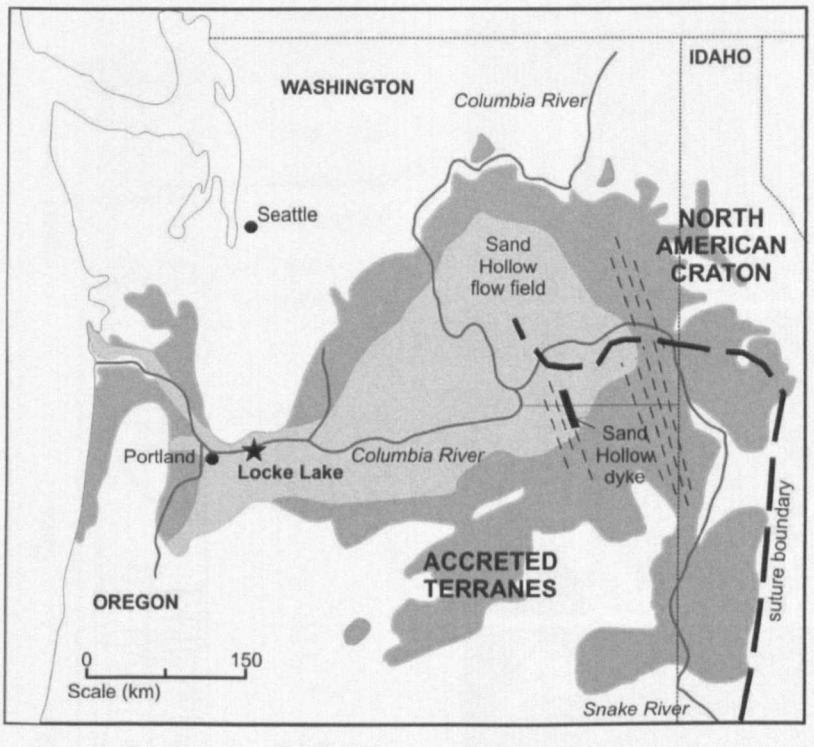

Figure 5.1 Location map for the sample site of the three crystals from a single lobe in the Sand Hollow flow field. Pale grey area indicates the extent of the Sand Hollow flow field within the Columbia River Basalt Group (dark grey).

The Locke Lake location (SH_11) was chosen because sufficient crystals are present within the samples to enable numerous crystals to be analysed at different heights within the lobe. Generally, the Sand Hollow flow field has a lower abundance of crystals

compared to other porphyritic flow fields of the Wanapum formation (e.g., Ginkgo and Roza). This prompts questions on the origin of the large crystals, such as whether they have a phenocrystic, antecrystic or xenocrystic relationship to the basalt in which they were erupted. Furthermore, the origin and mechanism facilitating the separation of crystals from the original melt may provide further information on the assembly of large melt bodies in the upper crust underlying flood basalt provinces.

Samples selected for intra-crystal analysis are CRB06_005 from the upper crust of the lobe, CRB06_014 from the lowermost part of the upper crust and CRB06_016 from the centre of the lobe core (Fig. 5.2).

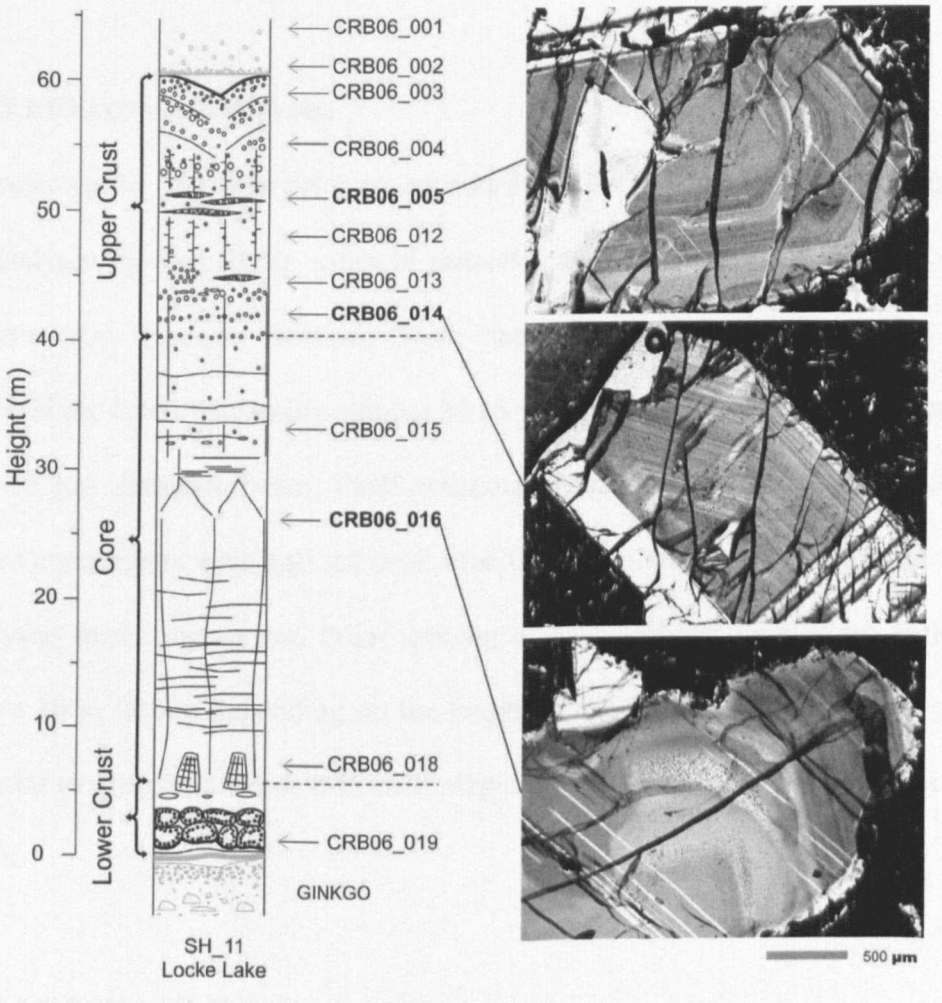

Figure 5.2 Log of the Sand Hollow flow field lobe at the Locke Lake locality indicating sample heights and the structure of the lobe according to the inflation model of pahoehoe lava (Self *et al.* 1996). Photomicrographs of the three crystals analysed within this chapter are shown relative to the samples from which the crystals are taken and the position of these within the lobe. All photos are at the same scale.

A relative timeline can be constructed from these samples, from the first emplaced lava (CRB06_005) to the youngest lava emplaced (CRB06_016). Samples gathered from the upper crust, rather than those from the lower crust, avoid potential complications caused by non-linear temporal evolution in the basal zone of the core.

5.3 Techniques

Polished thick sections (70 μm) of each sample were cut as close to the 'c' axis of each crystal as possible. Orientation of the crystals enables cross-correlation of zones in both character and width.

5.3.1 Electron microprobe

Electron microprobe analyses prior to microdrilling defined a sampling strategy for the isotopic analyses by identifying zones of potential variation, e.g. through large variations in anorthite (An) content. Sections were analysed on a Cameca SX-100 electron microprobe at the Open University using a 20 kV accelerating voltage, 20 nA beam current and a 10-15 μm diameter beam. Peak counting times ranged from 25-60 seconds and background count times were half the peak time for each element. Transects of each crystal were analysed from core to rim. Point spacing of each sample point along each transect varied from 10 to 20 μm depending on the length of the transect. Transects are orientated perpendicular to growth zones within each plagioclase crystal and cross all features within the crystals.

5.3.2 Whole-rock Sr isotopic analyses

Whole-rock analyses were conducted on powder splits of the same samples used for the Re-Os isotopic analyses in Chapter 4. Details of the methods are presented in Charlier *et*

al. (2006) but are outlined here. Sample digestion was conducted using conventional HF, HNO_3 and HCl digestions in Savillex® beakers. The residue was taken up in 500µL of 3M HNO_3 and left on a hotplate overnight. Finally 200µL of 3M HNO_3 was added to deliver the sample to column chemistry. Following sample loading to each column the Sr spec resin was rinsed with 50, 100, 200, 200µL batches of 3M HNO_3 to remove Rb and Ca (which have mass interference on ^{87}Sr and affect Sr ionisation during TIMS analysis respectively). Subsequently Sr was eluted from each column using batches of 50, 200, 200µL batches of 0.05M HNO_3 and evaporated prior to loading onto outgassed Re filaments. A TaF activator was also loaded onto each filament to enhance the Sr ionisation (Birck 1986). All samples were analysed on a Finnigan Triton thermal ionisation mass-spectrometer (TIMS) in static collection mode. Amplifier gains were calibrated at the start of each session and baselines were measured before each analysis. Sr isotope measurements were usually made at beam intensities of 5-6V ^{88}Sr and 300 ratios were measured for each analysis.

5.3.3 Intra-crystal Sr isotopic analyses

A full description of the methodologies employed within this chapter for micromilling and high precision isotope dilution thermal ionisation mass-spectrometry (ID-TIMS) are provided in Charlier *et al.* 2006.

5.3.3.1 Micromilling

The computer-controlled micromill consists of a binocular microscope, diamond-tipped milling bit and X-Y mobile stage with accompanying software that determines the drill tip location, sample surface location and drilling depth. Shallow troughs are drilled using multiple holes at 70 µm intervals and 45 µm depth to generate sufficient sample material of each growth band in turn. Sample recovery is accomplished using a drop of 18.2 MQ

water on the polished section surface. This water also serves as a cooling agent for the drill bit. The sample is drilled through the water drop and during drilling of the sample surface particulates collect in the water, generating a sample slurry. A micropipette is used to suction the section surface to collect the drilled sample. The section is bathed in methanol and rinsed to remove all traces of the drilled sample prior to drilling the next growth rim sample. Each sample slurry is deposited in a weighed small gold boat, dried and re-weighed to calculate the sample weight prior to deposition in a teflon beaker for digestion. The gold boats are resistant to digestion acids and standard dissolution techniques are employed in 3ml Savillex® Teflon beakers.

High concentrations of the target element require sampling of smaller quantities of material and offer the potential for finer spatial resolution of the samples. Small sample sizes enable detailed studies of individual growth rims but processing small samples (~0.001 – 0.01 mg) requires great care to produce 1 – 3 ng of Sr for a highly precise TIMS analysis (Charlier *et al.* 2006). Such analyses require a known and consistent blank with minimal correction.

5.3.3.2 Chemical preparation and separation

Sample dissolution was achieved using 200 µL HF added to each Savillex® beaker containing a gold boat. At this point each sample was also spiked using a mixed ^{87}Rb-^{84}Sr spike (made from IRMM-635 (99.89% ^{85}Sr) and IRMM-618 (97.99% ^{87}Rb) supplied by B.L.A Charlier). The samples were left to decompose and achieve sample-spike equilibration. Following extraction of the gold boat from each beaker a few drops of 3M HNO_3 was added to each beaker and reduced on a hotplate before addition of 200 µL of 6M HCl and placed on a hotplate for a minimum of 3 hours. On evaporation 200 µL 3M

HCl was added and left on a hotplate overnight before evaporation and finally being taken up in 50 µL 2.5M HCl ready for Sr spec column chemistry.

The samples were subsequently reduced before being taken up in 150 µL 3 M HNO_3 ready for column chemistry. Micro-cation columns were prepared with Dowex AG 50 WX8 cation exchange resin. After sample loading and elution of 1150 µL 2.5M HCl, the Rb fraction was collected in 700 µL 2.5M HCl. The Sr fraction was collected following elution of 450 µL 2.5M HCl and collection of 1450 µL which was dried down and dissolved in 100 µL 3M HNO_3. Sr separation was subsequently achieved using four stages of 50, 100, 200, 300 µL of 3M HNO_3 for the Rb fraction and batches of 50, 200, 200 µL of 0.05M HNO_3 for the Sr fraction. The Sr fraction was then dried down ready for TIMS analysis. Loading and analysis of isotope dilution samples follows the same method used for unspiked samples with correction for spike contribution applied offline.

5.3.3.3 Blanks and international standards

Total procedural blanks (TPB) include all stages of sample extraction, processing and analysis. The blanks were prepared by running the drill tip in a water droplet for the same period of time as for sample drilling. The water droplet was dried down on a gold boat that was then prepared for sample dissolution and column elution as if it were a powder sample. The isotopic composition of the TPB was $^{87}Sr/^{86}Sr$ 0.70878 ± 1.03 x 10^{-3} (n = 3). The sample data were not blank corrected as the contribution from the blanks are low, <1% of the sample loaded and close to the average isotopic composition of the samples.

International standards were run alongside every batch of sample analyses to determine external reproducibility. Repeat analyses for $^{87}Sr/^{86}Sr$ NBS 987 averaged 0.710260 ± 7.27818 x 10^{-6} (n=26) and are comparable to external values of this standard 0.710248 ±

1.1 x 10^{-5} (Thirlwall 1991). Run numbers 1-6 were conducted on 450 ng loads of the standard to enable comparison of TIMS analysis to the whole-rock data. The remaining run numbers using 12 ng load sizes for analysis alongside the micromilled samples (Fig. 5.3). Due to the disparity in results between these different load sizes a normalisation factor of 0.999982 is applied to the whole-rock data.

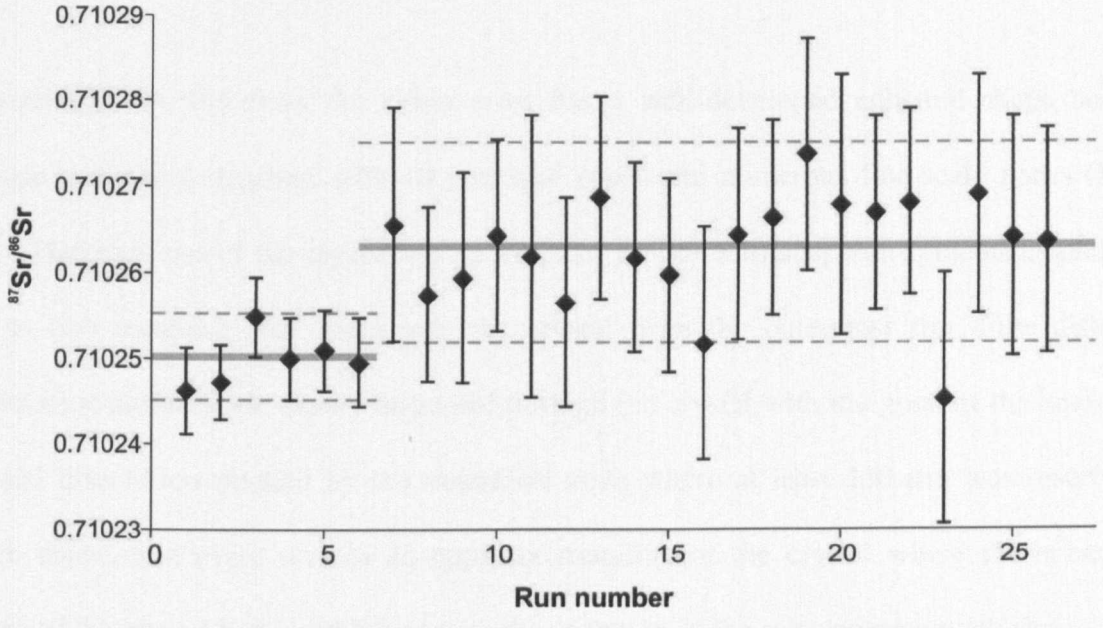

Figure 5.3 Results of the NBS 987 standards run throughout the time of sample analysis depicting external precision (2σ). Grey bar indicates the average value for 450 ng (run numbers 1-6) and 12 ng (run numbers 7-26) load sizes. Dashed lines indicate the average 2σ precision. Raw data is supplied in Appendix H.

5.4 Results

Whole-rock Sr isotope analyses for all samples within the Locke Lake lobe are presented for comparison with three large crystals (~1-2 cm diameter) analysed for intra-crystal elemental and isotopic heterogeneities as well as small whole plagioclase crystals (~1-3 mm) from the surrounding groundmass.

5.4.1 Petrology

A range of textural features and crystal morphologies are observed in each large crystal. Distinct dissolution surfaces and zones record a history of changing magmatic conditions. Crystal rims are irregular and pitted and crystals CRB06_005 and CRB06_016 have deep embayments suggesting compositional disequilibrium between the large crystals and groundmass.

Crystal CRB06_005 from the upper crust has a well-developed euhedral shape and a classic hexagonal structure with 10 principal zones and numerous fine-scale zones (Fig. 5.4). The outer rim of the crystal has an irregular profile with deep embayments extending up to two compositional zones into the crystal from the outermost rim. Five distinct dissolution surfaces are evenly dispersed through the crystal with the greatest thickness of crystal dissolution marked by the outermost zone where at least 250 μm was resorbed. Each dissolution event creates an apparent rounding of the crystal where the euhedral shape of the crystal is re-established with the accretion of the subsequent growth rim.

Crystal CRB06_014 from the lowermost part of the upper crust has the most growth zones of any of the crystals (Fig. 5.5). The zones are regular and thin (~50 to 200 μm wide) with few obvious dissolution surfaces. Some faceted growth zones may be representative of short time periods of resorption but the euhedral character of the crystal is maintained with all growth zones. This sample has the most complete outer rim.

Crystal CRB06_016 from the inner core of the lobe is a highly irregular crystal with a sub-rounded shape (Fig. 5.6). The last dissolution surface inside the crystal rim completely truncates interior growth zones. This may be in part due to the oblique cut through the crystal however the interior growth zones also suggest aggressive resorption events. Single

growth zones range from ~50 to 400 μm wide and some inner zones contain abundant inclusions. Five significant dissolution horizons produce a rounded grain and subsequent growth zones fail to re-establish an euhedral crystal geometry with rounded corners persistent throughout the crystal. A sharp compositional change is observed at the rim that cuts across previous zones but the outer boundary is irregular suggesting that this growth did not continue through to inclusion in the Sand Hollow flow field magma.

5.4.2 Electron microprobe analyses

Sample CRB06_005 from the upper part of the upper crust reveals a variable An content fluctuating around an average of 64.2 ± 2.2 (Fig. 5.4). A few strong inflections are associated with dissolution surfaces within the crystal, notably at 880 μm, 1180 μm, 1350 μm and 1910 μm distance along the transect from the crystal core. Low An values are observed at dissolution horizons. Values then increase into the associated growth zone. Anorthite decreases from the outer rim (An_{65} to An_{62}) to a dissolution horizon. With the exception of other dissolution horizons, the An content of the interior of the crystal displays limited compositional variation.

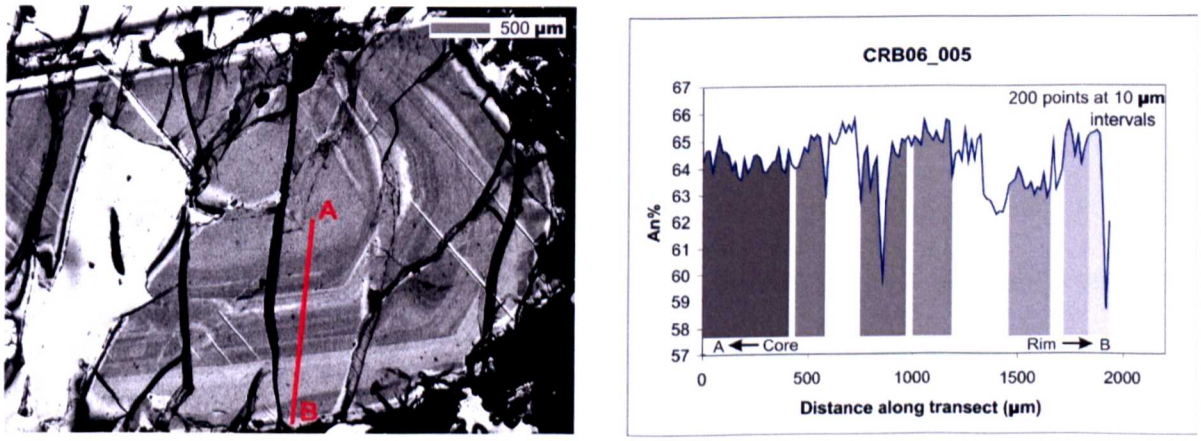

Figure 5.4 Photomicrograph of sample CRB06_005 indicating the transect analysed by microprobe from the crystal core (A) to the rim (B). Results of the transect plot An content against distance from the crystal core. Zones drilled for Sr isotope analysis are also shown in grey blocks.

Sample CRB_014 from the base of the upper crust varies slightly around An content 63 ± 0.8 (Fig. 5.5). Few peaks in inflections are observed in this profile with the exception of one increase in the middle of the profile and depletion in the crystal rim. The lack of compositional variation in this crystal is expected from the petrography because only minor resorption events can be visually discerned between the regular weak zones forming this crystal.

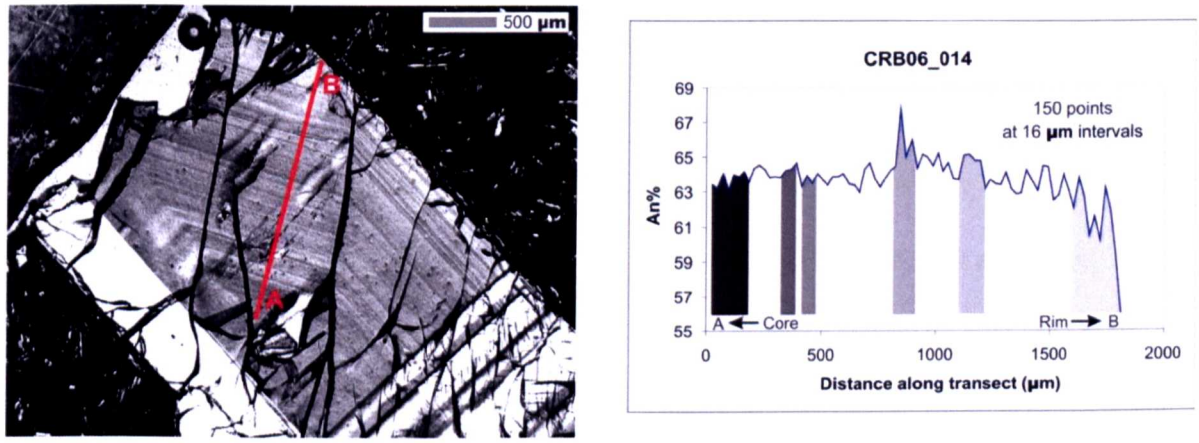

Figure 5.5 Photomicrograph of sample CRB06_014 indicating the transect analysed by microprobe from the crystal core (A) to the rim (B). Results of the transect are shown plotting An content against distance from the crystal core. Zones drilled for Sr isotope analysis are also shown in grey blocks.

Sample CRB_016 from the middle of the core of the lobe has a highly variable An content fluctuating around an average of 62.7 ± 4.3 (Fig. 5.6). Several data points have been omitted from the calculation of this mean (and from the display in the accompanying figure) because the transect crosses fractures in the crystal that do not provide a compositional analysis of the crystal. Decreases in An content are noted at some dissolution horizons but this is not a persistent characteristic in the profile. This may be due to the juxtaposition of growth zones of similar compositions due to extensive resorption of alternative compositions. This is seen at the first significant dissolution horizon close to the crystal core.

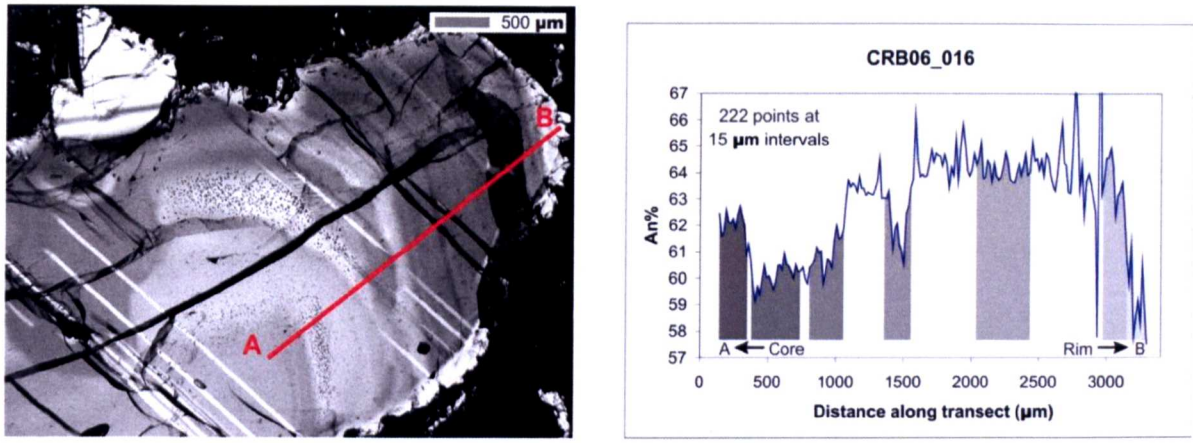

Figure 5.6 Photomicrograph of sample CRB06_016 indicating the transect analysed by microprobe from the crystal core (A) to the rim (B). Results of the transect are shown plotting An content against distance from the crystal core. Zones drilled for Sr isotope analysis are also shown in grey blocks.

The composition of the crystal core is slightly higher than the surrounding growth rims and slightly less than the cores of the other two crystals (CRB06_005 ~An_{64}, CRB06_014 ~An_{63}). The gross compositional profile of the crystal outlines increasing An content with increasing distance from the core until the outer rim.

5.4.3 $^{87}Sr/^{86}Sr$ whole-rock analyses

Results of the whole-rock analyses for samples within the Locke Lake lobe of the Sand Hollow flow field (Table 5.1) reveal little variation outside analytical error (2σ) (Fig. 5.7).

Sample Name	Height in lobe (m)	^{88}Sr average	$^{87}Sr/^{86}Sr$	1 std error	2 std error	$^{87}Sr/^{86}Sr$ normalised
3	59.8	4.40139	0.7051974	4.109E-06	8.21712E-06	0.7051845
4	55	6.42296	0.7052119	2.501E-06	5.0011E-06	0.7051990
5b	51	5.94345	0.7052109	2.956E-06	5.91247E-06	0.7051980
12	48	5.75664	0.7052062	2.896E-06	5.79191E-06	0.7051933
14	42	5.60446	0.7052044	2.99E-06	5.97934E-06	0.7051915
16	26	6.68358	0.7052237	2.45E-06	4.89919E-06	0.7052108
17	18	6.24617	0.7052225	2.81E-06	5.62077E-06	0.7052097
18	7	5.45204	0.7052096	2.795E-06	5.59061E-06	0.7051967
19	0.3	2.88981	0.705213	1.178E-05	2.35518E-05	0.7052001

Table 5.1 Whole-rock $^{87}Sr/^{86}Sr$ results showing the normalised isotope ratios to enable comparison between the whole-rock results and intra-crystal results.

The lava core samples show an increasingly radiogenic signature with height up to the upper crust boundary where there is a stepped decrease in $^{87}Sr/^{86}Sr$ (from 0.705224 ± 4.89919 x 10^{-6} to 0.705204 ± 5.97934 x 10^{-6}). The small compositional variations are exemplified by the analytical variance (2σ) associated with the sample from the lower crust. The standard deviation of analyses for this data point encompasses all the results for the other samples within this section.

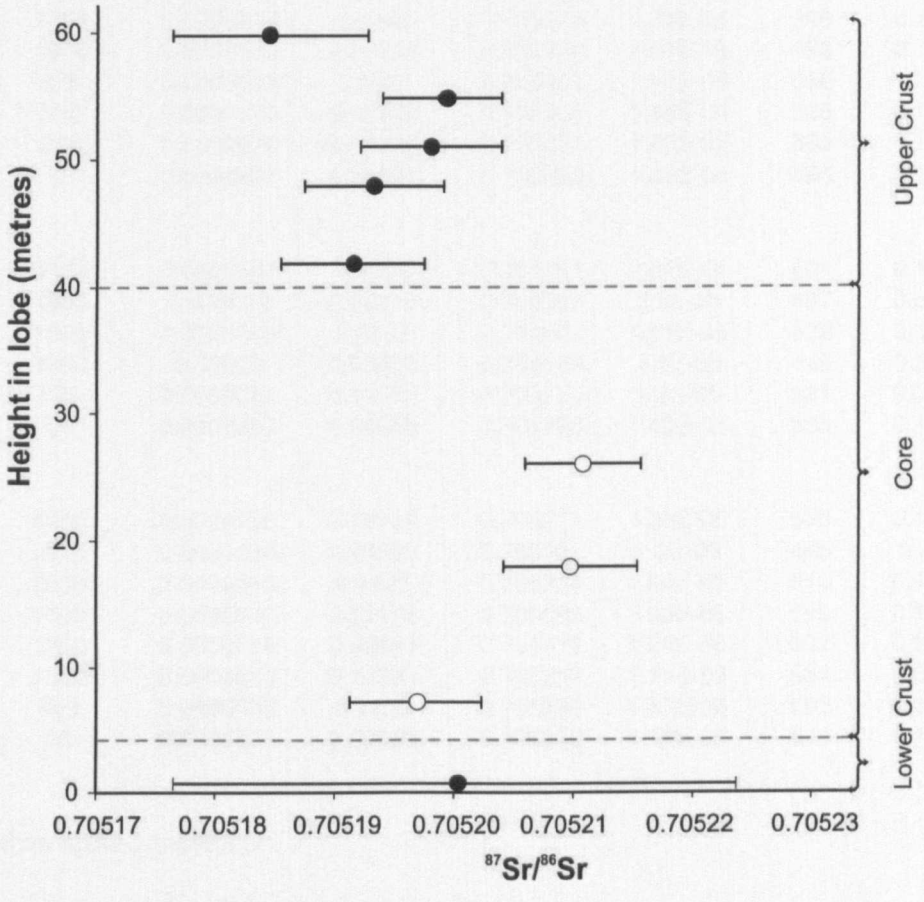

Figure 5.7 $^{87}Sr/^{86}Sr$ whole-rock analyses for the Locke Lake lobe within the Sand Hollow flow field. White circles indicate samples taken from the lobe core. Black circles indicate samples taken from the upper and lower crusts. Error bars associated with each sample represent 2σ.

5.4.4 $^{87}Sr/^{86}Sr$ drilled crystal sections

The $^{87}Sr/^{86}Sr$ results for each crystal are similar to the major element profiles, revealing varying characters for each crystal (Table 5.2). In a broad sense both the uppermost crust sample (CRB06_005) and the lobe core sample (CRB06_016) have increasingly radiogenic growth zones from the core of each crystal towards the rim. However, the lowermost crust

sample (CRB06_014) has significantly greater variation in $^{87}Sr/^{86}Sr$ than the other two crystals but the character of the variation is different. $^{87}Sr/^{86}Sr$ in this crystal decreases with increasing distance from the crystal core and a stepped increase to a radiogenic crystal rim.

sample name	distance from core	Sample weight (g)	Spike weight (g)	$^{87}Sr/^{86}Sr$ [1]	2σ	Sr ppm	2σ
CRB06_005							
groundmass	2000	0.00003	0.05283	0.705610	2.14E-05	433	0.130804
rim	1500	0.0000458	0.08182	0.705302	1.89E-05	572	0.44219
zone 4	1150	0.0000818	0.1449	0.705261	1.36E-05	599	0.136871
zone 3	1000	0.0000458	0.08108	0.705469	1.07E-05	572	0.111036
zone 2	675	0.0000543	0.0952	0.705301	1.42E-05	566	0.1529
zone 1	550	0.0000679	0.12029	0.705306	1.45E-05	566	0.150755
outer core	250	0.0000574	0.10089	0.705287	1.23E-05	585	0.122286
inner core	50	0.0000837	0.14822	0.705255	1.32E-05	596	0.156522
CRB06_014							
groundmass	3000	0.0000901	0.1564	0.705251	2.86E-05	501	0.116105
rim	1900	0.000019	0.03276	0.705987	3.5E-05	687	0.523768
zone 3	1500	0.0000486	0.0837	0.704803	1.81E-05	622	0.177027
zone 2	1000	0.00002	0.03476	0.704486	4.4E-05	645	0.293239
zone 1	625	0.0000686	0.11973	0.705170	1.2E-05	521	0.069742
core	50	0.0000257	0.04365	0.705188	1.45E-05	533	0.120529
CRB06_016							
groundmass	4000	0.0000736	0.12788	0.705271	1.26E-05	533	0.115537
rim	2875	0.0001354	0.23592	0.705257	1.3E-05	465	0.08353
zone 5	2650	0.0000816	0.1425	0.705324	1.08E-05	619	0.121222
zone 4	1500	0.0000642	0.11173	0.705282	1.32E-05	585	0.107187
zone 3	1250	0.0000515	0.08894	0.705312	1.24E-05	602	0.107701
zone 2	1000	0.0000813	0.14203	0.705239	1.14E-05	584	0.086565
zone 1	400	0.0000635	0.1105	0.705231	1.37E-05	599	0.122281
core	50	0.0000556	0.09559	0.705252	1.19E-05	619	0.115296

[1] Data corrected for spike contribution.

Table 5.2 Full results for the $^{87}Sr/^{86}Sr$ intra-crystal analyses.

In crystal CRB06_005 from the upper crust $^{87}Sr/^{86}Sr$ increases outward from the crystal core with each of the subsequent sampled growth zones (Fig. 5.8). There is a marked step increase in the radiogenic signature at the growth zone at 1000 μm (no. 5 in Fig. 5.8) along the transect from the crystal core. The crystallisation of this band follows a distinctive and complicated resorption horizon. The subsequent band (no. 6 in Fig. 5.8) returns to an unradiogenic signature similar to the crystal core. $^{87}Sr/^{86}Sr$ increases from this last band to the crystal rim. The groundmass plagioclase results are highly radiogenic and anomalously

elevated above the whole-rock analysis. Whilst the groundmass plagioclase sample is a combined analysis of 10 small single crystals, it is not possible to rule out that these crystals might be smaller fragments of antecrysts and are thus in disequilibrium with the melt composition (represented by the whole-rock analysis).

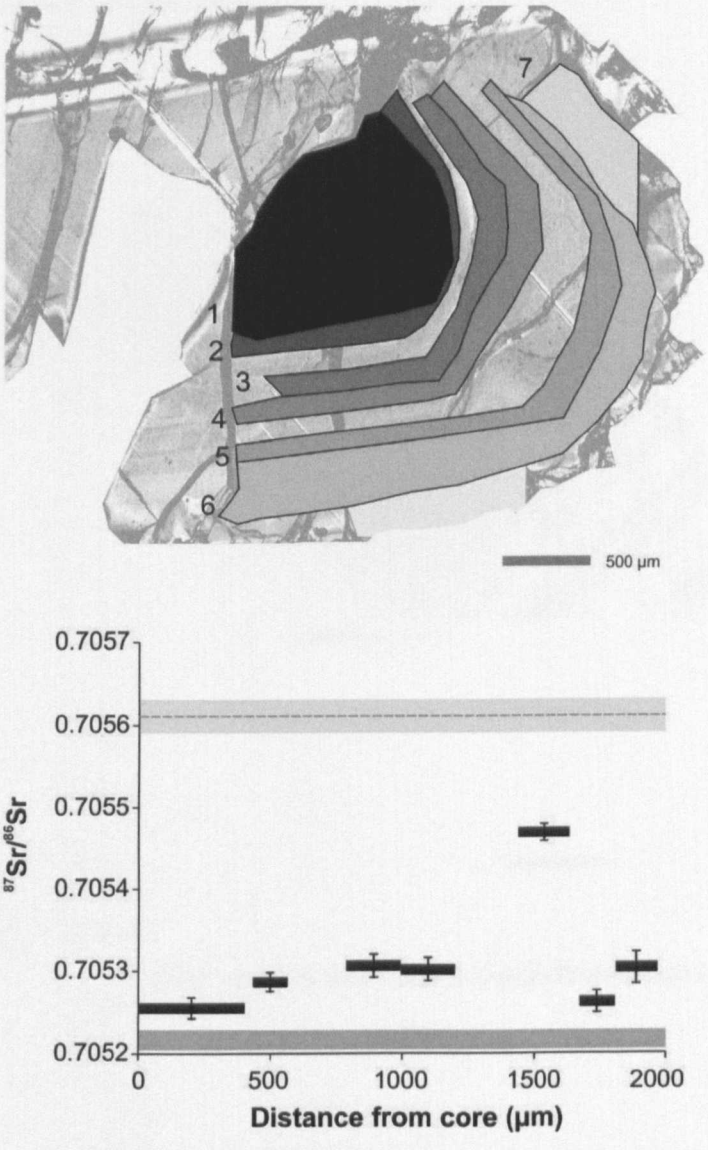

Figure 5.8 Single crystal $^{87}Sr/^{86}Sr$ results for crystal CRB06_005 from the upper crust of the lobe. The result of several whole single crystal analyses from groundmass plagioclase crystals (averaged from 10 samples) is indicated by a dashed line with 2σ analytical precision shown in pale grey. The dark grey solid bar shows the result of the whole-rock $^{87}Sr/^{86}Sr$ for this sample including 2σ analytical precision. Error bars indicate 2σ.

The composition of the core of crystal CRB06_014 is slightly lower than that from higher in the upper crust; $^{87}Sr/^{86}Sr$ is 0.705188 in this crystal relative to 0.705255 in crystal CRB06_005 (Fig. 5.9). The first growth rim (no.2) analysed outside the core (no.1 on Fig.

5.9) has a similar value to the crystal core, the groundmass crystals and the whole-rock analyses, all of which are in equilibrium. However, the intervening growth rims demonstrate the most variable compositions of any of the samples from the other crystals analysed. From the growth rim at 1000 µm along the transect (no.3) the subsequent two growth rims are increasingly radiogenic.

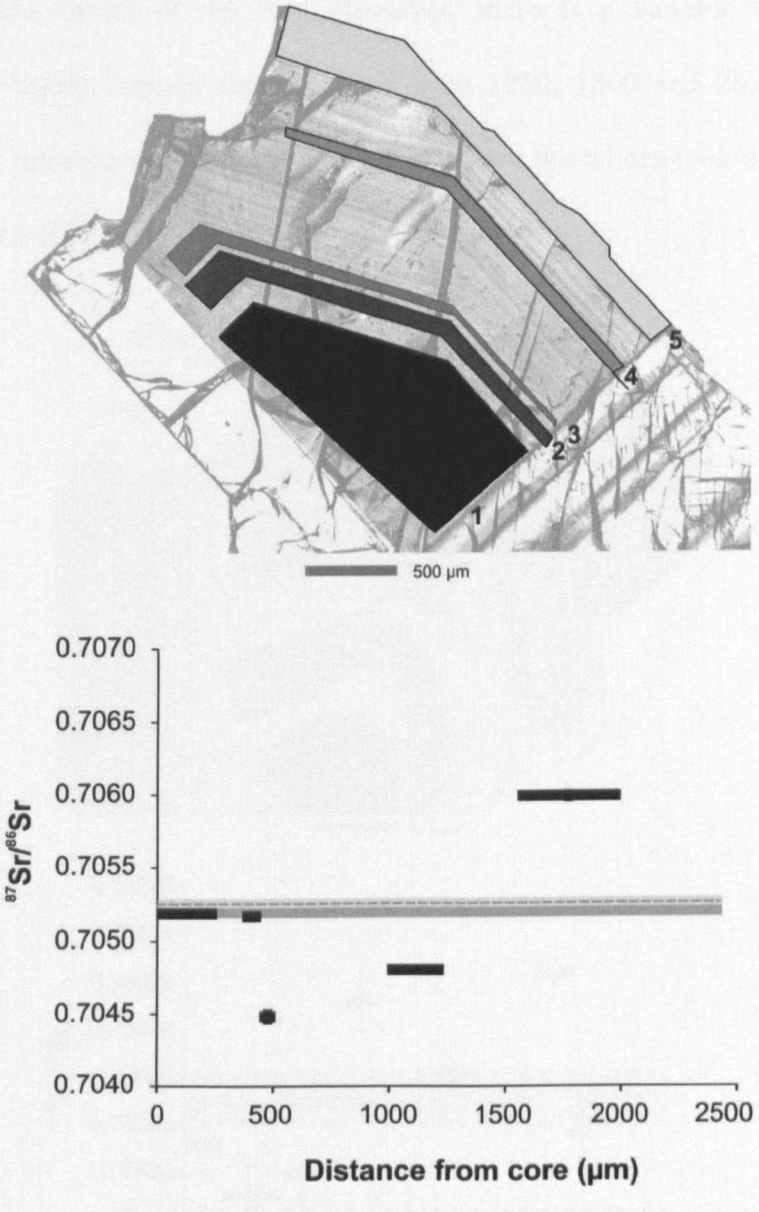

Figure 5.9 Compilation of single crystal $^{87}Sr/^{86}Sr$ results for crystal CRB06_014 from the lowermost part of the upper crust of the lobe. The result of several whole single crystal analyses from groundmass plagioclase crystals (averaged from 10 samples) is indicated by a dashed line with 2σ analytical precision shown in pale grey. The grey solid bar shows the result of the whole-rock $^{87}Sr/^{86}Sr$ for this sample including 2σ analytical precision. Error bars indicate 2σ.

Whilst crystal CRB06_016 from the lobe core demonstrates the most complex intra-crystal textures of any of the crystals, it has the most limited $^{87}Sr/^{86}Sr$ range. The composition of the crystal core is slightly elevated above the composition of the first growth zone (no.2 in Fig. 5.10). Like crystal CRB06_014, the rim of the crystal interestingly bears the same isotopic value as the crystal core and the groundmass plagioclase is within analytical error of the Sr isotope values of the rim. However, there is a variable set of high and intermediate radiogenic results for growth rims at 1250, 1500 and 2650 µm along the transect. All the intra-crystal results are elevated above the whole-rock analysis ($^{87}Sr/^{86}Sr$ $0.705224 \pm 4.90 \times 10^{-6}$).

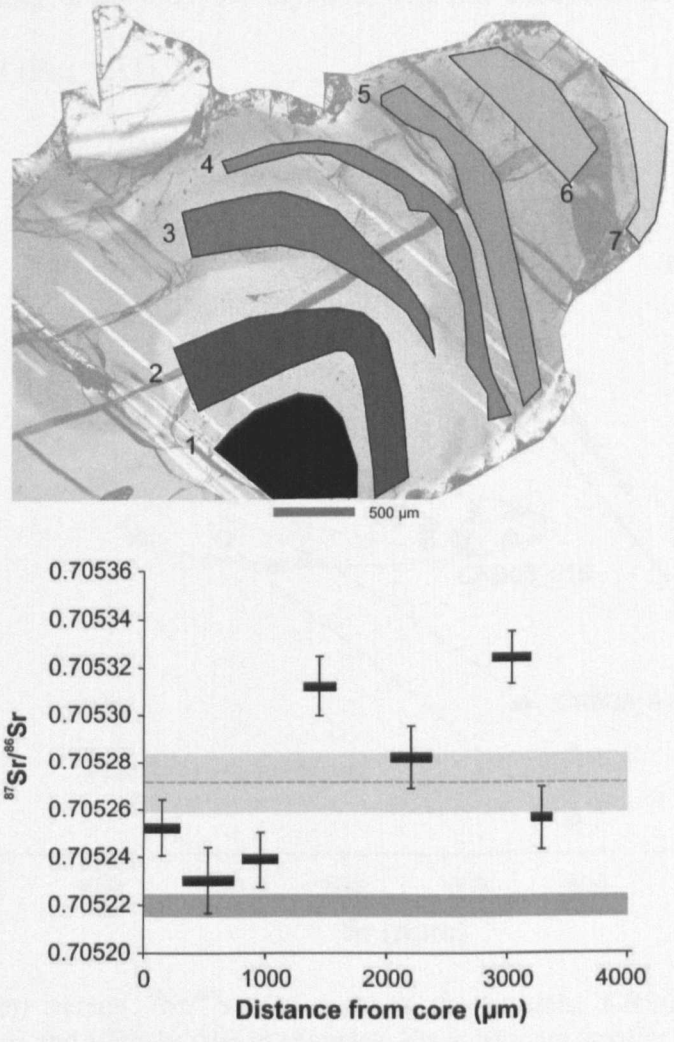

Figure 5.10 Compilation of single crystal $^{87}Sr/^{86}Sr$ results for crystal CRB06_016 from the lobe core. The result of several whole single crystal analyses from groundmass plagioclase crystals (averaged from 10 samples) is indicated by a dashed line with 2σ analytical precision shown in pale grey. The grey solid bar shows the result of the whole-rock $^{87}Sr/^{86}Sr$ for this sample including 2σ analytical precision. Error bars indicate 2σ.

A distinct profile emerges with height within the lobe when comparing the range of intra-crystal $^{87}Sr/^{86}Sr$ values for each of the three crystals. The crystal with the least isotopic variation is the found in the lobe core (CRB06_016) and the most variation is born within the crystal from the lower portion of the upper crust (CRB06_014). The most isotopically heterogeneous crystal bears the least elemental variation and appears to be petrographically simple with even, closely spaced growth rims. The crystal from the core with the most chemical and textural variation is isotopically the most restricted.

Isotopic compositions compared to Sr concentration for each crystal reveals overlaps between some portions of the analysed crystals, with one exception from the crystal rim of sample CRB06_014 (Fig. 5.11).

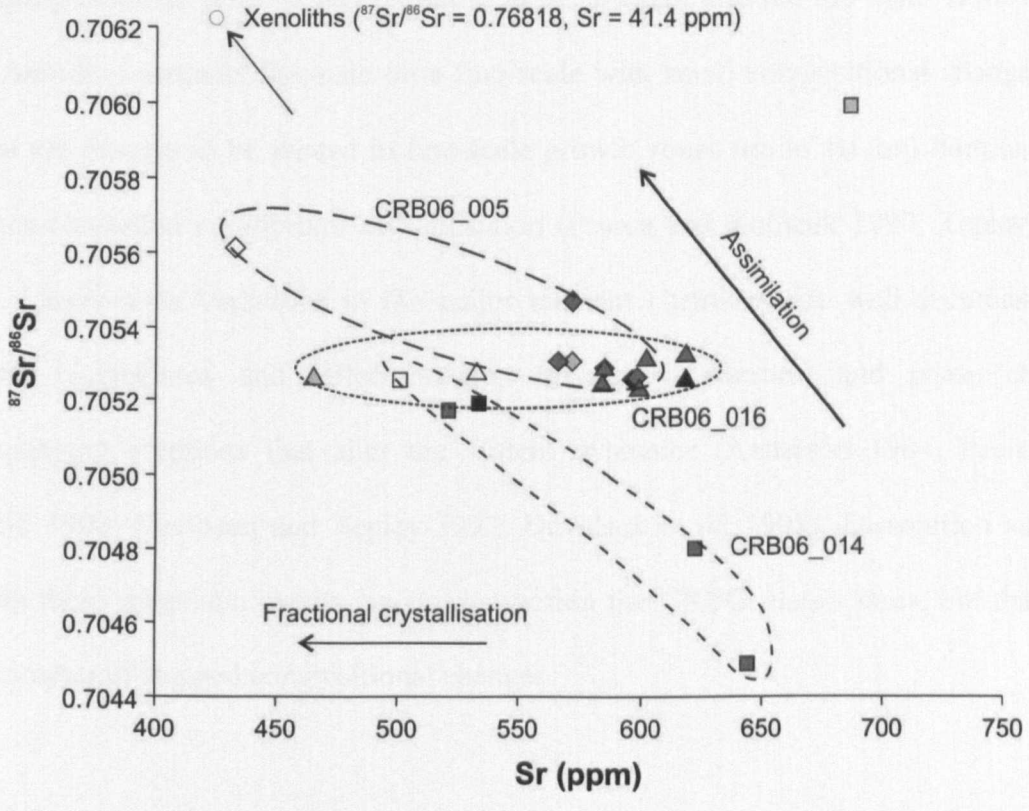

Figure 5.11 Sr (ppm) versus $^{87}Sr/^{86}Sr$ for each of the crystals: CRB06_005 in diamonds, CRB06_014 in squares and CRB06_016 in triangles. Error bars are smaller than the symbol size. Ellipses show the area of all the analytical points in each crystal with the exception of one outlier for sample CRB06_014. In all cases white symbols represent the mean groundmass plagioclase composition from each sample, pale grey symbols are the rim compositions, black symbols are the crystal cores and dark grey symbols represent samples from all the intervening growth rims. Composition of xenoliths from Carlson et al. (1981).

Groundmass plagioclase crystals mostly have lower Sr concentrations than those samples from within the antecrysts. Range in values for intra-crystal analyses of CRB06_005 and CRB06_016 overlap, whilst sample CRB06_014 is more distinct. Samples CRB06_005 and CRB06_014 both display a negative correlation between isotopic and chemical composition, whilst CRB06_016 has a comparatively limited range of isotopic values.

5.5 Discussion

5.5.1 Origin of intra-crystal compositions

5.5.1.1 *Major-element profiles*

The results presented for each crystal are unique in character suggesting that they had contrasting histories prior to incorporation in the magma that fed the Sand Hollow flow field. Anorthite contents fluctuate on a fine scale with small compositional changes (1-2 %) that are thought to be related to fine-scale growth zones (up to 10 μm) dominated by diffusion-controlled equilibrium crystallisation (Pearce and Kolisnik 1990; Tepley *et al.* 2000). Larger-scale variations in the major element chemistry are well-documented in volcanic plagioclases and reflect magma mixing or overturn and phase changes accompanying eruptions that alter the system dynamics (Anderson 1984; Pearce and Kolisnik 1990; Davidson and Tepley 1997; Davidson *et al.* 1998). Dissolution surfaces marking these magmatic events are present within the CRBG plagioclases, but there are few examples of stepped compositional changes.

Two explanations have been suggested for complex zoning of compositional and textural features: a) magma chamber convection, or b) changes in the volatile content of a system due to periodic eruptions (Belkin *et al.* 1984; McGee *et al.* 1987; Singer *et al.* 1995; Tepley *et al.* 2000). These processes cause variations in volatile saturation of the system;

increasing volatile contents lower the plagioclase solidus temperature and allow Ca-rich plagioclase to crystallise, whereas reduction of volatiles (e.g. through degassing and eruption) re-equilibrates lower An content plagioclase (Tepley *et al.* 2000; Costa *et al.* 2003). However, these closed-system processes cannot account for intra-crystal isotopic heterogeneities which require magma mixing events in an open magmatic system. Comparisons between crystals relative to the sample position within this lobe reveal a stepped profile in the lobe core, limited variation in the lower portion of the upper crust and slightly oscillatory zoning in the uppermost sample. Interpretations of the intra-crystal data involve magma chamber recharge and mixing of a more primitive melt causing dissolution horizons and subsequent crystallisation of Ca-rich plagioclase reflected in the anorthite content (Tsuchiyama 1985). The record of melting and crystallisation from multiple dissolution horizons within some crystals cannot be explained by a single simple event (Blundy and Cashman 2008).

5.5.1.2 *Isotope profiles*

Some intra-crystal isotopic characteristics are similar to each other, with sequential growth zones in each crystal having increasingly radiogenic $^{87}Sr/^{86}Sr$ towards the crystal rims. However, there are many textural and compositional characteristics that are not shared. The crystal from the lobe core exhibits less total variance in $^{87}Sr/^{86}Sr$ between growth rims and dissolution zones whereas the crystal from the lower portion of the upper crust has the greatest variance in $^{87}Sr/^{86}Sr$ and the least variation in major and trace elements. Whilst major-element profiles reflect levels of intra-crystal textural complexity, isotopic profiles must be related to complex open-system processes.

Variations in $^{87}Sr/^{86}Sr$ ratios seem independent of textural complexity and size of each of the crystals. Correlations between the antecrysts textural features such as disconformities

in crystal growth and decreases in $^{87}Sr/^{86}Sr$ reflect the addition of a more primitive less contaminated mantle-derived magma with lower $^{87}Sr/^{86}Sr$. Similar relationships between the crystal growth zones and isotopic signature of whole-rock analyses have been documented in other tectonic settings including volcanic arcs (Davidson and Tepley 1997).

The crystal from the lobe core (CRB06_016) is the only sample that reveals similar $^{87}Sr/^{86}Sr$ compositions in both the crystal core (0.705252) and crystal rim (0.705257). The composition of the groundmass plagioclase crystals is also within the error values for these analyses (0.705255). The similarity in the values from these samples may reflect numerous processes active during the growth of the crystal: 1) no contamination occurred in the magmatic system, 2) crystal growth occurred after contamination of the magma, 3) the magma from which the crystal grew was contaminated by an isotopically identical lithology to the composition of the melt (Font *et al.* 2008). The isotopic signature of the intervening growth rims suggest crystal growth occurred in a magmatic system with an increasing degree of crustal contamination. Recharge from a more primitive, less contaminated melt from the same source as the initial melt in which the crystal nucleated may have facilitated the growth of an isotopically identical crystal rim.

Intra-crystal isotopic signatures may be a result of modification processes within the lava following eruption. Davidson *et al.* (2007) suggest that variation may be achieved through: a) post-eruption growth of the crystals through crystallisation of a rim, b) radiogenic ingrowth or c) diffusional re-equilibration. In-situ crystallisation and proposed conditions from other research suggests crystal-mush compaction may influence the composition and texture of crystal rims (Dragovic *et al.* 2002). Overgrowths on crystals derived from progressive crystallisation of a residual intercumulus liquid have been identified in the Skaergaard intrusion (Humphreys 2009). Thick flood basalt lava flows are analogous to sill

bodies and the suggested lava emplacement times of a flow field (up to 15 years (Thordarson and Self 1998) are sufficient to allow prolonged post-emplacement crystallisation. In-situ crystallisation is demonstrated not to make a contribution to the crystals presented in this study as the crystal rims in each case are in both textural and compositional disequilibrium with the surrounding melt. This evidence is provided by both the 'average' $^{87}Sr/^{86}Sr$ composition of each sample derived from the whole-rock powder analyses and also single crystal analyses of microlites in the surrounding groundmass.

5.5.2 Open vs. closed system for flood basalt magmas

5.5.2.1 *Crustal contamination*

Broad-scale compositional variations within the crystals support the Re-Os isotopic data for sequential increases in the assimilation of crustal material in the Sand Hollow magma. Radiogenic signatures in whole-rock samples and within crystals are coupled to major element indications of magma recharge – the most mafic lavas, found in lobe cores, are generally the least contaminated by crustal materials. This holds true for the upper crustal samples CRB06_005 and CRB06_014 but the last crystal to be emplaced (CRB06_016) displays the reverse. This suggests the addition of an assimilant coincident with fractional crystallisation of the melt (AFC) (DePaolo 1981). This crystal from the lobe core also bears the least variation in $^{87}Sr/^{86}Sr$ and the most complex petrographic and chemical features.

Significant crustal contamination has been identified elsewhere within the products of flood basalt eruptions e.g. (Carter *et al.* 1978; Moorbath and Thompson 1980; Devey and Cox 1987; Ellam 1992) but not previously on the small-scales documented here. Distinctive contamination signatures are present within each of the crystals within this chapter but the location of contamination and the origin of the crystals are elusive.

Strontium compositions of country rock in the region are variable. Mesozoic granites intruding the North American craton are more radiogenic ($^{87}Sr/^{86}Sr$ = 0.7092-0.7140) than those intruding the accreted terranes ($^{87}Sr/^{86}Sr$ = 0.7033-0.7049) and country rock composition as a whole is known to be < 0.704 to the south and west, and > 0.706 to the north and east of the suture boundary (Armstrong *et al.* 1977) (Fig. 5.1). Therefore, assuming the contaminant came from the west of the boundary, the $^{87}Sr/^{86}Sr$ ratios of the contaminant would be similar to the isotopic signature of the CRB magmas. This may account for the lack of variability in whole-rock samples.

Whilst there are no constraints to isolate the timing of crustal contamination implied by Re-Os isotopic data in Chapter 4, a sense of relative timing is gleaned from the single crystal analyses presented here. Dungan (2005) suggests that rates of crustal assimilation may be significantly shorter than repose periods at arc volcanoes (an order of magnitude shorter than repose periods of flood basalt volcanic episodes – 100-10,000 years (Thordarson and Self 1998; Self *et al.* 2006; Jolley *et al.* 2008). Moreover, rates may be sufficiently rapid to operate during 'extended eruptive episodes (years-decades)' (Dungan 2005). These timescale ranges would lie in the typical range estimated for the duration of flood basalt eruptions (Self *et al.* 1996; Thordarson and Self 1998).

It is unlikely that assimilation of a homogeneous lithology or a partial melt will account for all contamination of even small magmatic systems (Dungan 2005). Uniform contamination on the scale of flood basalt magmatic systems is even less likely. Variations in conditions experienced during crustal contamination have been highlighted for $^{87}Sr/^{86}Sr$ (Knesel and Davidson 1996) as isotopic disequilibrium may not be maintained during partial melting of the crust. Whilst isotopic variations are known to be a product of mantle melting (Hofmann

and Hart 1978), the effect of isotopic disequilibrium between a melt and the host country rock on a contamination signature is poorly constrained and cannot be isolated here.

5.5.2.2 *Magma chamber recharge*

A growing number of investigations into intra-crystal heterogeneity identify magma chamber recharge as a common feature irrespective of the volcanic or tectonic setting (e.g. Davidson and Tepley 1997; Zellmer *et al.* 2005; Charlier *et al.* 2008). The combined intra-crystal data and whole-rock data reveal that antecrysts may represent a longer timeline of differentiation of the magmatic history than that revealed using whole-rock analyses. Small-scale compositional heterogeneity within the Sand Hollow flow field, shown in Chapter 2, also reveals patterns which may be explained by either sequential tapping of a zoned magma chamber or recharge of the magmatic system by more primitive, less radiogenic magma.

Co-linearity of Sr composition versus isotopic ratios between the data points for samples CRB06_005 and CRB06_014 suggests assimilation of crustal materials accompanying fractional crystallisation of the magma (Fig. 5.11). By contrast, sample CRB06_016 displays a dominant fractional crystallisation trend with the crystal core at the most primitive composition (high Sr) and the crystal rim at the most evolved (low Sr). The eruption sequence of these samples (CRB06_005 first – CRB06_016 last) supports the eruption of a less evolved composition in the latter stages of the eruption that may represent magma chamber recharge.

The compositional signature of melts acquired through open-system magmatic processes is complex due to the variety and interdependence of active processes. Magma recharge (or replenishment) enhances efficient assimilation of wallrock due to the influx of high

temperature mafic melt (Dungan 2005). Several recharge events into the magmatic system would explain initial decreases in $^{87}Sr/^{86}Sr$ as a less contaminated and more primitive melt entered the system and an elevated signature above the previous ratio in the subsequent growth rims.

5.5.3 Genesis and assembly of the Sand Hollow magma

The genesis and assembly of the magma that fed the Sand Hollow flow field can be fingerprinted for its crystal history and contributing melts. The antecrysts clearly did not crystallise from the melt in which they were erupted (represented by the host groundmass in these samples). Disequilibrium between crystals and the host melt may be caused by processes including magma mixing, crustal assimilation and entrainment of crystal mush (Philpotts and Asher 1993; Bohrson and Spera 2001; Spera and Bohrson 2001).

Disequilibrium between crystal rims and host magma imply that either a) the host magma changes composition at a rate that is greater than crystal growth rate (e.g. 10^{-10} to 10^{-14} ms^{-1} (Cashman 1993 and references therein) at the scale at which analyses can be conducted or b) crystal residence times in the melt were insufficient for either equilibration to the new conditions promoting renewed growth or crystals were still undergoing dissolution (Davidson *et al.* 2007). Experimental study suggests fast mixing timescales may be recorded if eruption occurs shortly after mixing as rims 10-100 μm wide take ~10 days to 4 months (Larsen 2005). The latter of the two hypotheses is favoured for these three crystals, which represent a crystal cargo incorporated into the magma in which they were erupted, because only a small portion of magmatic evolutionary history is shared between the crystal and melt components.

Decreasing height (and relative younging) of the crystal samples within the lobe is correlated with decreasing degrees of disquilibrium between the isotopic composition of the rims and the groundmass plagioclase crystals. The timeline represented by these three samples is interpreted here to reflect a longer residence time of crystals in magma emplaced later in the eruption sequence (CRB06_016 – lobe core) and shorter residence times early on (CRB06_005 – upper crust). It might be considered that incorporation of pre-existing crystals into the Sand Hollow magma occurred as one event immediately before eruption.

The combined $^{87}Sr/^{86}Sr$ results from whole-rock, single crystal and intra-crystal analyses suggest a multi-stage, complex genesis for flood basalt magmas with late stage assembly of the melt plus antecrysts. The plagioclase microlites (the groundmass plagioclase crystals) are crystallised from the Sand Hollow magma body and the antecrysts were mobilised and included in this melt during shallow crustal transport of the Sand Hollow magma to the fissure vent. The cause of disequilibrium between whole-rock $^{87}Sr/^{86}Sr$ analyses, plagioclase microlites and the antecrysts could be related to the style of crustal contamination, suggested by whole-rock Re-Os isotopes as an important component in the Sand Hollow magma.

5.5.4 Implications for magmatic plumbing systems of flood basalt provinces

Shallow crustal plumbing systems for other flood basalt provinces have been found to consist of extensive sills and dykes (e.g. Morrison *et al.* 1985; Chevallier and Woodward 1999; Elliot and Fleming 2008). Deeply eroded provinces have revealed giant dykes swarms inferred to have fed eruptions (Piccirillo *et al.* 1990; Ernst and Buchan 1997; Ray *et al.* 2007). These systems must be extensive and contain substantial volumes of unerupted magma (Crisp 1984; Walker 1993). Roberts *et al.* (1984) and White and

McKenzie (1989) propose that volume figures can be up to 10 times larger than the erupted volume. However, the nature of shallow-level exposures does not imply similarity in the character of magma transport at depth, illustrated by the range of possibilities presented by (Elliot and Fleming 2004) for the Ferrar Group, Antarctica. Lateral and vertical zones of melt generation and migration require evaluation to determine the nature of a flood basalt plumbing system.

Complex plumbing systems beneath flood basalt provinces are recorded from magma-crust interactions in the British Tertiary Volcanic Province (Morrison *et al.* 1985). Variable degrees of contamination of different lithologies are related to the transition and ponding of magma bodies at several depths in the crust. Evolution of a similarly complex magmatic system is described for the East Greenland flood basalt province (Peate *et al.* 2008). Complex plumbing systems with multiple transport pathways along extensive sill-dyke networks and ponding of magma bodies throughout the crust may be a common phenomena associated with flood basalt provinces.

The available data suggests that the physical structure of the magma storage system underlying the Columbia River province at the time of the Wanapum Formation eruptions contributed to compositional heterogeneity of the Sand Hollow flow field. Contributions of several different components including crystals with apparently different crystallisation histories to the Sand Hollow melt suggests re-use of an existing magmatic plumbing system and incorporation of crystal mush from pre-existing magmas. Eruptions preceding the Sand Hollow include the crystal-rich lavas of the Ginkgo flow field. Whilst no phenocrysts from these lavas have been analysed, unerupted melts from this system may provide the source of residual crystal mush. Such interpretation implies the occupation of a pre-existing and potentially long-lived plumbing system.

Comparison of the profiles for Sand Hollow antecrysts with published results from other flow fields within the CRBG (Ramos *et al.* 2005) reveal similarities with the Roza flow field, also of the Wanapum Formation. However, crystals from other formations within the province reveal contrasting styles or limited variation in isotopic profiles. Care must be taken in interpretations gleaned from only a few data points, in this case a single crystal that defines each stratigraphic zone, but a tentative relationship can be correlated with time and the evolution of the flood basalts. The changes in processes and melt assembly over time may be related to evolution of the plumbing system underlying the province. Bryce and DePaolo (2004) provide supporting data for the first CRBG eruptions forming the Imnaha Basalts as representing plume or mantle compositions. Low εNd values are coupled with low $^{87}Sr/^{86}Sr$ (Bryce and DePaolo 2004), low $^{187}Os/^{188}Os$ (Chesley and Ruiz, 1998) and a plume-like $^{3}He/^{4}He$ value. Dodson et al. (1997) suggests that intra-crystal and melt isotopic heterogeneities are mantle-derived with limited modification through crustal assimilation. By contrast, the voluminous, high frequency eruptions of subsequent Grande Ronde lavas have limited intra-crystal or whole-rock isotopic heterogeneity. It is not until the later erupted Wanapum and Elephant Mountain flow fields that intra-crystal heterogeneities demonstrate complex isotopic signatures.

Combination of the processes active in the assembly of the Sand Hollow melt are best explained by the existence of a crustal-level system of sills and dykes rather than a single magma chamber or conduit. It is unknown whether this system may be laterally or vertically extensive, or both. Wolff *et al.* (2008) suggest lateral flow of CRBG magma from a central source, which in this case was the Yellowstone plume. The suture boundary between the North American craton to the east and accreted terranes to the west has been identified as a lithospheric weak spot that may facilitate lateral transport of magma away from the plume. Seismic data indicates that the south-eastern region of the Columbia River

province, in which Wanapum Formation feeder dykes are located, contains a strong bend in the suture boundary (Mohl and Thiessen 1995). The change in lithospheric structure in this zone may act as a focal point for the eruption of the CRBG lavas and ponding of magma bodies contaminated by at least two isotopically significantly different lithologies.

5.6 Conclusions

- Intra-crystal Sr isotope data reinforce the conclusions gleaned from whole-rock Re-Os isotope data for the Sand Hollow flow field of variable contamination by both the North American craton and Jurassic accreted terranes through which the magma ascended.

- Each of the three crystals sampled are in disequilibrium with the host melt and are thus identified as antecrysts. All exhibit multiple compositional zones within the crystal and 3 to 5 principal resorption rims or dissolution surfaces suggesting numerous recharge events within shallow crustal reservoirs.

- Crystals are representative of pre-eruptive conditions only rather than any syn-eruption crystal growth as the last growth-stage (the crystal rims) are texturally undulating or wavy with deep embayments in some cases and isotopically distinct from both the whole-rock and groundmass plagioclase crystals.

- Isotopic variations from the core to the rim of each antecryst reveal growth in an open-system environment with a combination of recharge, mixing and crustal contamination producing an evolving magmatic composition.

- Co-variations in composition and isotopic ratios suggest AFC is a dominant process in the magmas erupted early in the eruption sequence with magma chamber recharge and fractional crystallisation dominant toward the latter stages of the eruption.

- Several items of evidence suggest aggregation of crystals and possibly also melt bodies from different sites of magma storage in the crust that are tapped during the eruption of this flow field:
  - Despite being from the same lobe in the flow field each crystal has varying core to rim isotopic characteristics although the overall pattern of increasingly radiogenic signatures with increasing distance from the core is similar.
  - The rim of two of the crystals is in disequilibrium with the surrounding groundmass plagioclase crystals and the whole-rock Sr isotope signature.
  - A varying number of recharge events and varying petrographic features in general between each crystal imply growth of each crystal under different conditions.

5.7 Further work

Assessments of timescales have been sought from intra-crystal compositions to demonstrate the rate of magmatic events (e.g. Hawkesworth *et al.* 2000; Smith *et al.* 2009). Residence times of an antecryst in a host melt may be calculated by diffusion profiles where the composition of the crystal and that of the surrounding melt are variable and chemical equilibrium is sought (Morgan *et al.* 2004; Costa and Dungan 2005; Morgan and Blake 2006). One-dimensional modelling of phenocrysts from the CRBG reveals a variety of residence times from 15-150 years (Ramos *et al.* 2005). The modelling application uses

diffusion profiles assuming the groundmass surrounding the crystal is representative of the melt composition from which the crystal grew. In the case of antecrysts in disequilibrium with the host melt this method is not applicable. However, the calculated residence times from crystals with rims in equilibrium with the host melt (interpreted to be phenocrysts) suggest short residence times and provide no evidence for a long-lived magma chamber (Wolff *et al.* 2008). Further work is required in the future to establish the interdependence of disruptions of the crystal lattice and changing anorthite content to the diffusion behaviour of Sr in plagioclase crystals before such modelling can be reliably calculated for texturally complex antecrysts.

Palouse River and exposures through the Wanapum Formation

Chapter 6. Conclusions

6.1 Summary

In this thesis I have used field investigations to investigate the emplacement style of flood basalt flow fields. The resulting structure in three-dimensions and the derived relative emplacement times have been used to asses the presence of geochemical variation vertically and laterally within these flow fields. Compositional heterogeneity is used to investigate the origin and petrogenetic history of magma bodies that fed individual flood basalt eruptive events. I have applied this research to three flow fields in the CRBG and the results show that:

1. Flow fields consist of a network of lobes, sequentially emplaced and controlled by endogenous processes enabling progressive lateral growth of each flow field. Emplacement of a single flow field, and by inference the duration of the eruptive event, takes months to decades.
2. Small-scale geochemical heterogeneity is a common feature within flow fields and comparison with a physical framework reveals compositional variations with time and eruption sequence.
3. The origin of compositional heterogeneity in major and trace elements alone is difficult to pin down. Isotopic systems sensitive to open system processes such as Re-Os and intra-crystal Sr isotopes reveal a complex magma plumbing system with concurrent AFC processes and aggregation of a melt body immediately prior to eruption.

6.2 General considerations

6.2.1 Styles of lava emplacement and flood basalt facies architecture

The Columbia River flood basalt eruptions that produced the three studied flow fields were voluminous (up to 2,660 km^3). The lavas have pāhoehoe and rubbly pāhoehoe surface morphologies and internal structures characterised by a three-tiered division comprising lower crust, lava core and upper crust. This structure is similar to smaller inflated pāhoehoe lobes on Hawaii, Tenerife, Iceland and in other flood basalt provinces. The inflation model is the most satisfactory mechanism for emplacement of the lavas. The field observations suggest that small flow fields develop thicker lobes near the vent, and that lobes thin with increasing distance from the vent with small precursor or two lobes in the distal reaches of the field. In small flow fields such as the Palouse Falls, many lobe cores are physically linked, despite separate upper crusts, indicating that the last emplaced lava in each lobe simultaneously inflates adjacent lobes. A single simple flow field with linked lobe cores may be considered to be one lava flow within the flow field.

Single lobes range in diameter from 0.2 to 10 km. The variation in the thicknesses of the upper crust and core indicates both a longer duration of inflation in the proximal lobes and a thicker lobe core from 1.9 to 19.2 years. The data suggest that proximal sheet lobes transport lava through lobe cores to the distal margins of a flow field without developing physically identifiable lava tubes and that the magmatic pressure driving inflation was higher nearer the vent. Longer duration and higher volume eruptions generate more complex flow fields where the genetic and spatial development of the flow field cannot be disentangled using field observations alone.

6.2.2 Styles of compositional heterogeneity

Progressive systematic variation with height through individual sheet lobes provides supporting evidence for the emplacement of individual lobes by pāhoehoe-type inflation. High resolution sampling and compositional analysis within a flow field offers a significant advance in the understanding of emplacement mechanisms that is not revealed by lower resolution datasets. Such compositional data provides a record of the sequential evolution of the magmatic system over time. Intra-lobe differentiation, syn-emplacement contamination and post-emplacement alteration are ruled out as processes generating the observed compositional heterogeneity.

Vertical and lateral variations within and between lobes constituting a single flow field reveal slightly more evolved upper and lower crusts and slightly more primitive cores. During emplacement of the flow field the composition of the magma became slightly more primitive. Small-scale major and trace element compositional heterogeneity on whole rock samples alone is insufficient evidence to constrain the petrogenesis of individual flood basalt eruptive units. Small scale geochemical heterogeneity, in both major and trace elements, within and between lobes produced during a single eruption, was present at the time of emplacement and was acquired from pre-eruptive magmatic contamination, rather than surface processes.

From current evidence in the Columbia River basalts, intra-lava flow compositional heterogeneity may cause miscorrelation or misinterpretation of eruption units when based on single sample characterisation. This has implications for sampling for the purpose of establishing a chemostratigraphy. Even on a small-scale, it cannot be assumed that samples from the same point or height in a lobe enable cross-correlation. Across a province, compositional variations may not distinguish between or correlate separate eruptions. Re-

Os isotopes, in this example at least, highlight the difficulty in applying a chemostratigraphy for a single flow field because the compositional variations vary at different sites across the flow.

6.2.3 Origin of compositional heterogeneity

Intra-crystal Sr isotope data and whole-rock Re-Os isotope data can be explained by variable contamination of the Sand Hollow magma by both the North American Craton and Jurassic accreted terrane through which the magma was transported. The Re-Os isotopic variations in the flow studied here suggest that there was a progressive crustal contamination during emplacement of the flow, ranging up to 10% assimilation. Thus, individual eruptions cannot be compositionally classified as either contaminated or primitive. During emplacement the magma was also affected by fractional crystallisation in parallel with the assimilation of continental material. Variable processes affecting melt erupted in a single event are not a special case limited to the CRB province. Preliminary data for an individual lava flow from the Deccan Traps indicate that a similar process of contamination has occurred. The juxtaposition of continental suture boundaries and flood basalt provinces may impart a cryptic contamination signature to the basalt composition.

Large plagioclase crystals are in disequilibrium with the host melt and are thus identified as antecrysts. All exhibit multiple compositional zones within the crystal and 3 to 5 principal resorption rims or dissolution surfaces suggesting numerous recharge events within shallow crustal reservoirs. Crystals are representative of only pre-eruptive conditions rather than syn-eruption crystal growth because the last growth-stage (the crystal rims) are texturally undulating or wavy with deep embayments in some cases and isotopically distinct from both the whole-rock and groundmass plagioclase crystals. Isotopic variations from the core to the rim of each antecryst reveal growth in an open-

system environment with a combination of recharge, mixing and crustal contamination producing an evolving magmatic composition. Several lines of evidence suggest aggregation of crystals and possibly also melt bodies from different sites of magma storage in the crust that are tapped during the eruption of this flow field. This evidence includes a) despite being from the same lobe each crystal has varying core to rim isotopic characteristics whilst the general intra-crystal pattern of increasingly radiogenic signatures with increasing distance from the core is similar; b) the rim of each crystal is in disequilibrium with both the surrounding groundmass plagioclase crystals and the whole-rock Sr isotope signature; c) a varying number of recharge events and varying petrographic features in general between each crystal imply growth of each crystal under different conditions.

It is evident from antecrysts found in other volcanic products in numerous tectonic settings that open system processes and magma recharge is common within small magmatic systems. To some extent it is unsurprising that similar features are present within voluminous melt bodies underlying flood basalt provinces. However few studies document chemical and isotopic heterogeneities in basaltic magmas which typically have shorter residence times, higher temperature and lower viscosity melts. The compositional heterogeneity presented within this thesis suggests that characterisation can provide insights into the petrogenetic processes active within repose periods between flood basalt eruptive events. Furthermore, heterogeneity requires characterisation prior to any interpretation of source mantle heterogeneities.

6.3 Concluding remarks

In this thesis I have identified the emplacement mechanism and physical structures of three flow fields from the CRBG. I have used the structure of these units to investigate the presence of compositional heterogeneity and evaluate, both quantitatively and qualitatively, the petrogenesis of large volumes of magma erupted in the province. The results show that continued augmentation of the methods introduced in this thesis will enhance knowledge of flood basalt genesis, storage, eruption style and emplacement of flow fields. These factors have important implications for future studies of mantle heterogeneity, and form the base control for insights to eruption rates and environmental impacts of flood basalt provinces.

References

Ali, J. R., Thompson, G. M., Zhou, M.-F. and Song, X. (2005). "Emeishan large igneous province, SW China." Lithos in Mantle Plumes: Physical Processes, Chemical Signatures, Biological Effects 79(3-4): 475-489.

Allègre, C. J., Birck, J. L., Capmas, F. and Courtillot, V. (1999). "Age of the Deccan traps using Re-^{187}-Os-^{187} systematics." Earth and Planetary Science Letters 170(3): 197-204.

Allègre, C. J., Dupré, B., Richard, P., Rousseau, D. and Brooks, C. (1982). "Subcontinental versus suboceanic mantle, II. Nd-Sr-Pb isotopic comparison of continental tholeiites with midocean ridge tholeiites and the structure of the continental lithosphere." Earth and Planetary Science Letters 57: 25-34.

Allègre, C. J. and Luck, J.-M. (1980). "Osmium isotopes as petrogenetic and geological tracers." Earth and Planetary Science Letters 48(1): 148-154.

Alves, S., Schiano, P., Capmas, F. and Allegre, C. J. (2002). "Osmium isotope binary mixing arrays in arc volcanism." Earth and Planetary Science Letters 198(3-4): 355-369.

Anderson, A. T. (1984). "Probably relations between plagioclase zoning and magma dynamics, Fuego Volcano, Guatemala." American Mineralogist 69: 660-676.

Anderson, A. T., Swihart, G. H., Artioli, G. and Geiger, C. A. (1984). "Segregations vesicles, gas filter-pressing and igneous differentiation." Journal of Geology 92: 55-72.

Anderson, D. L. (1994). "Superplumes or supercontinents?" Geology 22(1): 39-42.

Anderson, S. W., Stofan, E. R., Smrekar, S. E., Guest, J. E. and Wood, B. (1999). "Pulsed inflation of pahoehoe lava flows: implications for flood basalt emplacement." Earth and Planetary Science Letters 168: 7-18.

Anderson, S. W., Stofan, E. R., Smrekar, S. E., Guest, J. E. and Wood, B. (2000). "Reply to: Self et al. discussion of "Pulsed inflation of pahoehoe lava flows: implications for flood basalt emplacement"." Earth and Planetary Science Letters 179: 425-428.

Armstrong, R. L., Taubeneck, W. H. and Hales, P. O. (1977). "Rb-Sr and K-Ar geochronometry of Mesozoic granitic rocks and their Sr isotopic composition, Oregon, Washington, and Idaho." Geological Society of America Bulletin 88(3): 397-411.

Arndt, N. T., Czamanske, G. K., Wooden, J. L. and Fedorenko, V. A. (1993). "Mantle and crustal contributions to continental flood volcanism." Tectonophysics 223(1-2): 39-52.

Atwater, T. (1970). "Implications of plate tectonics for the Cenozoic tectonic evolution of western North America." Geological Society of America Bulletin 81: 3513-3556.

Aubele, J. C., Crumpler, L. S. and Elston, W. E. (1988). "Vesicle zonation and vertical structure of basalt flows." Journal of Volcanology and Geothermal Research 35(4): 349-374.

Bachmann, O. and Bergantz, G. W. (2008). "Deciphering magma chamber dynamics from styles of compositional zoning in large silicic ash flow sheets." Reviews in mineralogy and geochemistry 69(1): 651-674.

Baksi, A. K. and Farrar, E. (1990). "Evidence for errors in the geomagnetic polarity time-scale at 17-15 Ma: $^{40}Ar/^{39}Ar$ dating of basalts from the Pacific Northwest, USA." Geophysical Research Letters 17(8): 1117-1120.

Ballard, R. D., Holcomb, R. T. and van Andel, T. H. (1979). "The Galapagos Rift at $86^{0}W$: 3. Sheet flows, collapse pits, and lava lakes of the rift valley." Journal of Geophysical Research 84: 5407-5422.

Barnett, J. and Fisk, L. H. (1980). "Palynology and paleoecology of a sedimentary interbed in the Yakima basalt (Miocene), Palouse Falls, Washington." Northwest Science 54(4): 259-278.

Barth, G. A., Kleinrock, M. C. and Helz, R. T. (1994). "The magma body at Kilauea-Iki lava lake - potential insights into midocean ridge magma chambers." Journal of Geophysical Research-Solid Earth 99(B4): 7199-7217.

Beeson, M. H., Fecht, K. R., Reidel, S. P. and Tolan, T. L. (1985). "Regional correlations within the Frenchman Springs Member of the Columbia River Basalt Group: New insights into the middle Miocene tectonics of northwest Oregon." Oregon Geology 47(8): 87-96.

Beeson, M. H., Tolan, T. L. and Anderson, J. L. (1989). The Columbia River Basalt Group in western Oregon; geologic structures and other factors that controlled flow emplacement patterns. Volcanism and Tectonism in the Columbia River Flood-Basalt Province. S. P. Reidel and P. R. Hooper, Geological Society of America. Special Paper 239.

Belkin, H. E., McGee, J. J. and Tilling, R. I. (1984). "Plagioclase zonation as an indicator of the magmatic history of El Chichon Volcano, Chiapas, Mexico." Geological Society of America, Abstracts with Programs 16: 442.

Bennett, V. C., Esat, T. M. and Norman, M. D. (1996). "Two mantle-plume components in Hawaiian picrites inferred from correlated Os-Pb isotopes." 381(6579): 221-224.

Bennett, V. C., Norman, M. D. and Garcia, M. O. (2000). "Rhenium and platinum group element abundances correlated with mantle source components in Hawaiian picrites: sulphides in the plume." Earth and Planetary Science Letters 183(3-4): 513-526.

Bentley, R. D. and Campbell, N. P. (1983). Geologic map of the Yakima quadrangle, Washington. Washington Division of Geology and Earth Resources Geologic Map GM-29, scale 1:62,500.

Beresford, S. W. and Cas, R. A. F. (2001). "Komatiitic invasive lava flows, Kambalda, western Australia." The Canadian Mineralogist 39(2): 525-535.

Bideau, D. and Hekinian, R. (1984). "Segregation vesicles of ocean floor basalts, 1: Petrological study of the segregation products." Journal of Geophysical Research 89(B9): 7903-7914.

Birck, J. L., Barman, M. R. and Capmas, F. (1997). "Re-Os isotopic measurements at the femtomole level in natural samples." Geostandards Newsletter-the Journal of Geostandards and Geoanalysis 21(1): 19-27.

Blake, S. and Bruno, B. C. (2000). "Modelling the emplacement of compound lava flows." Earth and Planetary Science Letters 184: 181-197.

Blundy, J. D. and Cashman, K. (2008). "Petrologic reconstruction of magmatic system variables and processes." Reviews in mineralogy and geochemistry 69(1): 179-239.

Bohrson, W. A. and Spera, F. J. (2001). "Energy-constrained open-system magmatic processes II: Application of energy-constrained assimilation fractional crystallization (EC-AFC) model to magmatic systems." Journal of Petrology 42: 1019-1041.

Bondre, N. R., Dole, G., Phadnis, V. M., Duraiswami, R. and Kale, V. S. (2000). "Inflated pahoehoe lavas from the Sangamner area of the western Deccan Volcanic Province." Current Science 78(8): 1004-1007.

Bondre, N. R., Duraiswami, R. A. and Dole, G. (2004). "A brief comparison of lava flows from the Deccan Volcanic Province and the Columbia-Oregon Plateau Flood Basalts: Implications for models of flood basalt emplacement." Proceedings of the Indian Academy of Science (Earth Planet. Sci.) 113(4): 809-817.

Bondre, N. R., Duraiswami, R. A. and Dole, G. (2004). "Morphology and emplacement of flows from the Deccan Volcanic Province, India." Bulletin of Volcanology 66: 29-45.

Bondre, N. R. and Hart, W. K. (2008). "Morphological and textural diversity of the Steens Basalt lava flows, Southeastern Oregon, USA: implications for emplacement style and nature of eruptive episodes." Bulletin of Volcanology 70(8): 999-1019.

Brandon, A. D. and Goles, G. G. (1988). "A Miocene subcontinental plume in the Pacific Northwest - geochemical evidence." Earth and Planetary Science Letters 88(3-4): 273-283.

Brandon, A. D., Hooper, P. R., Goles, G. G. and Lambert, R. S. J. (1993). "Evaluating crustal contamination in continental basalts: the isotopic composition of the Picture Gorge Basalt of the Columbia River Basalt Group." Contributions to Mineralogy and Petrology 114: 452-464.

Branney, M. J. and Kokelaar, P. (2002). Pyroclastic density currents and the sedimentation of ignimbrites, Geological Society, London, Memoirs, 27.

Brauns, C. M., Hergt, J. M., Woodhead, J. D. and Maas, R. (2000). "Os isotopes and the origin of the Tasmanian dolerites." Journal of Petrology 41(7): 905-918.

Bruce, P. M. and Huppert, H. E. (1989). "Thermal control of basaltic fissure eruptions." Nature 342: 665-667.

Bruno, B. C., Taylor, G. J., Rowland, S. K. and Baloga, S. M. (1994). "Quantifying the effect of rheology on lava-flow margins using fractal geometry." Bulletin of Volcanology 56(3): 193-206.

Bryce, J. G. and DePaolo, D. J. (2004). "Pb isotopic heterogeneity in basaltic phenocrysts." Geochimica et Cosmochimica Acta 68: 4453-4468.

Bunge, H.-P. and Grand, S. (2000). "Mesozoic plate-motion history below the northeast Pacific Ocean from seismic images of the subducted Farallon slab." Nature 405: 337-340.

Burov, E., Guillou-Frottier, L., d'Acremont, E., Le Pourhiet, L. and Cloetingh, S. (2007). "Plume head-lithosphere interactions near intra-continental plate boundaries." Tectonophysics 434(1-4): 15-38.

Burton, K. W., Gannoun, A., Birck, J. L., Allegre, C. J., Schiano, P., Clocchiatti, R. and Alard, O. (2002). "The compatibility of rhenium and osmium in natural olivine and their behaviour during mantle melting and basalt genesis." Earth and Planetary Science Letters 198(1-2): 63-76.

Burton, K. W., Schiano, P., Birck, J. L. and Allegre, C. J. (1999). "Osmium isotope disequilibrium between mantle minerals in a spinel-lherzolite." Earth and Planetary Science Letters 172(3-4): 311-322.

Byerly, G. R. and Swanson, D. (1978). "Invasive Columbia basalt flows along the northwestern margin of the Columbia Plateau, north-central Washington." Geological Society of America, Abstract Programs 10: 98.

Calvari, S. and Pinkerton, H. (1999). "Lava tube morphology on Etna and evidence for lava flow emplacement mechanisms." Journal of Volcanology and Geothermal Research 90: 263-280.

Camp, V. E. and Hanan, B. B. (2008). "A plume-triggered delamination origin for the Columbia River Basalt Group." Geosphere 4: 480-495.

Camp, V. E. and Hooper, P. R. (1981). "Geologic Studies of the Columbia Plateau .1. Late Cenozoic evolution of the southeast part of the Columbia River Basalt Province." Geological Society of America Bulletin 92(9): 659-668.

Camp, V. E. and Ross, M. E. (2004). "Mantle dynamics and genesis of mafic magmatism in the intermontane Pacific Northwest." Journal of Geophysical Research-Solid Earth 109(B8): B08204.

Canon-Tapia, E. and Coe, R. (2002). "Rock magnetic evidence of inflation of a flood basalt lava flow." Bulletin of Volcanology 64: 289-302.

Caprarelli, G. and Reidel, S. P. (2005). "A clinopyroxene-basalt geothermobarometry perspective of Columbia Plateau (NW-USA) Miocene magmatism." Terra Nova 17(3): 265-277.

Carlson, R. W. (1984). "Isotopic constraints on Columbia River flood basalt genesis and the nature of the subcontinental mantle." Geochimica et Cosmochimica Acta 48(11): 2357-2372.

Carlson, R. W. (1991). "Physical and chemical evidence on the cause and source characteristics of flood-basalt volcanism." Australian Journal of Earth Sciences 38(5): 525-544.

Carlson, R. W., Lugmair, G. W. and Macdougall, J. D. (1981). "Columbia River volcanism - the question of mantle heterogeneity or crustal contamination." Geochimica Et Cosmochimica Acta 45(12): 2483-2499.

Carlson, R. W. and Turekian, K. K. (2005). The mantle and core, Elsevier.

Caroff, M., Maury, R. C., Cotten, J. and Clement, J. P. (2000). "Segregation structures in vapor-differentiated basaltic flows." Bulletin of Volcanology 62(3): 171-187.

Carrasco-Nunez, G. (1997). "Lava flow growth inferred from morphometric parameters; a case study of Citlaltepetl Volcano, Mexico." Geological Magazine 134(2): 151-162.

Carrasco-Nunez, G. and Branney, M. J. (2005). "Progressive assembly of a massive layer of ignimbrite with a normal-to-reverse compositional zoning: the Zaragoza ignimbrite of central Mexico." Bulletin of Volcanology 68(1): 3-20.

Carroll, M., Hill, J., Philpotts, A. R. and Anonymous (1995). "Physical and chemical characteristics of the coarse-grained segregation sheets in the Holyoke Basalt, CT " Geological Society of America, Northeastern Section, 30th annual meeting 27(1): 34.

Carter, S. R., Evensen, N. M., Hamilton, P. J. and O'Nions, R. K. (1978). "Nd- and Sr-isotopic evidence for crustal contamination of continental volcanics." Science 202: 743-747.

Cashman, K. (1993). "Relationship between plagioclase crystallization and cooling rate in basaltic melts." Contributions to Mineralogy and Petrology 113(1): 126-142.

Cashman, K., Pinkerton, H. and Stephenson, J. (1998). "Introduction to special section: Long lava flows." Journal of Geophysical Research 103(B11): 27,281 - 27,289.

Cashman, K. V. and Kauahikaua, J. P. (1997). "Re-evaluation of vesicle distributions in basaltic lava flows." Geology 25(5): 419-422.

Charlier, B., Ginibre, C., Morgan, D. J., Nowell, G. M., Pearson, D. G., Davidson, J. and Ottley, C. J. (2006). "Methods for the microsampling and high-precision analysis of strontium and rubidium isotopes at single crystal scale for petrological and geochronological applications." Chemical Geology 232(3-4): 114-133.

Charlier, B. L. A., Bachmann, O., Davidson, J. P., Dungan, M. A. and Morgan, D. J. (2007). "The upper crustal evolution of a large silicic magma body: evidence from crystal-scale Rb Sr isotopic heterogeneities in the Fish Canyon magmatic system, Colorado." Journal of Petrology 48(10): 1875-1894.

Charlier, B. L. A., Wilson, C. J. N. and Davidson, J. (2008). "Rapid open-system assembly of a large silicic magma body: time-resolved evidence from cored plagioclase crystals in the Oruanui eruption deposits, New Zealand." Contributions to Mineralogy and Petrology 156(6): 799-813.

Charlier, B. L. A., Wilson, C. J. N., Lowenstern, J. B., Blake, S., van Calsteren, P. W. and Davidson, J. (2005). "Magma generation at a large, hyperactive silicic volcano (Taupo, New Zealand) revealed by U-Th and U-Pb systematics in zircons." Journal of Petrology 46(1): 3-32.

Chenet, A.-L., Fluteau, F., Courtillot, V., Gerard, M. and Subbarao, K. V. (2008). "Determination of rapid Deccan eruptions across the Cretaceous-Tertiary boundary using paleomagnetic secular variation: Results from a 1200-m-thick section in the Mahabaleshwar escarpment." Journal of Geophysical Research 113(B04101).

Chesley, J., Ruiz, J., Righter, K., Ferrari, L. and Gomez-Tuena, A. (2002). "Source contamination versus assimilation: an example from the Trans-Mexican Volcanic Arc." Earth and Planetary Science Letters 195(3-4): 211-221.

Chesley, J. T. and Ruiz, J. (1998). "Crust-mantle interaction in large igneous provinces: Implications from the Re-Os isotope systematics of the Columbia River flood basalts." Earth and Planetary Science Letters 154(1-4): 1-11.

Chevallier, L. and Woodward, A. (1999). "Morpho-tectonics and mechanism of emplacement of the dolerite sills of the western Karoo, South Africa." South African Journal of Geology 102: 43-54.

Chitwood, L. A. (1994). "Inflated basaltic lava - examples of processes and landforms from central and southeast Oregon." Oregon Geology 56: 11-21.

Christensen, J. N. and Depaolo, D. J. (1993). "Time scales of large volume silicic magma systems: Sr isotopic systematics of phenocrysts and glass from the Bishop Tuff, Long Valley, California." Contributions to Mineralogy and Petrology 113: 100-114.

Cordrey, M. J., Davies, G. F. and Campbell, I. H. (1997). "Genesis of flood basalts from eclogite-bearing mantle plumes." Journal of Geophysical Research 102: 20179-20197.

Cortini, M. and van Calsteren, P. W. (1985). "Lead isotope differences between whole-rock and phenocrysts in recent lavas from southern Italy." Nature 314: 343-345.

Costa, A., Blake, S. and Self, S. (2006). "Segregation processes in vesiculating crystallizing magmas." Journal of Volcanology and Geothermal Research 153(3-4): 287-300.

Costa, F., Chakraborty, S. and Dohmen, R. (2003). "Diffusion coupling between trace and major elements and a model for calculation of magma residence times using plagioclase." Geochimica et Cosmochimica Acta 67(12): 2189-2200.

Costa, F. and Dungan, M. (2005). "Short time scales of magmatic assimilation from diffusion modeling of multiple elements in olivine." Geology 33(10): 837-840.

Creaser, R. A., Papanastassiou, D. A. and Wasserburg, G. J. (1991). "Negative thermal ion mass spectrometry of osmium, rhenium and iridium." Geochimica et Cosmochimica Acta 55(1): 397-401.

Crisp, J. (1984). "Rates of magma emplacement and volcanic output." Journal of Volcanology and Geothermal Research 20: 177-211.

Danyushevsky, L. V. (2001). "The effect of small amounts of H_2O on crystallisation of midocean ridge and backarc magmas." Journal of Volcanology and Geothermal Research 110(3-4): 265-280.

Davidson, J., Charlier, B., Hora, J. M. and Perlroth, R. (2005). "Mineral isochrons and isotopic fingerprinting: Pitfalls and promises." Geology 33(1): 29-32.

Davidson, J., Font, L., Charlier, B. and Tepley, F. I. (2006). "Mineral-scale Sr isotope variation in plutonic rocks - a tool for unravelling the evolution of magma systems." Transactions of the Royal Society of Edinburgh-Earth Sciences 97(4): 357-367.

Davidson, J., Holden, P., Halliday, A. N. and de Silva, S. L. (1990). "Small-scale disequilibrium in a magmatic inclusion and its more silicic host." Journal of Geophysical Research 95: 17661-17675.

Davidson, J., Hora, J. M., Garrison, J. M. and Dungan, M. (2005). "Crustal forensics in arc magmas." Journal of Volcanology and Geothermal Research 140(1-3): 157-170.

Davidson, J., Tepley, F. I., Palacz, Z. and Meffan-Main, S. (2001). "Magma recharge, contamination and residence times revealed by in situ laser ablation isotopic analysis of feldspar in volcanic rocks." Earth and Planetary Science Letters 184: 427-442.

Davidson, J., Tepley III, F. and Knesel, K. M. (1998). "Isotopic fingerprinting may provide insights into evolution of magmatic systems." EOS 79(15): 185, 189 and 193.

Davidson, J. P., Morgan, D. J., Charlier, B. L. A., Harlou, R. and Hora, J. M. (2007). "Microsampling and isotopic analysis of igneous rocks: Implications for the study of magmatic systems." Annual Review of Earth and Planetary Sciences 35(1): 273-311.

Davidson, J. P. and Tepley, F. J. (1997). "Recharge in volcanic systems: Evidence from isotope profiles of phenocrysts." Science 275(5301): 826-829.

Degraff, J. M. and Aydin, A. (1987). "Surface-morphology of columnar joints and its significance to mechanics and direction of joint growth." Geological Society of America Bulletin 99(5): 605-617.

Degraff, J. M., Long, P. E. and Aydin, A. (1989). "Use of joint-growth directions and rock textures to infer thermal regimes during solidification of basaltic lava flows." Journal of Volcanology and Geothermal Research 38: 309-324.

DePaolo, D. J. (1981). "Trace-element and isotopic effects of combined wallrock assimilation and fractional crystallization." Earth and Planetary Science Letters 53(2): 189-202.

DePaolo, D. J. (1983). "Comment on "Columbia River volcanism: the question of mantle heterogeneity or crustal contamination" by R. W. Carlson, G. W. Lugmair and J. D. Macdougall." Geochimica et Cosmochimica Acta 47(4): 841-844.

Devey, C. W. and Cox, K. G. (1987). "Relationships between crustal contamination and crystallisation in continental flood basalt magmas with special reference to the Deccan Traps of the Western Ghats, India." Earth and Planetary Science Letters 84(1): 59-68.

Dodson, A., Kennedy, B. M. and DePaolo, D. J. (1997). "Helium and neon isotopes in the Imnaha Basalt, Columbia River Basalt Group: Evidence for a Yellowstone plume source." Earth and Planetary Science Letters 150(3-4): 443-451.

Dragoni, M. and Santini, S. (2007). "Lava flow in tubes with elliptical cross sections." Journal of Volcanology and Geothermal Research 160: 239-248.

Dragovic, B., Philpotts, A. R. and Anonymous (2002). "Degree of crystal-mush compaction in the Holyoke Basalt, CT as inferred from overgrowths on plagioclase phenocrysts " Geological Society of America, Northeastern Section, 37th annual meeting 34(1): 70.

Dungan, M. A. (2005). "Partial melting at the earth's surface: implications for assimilation rates and mechanisms in subvolcanic intrusions." Journal of Volcanology and Geothermal Research 140(1-3): 193-203.

Duraiswami, R. A., Bondre, N., Dole, G. and Phadnis, V. (2002). "Morphology and structure of flow-lobe tumuli from Pune and Dhule areas, western Deccan Volcanic Province." Journal of the Geological Society of India 60(1): 57-65.

Duraiswami, R. A., Dole, G. and Bondre, N. (2005). "The Songir structure: Inflated lava flow or tube?" Journal of the Geological Society of India 65(3): 357-365.

Durand, S. R. and Sen, G. (2004). "Preeruption history of the Grande Ronde Formation lavas, Columbia River Basalt Group, American Northwest: Evidence from phenocrysts." Geology 32(4): 293-296.

Eckberg, A., Wolff, J. A., Ramos, F. C., Hart, G. L. and Tollstrup, D. L. (2006). "The purity of the COSYMA in the Imnaha basalt: Strontium isotope ratio variations in plagioclase phenocrysts." EOS Transactions 52(Abstract V51D-1703).

Ellam, R. M. (1992). "Lithospheric thickness as a control on basalt geochemistry." Geology 20: 153-156.

Ellam, R. M., Carlson, R. W. and Shirey, S. B. (1992). "Evidence from Re-Os isotopes for plume-lithosphere mixing in Karoo flood basalt genesis." 359(6397): 718-721.

Elliot, D. H. and Fleming, T. H. (2004). "Occurrence and dispersal of magmas in the Jurassic Ferrar Large Igneous Province, Antarctica." Gondwana Research 7: 223-237.

Elliot, D. H. and Fleming, T. H. (2008). "Physical volcanology and geological relationships of the Jurassic Ferrar Large Igneous Province, Antarctica." Journal of Volcanology and Geothermal Research 172(1-2): 20-37.

Ernst, R. E. and Buchan, K. L. (1997). "Giant radiating dyke swarms: Their use in identifying pre-Mesozoic large igneous provinces and mantle plumes." Geophysical Monograph 100: 297-333.

Ertel, W., O'Neill, H. S. C., Sylvester, P. J., Dingwell, D. B. and Spettel, B. (2001). "The solubility of rhenium in silicate melts: Implications for the geochemical properties of rhenium at high temperatures." Geochimica et Cosmochimica Acta 65(13): 2161-2170.

Esser, B. K. and Turekian, K. K. (1993). "The Osmium isotopic composition of the continental-crust." Geochimica Et Cosmochimica Acta 57(13): 3093-3104.

Fagents, S. A. and Greeley, R. (2001). "Factors influencing lava-substrate heat transfer and implications for thermomechanical erosion." Bulletin of Volcanology 62: 519-532.

Fehn, U., Teng, R., Elmore, D. and Kubik, P. W. (1986). "Isotopic composition of Osmium in terrestrial samples determined by accelerator mass spectrometry." Nature 323(6090): 707-710.

Fierstein, J. and Wilson, C. J. N. (2005). "Assembling an ignimbrite: Compositionally defined eruptive packages in the 1912 Valley of Ten Thousand Smokes ignimbrite, Alaska." Geological Society of America Bulletin 117(7-8): 1094-1107.

Font, L., Davidson, J. P., Pearson, D. G., Nowell, G. M., Jerram, D. A. and Ottley, C. J. (2008). "Sr and Pb Isotope Micro-analysis of Plagioclase Crystals from Skye Lavas: an Insight into Open-system Processes in a Flood Basalt Province." Journal of Petrology 49(8): 1449-1471.

Gamble, J. A., Wood, C. P., Price, R. C., Smith, I. E. M., Stewart, R. B. and Waight, T. (1999). "A fifty year perspective of magmatic evolution on Ruapehu Volcano, New Zealand: verification of open system behaviour in an arc volcano." Earth and Planetary Science Letters 170: 301-314.

Gannoun, A., Burton, K. W., Parkinson, I. J., Alard, O., Schiano, P. and Thomas, L. E. (2007). "The scale and origin of the osmium isotope variations in mid-ocean ridge basalts." Earth and Planetary Science Letters 259(3-4): 541-556.

Geist, D., Myers, J. D. and Frost, C. D. (1988). "Megacryst-bulk rock isotopic disequilibrium as an indicator of contamination processes: The Edgecumbe Volcanic Field, SE Alaska." Contributions to Mineralogy and Petrology 99(1): 105-112.

Geist, D. and Richards, M. (1993). "Origin of the Columbia Plateau and Snake River Plain - Deflection of the Yellowstone Plume." Geology 21(9): 789-792.

Gibb, F. G. F. and Henderson, C. M. B. (1996). "The Shiant Isles Main Sill: Structure and mineral fractionation trends." Mineralogical Magazine 60(398): 67-97.

Gibb, F. G. F. and Henderson, C. M. B. (2006). "Chemistry of the Shiant Isles Main Sill, NW Scotland, and wider implications for the petrogenesis of mafic sills." Journal of Petrology 47(1): 191-230.

Giletti, B. J. and Casserly, J. E. D. (1994). "Strontium diffusion kinetics in plagioclase feldspars." Geochimica et Cosmochimica Acta 58(18): 3785-3793.

Ginibre, C., Worner, G. and Kronz, A. (2002). "Minor- and trace-element zoning in plagioclase: implications for magma chamber processes at Parinacota volcano, northern Chile." Contributions to Mineralogy and Petrology 143: 300-315.

Glazner, A. F. and Farmer, G. L. (1992). "Production of isotopic variability in continental basalts by cryptic crustal contamination." Science 255(5040): 72-74.

Godinot, A. (1988). "Pipe vesicles in Hawaiian basaltic lavas - their origin and potential as paleoslope indicators - Comment." Geology 16(1): 90-90.

Goff, F. (1996). "Vesicle cylinders in vapor-differentiated basalt flows." Journal of Volcanology and Geothermal Research 71(2-4): 167-185.

Grattan, J. (2005). "Pollution and paradigms: lessons from Icelandic volcanism for continental flood basalt studies." Lithos 79(3-4): 343-353.

Greeley, R. (1971). "Observations of actively forming lava tubes and associated structures, Hawaii." Modern Geology 2: 207-223.

Greeley, R., Fagents, S. A., Harris, R. S., Kadel, S. D., Williams, D. A. and Guest, J. E. (1998). "Erosion by flowing lava: Field evidence." Journal of Geophysical Research-Solid Earth 103(B11): 27325-27345.

Griselin, R. A., Amdt, N. T. and Baragar, W. A. R. (1997). "Plume-lithosphere interaction and crustal contamination during formation of the Coppermine River basalts, Northwest Territories, Canada." Canadian Journal of Earth Sciences 34: 958-975.

Grove, T. L., Baker, M. B. and Kinzler, R. J. (1984). "Coupled CaAl-NaSi diffusion in plagioclase feldspar: Experiments and applications to cooling rate speedometry." Geochimica et Cosmochimica Acta 48: 2113-2121.

Guilbaud, M.-N. (2006). The origin of basaltic lava flow textures. PhD Thesis, Department of Earth Sciences, The Open University.

Guilbaud, M.-N., Thordarson, T. and Blake, S. (2005). Morphology, surface structures, and emplacement of lavas produced by Laki, A.D. 1783-1784. In: Manga, M., Ventura, G. (eds.) Kinematics and dynamics of lava flows, Geological Society of America Special Paper 396: 81-102.

Hales, T. C., Abt, D. L., Humphreys, E. D. and Roering, J. J. (2005). "A lithospheric instability origin for Columbia River flood basalts and Wallowa Mountains uplift in northeast Oregon." Nature 438(7069): 842-845.

Halliday, W. R. (2002). "What is a lava tube?" Association for Mexican Cave Studies Bulletin 19: 48-56.

Hart, S. R. and Ravizza, G. (1996). "Os partitioning between phases in lherzolite and basalt. In: Basu, A., Hart, S.R. (eds.), Earth processes: Reading the isotopic code." American Geophysical Union Geophysical Monographs 95: 123-134.

Hartley, M. E. and Thordarson, T. (2009 in press). "Melt segregations in a Columbia River Basalt lava flow: A possible mechanism for the formation of highly evolved mafic magmas." Lithos.

Hauri, E. H. and Hart, S. R. (1993). "Re-Os isotope systematics of HIMU and EMII oceanic island basalts from the south Pacific Ocean." Earth and Planetary Science Letters 114(2-3): 353-371.

Hauri, E. H. and Hart, S. R. (1997). "Rhenium abundances and systematics in oceanic basalts." Chemical Geology 139(1-4): 185-205.

Hauri, E. H., Lassiter, J. C. and DePaolo, D. J. (1996). "Osmium isotope systematics of drilled lavas from Mauna Loa, Hawaii." Journal of Geophysical Research-Solid Earth 101(B5): 11793-11806.

Hawkesworth, C. J., Blake, S., Evans, P., Hughes, R., Macdonald, R., Thomas, L. E. and Turner, S. P. (2000). "Time scales of crystal fractionation in magma chambers-Integrating physical, isotopic and geochemical perspectives." Journal of Petrology 41: 991-1006.

Heliker, C., Swanson, D. and Takahahshi, T. J. (2003). "The Pu'u' O'o-Kupaianaha eruption of Kilauea Volcano Hawaii: The first 20 years." US Geological Survey Professional Paper 1676: 206.

Helz, R. T., Heliker, C., Hon, K. and Mangan, M. (2003). "Thermal efficiency of lava tubes in the Pu'u 'O'o-Kupaianaha eruption." US Geol Survey Prof Paper 1676: 105-120.

Helz, R. T., Heliker, C., Mangan, M., Hon, K., Neal, C. A. and Simmons, L. (1991). "Thermal history of the current Kilauean East Rift eruption." Eos 72: 557.

Helz, R. T., Kirschenbaum, H. and Marinenko, J. W. (1989). "Diapiric transfer of melt in Kilauea Iki Lava Lake, Hawaii - a quick, efficient process of igneous differentiation." Geological Society of America Bulletin 101(4): 578-594.

Higgins, M. D. and Chandrasekharam, D. (2007). "Nature of sub-volcanic magma chambers, Deccan province, India: Evidence from quantitative textural analysis of plagioclase megacrysts in the Giant Plagioclase Basalts." Journal of Petrology 48: 885-900.

Hildreth, W. (1983). "The compositionally zoned eruption of 1912 in the Valley of Ten Thousand Smokes, Katmai National Park, Alaska." Journal of Volcanology and Geothermal Research 18: 1-56.

Hildreth, W. and Wilson, C. J. N. (2007). "Compositional zoning of the Bishop Tuff." Journal of Petrology 48(5): 951-999.

Hirt, B., Herr, W. and Hoffmeister, W. (1963). Age determination by the rhenium-osmium method. Radioactive dating. Internat. Atomic Energy Agency, Vienna: 35-44.

Ho, A. M. (1999). "Emplacement of a large lava flow - the Ginkgo flow of the Columbia River Basalt Group." PhD Thesis, University of Oregon, Eugene, 188 pp.

Ho, A. M. and Cashman, K. V. (1997). "Temperature constraints on the Ginkgo flow of the Columbia River Basalt Group." Geology 25(5): 403-406.

Hoefs, J., Faure, G. and Elliot, D. H. (1980). "Correlation of delta^{18}O and initial $^{87}Sr/^{86}Sr$ ratios in Kirkpatrick Basalt at Mt. Falla, Transantarctic Mountains." Contributions to Mineralogy and Petrology 48: 153-169.

Hofmann, A. W. and Hart, S. R. (1978). "An assessment of local and regional equilibrium in the mantle." Earth and Planetary Science Letters 38: 44-62.

Hon, K., Kauahikaua, J., Denlinger, R. and Mackay, K. (1994). "Emplacement and inflation of pahoehoe sheet flows: Observations and measurements of active lava flows on Kilauea Volcano, Hawaii." Geological Society of America Bulletin 106: 351-370.

Hooper, P., Camp, V., Reidel, S. and Ross, M. (2005). "The Columbia River basalts." Geochimica et Cosmochimica Acta 69(10): A138-A138.

Hooper, P. R. (1982). "The Columbia River Basalts." Science 215(4539): 1463-1468.

Hooper, P. R. (1985). "A case of simple magma mixing in the Columbia River Basalt Group: The Wilbur Creek, Lapwai, and Asotin Flows, Saddle Mountains Formation." Contributions to Mineralogy and Petrology 91: 66-73.

Hooper, P. R. (1988). "Crystal Fractionation and Recharge (RFC) in the American Bar Flows of the Imnaha Basalt, Columbia River Basalt Group." J. Petrology 29(5): 1097-1118.

Hooper, P. R. (1997). The Columbia River Flood Basalt Province: Current Status. In: Large Igneous Provinces: Continental, Oceanic and Planetary Flood Volcanism, American Geophysical Union. Geophysical Monograph 100: 1-27.

Hooper, P. R. (2000). "Chemical descrimination of Columbia River basalt flows." Geochemistry Geophysics Geosystems 1(6), 1024, doi:10.1029/2000GC000040.

Hooper, P. R., Binger, G. B. and Lees, K. R. (2002). "Ages of the Steens and Columbia River flood basalts and their relationship to extension-related calc-alkalic volcanism in eastern Oregon." Geological Society of America Bulletin 114(1): 43-50.

Hooper, P. R. and Camp, V. E. (1981). "Deformation of the southeast part of the Columbia Plateau." Geology 9: 323-328.

Hooper, P. R., Camp, V. E., Reidel, S. P. and Ross, M. E. (2007). The origin of the Columbia River flood basalt province: Plume versus nonplume models. In: Foulger, G. R., Jurdy, D M (eds.) Plates, Plumes and Planetary Processes, Geological Society of America Special Paper 430: 635-668.

Hooper, P. R. and Hawkesworth, C. J. (1993). "Isotopic and geochemical constraints on the origin and evolution of the Columbia River Basalt." Journal of Petrology 34(6): 1203-1246.

Hooper, P. R. and Swanson, D. (1990). The Columbia River Basalt Group and associated volcanic rocks of the Blue Mountains province. In: Walker, G W (ed.). Geology of the Blue Mountains region of Oregon, Idaho and Washington, USGS Technical Paper P1437.

Horan, M. F., Walker, R. J., Fedorenko, V. A. and Czamanske, G. K. (1995). "Osmium and neodymium isotopic constraints on the temporal and spatial evolution of Siberian flood basalt sources." Geochimica et Cosmochimica Acta 59(24): 5159-5168.

Houk, R. S. (1980). Inductively coupled plasma as an ion source for the determination of trace elements in solutions by mass spectrometry, Ames Lab.

Hulme, G. (1982). "A review of lava flow processes related to the formation of lunar sinuous rilles." Geophysical Survey 5: 245-279.

Humphreys, M. C. S. (2009). "Chemical evolution of intercumulus liquid, as recorded in plagioclase overgrowth rims from the Skaergaard intrusion." Journal of Petrology 50(1): 127-145.

Huppert, H. E., Sparks, R. S. J., Turner, J. S. and Arndt, N. (1984). "Emplacement and cooling of komatiite lavas." Nature 309: 19-22.

Iddings, J. P. (1886). "The columnar structures in the igneous rock on Orange Mountain, New Jersey." American Journal of Science 31(3): 321-331.

Iezzi, G. and Ventura, G. (2000). "Kinematics of lava flows based on folds analysis." Geophysical Research Letters 27(8): 1227-1231.

James, M. R., Bagdassarov, N., Muller, K. and Pinkerton, H. (2004). "Viscoelastic behaviour of basaltic lavas." Journal of Volcanology and Geothermal Research 132(2-3): 99-113.

Jay, A. (2005). Volcanic architecture of the Deccan Traps, Western Maharashtra, India: an integrated chemostratigraphic and palaeomagnetic study. PhD Thesis, Department of Earth Sciences, The Open University.

Jensen, A. (1980). "Mineralogical and geochemical variations across three basaltic lava flows from the Faeroe Islands." Bulletin of the Geological Survey of Denmark 28: 95-114.

Jerram, D. (2002). Volcanology and facies architecture of flood basalts. Volcanic Rifted Margins. M. A. Menzies, S. L. Klemperer, C. J. Ebinger and J. Baker, Geological Society of America. Special Paper 362: 121-135.

Jerram, D. A., Cheadle, M. C. and Philpotts, A. R. (2003). "Quantifying the building blocks of igneous rocks: are clustered crystal frameworks the foundation?" Journal of Petrology 44: 2033-2051.

Jerram, D. A., Mountney, N. P., Howell, J. A., Long, D. and Stollhofen, H. (2000). "Death of a sand sea: an active aeolian erg systematically buried by the Etendeka flood basalts of NW Namibia." Journal of the Geological Society 157: 513-516.

Johnston, S. T. and Thorkelson, D. J. (2000). "Continental flood basalts: episodic magmatism above long-lived hotspots." Earth and Planetary Science Letters 175(3-4): 247-256.

Jolley, D. W., Widdowson, M. and Self, S. (2008). "Volcanogenic nutrient fluxes and plant ecosystems in large igneous provinces: an example from the Columbia River Basalt Group." Journal of the Geological Society 165(5): 955-966.

Kattenhorn, S. A. and Schaefer, C. J. (2008). "Thermal-mechanical modeling of cooling history and fracture development in inflationary basalt lava flows." Journal of Volcanology and Geothermal Research 170(3-4): 181-197.

Kauahikaua, J., Cashman, K., Mattox, T. N., Hon, K., Heliker, C., Mangan, M. and Thornber, C. R. (1998). "Obervations on basaltic lava streams in tubes from Kilauea volcano, Hawaii." Journal of Geophysical Research 103: 27303-27324.

Keays, R. R. (1995). "The role of komatiitic and picritic magmatism and S-saturation in the formation of ore deposits." Lithos 34: 1-18.

Kent, R. W., Thomson, B. A., Skelhorn, R. R., Kerr, A. C., Norry, M. J. and Walsh, J. N. (1998). "Emplacement of Hebridean Tertiary flood basalts: evidence from an inflated pahoehoe lava flow on Mull, Scotland." Journal of the Geological Society 155: 599-607.

Kerr, R. C. (2001). "Thermal erosion by laminar lava flows." Journal of Geophysical Research-Solid Earth 106(B11): 26453-26465.

Keszthelyi, L. and Denlinger, R. (1996). "The initial cooling of pahoehoe flow lobes." Bulletin of Volcanology 58(1): 5-18.

Keszthelyi, L., Self, S. and Thordarson, T. (2006). "Flood lavas on earth, Io and Mars." Journal of the Geological Society 163: 253-264.

Keszthelyi, L. P. and Pieri, D. C. (1993). "Emplacement of the 75-km-long Carrizozo lava flow-field, south-central New-Mexico." Journal of Volcanology and Geothermal Research 59(1-2): 59-75.

Keszthelyi, L. P. and Self, S. (1998). "Some physical requirements for the emplacement of long basaltic lava flows." Journal of Geophysical Research 103(B11): 27,447-27,464.

Keszthelyi, L. P., Self, S. and Thordarson, T. (1999). Application of recent studies on the emplacement of basaltic lava flows to the Deccan Traps. In: Subbarao, K V (ed.) Deccan Flood Basalts, Memoirs of the Geological Society of India. 10: 485-520.

Keszthelyi, L. P., Thordarson, T., McEwan, A., Haack, H., Guilbaud, M.-N., Self, S. and Rossi, M. J. (2004). "Icelandic analogs to Martian flood lavas." Geochemistry Geophysics Geosystems 5(11): 1-32.

Kilburn, C. R. J. and Lopez, R. M. C. (1988). "The growth of lava flow fields on Mt Etna, Sicily." Journal of Geophysical Research 93: 14759-14772.

King, S. D. and Anderson, D. L. (1995). "An alternative mechanism of flood basalt formation." Earth and Planetary Science Letters 136: 269-279.

Kisakurek, B., Widdowson, M. and James, R. H. (2004). "Behaviour of Li isotopes during continental weathering: the Bidar laterite profile, India." Chemical Geology 212(1-2): 27-44.

Knesel, K. M. and Davidson, J. (1996). "Isotopic disequilibrium during melting of granit and implications for crustal contamination of magmas." Geology 24(3): 243-246.

Knesel, K. M. and Davidson, J. P. (1999). "Sr isotope systematics during melt generation by intrusion of basalt into continental crust." Contributions to Mineralogy and Petrology 136(3): 285-295.

Knesel, K. M., Davidson, J. P. and Duffield, W. A. (1999). "Evolution of silicic magma through assimilation and subsequent recharge: evidence from Sr isotopies in sanidine phenocrysts, Taylor Creek Rhyolite, NM." Journal of Petrology 40(5): 773-786.

Krahenbuhl, U., Geissbuhler, M., Buhler, F., Eberhardt, P. and Finnegan, D. L. (1992). "Osmium isotopes in the aerosols of the mantle volcano Mauna Loa." Earth and Planetary Science Letters 110(1-4): 95-98.

Krienitz, M. S., Haase, K. M., Mezger, K., Eckardt, V. and Shaikh-Mashail, M. A. (2006). "Magma genesis and crustal contamination of continental intraplate lavas in northwestern Syria." Contributions to Mineralogy and Petrology 151(6): 698-716.

Landon, R. D. and Long, P. E. (1989). Detailed stratigraphy of the N2 Grande Ronde Basalt, Columbia River Basalt Group, in the central Columbia Plateau. In: Reidel, S.P., Hooper, P.R. (eds.) Volcanism and Tectonism in the Columbia River Flood-Basalt Province, Geological Society of America. Special Paper 239: 55-66.

Larsen, J. F. (2005). "Experimental study of plagioclase rim growth around anorthite seed crystals in rhyodacitic melt." American Mineralogist 90(2-3): 417-427.

Larsen, L. M., Waagstein, R., Pedersen, A. K. and Storey, M. (1999). "Trans-Atlantic correlation of the Palaeogene volcanic successions in the Faeroe Islands and East Greenland." Journal of the Geological Society 156(6): 1081-1095.

Lassiter, J. C. (2003). "Rhenium volatility in subaerial lavas: constraints from subaerial and submarine portions of the HSDP-2 Mauna Kea drillcore." Earth and Planetary Science Letters 214(1-2): 311-325.

Lassiter, J. C., DePaolo, D. J. and Mahoney, J. J. (1995). "Geochemistry of the Wrangellia Flood Basalt Province: Implications for the role of continental and oceanic lithosphere in flood basalt genesis." Journal of Petrology 36(4): 983-1009.

Lassiter, J. C. and Hauri, E. H. (1998). "Osmium-isotope variations in Hawaiian lavas: evidence for recycled oceanic lithosphere in the Hawaiian plume." Earth and Planetary Science Letters 164(3-4): 483-496.

Latypov, R. M. (2003). "The origin of basic-ultrabasic sills with S-, D-, and I-shaped compositional profiles by in situ crystallization of a single input of phenocryst-poor parental magma." Journal of Petrology 44(9): 1619-1656.

Leopold, E. B. (1969). Late Cenozoic palynology. In: Tschudy, R. H., Scott, R. A. (eds.) Aspects of Palynology, John Wiley & Sons, Inc.: 510.

Lightfoot, P. C. and Keays, R. R. (2005). "Siderophile and chalcophile metal variations in flood basalts from the Siberian Trap, Noril'sk Region: Implications for the origin of the Ni-Cu-PGE sulfide ores." Economic Geology 100: 439-462.

Lindner, M., Leich, D. S., Russ, G. P., Bazan, J. M. and Borg, R. J. (1989). "Direct determination of the half-life of Re-187." Geochimica et Cosmochimica Acta 53(7): 1597-1606.

Lindstrom, M. M. and Haskin, L. A. (1981). "Compositional inhomogeneities in a single Icelandic tholeiite flow." Geochimica et Cosmochimica Acta 45(1): 15-31.

Lisitsyna, N. A. (1968). "Geochemistry of weathering zones of basic rocks." Geochemistry International 5: 210-244.

Lockwood, J. P. and Williams, I. S. (1978). "Lava trees and tree moulds as indicators of lava flow direction." Geological Magazine 115: 69-74.

Long, P. and Duncan, A. R. (1983). "$^{40}Ar/^{39}Ar$ ages of Columbia River Basalt from deep boreholes in south-central Washington." Eos American Geophysical Union Transactions 62: 61.

Long, P. E. and Wood, B. J. (1986). "Structures, textures, and cooling histories of Columbia River basalt flows." Geological Society of America Bulletin 97: 1144-1155.

Lore, J., Gao, H. J. and Aydin, A. (2000). "Viscoelastic thermal stress in cooling basalt flows." Journal of Geophysical Research-Solid Earth 105(B10): 23695-23709.

Luck, J.-M. and Allegre, C. (1992). "Osmium isotopes in ophiolites." Earth and Planetary Science Letters 107: 406-415.

Luck, J. M. and Allegre, C. J. (1982). "The study of molybdenites through the ^{187}Re-^{187}Os chronometer." Earth and Planetary Science Letters 61(2): 291-296.

Luck, J. M., Birck, J. L. and Allegre, C. J. (1980). "^{187}Re-^{187}Os systematics in meteorites; early chronology of the solar system and age of the Galaxy." Nature 283(5744): 256-259.

Luck, J. M. and Turekian, K. K. (1983). "$^{187}Os/^{186}Os$ in Manganese Nodules and the Cretaceous-Tertiary Boundary." Science 222(4624): 613-615.

Lui, L., Spasojevic, S. and Gurnis, M. (2008). "Reconstructing Farallon Plate subduction beneath North America back to the Late Cretaceous." Science 5309: 934-938.

Lustrino, M. (2005). "How the delamination and detachment of lower crust can influence basaltic magmatism." Earth-Science Reviews 72(1-2): 21-38.

Lyle, P. (2000). "The eruption environment of multi-tiered columnar basalt lava flows." Journal of the Geological Society 157: 715-722.

MacKenzie, J. M. and Canil, D. (2006). "Experimental constraints on the mobility of Rhenium in silicate liquids." Geochimica Et Cosmochimica Acta 70(20): 5236-5245.

Mackiewicz, M. C. (1978). "Lava trees." Earth Science 31: 5-8.

Mackin, J. H. (1961). A stratigraphic section in the Yakima Basalt and the Ellensburg Formation in south-central Washington, Washington Division of Mines and Geology Report of Investigations 19: 45.

Maclennan, J., McKenzie, D. and Hilton, F. (2003). "Geochemical variability in a single flow from northern Iceland." Journal of Geophysical Research 108(B1): 1-20.

Mahoney, J. J., MacDougall, J. D., Lugmair, G. W., Murali, A. V., Sankar, D. M. and Gopalan, K. (1982). "Origin of the Deccan Trap flows of Mahabaleschwar inferred from Nd and Sr isotopic chemical evidence." Earth and Planetary Science Letters 60: 47-60.

Mahoney, J. J., Sheth, H. C., Chandrasekharam, D. and Peng, Z. X. (2000). "Geochemistry of flood basalts of the Toranmal section, northern Deccan Traps, India: implications for regional Deccan stratigraphy." Journal of Petrology 41(7): 1099-1120.

Manea, V. C., Manea, M., Leeman, W. P. and Schutt, D. L. (2009). "The influence of plume head-lithosphere interaction on magmatism associated with the Yellowstone hotspot track." Journal of Volcanology and Geothermal Research In Press, Corrected Proof.

Mangan, M. T., Wright, T. L., Swanson, D. A. and Byerly, G. R. (1986). "Regional Correlation of Grande-Ronde Basalt Flows, Columbia River Basalt Group, Washington, Oregon, and Idaho." Geological Society of America Bulletin 97(11): 1300-1318.

Marcantonio, F., Zindler, A., Elliott, T. and Staudigel, H. (1995). "Os isotope systematics of La Palma, Canary Islands: Evidence for recycled crust in the mantle source of HIMU ocean islands." Earth and Planetary Science Letters 133(3-4): 397-410.

Marsh, B. D. (2004). "A magmatic mush column Rosetta Stone: the McMurdo Dry Valleys of Antarctica." EOS Transactions 85: 497-502.

Martin, B. (1989). "The Roza Member, Columbia River Basalt Group; Chemical stratigraphy and flow distribution." Geological Society of America Special Paper 239: 85-104.

Martin, B. (1991). Geochemical variations within the Roza Member, Wanapum basalt, Columbia River basalt group: Implications for the magmatic processes affecting continental flood basalts. PhD Thesis, Department of Geology and Geography, University of Massachusetts: 513.

Martin, C. E. (1991). "Osmium isotopic characteristics of mantle-derived rocks." Geochimica et Cosmochimica Acta 55(5): 1421-1434.

Martin, C. E., Carlson, R. W., Shirey, S. B., Frey, F. A. and Chen, C. Y. (1994). "Os-isotopic variation in basalts from Haleakala Volcano, Maui, Hawaii - a record of magmatic processes in oceanic mantle and crust." Earth and Planetary Science Letters 128(3-4): 287-301.

Martin, C. E., Esser, B. K. and Turekian, K. K. (1991). "Re-Os isotopic constraints on the formation of mantle and crustal reservoirs." Australian Journal of Earth Sciences 38(5): 569-576.

Martini, F., Hobbs, R. W., Bean, C. J. and Single, R. (2005). "A complex 3D volume for sub-basalt imaging." First Break 23: 41-51.

McBride, J. S., Lambert, D. D., Nicholls, I. A. and Price, R. C. (2001). "Osmium isotopic evidence for crust-mantle interaction in the genesis of continental intraplate basalts from the Newer Volcanics Province, Southeastern Australia." Journal of Petrology 42(6): 1197-1218.

McDaniel, D. K., Walker, R. J., Hemming, S. R., Horan, M. F., Becker, H. and Grauch, R. I. (2004). "Sources of osmium to the modern oceans: New evidence from the Pt-190-(OS)-O-186 system." Geochimica et Cosmochimica Acta 68(6): 1243-1252.

McDougall, I. (1976). "Geochemistry and origin of basalt of Columbia River Group, Oregon and Washington." Geological Society of America Bulletin 87(5): 777-792.

McGee, J. J., Tilling, R. I. and Duffield, W. A. (1987). "Petrologic characteristics of the 1982 and pre-1982 eruptive products of El Chichon volcano, Chiapas, Mexico." Geofisica Internacional 26(1): 85-108.

McKee, E. H., Swanson, D. A. and Wright, T. I. (1977). "Duration and volume of Columbia River Basalt volcanism, Washington, Oregon, and Idaho." Geological Society of America Abstracts with Programmes 9: 463-464.

McMillan, K., Cross, R. W. and Long, P. E. (1987). "2-Stage vesiculation in the Cohassett flow of the Grande-Ronde Basalt, south-central Washington." Geology 15(9): 809-812.

McMillan, K., Long, P. E. and Cross, R. W. (1989). "Vesiculation in Columbia River Basalts." Geological Society of America Special Paper 239: 157-167.

Meisel, T., Walker, R. J. and Morgan, J. W. (1996). "The osmium isotopic composition of the Earth's primitive upper mantle." Nature 383(6600): 517-520.

Merle, O. (1998). "Internal strain within lava flows from analogue modelling." Journal of Volcanology and Geothermal Research 81(3-4): 189-206.

Misra, K. S., Viswanathan, S., Dole, G., Bondre, N., Duraiswami, R. A. and Kale, V. S. (2002). "Arterial system of lava tubes and channels within Deccan volcanics of western India." Journal of the Geological Society of India 60(5): 595-600.

Mohl, G. and Thiessen, R. (1995). Gravity studies of an island arc - continent suture in west central Idaho and adjacent Washington. In: Vallier, T.L., Brooks, H.C. (eds.) The geology of the Blue Mountains Region of Oregon, Idaho and Washington: Petrology and tectonic evolution of Pre-Tertiary rocks of the Blue Mountains Region, U.S. Geological Survey Professional Paper. 1438: 497-516.

Molzahn, M., Reisberg, L. and Worner, G. (1996). "Os, Sr, Nd, Pb, O isotope and trace element data from the Ferrar flood basalts, antarctica: evidence for an enriched subcontinental lithospheric source." Earth and Planetary Science Letters 144(3-4): 529-545.

Moorbath, S. and Thompson, R. N. (1980). "Strontium isotope geochemistry and petrogenesis of the early Tertiary lava pile of the Isle of Skye, Scotland, and other basic rocks of the British Tertiary Province: An example of magma-crust interation." Journal of Petrology 21: 295-321.

Morgan, D. J. and Baedecker, P. A. (1983). "Elemental composition of sulphide particles from an ultramafic xenolith and the siderophile content of the upper mantle." Lunar Planetary Science Conference XIV: 513-514.

Morgan, D. J. and Blake, S. (2006). "Magmatic residence times of zoned phenocrysts: introduction and application of the binary element diffusion modelling (BEDM) technique." Contributions to Mineralogy and Petrology 151(1): 58-70.

Morgan, D. J., Blake, S., Rogers, N. W., De Vivo, B., Rolandi, G. and Davidson, J. P. (2006). "Magma chamber recharge at Vesuvius in the century prior to the eruption of AD 79." Geology 34(10): 845-848.

Morgan, D. J., Blake, S., Rogers, N. W., DeVivo, B., Rolandi, G., Macdonald, R. and Hawkesworth, C. J. (2004). "Time scales of crystal residence and magma chamber volume from modelling of diffusion profiles in phenocrysts: Vesuvius 1944." Earth and Planetary Science Letters 222(3-4): 933-946.

Morgan, D. J., Jerram, D., Chertkoff, D. G., Davidson, J., Pearson, D. G., Kronz, A. and Nowell, G. M. (2007). "Combining CSD and isotopic microanalysis: Magma supply and mixing processes at Stromboli volcano, Aeolian Islands, Italy." Earth and Planetary Science Letters 260: 419-431.

Morgan, J. W. (1986). "Ultramafic xenoliths: clues to Earth's late accretionary history." Journal of Geophysical Research 91: 12375-12387.

Morgan, J. W. (1997). Rhenium. Encyclopaedia of Geochemistry. R. Fairbridge. New York, Chapman-Hall.

Morrison, M. A., Thompson, R. N. and Dickin, A. P. (1985). "Geochemical evidence for complex magmatic plumbing during development of a continental volcanic centre." Geology 13: 581-584.

Murphy, M. T., Long, P. E. and Self, S. (1991). "Duration of flood basalt eruptions: Evidence from the Pomona flow, Columbia River Basalt." Eos 72: 567.

Nier, A. O. (1937). "The isotopic constitution of osmium." Physical Review 52(8): 0885-0885.

Paslick, C. R., Halliday, A. N., Lange, R. A., James, D. and Dawson, J. B. (1996). "Indirect crustal contamination: Evidence from isotopic and chemical disequilibria in minerals from alkali basalts and nephelinites from northern Tanzania." Contributions to Mineralogy and Petrology 125: 277-292.

Passey, S. R. and Bell, B. R. (2007). "Morphologies and emplacement mechanisms of the lava flows of the faroe islands basalt group, faroe islands, NE atlantic ocean." Bulletin of Volcanology 70(2): 139-156.

Pearce, T. H. and Kolisnik, A. M. (1990). "Observations of plagioclase zoning using interference imaging." Earth Science Reviews 29: 9-26.

Peate, D., Barker, A. K., Riishuus, M. S. and Andreasen, R. (2008). "Temporal variations in crustal assimilation of magma suites in the East Greenland flood basalt province: Tracking the evolution of magmatic plumbing systems." Lithos 102: 179-197.

Peng, Z. X., Mahoney, J., Hooper, P., Harris, C. and Beane, J. (1994). "A role for lower continental-crust in flood-basalt genesis - isotopic and incompatible element study of the lower 6 Formations of the Western Deccan Traps." Geochimica Et Cosmochimica Acta 58(1): 267-288.

Perini, G., Tepley, F. I., Davidson, J. and Conticelli, S. (2003). "The origin of K-feldspar megacrysts hosted in alkaline potassic rocks from central Italy: a track for low-pressure processes in mafic magmas." Lithos 66: 223-240.

Peterson, D. W. and Swanson, D. (1974). "Observed formation of lava tubes during 1970-1971 at Kilauea volcano, Hawaii." Studies in Speleology 2(6): 209-222.

Peucker-Ehrenbrink, B. and Jahn, B. M. (2001). "Rhenium-osmium isotope systematics and platinum group element concentrations: Loess and the upper continental crust." Geochemistry Geophysics Geosystems 2.

Philpotts, A. R. (1998). "Nature of a flood-basalt-magma reservoir based on the compositional variation in a single flood-basalt flow and its feeder dike in the Mesozoic Hartford Basin, Connecticut." Contributions to Mineralogy and Petrology 133(1-2): 69-82.

Philpotts, A. R. and Asher, P. M. (1993). "Wallrock melting and reaction effects along the Higganum diabase dike in Connecticut: contamination of a continental flood basalt feeder." Journal of Petrology 34(5): 1029-1058.

Philpotts, A. R., Brustman, C. M., Shi, J. Y., Carlson, W. D. and Denison, C. (1999). "Plagioclase-chain networks in slowly cooled basaltic magma." American Mineralogist 84(11-12): 1819-1829.

Philpotts, A. R. and Burkett, D. H. (1987). "Structures, textures, and cooling histories of Columbia River basalt flows." Geological Society of America Bulletin 99(6): 886-887.

Philpotts, A. R. and Lewis, C. L. (1987). "Pipe vesicles - an alternate model for their origin." Geology 15(10): 971-974.

Philpotts, A. R. and Philpotts, D. E. (2005). "Crystal-mush compaction in the Cohassett flood-basalt flow, Hanford, Washington." Journal of Volcanology and Geothermal Research 145(3-4): 192-206.

Philpotts, A. R. and Philpotts, D. E. (2006). "Reply to comment on : Crystal-mush compaction in the Cohassett flood-basalt flow, Hanford, Washington." Journal of Volcanology and Geothermal Research 152(1-2): 194-195.

Philpotts, A. R., Shi, J. and Brustman, C. (1998). "Role of plagioclase crystal chains in the differentiation of partly crystallized basaltic magmas." Nature 395(6700): 343-346.

Piccirillo, E. M., Bellieni, G., Cavvazini, G., Comin-Chiaramonti, P., Petrini, R., Melfi, A. J., Pinese, J. P. P., Zantadeschi, P. and De Min, A. (1990). "Lower Cretaceous tholeiitic dyke swarms from the Ponta Grossa Arch (southeast Brazil): petrology, Sr-Nd isotopes and genetic relationships with the Parana flood volcanics." Chemical Geology 89(1-2): 19-48.

Potts, P. J., Webb, P. C. and Watson, J. S. (1984). "Energy-dispersive x-ray-fluorescence analysis of silicate rocks for major and trace-elements." X-Ray Spectrometry 13(1): 2-15.

Powell, R. (1984). "Inversion of the assimilation and fractional crystallization (AFC) equations - characterization of contaminants from isotope and trace-element relationships in volcanic suites." Journal of the Geological Society 141: 447-452.

Price, R. C., Gamble, J. A., Smith, I. E. M., Stewart, R. B., Eggins, S. M. and Wright, I. C. (2005). "An integrated model for the temporal evolution of andesites and rhyolites and crustal development in New Zealand's North Island." Journal of Volcanology and Geothermal Research 140: 1-24.

Ramos, F. C. and Tepley, F. I. (2008). "Inter- and intracrystalline isotopic disequilibria: techniques and applications." Reviews in mineralogy and geochemistry 69: 403-443.

Ramos, F. C., Wolff, J. A. and Tollstrup, D. L. (2004). "Measuring $^{87}Sr/^{86}Sr$ variations in minerals and groundmass from basalts using LA-MC-ICPMS." Chemical Geology 211: 135-158.

Ramos, F. C., Wolff, J. A. and Tollstrup, D. L. (2005). "Sr isotope disequilibrium in Columbia River flood basalts: Evidence for rapid shallow-level open-system processes." Geology 33(6): 457-460.

Ray, R., Sheth, H. and Mallik, J. (2007). "Structure and emplacement of the Nandurbar-Dhule mafic dyke swarm, Deccan Traps, and the tectonomagmatic evolution of flood basalts." Bulletin of Volcanology 69(5): 537-551.

Reichow, M. K., Saunders, A. D., White, R. V., Al'Mukhamedov, A. I. and Medvedev, A. Y. (2005). "Geochemistry and petrogenesis of basalts from the West Siberian Basin: an extension of the Permo-Triassic Siberian Traps, Russia." Lithos 79(3-4): 425-452.

Reidel, S. P. (1983). "Stratigraphy and petrogenesis of the Grande Ronde Basalt from the deep canyon country of Washington, Oregon and Idaho." Geological Society of America Bulletin 94: 519-542.

Reidel, S. P. (1998). "Emplacement of Columbia River flood basalt." Journal of Geophysical Research 103(B11): 27,393-27,410.

Reidel, S. P. (2005). "A lava flow without a source: the Cohassett flow and its compositional components, Sentinel Bluffs Member, Columbia River Basalt Group." The Journal of Geology 113: 1-21.

Reidel, S. P. and Fecht, K. R. (1987). "The Huntzinger flow: evidence of surface mixing of the Columbia River Basalt and its petrogenetic implications." Geological Society of America Bulletin 98: 664-677.

Reidel, S. P., Fecht, K. R., Hagood, M. C. and Tolan, T. L. (1989). "The geologic evolution of the central Columbia Plateau." Geological Society of America Special Paper 239: 247-264.

Reidel, S. P. and Hooper, P. R., Eds. (1989). Volcanism and tectonism in the Columbia River Flood-Basalt Province. Geological Society of America Special Paper 239.

Reidel, S. P. and Tolan, T. L. (1992). "Eruption and emplacement of flood basalt: An example from the large-volume Teepee Butte Member, Columbia River Basalt Group." Geological Society of America Bulletin 104: 1650-1671.

Reidel, S. P. and Tolan, T. L. (1994). "Late Cenozoic structure and correlation to seismicity along the Olympic-Wallowa lineament, Northwestern United-States - discussion." Geological Society of America Bulletin 106(12): 1634-1638.

Reiners, P. W. (2002). "Temporal-compositional trends in intraplate basalt eruptions: Implications for mantle heterogeneity and melting processes." Geochemistry Geophysics Geosystems 3.

Reisberg, L. and Lorand, J. P. (1995). "Longevity of the sub-continental mantle lithosphere from osmium isotope systematics in orogenic lherzolite massifs." Nature 376: 159-162.

Reisberg, L., Zindler, A., Marcantonio, F., White, W., Wyman, D. and Weaver, B. (1993). "Os isotope systematics in ocean island basalts." Earth and Planetary Science Letters 120(3-4): 149-167.

Rhodes, J. M. (1983). "Homogeneity of lava flows: chemical data for historic Mauna Loan eruptions." Journal of Geophysical Research 88A: 869-879.

Richards, M. A., Duncan, R. A. and Courtillot, V. E. (1989). "Flood basalts and hot-spot tracks: plume heads and tails." Science 246(4926): 103-107.

Richardson, S. H. (1979). "Chemical variation induced by flow differentiation in an extensive Karroo dolerite sheet, southern Namibia." Geochimica et Cosmochimica Acta 43(9): 1433-1441.

Roberts, D. G., Backman, J., Morton, A. C., Murray, J. W. and Keene, J. B. (1984). "Evolution of volcanic rifted margins: synthesis of Leg 81 results on the west margin of Rockall Plateau." Initial reports of the Deep Sea Drilling Project 81: 883-911.

Rogan, W., Blake, S. and Smith, I. (1996). "In situ chemical fractionation in thin basaltic lava flows: Examples from the Auckland volcanic field, New Zealand, and a general physical model." Journal of Volcanology and Geothermal Research 74(1-2): 89-99.

Ross, M. E. (1983). "Chemical and mineralogic variations within four dikes of the Columbia River Basalt Group, southeastern Columbia Plateau." Geological Society of America Bulletin 94(9): 1117-1126.

Rossi, M. J. and Gudmundsson, A. (1996). "The morphology and formation of flow-lobe tumuli on Icelandic shield volcanoes." Journal of Volcanology and Geothermal Research 72: 291-308.

Rowland, S. K. and Walker, G. P. L. (1990). "Pāhoehoe and aa in Hawaii - volumetric flow-rate controls the lava structure." Bulletin of Volcanology 52(8): 615-628.

Roy-Barman, M. and Allegre, C. J. (1995). "$^{187}Os/^{186}Os$ in oceanic island basalts: tracing oceanic crust recycling in the mantle." Earth and Planetary Science Letters 129(1-4): 145-161.

Roy-Barman, M., Wasserburg, G. J., Papanastassiou, D. A. and Chaussidon, M. (1998). "Osmium isotopic compositions and Re-Os concentrations in sulfide globules from basaltic glasses." Earth and Planetary Science Letters 154(1-4): 331-347.

Rubin, K. H., Smith, M. C., Bergmanis, E. C., Perfit, M. R., Sinton, J. M. and Batiza, R. (2001). "Geochemical heterogeneity within mid-ocean ridge lava flows: insights into eruption, emplacement and global variations in magma generation." Earth and Planetary Science Letters 188(3-4): 349-367.

Ryan, M. P. and Sammis, C. G. (1978). "Cyclic fracture mechanisms in cooling basalt." Geological Society of America Bulletin 89(9): 1295-1308.

Saal, A. E., Rudnick, R. L., Ravizza, G. E. and Hart, S. R. (1998). "Re-Os isotope evidence for the composition, formation and age of the lower continental crust." Nature 393(6680): 58-61.

Saemundsson, K. (1970). "Interglacial lava flows in the lowlands of southern Iceland and the problem of two-tiered columnar jointing." Jokull 20: 62-77.

Salters, V. J. M. and Stracke, A. (2004). "Composition of the depleted mantle." Geochemistry Geophysics Geosystems 5(5).

Schaefer, B. F., Parkinson, I. J. and Hawkesworth, C. J. (2000). "Deep mantle plume osmium isotope signature from West Greenland Tertiary picrites." Earth and Planetary Science Letters 175(1-2): 105-118.

Schenato, F., Formoso, M. L. L., Dudoignon, P., Meunier, A., Proust, D. and Mas, A. (2003). "Alteration processes of a thick basaltic lava flow of the Parana Basin

(Brazil): petrographic and mineralogical studies." Journal of South American Earth Sciences 16(5): 423-444.

Schiano, P., Birck, J. L. and Allegre, C. J. (1997). "Osmium-strontium-neodymium-lead isotopic covariations in mid-ocean ridge basalt glasses and the heterogeneity of the upper mantle." Earth and Planetary Science Letters 150(3-4): 363-379.

Schiano, P., Burton, K. W., Dupre, B., Birck, J. L., Guille, G. and Allegre, C. J. (2001). "Correlated Os-Pb-Nd-Sr isotopes in the Austral-Cook chain basalts: the nature of mantle components in plume sources." Earth and Planetary Science Letters 186(3-4): 527-537.

Seims, B. A., Bush, J. G. and Crosby, J. W. (1974). "TiO_2 and geophysical logging criteria for Yakima Basalt Correlation, Columbia Plateau." Geological Society of America Bulletin 85: 1061-1068.

Selby, D., Creaser, R. A., Stein, H. J., Markey, R. J. and Hannah, J. L. (2007). "Assessment of the ^{187}Re decay constant by cross calibration of Re-Os molybdenite and U-Pb zircon chronometers in magmatic ore systems." Geochimica et Cosmochimica Acta 71(8): 1999-2013.

Self, S., Keszthelyi, L. P. and Thordarson, T. (1998). "The importance of pāhoehoe." Annual Review of Earth and Planetary Sciences 26: 81-110.

Self, S., Keszthelyi, L. P. and Thordarson, T. (2000). "Discussion of: "Pulsed inflation of pahoehoe lava flows: implications for flood basalt emplacement", by S.W. Anderson, E.R. Stofan, E.R. Smrekar, J.E. Guest and B. Wood [Earth Planet. Sci. Lett. 168 (1999) 7-18]." Earth and Planetary Science Letters 179: 421-423.

Self, S., Thordarson, T. and Keszthelyi, L. P. (1997). Emplacement of continental flood basalt lava flows. In: Large Igneous Provinces: Continental, Oceanic and Planetary Flood Volcanism, American Geophysical Union: 381-410.

Self, S., Thordarson, T., Keszthelyi, L. P., Walker, G. P. L., Hon, K., Murphy, M. T., Long, P. and Finnemore, S. (1996). "A new model for the emplacement of Columbia River basalts as large, inflated pahoehoe lava flow fields." Geophysical Research Letters 23(19): 2689-2696.

Self, S., Thordarson, T. and Widdowson, M. (2005). "Gas Fluxes from Flood Basalt Eruptions." Elements 1: 283-287.

Self, S., Widdowson, M., Thordarson, T. and Jay, A. E. (2006). "Volatile fluxes during flood basalt eruptions and potential effects on the global environment: A Deccan perspective." Earth and Planetary Science Letters 248(1-2): 518-532.

Shaw, H. R. and Swanson, D. A. (1970). "Eruption and flow rates of flood basalts." Proceedings of the Second Columbia River Basalt Symposium, Cheney, Washington: 271-299.

Sheldon, N. D. (2003). "Pedogenesis and geochemical alteration of the Picture Gorge subgroup, Columbia River basalt, Oregon." Geological Society of America Bulletin 115(11): 1377-1387.

Shen, J. J., Papanastassiou, D. A. and Wasserburg, G. J. (1996). "Precise Re-Os determinations and systematics of iron meteorites." Geochimica et Cosmochimica Acta 60(15): 2887-2900.

Sheth, H. C., Mahoney, J. J. and Chandrasekharam, D. (2004). "Geochemical stratigraphy of Deccan flood basalts of the Bijasan Ghat section, Satpura Range, India." Journal of Asian Earth Sciences 23(1): 127-139.

Shirey, S. B., klewin, K. W., Berg, J. H. and Carlson, R. W. (1994). "Temporal changes in the sources of flood basalts: Isotopic and trace element evidence from the 1100 Ma old Keweenawan Mamainse Point Formation, Ontario, Canada." Geochimica et Cosmochimica Acta 58(20): 4475-4490.

Shirey, S. B. and Walker, R. J. (1998). "The Re-Os isotope system in cosmochemistry and high-temperature geochemistry." Annual Review of Earth and Planetary Sciences 26: 423-500.

Singer, B. S., Dungan, M. and Layne, G. D. (1995). "Textures and Sr, Ba, Mg, Fe, K and Ti compositional profiles in volcanic plagioclase: clues to the dynamics of calc-alkaline magma chambers." American Mineralogist 80: 776-798.

Slater, L., McKenzie, D., Gronvold, K. and Shimizu, N. (2001). "Melt generation and movement beneath Theistareykir, NE Iceland." Journal of Petrology 42(2): 321-354.

Smith, A. D. (1992). "Back-arc convection model for Columbia River Basalt genesis." Tectonophysics 207(3-4): 269-285.

Smith, A. D. (2003). "Critical evaluation of Re-Os and Pt-Os isotopic evidence on the origin of intraplate volcanism." Journal of Geodynamics 36(4): 469-484.

Smith, V. C., Blundy, J. D. and Arce, J. L. (2009). "A temporal record of magma accumulation and evolution beneath Nevado de Toluca, Mexico, preserved in plagioclase phenocrysts." Journal of Petrology 50(3): 405-426.

Smoliar, M. I., Walker, R. J. and Morgan, J. W. (1996). "Re-Os ages of group IIA, IIIA, IVA, and IVB iron meteorites." Science 271(5252): 1099-1102.

Snavely, P. D., Macleod, N. S. and Wagner, H. C. (1973). "Miocene tholeiitic basalts of coastal Oregon and Washington and their relations to coeval basalts of Columbia Plateau." Geological Society of America Bulletin 84(2): 387-424.

Snow, J. E. and Reisberg, L. (1995). "Os isotopic systematics of the MORB mantle: results from altered abyssal peridotites." Earth and Planetary Science Letters 133(3-4): 411-421.

Solana, M. C., Kilburn, C. R. J., Badiola, E. R. and Aparicio, A. (2004). "Fast emplacement of extensive pāhoehoe flow-fields: the case of the 1736 flows from Montana de las Nueces, Lanzarote." Journal of Volcanology and Geothermal Research 132(2-3): 189-207.

Spera, F. J. and Bohrson, W. A. (2001). "Energy-constrained open-system magmatic processes I: general model and energy-constrained assimilation and fractional crystallization (EC-AFC) formulation." Journal of Petrology 42: 999-1018.

Spiegelman, M. and Kelemen, P. B. (2003). "Extreme chemical variability as a consequence of channelized melt transport." Geochemistry Geophysics Geosystems 4.

Stephenson, P. J., Burch-Johnston, A. T., Stanton, D. and Whitehead, P. W. (1998). "Three long lava flows in north Queensland." Journal of Geophysical Research-Solid Earth 103(B11): 27359-27370.

Stephenson, P. J., Zhang, M. and Spry, M. (2000). "Fractionation modelling of segregations in the Toomba Basalt, north Queensland." Australian Journal of Earth Sciences 47(2): 291-300.

Sumner, J. S. and Branney, M. J. (2002). "The emplacement history of a remarkable heterogenous, compositionally zoned, rheomorphic and locally lava-like

rheomorphic ignimbrite: 'TL' on Gran Canaria." Journal of Volcanology and Geothermal Research 115: 109-138.

Sun, S. S. and McDonough, W. F. (1989). "Chemical and isotopic systematics of oceanic basalts: Implications for mantle composition and processes. In: A.D. Saunders and M.J. Norry, Editors, Magmatism in the Ocean Basins, Special Publication 42, Geological Society (London)." 313-345.

Sun, W., Bennett, V. C. and Kamenetsky, V. S. (2004). "The mechanism of Re enrichment in arc magmas: evidence from Lau Basin basaltic glasses and primitive melt inclusions." Earth and Planetary Science Letters 222(1): 101-114.

Swanson, D. and Wright, T. L. (1981). The regional approach to studying the Columbia River Basalt Group. In: Subbarao, K.V., Sukheswala, R.N. (eds.) Deccan Volcanism and related basalt provinces in other parts of the World: Geological Society of India Memoir No. 3, p 58-80.

Swanson, D. A. (1967). "Yakima Basalt of Tieton river area south-central Washington." Geological Society of America Bulletin 78(9).

Swanson, D. A., Wright, T. I. and Helz, R. T. (1975). "Linear vent systems and estimated rates of magma production and eruption for the Yakima Basalt on the Columbia Plateau." American Journal of Science 275: 877-905.

Swanson, D. A., Wright, T. L., Hooper, P. R. and Bentley, R. D. (1979). Revisions in stratigraphic nomenclature of the Columbia River Basalt Group, US Geological Survey Bulletin.

Sweeney, R. J., Duncan, A. R. and Erlank, A. J. (1994). "Geochemistry and petrogenesis of central Lebombo basalts of the Karoo igneous province." Journal of Petrology 35(1): 95-125.

Takahahshi, E., Nakajima, K. and Wright, T. L. (1998). "Origin of the Columbia River basalts: melting model of a heterogeneous plume head." Earth and Planetary Science Letters 162(1-4): 63-80.

Tepley, F. I., Davidson, J. and Clynne, M. A. (1999). "Magmatic interactions as recorded in plagioclase phenocrysts of Chaos Crags, Lassen Volcanic Centre, California." Journal of Petrology 40: 787-806.

Tepley, F. I., Davidson, J., Tilling, R. I. and Arth, J. G. (2000). "Magma mixing, recharge and eruption histories recorded in plagioclase phenocrysts from El Chichon volcano, Mexico." Journal of Petrology 41: 1397-1411.

Thordarson, T. (1995). Volatile release and atmospheric effects of basaltic fissure eruptions, PhD Thesis, University of Hawaii, Manoa, Honolulu: 580 pp.

Thordarson, T., Miller, D. J., Larsen, G., Self, S. and Sigurdsson, H. (2001). "New estimates of sulfur degassing and atmospheric mass-loading by the 934 AD Eldgja eruption, Iceland." Journal of Volcanology and Geothermal Research 108(1-4): 33-54.

Thordarson, T. and Self, S. (1996). "Sulphur, chlorine and fluorine degassing and atmospheric loading by the Roza eruptions, Columbia River Basalt Group, Washington, USA." Journal of Volcanology and Geothermal Research 74: 49-73.

Thordarson, T. and Self, S. (1998). "The Roza Member, Columbia River Basalt Group: A gigantic pahoehoe lava flow field formed by endogenous processes?" Journal of Geophysical Research 103(B11): 27,411-27,445.

Tolan, T. L., Reidel, S. P., Beeson, M. H., Anderson, J. L., Fecht, K. R. and Swanson, D. A. (1989). "Revisions to the estimated of the areal extent and volume of the Columbia River Basalt Group." Geological Society of America Special Paper 239: 1-20.

Tomkeieff, S. (1940). "The basalt lavas of the Giant's Causeway district of northern Ireland." Bulletin of Volcanology 11(6): 89-143.

Tsuchiyama, A. (1985). "Dissolution kinetics of plagioclase in the melt of the system diopside-albite-anorthite, and origin of dusty plagioclase in andesites." Contributions to Mineralogy and Petrology 89: 1-16.

Turner, S., Hawkesworth, C., Gallagher, K., Stewart, K., Peate, D. and Mantovani, M. (1996). "Mantle plumes, flood basalts, and thermal models for melt generation beneath continents: Assessment of a conductive heating model and application to the Parana." Journal of Geophysical Research-Solid Earth 101(B5): 11503-11518.

Vallier, T. L. (1995). "Petrology of pre-Tertiary igneous rocks in the Blue Mountains region of Oregon, Idaho, and Washington: Implications for the geologic evolution of a complex island arc. In: Vallier, T.L and Brooks, H.C. (eds.) Geology of the Blue Mountains region of Oregon, Idaho and Washington: Petrology and tectonic evolution of pre-Tertiary rocks of the Blue Mountains Region." USGS Professional Paper 1438: 125-209.

Volkening, J., Walczyk, T. and G. Heumann, K. (1991). "Osmium isotope ratio determinations by negative thermal ionization mass spectrometry." International Journal of Mass Spectrometry and Ion Processes 105(2): 147-159.

Waagstein, R. (1988). "Structure, composition and age of the Faeroe basalt plateau." Geological Society, London, Special Publications 39(1): 225-238.

Wacaster, S. G. and McConnell, V. S. (2002). Segregation Structures in Diktytaxitic Basalt Flows of NE Oregon. Cordilleran Section - 98th Annual Meeting (May 13-15, 2002). Corvallis, Oregon, The Geological Society of America.

Waichel, B. L., de Lima, E. F., Lubachesky, R. and Sommer, C. A. (2006). "Pahoehoe flows from the central Parana Continental Flood Basalts." Bulletin of Volcanology 68(7-8): 599-610.

Walczyk, T., Hebeda, E. H. and Heumann, K. G. (1991). "Osmium isotope ratio measurements by negative thermal ionization mass spectrometry (NTI-MS)." Fresenius' Journal of Analytical Chemistry 341: 537-541.

Walker, G. P. L. (1971). "Compound and simple lava flows and flood basalts." Bulletin of Volcanology 35(3): 579-590.

Walker, G. P. L. (1973). "Lengths of lava flows." Philosophical Transactions of the Royal Society of London A 274: 107-118.

Walker, G. P. L. (1987). "Pipe vesicles in Hawaiian basaltic lavas - their origin and potential as paleoslope indicators." Geology 15(1): 84-87.

Walker, G. P. L. (1991). "Structure, and origin by injection of lava under surface crust, of tumuli, "lava rises", "lava-rise pits", and "lava-inflation clefts" in Hawaii." Bulletin of Volcanology 53: 546-558.

Walker, G. P. L. (1993). Basaltic-volcano systems. In: Magmatic processes and plate tectonics. H. M. Prichard, T. Alabaster, N. B. W. Harris and C. R. Neary, Geological Society, London, Special Publications. 76: 3-38.

Walker, G. P. L. (1996). Morphometric study of pahoehoe lava flows. Chapman Conference on Long Lava Flows, Dept of Earth Sci., James Cook Univ. of North Queensland, Townsville, Australia, Economic Geology Resources.

Walker, R. J. and Fassett, J. D. (1986). "Isotopic measurement of subnanogram quantities of rhenium and osmium by resonance ionization mass-spectrometry." Analytical Chemistry 58(14): 2923-2927.

Walker, R. J., Morgan, J. W., Naldrett, A. J., Li, C. and Fassett, J. D. (1991). "Re-Os isotope systematics of Ni-Cu sulphide ores, Sudbury Igneous Complex, Ontario - evidence for a major crustal component." Earth and Planetary Science Letters 105(4): 416-429.

Walker, R. J., Shirey, S. B. and Stecher, O. (1988). "Comparative Re-Os, Sm-Nd and Rb-Sr isotope and trace element systematics for Archean komatiite flows from Munro Township, Abitibi Belt, Ontario." Earth and Planetary Science Letters 87(1-2): 1-12.

Wang, C. Y., Zhou, M.-F. and Qi, L. (2007). "Permian flood basalts and mafic intrusions in the Jinping (SW China)-Song Da (northern Vietnam) district: Mantle sources, crustal contamination and sulfide segregation." Chemical Geology 243(3-4): 317-343.

Waters, A. C. (1960). "Determining direction of flow in basalts." American Journal of Science 258: 350-366.

Waters, A. C. (1961). "Stratigraphic and lithologic variations in the Columbia River basalt." American Journal of Science 259(8): 583-611.

Watkins, N. D. and Baksi, A. K. (1974). "Magnetostratigraphy and oroclinal folding of Columbia-River, Steens, and Owyhee basalts in Oregon, Washington, and Idaho." American Journal of Science 274(2): 148-189.

Watkins, N. D., Gunn, B. M. and Coy-yll, R. (1970). "Major and trace element variations during initial cooling of an Icelandic lava." American Journal of Science 268(1): 24-49.

White, R. and McKenzie, D. (1989). "Magmatism at rift zones - the generation of volcanic continental margins and flood basalts." Journal of Geophysical Research 94(7685-7729).

White, R. S. and McKenzie, D. (1995). "Mantle plumes and flood basalts." Journal of Geophysical Research-Solid Earth 100(B9): 17543-17585.

Whitehead, P. W. and Stephenson, P. J. (1998). "Lava rise ridges of the Toomba basalt flow, north Queensland, Australia." Journal of Geophysical Research-Solid Earth 103(B11): 27371-27382.

Widom, E. (1997). "Sources of ocean island basalts: A review of the osmium isotope evidence." Physica A: Statistical and Theoretical Physics 244(1-4): 484-496.

Widom, E., Hoernle, K. A., Shirey, S. B. and Schmincke, H. U. (1999). "Os isotope systematics in the Canary Islands and Madeira: Lithospheric contamination and mantle plume signatures." Journal of Petrology 40(2): 279-296.

Widom, E. and Shirey, S. B. (1996). "Os isotope systematics in the Azores: implications for mantle plume sources." Earth and Planetary Science Letters 142(3-4): 451-465.

Wignall, P. B., Sun, Y., Bond, D. P. G., Izon, G., Newton, R. J., Védrine, S., Widdowson, M., Ali, J. R., Lai, X., Jiang, H., Cope, H. and Bottrell, S. H. (2009). "Volcanism,

mass extinction and carbon isotope fluctuations in the middle Permian of China." Science 324(5931): 1179-1182.

Williams, D. A., Kadel, S. D., Greeley, R., Lesher, C. M. and Clynne, M. A. (2004). "Erosion by flowing lava: geochemical evidence in the Cave Basalt, Mount St. Helens, Washington." Bulletin of Volcanology 66(2): 168-181.

Wilson, L. and Head, J. W. (1981). "Ascent and eruption of basaltic magma on the Earth and Moon." Journal of Geophysical Research 86: 2971-3001.

Wimpenny, J., Gannoun, A., Burton, K. W., Widdowson, M., James, R. H. and Gislason, S. R. (2007). "Rhenium and osmium isotope and elemental behaviour accompanying laterite formation in the Deccan region of India." Earth and Planetary Science Letters 261(1-2): 239-258.

Wolff, J. A., Ramos, F. C. and Davidson, J. (1999). "Sr isotope disequilibrium during differentation of the Bandelier Tuff: Constraints on the crystallization of a large rhyolitic magma chamber." Geology 27: 495-498.

Wolff, J. A., Ramos, F. C., Hart, G. L., Patterson, J. D. and Brandon, A. D. (2008). "Columbia River flood basalts from a centralized crustal magmatic system." Nature Geoscience 1(3): 177-180.

Wood, D. A., Gibson, I. L. and Thompson, R. N. (1976). "Elemental mobility during zeolite facies metamorphism of the Tertiary basalts of eastern Iceland." Contributions to Mineralogy and Petrology 55(3): 241-254.

Worster, M. G., Huppert, H. E. and Sparks, R. S. J. (1993). "The crystallization of lava lakes." Journal of Geophysical Research-Solid Earth 98(B9): 15891-15901.

Wright, T. I., Mangan, M. and Swanson, D. (1989). "Chemical data for flows and feeder dikes of the Yakima basalt subgroup, Columbia River Basalt Group, Washington, Idaho and Oregon, and their bearing on a petrogenetic model." U.S. Geological Survey Bulletin 1821: 71 p.

Wright, T. L., Grolier, M. J. and Swanson, D. A. (1973). "Chemical variation related to stratigraphy of Columbia River basalt." Geological Society of America Bulletin 84(2): 371-385.

Xu, J.-F., Suzuki, K., Xu, Y.-G., Mei, H.-J. and Li, J. (2007). "Os, Pb, and Nd isotope geochemistry of the Permian Emeishan continental flood basalts: Insights into the source of a large igneous province." Geochimica et Cosmochimica Acta 71(8): 2104-2119.

Zablocki, C. J. (1978). "Applications of Vlf induction method for studying some volcanic processes of Kilauea volcano, Hawaii." Journal of Volcanology and Geothermal Research 3(1-2): 155-195.

Zellmer, G. F., Annen, C., Charlier, B. L. A., George, R. M. M., Turner, S. P. and Hawkesworth, C. J. (2005). "Magma evolution and ascent at volcanic arcs: constraining petrogenetic processes through rates and chronologies." Journal of Volcanology and Geothermal Research Energy and Mass Fluxes in Volcanic Arcs 140(1-3): 171-191.

Appendix A – Sample locality information.

Table 1 – 2005 Field season

Sample Number	Latitude	Longitude	Locality Number	Locality Description	Sample description	Stratigraphy	Position in flow	Height in section	Thin section	XRF	REE	Re-Os	Sr
CRB05_01	46. 56.142	119.57.229	05_2E	Sentinel Bluffs - Sand Hollow cliff section, starting at the top, base of the upper pillow pile	Glassy selvage - base of pillow pile	SG	pillow lobes	1	X	X			
CRB05_02	46. 56.142	119.57.231	05_2E	Sentinel Bluffs - Sand Hollow cliff section, starting at the top, base of the upper pillow pile	c. 10m along from sample 1. Highly vesicular flow top - an eroded top so the true flow top is not seen	SH	u/c	34	X	X	X	X	
CRB05_03	46. 56.126	119.57.229	05_2E	Sentinel Bluffs - Sand Hollow cliff section, starting at the top, base of the upper pillow pile	20m along section c.3m from top of the flow lobe. Upper core / crust transition zone	SH	u/c	25	X	X	X	X	
CRB05_04	46. 56.133	119.57.232	05_2D	Down section and transect across slope to the north - to one side of a grassy slope	Mid-core, 8m down from the top of the unit, above finely jointed black band	SH	core	18	X	X	X	X	
CRB05_05	46. 56.138	119.57.242	05_2D	Sentinel Bluffs - Sand Hollow cliff section	1m down from the top of the black band	SH	core	13	X	X	X	X	
CRB05_06	46. 56.155	119.57.252	05_2	Sentinel Bluffs - Sand Hollow cliff section	3 to 4m down from the top of the black band	SH	core	10	X	X	X	X	
CRB05_07	46. 56.161	119.57.258	05_2E	Sentinel Bluffs - Sand Hollow cliff section	1m from the top of the thickly jointed core - very close to the end truncation / fault zone on the Sentinel Bluff cliff section	SH	core	8	X	X	X	X	
CRB05_08	46. 56.168	119.57.265	05_2E	Sentinel Bluffs - Sand Hollow cliff section	4m beneath sample 7. Thickly jointed core on the opposite side of the disturbed zone	SH	core	3	X	X	X	X	
CRB05_09	46. 56.186	119.57.278	05_2C	Sentinel Bluffs - Sand Hollow cliff section	base of flow above Gingko. Base of the flow	SH	l/c	0.1	X	X	X	X	
CRB05_10	46. 56.186	119.57.278	05_2C	Sentinel Bluffs - Sand Hollow cliff section	50cm above sample 9. Base of the core	SH	l/c	0.5	X	X	X	X	
CRB05_11	46. 55.413	119.57.030	05_3B	Road section to the south of Sand Hollow on the Vantage-Richland road.	Vesicular zone marking an upper lobe within the Ginkgo	Ginkgo	l/c	0	X	X			
CRB05_12	46. 55.413	119.57.030	05_3B	Road section to the south of Sand Hollow on the Vantage-Richland road.	Xenocryst rich basalt, above the pipe vesicles at locality 2B	Ginkgo	core	1.5	X	X			
CRB05_13	46. 55.383	119.57.022	05_3C	Road section to the south of Sand Hollow on the Vantage-Richland road.	3m above the flow base	Ginkgo	core	4	X	X			
CRB05_14	46. 55.341	119.57.009	05_3D	Road section to the south of Sand Hollow on the Vantage-Richland road.	3-4m into the mid-core	Ginkgo	core	9	X	X			
CRB05_15	46. 55.271	119.56.985	05_3F	Road section to the south of Sand Hollow on the Vantage-Richland road.	Upper crust	Ginkgo	u/c	14	X	X			
CRB05_16	46. 55.884	119.56.986	05_1	Road section to the south of Sand Hollow on the Vantage-Richland road.	pillow pile	Ginkgo	u/c	u/k	X				
CRB05_17	46. 56.932	119.56.891	05_1D	Up the road cutting to the East from Sand Hollow and locality CVY1	middle of sheet lobe c.30m above the contact with the pillows	SH	core	5	X	X			

Sample Number	Latitude	Longitude	Locality Number	Locality Description	Sample description	Stratigraphy	Position in flow	Height in section	Thin section	XRF	REE	Re-Os	Sr
CRB05_18	46. 55.255	119.56.984	05_3H	Road section to the south of Sand Hollow on the Vantage-Richland road.	mid-core near to the top of the Ginkgo pile	Ginkgo	core	1.5					
CRB05_19	46. 55.255	119.56.984	05_3H	Road section to the south of Sand Hollow on the Vantage-Richland road.	1m up from the base of the unit with the black band into the lower core	SH	l/c	1	X	X			
CRB05_20	46. 55.237	119.56.976	05_3I	Road section to the south of Sand Hollow on the Vantage-Richland road.	70cm down from the contact with the black band in the lower core	SH	core	8.5	X	X			
CRB05_21	46. 55.186	119.56.957	05_3J	Road section to the south of Sand Hollow on the Vantage-Richland road.	50cm up from the base within the finely jointed black band	SH	core	10	X	X			
CRB05_22	46. 55.186	119.56.957	05_3J	Road section to the south of Sand Hollow on the Vantage-Richland road.	1m down from the top of the black band	SH	core	14	X	X			
CRB05_23	46. 55.109	119.56.928	05_3K	Road section to the south of Sand Hollow on the Vantage-Richland road.	1.5m up from the base of the thickly jointed core (above the black band finely jointed columns)	SH	core	16	X	X			
CRB05_24	46. 55.015	119.56.876	05_3L	Road section to the south of Sand Hollow, opposite the new vineyard entrance	Transition from core to upper crust	SH	core	20	X	X			
CRB05_25	46. 55.015	119.56.876	05_3L	Road section to the south of Sand Hollow, opposite the new vineyard entrance	Segregation vesicles from the upper crust	SH	u/c	24	X	X			
CRB05_26	46. 55.015	119.56.876	05_3L	Road section to the south of Sand Hollow, opposite the new vineyard entrance	Upper crust - within top 50cm of the exposed top of the flow	SH	u/c	26	X	X			
CRB05_27	46. 28.071	118.37.496	05_04	Gingko dyke section on the lower railroad section to the west of Devils Canyon	Ginkgo flow dyke - near edge	Ginkgo	n/a	n/a		X			
CRB05_28	46. 36.432	117.21.758	?	Gingko dyke section on the upper railroad level to the west of Devils Canyon on the north side of the Snake River.	Ginkgo flow dyke - near centre	Ginkgo	n/a	n/a		X			
CRB05_29	46. 36.432	117.21.758	05_5A	Road and rail cutting at Granite Knob	Just over the top of the granodiorite	GR	n/a	n/a					
CRB05_30	46. 01.724	117.00.923	05_6B	Chief Joseph Creek, track off main road	Feeder dyke	GR	n/a	n/a					
CRB05_31	46. 04.334	117.00.520	05_Y7	Dyke outcrop on the side of the hill above the bend in the Grand Rhonde Canyon and the small road bridge.	Feeder dyke	GR	n/a	n/a					
CRB05_32	46. 04.137	117.00.062	05_8	Buckhorn springs	Base of massive sheet flow	GR	l/c	u/k					

Sample Number	Latitude	Longitude	Locality Number	Locality Description	Sample description	Stratigraphy	Position in flow	Height in section	Thin section	XRF	REE	Re-Os	Sr
CRB05_34	46. 16.738	117.00.097	05_12	Weissenfels ridge, road/track cutting	Vesicle cylinder	GR	core	u/k					
CRB05_35	46. 16.738	117.00.097	05_12	Weissenfels ridge, road/track cutting	Base of bell vesicle segregation feature	GR	u/c	u/k					
CRB05_36	46. 16.738	117.00.097	05_12	Weissenfels ridge, road/track cutting	Base sample	GR	l/c	1					
CRB05_37	46. 16.738	117.00.097	05_12	Weissenfels ridge, road/track cutting	Soil from under GR R2 lobe in this locality	GR	n/a	n/a					
CRB05_38	46. 31.542	117.48.198	05_15	road cutting to the south east of Starbuck - approx - on the north cutting	Soil from top of flow	GR	n/a	n/a					
CRB05_39	46. 31.542	117.48.198	05_15	road cutting to the south east of Starbuck - approx - on the south side of the cutting	Basalt from core - basal 1m of exposure	GR	core	1					
CRB05_40	46. 39.828	118.13.377	05_16	west side of the Palouse Falls river canyon above the rapids	basal 5cm of FS - SH	SH	l/c	0.1	X	X			
CRB05_41	46. 39.969	118.13.492	05_16	west side of the Palouse Falls river canyon above the rapids	1m up from base of FS - SH	SH	core	1	X	X			
CRB05_42	46. 39.969	118.13.492	05_16	west side of the Palouse Falls river canyon above the rapids	2.40m up from base	SH	core	2.4	X	X			
CRB05_43	46. 40.094	118.13.512	05_19	The north side of the side canyon below the railroad by the rapids to the north of the Palouse River Falls	11, up from base, near base of finely jointed band	SH	core	12.5	X	X			
CRB05_44	46. 40.104	118.13.516	05_19	The north side of the side canyon below the railroad by the rapids to the north of the Palouse River Falls	2m below the large joints (within the finely jointed unit) c. 15m above the last sample point	SH	core	28	X	X			
CRB05_45	46. 40.111	118.13.528	05_19	The north side of the side canyon below the railroad by the rapids to the north of the Palouse River Falls	at the level of the joint horizon just below a vesicular zone (?core crust transition zone), 3m above the last point	SH	u/c	30	X	X			
CRB05_46	46. 40.052	118.13.564	05_19	2m below the level of the railroad above Palouse Falls	just above the main joint break	SH	u/c	32.5	X	X			
CRB05_47	46. 40.052	118.13.564	05_19	At the railroad level on the cutting above the rapids on the Palouse Falls River	slightly vesicular upper crust	SH	u/c	38	X	X			
CRB05_48	46. 40.052	118.13.564	05_19	5m down from the top of the cliff above the railroad level	upper part of the vesicular upper crust	SH	u/c	47.5	X	X			
CRB05_49	46. 32.373	118.08.995	05_20	Lower Goose Dam road	hackly jointed finely-crystalline	GR	core	4					
CRB05_50	46. 33.621	118.10.892	05_26	railway cutting off the Starbuck-Washtucna road	Upper part of the core (1m from the base of the exposure)	GR	core	1	X	X			
CRB05_51	46. 33.621	118.10.892	05_26	railway cutting off the Starbuck-Washtucna road	Top of the core at a megavesicle horizon	GR	u/c	4	X	X			
CRB05_52	46. 33.621	118.10.892	05_26	railway cutting off the Starbuck-Washtucna road	Base of the crust, in blackband horizon, beneath the first vesicle rich layer	GR	u/c	5	X	X			

Sample Number	Latitude	Longitude	Locality Number	Locality Description	Sample description	Stratigraphy	Position in flow	Height in section	Thin section	XRF	REE	Re-Os	Sr
CRB05_53	46. 33.621	118.10.892	05_26	railway cutting off the Starbuck-Washtucna road	First vesicular zone, just above the black band (9m up from base)	GR	u/c	7	X	X			
CRB05_54	46. 33.621	118.10.892	05_26	railway cutting off the Starbuck-Washtucna road	c.12m up in a major vesicular zone, v. large and closely spaced vesicles.	GR	u/c	10	X	X			
CRB05_55	46. 33.621	118.10.892	05_26	railway cutting off the Starbuck-Washtucna road	Third vesicular band up	GR	u/c	12.5	X	X			
CRB05_56	46. 33.621	118.10.892	05_26	railway cutting off the Starbuck-Washtucna road	Fourth vesicular band up, c.15m from the flow base	GR	u/c	14	X	X			
CRB05_57	46. 33.621	118.10.892	05_26	railway cutting off the Starbuck-Washtucna road	Fifth vesicular band up, c.18m from flow base	GR	u/c	18	X	X			
CRB05_58	46. 37.803	118.13.009	05_29	side canyon to the main Palouse Falls	6m from outcrop top, in vesicular crust	SH	u/c	7	X				
CRB05_59	46. 37.796	118.13.004	05_29	side canyon to the main Palouse Falls	50cm up from base of hackly fine joints (in core)	PF	core	1	X				
CRB05_60	46. 37.796	118.13.004	05_29	side canyon to the main Palouse Falls	Base crust / base core transition	PF	u/c	5	X				
CRB05_61	46. 37.510	118.12.772	05_31	side canyon to the main Palouse Falls	Upper core c.1m from gradual core-crust transition	GR	core	2	X				
CRB05_62	46. 37.510	118.12.772	05_31	side canyon to the main Palouse Falls	Middle of upper crust c.8m up from CRB05_061	GR	u/c	8	X				
CRB05_63	46. 37.413	118.12.799	05_32	W side of Palouse Falls river canyon	highly and regularly jointed vesicular upper crust	PF	u/c	8					
CRB05_64	46. 37.097	118.13.116	05_33	Joso locality on railway cutting, W side of Palouse Falls river canyon	few sparse vesicles in basal portion of the lobe core	PF	core	1	X	X			
CRB05_65	46. 37.097	118.13.116	05_33	Joso locality on railway cutting, W side of Palouse Falls river canyon	non-vesicular upper portion of the lobe core	PF	u/c	4	X	X			
CRB05_66	46. 37.097	118.13.116	05_33	Joso locality on railway cutting, W side of Palouse Falls river canyon	vesicular lower portion of the upper crust	PF	u/c	6.5	X	X			
CRB05_67	46. 37.097	118.13.116	05_33	Joso locality on railway cutting, W side of Palouse Falls river canyon	slightly less vesicular band within middle portion of the upper crust	PF	u/c	13	X	X			
CRB05_68	46. 37.990	118.13.400	SS	Joso locality on railway cutting, W side of Palouse Falls river canyon	finely jointed columns	SH	core	6					
CRB05_69	46. 37.990	118.13.400	SS	Joso locality on railway cutting, W side of Palouse Falls river canyon	slightly vesicular upper crust	SH	u/c	2					
CRB05_70	46. 35.172	118.13.346	05_36	railway cutting to the south side of the Snake River	1m into the base of flow 2	GR	core	1					
CRB05_71	46. 33.037	118.10.767	05_37	railway cutting to the south side of the Snake River	Fallout deposit on top of flow 3	GR	n/a	n/a					
CRB05_72	46. 33.048	118.10.768	05_37	railway cutting to the south side of the Snake River	50cm down into the upper crust beneath rubble and fallout	GR	u/c	u/k					
CRB05_73	46. 35.102	118.13.416	05_38	cliff outcrops above Lyons Ferry Marina	Top of the widely jointed columns - core	SH	l/c	1					

Sample Number	Latitude	Longitude	Locality Number	Locality Description	Sample description	Stratigraphy	Position in flow	Height in section	Thin section	XRF	REE	Re-Os	Sr
CRB05_74	46. 35.105	118.13.454	05_38	cliff outcrops above Lyons Ferry Marina	Halfway up the finely jointed core	SH	core	6					
CRB05_75	46. 35.128	118.13.477	05_38	cliff outcrops above Lyons Ferry Marina	Upper core - just beneath first vesicle horizon	SH	core	16					
CRB05_76	46. 35.135	118.13.473	05_38	cliff outcrops above Lyons Ferry Marina	Vesicle rich upper crust (beneath rubbly top)	SH	u/c	20					
CRB05_77	46. 35.135	46. 35.135	05_38	cliff outcrops above Lyons Ferry Marina	Non-vesicular upper crust	SH	u/c	23					
CRB05_78a	46. 33.977	118.32.684	05_39	Devils Canyon	Tephra from between flows	PF	n/a	n/a					
CRB05_78b	46. 33.977	118.32.684	05_39	Devils Canyon	Tephra from between flows	PF	n/a	n/a					
CRB05_79	46. 33.977	118.32.684	05_39	Devils Canyon	Windblown diatomitic mud / sediment from over lobe	PF	n/a	n/a					
CRB05_80	46. 33.977	118.32.684	05_39	Devils Canyon	Gingko lobe 50cm above base with PF (sampled the least phenocryst rich)	Ginkgo	l/c	0.5					
CRB05_81	46. 30.451	118.36.969	05_40	N side Snake River between Devils Canon and Ginkgo dyke site	Dodge flow	EM	core	3					
CRB05_82	46. 32.999	118.33.284	05_43	railroad cutting w of Lower Monumental Dam	Top of GR flows - contact with PF, tumuli top	GR	u/c	u/k					
CRB05_83	46. 33.640	118.32.874	05_44	railroad cutting w of Lower Monumental Dam	Base 1m (5m from top of lobe) of GR flow 1	GR	core	5					
CRB05_84	46. 34.015	118.32.502	05_45	Lower Monumental Dam	1m up from base in flow 2 of PF	PF	core	2					
CRB05_85	46. 34.015	118.32.502	05_45	Lower Monumental Dam	Middle of flow 3 - near thinned edge	GR	u/c	u/k					
CRB05_86	section/township/range	NESW36 12N 27E	-	Pasco Basin borehole DC8	sedimentary interbeds	Ginkgo	seds	49.5					
CRB05_87	section/township/range	NESW36 12N 27E	-	Pasco Basin borehole DC8	upper part of the lowermost Ginkgo flow	Ginkgo	u/c	49		X			
CRB05_88	section/township/range	NESW36 12N 27E	-	Pasco Basin borehole DC8	vesicle poor band within the u/c of Ginkgo flow 1	Ginkgo	u/c	45.65		X			
CRB05_89	section/township/range	NESW36 12N 27E	-	Pasco Basin borehole DC8	vesicle rich band in the u/c of Ginkgo flow 1	Ginkgo	u/c	42.15		X			
CRB05_90	section/township/range	NESW36 12N 27E	-	Pasco Basin borehole DC8	horizon with pods of segregation material	Ginkgo	u/c	39.75		X			
CRB05_91	section/township/range	NESW36 12N 27E	-	Pasco Basin borehole DC8	first vesicular zone in the u/c of Ginkgo flow 1	Ginkgo	u/c	31.75		X			
CRB05_92	section/township/range	NESW36 12N 27E	-	Pasco Basin borehole DC8	slightly vesicular portion mid-core	Ginkgo	core	14.35		X			
CRB05_93	section/township/range	NESW36 12N 27E	-	Pasco Basin borehole DC8	lower crust of Ginkgo flow 2	Ginkgo	l/c	1.15		X			
CRB05_94	section/township/range	NESW36 12N 27E	-	Pasco Basin borehole DC8	lower portion of Ginkgo flow 1 core	Ginkgo	core	5.35		X			
CRB05_95	section/township/range	NESW36 12N 27E	-	Pasco Basin borehole DC8	base of Ginkgo flow 1	Ginkgo	l/c	0.1		X			

Sample Number	Latitude	Longitude	Locality Number	Locality Description	Sample description	Stratigraphy	Position in flow	Height in section	Thin section	XRF	REE	Re-Os	Sr
CRB05_96	section/township/range	NESW36 12N 27E	-	Pasco Basin borehole DC8	vesicular upper crust of PF	PF	u/c	27		X			
CRB05_97	section/township/range	NESW36 12N 27E	-	Pasco Basin borehole DC8	vesicle poor band within the u/c of PF	PF	u/c	21		X			
CRB05_98	section/township/range	NESW36 12N 27E	-	Pasco Basin borehole DC8	mid-core	PF	core	11		X			
CRB05_99	section/township/range	NESW36 12N 27E	-	Pasco Basin borehole DC8	lower crust of PF - split into 2 sample for analysis	PF	l/c	0.1		X			
CRB05_100	section/township/range	NESW36 12N 27E	-	Pasco Basin borehole DC8	sedimentary interbeds	GR-Wanapum	n/a	n/a					
CRB05_101	section/township/range	NESW36 12N 27E	-	Pasco Basin borehole DC8	sedimentary interbeds	GR-Wanapum	n/a	n/a					
CRB05_102	section/township/range	NESW36 12N 27E	-	Pasco Basin borehole DC8	HVS	PF	u/c	26					
CRB05_103	section/township/range	NESW36 12N 27E	-	Pasco Basin borehole DC8	sedimentary interbeds	GR-Wanapum	n/a	n/a					
CRB05_104	46. 46.713	119.55.109	05_47	cliff section above Mattawa vineyard	pale green grey fine sand silt sed between two FS flows	GR-Wanapum	n/a	u/k					
CRB05_105	46. 56.385	119.57.478	05_49	Vantage	fallen blocks of pillow basalts from cliff tops	SG	u/k	u/k					
CRB05_106	47. 01.672	119.59.635	05_52	S side of Frenchman Springs Coulee	70cm above base in basal core	GR	l/c	0.7					
CRB05_107	47. 01.672	119.59.635	05_52	S side of Frenchman Springs Coulee	glassy base of flow	GR	l/c	0.1					
CRB05_108	47. 01.513	119.58.211	05_53	S side of Frenchman Springs Coulee	xenocryst found in loose block	u/k	u/k	u/k					
CRB05_109	47. 01.607	119.57.975	05_54	S side of Frenchman Springs Coulee	2m down from flow top - for pheno content	Ginkgo	u/c	7					
CRB05_110	47. 01.592	119.58.001	05_54	S side of Frenchman Springs Coulee	3cm from top of flow (top one of Ginkgo)	Ginkgo	u/c	8.95		X			
CRB05_111	47. 01.592	119.58.001	05_54	S side of Frenchman Springs Coulee	near base of upper crust in HVS zone	Ginkgo	core	2.95		X			
CRB05_112	47. 01.592	119.58.001	05_54	S side of Frenchman Springs Coulee		Ginkgo	l/c	0.1		X			

Table 2 – 2006 Field season

Sample Number	Latitude	Longitude	Locality Number	Locality Description	Sample description	Stratigraphy	Position in flow	Height in section	Thin section	XRF	REE	Re-Os	Sr
CRB06_001	N45.41.916	W121.23.684	06_1	Locke Lake upper old road cutting	30cm above base (lower core) of ?Sentinel Gap flow 1	SG	l/c	0.3		X			
CRB06_002	N45.41.916	W121.23.684	06_1	Locke Lake upper old road cutting	Vesicular base above thin soil of ?Sentinel Gap flow 1	SG	?l/c	0.1		X			
CRB06_003	N45.41.916	W121.23.684	06_1	Locke Lake upper old road cutting	Upper 10cm of upper crust of thick Sand Hollow flow, lobate v. vesicular u/c	SH	u/c	59.8	X	X	X	X	X
CRB06_004	N45.41.916	W121.23.684	06_1	Locke Lake upper old road cutting	40cm down from top into upper crust	SH	u/c	59.5	X	X	X	X	X
CRB06_005	N45.41.916	W121.23.684	06_1	Locke Lake upper old road cutting	6.50m down from top, within HVS zone but not including HVS material	SH	u/c	51	X	X	X		X
CRB06_006	N45.41.972	W121.24.395	06_4	Main road sections to the west of Locke Lake	Centre of core, 10m down from expo / cliff top	GR	core	10					
CRB06_007	N45.41.972	W121.24.395	06_4	Main road sections to the west of Locke Lake	Edge of small lobes which look like breakouts on the top of the flow sampled in 008-010	GR	breakouts	0.1					
CRB06_008	N45.41.972	W121.24.395	06_4	Main road sections to the west of Locke Lake	2 metres down from flow top, zone of irregular vesicle sheets / lobes	GR	u/c	4.5					
CRB06_009	N45.41.972	W121.24.395	06_4	Main road sections to the west of Locke Lake	Vesicle cylinder, 5 metres down from top	GR	core	2					
CRB06_010	N45.41.972	W121.24.395	06_4	Main road sections to the west of Locke Lake	40-50cm above base, just at core / lower crust transition, above inclines pipe vesicles.	GR	l/c	0.3					
CRB06_011	N45.41.972	W121.24.395	06_4	Main road sections to the west of Locke Lake	2m metres down into next flow, massive part inbetween vesicular layers.	GR	u/c	1.5					
CRB06_012	N45.41.916	W121.23.684	06_1	Locke Lake upper old road cutting	8-9 metres from top, within poorly vesicular area of u/c or upper core	SH	u/c	47.5		X	X	X	X
CRB06_013	N45.41.916	W121.23.684	06_1	Locke Lake upper old road cutting	second HVS zone, just above the first proper vesicular layer	SH	u/c	44		X	X		
CRB06_014	N45.41.916	W121.23.684	06_1	Locke Lake upper old road cutting	18metres from top, within vesicular layered zone	SH	u/c	42	X	X	X	X	X
CRB06_015	N45.41.916	W121.23.684	06_1	Locke Lake upper old road cutting	25 metres from top, just below u/c to core transition zone	SH	core	35		X	X		
CRB06_016	N45.41.916	W121.23.684	06_1	Locke Lake upper old road cutting	36 metres from top, massive, irregular curvy joints, few large feldspar crystals seen in sample	SH	core	24	X	X	X	X	X
CRB06_017	N45.41.916	W121.23.684	06_1	Locke Lake upper old road cutting	2 samples taken, 1.5 metres laterally apart from each other, 42 metres from top, poorly jointed zone	SH	core	18		X	X	X	X
CRB06_018	N45.41.916	W121.23.684	06_1	Locke Lake upper old road cutting	55 metres from top, 2 metres above the top of the tree moulds, at base of massive, balde like jointing pattern	SH	core	5		X	X	X	X
CRB06_019	N45.41.916	W121.23.684	06_1	Locke Lake upper old road cutting	30cm above contact (small lobes / pillows), sample taken from centre of a small lobe, above 20cm grey seds and coal.	SH	l/c	0.3		X	X	X	X
CRB06_020	N45.41.989	W121.24.994	06_4	Main road sections to the west of Locke Lake	lobe no. 7, 60cm above the contact with lobe no.8 - banded vesicular rich and poor areas in lower crust	GR	l/c	0.6		X			

Sample Number	Latitude	Longitude	Locality Number	Locality Description	Sample description	Stratigraphy	Position in flow	Height in section	Thin section	XRF	REE	Re-Os	Sr
CRB06_021	N45.41.989	W121.24.994	06_4	Main road sections to the west of Locke Lake	upper crust of lobe no.8, 3m down from flow top (flow top too rotten to sample)	GR	u/c	21					
CRB06_022	N45.41.989	W121.24.994	06_4	Main road sections to the west of Locke Lake	5.50m down from flow top within upper crust, just above megavesicle horizon	GR	u/c	18					
CRB06_023	N45.41.989	W121.24.994	06_4	Main road sections to the west of Locke Lake	11m down from flow top, 4m from the top of the core, well developed joints	GR	core	12		X			
CRB06_024	N45.41.989	W121.24.994	06_4	Main road sections to the west of Locke Lake	50cm above base, est 24.5m from top of flow, slightly vesicular, good ropes	GR	l/c	0.5		X			
CRB06_025	N45.41.390	W121.16.322	06_5	Cliff sections east of Lyle, N banks of the CR	2m from flow top within upper crust, highly weathered, ?some erosion from top of flow	FS #1	u/c	13					
CRB06_026	N45.41.390	W121.16.322	06_5	Cliff sections east of Lyle, N banks of the CR	7m from flow top (est 4m from u/c boundary) within flow core	FS #1	core	7		X			
CRB06_027	N45.41.390	W121.16.322	06_5	Cliff sections east of Lyle, N banks of the CR	1m above flow base	FS #1	l/c	1		X			
CRB06_028	N45.41.390	W121.16.322	06_5	Cliff sections east of Lyle, N banks of the CR	est 1-2m from flow top (v weathered, undulating flow top), vesicular zone within the u/c	FS #2	u/c	63		X			
CRB06_029	N45.41.390	W121.16.322	06_5	Cliff sections east of Lyle, N banks of the CR	14m from flow top, just within the core / at the core-u/c boundary, as defined by a zone of platy jointing.	FS #2	core	51		X			
CRB06_030	N45.41.390	W121.16.322	06_5	Cliff sections east of Lyle, N banks of the CR	20m from top of flow, at base of zone of patchy vesicles, above strong jointing horizon that makes this flow look like two units from a distance.	FS #2	core	47.5		X			
CRB06_031	N45.41.390	W121.16.322	06_5	Cliff sections east of Lyle, N banks of the CR	38m from the top of the flow, 2m down into a zone of tulip joints	FS #2	core	42		X			
CRB06_032	N45.41.390	W121.16.322	06_5	Cliff sections east of Lyle, N banks of the CR	Base of flow, no glass and no vesicles, welded to the underlying Ginkgo flow, est 80m from top of flow (thickness extremely laterally variable from 60 to 80m, mostly within the u/c and lowermost tulip jointed zone.	FS #2	l/c	0.2		X			
CRB06_033	N45.41.390	W121.16.322	06_5	Cliff sections east of Lyle, N banks of the CR	10m up from base, within tulip jointed zone	FS #2	core	9		X			
CRB06_034	N45.41.390	W121.16.322	06_5	Cliff sections east of Lyle, N banks of the CR	2m down from top of flow	Ginkgo	u/c	u/k		X			
CRB06_035	N45.41.390	W121.16.322	06_5	Cliff sections east of Lyle, N banks of the CR	53m down from top of flow, above the 2nd tulip jointed zone	FS #2	core	30		X			
CRB06_036	N45.40.758	W121.14.360	06_1	Locke Lake lower main road cutting	Hyaloclastite from the unit above the ?Sentinal Gap flow 1 unit.	?SG	-	-					

Sample Number	Latitude	Longitude	Locality Number	Locality Description	Sample description	Stratigraphy	Position in flow	Height in section	Thin section	XRF	REE	Re-Os	Sr
CRB06_037	N45.41.362	W121.16.619	06_5	Main road cutting to the east of Lyle	3.5m from flow top	Ginkgo	u/c	18.5		X			
CRB06_038	N45.41.362	W121.16.619	06_5	Main road cutting to the east of Lyle	7.5m from flow top within vesicular band	Ginkgo	u/c	15		X			
CRB06_039	N45.41.362	W121.16.619	06_5	Main road cutting to the east of Lyle	9m from flow top within weakly vesicular band within the u/c	Ginkgo	u/c	13.4		X			
CRB06_040	N45.41.362	W121.16.619	06_5	Main road cutting to the east of Lyle	10m from flow top, hackly and irregular jointed zone, forms a major bench on surrounding hillsides	Ginkgo	u/c	12		X			
CRB06_041	N45.41.362	W121.16.619	06_5	Main road cutting to the east of Lyle	12.5m from flow top, at top of commencement of vesicular rich bands again	Ginkgo	u/c	9.7		X			
CRB06_042	N45.41.362	W121.16.619	06_5	Main road cutting to the east of Lyle	16.5m from flow top, few weak horizontal joints, just below the u/c to core transition	Ginkgo	core	5.5		X			
CRB06_043	N45.41.196	W121.15.914	06_5	Main road cutting to the east of Lyle	21m from top of flow (? Fairly close to the base but unknown, not exposed in this general area)	Ginkgo	core	1		X			
CRB06_044	N46.34.652	W118.23.520	06_9	Railroad cutting near Ayer Road	1m above the base contact with the GRs	Eckler Mountain	core	1					
CRB06_045	N46.34.634	W118.23.349	06_9	Railroad cutting near Ayer Road	Red-orange weathered top / ash / soil	Eckler Mountain - GR contact	contact material	-					
CRB06_046	N46.35.194	W118.29.279	06_12	end of Fry Road, at contact with Snake River	1m above the u/c - core boundary, est 9-10m from flow top (undulating)	PF	u/c	23					
CRB06_047	N46.35.194	W118.29.279	06_12	end of Fry Road, at contact with Snake River	1m below the u/c - core boundary, est 11-12m from flow top (undulating)	PF	u/c	21					
CRB06_048	N46.35.719	W118.28.847	06_13	North side of Snake River, opposite Magallen	Rubbly, well-jointed lower crust with bands of 1-3mm sized vesicular zones 1-10cm of base	PF	l/c	0.1		X			
CRB06_049	N46.35.719	W118.28.847	06_13	North side of Snake River, opposite Magallen	1.40m above base, elongate, slightly inclined vesicles widely spaced, otherwise massive	PF	l/c to core transition zone	2.5		X			
CRB06_050	N46.35.719	W118.28.847	06_13	North side of Snake River, opposite Magallen	5m above base, just below first horizontally jointed zone	PF	core	7		X			
CRB06_051	N46.35.719	W118.28.847	06_13	North side of Snake River, opposite Magallen	12m above base, curvy jointed, non-vesc zone	PF	core	13		X			
CRB06_052	N46.35.719	W118.28.847	06_13	North side of Snake River, opposite Magallen	17m above base at u/c to core transition zone, defined by commencement of first vesicular zone	PF	core - u/c	19.5		X			
CRB06_053	N46.35.719	W118.28.847	06_13	North side of Snake River, opposite Magallen	20m above base at first major shatter zone / horizontal joints within vesicular zone of u/c	PF	u/c	24		X			

Sample Number	Latitude	Longitude	Locality Number	Locality Description	Sample description	Stratigraphy	Position in flow	Height in section	Thin section	XRF	REE	Re-Os	Sr
CRB06_054	N46.35.719	W118.28.847	06_13	North side of Snake River, opposite Magallen	24m above base, looks water chilled, non vesicular zone, above megavesicle horizon	PF	u/c	31		X			
CRB06_055	N46.35.719	W118.28.847	06_13	North side of Snake River, opposite Magallen	29m above base, vesicular zone of u/c (top of expo here), at time of collection believed to be only a few more metres on top, now believed to be at least another 5-10m of u/c.	PF	u/c	36		X			
CRB06_056	N46.36.480	W118.29.130	06_13	outcrop on hillside off corner of Fry Road with valley	very glassy lower crust of Roza or Ginkgo over PF	Ginkgo?	l/c	0.5					
CRB06_057	N46.36.480	W118.29.130	06_13	outcrop on hillside off corner of Fry Road with valley	2m above base, non-vesicular, thick well-developed joints	Ginkgo?	core	2					
CRB06_058	N46.36.635	W118.19.402	06_14	Cliffs on the N bank of the Snake River, to SW of Davin	30cm above base of flow	PF	l/c	0.3		X			
CRB06_059	N46.36.635	W118.19.402	06_14	Cliffs on the N bank of the Snake River, to SW of Davin	70cm above base of flow - contorted banding of vesicular bands	PF	l/c	2.5		X			
CRB06_060	N46.36.635	W118.19.402	06_14	Cliffs on the N bank of the Snake River, to SW of Davin	11m above base, few well-rounded vesicles, slightly banded appearance	PF	core	19		X			
CRB06_061	N46.36.635	W118.19.402	06_14	Cliffs on the N bank of the Snake River, to SW of Davin	25.5m above base, first vesicular band in upper crust (u/c to core transition at 25m)	PF	u/c	30		X			
CRB06_062	N46.36.637	W118.19.479	06_14	Cliffs on the N bank of the Snake River, to SW of Davin	numerous v small vesicles at 35m above base	PF	u/c	41		X			
CRB06_063	N46.36.637	W118.19.479	06_14	Cliffs on the N bank of the Snake River, to SW of Davin	very vesicular upper crust, est 59m above base	PF	u/c	58		X			
CRB06_064	N46.33.012	W118.10.766	06_15	Starbuck-Washtucna Road section	lower part of core, 7m from flow top in GR N2-1	GRs	core	5					
CRB06_065	N46.33.012	W118.10.766	06_15	Starbuck-Washtucna Road section	u/c - core transition, 5m from flow top in GR N2-2	GRs	u/c	22					
CRB06_066	N46.33.012	W118.10.766	06_15	Starbuck-Washtucna Road section	core with elongated vesicles creating a banded look to the rock (?location of u/c boundary in this flow), 15m from flow top in GR N2-2	GRs	core	11					
CRB06_067	N46.33.012	W118.10.766	06_15	Starbuck-Washtucna Road section	23m from flow top in massive thickly jointed flow, 2m from flow base in GR N2-2	GRs	core	2					
CRB06_068	N46.33.012	W118.10.766	06_15	Starbuck-Washtucna Road section	5m from flow top, just above first vesc band in u/c of GR N2-3	GRs	u/c	6					

Sample Number	Latitude	Longitude	Locality Number	Locality Description	Sample description	Stratigraphy	Position in flow	Height in section	Thin section	XRF	REE	Re-Os	Sr
CRB06_069	N46.41.361	W118.13.446	06_16	Railway tracks to the N of Palouse falls	abundant vesicles in a flow top ?top of the PF	?PF	u/c	u/k					
CRB06_070	N46.41.361	W118.13.446	06_16	Railway tracks to the N of Palouse falls	base exposure of the flow overyling the ?PF - sample taken from the core with vesicle cylinders ?PF breakout?	?PF	core	15					
CRB06_071	N46.44.165	W118.15.101	06_16	Top of the hill of the entrance road into Palouse Falls State Park	? SH with a pheno rich base or Rosa?	?Roza	core	u/k					
CRB06_072	N46.34.287	W118.32.549	06_18	Upper railway grade above Lower Monumental Dam	red-orange fine ash layers separated by pale grey tephra	?PF-Ginkgo contact	contact material	0					
CRB06_073	N46.34.287	W118.32.549	06_18	Upper railway grade above Lower Monumental Dam	vesicular and non-vesicular strongly banded areas, 1.5m below flow top within u/c	?PF	u/c	-2		X			
CRB06_074	N46.33.912	W118.32.759	06_18	Upper railway grade above Lower Monumental Dam	base 10cm of Ginkgo flow - lower crust	Ginkgo	l/c	0.1					
CRB06_075	N46.33.574	W118.33.045	06_18	Upper railway grade to the west of Lower Monumental Dam	1m below flow top in u/c	Ginkgo	u/c	9					
CRB06_076	N46.33.574	W118.33.045	06_18	Upper railway grade to the west of Lower Monumental Dam	5m below flow top at the core - upper crust transition, seems to be especially diffuse here	Ginkgo	core - u/c	5					
CRB06_077	N46.33.574	W118.33.045	06_18	Upper railway grade to the west of Lower Monumental Dam	9m below flow top - interpreted to be v near to the flow base, ie within 1m but full outcrop not actually seen	Ginkgo	core	1		X			
CRB06_078	N46.33.575	W118.33.044	06_18	Upper railway grade to the west of Lower Monumental Dam	top of the PF lobe	PF	u/c	u/k		X			
CRB06_079	N46.34.015	W118.32.502	06_19	Cliffs opposite the entrance to Lower Monumental Dam (N side)	1m up from flow base, fairly rich in phenos for the PFs, some onion skin weathering, ?just above l/c	PF	l/c - core	0.5		X			
CRB06_080	N46.34.015	W118.32.502	06_19	Cliffs opposite the entrance to Lower Monumental Dam (N side)	3m up from flow base	PF	core	2		X			
CRB06_081	N46.34.015	W118.32.502	06_19	Cliffs opposite the entrance to Lower Monumental Dam (N side)	4m up from flow base	PF	core	3.5		X			
CRB06_082	N46.34.015	W118.32.502	06_19	Cliffs opposite the entrance to Lower Monumental Dam (N side)	5.5m up from flow base, v weak horizontal joints	PF	core	5.5		X			

Sample Number	Latitude	Longitude	Locality Number	Locality Description	Sample description	Stratigraphy	Position in flow	Height in section	Thin section	XRF	REE	Re-Os	Sr
CRB06_083	N46.34.015	W118.32.502	06_19	Cliffs opposite the entrance to Lower Monumental Dam (N side)	slight break and a few horizontal joints, 7m up from base	PF	core	7.5		X			
CRB06_084	N46.34.015	W118.32.502	06_19	Cliffs opposite the entrance to Lower Monumental Dam (N side)	8.5m up from flow base - altered area with Fe staining and slight increase in the abundance of vesicles.	PF	core	10		X			
CRB06_085	N46.34.015	W118.32.502	06_19	Cliffs opposite the entrance to Lower Monumental Dam (N side)	densely jointed zone 10m up from flow base	PF	core	13		X			
CRB06_086	N46.34.015	W118.32.502	06_19	Cliffs opposite the entrance to Lower Monumental Dam (N side)	11.5m up from base, major joint break at the top of a densely jointed zone	PF	core	15.5		X			
CRB06_087	N46.34.015	W118.32.502	06_19	Cliffs opposite the entrance to Lower Monumental Dam (N side)	small HVS pod, 13.5m up from flow base	PF	core	18		X			
CRB06_088	N46.34.015	W118.32.502	06_19	Cliffs opposite the entrance to Lower Monumental Dam (N side)	top of thickly jointed zone with few rounded vesicles, 15m up from base	PF	core	19		X			
CRB06_089	N46.34.015	W118.32.502	06_19	Cliffs opposite the entrance to Lower Monumental Dam (N side)	16m up from base in finely jointed zone with abundant small rounded vesicles marking the top of the core	PF	core	20		X			
CRB06_090	N46.34.015	W118.32.502	06_19	Cliffs opposite the entrance to Lower Monumental Dam (N side)	hackly jointed zone 19m up from flow base	PF	u/c	27		X			
CRB06_091	N46.34.015	W118.32.502	06_19	Cliffs opposite the entrance to Lower Monumental Dam (N side)	22m up from flow base, slight horiz joints, separating zone of small abundant vesc from more irregular larger vesc above	PF	u/c	30		X			
CRB06_092	N46.34.015	W118.32.502	06_19	Cliffs opposite the entrance to Lower Monumental Dam (N side)	25m up from flow base increase in large vesc abundance	PF	u/c	32		X			
CRB06_093	N46.34.015	W118.32.502	06_19	Cliffs opposite the entrance to Lower Monumental Dam (N side)	27.5m up from flow base - top of exposure (lack of expo in grass slope above - unknown if still part of this PF lobe or if constituting smaller breakout lobes, 15-20m worth)	PF	u/c	34		X			
CRB06_094	N46.33.021	W118.33.206	06_21	lower railroad grade to the east of Windust	base 5cm of the PF lobe (the same lobe as that collected in samples 079 - 093)	PF	l/c	0.1		X			
CRB06_095	N46.35.334	W118.32.667	06_22	Railroad grade on west side of Devils Canyon	SEDS overlying the PF breakout lobes	PF - Ginkgo	contact material	0					

Sample Number	Latitude	Longitude	Locality Number	Locality Description	Sample description	Stratigraphy	Position in flow	Height in section	Thin section	XRF	REE	Re-Os	Sr
CRB06_096	N46.35.334	W118.32.667	06_22	Railroad grade on west side of Devils Canyon	upper core of first lobes overlying what is interpreted to the be the top of the PF, therefore ?Ginkgo	Ginkgo	core	1					
CRB06_097	N46.35.334	W118.32.667	06_22	Railroad grade on west side of Devils Canyon	lower 50cm of 3rd lobe stacked over the top the of the PF	Ginkgo	l/c - core	0.3					
CRB06_098	N46.34.794	W118.32.473	06_22	Exposures under the railroad grade on the western wall of Devils Canyon	vesicular upper crust of PF, est 10-15m below railroad grade (interpreted to lie at about the leve of the PF - Ginkgo contact)	?PF	u/c	u/k					
CRB06_099	N46.34.798	W118.32.444	06_22	Exposures under the railroad grade on the western wall of Devils Canyon	massive to vesicular upper crust, 25m below railway cut, cumulate phenos up to 2cm long!	PF	u/c	u/k					
CRB06_100	N46.37.287	W118.33.459	06_23	Road cutting at the northern end of Devils Canyon	SEDS over ash - overlying the ?Silver Falls unit	SF-SH SEDS	contact material	0					
CRB06_101	N46.37.287	W118.33.459	06_23	Road cutting at the northern end of Devils Canyon	5cm from base of flow - lower crust with inclined pipe vesicles	SH flow #1	l/c	0.05		X			
CRB06_102	N46.37.287	W118.33.459	06_23	Road cutting at the northern end of Devils Canyon	70cm up from flow base - at lower crust to core transition	SH flow #1	l/c - core	0.7		X			
CRB06_103	N46.37.287	W118.33.459	06_23	Road cutting at the northern end of Devils Canyon	1.5m up from flow base, abundant well developed jointing	SH flow #1	core	1.5		X			
CRB06_104	N46.37.287	W118.33.459	06_23	Road cutting at the northern end of Devils Canyon	2.5m up from flow base - upper part of the core	SH flow #1	core	2.5		X			
CRB06_105	N46.37.287	W118.33.459	06_23	Road cutting at the northern end of Devils Canyon	80cm down from flow top (5m from flow base)	SH flow #1	u/c	5		X			
CRB06_106	N46.37.287	W118.33.459	06_23	Road cutting at the northern end of Devils Canyon	near flow top - max 20cm down, very poorly developed columns, generally very heavily weathered with sub-horizontal fractures	SH flow #1	u/c	5.8		X			
CRB06_107	N46.32.738	W118.33.697	06_24	Upper railroad grade cutting to the E of Wilson Canyon	60-70cm up from the base	?Ginkgo	lower core	0.6		X			
CRB06_108	N46.32.738	W118.33.697	06_24	Upper railroad grade cutting to the E of Wilson Canyon	1.5m up from flow base, massive, non-vesicular, upper part of the core	?Ginkgo	core	1.5		X			
CRB06_109	N46.32.738	W118.33.697	06_24	Upper railroad grade cutting to the E of Wilson Canyon	2m up from flow base, v. messy irregular jointing, just passing into first vesicular band	?Ginkgo	u/c	2		X			
CRB06_110	N46.32.738	W118.33.697	06_24	Upper railroad grade cutting to the E of Wilson Canyon	80cm down from flow top (3m up from base), vesicular zone, slightly elongated	?Ginkgo	u/c	2.2		X			

Sample Number	Latitude	Longitude	Locality Number	Locality Description	Sample description	Stratigraphy	Position in flow	Height in section	Thin section	XRF	REE	Re-Os	Sr
CRB06_111	N46.32.738	W118.33.697	06_24	Upper railroad grade cutting to the E of Wilson Canyon	1m up into the core of this Ginkgo lobe	Ginkgo	l/c	1		X			
CRB06_112	N46.28.069	W118.37.498	06_25	Gingko dyke locality on N side of Snake	30cm from edge of dyke	Ginkgo	dyke	0.3		X			
CRB06_113	N46.28.069	W118.37.498	06_25	Gingko dyke locality on N side of Snake	70cm from edge of dyke	Ginkgo	dyke	0.7		X			
CRB06_114	N46.28.069	W118.37.498	06_25	Gingko dyke locality on N side of Snake	1.40m from edge of dyke	Ginkgo	dyke	1.4		X			
CRB06_115	N46.28.069	W118.37.498	06_25	Gingko dyke locality on N side of Snake	1.90m from edge of dyke	Ginkgo	dyke	1.9		X			
CRB06_116	N46.28.069	W118.37.498	06_25	Gingko dyke locality on N side of Snake	2.50m from edge of dyke	Ginkgo	dyke	2.5		X			
CRB06_117	N46.28.069	W118.37.498	06_25	Gingko dyke locality on N side of Snake	3.0m from edge of dyke	Ginkgo	dyke	3		X			
CRB06_118	N46.28.069	W118.37.498	06_25	Gingko dyke locality on N side of Snake	3.8m from edge of dyke	Ginkgo	dyke	3.8		X			
CRB06_119	N46.28.069	W118.37.498	06_25	Gingko dyke locality on N side of Snake	4.20m from edge of dyke	Ginkgo	dyke	4.2		X			
CRB06_120	N46.28.069	W118.37.498	06_25	Gingko dyke locality on N side of Snake	highly fractured, devitrified, glassy selvage to dyke	Ginkgo	dyke	0.01					
CRB06_121	N46.25.600	W118.36.279	06_26	Upper Railroad grade cutting, N bank of Snake, opposite Walker	50cm up from flow base in PF flow no.2	PF	l/c	0.5		X			
CRB06_122	N46.25.600	W118.36.279	06_26	Upper Railroad grade cutting, N bank of Snake, opposite Walker	1.40m from flow base in crystal rich core in PF flow no.2	PF	core	1.4		X			
CRB06_123	N46.25.600	W118.36.279	06_26	Upper Railroad grade cutting, N bank of Snake, opposite Walker	1.80m up from flow base in crystal rich core in PF flow no.2	PF	core	1.8		X			
CRB06_124	N46.25.600	W118.36.279	06_26	Upper Railroad grade cutting, N bank of Snake, opposite Walker	2.3m up from flow base at core - upper crust boundary	PF	core - u/c	2.3		X			
CRB06_125	N46.25.600	W118.36.279	06_26	Upper Railroad grade cutting, N bank of Snake, opposite Walker	3.5m up from flow base in upper crust (overlying flow top is too red and weathered to be sampled)	PF	u/c	3.5		X			
CRB06_126	N46.25.600	W118.36.279	06_26	Upper Railroad grade cutting, N bank of Snake, opposite Walker	crystal rich Ginkgo base - l/c - core	Ginkgo	l/c - core	1		X			

Sample Number	Latitude	Longitude	Locality Number	Locality Description	Sample description	Stratigraphy	Position in flow	Height in section	Thin section	XRF	REE	Re-Os	Sr
CRB06_127	N46.25.600	W118.36.279	06_26	Upper Railroad grade cutting, N bank of Snake, opposite Walker	mid-core crystal rich main Ginkgo lobe in this area	Ginkgo	core	15		X			
CRB06_128	N46.25.600	W118.36.279	06_26	Upper Railroad grade cutting, N bank of Snake, opposite Walker	upper part of the core, above horiz jointing zone with well-rounded vescs.	SH	core	60		X			
CRB06_129	N46.25.600	W118.36.279	06_26	Upper Railroad grade cutting, N bank of Snake, opposite Walker	SEDS overlying the Dodge / Eckler Mountain flow, under the PF	Eckler Mountain - PF contact	contact material	0					
CRB06_130	N46.24.677	W117.11.215	06_27	S side of Snake River, W of Clarkston	est 28m above base of flow - at top of outcrop within elongate vesicle zone, v.coarse, distinct greeny colour (?olivines)	Pomona	core	27					
CRB06_131	N46.24.677	W117.11.215	06_27	S side of Snake River, W of Clarkston	est 68m up (small exposures, all believed to be part of the same lobe but unknown - need to examine chemistry)	Pomona	?u/c	60					
CRB06_132	N46.24.677	W117.11.215	06_27	S side of Snake River, W of Clarkston	est 38m above base of flow, nr horiz joints and small well-rounded vesicles, radiating columns	Pomona	?u/c or upper core	37					
CRB06_133	N46.24.677	W117.11.215	06_27	S side of Snake River, W of Clarkston	14m above base of outcrop, 2m above colonnade to entablature contact and hackly zone associated with this, radiating columns	Pomona	core	16					
CRB06_134	N46.24.677	W117.11.215	06_27	S side of Snake River, W of Clarkston	10m above base of outcrop, well developed columnar zone (colonnade), 2m down from contact	Pomona	core	12					
CRB06_135	N46.24.677	W117.11.215	06_27	S side of Snake River, W of Clarkston	base of exposure, presumed to be near base of flow as is near base of modern day valley and this flow is a valley fill	Pomona	core	2					
CRB06_136	N46.25.396	W117.07.450	06_27	S side of Snake River, W of Clarkston	base 30cm of flow, massive and non-vesicular all the way to the base, chatter marks on the sides of columns	Pomona	l/c	0.1					
CRB06_137	N47.43.999	W119.14.572	06_28	E side of Banks Lake	1m from flow top, vesicular	?Ginkgo - sparse phenos only!	u/c	1.5		X			
CRB06_138	N47.43.999	W119.14.572	06_28	E side of Banks Lake	2m from flow top, below jointing horizon and into slightly less vesicular band	?Ginkgo - sparse phenos only!	u/c	5		X			
CRB06_139	N47.43.999	W119.14.572	06_28	E side of Banks Lake	3.5m from flow top, at discont HVS zone and horiz joints, interp upper crust - core boundary	?Ginkgo - sparse phenos only!	u/c - core	4		X			
CRB06_140	N47.43.999	W119.14.572	06_28	E side of Banks Lake	mid-core, 5m from flow top, irregular joints	?Ginkgo - sparse phenos only!	core	2		X			

Sample Number	Latitude	Longitude	Locality Number	Locality Description	Sample description	Stratigraphy	Position in flow	Height in section	Thin section	XRF	REE	Re-Os	Sr
CRB06_141	N47.43.999	W119.14.572	06_28	E side of Banks Lake	6m from flow top, between 30cm and 1m from flow base (rapidly undulates in response to topography on the underlying flow exposed here)	?Ginkgo - sparse phenos only!	core-l/c	1		X			
CRB06_142	N47.43.999	W119.14.572	06_28	E side of Banks Lake	1m from flow top, vesicular	?Ginkgo or SH	u/c	7.5		X			
CRB06_143	N47.43.999	W119.14.572	06_28	E side of Banks Lake	3m down from flow top, poorly vesicular	?Ginkgo or SH	u/c	6		X			
CRB06_144	N47.43.999	W119.14.572	06_28	E side of Banks Lake	7m down from flow top (1.8m down from u/c - core boundary) - has browny onion skin weathering, much like the uppermost Ginkgo flow, exposed underneath Roza, in Dry Falls Park	?Ginkgo or SH	core	1		X			
CRB06_145	N46.51.473	W119.58.024	06_29	N edge of Dry Falls Lake	top of core / upper crust, fine grained and no phenos	GRs	core - u/c	u/k		X			
CRB06_146	N46.51.473	W119.58.024	06_29	N edge of Dry Falls Lake	1.2m from flow top, abundant vesicles	Ginkgo	u/c	25		X			
CRB06_147	N46.51.473	W119.58.024	06_29	N edge of Dry Falls Lake	0-12cm from base of flow, inclined pipe vesicles	Roza	l/c	0.2		X			
CRB06_148	N46.51.473	W119.58.024	06_29	N edge of Dry Falls Lake	upper core, 9m below flow top, coarse, v. few phenos, 1m below u/c to core boundary	Ginkgo	core	15		X			
CRB06_149	N46.51.473	W119.58.024	06_29	N edge of Dry Falls Lake	5m below flow top, abundant phenos, v coarse, brown onion skin weathering	Ginkgo	u/c	19		X			
CRB06_150a	N46.47.591	W119.54.827	06_29	Cliff promintory from E side of Dry Falls	base of flow, no phenos	?Rosalia	l/c	0.01					
CRBo0_150b	N46.47.591	W119.54.827	06_29	Cliff promintory from E side of Dry Falls	10cm above flow base	?Rosalia	l/c	0.1					
CRB06_151	N46.47.591	W119.54.827	06_29	Cliff promintory from E side of Dry Falls	2m down from flow top, pheno rich	Roza flow #2	u/c	6					
CRB06_152	N46.47.591	W119.54.827	06_29	Cliff promintory from E side of Dry Falls	4m down from flow top, pheno rich	Roza flow #2	core	2					
CRB06_153	N46.47.591	W119.54.827	06_29	Cliff promintory from E side of Dry Falls	3m60 down from flow top, pheno rich	Roza flow #1	upper core	6					
CRB06_154	N47.51.721	W119.58.194	06_30	Road cutting just north of turning for Sun Lake State Park	small phenocrysts abundant	? Rosalia	u/c	u/k					
CRB06_155	N47.51.721	W119.58.194	06_30	Road cutting just north of turning for Sun Lake State Park	4m up from flow base, horiz jointing, aphyric, v.coarse core, v.fine u/c	?Rosalia flow no.4	core	3					
CRB06_156	N47.51.721	W119.58.194	06_30	Road cutting just north of turning for Sun Lake State Park	12m up from base, at core-upper crust boundary, above 1st megavesicle horizon	?Rosalia flow no.4	core-u/c	14					
CRB06_157	N47.51.721	W119.58.194	06_30	Road cutting just north of turning for Sun Lake State Park	1m up from flow base, v.ocassional pheno seen, otherwise aphyric, well-jointed	?Rosalia flow no 5a	core	1					

Sample Number	Latitude	Longitude	Locality Number	Locality Description	Sample description	Stratigraphy	Position in flow	Height in section	Thin section	XRF	REE	Re-Os	Sr
CRB06_158	N47.51.721	W119.58.194	06_30	Road cutting just north of turning for Sun Lake State Park	50cm up from flow base, within very short colonnade, underlain by v. fissile lava	?Rosalia flow no.5b	core	7.5					
CRB06_159	N47.35.289	W119.23.311	06_32	Cliff top outcrop above Lenore Caves	basal 20cm of Ginkgo flow no.1	Ginkgo	l/c	0.2		X			
CRB06_160	N47.35.289	W119.23.311	06_32	Cliff top outcrop above Lenore Caves	75cm up from base of Ginkgo flow no.1	Ginkgo	l/c - core	0.75		X			
CRB06_161	N47.35.289	W119.23.311	06_32	Cliff top outcrop above Lenore Caves	7m up from flow base in Ginkgo flow no.1, abundant large pheno cumulates	Ginkgo	core - u/c	7		X			
CRB06_162	N47.35.289	W119.23.311	06_32	Cliff top outcrop above Lenore Caves	13m up from the base of Ginkgo flow no.1 - flow top	Ginkgo	u/c	13		X			
CRB06_163	N47.35.289	W119.23.311	06_32	Cliff top outcrop above Lenore Caves	40cm above the base of Ginkgo flow no.2	Ginkgo	l/c	0.4		X			
CRB06_164	N47.35.289	W119.23.311	06_32	Cliff top outcrop above Lenore Caves	1.5m above the base of the flow, dixytaxitic, flow may be thinner here as it is thinning over the top of another small lobe, this sample is 1/2 way up the core	Ginkgo	core	4.5		X			
CRB06_165	N47.35.289	W119.23.311	06_32	Cliff top outcrop above Lenore Caves	top of the flow (est.12m thick in total)	Ginkgo	u/c	12		X			
CRB06_166	N47.35.289	W119.23.311	06_32	Cliff top outcrop above Lenore Caves	12m from base of the flow, tortoise shell joints and chatter marks, v.v. abundant phenocrysts	Roza	core	12		X			
CRB06_167	N47.35.289	W119.23.311	06_32	Cliff top outcrop above Lenore Caves	4m up from flow base, platy jointing / tulip joints - base of flow not seen	Roza	core	4					
CRB06_168	N47.35.289	W119.23.311	06_32	Cliff top outcrop above Lenore Caves	0.75m down from flow top	?SH	u/c	11.5		X			
CRB06_169	N47.35.289	W119.23.311	06_32	Cliff top outcrop above Lenore Caves	3m down from flow top	?SH	u/c	9		X			
CRB06_170	N47.35.289	W119.23.311	06_32	Cliff top outcrop above Lenore Caves	5.5m down from flow top, some phen cumulates (10%), fairly rare, less abundant than flow beneath, within HVS zone	?SH	u/c	6.5		X			
CRB06_171	N47.35.289	W119.23.311	06_32	Cliff top outcrop above Lenore Caves	7.5m down from flow top, v. poorly dev columns, v. coarse crystals	?SH	u/c?	4.5		X			
CRB06_172	N47.35.289	W119.23.311	06_32	Cliff top outcrop above Lenore Caves	10m down from flow top, just beneath u/c - core boundary, just above vesc cylinders	?SH	core	2		X			
CRB06_173	N47.35.289	W119.23.311	06_32	Cliff top outcrop above Lenore Caves	flow base (12m flow thickness)	?SH	l/c	0.1		X			
CRB06_174	N47.30.600	W119.29.200	06_32	Cliffs immediately above Lenore Caves	2.5m below flow top, vesicular u/c	GRs	u/c	28					
CRB06_175	N47.30.600	W119.29.200	06_32	Cliffs immediately above Lenore Caves	12m below flow top, 1m below u/c - core boundary, hackly water chilled	GRs	core	15					
CRB06_176	N47.33.896	W119.26.358	06_33	End of road past Rock Rim village, SE side of CR	SEDs c.10cm baked silty seds between Rosalia and Roza flows	Rosalia - Roza	contact material	0					

Sample Number	Latitude	Longitude	Locality Number	Locality Description	Sample description	Stratigraphy	Position in flow	Height in section	Thin section	XRF	REE	Re-Os	Sr
CRB06_177	N47.35.199	W119.22.220	06_33	cliffs above Rock Rim village	weathered flow top of flow underlying Roza, poor soil and evidence of mechanical weathering overlying the sampling locality, 20cm below flow top. ?SH or non-pheno rich breakout from centre of Ginkgo flow?	?SH or ?Ginkgo	u/c	0					
CRB06_178	N46.28.168	W116.25.118	06_34	Crater Coulee to Crater Lake	1m above base	Ginkgo	core	1					
CRB06_179	N46.28.168	W116.25.118	06_34	Crater Coulee to Crater Lake	2m above base	Ginkgo	core	2					
CRB06_180	N46.28.168	W116.25.118	06_34	Crater Coulee to Crater Lake	HVS area, just under core - upper crust boundary, 6m up from base	Ginkgo	core	6					
CRB06_181	N46.28.168	W116.25.118	06_34	Crater Coulee to Crater Lake	9m up from base, nr top of exposure	Ginkgo	u/c	9					
CRB06_182	N46.43.997	W119.14.572	06_34	railway track access track cutting	SEDS collected from within a dig for fossil trees ?paleosoil	GRs ?Museum	contact material	0					
CRB06_183	N47.43.997	W119.14.572	06_34	railway track access track cutting	glassy selvage of pillows	GRs	pillow selvages	0.1					
CRB06_184	N47.14.456	W119.59.074	06_35	Highway 28 at Lynch Canyon Junction	SEDs between Roza and Ginkgo, pale yellow-green with orange colouration - palagonisation and alteration with water and the seds	Ginkgo - Roza	contact material	0					
CRB06_185	N47.14.456	W119.59.074	06_35	Highway 28 at Lynch Canyon Junction	top of the core of the Ginkgo - possible erosion of the u/c here	Ginkgo	core	u/k					
CRB06_186	N47.14.960	W119.57.959	06_38	Type section of Vantage on Museum road, outside Vantage	SEDs, 30cm thick silty layer underlying pillows, GR to Ginkgo contact.	GR - Ginkgo	contact material	0					
CRB06_187	N47.01.535	W119.58.051	06_40	Road section on the south side of FSC	1.8m down from flow top (est 18m from flow base), vesicular u/c	?SH	u/c	18		X			
CRB06_188	N47.01.535	W119.58.051	06_40	Road section on the south side of FSC	vesicular band with poorly developed joints, 15m above flow base	?SH	u/c	15		X			
CRB06_189	N47.01.535	W119.58.051	06_40	Road section on the south side of FSC	10m up from flow base, non-vesicular zone just above first vesicular band and horizontal joints - core - upper crust	?SH	u/c	10		X			
CRB06_190	N47.01.535	W119.58.051	06_40	Road section on the south side of FSC	8m up from flow base, just below HVS zone	?SH	core	8		X			
CRB06_191	N47.01.535	W119.58.051	06_40	Road section on the south side of FSC	6m up from flow base, beginning to be slightly vesicular, BB horizon	?SH	core	6		X			
CRB06_192	N47.01.535	W119.58.051	06_40	Road section on the south side of FSC	5m up from flow base, hackly joints, non-vesicular, BB horizon	?SH	core	5		X			
CRB06_193	N47.01.535	W119.58.051	06_40	Road section on the south side of FSC	2m up from flow base, v thick columns	?SH	core	2		X			
CRB06_194	N47.01.535	W119.58.051	06_40	Road section on the south side of FSC	flow base, v pheno rich flow base	?SH	l/c	0.1		X			
CRB06_195	N47.01.535	W119.58.051	06_40	Road section on the south side of FSC	5cm down from top of flow, est 10.5m up from base	?SG	u/c	10.5		X			

Sample Number	Latitude	Longitude	Locality Number	Locality Description	Sample description	Stratigraphy	Position in flow	Height in section	Thin section	XRF	REE	Re-Os	Sr
CRB06_196	N47.01.535	W119.58.051	06_40	Road section on the south side of FSC	9m up from flow base, vesicular u/c, adjacent to tree moulds, just below zone of MVs	?SG	u/c	9		X			
CRB06_197	N47.01.535	W119.58.051	06_40	Road section on the south side of FSC	6.4m up from flow base, at core-upper crust boundary, zone of finer joints	?SG	core - u/c	6.8		X			
CRB06_198	N47.01.535	W119.58.051	06_40	Road section on the south side of FSC	5m up from flow base, near top of well-dev columns, up to 2m wide	?SG	core	5.1		X			
CRB06_199	N47.01.535	W119.58.051	06_40	Road section on the south side of FSC	1.8m up from flow base, thick well dev joints, v sparse phenos, v occasional vesicles	?SG	core	1.8		X			
CRB06_200	N47.01.535	W119.58.051	06_40	Road section on the south side of FSC	20cm above flow base, vesicular	?SG	l/c	0.2		X			
CRB06_201	N46.47.975	W119.54.800	06_41	Cliff exposures on S side of Sentinel Bluff	vesicular u/c of top of Ginkgo	Ginkgo	u/c	u/k		X			
CRB06_202	N46.47.975	W119.54.800	06_41	Cliff exposures on S side of Sentinel Bluff	upper part of the core of the uppermost Ginkgo flow, v coarse and v pheno rich	Ginkgo	core	u/k		X			
CRB06_203	N47.14.960	W119.57.959	06_38	Type section of Vantage on Museum road, outside Vantage	SEDs, 30cm thick silty layer underlying pillows, GR to Ginkgo contact.	GR - Ginkgo	contact material	0					
CRB06_204	N46.57.200	W119.59.200	06_38	end of Museum Road by CR	lower crust of lower flow ?Levering	?Levering	l/c	0.1					
CRB06_205	N46.57.200	W119.59.200	06_38	end of Museum Road by CR	mid-core, 3m up from flow base with some vesicle cylinders	?Levering	core	3					
CRB06_206	N46.57.200	W119.59.200	06_38	end of Museum Road by CR	upper crust, 5.5m up from flow base (total flow est 6m thick), max 1.5m thick u/c	?Levering	u/c	5.5					
CRB06_207	N46.57.200	W119.59.200	06_38	end of Museum Road by CR	section of small lobe, 6m found between the flows here (variable thickness)	?Levering or Rocky Coulee	core	1					
CRB06_208	N46.57.200	W119.59.200	06_38	end of Museum Road by CR	? Thin lobes at base of main flow - welded to flow ?first expressions?, 1m up from flow base, lightly hackly jointed	?Rocky Coulee	l/c-core	0.2					
CRB06_209	N46.57.200	W119.59.200	06_38	end of Museum Road by CR	7m up from flow base, crinkly joints and fractures	?Rocky Coulee	core	7					
CRB06_210	N46.57.200	W119.59.200	06_38	end of Museum Road by CR	12m up from base, very hackly area	?Rocky Coulee	core	12					
CRB06_211	N46.57.200	W119.59.200	06_38	end of Museum Road by CR	19m up from base, just at core - upper crust boundary as basalt starts to become vesicular	?Rocky Coulee	core-u/c	19					
CRB06_212	N46.57.200	W119.59.200	06_38	end of Museum Road by CR	25m up from base, vesicle poor zone between bands in the u/c	?Rocky Coulee	u/c	25					
CRB06_213	N46.57.200	W119.59.200	06_38	end of Museum Road by CR	70cm below flow top, est 29m from base, v.vesicular	?Rocky Coulee	u/c	0.7					
CRB06_214	N46.57.200	W119.59.200	06_38	end of Museum Road by CR	50cm up from flow base (nr top of section)	?Museum	l/c - core	0.5					
CRB06_215	N46.51.473	W119.58.025	06_42	W bank of CR, south of Dam	6.5m down from flow top, just above u/c - core boundary	?SG	u/c	10					

Sample Number	Latitude	Longitude	Locality Number	Locality Description	Sample description	Stratigraphy	Position in flow	Height in section	Thin section	XRF	REE	Re-Os	Sr
CRB06_216	N46.51.473	W119.58.025	06_42	W bank of CR, south of Dam	2m down from top of flow exposure, v vesicular u/c	?SG	u/c	16					
CRB06_217	N46.51.473	W119.58.025	06_42	W bank of CR, south of Dam	4m down from flow top, fairly large vesicles	?SG	u/c	13					
CRB06_218	N46.51.473	W119.58.025	06_42	W bank of CR, south of Dam	7m down from flow top, fairly finely jointed, non-vesicular core	?SG	core	9					
CRB06_219	N46.51.473	W119.58.025	06_42	W bank of CR, south of Dam	8.5m down from flow top, just below horiz jointing horizon, at top of thick well-dev joints	?SG	core	6					
CRB06_220	N46.51.473	W119.58.025	06_42	W bank of CR, south of Dam	12.5m down from flow top, 2m max above pillows.	?SG	core	2					
CRB06_221	N47.44.549	W119.13.880	06_43	Vantage cliffs above the parkway	basal 10cm with vertical pipe vesicles	Ginkgo	l/c	0.1					
CRB06_222	N47.44.549	W119.13.880	06_43	Vantage cliffs above the parkway	30-40cm up from flow base, v. pheno rich	Ginkgo	l/c - core	0.3					
CRB06_223	N47.44.549	W119.13.880	06_43	Vantage cliffs above the parkway	4m up from flow base, just above a series of scalloped joints	Ginkgo	core	4					
CRB06_224	N47.44.549	W119.13.880	06_43	Vantage cliffs above the parkway	10m up from flow base, at top of finely jointed zone, base of thick columns	Ginkgo	core	10					
CRB06_225	N47.44.549	W119.13.880	06_43	Vantage cliffs above the parkway	within HVS, just above core - u/c boundary, 16m up from flow base	Ginkgo	u/c	16					
CRB06_226	N47.44.549	W119.13.880	06_43	Vantage cliffs above the parkway	19m up from flow base, 1m down from top, within v vesicular 2-3m of top, abundant weathering.	Ginkgo	u/c	19					
CRB06_227	N47.35.199	W119.22.220	06_44	N cliffs of FSC, opposite the end of Roza on the south side	5cm thick max, rippled coarse sandstone	Ginkgo - SH	contact material	0					
CRB06_228	N47.35.199	W119.22.220	06_44	N cliffs of FSC, opposite the end of Roza on the south side	glassy base, 0 to 5cm thick	SH	l/c	0.03	X	X			
CRB06_229	N47.35.199	W119.22.220	06_44	N cliffs of FSC, opposite the end of Roza on the south side	2cm thick sample, taken 6cm up from base, v. small phenos	SH	l/c	0.06	X	X	X	X	
CRB06_230	N47.35.199	W119.22.220	06_44	N cliffs of FSC, opposite the end of Roza on the south side	orientated sample taken from 15cm to 25cm up from base, NW orientated pipe vesicles	SH	l/c	0.15	X	X			
CRB06_231	N47.35.199	W119.22.220	06_44	N cliffs of FSC, opposite the end of Roza on the south side	from 35cm up from base, v fine grained	SH	l/c	0.35	X	X			
CRB06_232	N47.35.199	W119.22.220	06_44	N cliffs of FSC, opposite the end of Roza on the south side	50cm up from base, few v small vesicles	SH	l/c - core	0.5	X	X			
CRB06_233	N47.35.199	W119.22.220	06_44	N cliffs of FSC, opposite the end of Roza on the south side	90cm up from base	SH	core	0.9	X				

Sample Number	Latitude	Longitude	Locality Number	Locality Description	Sample description	Stratigraphy	Position in flow	Height in section	Thin section	XRF	REE	Re-Os	Sr
CRB06_234	N47.35.199	W119.22.220	06_44	N cliffs of FSC, opposite the end of Roza on the south side	1.5m up from base, patchy vesicular areas, v weak banding	SH	core	1.5	X	X	X	X	
CRB06_235	N47.35.199	W119.22.220	06_44	N cliffs of FSC, opposite the end of Roza on the south side	4m up from base, v thick columns, slightly wavy joints	SH	core	4	X	X	X	X	
CRB06_236	N47.35.199	W119.22.220	06_44	N cliffs of FSC, opposite the end of Roza on the south side	7m up from base at the top of the thick columns	SH	core	7	X	X			
CRB06_237	N47.35.199	W119.22.220	06_44	N cliffs of FSC, opposite the end of Roza on the south side	9m up from base, at base of thinner, slightly radiating joints	SH	core	8.5	X	X	X	X	
CRB06_238	N47.35.199	W119.22.220	06_44	N cliffs of FSC, opposite the end of Roza on the south side	15m up from base	SH	core	15.5	X	X			
CRB06_239	N47.35.199	W119.22.220	06_44	N cliffs of FSC, opposite the end of Roza on the south side	19m up from base, joints beginning to radiate from this point upwards	SH	core	19	X	X	X	X	
CRB06_240	N47.35.199	W119.22.220	06_44	N cliffs of FSC, opposite the end of Roza on the south side	26m up from base, inbetween 1st and 2nd jointing horizons	SH	core	26	X	X			
CRB06_241	N47.35.199	W119.22.220	06_44	N cliffs of FSC, opposite the end of Roza on the south side	29m up from flow base, at top of thick columns, just beneath jointing horizon (top of core), v large cumulates up to 7cm diameter seen	SH	top of core	28	X	X			
CRB06_242	N47.35.199	W119.22.220	06_44	N cliffs of FSC, opposite the end of Roza on the south side	31m up from base, hackly v small columns	SH	u/c	31	X	X	X	X	
CRB06_243	N47.35.199	W119.22.220	06_44	N cliffs of FSC, opposite the end of Roza on the south side	33.5m up from base, at top of hackly jointed zone	SH	u/c	33.5	X	X	X	X	
CRB06_244	N47.35.199	W119.22.220	06_44	N cliffs of FSC, opposite the end of Roza on the south side	35m up from base, first strong vesicle band	SH	u/c	35.5	X	X			
CRB06_245	N47.35.199	W119.22.220	06_44	N cliffs of FSC, opposite the end of Roza on the south side	38m up from base, 1m from the top of the flow, v weathered, assumed to have erosion from top. Difficult to tell if unit overlying is a separate flow or part of this one - looks welded, assumed to be Roza	SH	u/c	38	X	X	X	X	
CRB06_246	N47.35.199	W119.22.220	06_44	N cliffs of FSC, opposite the end of Roza on the south side	1m above jointing horizon / contact, pockets of segregation material and v pheno rich.	?Roza	core	40.5	X	X			
CRB06_247	N47.32.623	W119.25.232	06_45	SE end of FSC	close to base of flow but contact not seen so unknown, 1m up from base of expo	Ginkgo flow #1	core	est. 3					
CRB06_248	N47.32.623	W119.25.232	06_45	SE end of FSC	5m up from flow base, just below principle HVS zone	Ginkgo flow #1	core	8					

Sample Number	Latitude	Longitude	Locality Number	Locality Description	Sample description	Stratigraphy	Position in flow	Height in section	Thin section	XRF	REE	Re-Os	Sr
CRB06_249	N47.32.623	W119.25.232	06_45	SE end of FSC	8m up from flow base, just above HVS zone	Ginkgo flow #1	u/c	11					
CRB06_250	N47.32.623	W119.25.232	06_45	SE end of FSC	top of flow, 12.5m up from flow base, within 30cm of flow top	Ginkgo flow #1	u/c	15.5					
CRB06_251	N47.32.623	W119.25.232	06_45	SE end of FSC	within base 1m of flow	Ginkgo flow #2	l/c - core	0.8					
CRB06_252	N47.32.623	W119.25.232	06_45	SE end of FSC	upper part of the core, just beneath HVS, adjacent to the vesicle cylinders which can be seen to be feeding these, 4m up from flow base	Ginkgo flow #2	upper core	4					
CRB06_253	N47.32.623	W119.25.232	06_45	SE end of FSC	7m up from flow base, v vesicular u/c	Ginkgo flow #2	u/c	7					
CRB06_254	N47.32.623	W119.25.232	06_45	SE end of FSC	3m up from flow base, within middle part of the core, slightly smaller columns that those observed in the two underlying flows	Ginkgo flow #3	core	3					
CRB06_255	N47.32.623	W119.25.232	06_45	SE end of FSC	base of upper crust, rest of u/c very weathered	Ginkgo flow #3	u/c	6					
CRB06_256	N47.32.623	W119.25.232	06_45	SE end of FSC	1m above flow base, just below horizontally jointed / fissile zone	?SH	core	1		X			
CRB06_257	N47.32.623	W119.25.232	06_45	SE end of FSC	top of fissile zone, 5m above flow base	?SH	core	5		X			
CRB06_258	N47.32.623	W119.25.232	06_45	SE end of FSC	top of thin thickly jointed, well dev columnar zone, v occasional pheno, 6-7m above flow base	?SH	core	7		X			
CRB06_259	N47.32.623	W119.25.232	06_45	SE end of FSC	12m above flow base, top of zone of chatter marks and undulating columns, just below horizontal jointing horizon marking core - u/c boundary	?SH	top of core	12		X			
CRB06_260	N47.32.623	W119.25.232	06_45	SE end of FSC	16m above flow base, fairly abundant phenos, weak joints and wide columns, few vesicles	?SH	u/c	16		X			
CRB06_261	N47.32.623	W119.25.232	06_45	SE end of FSC	18m above flow base, above zone of MVs / elongate large vesicles	?SH	u/c	18		X			
CRB06_262	N47.32.623	W119.25.232	06_45	SE end of FSC	top of flow, est 23m above base of flow, v. vesicular banded top. Small flow 2m thick overlying this, may be a breakout?	?SH	u/c	23		X			
CRB06_263	N47.33.896	W119.26.358	06_33	End of road past Rock Rim village, SE side of CR	flow top, 18m from flow base	?Ginkgo	u/c	18		X			
CRB06_264	N47.33.896	W119.26.358	06_33	End of road past Rock Rim village, SE side of CR	15.2m from flow base, v. abundant phenos, vesicular u/c	?Ginkgo	u/c	15.2					
CRB06_265	N47.33.896	W119.26.358	06_33	End of road past Rock Rim village, SE side of CR	very brown weathered u/c, 13m from flow base, v. brown weathered u/c, within HVS zone, just above (20cm) fissile horiz jointing zone (u/c - core boundary)	?Ginkgo	u/c	13					

Sample Number	Latitude	Longitude	Locality Number	Locality Description	Sample description	Stratigraphy	Position in flow	Height in section	Thin section	XRF	REE	Re-Os	Sr
CRB06_266	N47.33.896	W119.26.358	06_33	End of road past Rock Rim village, SE side of CR	9.5m from flow base, v. well developed columns some vesc cylinders	?Ginkgo	core	9.5					
CRB06_267	N47.33.896	W119.26.358	06_33	End of road past Rock Rim village, SE side of CR	5m above base of exposure, platy horiz jointing zone, v. few phenos	?Ginkgo	core	5					
CRB06_268	N47.33.896	W119.26.358	06_33	End of road past Rock Rim village, SE side of CR	base of expo, ?close of base of flow?, v. well dev columns with a few horiz joint features	?Ginkgo	core	0.5					
CRB06_269	N47.34.192	W119.25.365	06_49	mouth of Jasper Canyon with Blue Lake	0-15cm from base of flow, nr vertical pipe vesicles	Roza	l/c	0.15					
CRB06_270	N47.34.192	W119.25.365	06_49	mouth of Jasper Canyon with Blue Lake	SEDs 20cm thick separating Roza from ?Ginkgo	Roza - Ginkgo	contact material	0					
CRB06_271	N47.34.192	W119.25.365	06_49	mouth of Jasper Canyon with Blue Lake	upper 5-10cm fairly weakly weathered stretched vesc (no erosion) Ginkgo	Ginkgo	u/c	u/k					
CRB06_272	N47.34.192	W119.25.365	06_49	mouth of Jasper Canyon with Blue Lake	45cm below top of flow, last vesicular band	Ginkgo	u/c	u/k					
CRB06_273	N47.34.130	W119.25.372	06_49	mouth of Jasper Canyon with Blue Lake	3m down from flow top, within zones of vesc and non-vesc bands, but poorly developed	?SH	u/c	6.8					
CRB06_274	N47.34.130	W119.25.372	06_49	mouth of Jasper Canyon with Blue Lake	6m down from flow top within HVS zone, at u/c - core boundary	?SH	uc - core	4					
CRB06_275	N47.34.130	W119.25.372	06_49	mouth of Jasper Canyon with Blue Lake	8.5m down from flow top, between the end of HVS and start of vesc cylinders	?SH	core	2					
CRB06_276	N47.34.130	W119.25.372	06_49	mouth of Jasper Canyon with Blue Lake	50cm above flow base, pipe vesicles	?SH	l/c	0.2					
CRB06_277	N47.34.130	W119.25.372	06_49	mouth of Jasper Canyon with Blue Lake	50cm down from flow top, vesicular	?Ginkgo flow #2	u/c	6.5					
CRB06_278	N47.34.130	W119.25.372	06_49	mouth of Jasper Canyon with Blue Lake	3.5m down from flow top, just vesicular, above u/c - core boundary	?Ginkgo flow #2	u/c (base)	3					
CRB06_279	N47.34.130	W119.25.372	06_49	mouth of Jasper Canyon with Blue Lake	base 50cm of flow, vertical pipe vesicles	?Ginkgo flow #2	l/c	0.1					
CRB06_280	N47.34.130	W119.25.372	06_49	mouth of Jasper Canyon with Blue Lake	1m down from flow top, vesicular	?Ginkgo flow #1	u/c	u/k					
CRB06_281	N47.34.130	W119.25.372	06_49	mouth of Jasper Canyon with Blue Lake	4m down from flow top thickly jointed non-vesicular band with flow welded to top of flow beneath or v thick non-vesc band in u/c	?Ginkgo flow #1	?	u/k					
CRB06_282	N47.32.943	W119.24.974	06_49	junction of Jasper Canyon and Dry Coulee	from core of uppermost GR flow in this area	GRs	core	u/k					
CRB06_283	N47.32.622	W119.25.233	06_50	junction of Jasper Canyon and Dry Coulee	3m above u/c - core boundary	uppermost GR	u/c	8					
CRB06_284	N47.32.622	W119.25.233	06_50	junction of Jasper Canyon and Dry Coulee	just above the u/c - core boundary	uppermost GR	u/c	5					
CRB06_285	N47.32.622	W119.25.233	06_50	junction of Jasper Canyon and Dry Coulee	3m below the u/c - core boundary, wavy columns 30cm wide	uppermost GR	core	3					
CRB06_286	N46.38.516	W118.12.230	06_52	mouth of Winn Lake Canyon	1m below the top of the underlying GR flow, v weathered and red-orange	GRs	u/c	u/k		X			

Sample Number	Latitude	Longitude	Locality Number	Locality Description	Sample description	Stratigraphy	Position in flow	Height in section	Thin section	XRF	REE	Re-Os	Sr
CRB06_287	N46.38.516	W118.12.230	06_52	mouth of Winn Lake Canyon	3m above flow base, few v rounded vesicles	PF	core	2		X			
CRB06_288	N46.38.516	W118.12.230	06_52	mouth of Winn Lake Canyon	9m above flow base, beneath jointing horizon, below 6m gap in exposure	PF	core	8.5		X			
CRB06_289	N46.38.516	W118.12.230	06_52	mouth of Winn Lake Canyon	15m above base of flow	PF	core	11.5		X			
CRB06_290	N46.38.516	W118.12.230	06_52	mouth of Winn Lake Canyon	20m above base of flow, slightly thinner columns	PF	core	22		X			
CRB06_291	N46.38.516	W118.12.230	06_52	mouth of Winn Lake Canyon	13m above base of flow, between jointing horizons, just below u/c - core boundary	PF	core	26		X			
CRB06_292	N46.38.516	W118.12.230	06_52	mouth of Winn Lake Canyon	starting to become vesicular, just within u/c at 25m above flow base	PF	u/c	30		X			
CRB06_293	N46.38.516	W118.12.230	06_52	mouth of Winn Lake Canyon	36m above flow base, non vesicular band within u/c	PF	u/c	39.5		X			
CRB06_294	N46.38.516	W118.12.230	06_52	mouth of Winn Lake Canyon	42m above base of flow, above break that looks like a tumuli but has no core - is all vesicular	?PF breakout	u/c	47.5		X			
CRB06_295	N46.38.516	W118.12.230	06_52	mouth of Winn Lake Canyon	top of exposure and top of flow (forms a light bench), rounded top marking small lobes that have coalesced, 46-50m above base	PF	u/c	52		X			
CRB06_296	N46.39.409	W118.11.006	06-051	Winn Lake Canyon	vesicular top of the SH flow field	SH	u/c	u/k		X			
CRB06_297	N46.39.702	W118.10.543	06_53	Winn Lake Canyon	base of expo (presumed near base of flow) of flow above PF flow	FS flow #2	core	0		X			
CRB06_298	N46.39.702	W118.10.543	06_53	Winn Lake Canyon	7m above flow base, in horizontally jointed / fissile zone	FS flow #2	core	7		X			
CRB06_299	N46.39.702	W118.10.543	06_53	Winn Lake Canyon	11.5m above flow base at top of thick well-developed column zone	FS flow #2	core	11.5		X			
CRB06_300	N46.39.702	W118.10.543	06_53	Winn Lake Canyon	14.5m above flow base, just above core - u/c boundary at first vesicular zone	FS flow #2	u/c - core	14.5		X			
CRB06_301	N46.39.702	W118.10.543	06_53	Winn Lake Canyon	18m above flow base, within second vesicular band, with some large irregular shaped vesicles	FS flow #2	u/c	18		X			
CRB06_302	N46.39.702	W118.10.543	06_53	Winn Lake Canyon	22m above flow base (exposure top), vesicular (unknown if actual flow top but must be v close)	FS flow #2	u/c	22		X			
CRB06_303	N46.39.409	W118.11.006	06_53	Winn Lake Canyon	non-vesicular breakout on the top of the PF flow near the head of the canyon	?PF	core - breakout	1.5		X			
CRB06_304	N46.35.174	W118.13.345	06_54	Starbuck - Washtucna road section	High interval sampling across vesicular to non-vesicular bands, 10cm below core - u/c boundary	GR-N2 2	upper core	0		X			
CRB06_305	N46.35.174	W118.13.345	06_54	Starbuck - Washtucna road section	70cm above the u/c - core boundary above the MV horizon	GR-N2 2	u/c	0.8		X			
CRB06_306	N46.35.174	W118.13.345	06_54	Starbuck - Washtucna road section	1.1m above boundary, at base of vesc band #1	GR-N2 2	u/c	1.1		X			

Sample Number	Latitude	Longitude	Locality Number	Locality Description	Sample description	Stratigraphy	Position in flow	Height in section	Thin section	XRF	REE	Re-Os	Sr
CRB06_307	N46.35.174	W118.13.345	06_54	Starbuck - Washtucna road section	1.4m above boundary within vesc band #1	GR-N2 2	u/c	1.3		X			
CRB06_308	N46.35.174	W118.13.345	06_54	Starbuck - Washtucna road section	1.8m above boundary, at top of vesc band #1	GR-N2 2	u/c	1.9		X			
CRB06_309	N46.35.174	W118.13.345	06_54	Starbuck - Washtucna road section	2.3m above boundary at base of MV horizon within non-vesc zone	GR-N2 2	u/c	2.4		X			
CRB06_310	N46.35.174	W118.13.345	06_54	Starbuck - Washtucna road section	3m above boundary at base of vesc band #2	GR-N2 2	u/c	3		X			
CRB06_311	N46.35.174	W118.13.345	06_54	Starbuck - Washtucna road section	3.7m above boundary at top of vesc band #2	GR-N2 2	u/c	3.6		X			
CRB06_312	N46.35.174	W118.13.345	06_54	Starbuck - Washtucna road section	3.9m above boundary within non-vesc zone	GR-N2 2	u/c	3.9		X			
CRB06_313	N46.35.174	W118.13.345	06_54	Starbuck - Washtucna road section	4.2m above boundary within vesc band #3	GR-N2 2	u/c	4.3		X			
CRB06_314	N46.40.032	W118.13.380	06_55	Palouse Falls rapids	orientated samples, 75-80cm above base of flow	PF	core	0.8	X	X			
CRB06_315	N46.40.032	W118.13.380	06_55	Palouse Falls rapids	35-40cm above base of flow, few dispersed vesicles up to 1cm diameter	PF	l/c	0.4	X	X			
CRB06_316	N46.40.032	W118.13.380	06_55	Palouse Falls rapids	20-25cm above base of flow, banded vesicle zones	PF	l/c	0.3	X	X			
CRB06_317	N46.40.032	W118.13.380	06_55	Palouse Falls rapids	10-15cm above flow base	PF	l/c	0.2	X	X			
CRB06_318	N46.40.032	W118.13.380	06_55	Palouse Falls rapids	basal 5cm	PF	l/c	0.1	X	X			
CRB06_319	N46.41.277	W118.13.396	06_55	Palouse Falls railway cutting	high frequency sampling across vesicular to non-vesicular zones, well dispersed small vesicles 2m above railway line	PF	u/c	0		X			
CRB06_320	N46.41.277	W118.13.396	06_55	Palouse Falls railway cutting	1m above last sample, at base of vesicular zone	PF	u/c	1		X			
CRB06_321	N46.41.277	W118.13.396	06_55	Palouse Falls railway cutting	1.3m above first sample, in middle of vesicular zone	PF	u/c	1.2		X			
CRB06_322	N46.41.277	W118.13.396	06_55	Palouse Falls railway cutting	1.5m above first sample, at top of vesicular zone	PF	u/c	1.5		X			
CRB06_323	N46.41.277	W118.13.396	06_55	Palouse Falls railway cutting	1.8m above first sample, in poorly vesicular zone	PF	u/c	1.8		X			
CRB06_324	N45.41.916	W121.23.684	06_56	Locke Lake	50cm below flow top	Ginkgo	u/c	9.5					
CRB06_325	N45.41.916	W121.23.684	06_56	Locke Lake	2m below flow top, just beneath MV zone	Ginkgo	u/c	8.5					
CRB06_326	N45.41.916	W121.23.684	06_56	Locke Lake	3.6m below flow top, within zone of smaller vesicles in u/c	Ginkgo	u/c	6.3					
CRB06_327	N45.41.916	W121.23.684	06_56	Locke Lake	7.5m down from flow top, underneath last MV zone, above hackly joints ? Just beneath core - u/c boundary.	Ginkgo	?	3.2					
CRB06_328	N45.41.916	W121.23.684	06_56	Locke Lake	10m below flow top vesicular band ?another flow welded to this or still within the u/c	Ginkgo	?	1					

Sample Number	Latitude	Longitude	Locality Number	Locality Description	Sample description	Stratigraphy	Position in flow	Height in section	Thin section	XRF	REE	Re-Os	Sr
CRB06_329	N45.53.473	W118.17.192	06_57	S fork of the Walla Walla river	dyke contact	?SH	dyke	0		X			
CRB06_330	N45.53.473	W118.17.192	06_57	S fork of the Walla Walla river	50cm away from the contact into the dyke	?SH	dyke	0.5		X			
CRB06_331	N45.53.473	W118.17.192	06_57	S fork of the Walla Walla river	2m into the dyke	?SH	dyke	2		X			
CRB06_332	N45.53.473	W118.17.192	06_57	S fork of the Walla Walla river	8m into the dyke	?SH	dyke	8		X			
CRB06_333	N45.53.473	W118.17.192	06_57	S fork of the Walla Walla river	est 10m into the dyke (good pheno)	?SH	dyke	9		X			
CRB06_334	N45.53.473	W118.17.192	06_57	S fork of the Walla Walla river	country rock', unknown GR flow	?GR	country rock / u/c	-0.2		X			
CRB06_335	N45.56.980	W119.03.667	06_58	Wallula Gap	core	? Ginkgo	core	u/k					
CRB06_336	N45.57.757	W119.01.393	06_58	Wallula Gap	weathered u/c	?SH	u/c	0.2					
CRB06_337	N45.57.757	W119.01.393	06_58	Wallula Gap	u/c, est 6m above base of flow	?SH	u/c	6					
CRB06_338	N45.57.757	W119.01.393	06_58	Wallula Gap	u/c, est 5m above base of flow	?SH	u/c	5					
CRB06_339	N45.57.757	W119.01.393	06_58	Wallula Gap	top of core, just below u/c boundary, est 3m above base of flow	?SH	core	3					
CRB06_340	N45.57.757	W119.01.393	06_58	Wallula Gap	15cm above base of flow	?SH	l/c	0.15					
CRB06_341	N45.57.757	W119.01.393	06_58	Wallula Gap	top of Ginkgo flow, 1m below flow top	?SH	u/c	u/k					
CRB06_342	N45.58.102	W119.00.623	06_59	Wallula Gap	red weathered contact between two Ginkgo flows	Ginkgo	u/c	u/k					
CRB06_343	N46.01.835	W118.56.012	06_59	Wallula Gap	v pheno rich, top of flow (presumed as actual contact not seen) but believed to be as within 1.5-2m.	?Ginkgo	u/c	u/k					
CRB06_344	N46.01.835	W118.56.012	06_59	Wallula Gap	6m below flow top, base of v vesicular band	?Ginkgo	u/c	13					
CRB06_345	N46.01.835	W118.56.012	06_59	Wallula Gap	Base of third vesicular band, just above u/c - core boundary, 9m below flow top	?Ginkgo	u/c	11					
CRB06_346	N46.01.835	W118.56.012	06_59	Wallula Gap	top of core, 10m below flow top	?Ginkgo	core	9.5					
CRB06_347	N46.01.835	W118.56.012	06_59	Wallula Gap	14m below flow top, in middle of zone of finer columns with some horizon joints	?Ginkgo	core	5					
CRB06_348	N46.01.835	W118.56.012	06_59	Wallula Gap	base of middle zone, 16m below flow top	?Ginkgo	core	2.5					
CRB06_349	N46.01.835	W118.56.012	06_59	Wallula Gap	top of basal zone of v thick joints with v v large pheno cumulates, 2m above flow base	?Ginkgo	core	2		X			
CRB06_350	N46.01.835	W118.56.012	06_59	Wallula Gap	flow base, 5-10cm base	?Ginkgo	l/c	0.08		X			
CRB06_351	N46.46.823	W118.05.602	06_60	Washtucna State Road 126	Sampling strategy - 1m horizontal spacing	?	u/c	4		X			
CRB06_352	N46.46.823	W118.05.602	06_60	Washtucna State Road 126	351 to 353, 5m below top of exposure, at base of first principle vesicular band up from the core - u/c boundary, 351 is the most easterly of these three samples	?	u/c	4		X			
CRB06_353	N46.46.823	W118.05.602	06_60	Washtucna State Road 126	see above	?	u/c	4		X			

Sample Number	Latitude	Longitude	Locality Number	Locality Description	Sample description	Stratigraphy	Position in flow	Height in section	Thin section	XRF	REE	Re-Os	Sr
CRB06_354	N46.46.823	W118.05.602	06_60	Washtucna State Road 126	354 to 356, 5 cm above core - u/c boundary in fairly vesicular basalt, just beneath MV zone, 8m below top of exposure, 354 is the most easterly of these three samples	?	u/c	3		X			
CRB06_355	N46.46.823	W118.05.602	06_60	Washtucna State Road 126	see above	?	u/c	3		X			
CRB06_356	N46.46.823	W118.05.602	06_60	Washtucna State Road 126	see above	?	u/c	3		X			
CRB06_357	N46.46.823	W118.05.602	06_60	Washtucna State Road 126	357 to 359, samples 13m down from exposure top, just below HVS zone, 359 is the most easterly of these samples	?	core	2		X			
CRB06_358	N46.46.823	W118.05.602	06_60	Washtucna State Road 126	see above	?	core	2		X			
CRB06_359	N46.46.823	W118.05.602	06_60	Washtucna State Road 126	see above	?	core	2		X			
CRB06_360	N46.24.167	W118.38.615	06_61	S bank of Snake River, cliffs to the W of the Sheffler grain silos	SEDs, red with clasts of basalt	?PF / Ginkgo	contact material	0		X			
CRB06_361	N46.24.167	W118.38.615	06_61	S bank of Snake River, cliffs to the W of the Sheffler grain silos	glassy edge of small lobes / pillows at the base of the overlying flow, separated by splatter / hyaloclastite	?PF / Ginkgo	small lobes	-		X			
CRB06_362	N46.24.167	W118.38.615	06_61	S bank of Snake River, cliffs to the W of the Sheffler grain silos	50cm up from contact of small lobes with sediments, within core of 1m thick larger lobes beneath the main sheet	?PF / Ginkgo	small lobes	-		X			
CRB06_363	N46.24.167	W118.38.615	06_61	S bank of Snake River, cliffs to the W of the Sheffler grain silos	lowermost 20cm of flow, including glassy selvage (samples split into two - bottom and top), pipe vesicles with a slight orientation indicating flow to the south, very pheno rich at the base here	?PF / Ginkgo	l/c	0.1		X			
CRB06_364	N46.24.167	W118.38.615	06_61	S bank of Snake River, cliffs to the W of the Sheffler grain silos	vesicular upper to flow est.6m thick, deep red coloration	?PF / Ginkgo	u/c	5		X			
CRB06_365	N46.24.167	W118.38.615	06_61	S bank of Snake River, cliffs to the W of the Sheffler grain silos	large well developed columns, 2-3m wide, sample taken 1m above flow base, just below a major joint horizon, v.abundant phenos	?PF / Ginkgo	core	7		X			
CRB06_366	N46.24.167	W118.38.615	06_61	S bank of Snake River, cliffs to the W of the Sheffler grain silos	c.8m above base of this flow, at the core - u/c boundary, just above a few poorly developed vesicle cylinders, v few phenos in this area, those present usually large cumulates 1-2cm diam	?Ginkgo	core	12.7		X			
CRB06_367	N46.24.167	W118.38.615	06_61	S bank of Snake River, cliffs to the W of the Sheffler grain silos	30cm above u/c - core boundary	?Ginkgo	u/c	13.5		X			
CRB06_368	N46.24.167	W118.38.615	06_61	S bank of Snake River, cliffs to the W of the Sheffler grain silos	increase in the abundance of phenos, est 6m above last sample point, just below horiz joint	?Ginkgo	u/c	17		X			

Sample Number	Latitude	Longitude	Locality Number	Locality Description	Sample description	Stratigraphy	Position in flow	Height in section	Thin section	XRF	REE	Re-Os	Sr
CRB06_369	N46.24.167	W118.38.615	06_61	S bank of Snake River, cliffs to the W of the Sheffler grain silos	top of flow, just above c.3m of no exposure	?Ginkgo	u/c	22		X			
CRB06_370	N46.24.167	W118.38.615	06_61	S bank of Snake River, cliffs to the W of the Sheffler grain silos	base of overlying flow, above shattered basalt outcrop, v sparse phenos, few vesicles, basal 10cm	?SF	l/c	0.1		X			
CRB06_371	N46.24.167	W118.38.615	06_61	S bank of Snake River, cliffs to the W of the Sheffler grain silos	c. 4m above base of flow, well developed columns	?SF	core	4		X			
CRB06_372	N46.24.167	W118.38.615	06_61	S bank of Snake River, cliffs to the W of the Sheffler grain silos	7m above flow base, in horiz jointed / fissile zone,	?SF	core	7		X			
CRB06_373	N46.24.167	W118.38.615	06_61	S bank of Snake River, cliffs to the W of the Sheffler grain silos	12m above flow base, widening of columns and a few vesicles, top of core	?SF	core - u/c	12		X			
CRB06_374	N46.24.167	W118.38.615	06_61	S bank of Snake River, cliffs to the W of the Sheffler grain silos	13.5m above flow base, base of first vesicular zone, poor exposures	?SF	u/c	13.5		X			
CRB06_375	N46.24.167	W118.38.615	06_61	S bank of Snake River, cliffs to the W of the Sheffler grain silos	18m above flow base, thin columns, few vesicles	?SF	u/c	18		X			
CRB06_376	N46.24.167	W118.38.615	06_61	S bank of Snake River, cliffs to the W of the Sheffler grain silos	30-50cm below top of flow, lobate top - no erosion seen	?SF	u/c	20		X			
CRB06_377	N46.24.167	W118.38.615	06_61	S bank of Snake River, cliffs to the W of the Sheffler grain silos	SEDS - v thin layers of organic rich soil, overlying flow, no vesicles seen at base, v abundant conc of large single phenos in the basal 50cm	?SF - SH	contact material	0		X			
CRB06_378	N46.27.664	W118.37.781	06_63	cliffs to the west of the Gingko dyke outcrop	4m below flow top, top of core - non-vesicular, well developed columns	Dodge	core	u/k		X			
CRB06_379	N46.27.664	W118.37.781	06_63	cliffs to the west of the Gingko dyke outcrop	SEDS - from between the Dodge and PF flows	Dodge - PF	contact material	0					
CRB06_380	N46.27.664	W118.37.781	06_63	cliffs to the west of the Gingko dyke outcrop	basal 10cm of PF flow, elongate vesicles, parallel to the flow base	PF	l/c	0.1		X			
CRB06_381	N46.27.664	W118.37.781	06_63	cliffs to the west of the Gingko dyke outcrop	3.5m above flow base, top of thick columns	PF	core	8		X			
CRB06_382	N46.27.664	W118.37.781	06_63	cliffs to the west of the Gingko dyke outcrop	4.5m above flow base, base of thinly jointed columns	PF	core	11		X			
CRB06_383	N46.27.664	W118.37.781	06_63	cliffs to the west of the Gingko dyke outcrop	6.8m above flow base, start of vesicular band, core - u/c boundary	PF	core - u/c	17		X			
CRB06_384	N46.27.664	W118.37.781	06_63	cliffs to the west of the Gingko dyke outcrop	9.5m above flow base, middle of vesicular band	PF	u/c	23		X			
CRB06_385	N46.27.664	W118.37.781	06_63	cliffs to the west of the Gingko dyke outcrop	top of flow, 20cm below top (presumed top, direct contact with overlying Ginkgo not quite observed)	PF	u/c	32		X			
CRB06_386	N46.27.664	W118.37.781	06_63	cliffs to the west of the Gingko dyke outcrop	2m above base of Ginkgo	Ginkgo	core	2		X			

Sample Number	Latitude	Longitude	Locality Number	Locality Description	Sample description	Stratigraphy	Position in flow	Height in section	Thin section	XRF	REE	Re-Os	Sr
CRB06_387	N46.27.921	W118.37.640	06_64	Cliffs above the upper railroad grade, above the Gingko dyke	Base of flow, above baked soil (not sampled as couldn't reach), v weak stripey vesicular bands and horiz jointed	?Ginkgo	l/c	0.4		X			
CRB06_388	N46.27.921	W118.37.640	06_64	Cliffs above the upper railroad grade, above the Gingko dyke	1m above flow base, vesicular banding	?Ginkgo	l/c	2		X			
CRB06_389	N46.27.921	W118.37.640	06_64	Cliffs above the upper railroad grade, above the Gingko dyke	2m above flow base, vesicular banding	?Ginkgo	l/c	4.5		X			
CRB06_390	N46.27.921	W118.37.640	06_64	Cliffs above the upper railroad grade, above the Gingko dyke	5m above flow base, top of well developed columns	?Ginkgo	core	10		X			
CRB06_391	N46.27.921	W118.37.640	06_64	Cliffs above the upper railroad grade, above the Gingko dyke	irregular jointing, 6.5m above flow base, areas of segregation material, lacking particular shape	?Ginkgo	core	13		X			
CRB06_392	N46.27.921	W118.37.640	06_64	Cliffs above the upper railroad grade, above the Gingko dyke	core - u/c boundary, thin columns, 8.5m above flow base	?Ginkgo	core - u/c	16.5		X			
CRB06_393	N46.27.921	W118.37.640	06_64	Cliffs above the upper railroad grade, above the Gingko dyke	10.5m above flow base, poorly vesicular u/c	?Ginkgo	u/c	20		X			
CRB06_394	N46.27.921	W118.37.640	06_64	Cliffs above the upper railroad grade, above the Gingko dyke	13m above flow base, poorly vesc u/c	?Ginkgo	u/c	25		X			
CRB06_395	N46.27.921	W118.37.640	06_64	Cliffs above the upper railroad grade, above the Gingko dyke	16m above flow base, top of columns, above is horizon jointed and v vesciular (vesicles are orientated / stretched)	?Ginkgo	u/c	28		X			
CRB06_396	N46.27.921	W118.37.640	06_64	Cliffs above the upper railroad grade, above the Gingko dyke	19m above flow base, top of flow	?Ginkgo	u/c	33		X			
CRB06_397	N46.27.921	W118.37.640	06_64	Cliffs above the upper railroad grade, above the Gingko dyke	flow base of the overlying flow, abundant phenos	?SF	l/c	0.2		X			
CRB06_398	N46.27.921	W118.37.640	06_64	Cliffs above the upper railroad grade, above the Gingko dyke	sample from base of cliffs, 7m down in Dodge flow	Dodge	u/c - core?	u/k		X			
CRB06_399	N47.10.251	W119.58.757	06_65	Babcock Bench near Potholes Coulee	mid core, c 8m above outcrop base	Ginkgo - top flow	core	0		X			
CRB06_400	N47.10.251	W119.58.757	06_65	Babcock Bench near Potholes Coulee	4m above last sample, above HVS zone, lightly vesicular - diffuse core - u/c boundary	Ginkgo - top flow	core - u/c	4		X			
CRB06_401	N47.10.251	W119.58.757	06_65	Babcock Bench near Potholes Coulee	3.5m above flow base, flow top	Ginkgo - top flow	u/c	7		X			
CRB06_402	N47.10.251	W119.58.757	06_65	Babcock Bench near Potholes Coulee	flow base	?SH	l/c	0		X			

Sample Number	Latitude	Longitude	Locality Number	Locality Description	Sample description	Stratigraphy	Position in flow	Height in section	Thin section	XRF	REE	Re-Os	Sr
CRB06_403	N47.10.251	W119.58.757	06_65	Babcock Bench near Potholes Coulee	3.7m above flow base, horiz jointed / fissile zone	?SH	core	3.5		X			
CRB06_404	N47.10.251	W119.58.757	06_65	Babcock Bench near Potholes Coulee	6m above flow base, zone of thicker columns	?SH	core	6		X			
CRB06_405	N47.10.251	W119.58.757	06_65	Babcock Bench near Potholes Coulee	10.4m above flow base, core - u/c bnoundary	?SH	core - u/c	9		X			
CRB06_406	N47.10.251	W119.58.757	06_65	Babcock Bench near Potholes Coulee	14m above flow base, v vesicular u/c - flow top	?SH	u/c	11.5		X			
CRB06_407	N47.10.251	W119.58.757	06_65	Babcock Bench near Potholes Coulee	2m above flow base, irregular jointing	?Roza	core	15		X			
CRB06_408	N47.10.251	W119.58.757	06_65	Babcock Bench near Potholes Coulee	v vesicular u/c - 75cm below top of flow	?SH	u/c	33.5		X			
CRB06_409	N47.10.251	W119.58.757	06_65	Babcock Bench near Potholes Coulee	3m below flow top, vesicular u/c with phenos	?SH	u/c	31.5		X			
CRB06_410	N47.10.251	W119.58.757	06_65	Babcock Bench near Potholes Coulee	5.8m below flow top, 1m below the u/c - core boundary	?SH	core	28.5		X			
CRB06_411	N47.10.251	W119.58.757	06_65	Babcock Bench near Potholes Coulee	12m below flow top, top of thickly jointed area, below fissile zone	?SH	core	22.3		X			
CRB06_412	N47.10.251	W119.58.757	06_65	Babcock Bench near Potholes Coulee	second fissile zone, 16m below flow top	?SH	core	18.5		X			
CRB06_413	N47.10.251	W119.58.757	06_65	Babcock Bench near Potholes Coulee	19m below flow top, flow base, under vesicle cylinders	?SH	l/c	15.5		X			
CRB06_414	N47.10.251	W119.58.757	06_65	Babcock Bench near Potholes Coulee	8.2m above flow base, just below HVS zone	?SH	core	8.2		X			
CRB06_415	N65.55.109	W119.56.928	06_68	Road section to the south of Sand Hollow	top of columns, just below black band	SH	black band	-0.1		X			
CRB06_416	N65.55.109	W119.56.928	06_68	Road section to the south of Sand Hollow	1.5m above base of black band	SH	black band	1		X			
CRB06_417	N65.55.109	W119.56.928	06_68	Road section to the south of Sand Hollow	2.5m above base of black band	SH	black band	2.7		X			
CRB06_418	N65.55.109	W119.56.928	06_68	Road section to the south of Sand Hollow	4.2m above base of black band	SH	black band	4.5		X			
CRB06_419	N65.55.109	W119.56.928	06_68	Road section to the south of Sand Hollow	5.1m above base of black band	SH	black band	5.5		X			
CRB06_420	N65.55.109	W119.56.928	06_68	Road section to the south of Sand Hollow	5.8m above base of black band	SH	black band	5.8					
CRB06_421	N65.55.109	W119.56.928	06_68	Road section to the south of Sand Hollow	6.5m above base of black band	SH	black band	6.5					
CRB06_422	N65.55.109	W119.56.928	06_68	Road section to the south of Sand Hollow	20cm above top of black band	SH	black band	8					

Appendix B. Methods and analytical techniques

B.1 Sample preparation

The major and trace element and Re-Os isotope geochemistry in this thesis is based upon compositional data from whole rock analysis. Samples were split to remove any weathered or joint faces and powdered in an agate mill. Sample sizes of at least 300g were used to produce a homogenous powder representative of the whole rock sample. The quench cooled, glass-rich samples are finely crystalline in nature and contain very few phenocryst phases. As a result sample heterogeneities due to the irregular distribution of crystal phases are minimal ensuring analytical reproducibility. Avoidance of amydaloidal material where present, avoids the effects of secondary enrichment on the primary signature of elements such as Ba and Sr which may be susceptible to mobility during zeolite facies metamorphism (Wood *et al.* 76).

The samples were divided using a manual hydraulic rock splitter. These pieces were then fed into jaw crushers set on the finest setting. The crushate was placed in an agate Tema and milled until a fine powder (≤ 60 μm) formed. To reduce cross contamination thorough cleaning in addition to pre-contamination with a sample or cleaning with pure quartz was carried out at each stage.

B.2 Analytical Techniques

B.2.1 X-Ray Fluorescence Analysis

Major and trace element analyses were conducted on whole-rock powders, prepared as described above, following the XRF technique at the Open University as described by (Potts *et al.* 1984). Both major and trace element analyses were carried out using an ARL 8420+ dual goniometer wavelength dispersive XRF spectrometer equipped with 3kW

rhodium anode end-window X-ray tube, flow proportional and scintillation counters-fully collimated, diffracting crystals:AX06 (multilayer), PET (penta-erythrytol), Ge111, LiF200, LiF220.

B.2.1.1 Major element preparation

These analyses were performed on fused glass beads composed of exactly 0.7g of rock powder (dried over night at 1000C) and flux (lithium metaborate/tetraborate, Johnson Matthey Spectroflux 100B, dried at 110^{0}C over night). The rock and flux were mixed in Pt-5 % Au crucibles then fused at 1100°C for 15 minutes. The samples were swirled 3 times to ensure sample homogenisation, dissolution and removal of gas bubbles. The melt was transferred to the centre of a heated brass mould and pressed. The plunger was preheated to avoid thermal shock. The resulting glass beads were stored under glass evaporating dishes until cool in case of shattering.

To calculate the loss of volatiles during fusion, loss on ignition was carried out on approximately 1.2-1.25g of each sample of rock powder. Alumina crucibles were pre-ignited at 1000°C for at least 15 minutes and allowed to cool for 10 minutes before the rock sample was weighed out, recorded and the total mass of the sample plus crucible recorded. The samples were ignited in the furnace at 1000°C for 1 hour. After ignition the samples and crucibles were cooled and re-weighed. The percentage loss on ignition was calculated to two decimal places.

$$\text{Percentage loss on ignition} = \frac{\text{Loss or gain in weight of rock powder}}{\text{Original weight of rock powder}} \times 100$$

B.2.1.2. Trace element preparation

Trace element analysis was carried out on pressed pellets of approximately 10g of rock powder bound together with 0.7-1.0 ml of polyvinylpyrollidone (PVP). The moist powder

was pressed in a mould at 5 ton in^{-2} to a minimum thickness of 3.5 mm and dried overnight.

B.2.2 ICP-MS

Trace element concentrations were determined by ICP-MS following a method of Teflon® vial dissolution using HF, HNO_3 and HCl. Rock powders (~0.1 g) were digested in cleaned Teflon vessels using a 4:1 mixture of concentrated TD HF and TD HNO_3. After 24 hours on a hotplate at 130 °C, the solution was dried down, refluxed in 2ml of TD HNO_3 and 4ml of MQ H_2O for 24 hours at 130 °C, dried down again and refluxed in 3ml of TD HNO_3 and 6ml of MQ H_2O at 130 °C overnight. The sample was then transferred into a clean 125 ml Nalgene bottle and made up to 100 ml with MQ H_2O to form a 2 % HNO_3 solution. Trace element concentrations were determined by ICP-MS (Agilent 7500s) at the Open University. The instrument is fitted with a standard quartz spray chamber and a Babington nebuliser. Samples were aspirated at approximately 400µl min^{-1} with count rates of the order of 3 - 5 x 10^7 cps / ppm. Five international rock standards (BIR-1, W2, DNC-1, BHVO-2 and AGV-1) were simultaneously run and reproducibility is less than 4% (1σ).

Detection limits for elements with atomic masses greater than 85 are usually <10 ppt in solution (equivalent to 10 ppb in the rock), but they are somewhat higher for lighter elements (10-100 ppt in solution, 10-100 ppb in the rock). Precision is also routinely better than ±2 % for elements heavier than Rb (where concentrations exceed 0.5 ppm) and 2 – 4 % for elements lighter than Rb.

B.2.3 Sulphur determination by LECO

Sulphur concentrations were determined on a Leco CS230 at the University of Leicester using induction furnace combustion of samples followed by infra-red absorption to yield

sulphur content. The lower limit of detection is 23 ppm and average reproducibility is 1.32% (1σ). The methodology outlined below was utilised by operational staff to produce the sulphur abundances presented in chapter 4 of this thesis.

The sample (approximately 0.2 g) is weighed in to a ceramic crucible. Iron and tungsten/tin chip accelerants are added in order to facilitate burning and the crucible is loaded on to the machine. The system is initially purged with O_2 to drive off residual atmospheric gases. The O_2 then continues to stream throughout the combustion process. Power is applied until the accelerants are molten, with carbon given off as CO_2 and CO and sulphur given off as SO_2. A dust filter prevents silicates (a potential infra-red wavelength overlap) from entering the infra-red cells. The combustion gases are passed through a drying tube of magnesium perchlorate and then pass to the SO_2 infra-red cell. Once determined, the gases pass through a platinised silica gel catalyst to convert any CO to CO_2, with any SO_2 trapped out as SO_3. The CO_2 content is then determined in the CO_2 infra-red cell. The gases then vent from the system.

The infra-red absorption cells use a tungsten filament as the source, heated to approximately 850°C. The infra-red is then chopped *c.*85Hz and filtered to achieve a monochromatic infra-red wavelength corresponding to the energy of the CO_2 / SO_2 adsorption wavelengths respectively. The output of the cells were monitored at 4Hz, converted from an analogue signal to a digital signal and the areas of the peaks were integrated. These values are then corrected for sample weight, blank value and calibration factors to give a total sulphur result.

Appendix C – Repeat analyses of standards by XRF

Element (ppm)	Rb	Sr	Y	Zr	Nb	Ba	Pb	Th	U	Sc	V	Cr	Co	Ni	Cu	Zn	Ga	Mo	As	S
Approx. Detection Limit	2	2	2.0	2	1.5	12	5	4	3	5	5	4	2	3	3	3	3	2	5	50
BHVO-1 Recommended	11	403	27.6	179	19.0	139	3	1	0.4	32	317	289	45	121	136	105	21	1	0	102
BHVO-1	11	406	27.2	179	18.3	141	4	2	1	30	320	295	48	129	137	105	22	0	5	134
residual	*1.30*	*2.72*	*-0.49*	*1.31*	*-0.13*	*1.39*	*2.15*	*-0.11*	*0.74*	*-1.59*	*6.65*	*3.63*	*3.82*	*8.20*	*-0.97*	*1.64*	*0.45*	*-0.57*	*3.76*	*3.24*
BHVO-1	9	404	29.3	177	18.1	141	7	1	0	33	310	293	48	119	134	104	22	1	1	138
residual	*-0.50*	*0.22*	*1.61*	*-1.29*	*-0.33*	*1.79*	*5.05*	*-0.71*	*-0.26*	*0.71*	*-3.55*	*2.13*	*2.92*	*-1.60*	*-3.67*	*0.24*	*-0.25*	*0.13*	*-0.14*	*7.44*
BHVO-1	10	405	28.1	178	18.6	141	2	3	0	31	314	295	46	125	137	105	22	1	0	134
residual	*0.10*	*1.22*	*0.41*	*-0.19*	*0.17*	*2.09*	*0.35*	*0.69*	*-0.16*	*-0.59*	*1.15*	*4.03*	*1.82*	*4.10*	*-0.67*	*1.04*	*0.45*	*0.53*	*-0.64*	*3.24*
BHVO-1	9	405	29.1	178	19	139	2	2	1	32	318	289	47	122	135	103	23	2	0	126
residual	*-1.00*	*1.42*	*1.41*	*0.41*	*0.57*	*0.19*	*-0.15*	*-0.31*	*0.54*	*-0.29*	*5.15*	*-1.57*	*2.22*	*1.50*	*-3.17*	*-0.46*	*1.65*	*1.03*	*-0.94*	*-4.26*
BHVO-1	10	404	28.2	179	19	142	2	2	0	31	316	296	45	123	134	102	22	2	6	121
residual	*0.10*	*0.52*	*0.51*	*0.61*	*0.57*	*2.49*	*-0.05*	*0.49*	*-0.56*	*-0.59*	*3.15*	*5.13*	*0.72*	*2.40*	*-4.07*	*-1.46*	*-0.05*	*1.53*	*4.86*	*-9.06*
BHVO-1	9	407	29.5	179	19.5	137	2	3	0	31	313	289	44	126	140	105	24	2	1	131
residual	*-0.50*	*3.62*	*1.81*	*0.71*	*1.07*	*-2.31*	*0.15*	*1.59*	*-0.26*	*-1.29*	*0.35*	*-1.97*	*-0.18*	*4.70*	*1.93*	*1.34*	*2.05*	*1.03*	*-0.24*	*0.74*
BHVO-1	9	405	27.2	178	20.0	151	1	2	0	30	322	288	45	119	139	103	22	1	3	132
residual	*-0.205*	*1.023*	*-0.491*	*-0.191*	*1.568*	*11.786*	*-0.645*	*-0.009*	*0.236*	*-1.891*	*8.450*	*-2.673*	*0.118*	*-2.000*	*1.227*	*-0.259*	*-0.245*	*-0.068*	*1.859*	*1.241*
BHVO-1	10	403	27.0	179	20.2	141	0	1	1	33	316	296	47	121	136	104	22	1	2	132
residual	*0.295*	*-0.777*	*-0.691*	*1.309*	*1.768*	*2.186*	*-1.845*	*-0.909*	*0.736*	*1.109*	*3.050*	*4.927*	*2.018*	*-0.200*	*-1.573*	*-0.059*	*-0.245*	*0.632*	*0.959*	*1.741*
BHVO-1	9	403	27.5	179	18.5	145	0	1	1	36	314	291	44	118	139	105	22	0	2	135
residual	*-0.405*	*-0.777*	*-0.191*	*1.309*	*0.068*	*5.286*	*-1.845*	*-1.209*	*0.436*	*3.609*	*0.450*	*-0.073*	*-0.682*	*-3.100*	*1.127*	*1.041*	*-0.045*	*-0.568*	*-0.941*	*4.141*
BHVO-1	10	404	27.1	178	18.1	146	0	2	1	31	307	290	45	119	140	104	21	1	0	127
residual	*-0.005*	*0.923*	*-0.591*	*-0.391*	*-0.332*	*7.086*	*-1.845*	*-0.209*	*1.036*	*-1.291*	*-6.550*	*-0.973*	*0.618*	*-1.900*	*2.527*	*0.541*	*-0.445*	*-0.068*	*-0.941*	*-3.959*
BHVO-1	10	401	28.0	177	18.3	138	2	0	0	32	310	290	44	120	138	102	22	1	0	132
residual	*0.195*	*-2.177*	*0.309*	*-0.991*	*-0.132*	*-1.414*	*0.155*	*-1.909*	*-0.164*	*-0.391*	*-2.850*	*-1.273*	*-0.382*	*-0.600*	*-0.173*	*-1.259*	*-0.245*	*0.132*	*-1.141*	*1.841*
BHVO-1	9	402	26.8	178	17.8	133	2	0	0	29	320	289	43	120	137	101	22	0	-2	134
residual	*-0.405*	*-1.077*	*-0.891*	*0.009*	*-0.632*	*-6.114*	*-0.045*	*-2.209*	*-0.164*	*-2.691*	*7.150*	*-1.873*	*-1.382*	*-0.800*	*-0.473*	*-2.659*	*0.155*	*-0.168*	*-3.041*	*3.241*
BHVO-1	10	401	27.4	177	17.5	138	1	2	1	32	307	296	44	115	136	104	21	0	0	131
residual	*0.295*	*-2.177*	*-0.291*	*-0.591*	*-0.932*	*-1.614*	*-1.245*	*0.191*	*0.836*	*0.509*	*-6.550*	*4.627*	*-0.882*	*-5.800*	*-1.573*	*0.341*	*-0.645*	*-0.568*	*-1.141*	*0.441*
BHVO-1	10	405	28.0	177	18.5	125	2	3	0	31	307	287	42	120	143	103	23	1	-6	121
residual	*-0.005*	*1.823*	*0.309*	*-1.091*	*0.068*	*-13.814*	*0.355*	*1.191*	*-0.164*	*-0.891*	*-6.050*	*-4.273*	*-2.882*	*-1.100*	*5.127*	*-0.559*	*1.155*	*0.032*	*-7.341*	*-9.059*
BHVO-1	10	402	26.6	178	18.0	137	3	4	0	34	316	291	45	121	137	105	20	1	0	133
residual	*0.495*	*-1.177*	*-1.091*	*0.109*	*-0.432*	*-1.914*	*1.055*	*1.791*	*-0.164*	*1.609*	*2.650*	*0.327*	*0.318*	*0.300*	*-0.773*	*1.041*	*-1.445*	*0.032*	*-0.941*	*2.341*
BHVO-1	11	404	27.3	177	18.0	139	0	3	-3	32	315	288	43	119	139	104	20	1	0	125
residual	*0.895*	*0.623*	*-0.391*	*-0.691*	*-0.432*	*-0.314*	*-1.445*	*0.791*	*-2.864*	*-0.191*	*1.750*	*-3.173*	*-1.782*	*-1.400*	*1.327*	*0.741*	*-1.445*	*0.432*	*-0.941*	*-5.059*
BHVO-1	9	401	27.2	176	18.6	145	1	0	0	34	320	287	44	121	138	101	22	0	4	135
residual	*-0.905*	*-2.077*	*-0.491*	*-1.791*	*0.168*	*5.786*	*-0.545*	*-1.809*	*-0.164*	*1.709*	*6.450*	*-4.373*	*-0.282*	*0.300*	*0.127*	*-2.559*	*-0.245*	*-0.568*	*2.959*	*4.041*
BHVO-1	10	402	27.5	178	18.1	136	3	1	0	32	315	288	43	120	138	104	21	0	2	122
residual	*0.695*	*-1.477*	*-0.191*	*0.409*	*-0.332*	*-3.214*	*0.855*	*-1.009*	*-0.164*	*-0.191*	*2.350*	*-2.673*	*-2.082*	*-0.900*	*0.427*	*0.441*	*-0.345*	*-0.668*	*0.659*	*-8.259*
BHVO-1	9	403	28	179	18.2	136	4	2	1	32	303	288	43	121	139	103	21	0	1	139
residual	*-0.405*	*-0.777*	*-0.091*	*0.709*	*-0.232*	*-3.614*	*2.355*	*0.091*	*0.636*	*0.009*	*-9.650*	*-2.873*	*-1.682*	*-0.100*	*0.827*	*-0.759*	*-0.645*	*-0.368*	*-0.141*	*8.341*
BHVO-1	10	403	27	179	18.2	131	0	2	0	35	308	293	44	123	136	105	22	0	3	128
residual	*0.795*	*-0.377*	*-0.291*	*1.309*	*-0.232*	*-8.314*	*-1.945*	*-0.309*	*0.236*	*3.109*	*-4.950*	*1.727*	*-0.882*	*2.000*	*-1.973*	*1.341*	*-0.145*	*-0.768*	*1.859*	*-2.559*
BHVO-1	9	402	27.6	177	17.2	142	3	3	0	31	310	291	45	120	139	104	22	0	0	131
residual	*-0.705*	*-1.777*	*-0.091*	*-1.291*	*-1.232*	*2.486*	*0.955*	*1.191*	*-0.164*	*-0.991*	*-2.850*	*0.027*	*-0.082*	*-0.900*	*0.827*	*0.441*	*0.655*	*-0.568*	*-0.741*	*0.841*
BHVO-1	10	404	27.6	178	17.8	139	0	5	0	32	307	292	43	118	141	103	22	0	3	130
residual	*-0.105*	*0.523*	*-0.091*	*0.309*	*-0.632*	*0.086*	*-1.845*	*2.691*	*-0.164*	*0.509*	*-5.750*	*1.227*	*-1.382*	*-3.100*	*3.627*	*-0.159*	*0.055*	*-0.568*	*2.359*	*-0.659*
Average	9.605	403.477	27.691	177.891	18.432	139.214	1.845	1.809	0.164	31.891	313.050	290.873	44.582	120.800	137.673	103.559	21.745	0.568	0.941	130.459
sum of square residuals	7.450	53.899	12.418	18.438	11.468	611.626	60.575	33.058	12.751	49.918	573.295	192.904	61.153	187.200	106.884	29.473	14.995	8.528	131.553	503.553
Std Dev	0.582	1.565	0.751	0.915	0.722	5.273	1.659	1.226	0.761	1.506	5.105	2.961	1.667	2.917	2.204	1.157	0.826	0.623	2.445	4.784
Std Error	0.124	0.334	0.160	0.195	0.154	1.124	0.354	0.261	0.162	0.321	1.088	0.631	0.355	0.622	0.470	0.247	0.176	0.133	0.521	1.020

Table C.1 Repeat analyses of BHVO_1 standard.

Element wt %	SiO_2	TiO_2	Al_2O_3	Fe_2O_3	MnO	MgO	CaO	Na_2O	K_2O	P_2O_5	S%	LOI	Total
WS-E Recommended	**51.10**	**2.400**	**13.78**	**13.15**	**0.171**	**5.55**	**8.95**	**2.47**	**1.00**	**0.302**	**0.05**	**0.85**	**99.77**
WS-E	51.07	2.390	13.84	13.21	0.173	5.56	9.03	2.42	0.99	0.310	0.05	0.85	99.91
residual	0.01	-0.04	-0.05	0.06	0.00	0.00	0.02	-0.03	0.00	0.01	-0.02	0.00	-0.02
WS-E	51.16	2.393	13.95	13.13	0.175	5.58	8.94	2.42	0.99	0.303	0.05	0.85	99.95
residual	0.11	-0.03	0.06	-0.02	0.01	0.02	-0.07	-0.03	0.00	0.00	-0.02	0.00	0.02
WS-E	51.18	2.388	13.89	13.19	0.172	5.56	9.05	2.44	1.00	0.303	0.05	0.85	100.06
residual	0.12	-0.04	0.00	0.04	0.00	-0.01	0.04	-0.02	0.01	0.00	-0.02	0.00	0.13
WS-E	51.32	2.389	13.90	13.12	0.174	5.58	8.96	2.44	1.00	0.298	0.05	0.85	100.08
residual	0.26	-0.04	0.01	-0.02	0.00	0.02	-0.05	-0.02	0.01	0.00	-0.02	0.00	0.15
WS-E	51.25	2.382	13.90	13.15	0.173	5.56	8.97	2.45	0.99	0.306	0.05	0.85	100.03
residual	0.19	-0.05	0.01	0.00	0.00	0.00	-0.05	0.00	0.00	0.00	-0.02	0.00	0.10
WS-E	51.25	2.388	13.90	13.16	0.171	5.61	8.94	2.46	0.99	0.306	0.05	0.85	100.08
residual	0.19	-0.04	0.01	0.01	0.00	0.05	-0.07	0.00	0.00	0.00	-0.02	0.00	0.15
WS-E	51.02	2.431	13.97	13.18	0.167	5.52	9.07	2.47	1.00	0.303	0.07	0.85	100.06
residual	-0.03	0.00	0.08	0.03	0.00	-0.04	0.06	0.01	0.01	0.00	0.00	0.00	0.12
WS-E	50.97	2.440	13.99	13.16	0.169	5.56	9.03	2.46	0.99	0.297	0.07	0.85	99.98
residual	-0.09	0.01	0.10	0.01	0.00	0.00	0.02	0.00	0.00	-0.01	0.00	0.00	0.05
WS-E	50.96	2.436	13.90	13.16	0.169	5.59	9.06	2.46	0.99	0.307	0.07	0.85	99.95
residual	-0.10	0.01	0.01	0.02	0.00	0.03	0.05	0.00	0.00	0.00	0.00	0.00	0.02
WS-E	51.07	2.444	13.86	13.17	0.169	5.58	9.02	2.46	1.00	0.299	0.07	0.85	100.00
residual	0.01	0.02	-0.02	0.02	0.00	0.02	0.01	0.01	0.00	0.00	0.00	0.00	0.06
WS-E	50.95	2.442	13.87	13.16	0.170	5.58	9.02	2.48	0.99	0.299	0.07	0.85	99.88
residual	-0.11	0.01	-0.02	0.01	0.00	0.02	0.01	0.03	0.00	0.00	0.00	0.00	-0.05
WS-E	50.99	2.437	13.90	13.18	0.167	5.56	9.05	2.46	1.00	0.302	0.07	0.85	99.96
residual	-0.06	0.01	0.01	0.03	0.00	0.00	0.04	0.00	0.01	0.00	0.00	0.00	0.03
WS-E	50.95	2.429	13.88	13.14	0.168	5.58	9.05	2.48	0.99	0.309	0.07	0.85	99.90
residual	-0.10	0.00	-0.01	-0.01	0.00	0.01	0.04	0.03	0.00	0.01	0.00	0.00	-0.04
WS-E	50.96	2.442	13.89	13.14	0.167	5.55	8.99	2.46	0.99	0.303	0.07	0.85	99.81
residual	-0.10	0.01	0.00	-0.01	0.00	-0.02	-0.02	0.00	0.00	0.00	0.00	0.00	-0.12
WS-E	50.85	2.435	13.90	13.13	0.169	5.53	9.02	2.47	1.00	0.305	0.07	0.85	99.73
residual	-0.21	0.01	0.01	-0.02	0.00	-0.04	0.01	0.02	0.01	0.00	0.01	0.00	-0.20
WS-E	51.03	2.439	13.89	13.12	0.170	5.51	9.01	2.44	1.00	0.304	0.07	0.85	99.82
residual	-0.03	0.01	0.00	-0.03	0.00	-0.05	0.00	-0.02	0.00	0.00	0.00	0.00	-0.11
WS-E	51.11	2.440	13.87	13.13	0.170	5.56	9.00	2.46	0.98	0.303	0.07	0.85	99.93
residual	0.05	0.01	-0.02	-0.02	0.00	-0.01	-0.01	0.00	-0.01	0.00	0.01	0.00	0.00
WS-E	51.08	2.443	13.88	13.12	0.169	5.53	9.00	2.43	0.99	0.309	0.07	0.85	99.87
residual	0.02	0.01	-0.01	-0.02	0.00	-0.03	-0.01	-0.03	0.00	0.01	0.01	0.00	-0.06
WS-E	50.97	2.443	13.86	13.14	0.169	5.58	8.99	2.44	0.99	0.302	0.07	0.85	99.82
residual	-0.09	0.02	-0.03	0.00	0.00	0.02	-0.02	-0.02	0.00	0.00	0.01	0.00	-0.11
WS-E	51.13	2.434	13.87	13.12	0.168	5.55	8.99	2.47	0.99	0.298	0.07	0.85	99.94
residual	0.07	0.01	-0.01	-0.03	0.00	-0.02	-0.02	0.02	0.00	0.00	0.01	0.00	0.01
WS-E	51.04	2.450	13.84	13.15	0.170	5.51	8.99	2.46	1.00	0.305	0.07	0.85	99.84
residual	-0.01	0.02	-0.05	0.00	0.00	-0.05	-0.02	0.01	0.00	0.00	0.01	0.00	-0.09
WS-E	50.97	2.429	13.90	13.16	0.169	5.56	9.03	2.45	0.99	0.306	0.07	0.85	99.88
residual	-0.09	0.00	0.01	0.01	0.00	-0.01	0.02	0.00	0.00	0.00	0.00	0.00	-0.05
WS-E	51.02	2.438	13.86	13.16	0.169	5.58	9.00	2.45	0.99	0.300	0.07	0.85	99.88
residual	-0.04	0.01	-0.03	0.01	0.00	0.02	-0.01	-0.01	0.00	0.00	0.00	0.00	-0.05
WS-E	51.14	2.440	13.87	13.13	0.170	5.54	8.99	2.43	0.99	0.303	0.07	0.85	99.92
residual	0.08	0.01	-0.02	-0.02	0.00	-0.02	-0.02	-0.02	-0.01	0.00	0.01	0.00	-0.01
WS-E	51.11	2.446	13.89	13.14	0.172	5.58	9.03	2.49	0.99	0.301	0.07	0.85	100.06
residual	0.05	0.02	0.00	0.00	0.00	0.01	0.02	0.03	0.00	0.00	0.00	0.00	0.13
WS-E	51.07	2.427	13.87	13.12	0.168	5.59	9.00	2.43	0.98	0.303	0.07	0.85	99.88
residual	0.01	0.00	-0.02	-0.03	0.00	0.02	-0.01	-0.02	-0.01	0.00	0.01	0.00	-0.05
WS-E	50.97	2.439	13.88	13.15	0.168	5.59	9.03	2.50	0.99	0.301	0.07	0.85	99.92
residual	-0.09	0.01	-0.01	0.00	0.00	0.03	0.01	0.04	0.00	0.00	0.00	0.00	-0.01
WS-E	51.05	2.437	13.87	13.14	0.169	5.56	9.02	2.47	0.99	0.300	0.07	0.85	99.92
residual	-0.01	0.01	-0.02	-0.01	0.00	0.00	0.01	0.01	0.00	0.00	0.00	0.00	-0.01
Average	51.06	2.43	13.89	13.15	0.17	5.56	9.01	2.46	0.99	0.30	0.07	0.85	99.93
sum of square residuals	0.31	0.01	0.03	0.01	0.00	0.02	0.03	0.01	0.00	0.00	0.00	0.00	0.22
Std Dev	0.1058	0.0211	0.0331	0.0221	0.0020	0.0256	0.0325	0.0192	0.0051	0.0034	0.0085	0.0000	0.0880
std error	0.0200	0.0040	0.0063	0.0042	0.0004	0.0048	0.0061	0.0036	0.0010	0.0006	0.0016	0.0000	0.0166

Table C.2 Repeat analyses of WS_E standard.

	SiO_2	TiO_2	Al_2O_3	Fe_2O_3	MnO	MgO	CaO	Na_2O	K_2O	P_2O_5	S%	LOI	Total
OUG94 Recommended	**69.95**	**0.314**	**14.66**	**3.05**	**0.075**	**1.04**	**1.34**	**4.60**	**2.96**	**0.165**	**0.01**	**1.97**	**100.13**
OUG94	69.73	0.317	14.58	3.06	0.078	1.04	1.40	4.54	2.96	0.171	0.01	1.97	99.84
residual	-0.19	0.00	-0.05	0.01	0.00	-0.01	0.03	-0.06	-0.01	0.00	0.00	0.00	-0.27
OUG94	69.87	0.315	14.67	3.06	0.077	1.04	1.39	4.54	2.94	0.174	0.00	1.97	100.05
residual	-0.05	0.00	0.04	0.02	0.00	-0.01	0.02	-0.06	-0.02	0.00	0.00	0.00	-0.06
OUG94	69.88	0.318	14.55	3.06	0.080	1.06	1.39	4.58	2.96	0.173	0.00	1.97	100.02
residual	-0.04	0.01	-0.08	0.02	0.00	0.01	0.02	-0.03	-0.01	0.00	0.00	0.00	-0.09
OUG94	70.04	0.317	14.65	3.05	0.078	1.05	1.39	4.55	2.97	0.171	0.01	1.97	100.23
residual	0.12	0.01	0.02	0.00	0.00	0.00	0.02	-0.05	0.00	0.00	0.00	0.00	0.13
OUG94	69.76	0.307	14.62	3.05	0.077	1.04	1.37	4.59	2.94	0.173	0.01	1.97	99.91
residual	-0.16	-0.01	-0.01	0.01	0.00	-0.01	0.01	-0.01	-0.02	0.00	0.00	0.00	-0.20
OUG94	70.00	0.314	14.62	3.06	0.077	1.05	1.38	4.54	2.96	0.171	0.01	1.97	100.16
residual	0.08	0.00	-0.01	0.01	0.00	0.01	0.02	-0.06	-0.01	0.00	0.00	0.00	0.05
OUG94	69.81	0.312	14.74	3.04	0.075	1.04	1.36	4.61	2.98	0.167	0.01	1.97	100.11
residual	-0.11	0.00	0.11	0.00	0.00	-0.01	-0.01	0.01	0.01	0.00	0.00	0.00	0.00
OUG94	69.86	0.305	14.74	3.04	0.075	1.05	1.36	4.61	3.00	0.169	0.01	1.97	100.19
residual	-0.06	-0.01	0.11	0.00	0.00	0.00	-0.01	0.01	0.03	0.00	0.00	0.00	0.08
OUG94	69.86	0.314	14.61	3.04	0.075	1.06	1.36	4.63	2.96	0.169	0.01	1.97	100.05
residual	-0.06	0.00	-0.02	0.00	0.00	0.01	-0.01	0.03	-0.01	0.00	0.00	0.00	-0.06
OUG94	69.99	0.313	14.65	3.04	0.075	1.06	1.37	4.62	2.97	0.163	0.01	1.97	100.23
residual	0.07	0.00	0.02	0.00	0.00	0.01	0.00	0.02	0.00	-0.01	0.00	0.00	0.12
OUG94	69.91	0.306	14.61	3.05	0.078	1.06	1.36	4.63	2.97	0.172	0.01	1.97	100.12
residual	-0.01	-0.01	-0.02	0.00	0.00	0.02	-0.01	0.02	0.00	0.00	0.00	0.00	0.01
OUG94	69.63	0.315	14.62	3.04	0.076	1.04	1.36	4.59	2.97	0.171	0.01	1.97	99.80
residual	-0.29	0.00	-0.01	0.00	0.00	0.00	0.00	-0.01	0.01	0.00	0.00	0.00	-0.30
OUG94	69.92	0.313	14.60	3.04	0.075	1.03	1.37	4.63	2.97	0.168	0.01	1.97	100.10
residual	0.01	0.00	-0.03	0.00	0.00	-0.01	0.00	0.03	0.00	0.00	0.00	0.00	-0.01
OUG94	69.80	0.309	14.61	3.04	0.076	1.03	1.36	4.59	2.96	0.169	0.01	1.97	99.93
residual	-0.12	0.00	-0.01	0.00	0.00	-0.02	-0.01	-0.02	0.00	0.00	0.00	0.00	-0.18
OUG94	69.87	0.307	14.63	3.04	0.076	1.04	1.37	4.59	2.97	0.169	0.01	1.97	100.03
residual	-0.05	-0.01	0.00	-0.01	0.00	-0.01	0.00	-0.02	0.00	0.00	0.00	0.00	-0.08
OUG94	69.90	0.314	14.61	3.04	0.074	1.03	1.36	4.58	2.97	0.169	0.01	1.97	100.04
residual	-0.02	0.00	-0.02	-0.01	0.00	-0.01	0.00	-0.02	0.00	0.00	0.00	0.00	-0.07
OUG94	69.95	0.308	14.59	3.04	0.077	1.04	1.35	4.59	2.96	0.169	0.01	1.97	100.05
residual	0.03	0.00	-0.04	-0.01	0.00	0.00	-0.01	-0.01	0.00	0.00	0.00	0.00	-0.05
OUG94	69.98	0.308	14.60	3.04	0.075	1.05	1.36	4.61	2.98	0.173	0.01	1.97	100.15
residual	0.06	0.00	-0.03	-0.01	0.00	0.01	0.00	0.01	0.01	0.00	0.00	0.00	0.04
OUG94	70.02	0.315	14.63	3.04	0.077	1.04	1.36	4.60	2.97	0.171	0.01	1.97	100.21
residual	0.10	0.00	0.00	0.00	0.00	0.00	0.00	0.00	0.00	0.00	0.00	0.00	0.10
OUG94	69.97	0.311	14.59	3.04	0.075	1.06	1.35	4.62	2.97	0.171	0.01	1.97	100.13
residual	0.05	0.00	-0.04	-0.01	0.00	0.01	-0.02	0.02	0.00	0.00	0.00	0.00	0.02
OUG94	69.97	0.313	14.62	3.04	0.075	1.05	1.36	4.64	2.96	0.168	0.01	1.97	100.18
residual	0.05	0.00	-0.01	-0.01	0.00	0.00	-0.01	0.04	0.00	0.00	0.00	0.00	0.07
OUG94	69.88	0.309	14.61	3.04	0.076	1.03	1.37	4.62	2.96	0.167	0.01	1.97	100.04
residual	-0.04	0.00	-0.02	0.00	0.00	-0.01	0.00	0.02	0.00	0.00	0.00	0.00	-0.07
OUG94	70.06	0.307	14.62	3.05	0.076	1.06	1.35	4.60	2.96	0.172	0.01	1.97	100.23
residual	0.14	-0.01	-0.01	0.00	0.00	0.01	-0.02	0.00	-0.01	0.00	0.00	0.00	0.12
OUG94	70.07	0.314	14.59	3.04	0.076	1.05	1.36	4.63	2.97	0.171	0.01	1.97	100.24
residual	0.15	0.00	-0.04	-0.01	0.00	0.00	-0.01	0.03	0.01	0.00	0.00	0.00	0.14
OUG94	70.05	0.313	14.66	3.04	0.075	1.04	1.36	4.60	2.98	0.173	0.01	1.97	100.26
residual	0.13	0.00	0.03	0.00	0.00	-0.01	-0.01	-0.01	0.01	0.00	0.00	0.00	0.15
OUG94	69.95	0.313	14.67	3.04	0.075	1.04	1.36	4.65	2.95	0.169	0.01	1.97	100.20
residual	0.03	0.00	0.04	0.00	0.00	0.00	-0.01	0.05	-0.01	0.00	0.00	0.00	0.10
OUG94	70.04	0.316	14.65	3.05	0.078	1.06	1.36	4.64	2.98	0.170	0.01	1.97	100.33
residual	0.12	0.00	0.02	0.01	0.00	0.01	0.00	0.04	0.01	0.00	0.00	0.00	0.22
OUG94	69.95	0.317	14.69	3.04	0.076	1.07	1.36	4.63	2.97	0.169	0.01	1.97	100.25
residual	0.03	0.00	0.06	0.00	0.00	0.02	0.00	0.03	0.01	0.00	0.00	0.00	0.14
Average	69.92	0.31	14.63	3.04	0.08	1.05	1.37	4.60	2.97	0.17	0.01	1.97	100.11
sum of square residuals	0.31	0.00	0.05	0.00	0.00	0.00	0.00	0.03	0.00	0.00	0.00	0.00	0.46
Std Dev	0.1055	0.0038	0.0426	0.0075	0.0014	0.0100	0.0123	0.0306	0.0107	0.0023	0.0014	0.0000	0.1282
Std Error	0.0199	0.0007	0.0080	0.0014	0.0003	0.0019	0.0023	0.0058	0.0020	0.0004	0.0003	0.0000	0.0242

Table C.3 Repeat analyses of OUG94 standard.

Sample No. wt. %	FSc7	FSc7	FSc7	FSc7	FSc7	FSc7	FSc7	FSc7	FSc7	FSc7	Std Dev (2σ)
SiO2	50.81	50.58	50.66	50.47	50.74	50.82	50.65	50.76	50.64	50.65	0.215
TiO2	3.321	3.325	3.312	3.318	3.306	3.334	3.316	3.331	3.314	3.311	0.018
Al2O3	14.67	14.60	14.64	14.56	14.66	14.64	14.59	14.62	14.61	14.60	0.069
Fe2O3	13.44	13.45	13.40	13.41	13.40	13.41	13.39	13.37	13.37	13.39	0.051
MnO	0.206	0.207	0.205	0.207	0.208	0.207	0.205	0.208	0.203	0.205	0.004
MgO	3.33	3.32	3.35	3.33	3.33	3.32	3.36	3.35	3.36	3.34	0.030
CaO	9.13	9.13	9.13	9.12	9.12	9.13	9.09	9.07	9.09	9.07	0.050
Na2O	2.91	2.91	2.89	2.84	2.86	2.88	2.87	2.92	2.85	2.86	0.058
K2O	1.25	1.25	1.26	1.26	1.26	1.25	1.26	1.26	1.26	1.25	0.012
P2O5	0.719	0.709	0.715	0.704	0.711	0.710	0.704	0.709	0.710	0.714	0.010
LOI	0.48	0.48	0.48	0.48	0.48	0.48	0.48	0.48	0.48	0.48	
Total	100.28	99.98	100.05	99.70	100.07	100.19	99.92	100.08	99.89	99.87	

Sample No. ppm	FSc7	FSc7	FSc7	FSc7	FSc7	FSc7	FSc7	FSc7	FSc7	FSC7	FSC7	Std Dev (2σ)
Rb	31	33	32	33	32	32	32	33	33	33	33	1.184
Sr	338	341	341	343	338	340	337	340	341	340	339	3.247
Y	48.9	49.4	49.0	48.7	49.0	49.4	48.1	49.2	48.5	49.3	48.5	0.841
Zr	222	221	221	220	221	220	222	222	223	220	220	1.621
Nb	17.4	17.8	18.1	17.1	17.5	17.4	18.0	17.5	18.0	17.5	16.8	0.797
Ba	590	592	583	580	597	590	602	594	588	587	571	16.540
Pb	8	9	7	7	8	10	7	8	10	12	7	3.259
Th	5	3	5	3	5	8	5	3	5	5	6	2.495
U	4	4	4	1	2	4	3	4	4	3	5	2.008
Sc	40	39	40	40	42	40	39	40	42	39	39	2.136
V	505	508	511	512	498	498	501	506	501	507	513	11.009
Cr	31	34	33	34	34	36	38	37	34	34	32	4.125
Co	33	34	32	32	33	33	33	33	34	33	35	1.779
Ni	20	21	22	21	18	21	18	21	22	21	23	3.072
Cu	36	35	36	38	35	36	37	37	38	36	36	2.134
Zn	162	166	161	161	164	164	158	162	160	162	162	3.733
Ga	23	23	23	23	23	24	23	23	24	23	24	0.772
Mo	1	2	2	1	1	1	2	2	1	1	1	0.921
As	1	4	3	0	0	0	0	0	7	2	1	4.472
S	738	741	734	726	755	749	728	756	728	757	726	24.917

Sample No. wt. %	DCy5	DCy5	DCy5	DCy5	DCy5	DCy5	DCy5	DCy5	DCy5	DCy5	Std Dev (2σ)
SiO2	51.12	51.15	51.11	51.13	51.39	51.28	51.26	51.30	51.12	51.31	0.205
TiO2	1.677	1.672	1.675	1.689	1.691	1.682	1.691	1.676	1.673	1.685	0.015
Al2O3	14.53	14.53	14.58	14.59	14.66	14.58	14.55	14.55	14.53	14.62	0.087
Fe2O3	11.90	11.88	11.87	11.86	11.86	11.84	11.84	11.84	11.85	11.86	0.037
MnO	0.180	0.179	0.181	0.179	0.181	0.178	0.181	0.180	0.183	0.182	0.003
MgO	6.64	6.64	6.63	6.56	6.68	6.64	6.69	6.63	6.61	6.68	0.080
CaO	10.56	10.55	10.55	10.54	10.55	10.54	10.51	10.51	10.50	10.45	0.070
Na2O	2.36	2.39	2.37	2.38	2.35	2.34	2.38	2.35	2.35	2.38	0.037
K2O	0.66	0.66	0.66	0.65	0.66	0.67	0.66	0.66	0.65	0.66	0.011
P2O5	0.241	0.242	0.241	0.243	0.246	0.242	0.244	0.250	0.241	0.241	0.006
LOI	0.23	0.23	0.23	0.23	0.23	0.23	0.23	0.23	0.23	0.23	
Total	100.10	100.12	100.10	100.05	100.49	100.21	100.23	100.17	99.92	100.30	

Sample No. ppm	DCy5	DCy5	DCy5	DCy5	DCy5	DCy5	DCy5	DCy5	DCy5	DCy5	DCy5	Std Dev (2σ)
Rb	16	16	15	16	16	17	15	17	16	15	15	1.258
Sr	233	231	234	233	233	233	233	233	234	234	232	1.778
Y	31.8	30.4	31.6	32.1	32.3	31.5	30.9	31.3	31.1	31.5	31.0	1.124
Zr	147	144	148	146	146	146	148	148	147	148	147	2.424
Nb	13.0	13.3	14.3	13.4	12.2	13.1	13.0	14.3	13.3	13.9	13.7	1.289
Ba	265	261	268	269	262	276	265	265	271	262	279	9.491
Pb	5	5	4	4	5	4	5	4	3	3	6	1.137
Th	5	4	3	4	3	2	4	4	4	4	3	1.569
U	1	0	0	1	1	0	0	0	1	0	1	1.133
Sc	30	33	30	32	33	35	32	32	32	33	37	3.074
V	279	269	271	276	273	274	268	280	276	273	273	8.233
Cr	92	93	94	96	96	96	96	91	92	94	96	3.867
Co	41	43	42	39	43	38	40	41	41	37	39	3.651
Ni	46	48	48	45	44	45	45	44	46	44	49	2.877
Cu	54	52	55	52	55	57	55	55	53	53	55	2.926
Zn	97	95	99	99	96	94	96	96	97	97	97	3.084
Ga	18	20	19	21	19	20	19	20	21	19	19	1.717
Mo	0	1	1	1	0	1	0	2	1	1	1	1.219
As	3	0	2	2	5	5	3	4	2	2	0	3.183
S	283	271	272	289	272	279	276	286	279	266	269	14.782

Table C.4. Repeat XRF data for CRB samples FSc7 from the Roza flow field at Frenchman Springs Coulee (N47.01'45.62" W119.57'48.72") and DCy5 from the Pomona flow field at Devil's Canyon (N46.35' 31.70" W118.32'50.24"). Samples acquired by Steve Self in 2004 and analysed at the OU labs as part of this study.

Appendix D – XRF major and trace element results

Grey areas within these tables indicate samples that lie within the core of a lobe whilst clear areas indicate samples from the upper and lower crusts.

Table D.1 Major and trace element results of samples from the Palouse Falls flow field

Sample locality			N side snake middle-distal						N side Snake - middle										Lower Monumental Dam						
Sample no.	CRB06-048	CRB06-049	CRB06-050	CRB06-051	CRB06-052	CRB06-053	CRB06-054	CRB06-055	CRB06-058	CRB06-059	CRB06-060	CRB06-061	CRB06-062	CRB06-063	CRB06-073	CRB06-079	CRB06-080	CRB06-081	CRB06-082	CRB06-083	CRB06-084				
Flow field	PF	PF	PF	PF	PF	PF	PF	PF	PF	PF	PF	PF	PF	PF	PF	PF	PF	PF	PF	PF	PF				
Height in flow (m)	0.1	2.5	7.0	13.0	19.5	24.0	31.0	36.0	0.3	2.5	19.0	30.0	41.0	58.0	-	0.5	2.0	3.5	5.5	7.5	10.0				
Distance from source (km)	22	22	22	22	22	22	22	22	12	12	12	12	12	12	-	30	30	30	30	30	30				
Oxide wt. %																									
SiO2	50.68	51.05	49.77	50.12	49.10	49.81	49.45	50.69	50.34	50.93	49.94	50.42	50.31	50.28	50.07	50.17	50.29	50.34	49.47	49.81	49.59				
TiO2	3.07	3.05	2.92	3.05	2.87	3.03	2.98	3.01	2.88	2.96	2.81	2.82	2.86	2.91	2.98	2.96	3.08	2.98	2.92	2.95	2.96				
Al2O3	13.11	13.06	12.89	12.97	12.86	12.90	12.72	12.91	13.49	13.36	13.08	13.13	13.08	13.22	13.14	13.00	13.04	12.97	12.78	12.81	12.81				
Fe2O3	15.28	15.29	15.72	15.33	15.36	15.77	15.90	15.55	13.96	14.95	15.48	15.13	15.38	15.70	15.49	15.13	15.41	15.42	15.98	15.66	15.82				
MnO	0.22	0.22	0.27	0.27	0.26	0.24	0.25	0.25	0.23	0.22	0.24	0.22	0.22	0.23	0.21	0.25	0.23	0.24	0.25	0.24	0.26				
MgO	4.06	4.31	4.10	4.25	4.10	4.08	4.07	4.01	4.16	4.29	4.29	4.26	4.28	3.97	3.69	4.01	3.94	4.08	4.13	4.03	4.20				
CaO	7.92	8.09	8.09	8.23	8.14	8.10	8.03	8.02	8.52	8.47	8.19	8.29	8.29	8.12	8.06	8.08	8.25	8.13	7.98	7.93	8.04				
Na2O	2.95	2.93	2.80	2.87	2.67	2.60	2.54	2.61	2.73	2.78	2.63	2.80	2.71	2.71	2.57	2.75	2.79	2.85	2.63	2.80	2.76				
K2O	1.27	1.25	1.12	1.16	0.94	1.28	1.32	1.67	1.24	1.39	1.39	1.24	1.23	1.22	1.31	1.30	1.10	1.12	1.32	1.21	1.17				
P2O5	0.52	0.54	0.51	0.49	0.49	0.52	0.51	0.56	0.54	0.56	0.54	0.54	0.54	0.56	0.67	0.53	0.52	0.51	0.51	0.51	0.50				
LOI	0.25	0.32	0.07	0.70	1.37	0.54	0.23	0.15	0.25	0.13	0.07	0.82	0.68	0.43	1.08	0.17	0.76	0.52	-0.02	0.05	0.39				
Total	99.34	100.11	98.26	99.44	98.17	98.85	98.00	99.45	98.35	100.04	98.67	99.66	99.60	99.36	99.29	98.35	99.41	99.15	97.95	97.98	98.50				
S%	0.04	0.03	0.03	0.02	0.03	0.07	0.05	0.04	0.02	0.05	0.04	0.04	0.05	0.05	0.01	0.04	0.01	0.02	0.05	0.04	0.02				
Element ppm																									
Rb	34	31	20	32	14	31	33	36	31	35	37	32	32	26	42	33	31	25	31	32	30				
Sr	301	298	307	291	302	305	304	301	340	329	325	334	321	322	341	311	312	308	306	302	299				
Y	44.2	45.1	44.8	43.6	42.8	43.4	44.7	44.8	47.0	43.9	43.4	43.8	43.2	43.3	46.0	44.6	42.6	43.1	43.6	43.0	43.4				
Zr	175	178	174	167	170	178	177	189	204	198	201	201	198	201	198	181	178	174	176	180	173				
Nb	12.7	12.7	13.5	12.6	12.7	13.8	13.4	15.2	16.6	15.1	14.9	15.4	15.7	15.2	15.8	13.9	13.5	12.6	13.3	14.0	13.7				
Ba	595	611	584	565	574	538	531	620	634	569	554	605	509	575	546	599	602	586	577	591	578				
Pb	8	9	10	4	6	12	8	8	6	7	9	8	8	9	8	9	7	5	8	8	4				
Th	8	4	6	7	5	5	4	5	6	6	6	2	4	6	3	3	5	3	8	8	4				
U	0	0	3	0	0	2	0	2	0	0	0	2	2	1	0	2	1	1	0	2	0				
Sc	44	36	39	44	39	38	40	37	39	35	38	34	36	35	36	39	37	41	40	39	38				
V	376	365	364	374	361	386	373	345	449	425	421	384	399	444	379	369	375	376	371	370	384				
Cr	39	41	49	55	46	36	39	41	49	49	52	49	49	29	20	41	39	39	40	39	49				
Co	36	34	33	38	36	33	34	35	38	35	29	33	34	33	26	38	31	35	31	31	36				
Ni	29	29	29	34	32	30	28	29	27	22	24	21	18	21	18	32	28	31	31	29	37				
Cu	37	40	37	44	44	37	36	43	36	35	32	35	35	30	28	38	38	38	41	39	40				
Zn	141	138	134	136	131	150	151	145	147	137	138	134	142	137	141	138	131	136	136	139	135				
Ga	19	21	22	22	21	22	22	20	25	24	21	23	21	21	21	20	22	21	22	20	22				
Mo	1	1	2	2	1	1	1	2	2	2	2	2	2	2	3	1	1	1	1	1	3				
As	0	0	0	1	3	0	2	0	5	0	7	2	4	2	0	1	1	2	0	0	2				
S	235	216	240	157	381	655	434	304	161	343	392	355	314	487	59	373	31	207	495	393	210				

Sample locality												Opposite Sheffler					Winn Lake Canyon						
Sample no.	CRB06-085	CRB06-086	CRB06-087	CRB06-088	CRB06-089	CRB06-090	CRB06-091	CRB06-092	CRB06-093	CRB06-094	CRB06-121	CRB06-122	CRB06-123	CRB06-124	CRB06-125	CRB06-287	CRB06-288	CRB06-289	CRB06-290	CRB06-291	CRB06-292	CRB06-293	CRB06-294
Flow field	PF	PF	PF	PF	PF	PF	PF	PF	PF	PF	PF	PF	PF	PF	PF	PF	PF	PF	PF	PF	PF	PF	PF
Height in flow (m)	13.0	15.5	18.0	19.0	20.0	27.0	30.0	32.0	34.0	0.1	0.5	1.4	1.8	2.3	3.5	2.0	8.5	11.5	22.0	26.0	30.0	39.5	47.5
Distance from source (km)	30	30	30	30	30	30	30	30	30		53	53	53	53	53	5	5	5	5	5	5	5	5
Oxide wt. %																							
SiO2	50.72	49.98	49.84	50.14	50.36	50.43	50.57	-	50.39	51.30	50.14	49.78	50.45	49.78	49.73	49.98	49.22	50.23	50.58	50.41	50.81	50.49	50.43
TiO2	3.07	3.06	3.12	3.14	3.13	3.14	3.08	-	3.13	3.01	3.06	3.04	3.05	3.09	3.11	3.06	3.14	2.88	2.91	2.89	2.83	2.86	2.92
Al2O3	13.17	13.01	12.96	13.12	12.98	13.00	13.03	-	13.11	13.10	13.24	12.98	13.14	12.89	12.97	13.26	13.57	13.20	13.17	13.16	13.12	13.12	13.19
Fe2O3	15.02	15.35	15.45	15.13	16.05	15.38	15.79	-	14.71	15.16	15.96	15.85	15.51	15.83	16.58	15.77	15.77	15.54	15.59	15.38	15.25	15.33	15.19
MnO	0.23	0.23	0.25	0.24	0.25	0.26	0.25	-	0.24	0.19	0.21	0.22	0.22	0.20	0.25	0.23	0.25	0.23	0.25	0.24	0.24	0.25	0.24
MgO	4.20	4.33	4.22	4.22	4.16	4.10	4.21	-	4.02	3.37	3.78	3.90	4.00	3.86	3.87	4.25	4.31	4.36	4.34	4.23	4.11	4.19	4.22
CaO	8.30	8.33	8.47	8.46	8.29	8.34	8.26	-	8.52	7.43	8.09	8.06	7.97	8.23	7.81	8.43	8.61	8.24	8.23	8.19	8.12	8.24	8.39
Na2O	2.95	2.83	2.80	2.78	2.73	2.68	2.80	-	2.64	3.02	2.69	2.76	2.62	2.62	2.66	2.74	2.71	2.68	2.69	2.73	2.75	2.57	2.67
K2O	1.21	1.02	0.98	1.21	1.19	1.28	1.31	-	1.44	1.43	1.30	1.13	1.42	0.99	1.28	0.98	0.90	1.38	1.32	1.30	1.30	1.22	1.05
P2O5	0.52	0.49	0.49	0.51	0.52	0.52	0.52	-	0.52	0.57	0.66	0.64	0.67	0.65	0.66	0.50	0.52	0.54	0.55	0.53	0.55	0.54	0.54
LOI	0.42	1.02	0.79	0.63	0.29	0.49	-0.04	-	0.62	0.98	1.14	0.90	1.02	1.37	0.64	0.61	0.70	0.11	-0.01	0.24	0.43	0.85	1.16
Total	99.81	99.67	99.37	99.58	99.95	99.62	99.78	-	99.34	99.55	100.27	99.25	100.09	99.53	99.55	99.82	99.71	99.37	99.61	99.31	99.50	99.67	100.01
S%	0.04	0.06	0.07	0.07	0.08	0.08	0.07	-	0.02	0.01	0.04	0.06	0.02	0.05	0.05	0.01	0.02	0.06	0.06	0.06	0.05	0.05	0.06
Element ppm																							
Rb	32	16	20	28	31	28	-	32	29	54	41	31	37	25	35	24	24	35	34	37	36	34	30
Sr	300	300	318	318	311	309	-	311	323	311	352	356	341	348	336	313	321	328	326	328	327	316	323
Y	44.0	43.2	41.8	43.2	43.1	42.9	-	43.6	43.0	45.2	41.9	43.9	43.6	44.4	44.0	42.1	44.0	42.1	43.2	42.4	43.4	42.0	42.3
Zr	173	169	173	179	178	177	-	179	180	192	194	196	197	197	201	172	176	198	198	201	207	201	199
Nb	13.4	12.8	12.3	12.6	13.9	13.9	-	14.2	12.8	14.4	15.2	14.4	15.2	15.0	15.0	12.2	13.1	15.4	15.9	15.4	15.5	15.4	13.8
Ba	585	581	569	575	525	604	-	537	579	693	627	641	567	582	531	576	574	563	556	704	573	539	499
Pb	7	7	6	5	7	6	-	6	4	8	7	8	7	8	7	6	4	6	7	9	6	6	6
Th	2	4	7	5	6	4	-	5	5	6	6	6	6	6	6	6	5	4	7	3	6	7	7
U	2	3	1	3	1	0	-	2	2	1	0	5	1	2	0	2	0	0	0	3	1	2	0
Sc	41	39	42	38	38	41	-	40	41	41	34	34	34	33	37	41	47	34	35	36	35	36	36
V	386	367	398	397	383	397	-	394	397	343	371	363	383	363	374	380	400	413	423	412	395	411	412
Cr	45	50	44	43	44	36	-	46	38	36	23	20	22	16	23	51	48	53	54	55	52	50	51
Co	33	38	39	39	38	35	-	33	45	29	34	33	34	34	36	36	35	35	37	36	32	38	36
Ni	36	32	34	34	30	26	-	31	32	22	16	13	14	15	13	33	31	21	25	22	22	20	26
Cu	41	41	39	36	37	36	-	38	37	36	31	29	28	28	30	47	43	34	34	33	34	33	31
Zn	132	133	144	146	153	150	-	155	144	148	140	144	154	152	151	133	147	136	147	147	148	145	144
Ga	21	22	22	21	22	19	-	21	21	22	22	22	23	23	22	22	22	22	22	23	22	22	21
Mo	2	2	0	1	0	1	-	2	0	1	2	2	1	1	1	0	0	1	2	1	1	1	1
As	0	2	0	0	0	2	-	4	2	0	0	0	0	2	3	0	4	5	0	2	0	1	1
S	246	441	596	795	475	496	-	424	145	64	431	377	114	297	248	42	100	460	295	365	321	283	446

Sample locality	basal interval high density sampling						u/c high density sampling					W of Gingko dyke						Burr Canyon					
Sample no.	CRB06-295	CRB06-314	CRB06-315	CRB06-316	CRB06-317	CRB06-318	CRB06-319	CRB06-320	CRB06-321	CRB06-322	CRB06-323	CRB06-380	CRB06-381	CRB06-382	CRB06-383	CRB06-384	CRB06-385	CRB06-387	CRB06-388	CRB06-389	CRB06-390	CRB06-391	CRB06-392
Flow field	PF	PF	PF	PF	PF	PF	PF	PF	PF	PF	PF	PF	PF	PF	PF	PF	PF	PF	PF	PF	PF	PF	PF
Height in flow (m)	52.0	0.8	0.4	0.3	0.2	0.1	0.0	1.0	1.2	1.5	1.8	0.1	8.0	11.0	17.0	23.0	32.0	0.4	2.0	4.5	10.0	13.0	16.5
Distance from source (km)	5	-	-	-	-	-	-	-	-	-	-	40	40	40	40	40	40	39	39	39	39	39	39
Oxide wt. %																							
SiO2	50.60	50.52	50.85	51.61	50.84	50.89	49.87	49.92	50.61	50.18	50.59	51.25	50.94	50.60	50.44	50.38	49.54	49.50	50.49	50.86	50.81	50.72	50.71
TiO2	2.95	2.92	2.92	3.00	2.93	3.04	2.85	2.88	2.95	2.96	2.89	3.10	3.12	3.08	3.18	3.11	3.13	3.24	3.06	2.98	3.08	3.11	3.08
Al2O3	13.25	13.06	13.20	13.62	13.28	13.56	13.06	13.07	13.19	13.27	13.39	13.26	12.93	13.11	13.09	12.96	13.00	14.46	13.19	13.20	13.10	12.93	13.15
Fe2O3	14.87	15.67	15.52	14.57	15.20	14.42	15.00	15.31	15.08	15.04	14.90	15.98	15.47	15.97	16.11	16.02	16.05	12.93	15.59	15.63	15.87	16.28	16.15
MnO	0.22	0.22	0.23	0.23	0.23	0.23	0.23	0.22	0.25	0.22	0.25	0.23	0.22	0.25	0.24	0.24	0.24	0.23	0.23	0.23	0.23	0.24	0.24
MgO	4.16	4.19	4.28	3.63	3.93	3.49	4.36	4.23	4.09	3.98	4.19	3.24	3.97	4.23	4.08	4.13	3.95	3.48	4.03	3.77	4.01	4.03	4.16
CaO	8.46	8.19	8.33	8.57	8.35	8.54	8.25	8.23	8.30	8.41	8.36	7.74	8.11	8.28	8.31	8.26	8.23	9.33	8.15	8.08	8.11	8.06	8.21
Na2O	2.65	2.76	2.71	2.84	2.73	2.70	2.62	2.61	2.69	2.75	2.60	3.01	2.93	2.72	2.82	2.61	2.56	2.82	2.88	2.83	2.76	2.83	2.84
K2O	1.18	1.26	1.40	1.38	1.35	1.38	1.13	1.14	1.28	1.18	1.39	1.18	1.24	1.35	1.05	1.35	0.99	0.66	1.35	1.47	1.47	1.38	1.29
P2O5	0.55	0.54	0.55	0.57	0.56	0.58	0.53	0.53	0.54	0.55	0.54	0.56	0.54	0.55	0.54	0.54	0.55	0.71	0.64	0.70	0.68	0.68	0.66
LOI	0.80	0.03	-0.18	0.05	-0.05	0.40	1.01	1.13	0.53	0.49	0.47	0.86	0.39	0.16	0.63	0.44	1.15	2.29	-0.06	0.41	-0.14	-0.23	-0.12
Total	99.68	99.37	99.81	100.08	99.35	99.24	98.91	99.29	99.50	99.01	99.58	100.41	99.85	100.31	100.49	100.05	99.39	99.66	99.55	100.15	99.98	100.03	100.36
S%	0.06	0.07	0.06	0.06	0.06	0.08	0.05	0.05	0.06	0.06	0.05	0.01	0.04	0.06	0.05	0.05	0.04	0.02	0.03	0.02	0.07	0.07	0.07
Element ppm																							
Rb	32	33	37	35	36	35	31	35	35	32	38	32	30	33	30	33	27	18	36	36	38	37	35
Sr	323	327	325	335	327	332	324	322	325	333	329	319	312	319	318	317	305	394	345	353	340	339	343
Y	42.4	42.8	42.3	43.9	42.5	45.6	42.6	43.7	43.2	42.6	42.1	44.3	43.4	43.7	44.5	43.6	46.1	46.2	44.3	45.1	44.7	44.5	43.2
Zr	199	199	202	204	197	205	197	202	203	205	198	187	180	182	181	181	182	206	198	207	202	205	197
Nb	15.4	15.1	15.7	15.9	15.7	16.2	15.5	16.2	15.2	15.9	14.9	14.0	13.4	13.7	14.6	13.8	12.8	15.9	14.5	15.7	16.8	16.0	15.1
Ba	529	572	552	576	537	577	540	569	552	570	564	644	607	553	608	563	514	609	610	654	577	625	579
Pb	4	8	4	8	7	5	7	6	8	5	8	5	8	4	6	6	9	6	7	8	5	9	6
Th	7	5	5	2	6	6	5	5	5	5	5	5	5	6	6	5	5	4	6	6	8	7	7
U	1	0	2	1	0	2	1	2	2	1	-1	0	2	0	2	3	1	1	1	2	0	0	3
Sc	38	37	37	40	36	43	36	38	35	36	35	38	39	37	41	37	39	38	35	34	35	35	37
V	422	403	407	439	421	441	401	399	408	422	422	342	378	349	374	367	365	430	394	345	379	381	396
Cr	52	50	56	54	52	59	50	50	52	46	53	33	31	33	37	34	34	19	19	20	22	20	24
Co	39	37	39	38	39	34	36	34	38	36	35	32	36	34	33	35	37	37	39	35	37	34	37
Ni	21	26	24	24	24	18	21	20	21	22	17	23	25	27	27	27	23	14	16	19	15	16	15
Cu	32	35	35	34	32	33	32	33	37	36	30	37	40	39	37	38	37	26	28	29	31	32	32
Zn	146	140	144	150	146	159	147	148	149	147	144	149	140	141	152	145	150	161	145	145	147	151	147
Ga	24	22	21	23	22	23	22	23	22	22	22	21	21	23	22	22	20	23	23	23	21	24	22
Mo	1	1	0	0	0	0	1	0	0	0	0	0	0	1	0	0	0	1	0	0	2	0	1
As	0	0	3	0	4	0	0	0	0	0	1	1	0	0	4	1	0	2	4	0	0	0	2
S	309	406	367	383	333	504	343	479	325	298	377	75	263	329	303	344	210	141	183	154	327	391	410

Sample locality	Joso lobe								PF in DC8 borehole				
Sample no.	CRB06-393	CRB06-394	CRB06-395	CRB06-396	CRB05-064	CRB05-065	CRB05-066	CRB05-067	CRB05-096	CRB05-097	CRB05-098	CRB05-099B	CRB05-099T
Flow field	PF	PF	PF	PF	PF	PF	PF	PF	PF	PF	PF	PF	PF
Height in flow (m)	20.0	25.0	28.0	33.0	1.0	4.0	6.5	13.0	27.0	21.0	11.0	0.1	0.3
Distance from source (km)	39	39	39	39	8	8	8	8	78	78	78	78	78
Oxide wt. %													
SiO2	50.78	50.90	50.51	49.54	50.60	50.61	50.91	50.63	48.68	49.56	50.41	50.88	50.56
TiO2	3.08	3.08	2.99	3.21	2.83	2.82	2.82	2.84	3.04	3.01	3.06	3.14	3.07
Al2O3	13.12	13.19	13.27	13.45	13.22	13.25	13.31	13.28	12.99	13.10	12.96	13.37	12.99
Fe2O3	16.11	15.75	15.82	16.33	15.33	15.28	15.10	15.29	16.79	15.51	16.01	15.02	16.06
MnO	0.24	0.23	0.23	0.26	0.22	0.22	0.23	0.20	0.33	0.23	0.23	0.25	0.23
MgO	4.03	3.92	3.91	3.66	4.33	4.35	4.24	4.23	4.30	4.18	3.99	3.31	3.41
CaO	8.20	8.18	8.22	8.02	8.21	8.18	8.20	8.33	8.35	8.43	7.94	7.93	7.87
Na2O	2.77	2.91	2.65	2.63	2.75	2.72	2.69	2.52	2.68	2.94	2.91	3.12	2.94
K2O	1.34	1.37	1.47	0.92	1.27	1.34	1.41	1.29	0.82	0.84	1.21	1.26	1.24
P2O5	0.67	0.69	0.66	0.73	0.54	0.54	0.55	0.55	0.49	0.50	0.51	0.55	0.53
LOI	-0.06	-0.04	0.24	1.45	-0.03	-0.04	0.02	0.65	1.48	1.38	0.45	1.02	0.83
Total	100.27	100.18	99.96	100.21	99.27	99.27	99.48	99.82	99.95	99.69	99.68	99.85	99.73
S%	0.07	0.06	0.06	0.04	0.06	0.04	0.04	0.05	0.01	0.05	0.01	0.03	0.05
Element ppm													
Rb	36	35	37	26	34	35	35	33	25	13	30	32	33
Sr	343	345	344	352	317	319	322	312	303	305	298	303	294
Y	43.9	45.2	44.3	45.4	42.0	42.8	44.5	42.2	41.7	41.3	42.2	44.5	42.9
Zr	201	205	197	205	194	196	199	195	168	169	171	181	175
Nb	16.0	16.8	15.6	15.7	15.1	15.0	15.6	15.2	13.4	12.4	12.6	15.4	13.1
Ba	599	586	544	498	572	568	568	529	416	602	605	618	588
Pb	7	9	8	10	9	7	7	7	7	7	8	10	11
Th	7	7	7	6	5	5	3	3	6	5	4	5	6
U	0	1	2	2	1	2	0	0	0	1	2	0	3
Sc	36	33	35	40	35	39	35	38	40	38	38	42	41
V	396	379	358	354	426	420	422	423	367	361	378	407	379
Cr	25	19	23	23	44	45	45	47	35	35	29	28	31
Co	34	38	36	35	35	37	34	34	35	35	33	37	38
Ni	18	16	17	15	17	15	17	16	24	26	23	26	27
Cu	30	30	28	28	32	33	33	32	36	39	39	36	37
Zn	147	151	146	148	146	147	150	145	127	138	131	153	148
Ga	20	22	22	22	21	22	21	21	21	20	23	23	23
Mo	0	1	1	0	2	1	2	2	1	2	1	2	1
As	1	0	0	0	5	0	1	3	1	5	2	2	0
S	424	351	407	241	410	284	252	284	186	423	50	241	305

Table D.2 Major and trace element results of samples from the Sand Hollow flow field.

Sample locality	Locke Lake											Lyle					
Sample no.	CRB06-001	CRB06-002	CRB06-003	CRB06-004	CRB06-005	CRB06-012	CRB06-013	CRB06-014	CRB06-015	CRB06-016	CRB06-017	CRB06-018	CRB06-019	CRB06-027	CRB06-028	CRB06-029	CRB06-030	CRB06-031	CRB06-032
Flow field	SG f#1	SG f#1	SH	SH	SH	SH	SH	SH	SH	SH	SH	SH	SH	Ro	SH	SH	SH	SH	SH
Height in flow (m)	30	0	59.8	55	51	48	45	42	34	26	18	7	0.3		78	64	58	40	0.1
Distance from source (km)	242	242	242	242	242	242	242	242	242	242	242	242	242	235	235	235	235	235	235
Oxide wt. %																			
SiO2	52.13	52.78	49.90	51.09	50.83	50.55	50.37	50.52	49.98	50.45	50.77	50.31	50.06	50.48	50.34	49.94	50.24	50.16	51.50
TiO2	2.906	3.072	2.946	2.936	2.799	2.856	2.833	2.867	2.843	2.862	2.823	2.827	2.900	2.793	2.862	2.977	2.858	2.766	2.954
Al2O3	13.30	14.22	13.69	13.99	13.32	13.18	13.26	13.21	13.07	13.29	13.13	13.08	13.56	12.89	13.31	13.18	13.04	13.07	13.83
Fe2O3	14.24	12.49	15.13	14.02	15.38	15.61	15.95	15.57	15.84	15.67	15.78	15.61	14.62	15.76	15.08	15.41	15.18	15.46	13.72
MnO	0.204	0.183	0.196	0.208	0.224	0.235	0.255	0.227	0.222	0.244	0.231	0.227	0.289	0.231	0.221	0.217	0.225	0.247	0.184
MgO	3.37	3.56	3.87	3.52	4.50	4.51	4.46	4.45	4.52	4.23	4.55	4.43	3.09	3.86	4.27	4.38	4.13	4.36	3.73
CaO	7.58	7.16	8.69	8.78	8.35	8.40	8.32	8.35	8.21	8.10	8.25	8.06	8.47	7.53	8.47	8.49	7.91	7.89	8.19
Na2O	3.00	3.19	2.65	2.72	2.67	2.65	2.72	2.75	2.69	2.86	2.72	2.81	2.75	2.84	2.66	2.80	2.77	2.80	3.03
K2O	1.50	1.62	0.88	1.16	1.30	1.23	1.16	1.18	1.07	1.25	1.35	1.24	1.35	1.44	1.22	1.07	1.25	1.27	1.31
P2O5	0.655	0.731	0.609	0.575	0.543	0.544	(0.540)	0.547	0.547	0.546	0.551	0.536	0.556	0.628	0.521	0.536	0.524	0.528	0.591
LOI	0.53	0.81	1.31	1.11	0.41	0.34	0.11	0.32	0.70	0.20	0.01	0.03	1.22	0.12	0.72	0.41	-0.02	0.05	0.45
Total	99.42	99.82	99.88	100.11	100.32	100.10	99.98	99.98	99.69	99.71	100.17	99.15	98.86	98.56	99.68	99.42	98.10	98.60	99.49
S%	0.06	0.04	0.03	0.04	0.02	0.05	0.04	0.04	0.04	0.05	0.06	0.02	0.06	0.01	0.01	0.03	0.06	0.05	0.05
Element ppm																			
Rb	41	44	29	35	35	33	28	29	22	34	36	35	37	35	31	22	34	33	35
Sr	321	341	325	336	327	323	327	323	322	323	323	315	328	320	330	340	316	315	330
Y	49.3	51.4	43.7	43.9	42.4	42.6	41.5	42.7	42.2	42.6	42.7	42	43.2	47.3	41.8	41.7	43.2	42.8	44.3
Zr	228	241	200	201	191	191	190	188	191	196	196	192	199	219	187	196	198	198	200
Nb	17.6	18.5	15.8	15	14.7	14.2	15.2	14.6	15	15.1	14.5	14.2	15.8	16.3	14.1	14.7	15.6	14.7	15.6
Ba	695	738	489	511	554	546	577	587	582	577	598	592	595	679	557	595	592	593	600
Pb	10	9	7	6	8	7	6	7	7	5	9	8	11	8	8	8	9	10	8
Th	7	6	7	6	5	6	5	6	6	3	5	8	7	7	5	2	9	7	4
U	0	1	1	0	1	2	0	0	1	0	1	2	2	3	0	0	1	0	1
Sc	37	43	37	37	32	31	36	34	34	33	34	35	40	32	35	36	35	37	34
V	400	459	434	432	405	408	415	394	407	418	404	401	449	371	418	426	425	404	447
Cr	17	18	46	50	46	44	51	40	42	49	46	46	56	19	50	50	47	52	49
Co	31	33	34	40	36	34	34	34	32	36	34	33	33	32	32	35	34	35	40
Ni	16	17	21	25	21	21	22	20	22	24	21	20	27	16	24	22	22	23	23
Cu	27	29	32	33	34	34	37	34	34	33	34	32	35	28	32	33	33	33	34
Zn	153	165	146	150	132	134	132	122	129	134	127	131	152	141	132	133	132	131	150
Ga	23	23	22	23	22	22	22	22	24	23	24	23	22	23	22	22	22	22	23
Mo	4	3	1	1	2	1	1	2	2	1	2	1	2	2	2	1	3	1	3
As	0	1	2	9	1	2	6	3	0	5	2	1	2	3	0	0	0	1	1
S	505	295	186	414	264	530	461	472	414	353	513	178	442	108	80	365	432	447	548

Sample locality				Sand Hollow Road								Vantage Cliffs						
Sample no.	CRB06-033	CRB06-034	CRB06-035	CRB05-018	CRB05-019	CRB05-020	CRB05-021	CRB05-022	CRB05-023	CRB05-024	CRB05-026	CRB05-001	CRB05-002WA	CRB05-003WA	CRB05-004WA	CRB05-005WA	CRB05-006	CRB05-007
Flow field	SH	G	SH	SH	SH	SH	SH	SH	SH	SH	SH	SG	SH	SH	SH	SH	SH	SH
Height in flow (m)	10		25	0.5	1	8	10	14.5	18.5	22	25	1	34	25	18	13	10	8
Distance from source (km)	235	235	235	157	157	157	157	157	157	157	157	158	158	158	158	158	158	158
Oxide wt. %																		
SiO2	50.43	49.51	51.20	51.07	50.91	50.31	51.30	50.43	51.06	51.09	50.88	50.63	51.34	51.22	50.77	50.84	50.61	50.89
TiO2	2.811	2.972	2.824	2.854	2.853	2.850	2.877	2.816	2.737	2.908	2.881	3.008	2.936	2.938	2.868	2.854	2.856	2.873
Al2O3	13.22	13.00	13.20	13.36	13.34	13.28	13.40	13.33	13.58	13.43	13.55	13.21	13.83	13.86	13.39	13.33	13.30	13.13
Fe2O3	15.51	16.19	15.61	15.42	15.51	15.62	15.63	15.45	15.35	15.50	14.36	15.69	13.81	13.65	15.42	15.48	15.42	15.29
MnO	0.233	0.253	0.224	0.220	0.219	0.221	0.221	0.219	0.218	0.213	0.204	0.215	0.199	0.196	0.218	0.218	0.219	0.196
MgO	4.54	4.08	4.57	4.29	4.40	4.38	4.41	4.38	4.57	4.42	3.99	3.93	3.48	3.69	4.33	4.36	4.34	4.24
CaO	8.06	8.02	8.04	8.22	8.25	8.13	8.26	8.28	8.40	8.48	8.56	8.14	8.80	8.73	8.31	8.25	8.25	7.85
Na2O	2.85	2.71	2.86	2.69	2.82	2.78	2.77	2.73	2.77	2.70	2.74	2.39	2.77	2.73	2.76	2.71	2.61	2.83
K2O	1.26	1.29	1.24	1.45	1.22	1.18	1.40	1.21	1.21	1.27	1.30	1.35	1.17	1.15	1.29	1.36	1.51	1.34
P2O5	0.538	0.613	0.547	0.552	0.549	0.556	0.570	0.539	0.537	0.558	0.539	0.603	0.565	0.560	0.543	0.557	0.560	0.559
LOI	0.11	-0.20	0.14	-0.20	0.05	0.32	0.11	0.42	0.33	0.24	0.43	0.76	1.13	1.07	-0.11	-0.05	0.14	0.18
Total	99.56	98.44	100.46	99.93	100.11	99.63	100.95	99.80	100.77	100.80	99.43	99.95	100.02	99.78	99.79	99.92	99.81	99.39
S%	0.03	0.06	0.04	0.04	0.04	0.05	0.05	0.05	0.05	0.03	0.03	0.06	0.03	0.03	0.01	0.04	0.04	0.05
Element ppm																		
Rb	34	34	35	36	33	29	36	34	35	34	33	37	32	30	31	35	37	34
Sr	313	335	315	322	324	323	322	323	333	329	357	316	343	356	327	325	331	313
Y	41.2	41.8	42.1	42.9	43.4	42.7	42.2	42.1	40.6	41.8	43.7	46.1	44.7	44.4	43.1	42.9	43.2	43.7
Zr	191	184	192	195	197	198	193	191	190	193	199	212	203	202	192	198	195	201
Nb	14.8	14.2	15.1	14.5	15.6	14.8	14.6	14.9	13.6	15.8	15.2	16.2	16.0	16.2	15.3	15.7	15.4	14.4
Ba	602	553	574	563	588	594	580	544	545	550	578	583	581	616	582	564	576	617
Pb	7	6	5	8	9	9	8	7	8	8	9	5	7	10	7	7	9	6
Th	5	6	6	4	6	7	6	6	8	4	3	5	8	6	8	6	6	5
U	2	3	1	2	0	5	2	0	0	3	2	0	1	2	2	1	1	0
Sc	36	37	37	36	37	38	35	35	36	36	39	44	38	38	32	36	36	33
V	399	393	405	426	422	421	421	418	410	435	441	431	451	455	423	416	404	410
Cr	50	29	48	43	44	43	44	43	47	43	45	32	46	47	43	43	42	40
Co	36	32	34	36	35	35	39	37	38	36	33	34	34	37	38	37	36	31
Ni	23	17	22	18	17	18	17	20	17	19	19	19	15	21	18	18	16	16
Cu	31	28	34	34	35	36	31	33	35	33	33	29	33	33	31	38	36	34
Zn	128	143	131	147	137	140	139	141	137	143	148	155	153	150	136	144	134	134
Ga	24	22	22	22	23	22	21	23	23	22	22	22	22	23	22	25	22	22
Mo	1	1	3	1	2	2	0	1	1	3	2	2	1	1	2	1	1	0
As	2	2	3	0	2	0	1	0	1	0	0	0	0	0	0	1	0	2
S	252	441	514	253	340	404	360	296	328	305	219	482	259	203	96	289	500	368

Sample locality					Lenore Caves						Babcock Bench							
Sample no.	CRB05-008	CRB05-010	CRB05-009B	CRB05-009T	CRB06-168	CRB06-169	CRB06-170	CRB06-171	CRB06-172	CRB06-173	CRB06-408	CRB06-409	CRB06-410	CRB06-411	CRB06-412	CRB06-413	CRB06-402	CRB06-403
Flow field	SH	SH	SH	SH	SH	SH	SH	SH	SH	SH	SH	SH	SH	SH	SH	SH	SG	SG
Height in flow (m)	3	0.5	0.1	0	11.5	9	6.5	4.5	2	0.1	33.5	31.5	28.5	22.3	18.5	15.5	0	3.5
Distance from source (km)	158	158	158	158	195	195	195	195	195	195	180	180	180	180	180	180	180	180
Oxide wt. %																		3.5
SiO2	50.65	51.00	51.80	48.42	50.35	50.38	50.34	50.21	50.12	51.63	50.86	50.88	50.40	50.57	51.15	51.88	51.07	50.79
TiO2	2.845	2.845	2.937	2.851	3.042	2.959	2.925	2.959	2.904	2.977	2.826	2.923	2.955	2.917	2.913	2.983	2.889	2.864
Al2O3	13.38	13.29	13.89	13.30	13.69	13.25	13.28	13.23	13.05	13.46	13.54	13.27	13.23	13.16	13.29	13.93	13.28	13.03
Fe2O3	15.14	15.07	12.90	13.39	15.32	15.40	15.60	15.62	16.05	15.12	14.90	15.31	15.75	15.64	14.86	13.09	15.48	15.34
MnO	0.213	0.202	0.156	0.396	0.226	0.251	0.247	0.242	0.269	0.228	0.212	0.218	0.234	0.232	0.209	0.155	0.225	0.203
MgO	4.29	4.22	3.69	3.43	4.19	4.01	4.50	4.51	4.46	3.64	4.38	4.09	4.38	4.29	4.20	3.32	4.40	4.28
CaO	8.23	8.12	8.15	10.45	8.54	8.29	8.40	8.39	8.33	8.07	8.64	8.37	8.37	8.17	8.15	8.59	8.27	7.85
Na2O	2.81	2.86	3.00	2.89	2.71	2.72	2.69	2.72	2.78	2.95	2.67	2.74	2.73	2.82	2.92	2.97	2.74	2.87
K2O	1.30	1.23	1.33	1.09	1.18	1.33	1.29	1.27	1.15	1.30	1.19	1.26	1.28	1.26	1.26	1.19	1.48	1.31
P2O5	0.549	0.550	0.580	0.662	0.580	0.557	0.511	0.517	0.536	0.561	0.529	0.549	0.536	0.554	0.543	0.551	0.567	0.539
LOI	0.01	0.34	0.88	3.47	0.33	0.46	-0.08	0.02	0.25	0.06	0.55	0.43	-0.03	-0.35	0.18	1.06	-0.13	0.48
Total	99.42	99.74	99.32	100.36	100.15	99.62	99.71	99.69	99.89	100.00	100.29	100.03	99.85	99.26	99.69	99.71	100.28	99.55
S%	0.06	0.04	0.04	0.01	0.01	0.03	0.02	0.05	0.08	0.04	0.03	0.05	0.03	0.04	0.05	0.06	0.04	0.03
Element ppm																		
Rb	31	28	25	35	28	38	33	31	27	37	30	33	35	33	33	19	36	37
Sr	333	321	331	331	338	331	333	333	328	324	349	337	334	335	331	352	334	324
Y	44.3	42.3	43.0	43.6	45.5	43.5	40.3	41.4	40.5	43.6	39.8	42.5	41.7	44.3	42.5	43.8	43.0	42.2
Zr	200	199	195	202	208	207	191	189	193	205	189	201	196	203	202	206	204	199
Nb	15.1	15.1	16.0	15.4	15.9	15.2	15.2	13.9	14.0	15.3	16.0	17.4	14.7	16.9	14.7	17.2	14.7	15.5
Ba	590	594	764	610	601	565	567	559	579	582	570	636	582	613	616	648	585	603
Pb	8	7	6	10	7	4	7	6	6	7	4	6	10	5	4	6	4	6
Th	2	8	7	7	6	7	6	6	7	8	5	6	5	5	7	7	4	7
U	0	3	3	2	1	4	1	0	1	1	1	1	0	0	0	1	2	0
Sc	36	35	40	39	39	37	34	34	36	39	35	33	35	34	33	34	35	36
V	416	413	444	456	427	412	403	420	418	432	406	428	422	421	415	436	405	404
Cr	45	44	43	48	48	46	53	51	53	50	48	45	47	46	58	45	46	45
Co	34	36	33	38	41	38	39	37	39	39	38	39	35	40	36	48	37	36
Ni	21	19	18	23	20	24	23	21	25	23	23	19	19	23	23	27	21	23
Cu	35	33	31	34	32	33	34	34	34	32	34	34	33	33	35	35	34	35
Zn	139	140	145	152	145	139	134	132	135	148	135	143	132	142	136	156	139	135
Ga	23	22	22	22	22	23	22	23	22	25	22	22	23	23	23	23	23	22
Mo	1	1	1	1	0	0	0	0	0	0	0	1	0	1	0	1	0	1
As	2	1	4	1	0	0	2	0	1	2	0	1	0	0	0	0	1	1
S	756	414	98	415	75	225	94	484	1108	238	175	237	152	242	415	559	369	246

Sample locality					Frenchman Springs Coulee - north														
Sample no.	CRB06-404	CRB06-414	CRB06-405	CRB06-406	CRB06-228	CRB06-229	CRB06-230	CRB06-231	CRB06-232	CRB06-234	CRB06-235	CRB06-236	CRB06-237	CRB06-238	CRB06-239	CRB06-240	CRB06-241	CRB06-242
Flow field	SG	SG	SG	SG	SH	SH	SH		SH	SH	SH	SH	SH	SH	SH	SH	SH	SH
Height in flow (m)	6	9	11.5	15	0.03	0.06	0.15	0.35	0.5	1.5	4	7	8.5	15.5	19	26	28	31
Distance from source (km)	180	180	180	180	174	174	174	174	174	174	174	174	174	174	174	174	174	174
Oxide wt. %	6	9	11.5	14.9														
SiO2	50.71	51.11	50.81	50.80	50.28	52.00	51.80	51.88	51.45	51.44	50.83	50.51	50.59	50.47	50.79	50.24	50.54	50.43
TiO2	2.819	2.827	2.865	2.906	3.036	3.027	2.959	2.916	2.879	2.947	2.877	2.881	2.862	2.920	2.931	2.906	2.888	2.914
Al2O3	13.22	13.14	13.27	13.45	13.67	14.03	13.63	13.46	13.25	13.42	13.13	13.11	13.07	13.05	13.17	13.04	13.16	13.16
Fe2O3	15.17	14.87	14.85	14.68	15.26	12.22	13.36	14.53	15.38	14.68	15.79	15.67	15.78	15.79	15.82	15.45	15.58	15.55
MnO	0.227	0.218	0.220	0.216	0.246	0.172	0.167	0.190	0.215	0.205	0.242	0.241	0.240	0.240	0.243	0.229	0.239	0.237
MgO	4.19	4.13	4.23	3.82	3.61	3.69	3.74	4.04	4.30	4.11	4.31	4.37	4.58	4.35	4.37	4.20	4.27	4.26
CaO	8.19	8.23	8.27	8.70	8.42	8.34	8.19	8.10	8.06	8.16	8.15	8.17	8.28	8.22	8.30	8.27	8.24	8.24
Na2O	2.70	2.76	2.69	2.73	2.50	3.18	3.06	3.01	2.93	2.95	2.80	2.75	2.73	2.70	2.74	2.66	2.70	2.65
K2O	1.47	1.43	1.44	1.26	1.14	1.40	1.32	1.32	1.26	1.24	1.37	1.42	1.28	1.35	1.31	1.19	1.30	1.29
P2O5	0.552	0.574	0.550	0.567	0.597	0.647	0.591	0.568	0.551	0.539	0.550	0.532	0.544	0.554	0.559	0.541	0.543	0.552
LOI	0.19	0.58	0.17	0.78	1.07	1.63	1.09	0.51	0.14	0.44	-0.39	-0.13	0.05	0.00	-0.04	0.86	0.23	0.43
Total	99.45	99.88	99.38	99.91	99.83	100.34	99.92	100.51	100.42	100.12	99.66	99.54	100.01	99.65	100.19	99.59	99.68	99.71
S%	0.05	0.08	0.02	0.06	0.08	0.05	0.07	0.07	0.06	0.07	0.07	0.04	0.07	0.07	0.07	0.07	0.07	0.07
Element ppm																		
Rb	36	37	36	34	31	40	36		32	32	36	37	34	36	33	33	33	35
Sr	338	342	340	332	318	358	337		323	328	328	325	324	322	323	324	325	327
Y	43.2	44.4	42.8	43.5	45.8	44.0	43.2		42.5	43.5	43.5	42.4	41.8	42.5	42.2	42.7	44.0	42.6
Zr	206	211	206	203	211	214	208		202	200	202	204	198	203	202	202	200	201
Nb	14.9	15.6	15.3	15.6	16.1	16.8	18.7		15.1	17.0	18.0	16.8	13.9	15.0	15.5	17.2	16.5	18.2
Ba	611	632	599	637	557	639	593		582	597	606	602	545	547	549	516	564	513
Pb	4	6	8	6	7	1	4		5	6	7	7	8	4	7	4	5	7	7
Th	7	5	6	6	6	5	6		7	5	4	2	7	3	5	7	5	7
U	0	1	0	1	1	1	2		0	2	0	2	1	0	2	0	1	2
Sc	35	36	37	39	40	39	36		35	34	32	36	37	37	33	34	30	35
V	407	387	402	416	430	477	438		406	429	406	407	407	398	408	411	412	414
Cr	46	43	47	47	55	52	51		49	49	52	52	50	51	54	54	49	55
Co	35	35	37	35	29	47	40		38	39	38	39	35	37	31	43	40	40
Ni	21	20	22	18	17	36	22		22	25	23	22	21	23	24	22	23	23
Cu	31	32	33	32	31	33	30		31	33	34	34	33	33	34	35	34	33
Zn	135	137	137	148	152	153	149		141	138	136	138	140	146	146	145	142	148
Ga	23	21	21	21	21	22	21		22	22	23	22	23	21	23	21	22	21
Mo	0	1	1	0	0	1	2		0	1	1	0	0	1	1	1	0	1
As	0	1	1	2	2	1	2		0	1	1	0	0	4	2	0	2	0
S	520	1083	102	312	601	477	648		574	462	543	329	625	396	421	504	389	455

Sample locality					Frenchman Springs Coulee - South						Palouse Falls rapids									
Sample no.	CRB06-243	CRB06-244	CRB06-245	CRB06-246	CRB06-195	CRB06-196	CRB06-197	CRB06-198	CRB06-199	CRB06-200	CRB05-040B	CRB05-040T	CRB05-041	CRB05-042	CRB05-043	CRB05-044	CRB05-045	CRB05-046	CRB05-047	CRB05-048
Flow field	SH	SH	SH	SH	SH	SH	SH	SH	SH	SH	SH	SH	SH	SH	SH	SH	SH	SH	SH	SH
Height in flow (m)	33.5	35.5	38	40.5	10.5	9	6.8	5.1	1.8	0.2	0.1	0.2	1.0	2.4	12.5	28.0	30.0	32.5	38.0	47.5
Distance from source (km)	174	174	174	174	173	173	173	173	173	173	150	150	150	150	150	150	150	150	150	150
																	4.04	50.92	197.42	2.85
Oxide wt. %																				
SiO2	50.52	50.21	51.18	50.78	50.51	51.04	50.42	50.49	51.02	51.80	51.13	51.15	51.33	51.45	50.70	50.61	51.23	51.06	50.29	50.57
TiO2	2.915	2.995	2.968	2.884	3.025	3.003	2.915	2.881	2.927	3.038	2.89	2.88	2.86	2.90	2.87	2.85	2.76	2.75	2.82	2.88
Al2O3	13.13	13.27	13.31	13.21	13.77	13.63	13.21	13.26	13.20	13.96	13.60	13.38	13.36	13.53	13.31	13.29	13.32	13.38	13.32	13.50
Fe2O3	15.67	15.20	15.30	15.58	15.12	14.70	15.46	15.62	15.47	13.47	14.68	15.12	15.48	15.38	15.54	15.49	15.25	15.11	15.12	14.75
MnO	0.237	0.213	0.221	0.234	0.224	0.224	0.231	0.232	0.224	0.203	0.22	0.22	0.21	0.22	0.22	0.22	0.22	0.22	0.22	0.23
MgO	4.33	4.40	4.09	4.26	3.42	3.41	4.36	4.59	4.35	3.71	3.71	4.04	4.26	4.46	4.43	4.35	4.20	4.17	4.16	3.90
CaO	8.35	8.75	8.39	8.18	8.83	8.56	8.31	8.35	8.28	8.74	8.45	8.35	8.28	8.34	8.25	8.19	8.09	8.13	8.28	8.45
Na2O	2.65	2.61	2.75	2.66	2.85	2.71	2.66	2.69	2.70	2.88	2.78	2.75	2.84	2.85	2.74	2.75	2.93	2.76	2.65	2.57
K2O	1.27	1.02	1.32	1.45	0.91	1.25	1.32	1.34	1.41	1.46	1.40	1.39	1.26	1.27	1.22	1.28	1.27	1.28	1.14	1.26
P2O5	0.554	0.506	0.562	0.552	0.604	0.546	0.542	0.533	0.561	0.579	0.55	0.55	0.56	0.57	0.54	0.55	0.55	0.55	0.55	0.55
														4.36	51.00	194.73	2.85			
LOI	0.35	1.40	0.64	0.46	0.86	0.65	0.14	0.01	-0.02	0.40	0.13	0.03	0.02	-0.16	0.20	-0.02	0.08	0.54	0.93	1.28
Total	99.96	100.57	100.74	100.25	100.12	99.72	99.57	100.00	100.12	100.23	99.55	99.85	100.46	105.18	151.01	294.31	102.74	99.96	99.47	99.94
S%	0.07	0.01	0.04	0.04	0.05	0.05	0.10	0.12	0.05	0.06	0.05	0.05	0.05	0.04	0.05	0.04	0.05	0.04	0.04	0.04
Element ppm																				
Rb	33	30	37	36	28	37	34	34	36	37	35.70	35.30	32.40	31.30	33.30	34.40	28.40	32.10	28.80	34.40
Sr	321	334	329	325	338	338	334	332	329	347	323.90	320.60	320.90	328.10	319.80	318.00	322.30	316.20	319.60	321.20
Y	43.3	38.4	41.5	44.1	47.3	44.8	42.2	40.6	42.1	44.3	43.20	42.90	42.90	42.40	42.10	41.30	43.40	44.00	43.10	42.50
Zr	198	183	203	204	205	207	196	191	200	210	200.40	196.80	193.80	195.20	191.60	193.70	198.40	202.30	196.10	195.10
Nb	17.0	13.7	14.4	17.5	18.2	17.2	15.8	13.9	14.8	15.3	16.30	16.30	15.20	14.30	14.90	15.30	14.60	15.10	15.50	15.30
Ba	501	493	563	567	551	560	569	554	568	596	550.70	536.90	581.80	596.40	554.80	568.20	608.90	579.80	511.30	528.60
Pb	7	4	7	8	7	6	8	5	2	5	8.00	9.20	6.70	8.20	9.00	8.00	7.40	8.40	10.50	8.80
Th	6	3	5	6	7	5	4	5	7	5	8.70	4.60	6.10	2.20	6.40	4.70	4.70	6.20	4.40	6.10
U	0	1	3	1	1	3	0	1	2	2	0.60	2.00	1.40	1.70	1.70	2.50	2.20	0.90	1.10	0.90
Sc	38	34	32	36	38	38	36	37	34	36	37.80	38.90	40.40	34.80	36.90	35.70	34.00	38.20	33.60	36.50
V	409	416	408	397	439	426	404	412	418	443	435.70	430.10	410.20	431.50	418.90	418.40	399.80	399.30	410.10	427.10
Cr	60	47	43	46	50	48	45	50	47	44	47.80	48.90	44.10	43.50	47.00	40.40	43.70	44.20	47.30	44.30
Co	37	34	35	37	35	41	36	37	35	38	36.00	38.00	34.00	38.20	37.40	33.00	34.60	34.80	34.20	39.60
Ni	22	19	23	21	16	25	23	24	23	24	19.80	20.30	20.40	21.10	19.50	18.90	17.90	17.20	17.00	17.90
Cu	34	30	33	33	33	34	36	32	33	34	33.50	31.80	32.40	34.70	33.10	31.90	35.50	34.10	33.30	32.70
Zn	147	133	143	141	148	149	134	134	140	148	149.40	147.50	139.10	141.30	146.30	141.10	139.00	151.20	147.10	146.50
Ga	22	20	22	22	21	23	22	21	23	22	22.20	22.10	23.80	22.60	22.10	21.10	22.70	21.80	21.80	21.30
Mo	0	0	0	2	2	1	1	0	0	0	1.60	1.70	1.80	1.20	1.90	1.80	0.50	0.30	1.80	1.30
As	2	2	0	0	0	4	0	0	3	2	1.80	1.40	4.60	9.00	2.40	1.00	3.10	0.00	3.00	0.30
S	485	65	339	387	239	327	1125	1503	347	446	318.10	321.00	381.30	457.90	369.40	291.00	471.50	354.90	326.40	324.00

Sample locality	Black Band					Dyke				
Sample no.	CRB06-415	CRB06-416	CRB06-417	CRB06-418	CRB06-419	CRB06-329	CRB06-330	CRB06-331	CRB06-332	CRB06-333
Flow field	SH	SH	SH	SH	SH	SH	SH	SH	SH	SH
Height in flow (m)	-0.1	1	2.7	4.5	5.5	0	0.5	2	8	9
Distance from source (km)	157	157	157	157	157	0	0	0	0	0
Oxide wt. %										
SiO2	50.84	50.64	50.44	50.69	50.16	51.26	50.73	50.73	50.39	50.74
TiO2	2.915	2.880	2.895	2.905	2.890	2.898	2.850	2.890	2.904	2.925
Al2O3	13.21	13.25	13.15	13.17	13.12	13.69	13.25	13.29	13.16	13.22
Fe2O3	15.54	15.54	15.61	15.57	15.42	13.77	15.21	15.62	15.63	15.26
MnO	0.228	0.222	0.228	0.226	0.227	0.216	0.241	0.241	0.233	0.217
MgO	4.38	4.45	4.34	4.39	4.36	3.44	4.23	4.46	4.41	4.15
CaO	8.27	8.31	8.21	8.23	8.29	8.60	8.28	8.37	8.25	8.26
Na2O	2.67	2.63	2.71	2.75	2.70	2.71	2.69	2.75	2.71	2.81
K2O	1.43	1.46	1.33	1.28	1.25	1.33	1.42	1.24	1.32	1.20
P2O5	0.549	0.539	0.544	0.551	0.534	0.549	0.541	0.554	0.542	0.532
LOI	0.02	0.16	0.03	0.15	0.41	0.88	0.06	0.08	0.02	0.19
Total	100.06	100.08	99.48	99.92	99.35	99.35	99.50	100.21	99.56	99.52
S%	0.06	0.05	0.06	0.06	0.06	0.09	0.10	0.08	0.08	0.06
Element ppm										
Rb	38	38	37	36	34	39	34	32	36	29
Sr	333	333	326	327	325	336	325	324	326	323
Y	42.8	42.2	42.8	42.6	42.7	41.7	40.8	40.3	41.5	40.4
Zr	201	198	197	199	194	195	193	192	195	197
Nb	14.1	14.2	15.1	14.7	15.3	14.7	16.0	17.5	16.0	17.0
Ba	585	557	579	589	543	712	533	557	555	600
Pb	7	7	5	6	6	7	2	8	7	5
Th	6	7	5	6	6	4	7	6	4	7
U	2	0	0	2	0	0	0	1	0	1
Sc	36	35	38	35	35	37	36	38	36	34
V	410	414	408	414	411	426	424	413	410	424
Cr	49	48	50	44	44	56	59	60	58	52
Co	37	36	36	32	38	44	38	39	40	39
Ni	22	24	19	22	19	26	28	26	25	25
Cu	34	31	32	34	33	32	33	31	34	33
Zn	135	134	134	139	141	148	141	141	137	140
Ga	23	24	21	22	22	22	21	21	25	23
Mo	1	1	0	0	0	1	1	3	0	1
As	0	0	3	0	1	0	1	0	0	4
S	453	347	336	328	316	416	513	477	419	423

Table D.3 Major and trace element results of samples from the Ginkgo flow field.

Sample locality	Sand Hollow road (G_4)						DC-8 Borehole (G_8)							Frenchman Springs Coulee			Lyle (G_13)					
Sample no.	CRB05-011	CRB05-012	CRB05-013	CRB05-014	CRB05-015	CRB05-016	CRB05-017	CRB05-087	CRB05-088	CRB05-089	CRB05-090	CRB05-091	CRB05-092	CRB05-094	CRB05-095	CRB05-110	CRB05-111	CRB05-112	CRB06-037	CRB06-038	CRB06-039	CRB06-040	CRB06-041
Flow field	G -flow 1	G -flow 1	G -flow 1	G -flow 1	G -flow 1	G - flow 2	G - flow 2	G - flow 2	G - flow 2	G - flow 2	G - flow 2	G - flow 2	G - flow 2	G - flow 2	G - flow 2	G - flow 1	G - flow 1	G - flow 1	G - flow 1	G - flow 1	G - flow 1	G - flow 1	G - flow 1
Height in flow (m)	0	1.5	4	9	14			49	45.65	42.15	39.75	31.75	14.35	5.35	0.1	8.95	2.95	0.1	18.5	15	13.4	12	9.7
Distance from source (km)	113.8	113.8	113.8	113.8	113.8	113.8	113.8	65	65	65	65	65	65	65	65	123	123	123	227.2	227.2	227.2	227.2	227.2
Oxide wt. %																							
SiO2	50.12	50.13	49.77	50.06	50.73	50.60	50.25	49.47	50.16	49.90	49.77	49.54	50.23	49.84	49.55	50.92	49.90	50.62	50.24	50.01	50.57	50.33	49.42
TiO2	3.018	2.993	3.006	2.994	3.076	3.003	3.065	2.989	3.018	2.986	2.954	2.943	2.993	2.972	3.195	2.909	3.027	3.047	2.952	2.934	3.016	2.972	2.956
Al2O3	13.35	13.42	13.04	13.15	13.39	13.35	12.95	13.12	13.20	13.09	13.05	13.01	13.08	13.05	14.22	13.51	13.22	13.52	13.07	13.14	13.06	13.00	12.84
Fe2O3	15.33	15.60	16.11	15.72	15.28	15.54	16.25	15.98	15.61	15.83	15.69	15.92	16.08	16.07	14.78	14.90	15.97	14.38	15.78	16.03	16.40	16.45	16.11
MnO	0.213	0.214	0.213	0.217	0.209	0.237	0.231	0.216	0.226	0.226	0.248	0.225	0.229	0.228	0.267	0.220	0.220	0.197	0.229	0.234	0.254	0.272	0.247
MgO	3.81	4.06	4.26	3.98	4.00	3.92	4.06	3.42	3.97	3.98	3.90	3.89	3.94	3.96	3.54	4.15	4.31	2.93	3.95	3.98	4.08	3.64	3.93
CaO	8.45	8.29	7.92	7.97	8.34	8.22	8.03	8.07	8.18	8.11	8.06	7.98	8.02	7.99	7.66	8.39	8.30	8.54	8.10	8.13	8.07	7.89	7.95
Na2O	2.73	2.83	2.85	2.88	2.71	2.73	2.70	2.74	2.84	2.80	2.86	2.82	2.86	2.86	3.19	2.74	2.74	2.89	2.75	2.65	2.74	2.81	2.64
K2O	1.13	1.24	1.22	1.31	1.42	1.47	1.47	1.42	1.24	1.24	1.18	1.33	1.37	1.33	1.20	1.42	1.32	1.30	1.25	1.26	1.39	1.29	1.41
P2O5	0.660	0.620	0.598	0.616	0.639	0.682	0.659	0.657	0.661	0.634	0.650	0.649	0.666	0.644	0.696	0.568	0.615	0.637	0.665	0.648	0.657	0.648	0.626
LOI	1.07	0.15	0.58	0.51	0.33	0.06	0.03	1.25	0.87	0.81	1.22	0.96	0.18	0.33	1.32	0.01	0.11	1.41	0.46	0.55	0.04	0.49	0.08
Total	99.89	99.54	99.57	99.40	100.12	99.81	99.69	99.34	99.98	99.61	99.59	99.27	99.64	99.27	99.62	99.74	99.72	99.47	99.45	99.57	100.28	99.79	98.23
Element ppm																							
Rb	29	34	28	35	37	35	37	34	34	36	31	35	36	37	17	36	31	25	34	34	33	35	38
Sr	350	342	326	331	339	334	333	319	332	328	331	323	327	333	355	325	336	338	339	343	324	318	334
Y	44.7	42.7	43.1	44.7	44.0	43.2	44.4	44.6	42.9	42.1	43.4	43.4	43.7	43.7	45.6	43	43	44.7	43.1	43.9	43.4	44	44.1
Zr	193	194	190	202	201	194	197	194	196	189	194	194	193	190	208	201	187	201	186	192	190	195	195
Nb	16.1	15.1	15.6	15.5	15.3	16.1	15.7	16.4	14.5	14.9	15.6	15.6	16.1	15.6	15.7	16	15	16.3	15.6	14.4	14.9	15.2	15.1
Ba	554	550	609	621	585	561	608	528	575	572	563	544	562	609	653	550	561	575	559	580	554	571	582
Pb	10	9	10	8	5	6	10	9	8	10	10	9	7	9	7	9	10	7	8	12	7	8	10
Th	4	6	8	6	8	5	6	6	7	5	5	3	9	8	4	7	5	3	6	7	7	5	7
U	3	1	1	1	4	2	0	0	0	2	0	1	1	1	0	2	2	2	2	3	0	3	2
Sc	39	34	33	34	36	38	34	38	39	37	34	38	36	35	41	36	37	40	33	34	36	37	36
V	405	395	398	400	421	392	392	384	398	392	389	379	372	371	444	431	408	416	373	363	386	386	372
Cr	19	18	17	19	20	15	14	17	15	15	17	19	17	14	16	46	19	20	15	24	23	28	21
Co	35	37	34	37	38	35	35	33	34	35	36	34	39	33	46	34	34	40	31	33	33	36	34
Ni	11	12	12	15	15	12	11	11	15	12	13	15	12	13	16	20	16	14	14	16	16	17	18
Cu	27	30	30	32	32	28	30	26	29	29	27	27	27	28	30	35	27	30	28	30	29	28	29
Zn	153	149	142	142	153	154	141	155	145	143	151	149	148	137	163	149	139	155	137	142	145	147	139
Ga	20	23	23	23	23	23	24	22	21	22	23	23	22	21	25	24	23	21	23	23	23	21	23
Mo	1	1	3	2	1	2	1	3	1	2	1	1	1	3	3	2	1	2	1	2	2	1	2
As	2	3	3	1	2	0	0	0	4	0	4	1	0	1	0	0	5	3	0	0	4	0	3
S	223	286	541	562	219	295	766	249	311	342	294	316	341	431	168	263	843	297	358	318	450	592	459

Sample locality			Upper railway grade, Wilson Canyon (G_2)					opposite Sheffler				Lenore Caves (G_11)									
Sample no.	CRB06-042	CRB06-043	CRB06-077	CRB06-107	CRB06-108	CRB06-109	CRB06-110	CRB06-111	CRB06-126	CRB06-127	CRB06-128	CRB06-159	CRB06-160	CRB06-161B	CRB06-161T	CRB06-162	CRB06-163	CRB06-164	CRB06-165	CRB06-343	CRB06-344
Flow field	G - flow 1	G - flow 1	G - flow 1	G - flow 3	G - flow 3	G - flow 3	G - flow 3	G - flow 3	G - flow 1	G - flow 1	G - flow 1	G - flow 2	G - flow 2	G - flow 2	G - flow 2	G - flow 2	G - flow 1	G - flow 1	G - flow 1	G - flow 1	G - flow 1
Height in flow (m)	5.5	1		0.6	1.5	2	2.2		1	15	60	0.2	0.75	7	7.1	13	0.4	4.5	12	18.5	17
Distance from source (km)	227.2	227.2		19.3	19.3	19.3	19.3	19.4	2	2	2	134.4	134.4	134.4	134.4	134.4	134.4	134.4	134.4	42.6	42.6
Oxide wt. %																					
SiO2	49.63	49.25	51.04	50.11	50.35	50.18	49.93	50.95	50.05	49.45	50.95	49.37	49.95	49.37	50.38	49.12	49.83	49.56	49.10	49.48	49.53
TiO2	3.005	2.948	2.834	2.991	3.060	3.052	3.084	3.080	3.021	3.028	2.836	2.999	3.061	3.221	3.072	3.231	3.063	3.073	3.313	2.942	3.222
Al2O3	12.87	12.91	13.42	13.49	13.11	13.15	13.05	13.24	13.27	13.35	13.23	13.24	13.07	13.46	13.40	13.69	13.23	13.12	13.67	13.21	12.97
Fe2O3	15.84	16.05	15.33	15.97	16.33	16.16	16.34	15.43	15.83	15.80	15.47	15.42	16.05	16.24	15.26	14.98	15.15	15.80	15.97	13.61	13.58
MnO	0.222	0.231	0.222	0.231	0.238	0.235	0.239	0.231	0.230	0.211	0.228	0.248	0.240	0.233	0.235	0.203	0.172	0.220	0.228	0.195	0.213
MgO	4.02	4.08	4.38	3.96	4.05	4.11	4.02	3.97	4.14	4.40	4.30	4.07	4.26	3.80	3.56	3.67	3.95	4.17	3.79	4.11	3.98
CaO	7.87	7.74	8.31	8.07	7.98	7.99	7.94	8.26	7.92	8.14	8.17	8.33	8.10	8.39	8.23	8.73	8.04	8.29	8.78	8.40	8.53
Na2O	2.74	2.78	2.68	2.70	2.73	2.72	2.76	2.81	2.83	2.86	2.80	2.65	2.72	2.77	2.66	2.78	2.88	2.62	2.63	2.66	2.71
K2O	1.25	1.26	1.32	1.39	1.26	1.27	1.29	1.45	1.29	1.15	1.34	1.51	1.37	1.02	1.37	1.09	1.12	1.26	0.84	1.07	1.11
P2O5	0.596	0.570	0.544	0.660	0.659	0.642	0.682	0.681	0.585	0.521	0.550	0.676	0.600	0.605	0.623	0.637	0.571	0.580	0.682	0.570	0.576
LOI	0.62	0.06	0.13	0.56	0.32	0.19	0.19	-0.02	0.43	0.54	0.00	0.78	0.19	0.63	0.63	1.94	1.86	0.81	1.57	-	-
Total	98.67	97.89	100.21	100.12	100.08	99.71	99.52	100.07	99.61	99.43	99.87	99.30	99.60	99.74	99.42	100.07	99.86	99.51	100.56	96.25	96.41
Element ppm																					
Rb	32	37		36	37	37	37	37	34	31	36	39	35	25	34	27	15	32	21	24	25
Sr	319	318		355	344	343	343	352	326	331	329	353	335	351	340	353	340	344	355	322	316
Y	42.1	41.6		42.7	43.1	44.6	44.3	45.0	43.0	39.1	43.5	41.8	43.4	44.9	44.7	46.1	42.2	42.5	47.3	169	174
Zr	194	193		192	196	198	199	200	195	171	200	197	197	207	205	210	191	196	211	37	38
Nb	15.9	15.4		15.4	15.2	14.9	14.0	15.3	15.4	12.6	14.9	14.6	15.3	15.1	16.2	15.6	14.6	15.5	16.3	12.4	12.6
Ba	583	574		571	564	565	594	595	578	548	560	589	547	586	581	557	608	559	569	491	534
Pb	7	7		6	8	7	8	6	5	4	8	5	5	7	7	6	7	7	8	7	8
Th	7	6		7	5	5	6	6	7	6	6	5	5	8	7	5	5	6	6	3	4
U	2	0		0	2	0	0	3	3	0	0	1	2	0	2	0	2	0	2	-	-
Sc	36	33		36	36	36	34	35	32	32	35	34	36	35	36	39	33	34	34	35	38
V	400	414		365	363	368	388	386	401	428	399	420	406	415	421	449	419	415	451	406	443
Cr	20	22		22	19	20	20	19	23	25	43	28	28	26	27	22	25	27	25	20	20
Co	34	34		33	38	33	35	35	33	38	34	39	38	39	36	42	37	38	37		
Ni	17	19		14	11	15	16	16	17	17	20	22	19	20	20	18	19	22	19	14	15
Cu	30	29		30	29	28	28	27	29	29	35	32	34	32	33	31	32	33	35	23	22
Zn	134	132		139	151	152	147	151	139	127	150	146	145	154	151	149	137	136	153	138	141
Ga	23	22		23	21	22	23	23	23	23	22	21	23	24	23	24	21	23	21	21	22
Mo	3	2		2	1	1	0	1	2	0	0	2	2	1	1	1	1	1	0	-	-
As	3	4		0	0	0	0	1	3	1	1	4	0	0	1	5	0	0	0	-	-
S	511	498		373	412	286	189	469	261	77	290	876	1125	587	298	2798	883	350	652	-	-

Sample locality	Wallula Gap (G_3)						Sheffler (G_1)										Babcock Bench		
Sample no.	CRB06-345	CRB06-346	CRB06-347	CRB06-348	CRB06-349	CRB06-350	CRB06-361	CRB06-362	CRB06-363	CRB06-364	CRB06-365	CRB06-366	CRB06-367	CRB06-368	CRB06-369	CRB06-386	CRB06-399	CRB06-400	CRB06-401
Flow field	G - flow 1	G - flow 1	G - flow 1	G - flow 1	G - flow 1	G - flow 1	G precursor lobes	G precursor lobes	G	G	G	G	G	G	G	G	G - flow 1	G - flow 1	G - flow 1
Height in flow (m)	12	9	6.5	5	2	0.8			0.1	5	7	12.7	13.5	17	22		0	4	7
Distance from source (km)	42.6	42.6	42.6	42.6	42.6	42.6	2.3	2.3	2.3	2.3	2.3	2.3	2.3	2.3	2.3	0.4	140.6	140.6	140.6
Oxide wt. %																			
SiO2	49.89	49.78	50.22	50.08	50.56	51.24	50.37	50.20	50.12	50.15	50.17	49.77	49.43	50.22	49.32	49.92	50.25	50.88	50.29
TiO2	3.209	3.126	3.114	3.079	3.041	3.020	3.068	3.014	3.053	3.036	3.027	3.170	3.231	3.068	3.254	3.068	3.040	3.027	3.050
Al2O3	12.95	12.82	12.80	12.82	13.90	13.79	13.04	13.21	13.09	12.98	13.19	13.16	13.14	13.16	14.00	13.01	13.03	13.56	13.20
Fe2O3	13.38	13.84	14.18	14.34	14.62	14.50	16.20	15.67	15.80	16.42	16.03	15.72	16.12	15.79	15.58	16.21	16.24	15.25	15.67
MnO	0.203	0.205	0.229	0.216	0.196	0.152	0.235	0.202	0.197	0.239	0.238	0.184	0.229	0.235	0.216	0.245	0.235	0.218	0.214
MgO	3.77	4.10	4.33	4.18	3.65	3.52	3.88	3.79	3.28	4.05	4.14	3.78	4.11	3.99	3.02	4.36	4.04	4.02	3.72
CaO	8.20	7.96	7.98	7.78	7.95	7.88	7.79	8.08	8.00	7.88	7.91	8.32	8.34	8.17	8.77	8.21	8.00	8.36	7.91
Na2O	2.85	2.87	2.90	2.88	2.98	2.94	2.32	2.70	2.76	2.69	2.87	2.81	2.75	2.67	2.70	2.69	2.76	2.83	2.71
K2O	1.25	1.27	1.25	1.25	1.31	1.30	1.31	1.27	1.15	1.32	1.27	1.09	1.09	1.44	0.78	1.23	1.43	1.37	1.47
P2O5	0.611	0.588	0.598	0.594	0.591	0.571	0.650	0.648	0.657	0.647	0.586	0.572	0.580	0.594	0.627	0.511	0.681	0.679	0.914
LOI	-	-	-	-	0.68	1.06	0.74	0.80	1.50	0.35	0.28	0.92	0.89	0.39	1.67	0.22	-0.24	0.24	0.61
Total	96.32	96.55	97.61	97.22	99.48	99.97	99.61	99.59	99.61	99.77	99.71	99.50	99.89	99.73	99.94	99.68	99.47	100.44	99.76
Element ppm																			
Rb	23	30	33	33	35	33	38	41	33	36	35	24	25	37	23	28	37	35	37
Sr	309	298	298	294	339	343	329	348	346	336	328	343	346	345	347	304	347	360	348
Y	181	179	182	181	43.2	41	44.5	42	43.2	42.5	42.2	43.2	43	44	46.5	42.2	43.8	42.9	43.5
Zr	39	38	39	38	198	197	194	197	199	197	194	197	195	201	209	169	198	191	198
Nb	13.7	13.2	13.8	13.1	15.7	14.9	14.6	16	14.8	15.1	15.2	15.9	15	15	16.5	11.8	15.5	14.4	15.1
Ba	554	545	562	562	601	600	548	579	562	590	580	606	579	602	485	557	596	569	590
Pb	8	6	8	8	6	4	9	7	8	6	6	7	5	7	5	6	5	7	4
Th	3	4	3	4	6	6	5	5	7	4	7	4	7	4	8	7	6	5	5
U	-	-	-	-	3	0	0	1	1	0	1	1	3	1	1	2	0	2	2
Sc	38	36	37	36	37	35	37	34	36	38	34	33	38	38	36	39	33	34	35
V	431	420	425	416	413	398	367	370	378	356	403	413	411	394	428	389	355	370	365
Cr	19	21	19	19	24	22	25	22	21	20	23	18	22	24	27	39	17	20	20
Co					37	41	33	34	29	36	32	40	37	37	29	37	29	35	34
Ni	15	15	15	19	18	19	15	16	16	19	19	18	21	18	13	30	15	17	16
Cu	24	23	22	24	31	28	28	30	25	28	30	33	32	34	30	41	29	26	30
Zn	143	144	144	143	138	147	154	140	146	151	139	126	128	131	148	138	140	141	153
Ga	22	24	22	21	23	25	22	23	22	22	23	23	21	23	23	22	24	24	22
Mo	-	-	-	-	0	0	0	0	0	0	1	2	0	0	0	0	1	0	1
As	-	-	-	-	1	3	0	0	0	1	0	4	3	0	2	0	0	0	2
S	-	-	-	-	256	304	378	445	105	378	162	43	259	262	162	103	203	1390	606

Table D.4 Major and trace element results of samples from the Grande Ronde Basalts.

Sample locality		Locke Lake			Starbuck_Washtucna										High interval - Starbuck road									
Sample no.	CRB06-020	CRB06-023	CRB06-024	CRB05-050	CRB05-051	CRB05-052	CRB05-053	CRB05-054	CRB05-055	CRB05-056	CRB05-057	CRB06-304	CRB06-305	CRB06-306	CRB06-307	CRB06-308	CRB06-309	CRB06-310	CRB06-311	CRB06-312	CRB06-313			
Flow field	GR-N2	GR-N2	GR-N2	GR-N2	GR-N2	GR-N2	GR-N2	GR-N2	GR-N2	GR-N2	GR-N2	GR-N2	GR-N2	GR-N2	GR-N2	GR-N2	GR-N2	GR-N2	GR-N2	GR-N2	GR-N2			
Height in flow (m)	0.6	1	0.5	1	4	5	7	10	12.5	14	18	0	0.8	1.1	1.3	1.9	2.4	3	3.6	3.9	4.3			
Distance from source (km)	-	-	-	-	-	-	-	-	-	-	-	-	-	-	-	-	-	-	-	-	-			
Oxide wt. %																								
SiO2	53.65	53.58	53.35	52.98	52.80	52.77	52.58	52.72	52.58	52.59	52.95	52.76	52.72	52.76	52.89	52.32	52.51	52.37	52.19	52.85	52.34			
TiO2	1.962	1.946	1.992	1.897	1.849	1.854	1.792	1.859	1.912	1.879	1.945	1.884	1.876	1.865	1.890	1.862	1.869	1.858	1.907	1.921	1.897			
Al2O3	13.87	13.83	13.66	13.87	13.88	14.09	14.10	14.16	14.02	13.86	13.81	13.86	13.93	13.85	13.92	13.85	13.94	13.79	13.94	13.87	13.95			
Fe2O3	13.43	13.77	13.65	13.12	12.84	12.81	12.80	12.98	13.03	13.24	13.19	12.64	13.14	12.96	12.80	12.94	12.99	12.99	13.50	13.22	12.85			
MnO	0.237	0.240	0.218	0.202	0.198	0.216	0.207	0.203	0.202	0.207	0.210	0.206	0.227	0.221	0.213	0.208	0.211	0.212	0.247	0.236	0.229			
MgO	4.42	4.73	4.34	4.64	4.79	4.38	4.78	4.76	4.68	4.67	4.52	4.72	4.80	4.60	4.82	4.95	4.78	4.63	4.85	4.60	4.53			
CaO	8.53	8.55	8.15	8.54	8.74	8.79	8.85	8.82	8.80	8.52	8.45	8.72	8.78	8.77	8.86	8.85	8.82	8.71	8.81	8.72	8.79			
Na2O	2.79	3.00	2.95	2.82	2.87	2.86	2.82	2.83	2.78	2.82	2.85	2.89	2.88	2.83	2.72	2.68	2.79	2.79	2.77	2.88	2.80			
K2O	1.11	1.09	1.14	1.23	1.02	0.97	0.94	0.91	0.83	1.04	1.14	1.05	0.98	1.00	0.97	0.84	0.87	0.93	0.81	0.96	0.97			
P2O5	0.308	0.307	0.324	0.288	0.275	0.272	0.267	0.274	0.288	0.282	0.307	0.270	0.278	0.273	0.276	0.273	0.279	0.263	0.280	0.287	0.277			
LOI	0.57	0.20	0.15	0.20	0.45	0.55	0.68	0.49	1.19	0.53	0.33	0.32	0.49	0.64	0.78	1.12	0.75	0.94	0.63	0.67	0.71			
Total	100.88	101.24	99.92	99.79	99.72	99.56	99.81	99.99	100.31	99.64	99.71	99.33	100.10	99.76	100.15	99.90	99.81	99.49	99.93	100.21	99.35			
Element ppm																								
Rb	31	26	29	30	25	26	27	24	24	28	29	25	24	27	26	24	25	25	22	27	26			
Sr	324	320	324	319	320	321	325	328	324	320	318	333	327	325	326	327	332	326	325	324	334			
Y	35.8	35	35.4	33.9	34.7	34.1	33.2	35.1	35.2	34.0	35.4	34.7	33	32.6	33.3	33.0	34.5	33.9	35.0	35.4	35.8			
Zr	170	164	171	164	158	160	154	161	163	163	166	161	162	160	163	160	162	161	165	164	166			
Nb	13	12.1	13	13.2	11.5	11.9	11.7	11.9	12.8	12.6	12.6	12.0	12.0	11.4	12.1	11.8	11.4	11.6	13.0	12.1	12.1			
Ba	487	490	531	489	461	457	422	438	426	447	545	474	465	456	429	410	437	436	417	476	447			
Pb	7	5	8	5	6	8	6	8	6	8	6	5	4	5	2	2	4	3	4	6	5			
Th	1	2	3	5	4	5	2	3	2	3	4	5	6	2	3	5	5	6	4	5	6			
U	1	1	2	0	1	1	0	0	1	1	0	2	1	1	1	0	0	0	2	1	0			
Sc	36	36	35	35	37	40	37	38	38	39	39	36	34	35	35	33	35	36	36	38	37			
V	343	336	352	337	333	338	325	349	346	345	342	328	325	334	337	337	333	329	341	331	336			
Cr	27	32	22	27	30	32	32	31	29	27	26	34	38	41	39	34	38	36	40	35	33			
Co	35	36	36	35	39	39	39	38	36	37	37	41	38	38	43	41	41	35	39	40	42			
Ni	15	15	13	12	14	13	15	16	13	11	11	17	19	16	18	15	17	17	18	16	19			
Cu	28	31	29	33	35	37	34	33	34	31	34	37	36	34	35	34	34	35	40	36	35			
Zn	116	111	118	114	114	122	116	124	120	124	123	111	112	117	114	113	118	115	120	120	119			
Ga	21	21	22	20	22	22	19	22	21	21	21	21	22	20	22	20	21	22	22	23	20			
Mo	1	2	2	1	1	0	1	0	2	2	1	1	0	1	0	1	0	0	2	0	1			
As	4	2	2	2	1	0	1	0	3	2	1	0	0	0	0	0	0	2	2	0	0			
S	152	59	141	331	296	284	250	177	143	197	209	160	146	260	133	80	139	172	176	224	101			

Table D.5 Major and trace element XRF results analysed at Washington State University

Sample	CRB06_006	CRB06_007	CRB06_008	CRB06_009	CRB06_010	CRB06_011	CRB06_046	CRB06_047	CRB06_056	CRB06_057	CRB06_064	CRB06_065	CRB06_066	CRB06_067	CRB06_068	CRB06_071	CRB06_074	CRB06_075
Oxide wt. %																		
SiO_2	53.07	53.74	53.32	53.51	52.83	53.03	53.43	49.86	46.89	50.52	53.28	52.43	53.12	53.01	52.86	50.78	49.54	49.27
TiO_2	1.735	1.702	1.705	2.158	1.848	1.790	1.756	3.112	3.551	3.040	1.816	1.694	1.788	1.800	1.911	2.856	2.962	3.171
Al_2O_3	13.86	14.17	14.03	13.41	13.97	14.03	13.87	12.73	14.69	12.94	13.97	14.20	13.97	14.04	13.78	13.09	13.15	12.88
FeO	11.12	10.64	10.55	12.06	10.83	10.81	10.76	14.04	10.74	13.99	11.47	11.04	11.25	10.92	11.63	12.97	13.54	14.32
MnO	0.193	0.190	0.186	0.202	0.197	0.191	0.191	0.253	0.292	0.227	0.202	0.182	0.192	0.191	0.206	0.215	0.179	0.235
MgO	4.81	4.77	4.77	4.10	4.36	4.68	4.64	4.22	2.84	3.93	5.09	5.21	5.12	5.03	4.86	4.14	4.05	3.86
CaO	8.49	8.55	8.56	8.08	8.63	8.74	8.23	8.23	8.20	8.03	8.84	8.78	8.53	8.35	8.62	8.16	7.92	8.23
Na_2O	2.94	2.90	2.86	2.84	2.85	2.80	2.76	2.76	2.89	2.85	2.81	2.91	2.97	3.01	2.86	2.70	2.84	2.70
K_2O	1.13	1.23	1.18	1.36	1.12	1.11	1.53	1.23	0.52	1.33	1.18	0.98	1.09	1.12	0.96	1.48	1.22	1.03
P_2O_5	0.303	0.307	0.301	0.349	0.300	0.282	0.326	0.538	0.831	0.688	0.280	0.257	0.285	0.302	0.278	0.530	0.579	0.743
Total	97.65	98.20	97.47	98.07	96.94	97.45	97.49	96.98	91.45	97.54	98.94	97.67	98.32	97.78	97.96	96.93	95.97	96.44
Element ppm																		
Ni	17	16	18	15	19	20	13	24	7	13	18	18	17	19	13	17	15	13
Cr	41	44	44	28	42	48	38	32	19	17	49	54	48	45	29	42	19	18
Sc	36	38	35	37	37	36	35	41	43	36	38	37	37	36	37	36	35	37
V	308	303	303	345	328	326	306	386	404	378	326	314	316	317	330	408	401	417
Ba	541	519	515	551	493	465	539	543	1136	573	453	448	466	479	422	599	547	561
Rb	23	31	30	35	31	30	35	28	9	31	27	23	28	29	23	33	26	25
Sr	306	313	310	294	307	306	306	288	393	319	302	304	297	298	309	306	304	319
Zr	153	153	152	183	157	150	155	161	210	182	153	141	151	153	153	187	174	191
Y	30	30	30	36	31	30	30	39	48	40	31	29	31	30	31	38	37	41
Nb	9.9	10.0	9.5	12.3	10.8	9.9	10.8	11.5	15.4	12.9	10.2	9.2	9.9	10.1	10.1	13.9	12.7	13.8
Ga	21	18	20	23	21	22	20	22	25	23	21	20	19	20	22	22	22	20
Cu	28	24	23	34	32	31	27	29	25	20	36	32	34	33	32	24	22	21
Zn	113	112	110	125	116	110	115	141	178	144	114	110	111	119	116	136	136	146
Pb	7	7	7	8	8	6	7	7	8	7	6	5	6	7	7	6	7	6
La	18	23	17	22	20	21	22	25	31	23	20	15	16	20	17	26	23	28
Ce	46	46	40	50	38	40	46	50	65	60	44	39	46	48	43	54	51	58
Th	2	2	1	3	2	2	1	2	4	2	1	1	1	3	1	2	2	3
Nd	23	25	25	29	23	23	25	30	38	34	26	21	23	23	25	31	30	34

Sample	CRB06_076	CRB06_077	CRB06_096	CRB06_097	CRB06_098	CRB06_099	CRB06_112	CRB06_113	CRB06_114	CRB06_115	CRB06_116	CRB06_117	CRB06_118	CRB06_119	CRB06_130	CRB06_131	CRB06_132	CRB06_133	CRB06_134	CRB06_135
Oxide wt. %																				
SiO_2	48.35	50.39	48.73	49.88	49.56	50.36	50.55	50.28	50.35	50.57	50.45	50.67	50.35	50.44	51.17	52.46	51.42	51.40	51.31	51.19
TiO_2	3.206	3.142	3.120	3.113	3.092	3.061	3.065	3.049	3.079	3.097	3.079	3.068	3.069	3.076	1.641	2.729	1.697	1.651	1.651	1.631
Al_2O_3	12.79	12.98	12.82	12.83	12.93	12.88	12.95	12.92	12.92	13.05	12.82	12.97	12.87	12.89	14.41	13.37	14.49	14.43	14.51	14.62
FeO	13.02	14.39	13.63	14.08	13.76	14.02	13.83	14.12	14.32	14.38	14.22	14.03	14.18	14.31	10.45	12.06	10.59	10.48	10.60	10.42
MnO	0.133	0.235	0.199	0.189	0.218	0.243	0.223	0.230	0.233	0.236	0.234	0.235	0.232	0.233	0.177	0.187	0.181	0.178	0.181	0.180
MgO	4.53	4.33	4.06	4.06	3.53	4.03	4.17	4.21	4.23	4.28	4.22	4.30	4.23	4.22	6.74	3.68	6.70	6.79	6.93	6.97
CaO	6.93	8.18	8.22	8.01	8.17	8.10	8.12	8.08	8.10	8.14	8.03	8.10	8.06	8.03	10.63	7.74	10.58	10.56	10.65	10.65
Na_2O	2.77	2.89	2.57	2.88	2.63	2.71	2.81	2.85	2.79	2.79	2.80	2.77	2.81	2.81	2.34	2.64	2.35	2.37	2.36	2.39
K_2O	1.28	1.28	1.12	1.24	1.13	1.42	1.40	1.24	1.41	1.42	1.43	1.41	1.35	1.40	0.63	1.69	0.68	0.69	0.66	0.62
P_2O_5	0.602	0.603	0.585	0.590	0.698	0.681	0.664	0.660	0.661	0.646	0.667	0.662	0.666	0.662	0.230	0.372	0.238	0.228	0.227	0.226
Total	93.62	98.42	95.05	96.85	95.73	97.50	97.78	97.64	98.10	98.61	97.95	98.23	97.82	98.08	98.41	96.93	98.91	98.79	99.08	98.90
Element ppm																				
Ni	17	17	17	17	13	15	17	17	16	15	16	17	18	18	54	23	50	54	54	53
Cr	20	21	20	20	16	17	18	19	18	20	20	18	17	17	114	31	103	113	110	113
Sc	37	38	37	38	37	37	36	36	37	36	35	37	35	37	36	29	35	36	36	36
V	429	426	424	426	380	381	394	388	392	400	388	391	388	393	279	331	281	278	281	278
Ba	563	569	522	550	557	580	585	564	578	564	574	564	566	574	246	589	242	251	237	242
Rb	33	31	25	32	30	34	34	29	35	35	35	35	34	35	14	48	14	15	14	14
Sr	297	307	310	296	328	319	317	316	312	315	310	311	311	312	230	254	230	222	226	224
Zr	185	182	178	181	184	181	181	181	180	175	182	178	180	179	134	216	138	134	131	129
Y	38	38	38	38	41	39	40	39	38	38	39	38	39	39	28	37	28	27	27	27
Nb	13.8	12.6	12.5	13.1	13.8	13.7	13.3	12.9	13.7	13.5	14.0	12.8	13.2	12.4	11.2	20.7	11.6	10.6	11.1	11.2
Ga	21	22	23	21	20	22	23	22	22	20	23	21	21	21	20	21	19	20	18	19
Cu	24	23	24	24	18	21	19	21	22	20	21	22	23	22	51	26	50	53	48	49
Zn	139	146	137	145	142	143	146	144	143	144	143	145	143	144	93	123	95	91	93	94
Pb	8	7	6	7	7	8	7	8	8	6	6	6	8	7	4	11	4	5	5	4
La	22	26	22	21	26	26	27	26	24	26	25	23	28	26	18	36	17	19	15	19
Ce	57	64	52	56	56	62	58	57	60	56	59	59	56	57	40	78	43	38	36	34
Th	2	2	2	2	3	3	2	3	3	2	3	2	2	3	1	7	1	1	1	0
Nd	34	34	31	32	32	36	32	34	33	33	35	36	32	32	20	38	22	20	21	21

Sample	CRB06_136	CRB06_154	CRB06_155	CRB06_156	CRB06_157	CRB06_158	CRB06_175	CRB06_179	CRB06_185	CRB06_204	CRB06_205	CRB06_206	CRB06_207	CRB06_208	CRB06_209	CRB06_210	CRB06_211	CRB06_212	CRB06_213	CRB06_214
Oxide wt. %																				
SiO_2	50.96	49.47	49.40	48.26	49.13	48.79	53.65	53.81	50.79	53.03	53.19	52.82	53.66	54.20	54.14	54.18	53.95	53.86	53.32	52.94
TiO_2	1.748	3.666	3.631	3.658	3.595	3.573	1.789	1.805	2.983	1.749	1.798	1.832	1.733	1.741	1.750	1.754	1.741	1.765	1.714	1.660
Al_2O_3	14.63	12.69	12.57	12.61	12.54	12.48	14.12	14.39	13.14	13.91	14.22	14.06	14.04	14.11	14.13	14.19	14.22	14.00	14.09	14.20
FeO	10.06	14.50	14.62	13.87	14.70	14.68	11.32	10.85	14.02	11.06	10.70	10.42	10.85	10.99	11.17	10.98	10.97	10.91	10.93	10.24
MnO	0.175	0.239	0.243	0.233	0.237	0.239	0.201	0.200	0.223	0.192	0.187	0.192	0.194	0.194	0.197	0.196	0.196	0.191	0.196	0.174
MgO	6.47	4.45	4.48	3.91	4.51	4.49	5.18	5.07	4.16	5.06	4.84	4.25	4.63	4.76	4.93	4.82	4.59	4.58	4.85	4.44
CaO	10.84	8.62	8.43	8.68	8.39	8.33	8.89	9.10	8.12	8.85	9.06	9.04	8.48	8.53	8.56	8.57	8.46	8.40	8.60	8.80
Na_2O	2.43	2.69	2.64	2.68	2.59	2.56	2.79	2.79	2.83	2.72	2.79	2.64	2.82	2.87	2.84	2.85	2.90	2.78	2.70	2.83
K_2O	0.60	1.30	1.30	1.05	1.27	1.29	1.22	1.16	1.40	1.10	1.09	1.06	1.31	1.32	1.30	1.27	1.27	1.41	1.28	0.94
P_2O_5	0.295	0.766	0.783	0.785	0.773	0.769	0.274	0.270	0.668	0.267	0.276	0.314	0.313	0.312	0.311	0.312	0.339	0.329	0.309	0.282
Total	98.22	98.37	98.10	95.74	97.73	97.20	99.44	99.45	98.33	97.93	98.14	96.63	98.04	99.03	99.34	99.11	98.64	98.23	97.99	96.50
Element ppm																				
Ni	56	20	18	18	20	20	19	19	15	18	20	15	18	15	16	16	15	17	16	15
Cr	106	15	12	13	14	14	48	51	17	48	48	46	41	42	42	43	41	39	44	51
Sc	36	40	40	38	39	38	38	38	35	37	37	37	34	35	37	35	34	35	35	37
V	287	431	428	429	421	413	323	333	373	325	335	330	306	307	306	309	288	306	307	304
Ba	295	576	562	631	554	545	456	448	561	429	469	548	523	523	520	530	544	527	527	542
Rb	12	28	31	26	31	29	27	23	33	26	25	25	32	32	32	32	31	36	28	19
Sr	232	286	277	293	278	275	304	312	326	308	320	325	309	309	309	312	320	311	314	321
Zr	145	217	218	217	217	216	150	151	177	144	149	154	157	157	156	156	157	159	153	146
Y	30	48	48	48	47	47	31	32	38	29	31	32	31	31	31	31	31	32	30	31
Nb	12.0	18.0	17.2	17.0	16.6	16.9	9.5	10.4	13.0	9.2	9.9	10.2	10.4	10.1	10.2	9.3	9.5	9.8	9.2	9.0
Ga	20	22	22	23	24	21	22	20	22	21	20	21	21	20	21	20	21	19	18	22
Cu	51	21	21	23	21	20	37	38	18	32	33	32	27	26	24	26	24	25	25	28
Zn	97	160	159	157	154	153	115	114	143	112	110	118	115	114	117	115	114	116	114	109
Pb	4	10	8	8	8	6	8	6	7	6	6	8	5	8	7	6	8	8	7	7
La	23	27	27	30	30	28	22	19	25	18	17	18	21	23	19	22	19	24	19	18
Ce	41	71	67	70	69	69	38	42	50	39	41	46	45	47	43	42	47	46	43	41
Th	1	5	5	5	4	2	3	2	4	4	3	4	3	4	3	4	3	5	3	3
Nd	22	40	38	41	40	42	24	24	31	20	26	24	22	26	24	25	25	27	23	24

Sample	CRB06_335	CRB06_336	CRB06_337	CRB06_338	CRB06_339	CRB06_340	CRB06_341	CRB06_343	CRB06_344	CRB06_345	CRB06_346	CRB06_347	CRB06_348	CRB06_349	CRB06_350
Oxide wt. %															
SiO_2	50.66	50.88	50.67	51.89	49.88	50.93	49.42	49.48	49.53	49.89	49.78	50.22	50.08	50.55	50.59
TiO_2	2.948	2.927	2.950	2.993	2.867	2.950	3.195	2.942	3.222	3.209	3.126	3.114	3.079	3.057	2.949
Al_2O_3	13.09	13.07	13.24	13.46	13.09	13.21	13.28	13.21	12.97	12.95	12.82	12.80	12.82	13.13	13.68
FeO	13.74	13.78	12.91	13.27	13.15	12.34	13.80	13.61	13.58	13.38	13.84	14.18	14.34	13.89	12.84
MnO	0.228	0.226	0.205	0.258	0.208	0.266	0.248	0.195	0.213	0.203	0.205	0.229	0.216	0.191	0.147
MgO	4.36	4.47	4.27	4.39	4.54	3.83	3.98	4.11	3.98	3.77	4.10	4.33	4.18	4.01	3.50
CaO	8.25	8.28	8.59	8.46	8.49	8.15	8.47	8.40	8.53	8.20	7.96	7.98	7.78	7.86	7.85
Na_2O	2.83	2.76	2.71	2.66	2.59	2.92	2.64	2.66	2.71	2.85	2.87	2.90	2.88	2.93	2.94
K_2O	1.25	1.38	1.19	1.47	1.11	1.24	1.10	1.07	1.11	1.25	1.27	1.25	1.25	1.29	1.27
P_2O_5	0.555	0.560	0.555	0.568	0.521	0.560	0.615	0.570	0.576	0.611	0.588	0.598	0.594	0.605	0.578
Total	97.92	98.32	97.29	99.42	96.44	96.40	96.75	96.25	96.41	96.32	96.55	97.61	97.22	97.52	96.34
Element ppm															
Ni	19	21	21	20	20	20	17	14	15	15	15	15	19	15	18
Cr	44	47	48	46	49	46	21	20	20	19	21	19	19	19	19
Sc	38	36	37	37	37	37	37	35	38	38	36	37	36	36	35
V	415	415	423	429	424	418	438	406	443	431	420	425	416	408	386
Ba	567	566	544	562	525	587	512	491	534	554	545	562	562	569	592
Rb	29	33	28	35	27	31	31	24	25	23	30	33	33	33	30
Sr	306	307	314	315	314	308	319	322	316	309	298	298	294	305	326
Zr	182	183	180	183	170	183	184	169	174	181	179	182	181	182	175
Y	38	39	38	38	36	38	38	37	38	39	38	39	38	38	37
Nb	14.1	13.6	13.6	13.5	12.4	13.6	13.7	12.4	12.6	13.7	13.2	13.8	13.1	13.6	13.7
Ga	21	21	22	26	20	21	23	21	22	22	24	22	21	21	21
Cu	25	26	27	26	25	26	24	23	22	24	23	22	24	24	23
Zn	140	139	142	142	138	140	145	138	141	143	144	144	143	140	135
Pb	9	8	9	9	7	8	8	7	8	8	6	8	8	8	7
La	25	24	20	26	23	26	26	25	25	25	27	25	24	27	25
Ce	60	57	56	53	52	55	56	50	51	52	48	52	61	56	57
Th	5	4	4	4	2	3	3	3	4	3	4	3	4	4	3
Nd	32	31	33	29	28	31	33	30	28	31	30	30	36	32	32

Appendix E – Cross-laboratory compatibility – XRF results

There are a large number of published geochemical analyses for the Columbia River Basalts. Many of these analyses were conducted at Washington State University XRF laboratory. To enable comparisons between samples from this study analysed at the OU and those reported in the literature a suite of samples were run in both labs. The results of these analyses are reported below.

Sample No.	DCy3a		DS1		CJC5		FSc7		DCy5		CJC7		FSc8	
Location	N46.35.632 W118.32.895		N45.35.950 W121.08.370		N46.04.148 W116.59.119		N47.01.456 W119.57.487		N46.35.317 W118.32.502		N46.04.148 W116.59.119		N47.01.771 W119.57.825	
Stratigraphy	Silver Falls		Rosalia		Imnaha		Roza		Pomona		Grande Ronde		Ginkgo	
Lab.	OU	WSU	OU	WSU	OU	WSU	OU	WSU	OU	WSU	OU	WSU	OU	WSU
(wt. %)														
SiO_2	50.46	51.56	49.73	50.91	49.27	50.77	50.68	51.71	51.13	51.92	51.78	52.59	50.17	51.43
TiO_2	3.00	3.13	3.27	3.39	2.08	2.19	3.32	3.45	1.68	1.73	2.74	2.83	2.93	3.05
Al_2O_3	13.13	13.14	12.42	12.47	16.77	17.01	14.62	14.60	14.55	14.65	13.33	13.36	13.37	13.44
Fe_2O_3	15.77	14.56	16.91	15.42	11.47	11.07	13.40	12.31	11.84	10.80	14.99	13.73	15.80	14.62
MnO	0.24	0.25	0.24	0.25	0.14	0.14	0.21	0.21	0.18	0.18	0.22	0.23	0.23	0.24
MgO	4.23	4.33	3.94	4.03	5.27	5.36	3.34	3.40	6.63	6.68	4.09	4.15	4.06	4.12
CaO	8.06	8.33	8.11	8.41	9.45	9.86	9.11	9.38	10.51	10.76	7.98	8.15	8.02	8.33
Na_2O	2.91	2.95	2.62	2.68	2.82	2.83	2.88	2.94	2.36	2.37	3.24	3.30	2.89	2.95
K_2O	1.19	1.22	1.52	1.53	0.47	0.50	1.26	1.26	0.66	0.68	1.17	1.18	1.16	1.18
P_2O_5	0.52	0.54	0.88	0.91	0.26	0.26	0.71	0.74	0.24	0.24	0.46	0.48	0.62	0.64
(ppm)														
Rb	31	28	39	36	7	8	31	33	16	16	23	23	25	26
Sr	305	286	297	283	404	406	338	335	233	229	327	314	334	323
Y	42.6	42.0	59.8	60.0	29.5	32.0	48.9	49.0	31.8	31.0	52.5	52.0	43.2	42
Zr	165	165	270	260	154	157	222	211	147	143	253	242	190	182
Nb	12.4	11.6	21.4	19.5	11.3	10.7	17.4	16.0	13.0	12.3	16.7	16.9	15.1	12.8
Ba	593	566	672	683	345	320	590	598	265	261	562	523	602	576
Pb	8	6	11	7	3	5	8	7	5	4	6	5	10	6
Th	6	3	3	3	3	2	5	4	5	1	2	1	6	3
U	2	-	3	-	0	-	4	-	1	-	2	-	4	-
Sc	36	41	32	38	22	27	40	41	30	38	35	37	33	36
V	338	386	363	395	223	249	505	481	279	288	399	407	379	398
Cr	29	35	12	11	76	82	31	34	92	101	15	18	15	18
Co	34	-	32	-	42	-	33	-	41	-	33	-	34	-
Ni	22	25	14	16	35	38	20	18	46	47	20	23	11	12
Cu	38	31	32	24	65	62	36	30	54	52	87	80	30	19
Zn	123	141	164	167	103	104	162	155	97	96	132	141	136	141
Ga	23	19	24	21	21	23	23	23	18	18	23	22	24	21

There is a good correlation between the analyses at both labs. The diagram below shows the OU laboratory results plotted against the WSU results for all major oxides with the exception of SiO_2. Thus data reported in this thesis can be compared to existing data published in the literature.

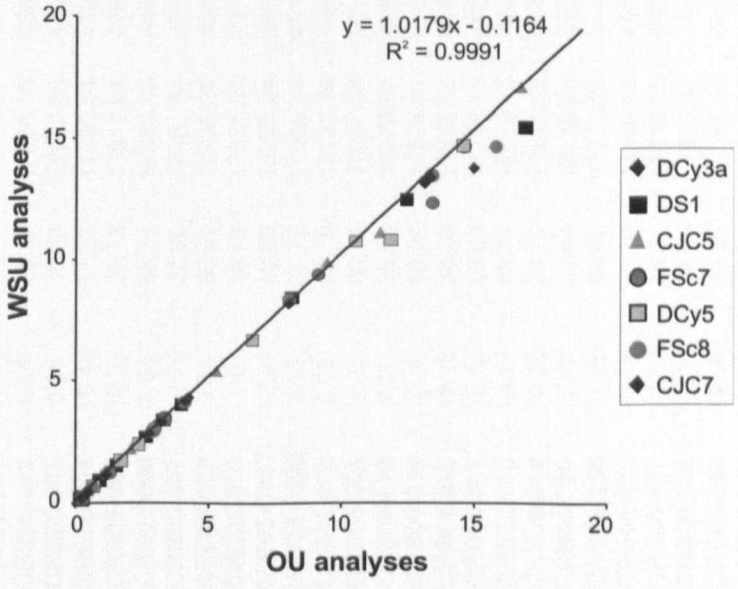

Appendix F – Trace elements determined by ICP-MS

Samples	Li	Sc	Ti	V	Cr	Mn	Co	Ni	Cu	Zn	Ga	Rb	Sr	Y
CRB05-002	8.34	40.35	18296.16	454.96	47.54	1599.99	37.75	13.99	29.37	150.42	22.46	32.16	349.05	47.00
CRB05-003	8.35	39.68	17930.56	448.12	48.01	1561.43	40.89	19.10	29.79	151.42	22.52	31.30	359.90	46.14
CRB05-004	10.42	37.93	17393.84	439.07	47.27	1709.11	39.59	17.52	26.74	144.38	21.41	31.56	329.03	44.15
CRB05-005	10.33	39.12	17860.82	449.69	47.60	1755.56	40.06	18.13	30.17	149.64	22.08	34.66	328.41	45.12
CRB05-006	9.58	38.74	17556.46	442.03	46.84	1745.25	39.57	16.67	27.81	146.82	22.00	35.60	326.59	43.87
CRB05-007	12.78	37.96	17461.64	434.29	43.21	1585.10	39.56	17.01	30.95	148.50	21.91	34.53	312.97	45.53
CRB05-008	9.84	38.81	17736.24	443.47	46.74	1716.88	40.09	18.03	29.79	147.14	22.09	31.65	330.25	44.85
CRB05-010	11.07	38.69	17631.26	438.22	46.08	1603.82	40.28	18.03	30.05	147.24	21.98	28.58	321.78	44.42
CRB05-009T	12.41	40.23	18273.34	460.83	49.25	1246.23	41.72	20.02	30.94	153.45	23.11	36.22	343.35	46.08
CRB05-009B	9.19	37.72	17395.76	433.54	46.20	3138.97	35.71	15.76	27.56	142.36	21.75	25.29	330.85	44.44
CRB06-003	8.78	38.75	17752.78	446.86	50.29	1525.65	37.08	17.54	29.23	145.49	22.28	28.40	326.08	45.29
CRB06-004	10.88	39.51	17901.94	451.29	53.13	1628.97	41.60	22.44	29.91	153.16	22.36	35.22	339.40	45.75
CRB06-012	9.29	38.23	17378.97	446.28	52.72	1878.67	40.85	20.57	28.81	144.15	21.70	33.51	324.31	42.89
CRB06-014	10.26	38.05	17574.81	446.90	49.81	1793.71	40.11	18.94	29.05	144.76	21.65	28.73	320.40	42.83
CRB06-016	13.12	38.23	17658.45	448.75	52.07	1950.14	40.73	20.92	30.43	147.62	22.22	34.75	320.40	43.78
CRB06-017	12.12	39.04	17713.16	448.25	51.10	1891.46	42.20	20.60	29.35	149.35	22.35	37.49	329.04	44.91
CRB06-018	14.17	38.34	17519.15	444.23	49.89	1824.08	40.69	19.18	29.47	148.00	21.99	34.89	318.18	43.84
CRB06-019	10.06	39.72	17988.95	454.20	60.87	2333.29	42.01	25.59	31.15	152.04	22.83	37.61	336.60	46.65
CRB06-229	12.97	39.44	18116.99	460.94	54.24	1380.95	47.33	30.26	31.00	154.41	23.04	40.86	356.96	46.60
CRB06-234	11.85	38.47	17519.26	444.37	52.11	1668.59	40.26	21.11	29.22	147.65	22.09	32.03	325.09	44.13
CRB06-235	10.73	38.16	17409.28	435.65	54.81	1966.68	40.49	22.28	30.01	150.03	22.32	35.24	326.34	45.53
CRB06-237	11.87	38.81	17446.55	443.75	57.28	1962.20	41.76	22.79	29.97	149.01	22.24	34.13	328.70	45.05
CRB06-239	13.34	38.46	17610.44	441.64	58.10	1990.51	40.70	22.77	30.00	156.01	22.49	35.32	328.25	45.44
CRB06-242	12.08	38.16	17564.92	440.19	56.60	1937.78	40.39	22.87	29.85	147.97	22.25	34.86	328.06	45.34
CRB06-243	11.13	38.58	17691.84	446.42	60.18	1952.58	40.80	23.63	30.06	148.57	22.33	34.23	331.30	45.70
CRB06-245	9.99	38.41	17555.79	436.46	49.58	1796.76	39.28	19.72	29.54	147.90	22.20	37.97	332.35	45.72

Samples	Zr	Nb	Mo	Sn	Sb	Cs	Ba	Hf	Ta	Pb	Th	U
CRB05-002	208.40	16.39	1.38	2.14	0.10	0.89	583.41	4.94	0.97	6.54	4.49	1.34
CRB05-003	204.15	16.24	1.33	2.12	0.11	0.85	596.41	4.97	0.97	6.54	4.50	1.74
CRB05-004	196.95	15.60	1.46	0.59	0.09	0.78	565.62	4.79	0.94	6.19	4.32	1.25
CRB05-005	202.50	16.06	1.51	2.11	0.10	0.90	561.81	4.82	0.93	6.43	4.36	1.24
CRB05-006	198.45	15.79	1.56	0.75	0.09	0.89	558.71	4.77	0.92	6.40	4.40	1.29
CRB05-007	206.75	16.19	1.45	1.03	0.09	0.49	585.41	4.92	0.96	6.51	4.52	1.29
CRB05-008	202.05	15.94	1.55	0.93	0.09	0.70	573.13	4.79	0.95	6.28	4.43	1.25
CRB05-010	200.35	15.88	1.44	2.01	0.10	0.54	576.02	4.79	0.94	6.26	4.36	1.25
CRB05-009T	207.10	16.35	1.69	0.35	0.09	0.78	596.51	4.90	0.97	6.56	4.52	1.31
CRB05-009B	194.60	15.59	1.37	1.90	0.10	0.68	748.17	4.62	0.91	6.23	4.33	2.32
CRB06-003	198.85	15.74	1.32	1.60	0.09	1.14	494.82	4.82	0.95	6.24	4.37	1.23
CRB06-004	200.20	16.04	1.45	2.06	0.10	1.14	520.10	4.84	0.95	6.38	4.42	1.25
CRB06-012	190.95	15.35	1.50	1.28	0.10	0.89	548.43	4.55	0.89	6.12	4.28	1.26
CRB06-014	192.35	15.39	1.42	0.72	0.09	0.72	558.53	4.63	0.92	5.98	4.18	1.18
CRB06-016	198.35	16.01	1.58	1.94	0.10	0.63	565.57	4.72	0.94	6.07	4.31	1.22
CRB06-017	202.25	16.16	1.52	2.06	0.10	0.96	578.77	4.80	0.95	6.37	4.45	1.26
CRB06-018	196.85	15.81	1.48	1.91	0.09	0.48	573.42	4.71	0.93	6.89	4.35	1.23
CRB06-019	204.40	16.42	1.79	0.80	0.11	1.04	628.01	4.88	0.96	6.55	4.53	1.28
CRB06-229	212.95	17.04	1.83	1.69	0.12	1.14	654.18	5.04	0.99	6.68	4.69	1.42
CRB06-234	200.30	16.02	1.62	1.79	0.10	0.63	576.53	4.82	0.95	6.28	4.40	1.24
CRB06-235	206.15	16.47	1.67	0.80	0.11	0.81	589.94	4.91	0.95	6.55	4.58	1.31
CRB06-237	202.60	16.20	1.57	1.90	0.10	0.94	565.33	4.77	0.93	6.41	4.44	1.26
CRB06-239	205.70	16.45	1.63	2.12	0.11	0.93	578.53	4.87	0.95	6.46	4.51	1.29
CRB06-242	204.25	16.34	1.62	0.77	0.10	0.90	549.37	4.83	0.94	6.40	4.48	1.27
CRB06-243	204.80	16.42	1.68	0.67	0.10	0.86	545.61	4.85	0.96	6.45	4.50	1.28
CRB06-245	207.10	16.52	1.55	1.60	0.11	0.95	564.19	4.88	0.96	6.59	4.59	1.31

Rare earth elements (REE) determined by ICP-MS

REE	La	Ce	Pr	Nd	Sm	Eu	Gd	Tb	Dy	Ho	Er	Yb	Lu	La/Yb
Vantage														
CRB05-002	113.54	95.04	86.85	72.80	54.22	43.61	41.93	37.09	31.69	29.71	28.00	24.63	24.30	4.61
CRB05-003	113.12	94.81	86.93	72.90	53.74	43.27	41.77	36.84	31.50	29.14	27.96	24.18	23.71	4.68
CRB05-004	104.85	87.81	81.40	69.91	51.37	41.46	39.75	35.18	29.80	28.04	26.38	23.14	22.59	4.53
CRB05-005	108.40	90.78	83.81	71.49	52.46	42.36	40.31	36.07	30.51	28.57	27.17	23.64	23.36	4.58
CRB05-006	107.59	89.41	82.25	69.63	52.11	41.56	40.27	35.73	29.92	28.32	26.65	23.44	22.59	4.59
CRB05-007	111.86	93.54	85.03	71.96	53.81	42.54	41.48	36.62	30.92	28.96	27.50	24.07	23.16	4.65
CRB05-008	108.27	90.65	83.17	69.92	52.06	41.88	40.43	35.73	30.28	28.17	26.97	23.36	22.93	4.64
CRB05-009B	106.50	88.61	81.81	69.21	51.52	41.47	39.59	35.12	29.69	27.82	26.44	23.21	22.70	4.59
CRB05-009T	112.36	94.16	86.21	72.43	53.73	43.49	41.42	36.68	31.19	28.99	27.53	23.82	23.28	4.72
CRB05-010	108.69	90.72	82.91	70.09	52.20	41.66	40.29	35.48	30.01	28.08	26.74	23.47	22.70	4.63
Locke Lake														
CRB06-003	113.42	93.62	85.28	71.76	53.44	42.49	41.61	36.68	30.82	29.19	27.81	23.98	23.74	4.73
CRB06-004	110.84	92.45	84.09	71.11	52.81	42.42	40.68	36.20	30.56	28.42	27.19	23.73	23.23	4.67
CRB06-012	104.35	87.42	79.81	67.12	50.09	40.40	38.61	34.46	29.13	27.16	25.79	22.62	22.22	4.61
CRB06-014	104.68	87.72	79.95	67.87	50.79	40.42	39.26	34.54	29.17	27.22	26.04	22.56	22.29	4.64
CRB06-016	107.05	89.66	82.16	69.67	51.64	41.77	39.95	35.35	29.84	27.82	26.45	23.17	22.73	4.62
CRB06-017	111.60	92.82	84.55	71.02	52.58	41.91	40.93	36.12	30.45	28.52	27.11	23.80	23.07	4.69
CRB06-018	108.44	90.52	82.54	69.80	51.72	41.61	39.98	35.37	30.04	28.15	26.65	23.41	22.89	4.63
CRB06-019	113.67	94.65	85.97	73.19	53.98	43.20	41.84	36.98	31.32	29.08	27.88	24.39	24.11	4.66
Frenchman Springs														
CRB06-229	116.29	97.00	87.67	74.49	54.91	44.14	42.54	37.42	31.71	29.71	28.22	24.57	23.98	4.73
CRB06-234	109.45	90.91	82.49	70.20	52.06	41.73	40.21	35.43	30.01	28.04	26.61	23.45	22.89	4.67
CRB06-235	113.80	93.59	85.50	72.36	53.55	42.81	41.57	36.48	30.92	28.90	27.56	24.10	23.64	4.72
CRB06-237	111.10	92.72	84.38	71.15	52.65	42.17	40.90	35.73	30.56	28.77	27.06	23.89	23.37	4.65
CRB06-239	112.53	93.41	84.68	72.16	53.54	42.72	41.25	36.40	30.86	28.94	27.41	24.03	23.46	4.68
CRB06-242	111.81	93.38	84.36	71.53	52.94	42.26	40.91	36.34	30.58	28.66	27.30	23.86	23.55	4.69
CRB06-243	112.49	93.65	84.97	71.88	53.20	42.81	41.33	36.45	30.74	28.99	27.53	24.22	23.77	4.64
CRB06-245	113.16	94.21	85.18	72.16	53.28	42.50	41.36	36.34	30.78	28.83	27.53	24.17	23.67	4.68

Appendix G – Re-Os isotope data for samples from the Deccan Province, India

Sample number	Height above lobe base	[Re] (ppt)	[Os] (ppt)	$^{187}Re/^{188}Os$	$^{187}Os/^{188}Os$	2σ	$^{187}Os/^{188}Os$ initial age corrected to 65 Ma
APMh29.8	29.8	337	57	28.97	-	-	-
APMh28.0	28	343	49	34.98	-	-	-
APMh27.0	27	355	65	26.68	0.1921	0.00023	0.163
APMh25.0	25	388	73	26.10	0.1979	0.00108	0.170
APMh18.0	18	741	77	47.24	0.1861	0.00014	0.135
APMh17.0	17	492	65	37.00	0.1921	0.00023	0.152
APMh14.0	14	511	66	37.95	0.1955	0.00007	0.154
APMh5.0	5	381	46	40.72	0.1981	0.00014	0.154
APMh0.65	0.65	410	65	31.17	0.1960	0.00009	0.162
APMh0.17	0.17	590	66	44.20	0.1922	0.00012	0.144

Appendix H – Sr isotope standards

STD no.	Sample Name	^{88}Sr ave (V)	$^{87}Sr/^{86}Sr$	1σ	2σ	^{84}Sr ave (V)	$^{84}Sr/^{86}Sr$	1σ	2σ
1	NBS987	7.34000	0.710246	2.52E-06	0.00000504	0.05000	0.056489	1.09E-06	2.18E-06
2	NBS987	8.16000	0.710247	2.18E-06	4.35601E-06	0.05000	0.056491	9.59E-07	1.92E-06
3	NBS987	8.14000	0.7102546	2.31E-06	4.61729E-06	0.05600	0.05649	1.04E-06	2.09E-06
4	NBS987	7.07514	0.7102497	2.4E-06	4.79539E-06	0.04823	0.056492	1.09E-06	2.18E-06
5	NBS987	7.01084	0.7102507	2.36E-06	4.7254E-06	0.04779	0.056493	1.28E-06	2.56E-06
6	NBS987	6.75132	0.7102493	2.59E-06	5.18391E-06	0.04602	0.05649	1.24E-06	2.48E-06
7	NBS987	3.50661	0.7102652	6.75E-06	1.34946E-05	0.02394	0.056503	4.07E-06	8.14E-06
8	NBS987	4.68205	0.7102572	5.05E-06	1.01048E-05	0.03171	0.056498	3.22E-06	6.44E-06
9	NBS987	4.66066	0.7102591	6.08E-06	1.21628E-05	0.03152	0.0565	3.41E-06	6.81E-06
10	NBS987	4.86312	0.710264	5.51E-06	1.10102E-05	0.03281	0.0565	3.55E-06	7.11E-06
11	NBS987	2.59803	0.7102615	8.15E-06	1.63021E-05	0.01753	0.056498	6.21E-06	1.24E-05
12	NBS987	4.61140	0.7102562	6.06E-06	1.21152E-05	0.03132	0.056494	3.83E-06	7.66E-06
13	NBS987	3.85224	0.7102684	5.84E-06	1.16728E-05	0.02631	0.056499	4.05E-06	8.09E-06
14	NBS987	4.90097	0.7102614	5.47E-06	1.09319E-05	0.03329	0.0565	3.1E-06	6.19E-06
15	NBS987	4.29343	0.7102594	5.6E-06	1.1208E-05	0.02903	0.056494	5.88E-06	1.18E-05
16	NBS987	3.81299	0.7102515	6.75E-06	1.35077E-05	0.02579	0.0565	5.01E-06	1E-05
17	NBS987	4.79043	0.7102641	6.08E-06	1.21681E-05	0.03245	0.056494	3.9E-06	7.8E-06
18	NBS987	3.85443	0.710266	5.61E-06	1.12219E-05	0.02610	0.056488	4.01E-06	8.02E-06
19	NBS987	3.25733	0.7102734	6.73E-06	1.34689E-05	0.02214	0.056502	5.21E-06	1.04E-05
20	NBS987	3.41114	0.7102676	7.49E-06	1.49742E-05	0.02321	0.056487	4.37E-06	8.74E-06
21	NBS987	5.45455	0.7102666	5.6E-06	1.11927E-05	0.03706	0.056494	3.58E-06	7.16E-06
22	NBS987	4.11882	0.7102679	5.36E-06	1.07213E-05	0.02789	0.056505	3.44E-06	6.87E-06
23	NBS987	3.03355	0.7102451	7.27E-06	1.45347E-05	0.02060	0.056501	5.11E-06	1.02E-05
24	NBS987	3.60803	0.7102688	6.88E-06	1.37519E-05	0.02409	0.056511	6.12E-06	1.22E-05
25	NBS987	3.40256	0.7102639	6.93E-06	1.38596E-05	0.02322	0.056508	4.6E-06	9.2E-06
26	NBS987	3.94581	0.7102634	6.51E-06	1.30271E-05	0.02654	0.056504	4.43E-06	8.85E-06

View down the Palouse River canyon at the end of fieldwork